Thèse préparée
à L'UNIVERSITÉ de PARIS
École doctorale STEP'UP - ED N°560
IPGP - Tectonique et mécanique de la lithosphère
et à L'UNIVERSITÉ de Granada
Departamento de Mineralogía y Petrología

Fluid pulses along the subduction interface: Integrated field and petro-geochemical approaches

Par

Jesús Muñoz Montecinos

Présentée et soutenue publiquement
22 Novembre 2021

Thèse de doctorat de Sciences de la Terre et de l'environnement
Programa de Doctorado en Ciencias de la Tierra

Dirigée par : ***Samuel Angiboust***
Antonio García Casco

Devant un jury composé de:

Editor: Universidad de Granada. Tesis Doctorales
Autor: Jesús Muñoz Montecinos
ISBN: 978-84-1117-150-2
URI: http://hdl.handle.net/10481/71759

Résumé

La relation entre la pression de fluide et les séismes lents et réguliers dans les zones de subduction est essentielle à la compréhension de leurs propriétés mécaniques, puisque les fluides contrôlent la rhéologie, et donc l'occurrence de ces phénomènes sismologiques particuliers. Cependant, les mécanismes à l'origine des glissements lents ne sont que très imparfaitement compris d'un point de vue de l'enregistrement géologique. Cette thèse apporte de nouvelles connaissances sur ce sujet en étudiant des complexes métamorphiques de haute pression formés par roches représentatives des régions où ces séismes se produisent. La première localité étudiée est un fragment du paléo-prisme d'accrétion du centre du Chili. Ce terrain de haute pression (400°C et 0,8GPa) est composé d'une association lithologique cohérente de schistes verts et bleus. Le second terrain étudié, le complexe de Seghin (suture de Zagros) dans le faciès schiste bleu à lawsonite (480°C-1.8GPa, Crétacé supérieur), est un paléochenal de subduction composé de blocs mafiques dans une matrice serpentinitique.

Les observations de terrain, les mesures structurales et les données pétro–géochimiques sur les veines et les roches hôtes révèlent que les premières veines ont été formées par des réactions prograde de déshydratation de minéraux de basse pression. Ces veines, ainsi que d'autres formées plus tard, ont évolué et ont été remplies de minéraux de haute pression. Des événements d'hydro-fracturation, caractérisés par la précipitation de carbonates, recoupent toutes les structures précédentes dans des conditions proches du pic métamorphique. Les analyses pétro-géochimiques suggèrent différentes sources de fluides, la plupart pouvant être associées à une source profonde proche de la transition schiste bleu-eclogite. Ainsi, il est suggéré qu'un mélange de fluides chenalisés et poreux soit le mécanisme d'écoulement dominant le long de l'interface de subduction. On note que les lithologies mafiques présentent des veines de lawsonite bréchique contenues dans une matrice (ultra) cataclastique. La caractérisation du système veine-matrice révèle que l'écoulement fragile et l'écoulement par pression-dissolution sont les principaux mécanismes de déformation dans les faciès schistes bleus. Ainsi, un scénario est établi dans lequel des «pulses» de fluides externes affaiblissent la zone de cisaillement et déclenchent un glissement lent et des séismes de basse fréquence. Une étude complémentaire décrit une première occurrence de roches liées à des failles sismiques dans les faciès de schistes bleus, y compris des brèches et des (ultra-) cataclasites. Dans les niveaux cataclastiques, la présence de minéraux de haute pression (20-35 km de profondeur) indique des conditions représentatives de la zone sismogène. Les relations de cisaillement entre les ultracataclasites, les brèches et les veines montrent que les processus de glissement sismique et d'hydrofracturation sont contemporains. Les modèles mécaniques confirment que ces structures ne peuvent s'être formées que dans un régime d'instabilité critique à des pressions de fluides quasi-lithostatique, tel documenté dans les subductions actives. Enfin, un modèle à grande échelle est proposé, dans lequel les fluides expulsés près de la transition schiste bleu-éclogite sont capables de circuler le long de l'interface de subduction en produisant une hydrofracturation trémorgène, des veines bréchiques (associées à un cisaillement lent) et des ultracataclasites, marqueurs de probables évènements sismiques réguliers et de basse fréquence.

Resumen

Entender la relación entre la presión de fluidos y los terremotos lentos y regulares en la zona de subducción es clave para determinar sus propiedades mecánicas, ya que los fluidos controlan su reología, y, por tanto, la ocurrencia de dichos fenómenos sismológicos. Sin embargo, estos efectos aún no han sido validados desde una perspectiva geológica. Esta tesis aporta nuevo conocimiento sobre esta temática al investigar complejos metamórficos de alta presión que exponen rocas representativas de las regiones donde estos terremotos ocurren. La primera localidad estudiada es un fragmento del paleo-prisma de acreción de Chile central. Este terreno de alta presión (400°C y 0.8GPa) está compuesto por una asociación litológica coherente de esquistos verdes y azules. El segundo terreno estudiado, el complejo de Seghin (sutura de Zagros) en facies de lawsonita-esquisto azul (480°C-1.8GPa, Cretácico tardío), es un paleocanal de subducción compuesto por bloques máficos en matriz serpentinitica.

Observaciones de campo, mediciones estructurales y datos petro-geoquímicos de las vetas y las rocas de caja revelan que las vetas tempranas se formaron mediante reacciones progradas de minerales de baja presión. Estas vetas, junto con otras formadas posteriormente, evolucionaron y fueron rellenadas con minerales de alta presión. Eventos de hidrofracturamiento, caracterizados por la precipitación de carbonatos, se sobrepusieron a todas las estructuras previas en condiciones cercanas al pico metamórfico. Los análisis petro-geoquímicos sugieren diferentes fuentes de fluidos, en su mayoría, posiblemente asociados a una fuente profunda cercana a la transición esquisto azul-eclogita. Así, se sugiere que una mezcla entre fluidos canalizados y porosos, fue el mecanismo de flujo dominante a lo largo de la interfaz de subducción. Se destaca que las litologías máficas presentan vetas de lawsonita brechificadas y contenidas en una matriz (ultra) cataclastica. Caracterización del sistema veta-matriz revela que el flujo frágil y el flujo por presión-disolución fueron los principales mecanismos de deformación en facies de esquisto azul. De este modo, se establece un escenario en el que «pulsos» de fluidos externos acompañaron y precedieron al flujo frágil en la zona de terremotos lentos, debilitando la zona de cizalle y desencadenando un deslizamiento lento y terremotos de baja frecuencia. Investigaciones posteriores dan cuentan de un primer registro de rocas relacionadas a fallas sísmicas en facies de esquisto azul, incluyendo brechas y (ultra) cataclasitas. En los materiales cataclásticos, la presencia de minerales de alta presión (20-35km de profundidad) indica condiciones representativas de la zona sismogénica. Las relaciones de corte entre las ultracataclasitas, las brechas y las vetas muestran que los procesos de fallamiento recurrente e hidrofracturamiento fueron contemporáneos. Los modelos mecánicos confirman que estas estructuras sólo pueden haberse formado en un régimen críticamente inestable a presiones de fluidos cercanas a las litostáticas, como se observa en márgenes activos. Por último, se propone un modelo a gran escala, en el que los fluidos expulsados cerca de la transición esquisto azul-eclogita son capaces de circular a lo largo de la interfaz de subducción produciendo hidrofracturación tremorogénica, vetas brechificadas (asociadas a cizallamiento lento) y ultracataclasitas, representando así posibles marcadores de señales sísmicas regulares y de baja frecuencia.

Abstract

Understanding the feedbacks between fluid overpressures and subduction slow and regular earthquake-related processes is critical to constrain the physical nature of the megathrust. Recently, the influence of fluids as weakening agents has been proven as a major factor controlling the rheology of the megathrust and thus the occurrence of a variety of earthquakes. Yet, a significant scientific gap in validating this knowledge from a geological perspective exists. This thesis provides new insights into this issue by investigating blueschist-facies metamorphic complexes that expose rocks representative of the slow and regular earthquakes regions. The first chosen locality is a fragment of the late Paleozoic accretionary wedge exposed in central Chile. This high pressure (400 °C and 0.8 GPa) terrane is composed by a coherent greenschist-blueschist lithological association. The second studied terrane is a late Cretaceous lawsonite-blueschist-facies (480 °C-1.8 GPa) segment of the Zagros suture: the Seghin complex, a well-preserved blueschist block-in-serpentinite matrix paleo-subduction channel.

We herein combine extensive field observations, structural measurements and petro-geochemical data on vein and host rock materials. In both studied localities, early veins formed after prograde breakdown of low-pressure minerals. These veins, along with newly formed ones, have evolved and re-filled by further high-pressure minerals. Subsequent massive carbonate-bearing hydrofracturing events overprinted all previous structures at near-peak conditions. Petro-geochemical analyses suggest different fluid sources for the veining stages, in most cases, likely associated with a deep-seated source near the blueschist-to-eclogite transition. In addition, we concluded that a mixture of channelized and porous flow was the dominant fluid flow mechanism along the subduction interface. Interestingly, mafic lithologies exhibit brecciated lawsonite veins hosted in a variably foliated (ultra) cataclastic host. Characterization of the host-vein system reveals that brittle creep and pressure solution processes were the dominant deformation mechanisms at blueschist-facies depths. Thus, supporting a scenario where external fluids accompanied and predated brittle creep in the slow earthquakes window. Consequently, episodic injection of fluid «pulses» weakened the megathrust and triggered subsequent slow slip and low frequency earthquakes. Further investigations led to a first report of blueschist-facies seismic fault-related rocks including breccias and foliated (ultra) cataclasites. In the cataclastic materials, the occurrence of newly-formed lower lawsonite-blueschist-facies (20-35 km depth) minerals point to conditions representative of the seismogenic zone. Crosscutting relationships among fluidized ultracataclasites, breccias and veins suggest that episodic faulting and hydrofracturing were contemporaneous processes. Mechanical modelling confirms that these fault-related structures can only have formed in a critically unstable regime at near lithostatic fluid pressure conditions, promoting recurrent seismic faulting as monitored in active margins. Last, we propose a large-scale scenario, where fluids expulsed near the blueschist-to-eclogite transition travelled upwards along the subduction interface producing massive, tremor-genic hydrofracturing, vein breccias (associated with slow slips) and ultracataclasites, representing a potential record of some of the slow and regular earthquakes phenomena.

Acknowledgements

I would like to start by thanking my advisor and friend Samuel Angiboust, who has offered me all his infinite patience, willingness, friendship and wisdom during the last 4 years and more. In fact, even without knowing me before, he agreed to take me on the expedition to Chilean Patagonia. From that moment on, I have felt enormously grateful and inspired by him. In fact, thanks to this experience, I decided to come to France to continue my career, but, this time, studying the Zagros blueschists, on the other side of the world. I hope that our friendship and scientific collaboration will continue for a long time to come, especially in the field. I would also like to thank Thais Hyppolito, who, like Samuel, I had the pleasure to meet on the expedition to Chilean Patagonia. Her support during these years has been fundamental, especially in the most difficult moments with advice and reassuring words. I wish you and Juliette all the best in your new life to come in Lyon.

Thanks to this project and crazy string of events and coincidences, I also had the pleasure and honour of meeting Antonio Garcia Casco, my co-supervisor. I must admit that despite his great hospitality, it was hard for me to understand that, in general, he was not scolding me and that is his way of talking. Despite my episodic stays in Granada, I consider that Antonio has become a great friend and a key piece in my learning process, both scientifically and personally speaking. I hope I can learn much more from him in the future!

During my career in Chile as well as in France and Spain, I have had the pleasure of meeting wonderful colleagues who have contributed to do one's bit in my learning process. I want to thank the professors I have had at the Andrés Bello University, especially Francisco Fuentes, who in spite of his craziness, always trusted me and established the contact so that I could embark on the trip to Diego de Almagro Island with Samuel. I also thank Mauricio Calderón, my former undergraduate supervisor; Francisco Hervé, Herné Etchart, Reynaldo Charrier, Cristobal Ramirez, Pierre-Yves and Jean-Baptiste, who ultimately advised me before my journey to Paris. At the IPGP, I would like to thank Alexandre Fournier and Clément Narteau for their excellent hospitality during my arrival at the institute. To Professor Gaston Godard for his help in some specific topics of crystallography and petrology. To the whole Tectonics department, especially to the PhD students and postdocs: Tara, Tania, Roxane, Matthieu, Armel, Francisco, Solene, and Liqing, with whom I had the pleasure to share to a greater or lesser extent. In Granada, I would like to thank the unconditional support of Aitor Cambeses, with whom I had the pleasure to share a short but fun field mission to Pichilemu. To Olga Cazalla for her help and infinite patience in the LA-ICP-MS. To "chipi" for being part of my "defensa de plan de investigación" tribunal and for showing samples of the Nevado-Filábride. Finally, I would like to thank my colleagues Irene Morales, Fabián VIllares, Júlia Farré and Maria Repczyńska with whom I shared an office and a lot of well-deserved beers after long-lasting work sessions; their friendship and affection were essential during my stays at Granada. ¡Les deseo mucho exito en todo lo que se propongan!

The friendships made at “Cité Universitaire Paris” were a key pillar to get through this process. Throughout my four years living there, I had the pleasure of meeting and enjoying with hundreds of beautiful people. However, Etienne, Hakim, Manuelini, Camilo, Erick and Gloria, were the most important for me, and we still keep in touch and maintain a beautiful friendship. I would also like to give special thanks to Valeria for the good times we have had in the last years and those to come.

My friends in Chile were also fundamental in this process, through moral support, good times, parties, and geological help. Unfortunately, I cannot thank all the beautiful people I met at Universidad Andrés Bello, as this section would extend for dozens of pages, but I would especially like to thank my first group of friends formed by Braulito, Andy, Leandro and Sebix. I would also like to thank Caro and Gustavo, who despite not having seen each other for years, I am sure that the friendship is still intact. In a more advanced stage of my career, I also had the pleasure and honour of meeting Mati Villa and Sandstone, with whom I have shared countless moments, parties, beers and geological discussions; I will always remember those field mission nights dancing, singing and playing guitar around a bonfire ¡ Qué buenos momentos! My childhood friends have also been key in this process. Every time I go to Chile I feel that in spite of time and distance, our friendship remains the same as the last time we saw each other. I wish to the “Diario de unos Borrachos”: Mathiew, Cristobal, el mono, il papiño and shipakyuxp_14 success in their lives.

Finalmente, me gustaría agradecer a mi familia, quienes me han apoyado incondicionalmente y con todas sus fuerzas a lo largo de mi vida y en todas las decisiones y proyectos que he tomado. Se que la distancia ha sido difícil de conllevar, especialmente durante estos momentos de pandemia con tantas incertidumbres e inseguridades, pero al final, estoy seguro de que todo ha sido para mejor. Elvi, Ñaña, Nico y Gustavo, les deseo lo mejor en sus vidas y espero verlos pronto ¡Los amo!

Left = Antonio García Casco; Center = Samuel Angiboust; Right = me

Contents

Table of figures

1. Introduction

1.1 Subduction zones: the most active (and risky) geological environments.

Subduction zones are a manifestation of the internal Earth's dynamic forces and represent the most geologically active environment controlling processes as important as orogenesis, climate and even may represent a locus for the origin of the earliest living organisms (Guillot and Hattori, 2013). In general, subduction of a tectonic plate underneath another one may occur in three different configurations (i) ocean-ocean, (ii) oceanic-continent and (iii) continent-continent (or collision zones). Although most of the subduction-related effects on our planet are indistinguishable for the human eyes and lifespan, some of them are of extreme importance, especially in terms of hazard. In particular, places where an oceanic plate subducts beneath the continental margin are the locus of the largest and most catastrophic earthquakes on Earth. The most spectacular example is undoubtedly the Valdivia (Chile; 1960) megathrust earthquake of Mw 9.5; the largest ever recorded. During this cataclysm, the rupture system propagated through more than 1000 km along strike for more than 10 minutes, critically affecting a surface of more than 400.000 km^2 from Chiloe to Talca (two thirds of the metropolitan French territory). The energy liberated by this earthquake represents ~20% of the cumulative seismic moment released by the Earth from 1906 to 2005 (according to the USGS). This event was followed by the eruption of the Puyehue volcano and a tsunami that reached Hawaii and Japan shorelines. Thus, an extreme effort is needed to understand the physics behind megathrust earthquakes and maybe, in the future, be able to forecast the occurrence of such complex phenomena.

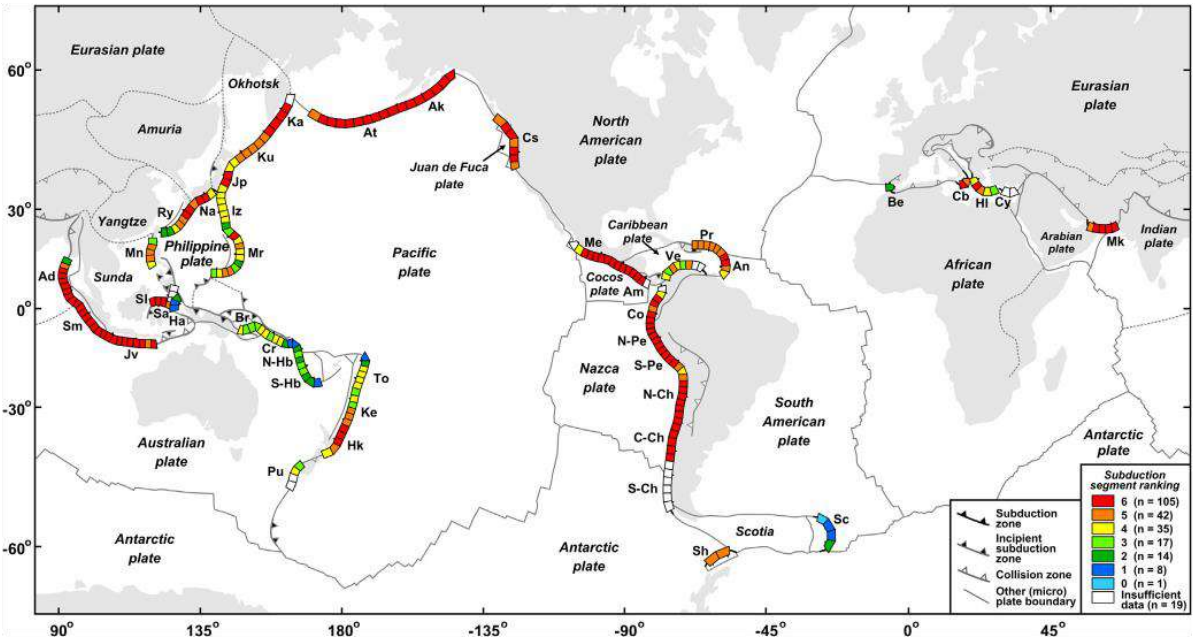

Figure 1.1.Distribution of present-day and ancient subduction settings worldwide. The color code represents the potential risk of generating a mega earthquake (Mw>8.5). Note that ancient suture zones are depicted as collision zones (after Schellart and Rawlinson, 2013).

The present state of knowledge on megathrust earthquakes has been mostly gained through indirect observations such as teleseismic waves (or receiver functions) and tomographic models, geodetic measurements using novel inSar and GPS instrumentations, sedimentary records and historic anthropologic vestiges. However, **direct observations are up to date instrumentally limited and further approaches are needed**. In the last decades, geologists realized about **the importance of studying the rock record to understand some aspects of earthquakes**, opening a new perspective towards a comprehensive view of fossilized in situ structures. These investigations have shown that the most widely accepted marker of an ancient earthquake are pseudotachylytes (Sibson, 1975); a rock formed by solidified/crystallized frictional melts (or shock melting). It is just in the last 30 years that such features have been recognized in exhumed rocks thought to represent the deep roots of ancient subduction environments (e.g., Austrheim and Boundy, 1994), opening a new route to study subduction earthquake-related processes that has considerably evolved nowadays (e.g., Rowe and Griffith, 2015).

1.2 Earthquakes and earthquakes

The complexities of subduction earthquakes are evident when looking at the heterogeneities among different tectonic settings (***Figure 1.1***). Parameters such as temperature, age, velocity, composition and geometry may all have an effect in controlling the magnitudes and velocities at which an earthquake slip (***Figure 1.2***). In a broad sense, all these parameters can be seen in the context of mechanical coupling, which eventually controls the magnitude, and therefore the hazard of an earthquake setting (Scholz and Campos, 2012). In a human lifespan (or several), the mechanical coupling corresponds to how much of the subducting plate convergence is transferred and accommodated in the hanging wall in the form of elastic strain. Nowadays, mechanical coupling is modelled and measured using geodetic GPS-based data acquired in forearc regions (e.g., Moreno et al., 2014; Jara et al., 2017). Thus, a fully coupled region will theoretically have a coupling factor of 1 (all the displacement is transferred to the hanging wall) while a decoupled margin will not accommodate stress between the subducting and the overriding plates (coupling factor of 0). In consequence, strongly coupled regions (or locked zones) are thought to have the potential to generate large megathrust earthquakes (Mw>9) while decoupled regions are thought to behave “aseismically” (Uyeda and Kanamori, 1978; Cloos and Shreve, 1996) with the largest events in the order of 7 Mw with very rare occurrences of earthquakes below 8.5 Mw. Unfortunately, a large part of America and Asia shorelines are located within the Pacific Ring of Fire associated with highly coupled zones and therefore, risky (Chilean-type margins; ***Figures 1.1*** and ***1.2***). While other regions are located near decupled settings such as the Mariana-Izu-Bonin margin (Mariana-type margins) where large megathrust earthquakes are very unlikely (Emry et al., 2011; Scholz and Campos, 2012).

On a different perspective, the geological record of long-term coupling and decoupling states are geologically challenging to illuminate. Some enlightenment can be gained through the study of exhumed metamorphic terranes considering that mechanical coupling is a prerequisite to allow detachment and underplating (c.f., the process of mass transfer from the subducting lithosphere

towards the base of the hanging wall; see Platt, 1986). Thus, a few studies, focusing mostly on high-pressure rocks (now exhumed to the surface), were able to document the long-term bulk mechanical coupling state of subduction interfaces (e.g., Glodny et al., 2005; Angiboust et al., 2015; Zak et al., 2020). However, it is still impossible to determine the coupling state of subduction interfaces at resolutions shorter than few Ma (Menant et al., 2019), being a weak point for the understanding of the seismic cycle during past geological time.

The complexities do not end here. In addition to the fast and destructive megathrust earthquakes described above, a "new" type of earthquake, the so-called slow earthquakes, has been recently discovered giving rise to a large number of studies in the last 20 years (e.g., Behr and Burgmann, 2021 and references therein). In the early 2000's, by means of GPS-based investigations, Dragert et al. (2001) noticed that aseismic slip, occurring in a time window of several years (versus seconds to minutes for fast megathrust earthquakes), was accommodating deformation at the downdip end of the seismogenic zone in Cascadia. Concurrently, Obara (2002) observed non-volcanic tremors at ~30 km depth in southwest Japan as a consequence of the installation of a high sensitivity seismograph network designed to study very small amplitude tremors. Just one year later, Rogers and Dragert (2003) realized that non-volcanic tremors and "aseismic" slips are temporally and spatially correlated. The association of events was defined as the episodic tremor and slip (ETS) phenomenon, which commonly occur in the transition zone between the seismogenic and the deep stably creeping region (***Figure 1.3***), with magnitudes up to c. 7 Mw. **They also concluded that ETS activity may help illuminating how stress loads the subduction megathrust** in the Cascadia margin; such observations have been validated recently by Obara and Kato (2016) who proposed a **possible link between ETS occurrences and megathrust earthquakes.**

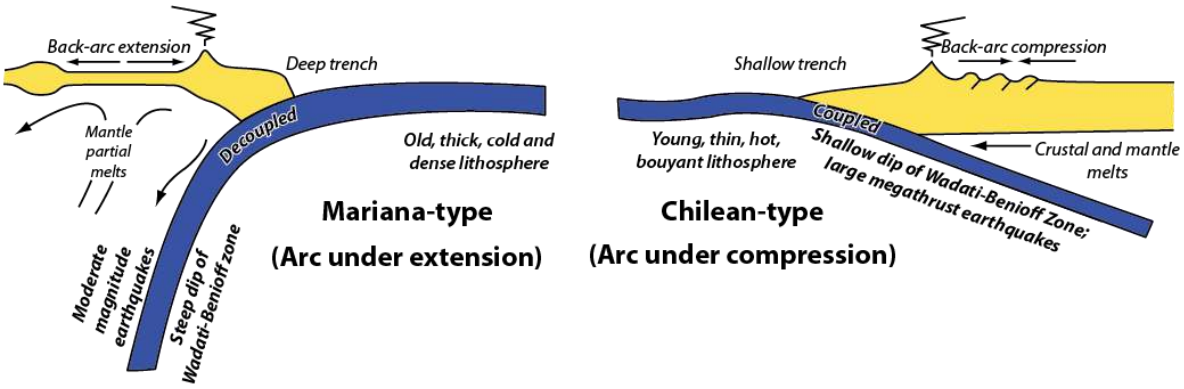

Figure 1.2. Mariana- and Chilean-type subduction endmembers (modified from Uyeda and Kanamori, 1979 and Stern, 2002).

1.3 Illuminating earthquakes through rocks

The discovery of ETS has had a great impact in the understanding of the physical properties of subduction zones, mainly due to a potential connection with large megathrust events and an unknown rheological behaviour of the subducting slab at the downdip end of the seismogenic zone (***Figure 1.3***). In consequence, a large number of geological studies aim at characterizing the processes occurring at depths (Kirkpatrick et al., 2021 and references therein). The best candidates to image earthquake-related processes occurring at depths correspond to exhumed high pressure-low (HP-LT) temperature metamorphic rocks. Since the study of subduction earthquake-related features in the rock record is a novel approach, there are no widely accepted structures nor fabrics that can be directly linked with any type of seismic event (except for pseudotachylytes; Kirckpatrick et al., 2021). In the geological record, well-preserved HP-LT localities are extremely scarce, being some of the best examples the Franciscan Complex (California, USA), Wester Alps, Tianshan belt (China), Tavşanlı belt (Turkey), Western Series (Chile) and the Seghin complex (Zagros orogen, Iran).

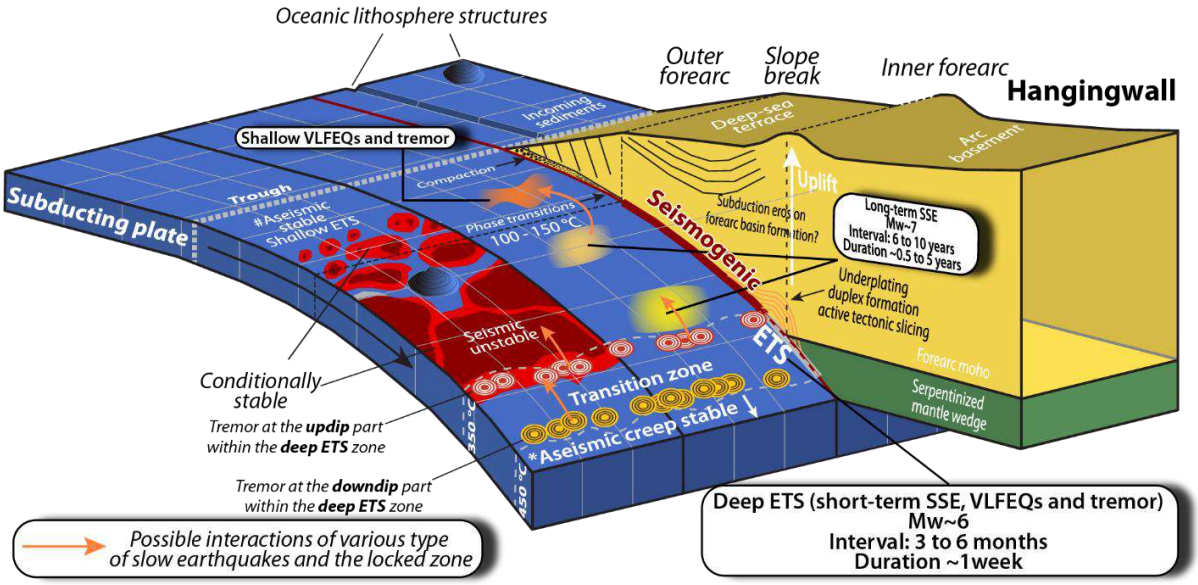

*Figure 1.3. Simplified representation of the frictional and seismic segmentation In subduction zones (modified from Bassett and Watts, 2015). Various earthquakes phenomena are depicted as well as their general properties and interactions (inspired in Obara and Kato, 2016). Note the uplift of the forearc (thick white arrow) as suggested by numerical modelling (inspired in Menant et al., 2019). *aseismic creep stable – although this convention is used by geophysicists to refer to what is downdip the transition (ETS) region, this concept should be dropped since it does not consider intermediate depth seismicity. # aseismic stable – this term is not accurate since tsunamigenic earthquakes can well propagate towards these conditions. SSE – slow slip event; VLFEQs – very low-frequency earthquakes.*

Two main issues must be solved before linking geological observations with earthquake-related processes. On the one hand, subduction rocks record a protracted sequence of prograde burial, peak and exhumation fabrics that occur at different times and at time scales far longer than any type of earthquake-related processes. On the other hand, it is still poorly constrained whether experimental and seismological observations match the large-scale source properties of any earthquake-related

processes with outcrops which in general cannot be imaged for more than a few hundreds of meters. Nevertheless, the present state of knowledge allows characterizing deformation mechanisms, fabrics and structures that are compatible with different types of slip at certain pressure-temperature (PT) conditions, geometries, strain rates, fluid pressures and types of rheological heterogeneities (e.g., Fagereng et al., 2010; Behr et al., 2018; Platt et al., 2018; Tarling et al., 2019). In addition, a few experimental studies and numerical simulations have aimed at reproducing different aspects of natural earthquake-related processes (e.g., Di Toro et al., 2009; Beall et al., 2019; Ioannidi et al., 2021), providing thus an independent perspective on the poorly known ETS region.

1.4 Thesis organization

This thesis – motivated by recent investigations proposing an active control of fluids in the occurrence of slow and fast earthquakes – aims at characterizing the mechanical and chemical role of fluid circulation along the subduction interface, by means of a field-based investigation on high-pressure-low temperature metamorphic terranes and a comparison with present-day geophysical observations. The chosen exhumed terranes correspond to the blueschist-facies Western Series (Central Chile) and the Seghin complex (Zagros orogen, Southeastern Iran). This selection is justified by an exceptional degree of preservation of prograde to peak structures and mineral assemblages, along with well visible vein network structures that allow mapping large-scale fabrics. Thus, the Western Series represent conditions compatible with the base of the seismogenic zone (in the transitional region) while the Seghin complex show structures and P-T conditions compatible with the deep ETS region (probably near the downdip end of the transition zone) and the seismogenic region (see **Chapters 6** and **7**).

Among many other questions, this work will focus on the following ones:

1. **What are the relative P-T conditions of fluid circulation and further veining? What deformation regimes are associated with veining? What are the possible fluid sources and to what extent these fluids may circulate along the subducting interface?**
2. **What evidence of transient deformation patterns can we identify in the geological record that compares to conditions imaged for the slow earthquakes source?**
3. **Can we identify brittle deformation patterns that can be witness of slow or fast slip? If so, how does fluid pressure variations affect or trigger the transition from a steady-state deformation mechanism (e.g., pressure-solution creep) towards a transient one (e.g., brittle creep)?**
4. **Can we establish rock textures/fabrics/structures/features that may be considered as guidelines for further identification of earthquakes in the rock record? Is there any large-scale relationship linking fluids in the overpressurized slow earthquakes region with the shallower unstable seismogenic zone?**

To address these questions, the **second Chapter** offers an updated compilation of the state-of-art information on the slow and fast earthquake phenomenology focusing on their respective geologic record. Thus, the conceptual basis of rheology, earthquakes, fluid sources, deformation mechanisms and geological record will be clarified.

The **third Chapter** introduces the geological and regional context relevant for this study. In the first place, the geology from the Western Series in Central Chile and the subduction dynamics below Gondwanaland in late Paleozoic times. Then, the geology associated with the meta-ophiolites from the Zagros orogen is described focusing on the subduction of the Neo-tethys ocean below the Eurasia continent.

After introducing the geological context, the **fourth Chapter** presents a first approach on the veined sequence of Infiernillo (Western Series) which corresponds to a published article in the journal **Geosphere**. Here, we offer the petrological and geochemical characteristics of host materials as well as the petrology and deformation structures of the vein networks observed in the field and at the microscale. We propose a scenario of vein formation during subduction and fluid-rock interaction processes. The **fifth Chapter** and further investigations focus on the Seghin complex. This **Chapter** is published in the journal **Chemical Geology** and offers a field-based investigation with a strong emphasis on the petrology and geochemistry of the different vein systems. We aim at characterizing different fluid sources and conditions of vein formation and deformation along the subduction history of these rocks. We propose a model of fluid circulation to explain the petro-geochemical characteristics of these veins. Furthermore, a **sixth Chapter** offers preliminary results and corresponds to an article in preparation aiming at characterizing the deformation structures and fabrics observed in sheared and brecciated lawsonite-bearing veins as well as in their host rock. This potential article will be hopefully submitted to a short format journal ("letter"). It is worth noting that **Chapters** fourth, fifth and sixth focus on conditions compatible with the slow earthquake region. In the **seventh Chapter** (published in the journal **Earth and Planetary Science Letters**) we report the first occurrence of upper plate blueschist-facies paleo-earthquakes and characterize the chemistry of fault products. We propose a mechanical model to explain the effects of fluid pressure on controlling transient brittle deformation patterns as well as a large-scale tectonic scenario for fluid circulation. The last **Chapter** aims at integrating the major outcomes of this research into a comprehensive tectonic model comparing the two localities studied here. Finally, I propose further perspectives for future research in subduction-related settings worldwide. Attached to this thesis are two additional papers I participated during my PhD. The **Appendix A** corresponds to which Angiboust et al., 2021 published in the journal **Earth-Science Reviews**, while **Appendix B** is a paper submitted to the **Lithos Journal**.

2. State-of-art on subduction zones earthquake-related processes with a focus on what rocks can tell

2.1 Seismic segmentation along dip

The megathrust is seismically heterogenous and therefore segmented along (and across) dip. Four main regions have been detected based on seismological and geodetical data: (i) the shallow portion extending from near the trench to c.15 km depth, (ii) the seismogenic region where large megathrust earthquakes nucleate (15-35 km depth), (iii) a transition region with an intermediate slip behaviour between unstable stick-slip and creep and (iv) "aseismic" and creeping region at c. 60 km depths and beyond (e.g., Lay et al., 2012; Audet and Kim, 2016; Bürgmann, 2018; ***Figure 1.3***).

The shallow part of an increasingly high number of megathrusts has recently been the subject of detailed imaging and is believed to behave similarly to the deeper transition region, i.e., through transitional frictional behaviour (Ito et al., 2015; Saffer and Wallace, 2015; Tanaka et al., 2019). Studies conclude that in this region, high pore fluid pressures as well as fault zone heterogeneities can be invoked as triggers for slow slip transients (Meneghini and Moore, 2007; Fagereng and Sibson, 2010; Skarbek et al., 2012; Basset et al., 2014; Melgar et al., 2015; e.g., ***Figure 2.1***). These transients are of extreme importance for geological hazards since they may trigger tsunamis or load the underlying seismogenic region (Saffer and Wallace, 2015; Obara and Kato, 2016). Some exhumed examples directly imaging the fault zone décollement and/or megathrust splays are located in the Chrystalls beach complex (New Zealand; Fagereng and Sibson, 2010), the Franciscan complex (California; Meneghini and Moore, 2007) and the Shimanto accretionary complex (Japan; Raimbourg et al., 2014; Phillips et al., 2020).

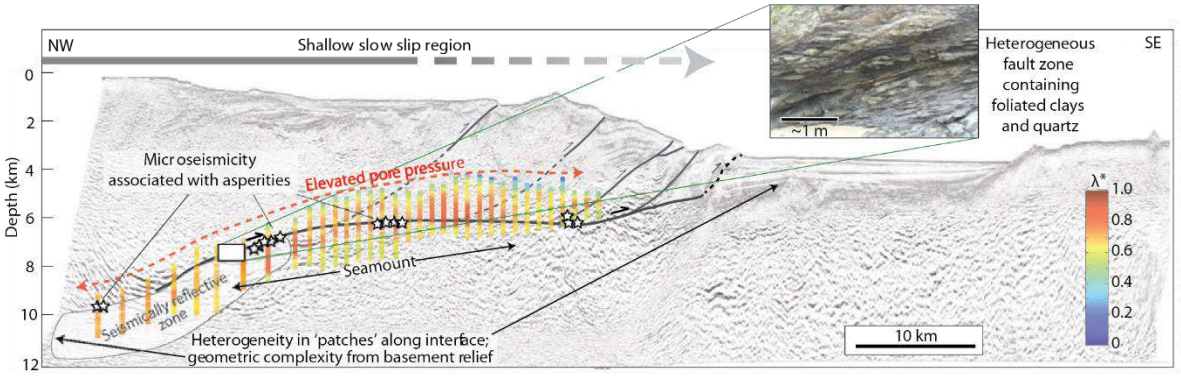

Figure 2.1. Schematic representation of a seismic reflection profile (Hikurangi margin) of the shallow ETS region highlighting fault complexities and lithological heterogeneities, fluid pressure and effective normal stresses variations. The vertical scale is exaggerated for aesthetical reasons (after Saffer and Wallace, 2015).

The seismogenic region is the locus of large megathrust earthquakes and is composed of large asperities or highly coupled patches that break by fast and frictional slip (Kanamori and Brodsky, 2004). It seems that these asperities are larger in Chilean-type rather than in Mariana-type margins, since in the latter events of magnitude above 7 are extremely rare and Mw 9 events have never been

reported there (e.g., Scholz and Campos, 2012). Their study is challenging since they do not occur frequently, with recurrence times in the order of tens to hundreds of years, making it difficult to investigate the complete seismic cycles (e.g., Anderson, 1975; Lay, 2015). Several mechanisms have been proposed to explain the occurrence of regular earthquakes including: transient shear stress highs related to plate convergence acceleration (e.g. Anderson, 1975), shear stress redistribution (e.g. Lin and Stein, 2004; Freed, 2005), pore fluid pressure variations (e.g. Li et al., 2018) and viscoelastic stress redistribution in the mantle (Melnick et al., 2017). Regular earthquakes are evidenced in the rock record by the occurrence of pseudotachylytes (e.g., Rowe et al., 2005; Meneghini et al., 2010; ***Figures 2.2A*** to ***C***). However, recent experimental studies have succeeded in generating pseudotachylytes at slow displacement velocities (i.e., 10^{-7} ms^{-1}), questioning the widely accepted vision of pseudotachylytes as seismic markers (Pec et al., 2012). In addition, other structures such as ultracataclasites (e.g., ***Figures 2.2D*** and ***E***) or silica gels may also be witnesses of ancient earthquakes (e.g., Ujiie et al., 2007; Stünitz et al., 2010; Lin, 2011; Rowe and Griffith, 2015; this study).

At the downdip end of the seismogenic region (or in decoupled patches), the subduction megathrust behaves by a mixture of viscous and frictional slip which seems to characterise the slow earthquake region (e.g., Behr and Platt, 2013; Fagereng et al., 2014; Angiboust et al., 2015; Ujiie et al., 2018; Behr et al., 2018; Tewksbury-Christle et al., 2021). However, the precise deformation mechanisms of the ETS region are still very poorly constrained (see below; Kirckpatrick et al., 2021). On a geophysical perspective, double-couple focal mechanisms and S-wave arrivals suggest that tectonic tremors, from which a great part corresponds to (very) low-frequency earthquakes, are produced by shear slip (Shelly et al., 2006; Bostock et al., 2012). These low- and very low-frequency events correspond to seismic signals that are a part, but not exclusive, of the slow earthquake phenomena; their source properties are described in section 2.4.

Interestingly, the region at which ETS and slow earthquakes occur also coincides with a low velocity (lower values of S-wave velocities with respect to elsewhere) and highly conductive zone at which high Vp/Vs and Poisson's ratio indicate the presence of overpressurized fluids: shear waves do not propagate in fluids or porosity, the latter reaching values up to 4 vol% (e.g., Audet et al., 2009; Peacock et al., 2011; Bostock, 2013; Audet and kim, 2016). It is worth noticing that in some cases, rock seismic anisotropies may lead to a bias capable of explaining the high Vp/Vs ratios (Wang et al., 2012; Pimienta et al., 2018). However, the consistency of these observations along a great number of subduction margins suggest that these ratios are very likely the product of fluid pressure highs (Audet and Kim, 2016). In most of the aforementioned investigations, a fluid-saturated environment is suggested to be intimately associated with the transient occurrence of ETS. In consequence, one should focus on analogues of these first order and transient features to illuminate ETS-related processes from the exhumed geological record.

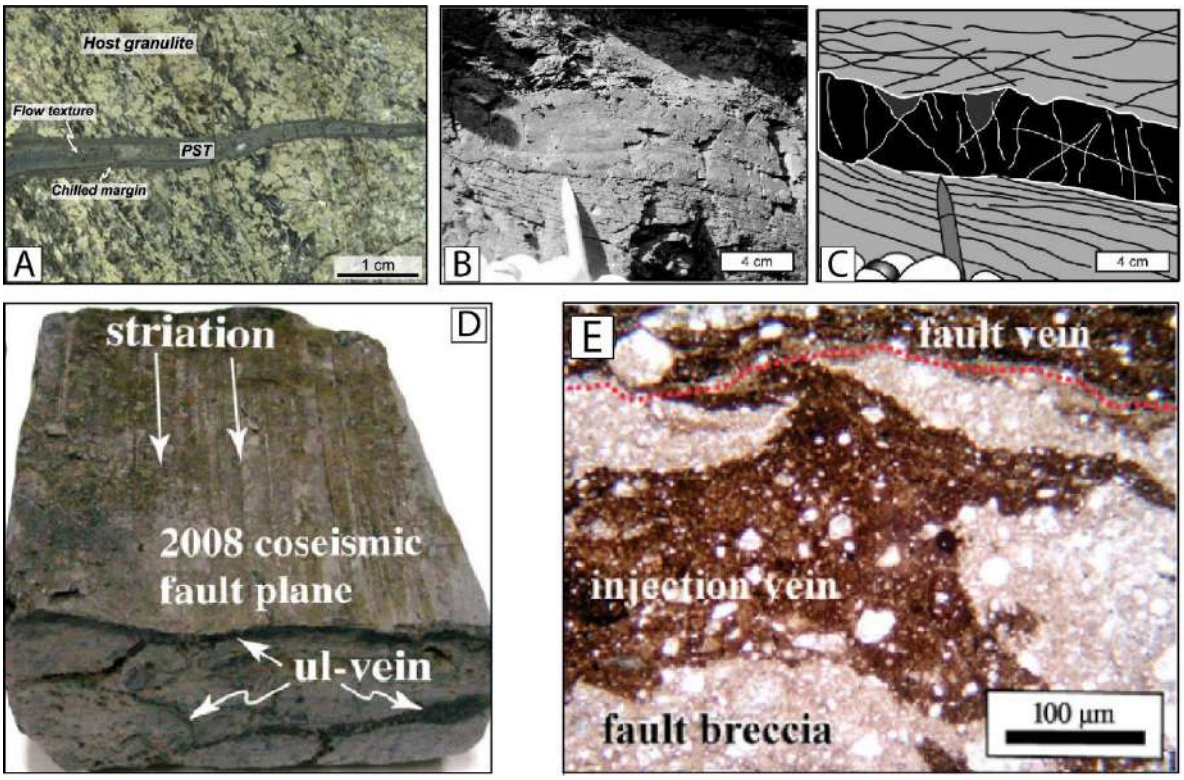

Figure 2.2. Examples from structures attributed to regular earthquakes. A. Pseudotachylyte interpreted to have formed by low magnitude regular earthquakes at depths of 30 km in a subduction environment hosted in a granulite from the Dent Blanche complex (after Menant et al., 2018). B. Massive pseudotachylyte crosscutting argillaceous mélange lithologies in the Kodiak accretionary complex (after Rowe et al., 2005). C. Sketch of panel B. D. Hand specimen showing striations and fluidized ultracataclasites vein networks (ul-vein) extracted from a coseismic fault scarp after the continental Wenchuan Mw 7.9 earthquake in 2008 (China). E. Photomicrograph of the structures shown in panel D (after Lin, 2011).

Furthermore, at depths coinciding with the onset of eclogite-facies (c. > 40-60 km) and beyond, it is believed that a transition towards a stably creeping and aseismic region occurs, culminating thus with seismic activity (e.g., Obara and Kato, 2016). This region is extremely poorly known. However, an aseismic and often purely ductile (see below; Tichelaar and Ruff 1993; Holtkamp and Brudzinski 2010) conception should not be used since evidence of brittle deformation and large-magnitude earthquakes in the form of eclogite-facies extensional veins, cataclasites, breccias and pseudotachylites are being increasingly reported (Austrheim and Andersen, 2004; John and Schenk, 2006; Angiboust et al., 2012; Andersen et al., 2014; Locatelli et al., 2019). Even the serpentinized ultramafic lithologies bear evidence of brittle, possibly seismogenic deformation events (e.g., Margott et al., 2020).

2.2 Rheology of the subduction interface environment

2.2.1 General rheological properties of the subduction interface

As the materials comprising the subducting slab are buried, it is expected that their rheological properties evolve along their journey towards great depths. Indeed, recent investigations in the shallower ETS portion of the Hikurangi margin suggest that the main décollement zone is composed of undercompacted sediments, that experience granular and subordinate pressure-solution ductile flow as dominant deformation mechanisms (e.g., Fagereng, 2011; Plaza-Faverola et al., 2016). These deformation mechanisms are associated with high pore fluid pressure conditions triggered due to pore collapse and fluid expulsion from the sedimentary pile (e.g., Meneghini and Moore, 2007). Experimental investigations on drilled materials from a number of active subduction trenches have found that the main constituents of the shallow ETS regions (clays) show variable slip responses (velocity-strengthening and velocity-weakening) to friction depending on slip rates. Thus, explaining the unstable slip behaviour of the shallowest and weak part of the megathrust hosting ETS and regular earthquakes (Ikari and Kopf, 2017).

As the lithologies forming the subduction interface are progressively buried towards seismogenic depths, compaction lithifies most lithologies and granular flow processes are no longer important (Meneghin and Moore, 2007; Rowe et al., 2011). Instead, the subduction interface will be composed of a mixture of stiffer oceanic materials underlying metasandstones and metamudstones, among other litholgies, whose general fabric range from tectonic melanges to coherent sequences (e.g., Fagereng et al., 2011; Ujiie et al., 2018; Muñoz-Montecinos et al., 2020). At these conditions (i,e., seismogenic depths), the subducting interface may slip at fast (in the order of 1 m/s) or slow (in the order of 10^{-7}-10^{-8} m/s) slip rates, overcoming the background plate subduction rates (10^{-12} m/s; ***Figure 2.3***). In subduction zones, fast slip and rupture may result in frictional heating of the fault surface at geometrically or rheologically (i.e., higher friction coefficients) favourable points resulting in melting of the host or gouge materials (e.g., Rowe et al., 2005; Bjørnerud, 2010). Nevertheless, occurrences of pseudotachylytes formed at seismic slip rates (e.g., ***Figure 2.3***) in subduction environments are rarely reported. One simple explanation is that once formed, pseudotachylytes are so reactive that retrogression or recrystallization during further metamorphism or exhumation erase any evidence (e.g., Fondriest et al., 2020), especially in subduction zones where hydrothermal alteration is abundant. Following this idea, it is also likely that pseutachylytes are not recognized in the rock record due to overprinting, and the need of microscopical techniques to identify such structures will ultimately result in a sampling bias (see Kirkpatrick et al., 2009 for an example in a crustal fault system). Recent studies show that pseudotachylytes and fault gouges (i.e., ultracataclasites) may form in fluid-saturated environments (Magloughlin, 1992; Rowe et al., 2005; Bachmann et al., 2009; Meneghini et al., 2010; Menant et al., 2018; Dobson et al., 2020; Ujiie et al., 2021a), and not only restricted to dry crystalline rocks (Sibson and Toy, 2006). In a recent study, however, it has been suggested that some of the aforementioned pseudotachylyte examples (e.g., Kodiak Island and Shimanto belt, USA and Japan, respectively) may indeed correspond to fluidized ultracataclasites

according to the maturation of carbonaceous materials (Moris-Muttoni et al., submitted). In subduction zones, where overpressurized conditions are inferred, the lack of pseudotachylytes seems to be a rather common scenario with strong mechanical effects to be discussed below.

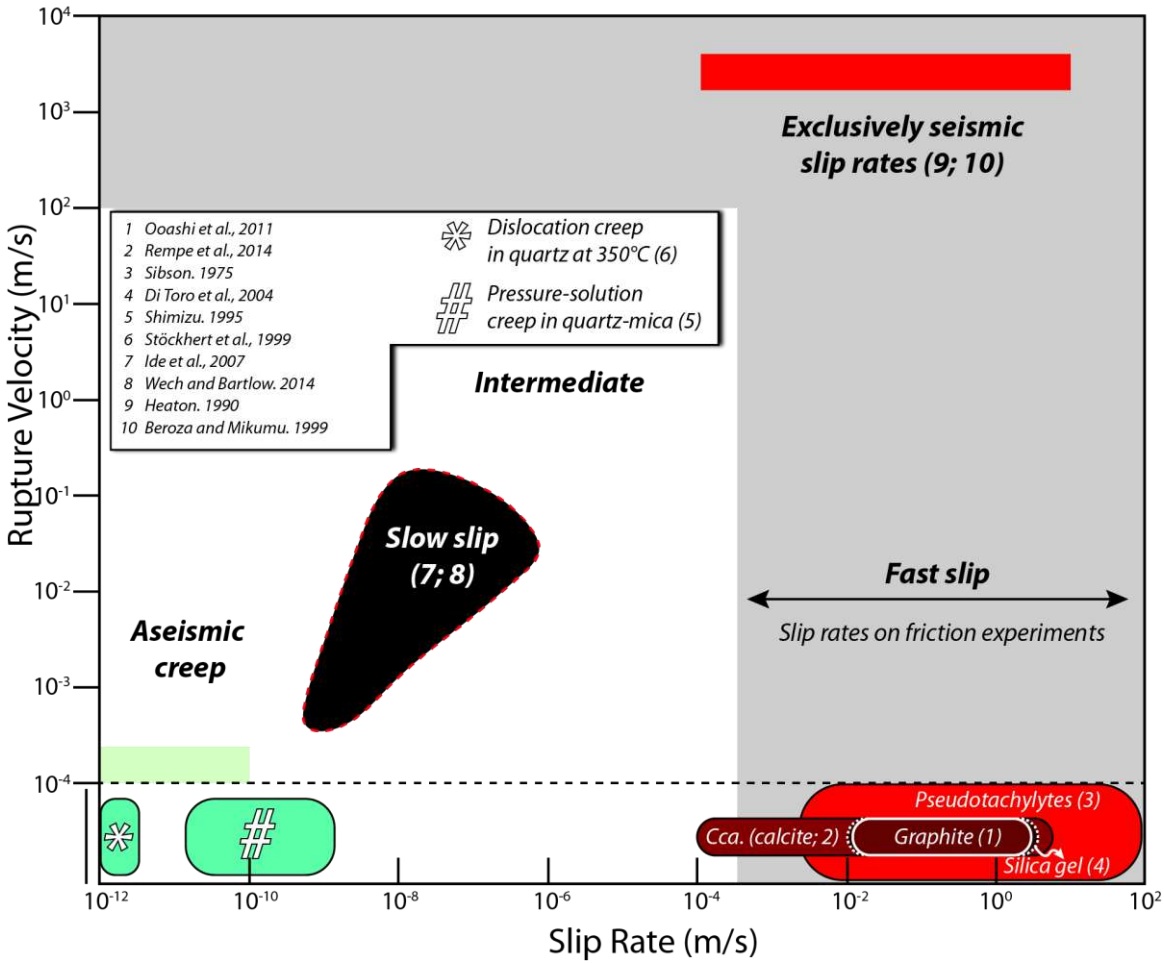

Figure 2.3. Slip rate versus rupture propagation velocity diagram depicting regular earthquakes (fast), slow slips (intermediate) and creep slip rates. Slip rates of deformation mechanisms as well as experimentally reproduced structures are shown for comparison. Modified from Rowe and Griffith (2015).Cca – clast cortex aggregates.

At plate convergence strain rates within the seismogenic zone, deformation seems to be accommodated by a combination of brittle-viscous flow with dissolution-precipitation creep around rigid objects and frictional sliding along foliation planes as dominant deformation mechanisms (e.g., Rutter and Elliott, 1976; Bos and Spiers, 2002; Den Hartog and Spiers, 2014). Physical models predict a transition from velocity-strengthening (stable creep) to velocity-weakening (unstable slip) with increasing slip rates triggering earthquakes (or slow slips), whose magnitude is restricted to the occurrences of barriers (e.g., seamounts and guyots) arresting earthquakes (e.g., Fagereng and Den Hartog, 2016; Bonnet et al., 2019). Thus, subduction zones with smooth topography may host larger megathrust earthquakes than highly rugged ones. This vision is not widely accepted since investigations have suggested that oceanic reliefs may indeed behave as asperities (highly coupled regions) promoting increments in slip rates and further dynamic weakening and rupture of the fault

(Bilek et al., 2003; Yang et al., 2012). In addition, the occurrence of abundant subducted sediments has been also proposed as a factor controlling giant earthquake nucleation. In this case, sediments are seen as pore fluid sources or smooth layers of low friction coefficients that may weaken the megathrust facilitating seismic slip (e.g., Ruff, 1989; Heuret et al., 2012; Li et al., 2018; Behr and Becker, 2018; Muldashev and Sobolev, 2020) or controlling the long-term stress transfer towards the upper plate (Oncken et al., 2006). Interestingly, there appears to be complex feedback between the subduction of trench sediments and oceanic reliefs, whereby the latter may favour sediments inflow into the subduction channel towards seismogenic depths and beyond (e.g., Lallemand et al., 1994; Noda et al., 2020).

2.2.2 Natural fabrics from exhumed metamorphic terranes

It has been classically believed that the seismogenic zone terminates at the onset of crystal plasticity in quartz at c. 350°C or whenever the materials forming the subduction channel starts to flow rather than unstably slip (Hirth et al., 2001; Hirauchi et al., 2010; Peacock et al., 2011; Behr and Platt, 2014; Lusk and Platt, 2020; the "aseismic-seismic transition zone"). For example, Platt et al. (2018) reported quartz fabrics in the Pelona Schists and the Franciscan Complex (California) indicating that pressure-solution and minor dislocation creep processes may accommodate plate boundary strain rates within a 1 km-wide shear zone. The authors also observed abundant extensional structures interpreted as transient bursts of brittle cracking under high pore fluid pressure conditions. Behr and Platt (2013) noticed that pressure-solution creep was the dominant prograde deformation mechanism in a HP-LT exhumed terrane (Nevado Filabride, Betic Cordillera, Spain; see also Platt et al., 2014). It was not until the temperatures exceeded c. 560°C that dislocation creep began to become important, as a result of prograde devolatilization and recrystallization, ultimately increasing pore fluid pressure and a grain size, both factors potentially promoting crystal plasticity (Holyoke and Kronenberg, 2013). More relevant for this study, Wassmann and Stöckhert (2012) studied deformation mechanisms of jadeite-bearing blueschists constituting the matrix of the Franciscan mélange at Angel Island (San Francisco Bay). The authors found that pressure-solution creep was the dominant deformation mechanism accommodating the bulk plate boundary convergence with dislocation creep restricted within quartz aggregates or veins. In agreement with previous investigations, the authors also found that brittle features and vein formation occurred at high pore fluid pressure conditions. The aforementioned observations demonstrate that, in general, the transition zone is (i) dominated by pressure-solution creep with dislocation creep occurring only locally, e.g., within monomineralic bands like veins or layers, (ii) weak, with stresses too low to produce important crystal-plastic creep and (iii) transient in deformation patterns, as evidenced by the episodic nature of brittle deformation associated with high pore fluid pressure conditions (e.g., Bachmann et al., 2009; Wassmann and Stöckhert, 2013; Angiboust et al., 2015; Platt et al., 2018; Kotowski and Behr, 2019; Behr and Bürgmann, 2021).

2.2.3 Rheological controls of minerals

Many microtextural investigations focus on metasedimentary materials. However, in a large number of subduction margins, the sedimentary supply to the trench is scarce (e.g., Northern Chile; Von Huene and Ranero, 2003). A similar scenario occurs in Chilean-type margins, where the subduction channel becomes thinner at depth (e.g., Cloos and Shreve, 1996) inhibiting subduction of sediments to greater depths (e.g., blueschist-facies conditions and beyond). In this context, the megathrust shear zone bulk rheology should be controlled by the mafic oceanic crust making the study of deformation mechanisms of mafic materials relevant. As viscous deformation mechanisms are activated towards depth, a transition from dominantly frictional to viscous creep occurs (Phillips et al., 2020). Depending on the subduction thermal gradient, the mafic oceanic crust in the ETS region will be dominated by lawsonite-blueschists or epidote-blueschists, representing a cold and an intermediate end member, respectively, whereas amphibolite-facies lithologies are expected in a hot scenario (e.g., Evans, 1990; Garcia-Casco et al., 2008; Peacock, 2011; Tsujimori and Ernst, 2014; Angiboust et al., 2017). In this regard, clinoamphibole (e.g., actinolite, glaucophane and hornblende) are key minerals in controlling the rheology of the oceanic and lower crust (e.g., Mainprice and Nicolas, 1989; Ko and Jung, 2015).

Natural microstructural observations show that clinoamphibole may deform by dislocation creep through gliding of several slip systems and mechanical twinning (see Dollinger and Blacic, 1975 and Reynard et al., 1989 for further details). For glaucophane, slip is favored due to internal crystal occupancies where Na can jump from the M4 to the A sites, the latter being commonly empty. EBSD results on natural blueschist examples show weak to somehow strong crystallographic preferred orientations (CPO) that are interpreted as the result of dislocation creep (e.g., Kim et al., 2013; Kotowki and Behr, 2019; Cao et al., 2021) with the [001] axe parallel to the stretching orientation (lineation) and [100] axe perpendicular to the foliation plane (e.g., ***Figures 2.4A*** and ***B***). In addition, other geological and experimental investigations in glaucophane-rich materials emphasize rigid body rotation and cataclastic deformation to dominate in the blueschist-facies field (e.g., Ildefonse et al., 1990; Kim et al., 2015) accompanying dislocation creep (Zucali et al., 2002). In the case of epidote-blueschists, experimental investigations show that glaucophane may deform in a variety of manners such as distributed dislocation creep, cataclastic flow and localized ductile shear depending on the grain sizes and the imposed magnitude of shear strain (***Figure 2.4E***). In contrast, the epidote grains, which occur as blasts surrounded by a glaucophane matrix, show structures consistent with cataclastic flow and rigid body rotation suggesting that epidote is stronger (Park et al., 2020). Similar observations have been drawn for lawsonite-blueschists in which lawsonite deforms in the brittle field by rigid body rotation with the development of minor traces of crystal plasticity highlighting strain localization within a weak glaucophane matrix or layers (Teyssier et al., 2010; Kim et al., 2013; Philippon et al., 2013; Kim et al., 2015; e.g., ***Figures 2.4C*** and ***D***). The lawsonite aspect ratios and shape preferred orientations (SPO) with respect to the foliation (vorticity analysis; e.g., Passchier, 1987) have been used to provide insights into the deformation regimes of subduction and exhumation processes, demonstrating that a combination of pure and simple shear dominates (Teyssier et al.,

2010). Investigations on natural lawsonite-blueschist samples comparing fine-grained foliated with respect to massive coarse-grained lithologies show that CPO of minerals are much stronger in the former (Cao et al., 2014). These results may explain discrepancies between studies proposing dislocation (e.g., Behr et al., 2018) versus pressure-solution creep (e.g., Wassmann and Stöckhert, 2012) as the dominant deformation mechanisms within the ETS region since the latter is favored at smaller grain sizes (e.g., Renard et al., 2001; Kilian et al., 2011). A similar debate exists among serpentinized ultramafic lithologies comprising the subduction environment, which are believed to deform mostly by pressure-solution (Wassmann et al., 2011) or dislocation creep (Padrón-Navarta et al., 2010). In addition, quartz also plays a dominant role in metasedimentary lithologies (Platt et al., 2018). These observations are relevant when explaining seismic anisotropies in the subduction environment which are commonly produced by the occurrence of cracks filled with fluids (e.g., Healy et al., 2009) or rock fabrics (Bezacier et al., 2010; Padrón-Navarta et al., 2012).

2.2.4 Implications of serpentinite rheology

In Mariana-type subduction margins, serpentinization of the forearc mantle may reach ratios from 40 to 100% being exposed towards the sea bottom (Fryer et al., 2020). However, core drilling programs have dredged peridotites from the forearc, suggesting that the highest serpentinization ratios are likely related to fluid pathways (Fryer, 1996; Hyndman and Peacock, 2003). These margins are largely considered as “aseismic” and non-accretionary (as opposed to Chilean-type margins), whereas seismicity occur mostly in the form of moderate-magnitude earthquakes (Emry et al., 2011 and references therein). The massive amount of serpentinite comprising the subduction channel has been considered as a first-order rheological control inhibiting earthquake nucleation (Hyndman et al. (1997); Hirauchi et al., 2010) due to an apparent – although strongly debated (e.g., Reinen, 2000)– velocity strengthening behavior. Nevertheless, this idea has been contradicted by Emry et al. (2011) and Eimer et al. (2020) who, by means of on-land and ocean bottom seismographs, determined that the active seismogenic region spans a depth range from 10 to 60 km, well within the serpentinized subduction channel and forearc. The authors agree in that a strongly rough subducting slab (delimiting potential seismogenic patches), or an extremely weak subduction channel (fluid overpressures) may explain the “aseismic” behavior of such margins. Similarly, the Maule (Chile) megathrust earthquake (Mw = 8.8) in 2010 ruptured the seismogenic region apparently dominated by metasediments and basaltic materials, but propagated downdip through the serpentinized forearc mantle (Vigny et al., 2011; Wang et al., 2020). Interestingly, aftershock distribution patterns reveal a seismic gap in the shallower part of the mantle wedge, but seismicity becomes abundant at greater depths (up to 50 km depth). The authors proposed that a velocity-strengthening behavior of lizardite/chrysotile (Moore and Lockner, 2011) favored afterslip while the apparently velocity-weakening behavior of antigorite promoted unstable slip (Proctor and Hirth, 2016) on a fluid-saturated environment. These considerations may also apply, at least partially, to slow-spreading contexts. There, the seafloor-forming materials are largely composed of mantle, commonly serpentinized, peridotites (Cannat, 1993) rather than a basaltic oceanic crust as in fast (e.g., central Pacific) spreading ridges. In fact, uplift of the mantle, via a complex mechanism of extensional detachment faults, results in brittle-

viscous rock fabrics before subduction, as observed in dredged specimens (e.g., Bickert et al., 2021) and in metamorphosed, now exhumed, subducted former slow-spreading seafloor complexes (e.g., meta-ophiolites from the Western Alps; Lagabrielle and Cannat, 1990). Thus, an already deformed serpentinized oceanic lithosphere is expected to be exposed to and in contact with the hanging wall upon subduction (Agard and Handy, 2021).

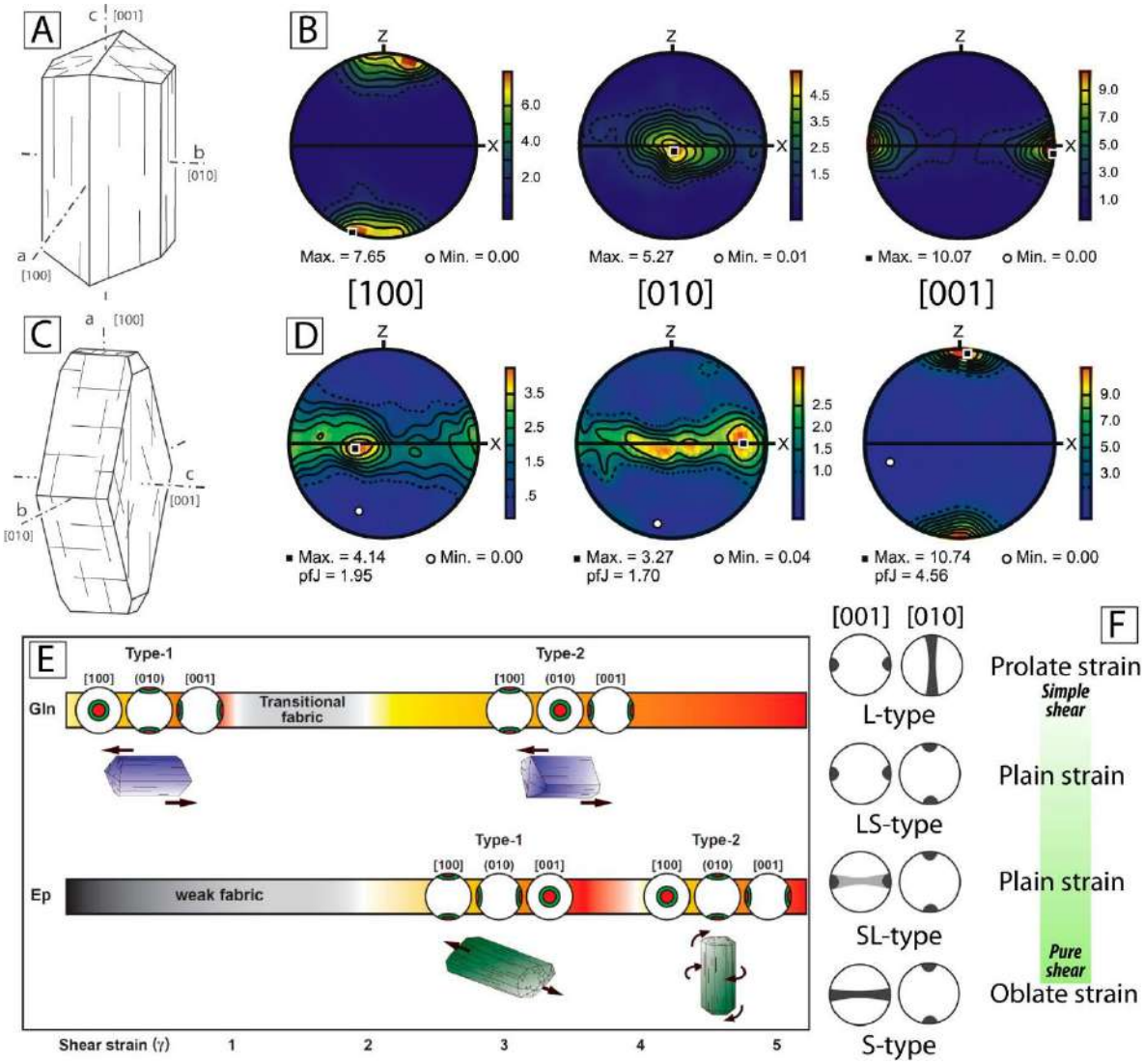

Figure 2.4. A. Lawsonite crystal morphology and axis notation used in the pole figures from panel B. B. Pole figures from lawsonite in a highly strained foliated blueschist. c. Glaucophane crystal morphology and axis notation used in the pole figures from panel C. C. Pole figures from glaucophane in a highly strained foliated blueschist showing a SL-type fabric (see panel F for details). The single crystal illustrations are from Nesse (2004) and the pole figure examples from Cao et al. (2014). D. Schematic representation of the development of LPOs of glaucophane and epidote with respect to the magnitude of shear strain (after Park et al., 2020). Note that the LPOs do not necessarily represent crystal plastic deformation mechanisms. E. Common fabrics for monoclinic symmetries (e.g., clinopyroxene and clinoamphibole) together with interpretation of the strain geometry (after Keppler, 2018).

2.2.5 Rheology of the deep subduction environment

Further at depths, the transformation of blueschists to eclogites result in a bulk rheology controlled by virtually dry omphacite and garnet mixtures with minor phengite, amphibole, lawsonite, epidote and rutile (the main stable mineral assemblage is volumetrically composed mostly by anhydrous phases). These facies transition dramatically modifies the slab structure affecting parameters such as density, fluid abundance and the stress regime (Rondenay et al., 2008). The deformation mechanisms are strongly debated, but it seems to be a consensus in that viscous flow – a combination of pressure-solution and dislocation creep – is the active deformation mechanism in mafic lithologies (e.g., Godard and Van Roermund, 1995; Zhang et al., 2006; Stünitz et al., 2020). Although geophysicial investigations, especially those developed by the ETS community, consider this region as aseismic, the occurrences of high-pressure vein systems (Taetz et al., 2016), eclogite breccias (Angiboust et al., 2012) and eclogite-facies pseudotachylytes (John and Schenk, 2006; Andersen et al., 2014), demonstrate that transient brittle deformation occurs associated with intermediate-depth earthquakes (Peacock, 2001). In Alpine Corsica, the pseudotachylyte networks found in the interface between the lithospheric mantle and overlying gabbro, interpreted as lower plane seismicity, suggest earthquake magnitudes in the order of 8 (Austrheim and Andersen, 2004; Andersen et al., 2014). The authors emphasize that this rupture required sliding over a surface of hundreds of kilometers and likely represent the same event that produced the earthquakes recorded in the eclogite breccia from Angiboust et al. (2012). In addition, experimental and geophysical observations enable linking the breakdown of antigorite (the high-pressure and high-temperature serpentine polymorph) with the location of intermediate-depth earthquakes in active subduction settings (e.g., Hacker et al., 2003). Although antigorite and mafic crust dehydration have been classically believed to generate double seismicity planes (an upper one along the interface itself and a lower one lying a few tens of km within the downgoing plate), recent investigations suggest that the lower plane of seismicity could be explained by localized deformation in a seismically anisotropic anhydrous slab mantle (Reynard et al., 2010). Furthermore, breakdown of antigorite and other hydrous minerals in the uppermost part of the hydrated oceanic lithosphere has been suspected to promote brittle failure inducing Intermediate-depth earthquakes (Hacker et al., 2003) via dehydration embrittlement processes (Raleigh and Paterson, 1965; Padrón-Navarta et al., 2011). Nevertheless, experimental investigations are yet inconclusive in this regard due to the poorly constrained rheological and hydro-mechanical properties of antigorite-rich serpentinites (Padrón-Navarta et al., 2010; Hirth and Guillot, 2013; Gasc et al., 2017).

The aforementioned investigations suggest that a rheological control, as for example the onset of crystal plasticity at a determined temperature, plays an important but not decisive role in controlling earthquake nucleation nor magnitude. Alternatively, it seems that fluid pressure is a more decisive factor in driving the subduction steady-state creep from background plate boundary rates towards fast and slow seismic slip rates (regular earthquakes and ETS; ***Figure 2.3***).

2.3 Sources of fluids and their mechanical effects along the subduction interface

2.3.1 Fluid sources and pathways

The importance of fluids and their mechanical effects on the Earth's lithosphere are considered as a key factor controlling processes at a wide range of scales (e.g., Peacock, 1990a). Fyfe et al (1978) state that strain rates in the lithosphere are so slow that deformation, and therefore orogenesis and plate tectonics would be impossible without considering the influence of fluids. While O'Neill et al. (2007) consider that the onset of plate tectonics in the Earth and other planets and moons is only possible if the effects of H_2O fluids are considered. From a chemical perspective, fluids are known to serve as mass transport agents or heat transfer media for magmatic to supergene processes resulting in ore enrichment in a number of geological contexts (e.g., Kesler, 2005). In most environments, hydrothermal fluids are mainly composed by C-O-H-Na-Cl mixtures with metal concentrations being particularly high only at specific conditions, resulting in anomalous enrichments and further giant deposits (Brimhall and Crerar, 1987; Yardley, 2005; Gottschalk, 2007), as for example La Escondida (Chile) copper deposit – the largest copper mine in the world. The physicochemical nature of low temperature and pressure fluids is well characterized with respect to high-pressure metamorphic fluids since, in the former, direct sampling is possible as for example in geothermal, basinal and seafloor hydrothermal systems (Liebscher, 2010). In supergene to deep environments, valuable information on the physical and geochemical properties of fluids can be gained through the study of breccias, metasomatic rocks and vein systems (e.g., Fyfe and Zardini, 1967; Moore et al., 1981; Heinrich, 2007; Angiboust et al., 2011; Vitale Brovarone et al., 2014).

Although subduction zones are believed to represent highly dynamic and fluid-saturated environments, direct information from deep fluids has been only acquired in the Mariana subduction margin through the study of pore waters contained in expelled rock fragments from mud volcanoes (e.g., Hulme et al., 2010). In most cases, the most obvious and accessible evidence of deep fluid flow are metamorphic vein networks (e.g., Philippot and Selverstone, 1991; Spandler et al., 2011; Raimbourg et al., 2015; Angiboust et al., 2020) and metasomatic rinds or black walls (Harlow and Sorensen, 2005; Spandler et al., 2008; Penniston-Dorland et al., 2014). In addition, indirect geophysical information led some authors to propose models of mineral precipitation and recovery of cohesion, processes that are intimately related to the slip behaviour of the slab enhancing healing of the shear zone (e.g., Saffer and Tobin, 2011; Audet and Bürgman, 2014; Fisher and Brantley, 2014; Ujiie et al., 2018). In particular, metamorphic vein systems and other metasomatic features provide information regarding the complex fluid-rock interaction processes occurring at depths as well as the fluid pathways and the pressure-temperature conditions of fluid circulation and/or precipitation.

In general, two scenarios are commonly invoked to explain the origin of deep fluids. One case corresponds to locally-derived fluids, which considers closed-system devolatilization (and advection) or diffusive mass transfer from the host rock towards a fracture, ultimately resulting in fluid stagnation and solute precipitation (Nadeau et al., 1993; Hermann et al., 2006; Spandler and Hermann, 2006; Fisher and Brantley, 2014). This mechanism requires a pressure gradient from near-lithostatic fluid

pressure values in the matrix towards a crack, which at the moment of opening will experience a fluid pressure drop until the crack is sealed. Right after fracturing (Secor and Pollar, 1975), little advection of solutes near the crack will sink into the opened crack. However, further diffusion of material will occur until the crack is closed (Fisher and Brantley, 1992). This mechanism is especially favourable in low permeability rocks (Etheridge et al., 1983; Cox, 1999). In metamorphic environments, hydrofracturing is enhanced by mineral dehydration reactions, differential stresses and viscous deformation accompanying porosity and permeability reduction (Rumble and Spear, 1983; Oliver, 1996; Oliver and Bons, 2001).

The opposite scenario corresponds to externally-derived fluids which are transported via advection up to the kilometres-scale (e.g., Etheridge et al., 1984; Vrolijk et al., 1988; Breeding and Ague, 2002; John et al., 2012; Angiboust et al., 2014; Taetz et al., 2018). In this case, the porous fluid pathways likely correspond to microcracks (pervasive; Holness and Graham, 1995; see also cavitation creep processes in shear zones; Précigout et al., 2017) or macrofractures (channelized). In the former case, it is likely that the fluid will reach a near-equilibrium state with the host rock (e.g., Dipple and Ferry, 1992) while in the latter a strong chemical gradient between the vein and host will occur (e.g., Bons, 2001). The current state of knowledge agrees that advective and diffusive fluid-rock interactions occur along the subduction path (Kastner et al., 1993), even at depths compatible with the blueschist-to-eclogite transition – conditions at which tremendous amounts of fluids are released by the oceanic and ultramafic section of the slab (***Figure 2.5A***). These interactions have been suggested to occur episodically, as evidenced by multiple events of vein re-opening, strong oscillatory zoning patterns (***Figures 2.5B*** and ***C***) and numerical simulations (e.g., Ramsay, 1980; Nur and Walder, 1992; Wiltschko and Morse; 2001; Spandler et al., 2011; Angiboust et al., 2014). Note that petrological observations and thermal modelling suggest no obvious relationships between any specific metamorphic dehydration reaction and temperature with the occurrence of ETSs (Peacock and Wang, 1999; Peacock, 2009; Peng and Gomberg, 2010).

In any case, the possible fluid sources are diverse and vary according to the followed metamorphic path. Based on isotopic and fluid inclusion studies, it has been shown that shallow subduction fluids are in great part produced by pore collapse and/or clay devolatilization of the sedimentary lithologies (e.g., Suess and Whiticar, 1989; Chan and Kastner, 2000; Saffer and Tobin, 2011). Moreover, very low-grade metamorphic minerals formed during seafloor alteration of metamafic lithologies (e.g., zeolites) may supply dehydrated fluids upon reaching sufficient temperature (e.g., Liou, 1971; Fyfe et al., 1978; Spear, 1993). Ernst (1990) emphasized that most fluids are released at low-grade conditions relative to the higher-grade dehydration reactions. Further at depths, fluid expulsion due to the breakdown of water-bearing minerals such as lawsonite, epidote, chlorite, micas, amphibole and serpentinite (Poli and Schmidt, 1995; Padrón-Navarta et al., 2011; Zheng and Hermann, 2014) strongly impacts processes such as seismicity, melting and further arc magmatism (Peacock, 1990a; Poli and Schmidt, 1995; Hacker et al., 2003; Padrón-Navarta et al., 2010; van Keken et al., 2011). In this regard, a large palette of analytical and numerical investigations suggests the complete spectrum

of subducting lithologies as likely fluid sources. In other words, the fluid sources for veining, mas-transport (including CO_2 mobility) and metasomatic formation of hybrid lithologies may correspond to metasediments, metabasites and/or serpentinites. Thus, careful evaluation of each particular study case is a prerequisite (Bebout and Barton, 1989; Nelson, 1995; Breeding et al., 2004; Hermann et al., 2006; Zack and John, 2007; Spandler et al., 2008; van der Straaten et al., 2008; 2012; Putnis and Austrheim, 2010; Spandler and Pirard, 2013; Angiboust et al., 2014; 2017; Taetz et al., 2016, 2018; Jaeckel et al., 2018; Epstein et al., 2020).

The most important carrier of volatiles in the subduction environment are serpentinized ultramafic lithologies. Serpentinites formed during seafloor alteration and outer rise bending of the oceanic lithosphere (Bach and Früh-Green, 2010) can contain up to 13 wt% of H_2O. Potential serpentinite devolatilization occurs by a series of discontinuous reactions down to ~200 km (Ulmer and Trommsdorff, 1995; Padrón Navarta et al., 2013), far beyond devolatilization depths for metamafic lithologies which expel their H_2O largely during the blueschist to eclogite transition at ~70 km depth (Schmidt and Poli, 1998; Gao and Klemd, 2001; Hilairet et al., 2006; John et al., 2012), leaving a virtually dry eclogite residue (<1 wt% of H_2O). It should be noted that devolatilization reactions are strongly dependent on the subduction thermal gradient, and that the greatest amount of H_2O is released in warm environments (van Keken et al., 2011; ***Figure 2.6***). Thus, it is widely accepted that a large part of the arc magmatism is triggered by melting of the mantle wedge hydrated by the influx of serpentinite-breakdown fluids at ~100 km depth (Stern et al., 2006; Padrón-Navarta et al., 2010; see ***Figure 2.7*** for a general review of devolatilization processes in a subduction context), leaving a diagnostic trace element signature to arc volcanic products (e.g., Scambelluri et al., 2019 and references therein).

2.3.2 Mechanical response of rocks to fluids

In the Earth's crust and mantle, pore fluid pressure is of great importance to understand earthquake mechanics since it can strongly affect the mechanical stability of a fault ultimately resulting in fast slip. For tectonic stress regimes (i.e., the principal components of the stress tensor $\sigma_1 > \sigma_2 > \sigma_3$), the most direct implication of pore fluids pressure is to decrease the effective normal stress, σ_n', of a fault plane which is defined as:

$$\sigma_n' = \sigma_n - P_f \quad (2.1)$$

where σ_n is the normal stress and P_f the fluid pressure (Hubbert and Rubey (1959). If the system is not connected to the Earth's surface, fluid pressures deviate from hydrostatic and can be associated with the overburden pressure or vertical stress, σ_v, as:

$$\lambda_v = \frac{P_f}{\sigma_v} = \frac{P_f}{\rho g z} \quad (2.2)$$

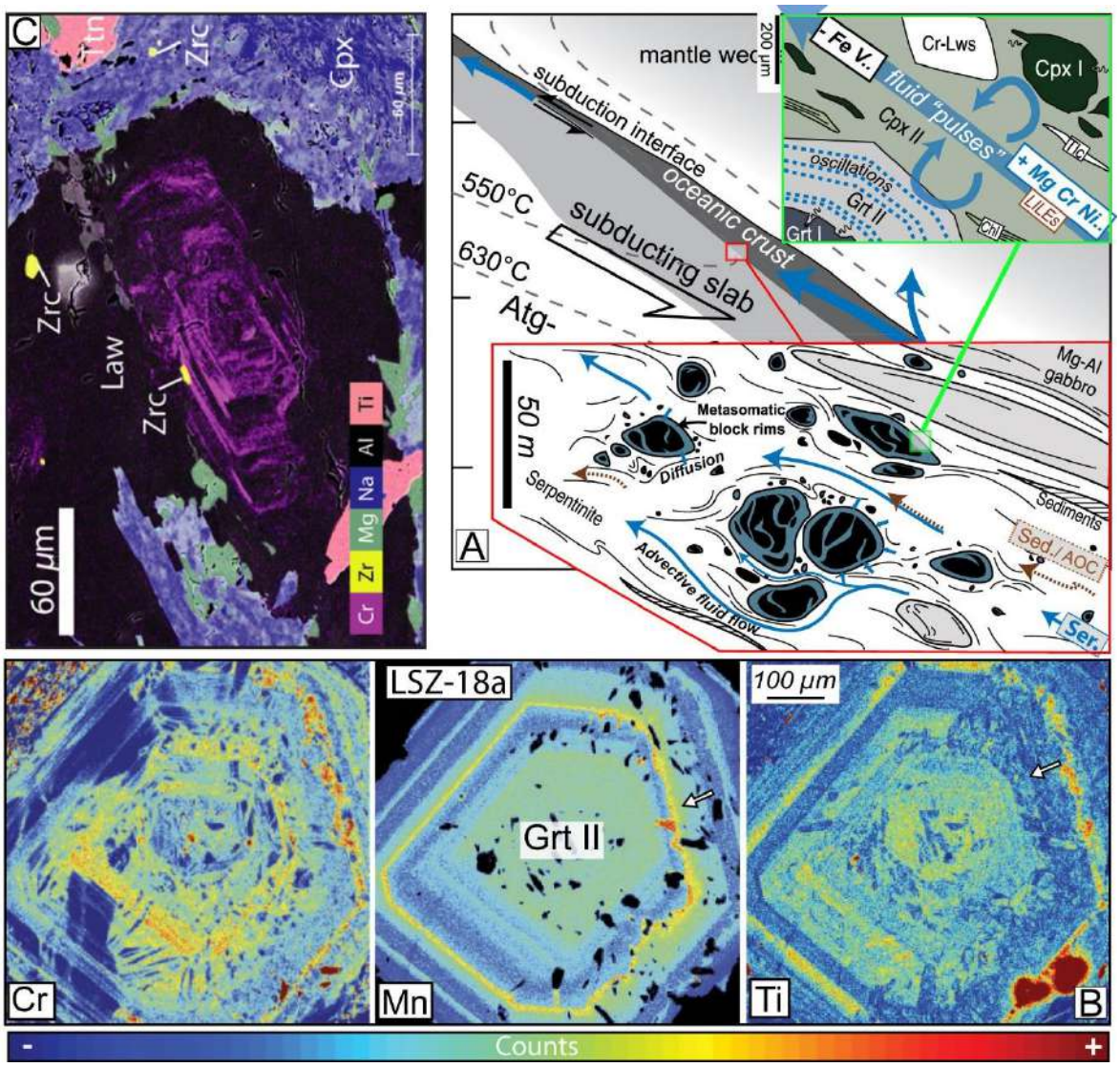

Figure 2.5. A. Illustration of a subduction shear zone in the Monviso metaophiolite context depicting fluid pathways, sources, lithologies and interactions at different scales (see insets). The circular arrow in the top right panel aims at representing fluid-mineral interactions. In this case, the major fluid contribution has been inferred to be serpentinite (Ser.)-derived but a signal of a sedimentary (Sed.)- or altered oceanic crust (AOC) has been also detected. B. Oscillatory zoning pattern (WDS X-Ray maps) in garnet from an eclogite (Monviso ophiolite) interpreted as formed due to the influx of fluid pulses. Panels A and B modified from Angiboust et al., (2014). C. Oscillatory zoning pattern (WDS X-Ray map) in a vein lawsonite crystal from a lawsonite eclogite (Alpine Corsica) interpreted as a result of multiple fluid-rock interaction events (after Vitale Brovarone et al.,2014).

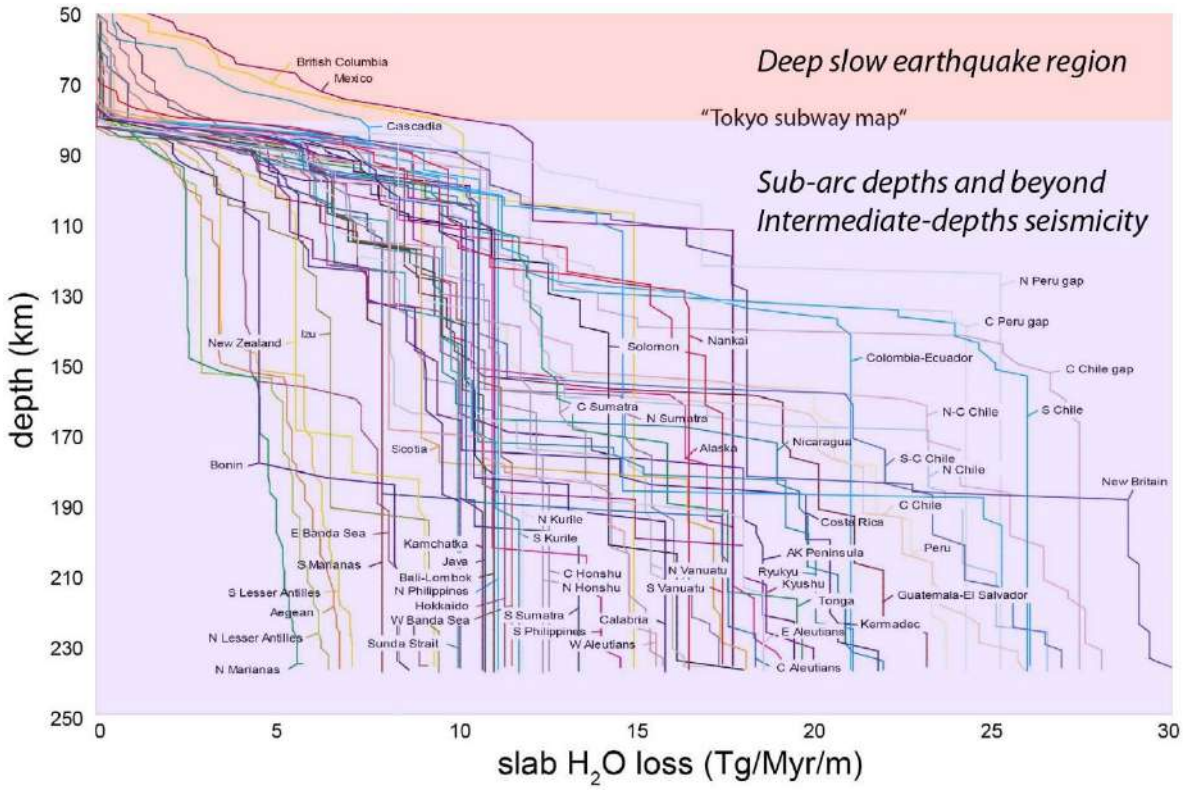

Figure 2.6. H_2O release in several subduction margins. Note that warm subduction slabs (e.g., Cascadia) largely devolatilize at shallower conditions compared to cold environments (e.g., Marianas; after van Keken et al., 2011).

In this formulation, λ_v, represents the pore fluid factor and ρ, g and z are the density, acceleration of gravity and depth, respectively. Thus, the effective normal stress can be related to the vertical stress as:

$$\sigma_v' = (\sigma_v - P_f) = \rho g z(1 - \lambda_v) \quad (2.3)$$

where, assuming an Andersonian stress state, $\sigma_v = \sigma_3$ for a compressional regime and $\sigma_v = \sigma_1$ for an extensional one (Anderson, 1951). From equations (2.2) and (2.3), it is easily deduced that in the case of fluid overpressures approaching lithostatic values (e.g., $\lambda_v > 0.9$; $\lambda_v = 1.0$ is the lithostatic threshold), the effective stresses are strongly reduced. These conditions are inferred according to geological, numerical force-balance and seismological studies which conclude that fault zones, in particular megathrusts, are weak (Magee and Zoback, 1993; Lamb, 2006; Seno, 2009; Fisher and Brantley, 2014; Dielforder, 2020). The shear strength of the megathrust and therefore the conditions for shear failure are commonly expressed by the linear Coulomb criterion:

$$\tau = C + \mu_s(\sigma_n - P_f) \quad (2.4)$$

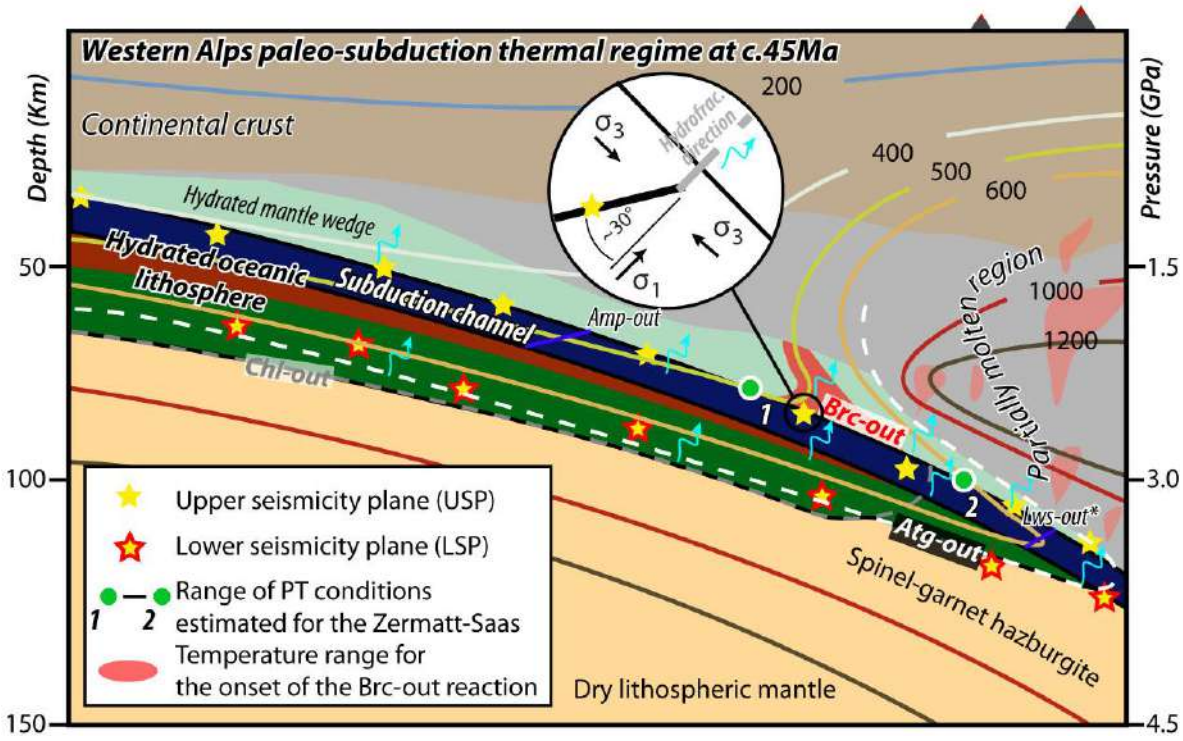

Figure 2.7. Relevant dehydration reactions in a subduction context, with Alpine paleosubduction system as an example. Intermediate depth earthquakes planes are depicted as yellow stars. The positions of main dehydration reactions are derived from Ulmer and Trommsdorff (1995; Atg out), Schmidt and Poli (1998; Chl out), Kempf et al. (2020; Brc out) and Hacker et al. (2003; Amp and Lws out). The phengite breakdown is not shown here for aesthetical reasons since it is expected to occur at c. 300 km depth. Similarly, the Lws-out reaction, strongly dependent on the subduction thermal regime, may occur at maximum depths of c. 280 km (Schmidt and Poli, 1998). Note that the subduction thermal gradient represents a snapshot of the Alpine subduction recorded in the Zermatt-Saas unit at c.45 Ma (after Dragovic et al., 2020). The inset represents schematic relationships between an intermediate depth earthquake fault plane (as inferred from focal mechanisms; bold black line) and hydrofracturing towards the subarc mantle (after Davies, 1999).*

here, C and μ_s are material properties for static frictional coefficient and cohesive strength, respectively. While τ and σ_n are the shear and normal stress components acting on the fault, respectively. From equation (2.4), it can be deduced that faulting can occur due to variations in σ_n (stress), P_f (fluid pressure), or a combination of both, since C and μ_s are considered as material properties. Although the friction coefficient has been classically believed to range between $0.5 < \mu_s < 1.0$, with a typically assumed value of 0.75 to be representative of crustal rocks, it is demonstrated that this parameter is variable in all lithologies forming the subduction slab, with values lower than 0.5 considered to be more realistic (e.g., Kopf and brown, 2003; Ikari et al., 2009 ; Tan et al., 2012; Hardebeck and Loveless, 2018; Okazaki and Hirth, 2020). It has been shown that changes in fluid pressure rather than stresses during the seismic cycle can also greatly affect the possibility of earthquake nucleation and recurrence in the subduction environment (Sibson, 2013). The opposite scenario corresponds to pure extensional fracturing or hydrofracturing (zero shear stress), which occurs when fluid pressure equals or exceed the sum of the least principal stress, σ_3, and the tensile strength of a rock, T, such that:

$$P_f = \sigma_3 + T \quad (2.5)$$

These conditions are represented in a generic Mohr diagram at the point (-T,0) by a circle touching the composite Griffith-Coulomb failure criterion. It should be noted that hydrofracturing can only occur when the differential stress is less than four times the tensile strength of the rock, $\sigma_1 - \sigma_3 < 4T$. Previous investigations have demonstrated that fluid pressure is time-dependent and therefore not constant during the seismic cycle (e.g., Sibson, 1992). Recent seismological studies have detected temporal and spatial (updip) variations of fluid pressure along the subduction interface, suggesting a fault-valve mechanism to occur in this environment (Gosselin et al., 2020) as proposed originally for continental faults (Sibson, 1990). Other lines of evidence allow estimating porosities, with values as high as 4%, resulting from hydrofracturing at depths (e.g., Peacock et al., 2011). An intermediate state between hydrofracturing and shear faulting is hybrid extensional-shear failure (Hancock, 1985), which occurs at critical stresses in the range of $4T < (\sigma_1 - \sigma_3) < 5.66T$ following the expression:

$$(\sigma_1 - \sigma_3)^2 = 8T(\sigma_1' + \sigma_3') \quad (2.6)$$

In the geological record, this process is evidenced, for example, by the occurrence of shear veins (e.g., Fagereng et al., 2010; see ***Figures 2.8A, B*** and ***C*** for a schematic illustration of the three modes of failure defined above).

With this theoretical background, it is now clear that fluid pressure can influence a number of failure processes in the continental crust but also within the subduction interface (Gosselin et al., 2020). For example, Cerchiari et al. (2020) applied these concepts to a veined sequence in the Northern Apennines thought to represent a subduction mélange. The authors conclude that the vein networks record a protracted sequence of fracturing associated with changes of the stress regime from compressional to extensional during the seismic cycle in a weak interface (see Mage and Zoback, 1993 for more details on the stress inversion process). Furthermore, Otsubo et al., 2020 studied the geometry of quartz veins in a fossilized megasplay fault in the Shimanto Belt (Japan). It is concluded that fluid drainage associated with hydrofracturing during post-seismic periods, plays a limited role in recovering the shear zone strength, which seems to be permanently very weak.

Another example is the Dent Blanche (Penninic Austroalpine transition realm) tectonic system, which exposes a blueschist-facies mixing zone. Angiboust et al. (2015) reported the existence of a number of brittle and viscous fabrics in mutual overprinting relationships including folded epidote veins, mylonites, breccias, cataclasites and foliated cataclasite networks. By investigating the rheological properties of the shear zone, the authors suggested that in order to promote brittle deformation as from background plate convergence rates viscous flow, variations in strain rates of at least 2 orders of magnitude are required under highly pressurized pore fluid pressure conditions – below the lithostatic threshold, i.e., $0.95 < \lambda_v < 0.98$. The triggers for higher slip rate bursts are thought to correspond to aftershock propagation downdip the seismogenic region or to slow slip events along the subduction interface. A model was proposed where fluids responsible for the formation of epidote veins percolated through porosity networks produced during cataclasis. Similarly, Bachmann et al. (2009) documented a mixing zone (also in the Penninic-Austroalpine transition realm) believed to

represent an exhumed fragment of the seismogenic region and slightly below. It was concluded that the role of fluids is active, affecting the coseismic and interseismic deformation patterns of the seismic cycle. In the latter case, by enhancing mylonitization of pseudotachylytes and pressure solution-creep, while in the former by triggering fracturing. Interestingly, the authors reported the existence of **hydraulic breccias** (similar to those reported in **Chapters 4** and **5**) which, according to their spatial distribution associated with pseudotachylytes and similarities in the internal structures of veins and pseudotachylyte networks, are inferred to have formed due to fast slip, potentially at seismic velocities.

In summary, it is clear that despite the range of fluid sources, the injection or flow of overpressurized fluids along the megathrust is critical in controlling different aspects of the seismic cycle. Nevertheless, very little is known about the mechanical effects of fluids at depths compatible with the transition zone, where a vast number of ETS seems to nucleate (e.g., Behr and Bürgmann, 2021).

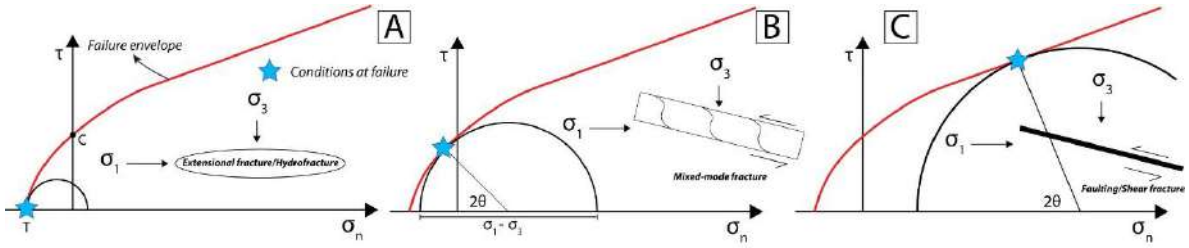

Figure 2.8. A to C. 2-D schematic representation of the stress state on a Mohr diagram showing different conditions of failure according to the principle of effective stress and fluid pressure variations. Failure orientation and basic characteristics of a fault or vein relative to the stress orientations are also depicted.

2.4 Potential geological records of slow earthquakes

Before explaining models for ETSs generation and possible rock records, it is worth introducing basic aspects for a series of seismological manifestations that are intimately associated with the ETS phenomena. First, slow earthquakes correspond to two families of processes. On the one hand, slow slips, defined as geodetically detectable slip events with sufficiently slow rupture and slip velocities to radiate seismic energy. On the other hand, tectonic tremors, commonly considered as clusters of low and very low frequency earthquakes (e.g., Audet and Kim, 2016), correspond to seismic signals that are a part, but not exclusive of, the slow earthquake phenomena. They are characterized by low- and very low-frequencies (more than 1 an 0.02 Hz, respectively) and durations in the order of deciseconds to a few minutes as well as magnitudes less than 4 (Shelly et al., 2006; Ito et al., 2007; Beroza and Ide, 2011; Bostock et al., 2015; Nakano et al., 2019; Behr and Burgmann,2021 and references therein). All these manifestations are believed to constitute the whole of the slow earthquake process (Kaneko et al., 2018). Very low- and low-frequency earthquakes are associated with minimum stress drops and may result from stick-slip in the order of few millimetres on a very weak and overpressurized fault zone (Ito and Obara, 2006). Subduction deep slow earthquakes are largely recorded in the 25 to 80 km depth range (e.g., Dragert et al., 2001; Wallace and Beavan, 2006; Wei e tal., 2012), generally occurring at greater depths in cold subduction margins (e.g., Alaska: Fu

and Freymueller, 2013; ***Figure 2.9***). Theoretical investigations suggest that, despite the observed S-wave radiation patterns, a shear mechanism is not obvious. Similar patterns can be produced by transient mechanical forces acting in the direction of fast fluid flow (Shapiro et al., 2018), ultimately resulting in hydrofracturing. In this perspective, it should be noted that fluid migration can occur both along strike and updip within the subduction interface (e.g., Frank et al., 2015; Cruz-Atienza et al., 2018). Such fluid migrations involve transient changes in permeability as depicted in the fault-valve model (Gosselin et al., 2020; Farge et al., 2021). In any case one of the most remarkably features of these seismic events is that hundreds or thousands of them occur during a major slow earthquake.

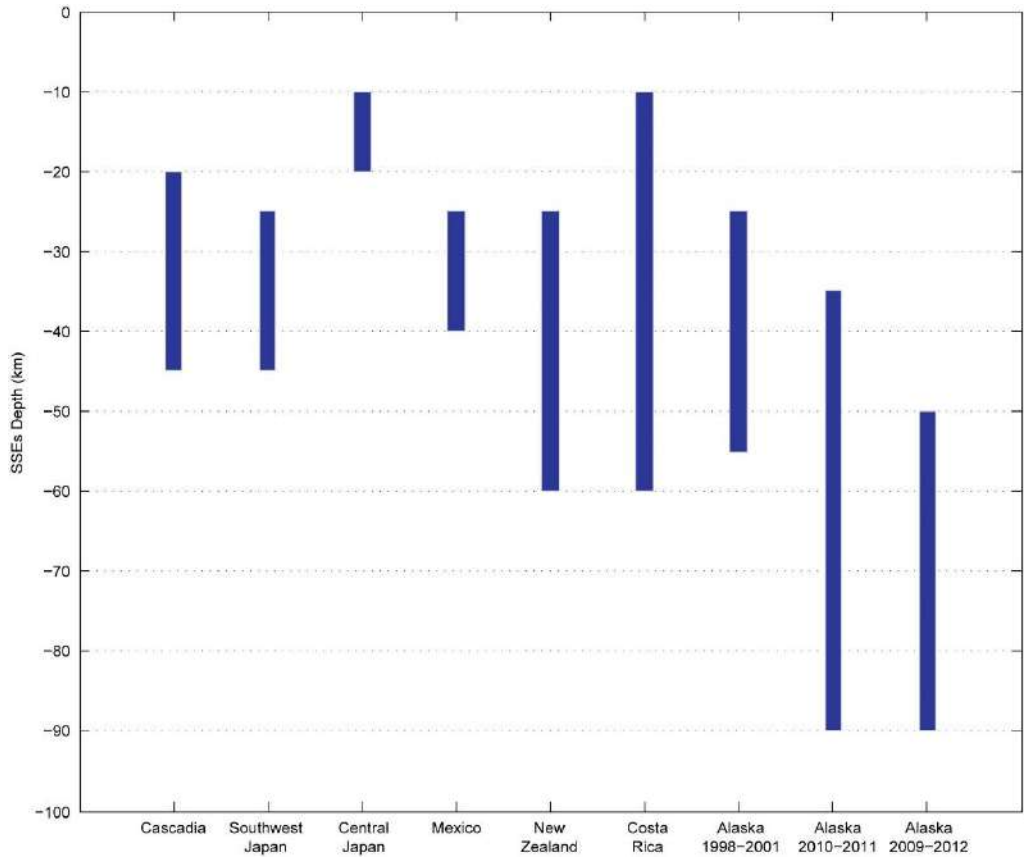

Figure 2.9. SEEs depth range for several subduction margins (after Fu and Freymueller, 2013).

Geological observations from exhumed shear zones representative of the ETS region represent the best approach to validate or provide new insights into the physical properties acting within the slow earthquake source. Up to date, there is no obvious geological or rock record which can be unequivocally attributed to the occurrence of a slow earthquake event. Here I review some general aspects of the slow earthquake source. The shear zone in the ETS region is composed of both localized and distributed shear fabrics, with evidence of synchronous viscous and brittle deformation patterns accommodating deformation within centimetre to hectometre-wide shear zones, although localized deformation seems to occur at the very top of the subduction channel (e.g., Bachman et al., 2009; Fagereng et al., 2010; Angiboust et al., 2014; Hayman and Lavier, 2014; Palazzin et al., 2016; Behr

et al., 2018; Kirkpatrick et al., 2021; Oncken et al., in press and references therein). Rheological heterogeneities are common within the subduction interface at a wide depth range (e.g., Fagereng et al., 2011; Kotowski and Behr, 2019). In all these environments, the development of foliations or cleavages are ubiquitous features (e.g., Kimura et al., 2012), while brittle deformation has been observed in the form of cataclasites, shear bands, extensional veins and off-sets around blocks of higher viscosity than the respective surrounding matrix (e.g., Bachman et al., 2009; Dielforder et al., 2015; Angiboust et al., 2015; Fagereng et al., 2018; Behr et al., 2018). Importantly, these features have been described in mutual crosscutting relationships, suggesting switches in the mode of deformation processes and fluid interactions (Angiboust et al., 2015). A general picture of how the slow earthquake source may looks like is presented in ***Figure 2.10***.

In the last decades, a number of mechanisms have been proposed to drive slip from background plate boundary velocities to slow earthquake rates: three review papers have been published in 2021 on the topic (Behr and Bürgmann, 2021; Kirkpatrick et al., 2021; Oncken et al., in press), highlighting the importance of the ETS processes. One possible explanation are rheological heterogeneities of the shear zone materials slipping faster than subduction convergence rates, causing a transition from

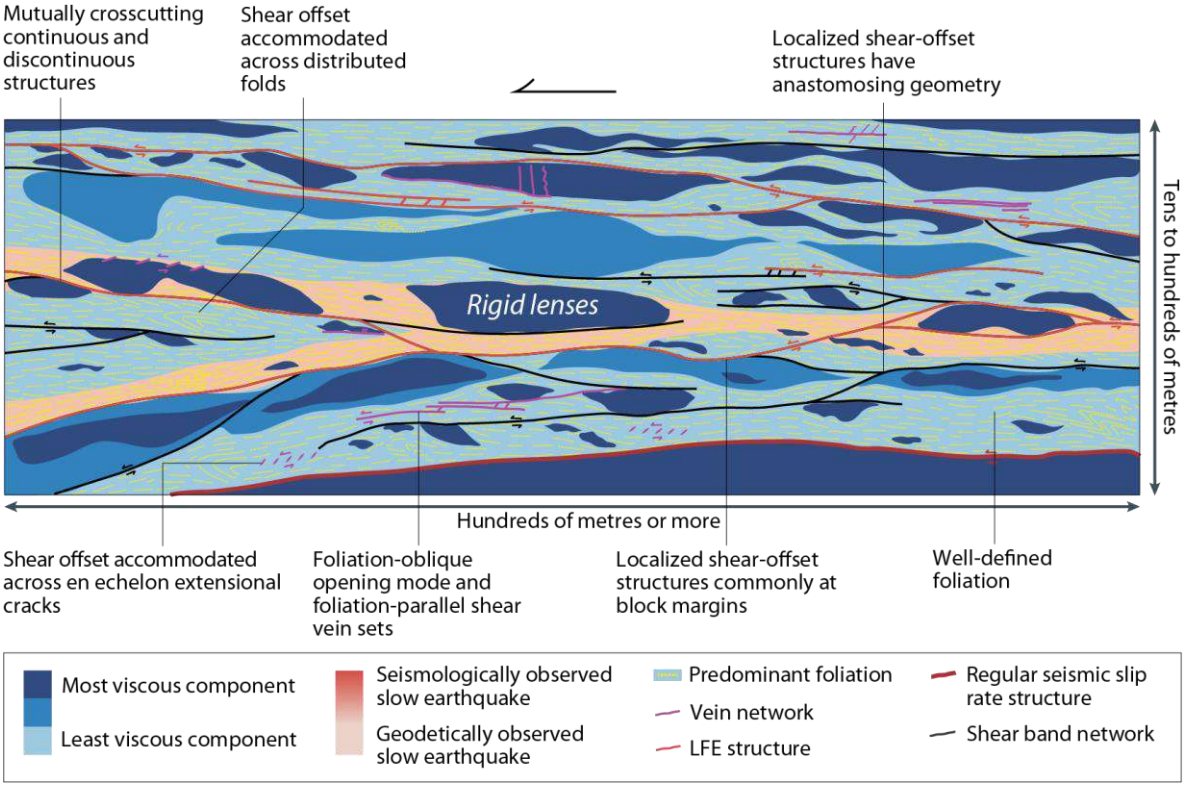

Figure 2.10. Illustration depicting general aspects of the slow earthquake source (after Kirkpatrick et al., 2021).

velocity-weakening to velocity neutral at increasing slip velocities or rates, as depicted by numerical simulation applying the rate-and-state friction formalism (e.g., Im et al., 2020). Under this perspective, Behr et al. (2018; see also Kotowski and Behr, 2019) suggested that rheological heterogeneities between eclogite pods within a blueschist matrix, the former representing stiffer

velocity-weakening materials, whereas the latter a weaker and velocity-strengthening domain, represent prone conditions for deep ETS. The authors also documented block distributions and scales within the weak matrix and found correlations with potential slip surface sizes as inferred from geophysical observations. The mixture of materials with contrasting viscosities, whose frictional behaviour depends on their distribution and abundance, as well as the occurrence of anastomosing shear bands and veins (Collettini et al., 2011; Fagereng, 2011), could represent a favourable environment for slow earthquakes – at least at shallow conditions (e.g., Phillips et al., 2020; Fagereng and Beall, 2021). Note that a main difference between shallow and deep environments is that plastic deformation could be active in the latter (see above). However, the triggering mechanisms are probably the same: increases of slip rates (or stress) and/or pore fluid pressures, enhancing brittle yield of the more viscous materials and viscous flow of the less competent lithologies around.

Transient deformation can also be associated with metasomatic reactions of the shear zone-forming lithologies. It has been suggested that dehydration results in hardening of the reaction products (Wintsch and Yeh., 2013). A recent investigation in shear zone-forming lithologies (e.g., the Livingstone Fault in New Zealand, considered as an analogue of the slab-mantle interface; see Tarling et al., 2019) suggests that serpentinite breakdown may release sufficient H_2O to generate fluid overpressures, and switch from distributed viscous to localized brittle deformation (Tarling et al., 2019). The low permeabilities of serpentinites perpendicular to foliation planes are support these conclusions (Kawano et al. 2011). Ujiie et al. (2021b) envision a similar scenario where metasomatic reactions in lithological boundaries may allow the formation of weak albitite bands, that eventually localize deformation possibly hosting ETS-genic processes. Other processes such as dehydration embrittlement of relevant minerals and associated shear instabilities (e.g., lawsonite; Okazaki and Hirth, 2016) have been also considered as a source for brittle instabilities and ETS (Behr and Bürgmann, 2021).

Further hypotheses have been proposed in literature. Nevertheless, the difficulty of correlating structures and fabrics with deep earthquake sources properties may account for the large number of hypotheses, as stated by Oncken et al. (in press). It is interesting to note that to date, the effects of other brittle structures, such as cataclasites or ultracataclasites have received little attention in the context of deep ETS (e.g., Essene and Fyfe, 1967; Rowe et al., 2011; Angiboust et al., 2015). This is reasonable owing to their extremely fine grain sizes enhancing metamorphic overprint and deformation (pressure-solution creep) of the original fabrics. By studying the constitutive flow laws of brittle creep (e.g., Brantut et al., 2012), Oncken et al. (in press) demonstrated that strain localization within cataclastic or ultracataclastic slip zones could accommodate the full spectrum of subseismic processes (e.g., shallow tremors, afterslips and deep ETS; see ***Figures 2.11A*** and ***B***). It is therein suggested that departure from steady-state pressure solution to brittle creep is the result of high pore fluid pressure conditions and stress build up. The authors also suggested that brittle creep transients may represent a good indicator of fault zone instabilities. Thus, in the framework of the seismic cycle, pressure solution creep and subordinately dislocation creep, the latter acting likely at higher

temperatures, are thought to be important in early stages, during loading (Gratier et al., 2014). Furthermore, due to healing of a previous brittle fabric and related porosity, brittle creep, and associated strain rate bursts, will become more important towards latter stages (or the end) of the seismic cycle associated with fluctuations of pore fluid pressure highs (Oncken et al., in press). Note that in extremely fine-grained and highly porous lithologies, pressure solution creep may also accommodate some of the slow slip transients. However, this scenario is unlikely since porosities in subduction zone rocks are one order of magnitude lower, as inferred from Vp/Vs ratios analyses (e.g., Peacock et al., 2011) or exhumed analogues (Rowe et al., 2011). Such conditions can be optimal in the post-seismic period just before fault strength recovery. Similarly, aseismic and pulsing afterslip distributions associated with aftershocks following the Maule megathrust earthquake (2010) also support an active role of fluid pressure highs as triggers of subseismic slip, rather than static stress variations (Bedford et al., 2013) Nevertheless, these complex feedbacks have not been naturally nor experimentally reported yet, although overprinting fabrics between brittle and viscous features may give a light on these complex interactions (e.g., Rowe et al., 2011; Angiboust et al., 2015).

2.5 What is next?

Despite the great efforts done in the last 20 years aiming at imaging and documenting possible geological records of slow earthquakes, an obvious lack of in situ natural observations represent a major scientific gap. Most observations come from geophysical or geological studies from the shallow part of the ETS source. Although the mechanisms for shallow and deep ETS generation may be similar, obvious differences exist in the materials, rheological properties and metamorphic processes towards greater depths. Through multidisciplinary approaches, it is however possible to illuminate source properties of the deep ETS source. The broad spectrum of geophyisical studies suggesting a transient nature of ETS intimately associated with fluid overpressures, represent a good guideline to seek in the geological record. To date, most studies aiming at characterizing fluid sources and processes in the blueschist-facies and beyond, focus on single outcrops or samples comprising unique lithologies; such approach is certainly limited considering the kilometre-scale and the diversity of materials associated with slow earthquakes. In addition, studies characterizing the deformation mechanisms operating in deep vein networks are missing. This thesis aims at filling these scientific gaps – at least to provide a light – through the study of exhumed metamorphic complexes belonging to the Western Series (Central Chile) and the Seghin complex (Zagros Orogen). Both representing well exposed former high-pressure subduction complexes from the shallower and deeper regions of the deep ETS zone, respectively, and both bearing plenty of evidence for brittle-viscous flow associated with fluid overpressures, including HP-LT metamorphic veins, breccias and foliated cataclasites.

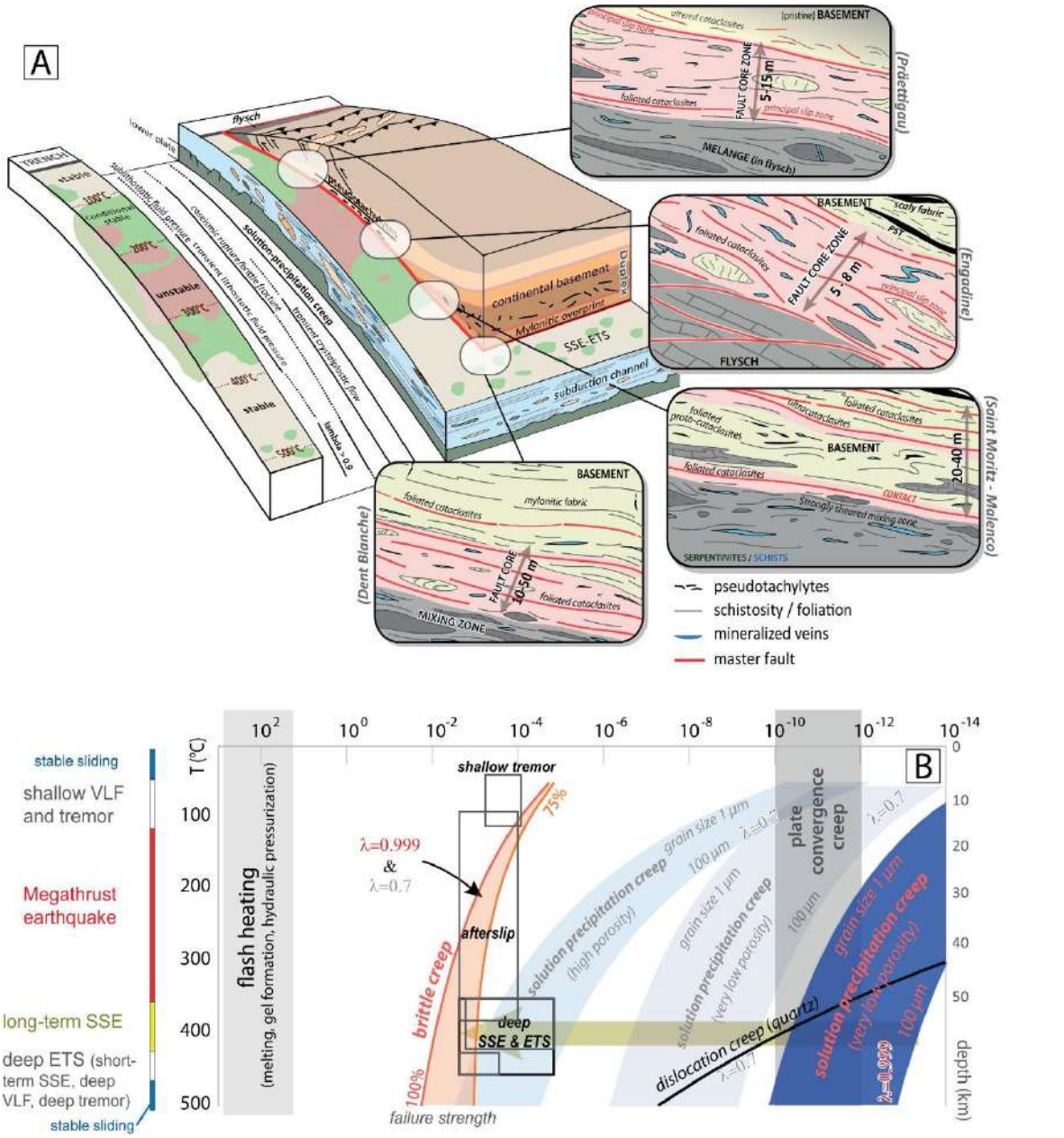

Figure 2.11. A. Illustration of the structure of a subduction interface and related deformation mechanisms. The insets depict schematic views of foliated cataclasites (pink colours) and ultracataclasites slip zones (red lines) at a range of depths using studied exhumed analogues. PST – pseudotachylytes; SSE – slow slip event. B. Deformation mechanism map correlating strain rate versus temperatures at pore fluid pressure ratios of 0.7 and 0.999; solution precipitation creep flow laws are plotted considering different porosities and grain sizes. Stresses are fixed at 100% and 75% of the peak strength (failure threshold). The black boxes show the range of strain rate estimates for a number of instrumentally observed seismic manifestations belonging to the slow earthquakes family. Panels A and B modified from Oncken et al. (in press).

3. Geological context

3.1 Geodynamic evolution of South-Central Chile

Most of the continental margin that now hosts the Cenozoic and Mezosoic Andean sequences is constituted of Proterozoic (?) to Jurassic igneous and metamorphic complexes, referred to in the Chilean literature as the “basement” or “crystalline basement” that records several stages of subduction, collision, terrane accretion and passive margin tectonics (e.g., Hervé et al., 2007 and references therein). In northern Chile, the occurrence of Early Cambrian to pre-Devonian metamorphic and igneous complexes represents evidence of subduction followed by continental collision, causing the Cambrian Pampean Orogeny and the subsequent Ordovician Famatinian Orogeny (e.g., Ramos et al., 1986; Rapela et al., 1988; Dalla Salda et al., 1992), the later related to the accretion of the Cuyania terrane (Ramos, 2004). During Devonian times, the Chilenia terrane (and Chaitenia island arc further south; see Hervé et al., 2016) accreted against Gondwana (see ***Figure 3.1A*** for details regarding present-day geological distribution; Ramos et al., 1986) marking the end of the Chanic Orogeny and the beginning of the Gondwanan Orogeny (see ***Figure 3.2*** for a synthesis of the geodynamic evolution in central Chile).

The Gondwanan Orogeny (Ramos 1988) begun in Late Paleozoic times showing significant variations from N to S; its remnants constitute de pre-Andean Chilean (and Argentinian) basement. In the Patagonia region (c. south of 40 °S), this tectonic cycle is related to the collision of Western Antarctica against Gondwana as evidenced by high-grade metamorphism, shear zones and anatectic synorogenic granitoids (Heredia et al., 2018 and references therein). On the other hand, north of 38 °S, the Gondwanan Orogeny is characterized by subduction of a fairly inclined oceanic lithosphere under the continental margin of Gondwana (Ramos, 1988; Willner et al 2005; Hyppolito et al., 2014a,b), except in the northern part (c. 30 °S) where flat-slab subduction developed allowing the migration of deformation, magmatism and synorogenic depocenters towards the east (Parada, 1990; Busquets et al., 2005, 2013; Hervé et al., 2014; Sato et al., 2015).

In the Coastal Range of Central Chile (***Figures 3.1A*** and ***B***), metamorphic rocks formed at the active Paleozoic continental margin during the Gondwanan Orogeny are exposed (Hervé, 1988). This tectonic cycle (Late Devonian-Late Permian) is related to subduction of the Panthalassan oceanic lithosphere under the continental margin of southwestern Gondwana in the rear of the accreted Chilenia Terrane (e.g., Hyppolito et al., 2014a). The corresponding accretionary complexes were intruded by N-S trending syn- and post-accretion subduction-related batholiths (inset ***Figure 3.1A***; Charrier, 1973; Hervé et al., 1974; Ramos, 1988; Willner et al., 2005; Willner, 2005; Charrier et al., 2007; Hervé et al., 2013; Hyppolito et al., 2014a, b; Charrier et al., 2015 and references therein) constituting the latest stages of terrane accretion that assembled the western margin of the Gondwana supercontinent. This orogenic cycle is followed by the pre-Andean tectonic cycle (latest Permian-earliest Jurassic), which is characterized by NNW-SSE extensional basins, felsic magmatism and absent or very diminished subduction (Charrier, 1979; Uliana and Biddle 1988; Mpodozis and Ramos 1989; Mpodozis and Kay 1990; Charrier et al., 2007 and references therein). It is interesting to note

that the major faults controlling rifting during the pre-Andean cycle, prior to Gondwana break-up, coincide with zones of structural weakness matching the sutures of the previously accreted terranes (Ramos, 1994). After the quiescent of subduction during the pre-Andean cycle, a reactivation in Early Jurassic times took place, characterized by the development of a volcanic arc and related back-arc basins parallel to the western margin of Gondwana as well as trench-parallel shear zones several hundreds to thousands of kilometres long (e.g., the Atacama Fault zone; Coira et al., 1982; Charrier et al., 2007; Charrier et al., 2014 and references therein). All these features developed in the framework of the Andean tectonic cycle, Gondwana break-up and subsequent drifting to its present-day position related to an almost continuous subduction of the Nazca-Farallon plate (Charrier et al., 2014 and references therein).

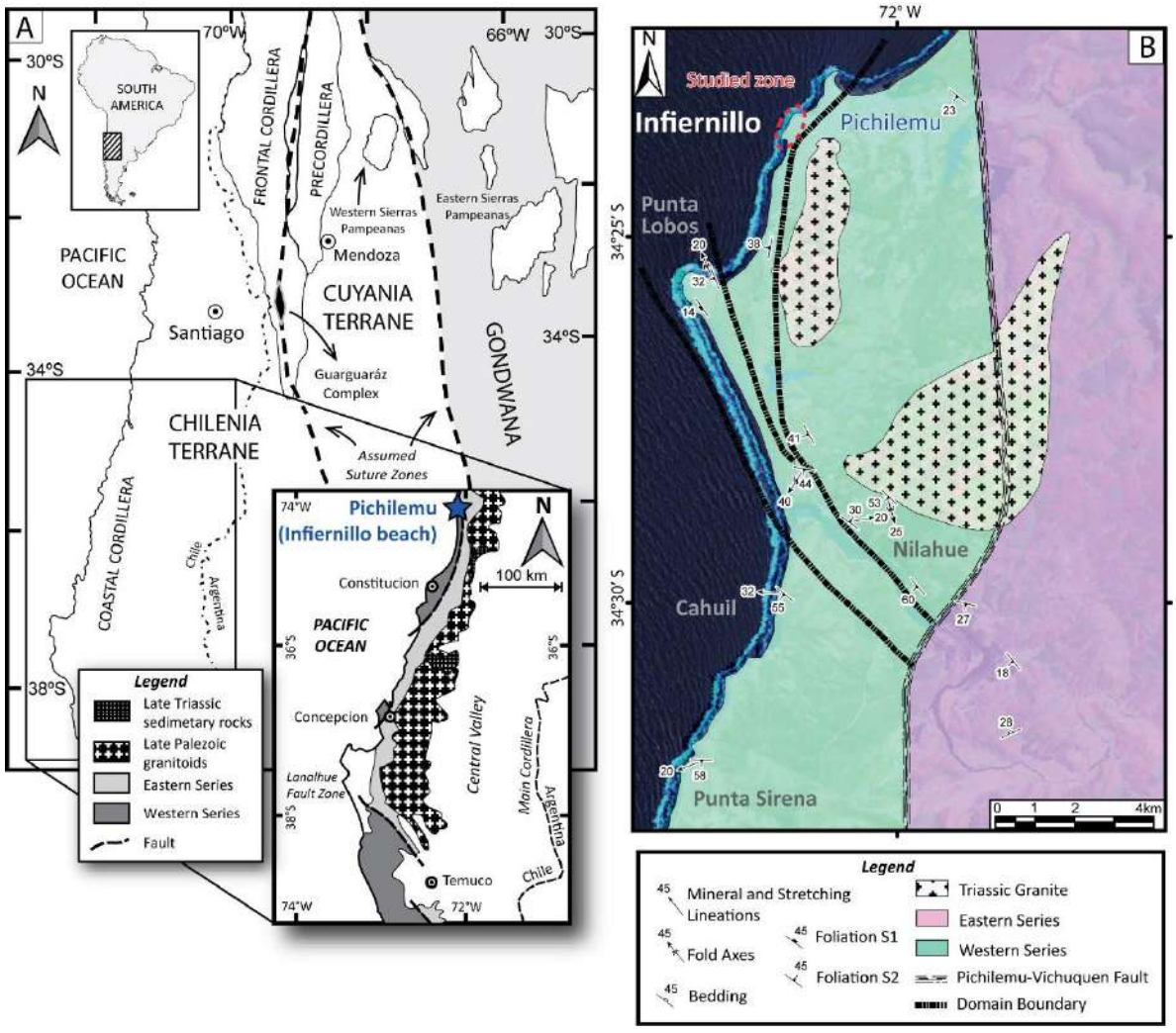

Figure 3.1. A. Geological map of Central Chile and adjacent Argentina including important geological features. The location of the Western and Eastern series is after Willner et al. (2004). For details regarding Chilenia and Cuyania Terranes in the framework of the Gondwanan margin during late Palaeozoic times the reader is referred to Hervé et al. (2013) and references therein. In the inset, the white areas correspond to Mesozoic and Cenozoic covers. B. Geological map of the studied zone after Hyppolito et al. (2014a).

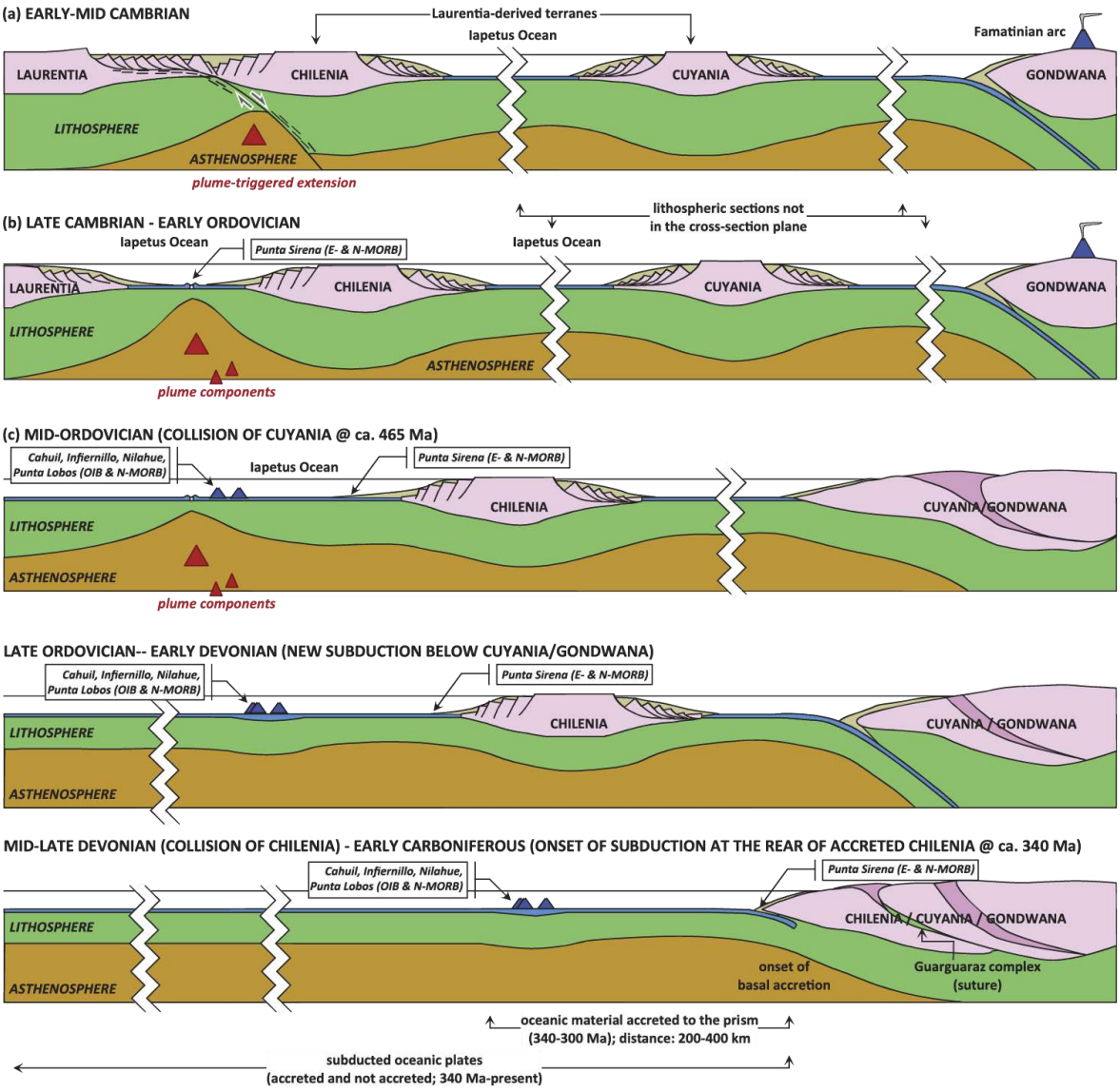

Figure 3.2. Sketch depicting the Palaeozoic geodynamic evolution of the southwestern margin of Gondwanaland emphazising the Chilenia terrane and adjacent oceanic realm (after Hyppolito et al., 2014a). The location of the former Infiernillo and in particular Punta de Lobos are purely schematic.

3.2 Geology of South-Central Chile with an emphasis in the Pichilemu region

Well-preserved remnants of the metamorphic basement and related magmatic complexes that developed during the Gondwanan Orogeny (***Figures 3.1A*** and ***B***), are now exposed in South-Central Chile (32 to 42 °S). These rocks make up an almost continuous metamorphic belt limited to the east by the Coastal Batholith and to the west by the Pacific Ocean. Early works from González-Bonorino (1970, 1971) and González-Bonorino and Aguirre (1970) identified the Curepto, Nirvilo and Pichilemu "series" or metamorphic belts. Nowadays, the most accepted terminology was proposed by Godoy (1970) and Aguirre et al. (1972) who subdivided the metamorphic complex into the juxtaposed Western and Eastern series, as depicted by contrasting PT metamorphic gradients (***Figures 3.1A*** and ***B***). Both series define a N-S elongated paired metamorphic belt in the sense of

Miyashiro (1961), in which the Western series represents the high pressure-low temperature (HP-LT) part of the belt while the Eastern series the low pressure-high temperature (LP-HT) counterpart. The Eastern series is mostly composed of turbiditic metagreywackes and minor calcsilicates in stratigraphic continuity, representing the forearc portion of a retro-wedge system (Hervé et al., 1988; Willner et al., 2001). Such lithologies are interpreted as frontally-accreted, former passive margin sediments scrapped off at the earliest stages of accretion at c. 340 Ma (Aguirre et al., 1972; Hervé et al., 1988; Glodny et al., 2008; Hyppolito et al., 2014b). A LP-HT thermal imprint affected the Eastern Series, as a result of the intrusion of a Late Paleozoic batholith (González Bonorino, 1971; Hervé, 1977). The latter now constitutes the Coastal Range of Central Chile and generated an increasingly high metamorphic grade towards the intrusive body, which locally reached transitional amphibole-granulite-facies at c. 305 My ($^{207}Pb/^{206}Pb$ ages; Willner et al., 2005; Willner, 2005). The end of the magmatic activity is recorded by late granitoids that yielded U-Pb and Rb-Sr ages from 257 to 220 Ma (mineral and whole rock; Lucassen et al., 2004; Willner et al., 2005) and have been associated with the retreat of the subducting slab, thus, marking the end of the tectonic cycle.

In this thesis, we focus on the HP-LT Western series that crops out in the Pichilemu city and its surroundings within the frame of the Coastal Range of Central Chile (***Figure 3.1A***), specifically in the Infiernillo locality (***Figure 3.1B***; 34° 23’ 30” S, 72° 1’ 30” W). There, the Western series corresponds to a coherent NE-NNE oriented blueschist-facies meta-volcanosedimentary sequence composed by a mixture of continent-derived metasedimentary rocks (Willner et al., 2005), metapyroclastic rocks, metalavas and metapillow lavas (Hervé, 1988; Hyppolito et al., 2014b), interpreted as a subduction-related complex (Hervé et al., 1976; Hervé, 1977; Hervé et al., 1981; Forsythe, 1982). The mafic metavolcanic materials have been classified as E-MORB, N-MORB and OIB (see ***Figure 3.2***; e.g., Hervé et al., 1984; Willner, 2005; Hyppolito et al., 2014a), the latter signature particularly important in Infiernillo metavolcanics interpreted as scraped off slices at the uppermost section of the subducted slab (Willner, 2005; Hyppolito et al., 2014a). $^{40}Ar/^{39}Ar$ plateau ages in phengite defining the main foliation in blueschists and metapsammopelites from the Wester Series range between 292 ± 1 Myr and 308 ± 1 Myr, interpreted as the age of the high-pressure basal accretion stage and the development of the ubiquitous main foliation S2 (Willner et al., 2005; see below for further details). The same method applied in phengite lining microfolds resulted in ages ranging from 259 to 329 Myr interpreted as retrograde crystallization during cooling and exhumation (Willner et al., 2005). The metabasites yielded peak metamorphic conditions of 0.75-0.80 GPa at 380-420 °C (Hyppolito, 2014; see **Chapter 4** for further details) in the transition from greenschist- to blueschist-facies, followed by an incipient greenschist-facies overprint. Recent petrological studies including multi-equilibrium calculations have demonstrated that the maximum P-T conditions attained in the Western Series along different locations further south, reached amphibolite- to eclogite-facies, which translates into maximum burial depths of around c. 60 km down deep in the subduction channel (Los Pabilos: e.g., Kato et al., 2008; Punta Sirena: Hyppolito et al., 2014b; La Cabaña: Plissart et al., 2019). Kato and Godoy (1995) observed a blueschist-facies mineral assemblage overprinting an earlier prograde amphibolite-facies metamorphism, while Willner et al.

(2004) suggested a counter-clockwise metamorphic trajectory that has been interpreted as resulting from a protracted sequence of subduction initiation and further isobaric cooling (see also Willner et al., 2005 and Hyppolito et al., 2014b) The HP-LT events were contemporaneous with the intrusion of the arc-related granitoids that caused the HT imprint in the Eastern Series at c. 305 Ma (U-Pb zircon; Willner et al., 2005).

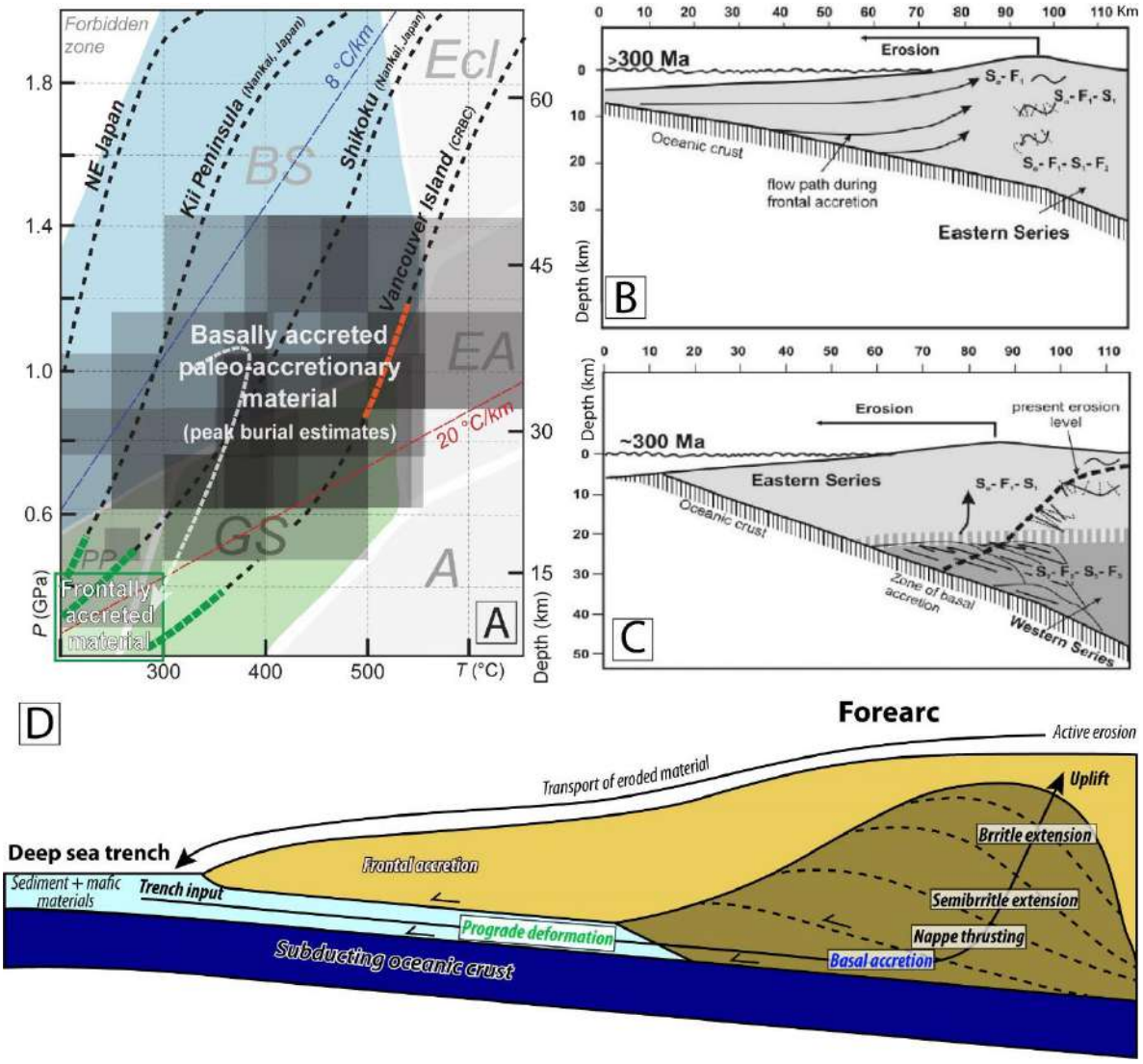

Figure 3.3. A. P-T diagram showing peak metamorphic conditions of basally accreted slivers compiled from 25 localities within circum-Pacific paleo-accretionary wedges. In addition, active basal (Orange dashed lines) and frontal accretion (green dashed lines) conditions from modern margins are depicted (see Angiboust et al., in press for further details and references). B and C. Tectonic evolution model during Late Palaeozoic times empahasizing frontal (B) and basal (C) modes of accretion for the Eastern and Western Series, respectively (after Richter et al., 2007). D. Illustration summarizing the main findings of mass transfer patterns during basal accretion after 2-D sandbox simulations, based on the Western Series from the South-Central Chilean Margin (modified from Glodny et al., 2005).

The transition from the Western towards the adjacent Eastern series has been preliminarily considered as a deep structural discontinuity referred as the "Coastal Suture Zone" (Ernst, 1975). Recently, the Vichuquén-Pichilemu fault (***Figure 3.1B***), which separates the HP-LT and the LP-HT series, has

been interpreted by Willner et al. (2005) to represent a brittle strike-slip fault developed during Cretaceous times instead of a suture zone as suggested by Ernst (1975), while Kato and Godoy (2015) pointed that some of the mélange-like fabric at Infiernillo and further south, may be the result of transpresional faulting tectonics. However, further investigations have suggested that the contact is indeed transitional, characterized by an increment in the penetrative deformation towards the Western series (Hervé, 1988). A main tectonic, sub-vertical foliation at the Eastern Series changes gradually towards a sub-horizontal main foliation S2 (Richter et al., 2007). In the Western Series, the S0 structures are parallel to the S1 foliation, and have been associated with depositional sedimentary and early subduction-related structures, respectively. The S2 represents the transposition main foliation developed during basal accretion. These fabrics are variably overprinted, depending on the competence of the affected lithology, developing a cleavage S3 which resulted from differential crenulation and further cleavage development likely during exhumation (e.g., Richter et al., 2007; Hyppolito et al., 2014a). The progressive structural evolution has been interpreted as different styles of deformation due to a non-steady tectonic regime affecting the accretionary wedge, resulting in changes in the mode of accretion from frontal to basal accretion, being the HP-LT metamorphism the marker of basal accretion (underplating; Willner, 2005; Richter et al., 2007; ***Figures 3.3A, B*** and ***C***). The progressive stack of slices during basal accretion site and nearly coaxial deformation allowed the formation of an antiformal deep duplex and the subsequent exhumation and erosion of the forearc (Willner et al., 2005; Glodny et al., 2005; ***Figure 3.3D***). The deep Western series duplex system is considered as an archetype of long-lived basal and frontal accretion processes that allow to understand the long-term underplating and forearc dynamics (Menant et al., 2019).

3.3 Geodynamic evolution of South Iran with emphasis in the Zagros orogeny and related ophiolitic rocks

The Zagros orogen, whose highest topographic point is the Dena Mount (c. 4400 m.a.s.l), is the largest mountain range in Iran, extending for more than 3000 km from Turkey to the westernmost part of the active Makran subduction system (***Figure 3.4A***; McCall and Kidd, 1981; Platt et al., 1988). This mountain range is considered as an analogue to the Himalayas range and, at the same time, regarded as an Alpine collision zone (e.g., Agard et al., 2005). Despite its increasingly recognized geological value in understanding the Alpine orogeny and geodynamic evolution of the Mesozoic Eurasian margin to present-day Asia continent, the Zagros orogen has been poorly characterized compared to the Himalayas and the Alps. In the contect of the Zagros collision, the oceanic realm corresponds to the Neo Tethys Ocean (e.g., Berberian and King, 1981; Dercourt et al., 1986; Barrier and Vrielynck, 2008) that once separated Eurasia from Arabia, the latter representing a former fragment of the Gondwana continent. The initiation of this collision event is debated, ranging from the Late Cretaceous to Paleogene (Stöcklin, 1968; Berberian and King, 1981). Nowadays, it seems to be a rough consensus on a Paleogene timing for the initiation of the collision (e.g., Jolivet and Faccenna, 2000; Agard et al., 2005), which is still active at convergence velocities in the order of 30 mm/yr (Vernant et al., 2004).

According to structural-deformational as well as orographic patterns, the Zagros orogen has been subdivided into sub-parallel tectonostratigraphic sequences, from SW to NE: the Zagros foreland basin, the Simply Fold Belt, the High Zagros, the Sanandaj–Sirjan zone (SSZ) and the Urumieh-Dokhtar magmatic province (UDMA; ***Figure 3.4B***). The Zagros Simply Fold Belt is a folded and thrusted belt comprising Arabian plate lithologies such as Proterozoic sediments and whose deformation was likely associated with a salt evaporitic décollement fault (e.g., Molinaro et al., 2005; Mouthereau et al., 2007). The High Zagros is similar to the fold and thrust belt but with subtle structural differences, remarkably, higher temperature of deformation. This structural domain is limited to the north by the Main Zagros Thrust (***Figure 3.4B***; see below) (Berberian and Berberian, 1981; McQuarrie and Van Hinsbergen, 2013).

The SSZ represents the southwestern part of the Euroasian continent considered as an Andean-like arc and comprises Mesozoic calc-alkaline magmatic rocks as well as fragments of the Tethyan margin (e.g., Stöcklin, 1968; Agard et al., 2006). Ultramafic lithologies, thought to represent the subcontinental forearc mantle, are also found therein (Shafaii Moghadam and Stern, 2011). On the other hand, the UDMA comprises tertiary calc-alkine magmatic rocks (Berberian and Berberian, 1981) emplaced in the upper plate within the SSZ during Jurassic to Eocene times (Alavi, 1994), representing an evidence of active subduction processes at least since Jurassic times associated with subduction of the Neo-Tethys oceanic realm. The occurrence of adakitic magmatism, with ages younger than c. 10 Ma (e.g., Jahangiri, 2007) in the UDMA, led to Omrani et al. (2008) to suggest slab break-off of the subducting plate below the Zagros orogen. Note that the SSZ shows no evidence of HP-LT metamorphic overprint, at least during the Zagros orogeny (e.g., Omrani et al., 2008; Agard et al., 2011).

The suture of the collision event between Eurasia and Arabia is depicted as the Main Zagros Thrust (e.g., Stöcklin, 1986; Agard et al., 2006; Paul et al., 2010): a tectonic plate boundary that reaches the mantle and is associated with ophiolites and ophiolitic lithologies, among them, the herein studied Seghin blueschists (see below; Sabzehei et al., 1974; Agard et al., 2006; Paul et al., 2010). In the Hajiabad-Esfandagheh region (e.g., ***Figures 3.4A*** and ***C***; Sabzehei, 1974) are exposed the rare HP-LT metamorphic rocks witnessing for a Cretaceous subduction event in the Eurasia margin. The geodynamic evolution of this suture and related collisional event has been summarized by Agard et al. (2011; see also **Appendix B**) as: (1) Neo Tethys Ocean opening due to a Permian rifting stage. (2) Onset of subduction during Lower Jurassic times as evidenced by arc magmatism in the SSZ and the occurrence of the oldest oceanic rocks accreted to the upper plate at c. 180Ma, comprising now the Zagros suture (Arvin et al., 2007; Moghadam et al., 2017). (3) Extension in the Eurasian continental margin resulting in extensional back arc basin opened around 105 to 70 Ma (Arvin and Robinson 1994; Moghadam et al., 2013). Concurrently, subduction and exhumation of HP rocks at c. 113 Ma until c. 60 Ma (Monié and Agard, 2009; Angiboust et al., 2016; this study **Appendix B**). (4) Migration of the magmatic front towards the UDMA at c. 50 Ma and further onset of collision at Late Eocene or younger (Agard et al., 2005). The stage 3 of this summary is illustrated in ***Figure 3.5A*** with

emphasis on Hajiabad-Esfandagheh metamorphic rocks, since they are relevant for the purpose of this thesis.

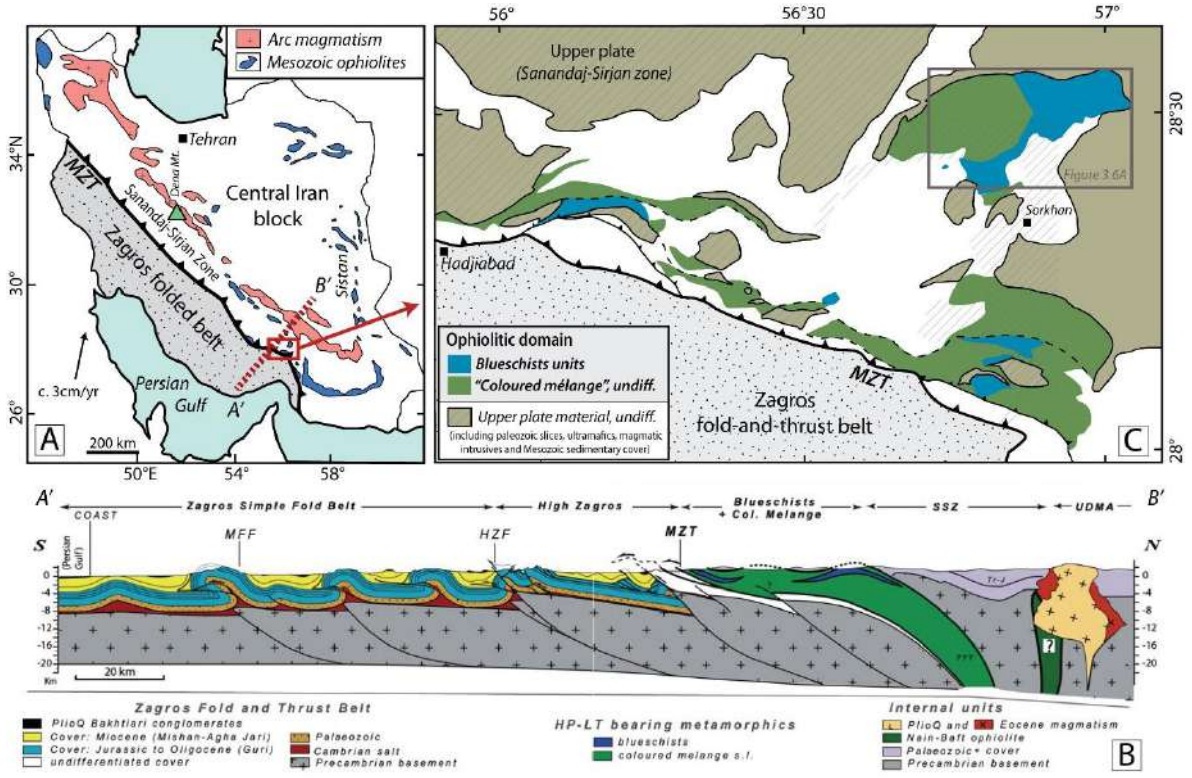

Figure 3.4. A. Simplified geological map of the Iranian region with emphasis in the Mesozoic ophiolites and arc mamgmatic complexes (after ShafaiiMoghadam and Stern, 2011 and Angiboust et al., 2016). The inset represents a zoom in the studied region. B. NE-SW cross-section (see red transect in panel A) of southern Iran (after Agard et al., 2006) highlighting the architecture of the Zagros fold and thrust belt and the internal zones. C. Hajiabad-Esfandagheh region depicting the occurrence of ophiolitic domains (after Agard et al., 2006 and Angiboust et al., 2016). HZF – High Zagros fault; MFF – Main front fault; MZT – Main Zagros Thrust.

3.4 Geology of the Hajiabad-Esfandagheh metaophiolites

In the Zagros orogen, the only HP-LT witnesses of subduction of the Neo-Tethys ocean under Eurasian continent crop out in the Hajiabad-Esfandagheh region (Sabzehei, 1974; ***Figure 3.6A***). These metamorphic rocks occur as a mega antiformal stack of slices forming a tectonic window below the Sikhoran-Sargaz-Abshur Sikhoran massif (e.g., Agard et al., 2006). Three metamorphic complexes are clearly differentiated in the region according to its structural characteristics, overall fabrics and petrological records which are differentiated by contrasting P-T-t trajectories (e.g., Agard et al., 2006; Angiboust et al., 2016; ***Figure 3.5B***).

Starting with the older and highest temperature member, the Ashin complex forms the uppermost part of the nappe stack which comprises a variably serpentinized, hazburgitic to dunitic ultramafic lithologies (with local chromitite pods and jadeite veins, see Oberhänsli et al., 2007; ***Figure 3.6B***) towards its base. This sequence is overlain by glaucophane-bearing quartzites and strongly strained garnet micaschists with minor amphibolites, marbles and cherts. The uppermost part of the Ashin

complex is composed of an apparently coherent decametre thick garnet-bearing amphibolite and metasedimentary sequence. Agard et al. (2006) and Angiboust et al. (2016) estimated peak conditions around 550 °C (at c. 1.2 GPa) on Ashin garnet micascshits. However, further investigations (presented here as part of **Appendix B**) demonstrate that, based on the finding of leucosomes in the mafic amphibolites, higher temperatures were reached by this complex up to the point of reaching partial melting. The sequence is bounded to the top by a tectonic contact (thrust), comprising strongly sheared serpentinties juxtaposing Ashin against ultramafic lithologies from the Sikhoran-Sargaz-Abshur massif. Ages of the peak amphibolite-facies range between 79 to 136 Ma (using multi-mineral and whole rock K/Ar, Ar-Ar and Rb-Sr isochron ages; see Ghasemi et al., 2002; Delaloye and Desmons, 1980; Agard et al., 2006; Angiboust et al., 2016 and Shafaii Moghadam et al., 2017 for further details regarding dating methods). However, none of these studies considered the presence of partial melts and further investigations are needed to refine the metamorphic history and associated

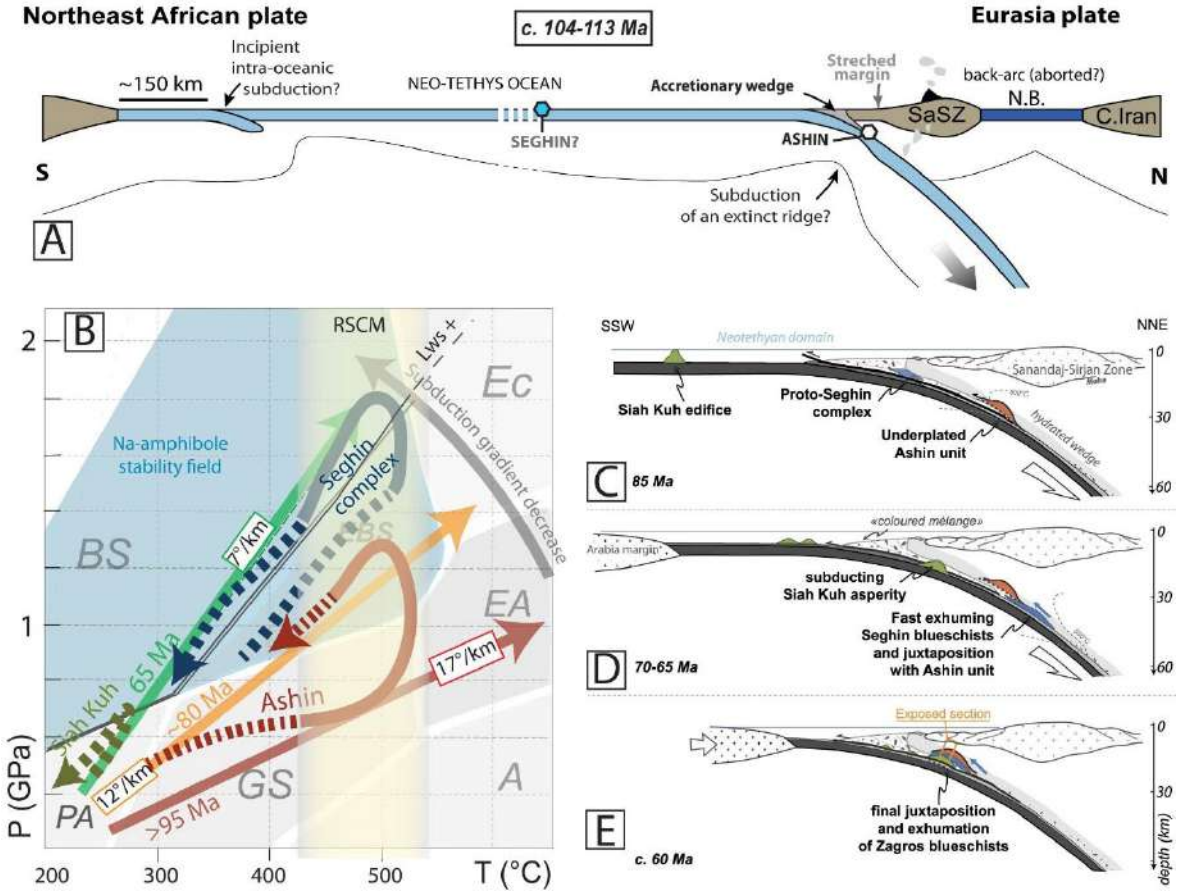

Figure 3.5. A. Illustration depicting the geodynamic framework across the Tethyan realm showing the subduction accretionary complex, a back-arc basin and a speculated ridge subduction under the SSZ at c. 104-113 Ma (Modified from Burg, 2018 and Bonnet et al., 2020; see also Appendix B). B. P-T-t grid depicting the cooling of the subduction thermal gradient along the Zagros subduction zone. Tectonic evolution and juxtaposition of the Hajiabad-Esfandagheh blueschists at (C) c. 85 Ma, (D) 70 to 65 Ma and (E) 60 Ma (after Angiboust et al., 2016). For more details, see the main text of this thesis. The metamorphic grid is after Evans (1990). A—amphibolite-facies; BS—blueschist-facies; EBS—epidote blueschist-facies; EA—epidote amphibolite-facies; Ecl—eclogite-facies; GS—greenschist-facies; PA—pumpellyite actinolite-facies.

geodynamics. A blueschist-facies overprint affected the earlier HT stage (Agard et al., 2006; Angiboust et al., 2016) as evidenced by the occurrence of riebeckite and omphacite overgrowths and the herein documented presence of lawsonite in the leucosomes (**Appendix B**).

Underlying the Ashin complex and in tectonic contact is located the Seghin complex (***Figure 3.6A*** and ***B),*** the main focus of this thesis and, for this reason, the reader is referred to **Chapters 5** and **7** for a more detailed characterization. Its main fabric is characterized by an antigorite-rich matrix wrapping hectometre-sized lawsonite blueschist blocks (block-in-matrix mélange) associated with minor marbles, calcschists and metapelites (e.g., Angiboust et al., 2016). Widespread aragonite + lawsonite-bearing veins occur therein (Angiboust et al., 2016). Such geological structures are the cornerstones of this investigation (see **Chapter 5** and **7**). The age of the peak blueschist-facies metamorphism (1.6-1.8 GPa at c. 430-520 °C), as inferred by multi-mineral and whole rock Rb-Sr dating, is in the range of 62 to 75 Ma (Angiboust et al., 2016), while an older Ar-Ar age of c. 80 Ma may represent excess argon (Monié and Agard, 2009). The peak metamorphic assemblage is only locally retrogressed or even devoid of further exhumation-related overprints, representing thus one of the best-preserved blueschist-facies assemblages on Earth. Although according to Angiboust et al. (2016) all the blueschist blocks from the Seghin mélange record similar upper blueschist-facies metamorphism, we note, based on this investigation, that some of the blocks record lower-blueschist-facies conditions. The significance of these blocks is detailed in **Chapter 7**, but it is likely that they may represent exotic blocks incorporated to the tectonic mélange during the return flow and further exhumation.

The lowermost Siah Kuh unit (***Figure 3.6B***) is part of what is referred in literature to as the "Coloured Mélange" (Stöcklin, 1974). It consists of a kilometre-sized ophiolite metamorphosed to incipient blueschist-facies conditions in the range of 200-300 °C and 0.5-0.9 GPa, allowing the preservation of primary magmatic and sedimentary features (Bonnet et al., 2020b). This massif has been recently interpreted as a subducted seamount accreted against the Iranian margin, more precisely below the Seghin complex during early Cenozoic times (Bonnet et al., 2020a). The magmatic rocks comprise pillow, hyaloclastites and breccias of basaltic composition as well as felsic sub volcanic intrusions overlaid by a limestone-sedimentary cover, the latter representing shallow platform environments deposited at c. 70 Ma (Sabzehei, 1974). Even though this volcanic edifice is largely undisturbed, some subduction-related features include (i) shearing of the pillow lavas, (ii) folding of the sedimentary cover, (iii) thrusting along pelagic sequences acting as decollement level, (iv) formation of HP mineral assemblages such as lawsonite, pumpellyite, sodic amphibole, sodic pyroxene and aragonite and (v) lawsonite-bearing extensional veins. Although out of the main scope of this work, one point of particular relevance is the finding of "only" one pseudotachylyte vein showing displacement in the order of up to tens of centimetres. According to Bonnet et al. (2019), this may be the record of a single <3 Mw earthquake within the lower blueschist-facies as evidenced by the presence of HP glaucophane and phengite. Based on these observations, the authors concluded that

subducted seamounts act as barriers rather than asperities, hampering earthquake nucleation and propagation.

As noted above, the contrasted P-T trajectories as well as spread in metamorphic ages were integrated in a model involving a long-lasting cooling of the subduction thermal gradient ranging from high temperature amphibolites towards lawsonite blueschist-facies rocks (***Figure 3.5A***; e.g., Angiboust et al., 2016; see also the **Appendix B** of this study). In this model (***Figures 3.5C*** to ***E***), the architecture of the aforementioned three metamorphic complexes resulted from tectonic slicing and accretion of apparently coherent oceanic materials subducted at different depths under a decreasing thermal gradient. First, the Ashin complex subducted and got accreted to the upper plate at c. 35 km depth (c. 85 Ma). Concurrently, the Seghin complex was just entering in the subduction factory while the Siah Kuh seamount was still occupying a seafloor position. The second stage involved attainment of peak higher blueschist-facies conditions (c. 55 km depth) in the Seghin slice and further return flow (or exhumation in the model of Angiboust et al., 2016) approaching the site of accretion of the Ashin complex at c. 30 km depth (at c. 75-65 Ma). Synchronously, the Siah Kuh seamount was likely just entering in the subduction zone. The last stage involves the juxtaposition of the three tectonic slices at maximum depths of 25-30 km, as delimited by peak conditions of the Siah Kuh unit and further exhumation and migration of the shear zone towards another downward thrust. During all these processes of subduction, accretion and exhumation, a progressive cooling of the subduction environment from c. 17 to 7 °C/km took place, as also observed with slightly different temperature values in the Franciscan complex (e.g., Grove and Bebout, 1995; Cooper et al., 2011) – a metamorphic complex sharing similarities with modern Mariana-type subduction margins (e.g., Stern and Bloomer, 1992). This cooling event has been considered as the product of convergence acceleration due to a Cretaceous plate reorganization event or, subduction of an “old” oceanic lithosphere (e.g., Peacock, 1996; Agard et al., 2011; Angiboust et al., 2016).

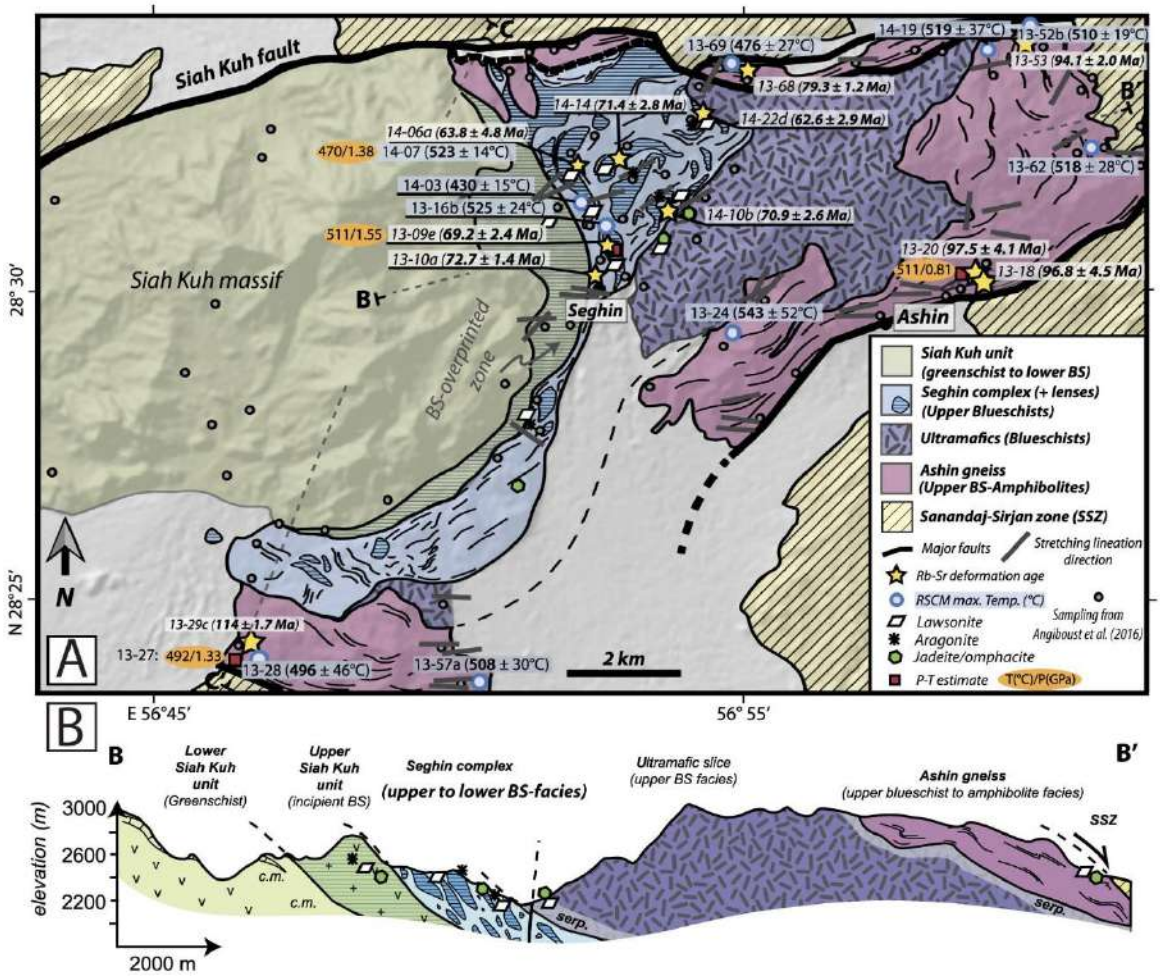

Figure 3.6. A. Geological sketch of the Seghin area depicting general features among the different tectonic slices as well as the sampling localities. B. Geological cross-section (B to B' in panel A) showing the different slices comprising the nappe-stack of blueschist-, amphibolite- and greenschist- facies lithologies in the studied region. Both panels are from Angiboust et al. (2016).

4. Multiple veining in a paleo-accretionary wedge: The metamorphic rock record of prograde dehydration and transient high pore fluid pressures along the subduction interface (W. Series, central Chile)

Muñoz-Montecinos et al. (2020)

Multiple veining in a paleo-accretionary wedge: The metamorphic rock record of prograde dehydration and transient high pore fluid pressures along the subduction interface (W. Series, central Chile)

Jesús Muñoz-Montecinos[1,2], Samuel Angiboust[1], Aitor Cambeses[3], Antonio Garcia-Casco[2,4]

[1] Université de Paris, Institut de physique du globe de Paris, CNRS, F-75005 Paris, France, jesus.munozmontecinos@gmail.com; angiboust@ipgp.fr

[2] Department of Mineralogy and Petrology, Faculty of Sciences, University of Granada, Campus Fuentenueva s/n, 18002 Granada, Spain, agcasco@ugr.es

[3] Institut für Geologie, Mineralogie and Geophysik Ruhr-Universität Bochum, Germany, aitor.cambeses.rub.de

[4] Instituto Andaluz de Ciencias de la Tierra, CSIC-Universidad de Granada, 18100 Armilla, Granada, Spain.

Published in: Geosphere (2020) 16 (3): 765–786

Reference: Jesús Muñoz-Montecinos, Samuel Angiboust, Aitor Cambeses, Antonio García-Casco; Multiple veining in a paleo–accretionary wedge: The metamorphic rock record of prograde dehydration and transient high pore-fluid pressures along the subduction interface (Western Series, central Chile). Geosphere 2020; 16 (3): 765–786.

DOI: https://doi.org/10.1130/GES02227.1

Journal Impact Factor (IF): 2.577

WoS Quartile: Q2 (Geosciences, Multidisciplinary)

ABSTRACT

High pressure-low temperature metamorphic rocks from the late Paleozoic accretionary wedge exposed in central Chile (Pichilemu region) are characterized by a greenschist-blueschist lithological association with interbedded metasediments which reached peak burial conditions of c. 400 °C and 0.8 GPa during late Carboniferous times. We herein combine new extensive field observations, structural measurements, geochemical and petrological data on vein and matrix material from Pichilemu transitional greenschist-blueschist facies rocks. The studied veins were first filled by albite followed by quartz and calcite as well as glaucophane and winchite. Field, structural and microscopic zoning patterns show that these rocks underwent a protracted sequence of prograde vein opening events, which have been largely transposed to the main foliation before and during underplating in the basal accretion site near 25 - 30 km depth. While some of the earliest albite-filled vein sets may have formed after prograde breakdown of sub-greenschist facies minerals (below 250 °C), our thermodynamic modeling shows that relatively minor amounts of fluid are produced in the subducted pile by dehydration reactions between 250 and 400 °C along the estimated geothermal gradient. It also confirms that the formation of interlayered blueschist and greenschist layers in Pichilemu metavolcanics is a consequence of local bulk composition variations and that greenschists are generally not formed due to selective exhumation-related retrogression of blueschists. The early vein sets are a consequence of prograde internal fluid production followed by sets of hydrofractures formed at near-peak burial that are interpreted as a record of external fluid influx. We postulate that such fractured sequence represents a close analogue to the high V_p/V_s regions documented by seismological studies within the base of the seismogenic zone in active subduction settings.

4.1 Introduction

Blueschist-facies metamorphic rocks exhumed from ancient subduction interfaces enable documenting and understanding fluid-rock interaction occurring near the downdip end of the seismogenic zone (Bebout and Barton, 1993, Halama et al., 2014; Angiboust et al., 2015) where episodic tremor and slow slip events nucleate (ETS and SSE; Obara, 2002; Audet et al., 2009; Peng and Gomberg, 2010). The most obvious marker of fluid transport in metamorphic rocks is vein systems (e.g. Fyfe et al., 1978; Fisher and Brantley, 1992). Their geometry sheds light on the connectivity of fluid pathways as well as on the spatial and temporal scale of the fluid-rock interaction events (Zack and John, 2007). Textures recorded in veins yield information on crack aperture as well as crystal growth kinetics during each veining event (Cox and Etheridge, 1983; Bons, 2001), while vein filling mineral assemblages and fluid inclusions provide a valuable source of information on fluid chemistry and pressure-temperature regimes of fluid migration (e.g. Philippot and Selverstone, 1991; Scambelluri and Philippot, 2001; Raimbourg et al., 2018).

Previous work on metamorphic rocks have demonstrated that the vein-filling material can either be of local origin, resulting from diffusion processes between the host and an almost stagnant fluid produced by local dehydration reactions (e.g. Spandler and Hermann, 2006) or from external provenance, resulting from advective transport over kilometer-scale distances before deposition in the crack (Etheridge et al., 1984; Cartwright and Barnicoat, 1999; Bebout and Penniston-Dorland, 2016; Lewerentz et al., 2017; Jaeckel et al., 2018). Fluid inclusion thermometry has been also used to propose that the fluid phase from which the vein filling material precipitates was warmer than the host, thus advocating for fast advective flow (Vrolijk et al., 1988). While short-distance diffusive transport does not require large scale connectivity, transportation over hundreds or thousands of meters implies the presence of highly permeable pathways such as brittle faults (e.g. Sibson, 2013; Angiboust et al., 2015; Dielforder et al., 2015). Yet, the genetic link between individual veining events, connection of vein networks by larger fault systems and the fate of fluids along the interface over several seismic cycles requires further investigation (e.g. Husen and Kissling, 2001; Fagereng et al., 2010). The relative timing of vein formation with respect to matrix deformation during burial/exhumation as well as the link with paleo-seismic events also requires further documentation (e.g. Dielforder et al., 2015).

Another consequence of fluid/rock interaction at depth is the variable metasomatic imprint that obliterates the original geochemical signature of the affected lithologies (e.g. Harlow and Sorensen; 2005; Vitale Brovarone et al., 2014; Bebout and Penniston-Dorland, 2016). Selective retrogression due to exhumation-related fluid circulation may enhance, in specific cases, the formation of blueschists and greenschists interlayered at centimeter to meter-scale (e.g. Bröcker, 1990; Barrientos and Selverstone, 1993; Halama and Konrad Schmolke 2015). However, many studies have proposed that bulk-rock geochemical differences may lead to the equilibration of cofacial greenschists and blueschists in the subducted material (Dungan et al., 1983; Owen, 1988; Baziotis and Mposkos, 2011; Hyppolito, 2014). Specifically, it has been proposed that Fe_2O_3, Fe/Mg, Na_2O and Na/Ca abundances

can control the occurrence of actinolitic and glaucophanitic amphiboles allowing for the formation of blueschists and/or greenschists (e.g. Dungan et al., 1983; Owen, 1988). This example highlights the importance of accurately constraining the metamorphic conditions of fluid-rock interaction since the consequences in terms of subduction zone fluid budget are drastically different.

Here we study a fully-exposed, exhumed transitional greenschist-blueschist facies segment of a late Paleozoic paleo-accretionary wedge from Central Chile (Pichilemu region) that provides a great opportunity for linking fossil subduction-related markers of fluid mobility such as vein systems together with structures and deformation patterns. The first part of this work aims at determining the controlling factors that result in the occurrence of layered blueschists and greenschists in this region as no consensus exists regarding the origin of this layering, either interpreted as a retrogressive fluid imprint or as a consequence of centimeter-scale bulk-rock composition variations (Hyppolito, 2014; Halama and Konrad-Schmolke, 2015). Resolving this issue is critical for the second part of this study, namely the design of a prograde fluid production model that aims at understanding the chronology of vein-formation events, which will ultimately refine our vision of fluid mobility in active subduction margins.

4.2 Geological setting

In the Chilean Coastal Range, metamorphic rocks formed at the active Paleozoic continental margin representing deformational records of the Gondwanan tectonic cycle are exposed (Hervé, 1988) (***Fig. 4.1***). This tectonic cycle (Late Devonian-Late Permian) is characterized by the subduction of oceanic crust under the continental margin of the southwestern part of Gondwana and formation of accretionary complexes (Ramos, 1988; Willner et al., 2005; Hyppolito et al., 2014a, 2014b), which were intruded by N-S trending syn- and post-accretion subduction-related batholiths (Hervé et al., 2013; Charrier et al., 2015). The remnants of this paleo-accretionary wedge are now preserved in the Eastern (low-pressure) and Western (high-pressure) Series that form an almost continuous metamorphic belt (Aguirre et al., 1972; Hervé, 1988) extending between 34 °S to 54 °S for more than 2000 km (Hervé, 1988; Angiboust et al., 2018) and interpreted as the result of coupled frontal and basal accretion in the subduction system (Richter et al., 2007; Willner et al., 2008).

At the Infiernillo locality (***Fig. 4.1a*** to ***c***), close to Pichilemu city (34° 23’ 30” S, 72° 1’ 30” W), a NE-NNE oriented meta-volcanosedimentary sequence belonging to the Western Series is composed by a mixture of continent-derived metasedimentary rocks (Willner et al., 2005), metapyroclastic rocks, metalavas and metapillow lavas (Hervé, 1988; Hyppolito et al., 2014a). The main tectonic structure is characterized by a sub-horizontal to sub-vertical penetrative foliation S2 that transposes the previous burial-related S1 and D1 fabrics (see below). Importantly, almost all outcrops at the Infiernillo locality show abundant veins ranging in size from millimeter to centimeter-wide that have not been studied in detail so far. Willner et al. (2005) suggested that albite veins (± sodic amphibole) probably reflect precipitation from metamorphic fluids under peak metamorphic conditions. The metavolcanic rocks in the Pichilemu region exhibit relict pillow and hyaloclastite structures (e.g., Hervé et al., 1984; Willner, 2005) and have Ocean Island Basalt (OIB), Enriched-MORB and Normal-

MORB geochemical signatures, suggesting scraped-off sections of the subducting upper oceanic crust (Hyppolito et al., 2014a). These metabasites form meter to decimeter-sized layers of greenschists and blueschists that underwent peak pressure-temperature (P-T) conditions of 0.70 - 0.93 GPa at 380 - 420 °C and 0.95 - 1.07 at 350 - 385 °C, respectively (Willner, 2005). Their contrasting P-T conditions led Willner (2005) to suggest that greenschists and blueschists may represent different sections of the zone of basal accretion in the range from 25 to 40 km depth. At Infiernillo locality, Hyppolito (2014) and Hyppolito et al. (2014a) classified the greenschist and blueschist metavolcanics as mostly OIBs that underwent uniform peak conditions of 0.75 - 0.80 GPa at 380 - 420 °C and emphasized that such conditions correspond to the greenschist-blueschist transition (***Fig. 4.1d***). In contrast, Halama and Konrad-Schmolke (2015) proposed that interlayered greenschist and blueschist pairs are the result of selective retrogression of blueschists in the greenschist facies during exhumation. Retrograde metamorphism was estimated by Willner (2005) and Hyppolito (2014) at conditions of 0.40 - 0.80 GPa at 300 - 380 °C and 0.65 GPa at 360 °C, respectively (***Fig. 4.1d***).

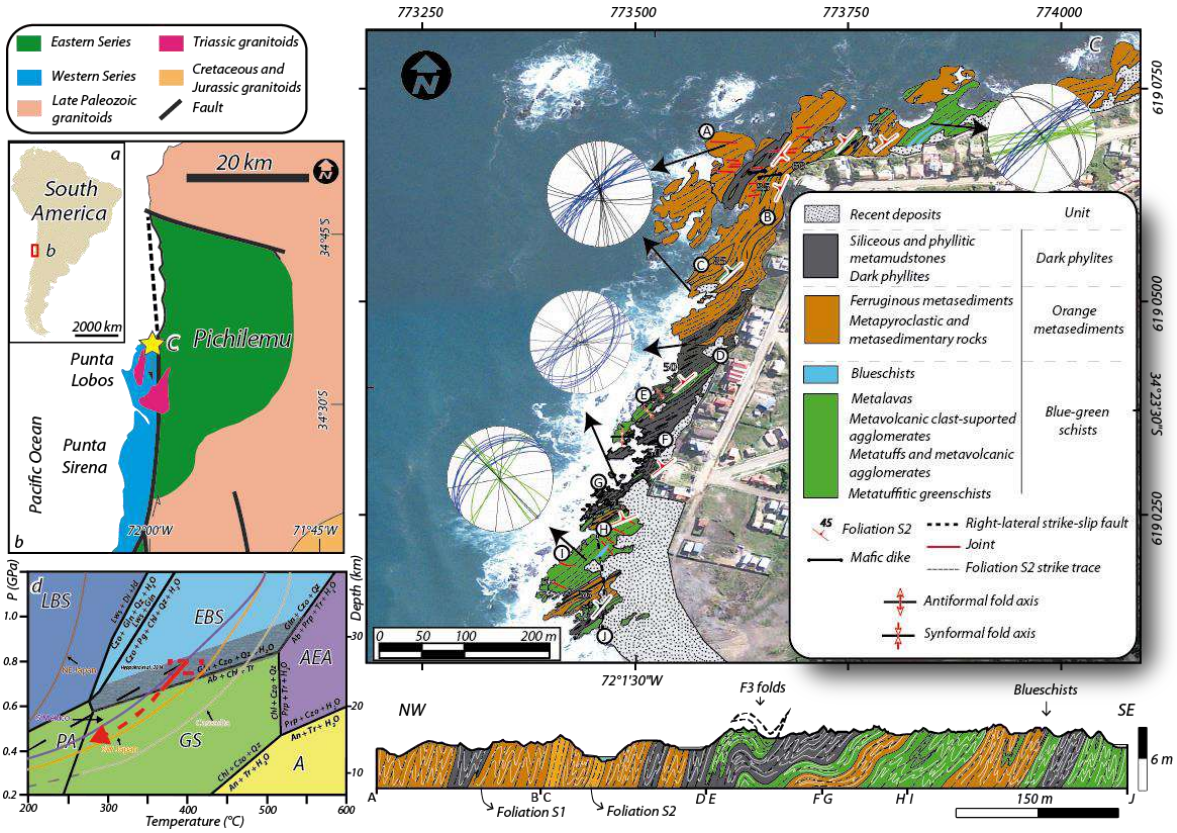

Figure 4.1. a. Location of the studied zone relative to South America. b. Simplified geological map of the Pichilemu region. c. Detailed geological-structural map and cross-section profile of the studied zone (modified from Hyppolito et al., 2014). Blue, green and black planes in the lower-hemisphere, equal-area stereoplots correspond to veins oriented parallel to the main foliation, transposed (oblique section) and cross-cutting veins, respectively. d. P-T diagram showing calculated peak and retrograde metamorphic conditions of the Blue-Green Schists at Infiernillo locality (after Hyppolito, 2014). Dashed black line correspond to a subduction P-T path of 15 °C/km. P-T paths from Cascadia, Japan and Mexico are shown (after Peacock et al., 2002). Background metamorphic grid after Evans (1990). PA – Pumpellyite-actinolite facies, GS – Greenschist facies, A – Amphibolite facies, AEA – Albite-epidote amphibolite facies, EBS – Epidote-blueschist facies, LBS – Lawsonite-blueschist facies. The red solid path corresponds to calculated conditions of Infiernillo (Hyppolito, 2014). The grey-shaded area corresponds to the overlap among stability fields of the different metamorphic facies from Evans (1990).

Hyppolito et al. (2014b) concluded that garnet micaschists and amphibolites from the Western Series (Punta Sirena locality) formed under a hot subduction scenario (up to 16 ºC/km) at c. 340 Myr (^{40}Ar-^{39}Ar amphibole and phengite ages) representing the earliest stages of the subduction event. Phengite ages from mature subduction blueschists and metapsammopelitic rocks from the Western Series yielded ages ranging between 292 ± 1 Myr and 308 ± 1 Myr (^{40}Ar/^{39}Ar plateau ages), interpreted as reflecting the peak of the high-pressure (HP) metamorphism and the formation of the transposition foliation (S2 in Willner et al., 2005). In addition, in situ ^{40}Ar/^{39}Ar UV laser ablation ages in microfolds yielded variable ages ranging between 329 to 259 Myr with differences in individual samples of 32 - 44 Myr. These values were considered as retrograde mineral growth and recrystallization events during exhumation-related pressure release and slight cooling (Willner et al., 2005). U-Pb zircon ages of c. 305 Myr were obtained in subduction-related granitoids intruding the Eastern Series (Willner et al., 2005). The HP event of the Western Series and the main pulse of the magmatic activity and low-pressure metamorphism of the Eastern Series were therefore considered as coeval by Willner et al. (2005). The sequence has been lately intruded by granitoids which yielded U-Pb zircon and Rb-Sr mineral and whole rock isochron ages between 257 and 220 Myr (Lucassen et al., 2004; Willner et al., 2005) and considered as the late magmatic activity associated with the retreat of the subducting slab.

4.3 Field observations

4.3.1 General Structure

Petrological and structural observations at Infernillo locality led to the identification of three coherent intercalated units: a) Blue-Green Schists, b) Dark Phyllites and c) Orange Metasediments (***Fig. 4.1c; Fig. 4.2a***). The Blue-Green Schists unit is characterized by abundant metatuffs, metalavas and metapillow lavas metamorphosed under high pressure-low temperature (HP-LT) transitional greenschist-blueschist facies (***Fig. 4.1d; Fig. 4.2a*** to ***d***; Willner et al., 2005; Hyppolito et al., 2014a; Hyppolito, 2014). Blueschists and greenschists occur intercalated at centimeter to meter scale (***Fig. 4.2c***). Massive decameter sized bodies of metabasalts are present in the Infernillo locality and also further to the south (Punta Lobos locality). Blue rims in metapillow lavas and epidote-bearing veins in the interpillow space reflect spilitization during sea-floor fluid/rock interaction (***Fig. 4.2b***). Evidence for HP-LT metamorphism event is attested by the ubiquitous presence of Na-amphibole as cores, rims and euhedral pristine crystals in the blueschist and greenschist host rock and vein domains (***Fig. 4.2d***). Previous works have suggested that the peak metamorphic event occurred related to underplating and basal accretion processes allowing the formation of a sub-horizontal transposition main foliation S2 and intrafolial isoclinal folds, the later corresponding to remnants of a (poorly-preserved) prograde, S1 foliation (Glodny et al., 2005; Richter et al., 2007; Hyppolito, 2014; ***Fig. 4.2a***). The main foliation structure is heterogeneously folded (F3) allowing a crenulation cleavage S3 much more developed in the Dark Phyllites, likely related with exhumation (Richter et al., 2007). Local S-C mylonitic fabrics suggest a non-coaxial kinematic regime.

The Dark Phyllites unit (***Fig. 4.2e***) corresponds to a strongly foliated sequence of phyllites with abundant carbonaceous (graphitic) matter and vein networks oriented mostly parallel to the main foliation (***Fig. 4.2e***). Thermometric studies based on Raman spectroscopy of organic matter indicate peak metamorphic temperatures of 400 ± 50 °C (S. Angiboust, unpublished data), in agreement with the previous estimates of Hyppolito (2014). The Orange Metasediments unit is a metasedimentary sequence with abundant iron oxides and stilpnomelane giving its characteristic orange-reddish color. The protoliths correspond to felsic pyroclastic rocks, conglomerates, breccias with volcanogenic fragments, quartzite, cherts and sandstones, most of them representing terrigenous trench filling sediments supplied from the overriding continental crust (e.g. Willner, 2005). As in the previous cases, the main structural fabric is a well-developed foliation S2 comprising abundant veins oriented parallel to the main foliation (***Fig. 4.S1a***). Interestingly, quartzite boudins stretched parallel to the main foliation are wrapped by metatuffs from the Blue-Green Schists (***Fig. 4.S1e***). Field markers of potential co-seismic deformation such as pseudotachylytes and cataclasites (e.g. Fagereng and Toy, 2011; Angiboust et al., 2015) were not observed. Some albite veins exhibit brittle deformation overprinted by transitional greenschist-blueschist facies ductile shearing (***Fig. 4.2f***). In many cases such prograde brittle features have been erased due to deformation during peak to retrograde metamorphism.

4.3.2 Structure and Distribution of Vein Networks

Three main vein sets were identified after structural characterization (stereonets shown in ***Fig. 4.1c***). In the Blue-Green Schists, the most abundant set corresponds to centimeter to tens of centimeters-wide veins oriented parallel to the main foliation (blue planes in ***Fig. 4.1c***) which contains albite + quartz + calcite ± amphibole (***Fig. 4.2d***). The distribution of these minerals is heterogenous, ranging from complex veins containing all the aforementioned minerals to almost monomineralic veins. Additionally, veins of this type have been boudinaged (***Fig. 4.S1b***) as a consequence of shearing likely during subduction (see below). No relationship was observed between vein density and the nature of the blueschist or greenschist host as well as no retrogression is present in wall-rock adjacent to veins. Millimeter to tens of centimeter-wide quartz ± albite ± calcite veins occur in the Dark Phyllites and Orange metasediments following the main foliation (e.g. ***Fig. 4.2e; Fig. 4.S1a***). These veins are heterogeneously distributed, showing striking differences in abundances at centimeter scale or in adjacent lithotypes (***Fig. 4.S1c*** and ***d***). A second vein set is present in the Blue-Green Schists and Dark Phyllites. Its mineral assemblage is similar to the first vein set. This vein set is distinguished from the first vein set by the fact that these planes clearly exhibit re-orientation due to shearing (see green planes in ***Fig. 4.1c***). They systematically exhibit segments of the veins that obliquely cut across the main foliation (as shown on the stereographic projections in ***Fig. 4.1c***). We refer here as transposed veins for this category (***Fig. 4.2f***; see discussion). The third set of millimeter to centimeter-wide quartz-rich veins occurs nearly perpendicular to the main foliation (see black planes in ***Fig. 4.1c***). No clear cross-cutting relationship was observed between transposed and foliation-parallel

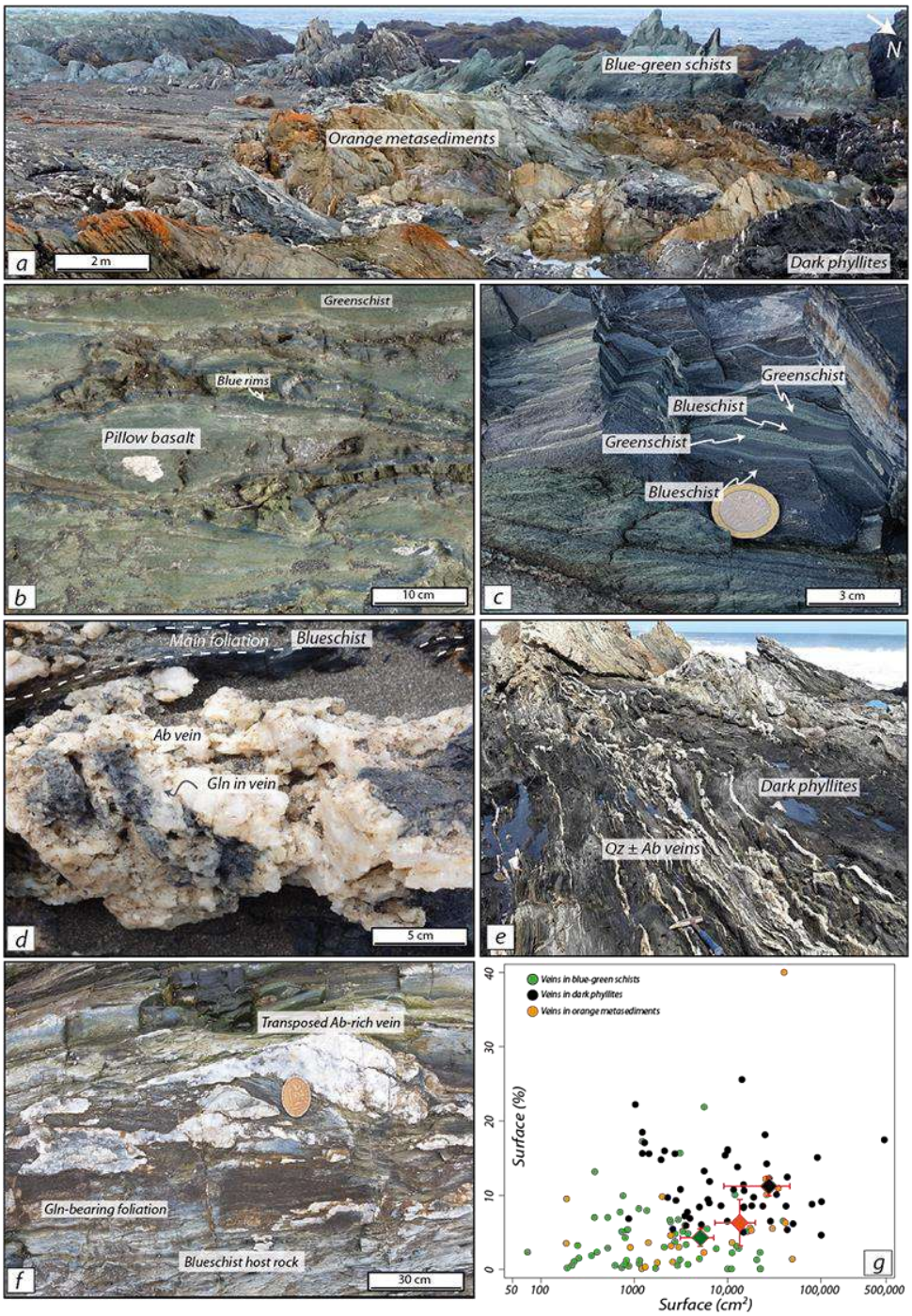

Figure 4.2. a. General views of Infiernillo exposures; note the complex relationship between the Blue-Green Schists, Dark Phyllites and Orange Metasediments. b. Pillow lava structure in a metabasalt from the Blue-Green Schists, in which the rim is richer in blue amphibole relative to the central green core c. Sharp contact relationship between centimeter to millimeter-wide blueschist and greenschist layers in the Blue-Green Schists. d. Blue amphibole in albite vein from the Blue-Green Schists following the main foliation. e. General view of the Dark Phyllites. Note the great abundance of quartz ± albite veins following the main foliation. f. Sheared and transposed albite-rich veins in blueschist; note the sigmoidal shape of the albite veins and how they follow and at the same time transect the main foliation. The veins are fragmented at the tip of the sigmoid. g. Surface measurements diagram showing the surface percentage of veins (surf. %) relative to the surface in cm^2 including the mean values and error bars for each unit. For further calculations, the value of 0.9 surf. % for the Blue-Green Schists relative to the entire beach is considered here composed of 0.45 and 0.45 surface % of albite and quartz, according to textural analysis.

veins. In addition, the third set of quartz-rich veins is folded with axial planes sub-parallel to the main foliation forming ptygmatic veins and rootless folds as a consequence of flattening and shearing (***Fig. 4.S1f*** and ***g***). In the Blue-Green Schists, high-density and chaotic calcite-rich vein networks are also present, ranging from millimeter to several centimeters in width (***Fig. S1i***). Up to tens of centimeter-wide host rock fragments are bounded by these calcite-rich networks (***Fig. 4.S1i***). Some of these veins are also folded with an axial plane sub-parallel to the main foliation, suggesting similar deformation conditions to those invoked for the ptygmatic veins. Quartz-rich necks and hydrofractures are observed perpendicular to the stretching direction of boudinaged Orange Metasediments (***Fig. 4.S1h***). These vein sets were folded with axial planes sub-parallel to the boudins stretching direction and main foliation orientation (***Fig. 4.S1h***).

4.4 Methods

4.4.1 Vein Abundance Estimations

Total vein surface proportions (surf. %) were estimated after processing 136 selected high-resolution field pictures supported with field measurements for each unit. An infinite projection in the dip direction is assumed, thus enabling direct conversion from surface (%) to volume (%) considering the mean value to a 95 % confidence interval. The absolute amount of veins in the studied locality is calculated by multiplying the mean by the respective proportion of each unit at the scale of the beach.

4.4.2 Analytical Methods

Petrological studies have been performed on representative vein and matrix samples from the Blue-Green Schists, Orange Metasediments and Dark Phyllites. Electron probe microanalyses were performed at Sorbonne Université with a CAMECA SX-Five instrument under common analytical conditions (15 kV, 20 nA, wavelength-dispersive spectroscopy mode) using a 5 µm beam diameter. Standards used for the calibration are the following: orthoclase (Al, Si, K), fluorite (F), rutile (Ti), Cr_2O_3 (Cr), wollastonite (Ca), tugtupite (Cl), albite (Na), MgO (Mg), Fe_2O_3 (Fe) and rhodonite (Mn). ***Table 1*** presents selected analyses of major phases. Elemental X-Ray maps were obtained with the same instrument applying the ZAF correction and with a scanning electron microscope (SEM) Zeiss model Evo MA10 at the Institut de Physique du Globe de Paris using internal calibration standards. The images were processed with DWImager (Torres-Roldán and García-Casco, unpublished) and Matlab (version 2012) softwares. ACF and AMF projections were developed using the CSpace software (Torres-Roldán et al., 2000), projected from and along the appropriate phases and vectors necessary to condense the 10- and 11-dimensions compositional space, respectively. This type of diagram enables the identification of schematic phase relations and the compositional influence of the protoliths in the observed paragenesis as well as compositional trends expected after alteration (or other processes)

Amphibole nomenclature, structural formulae and Fe^{3+} calculation are based on the recommendations of Leake et al. (1997). White mica structural formula was normalized to 11 equivalent oxygens

assuming no Fe^{3+} in the octahedral site. Mineral compositions are given in atoms per formula unit (a.p.f.u). Mineral abbreviations are from Whitney and Evans (2010).

Representative samples from each unit (6 from the Blue-Green Schists, 3 from the Orange Metasediments and 3 from the Dark Phyllites) were pulverized for major and trace element determinations performed by X-Ray fluorescence and inductively coupled plasma mass spectroscopy (ICP-MS) at Centro de Instrumentación Científica of the University of Granada. The first method after fusion with lithium tetraborate with typical precision better than ± 1.5 % for an analyte concentration of 10 wt% and the second after lithium metaborate/tetraborate fusion and nitric acid digestion of 0.2 g of the sample. It is likely that Zr determinations were underestimated due to instrumental limitations of the ICP-MS method. For practical reasons, FeO values were calculated from original Fe_2O_3. Some of the whole rock data presented here (***Table S1***) have been acquired after scanning with SEM the surface of polished thin sections, averaging 3 x 1.5 mm^2 local compositional estimates after a counting time of 20 s for each sector. Mg-number ($Mg/(Mg+Fe^{2+})$) is abbreviated as Mg#.

4.4.3 Pseudosections: Model Design

Calculations performed with the Perple_X software version 6.8.1 (Connolly, 2005) provide information on rock mineral composition, proportions, in addition to the assessment of phase relations at the P-T conditions of interest.

Blue-Green Schists pseudosections were calculated based on two chemical compositions (GS and BS, see below) obtained using SEM surface estimations in the system Na_2O-CaO-K_2O-FeO-MgO-Al_2O_3-SiO_2-H_2O-TiO_2-O_2 (NCKFMASHTO), considering water saturated conditions from 250 °C to 450 °C and from 0.50 to 1.00 GPa. Similar conditions were used for the Dark Phyllites and Orange Metasediments using averaged XRF whole rock compositions (see Perple_X compositions in ***Table S2***). For mineral solutions and aqueous fluid, the thermodynamic mineral database from Holland and Powell (1998, updated 2002) was used. The following solid solution models were chosen according to the recommendations of Willner et al. (2016) for low grade metamorphic conditions: Holland and Powell (2003) and Powell and Holland (1999) for white mica, epidote, chlorite and biotite, Massonne and Willner (2008) for amphibole, pumpellyite and stilpnomelane and Holland and Powell (1996) for clinopyroxene. CO_2 is not considered in the pseudosection modelling approach since carbonates are almost absent in the host rock matrix. The resulting pseudosections are presented as supplementary material (***Fig. 4.S2***).

4.5 Results

4.5.1 Vein Abundance Estimates

The results of the relative amount of vein abundance at the scale of the entire Infiernillo beach are shown in ***Fig. 4.2g***. Our estimates yield surf. % values of c. 4.3 ± 1.2, 6.3 ± 3.1 and 11.2 ± 1.3 for the Blue-Green Schists, Orange Metasediments and Dark Phyllites, respectively. Histograms showing the mean values and the confidence interval together with individual results are presented as supplementary material (***Fig. 4.S3*** and ***Table S3***). The proportion of each unit at the scale of the entire Infiernillo locality (based on the high-resolution map from Hyppolito et al., 2014a) are 21, 50 and 29 surf. % of Blue-Green Schists, Orange Metasediments and Dark Phyllites, respectively. Thus, the resulting vein proportion in the full Infiernillo sequence yields a total value c. 7.3 % of veins for the entire locality, with c. 0.9, 3.1 and 3.3 % for the Blue-Green Schists, Orange Metasediments and Dark Phyllites, respectively (see ***Table 2***).

4.5.2 Bulk Rock Geochemistry and Petrology

In this section, geochemical analyses of the Blue-Green Schists are presented in order to constrain the controlling factors resulting in the occurrence of interlayered blueschists and greenschists exposed at the Infiernillo locality. Petrographic and petrological analysis will also serve as a basis for a fluid production model, which includes the three lithotypes of the studied sequence. Representative geochemical analyses of Blue-Green Schists metavolcanics, avoiding outer rims of pillows, inter-pillows and apparently spilitized metapillow lavas, together with compositions from previous studies are shown in ***Fig. 4.3a*** to ***h***. We have plotted major elements against Mg#, since previous studies (e.g. Dungan et al., 1983; Palin and White, 2015) emphasized the important role of Mg in controlling the formation of blueschists and greenschists.

The Mg# is slightly higher in greenschists than in blueschists (***Fig 4.3a*** to ***d***). Al_2O_3 systematics (***Fig. 4.3a***) show extensive scatter with considerable overlap between blueschists and greenschists. CaO is higher in greenschists than in blueschists but with some overlap (***Fig. 4.3b***). Na_2O content is on average higher in blueschists than in greenschists (***Fig. 4.3c***) while the Na/Ca ratio (***Fig. 4.3d***) is commonly lower in greenschists than in blueschists.

The systematics described above are classically interpreted as the consequence of (i) magmatic differentiation and/or cryptic sea-floor spilitization or (ii) metasomatism during subduction or exhumation, as proposed by Halama and Konrad-Schmolke (2015). The abundance of immobile trace elements (***Fig. 4.3e*** and ***f***) show that the studied Blue-Green Schists are basaltic in composition and similar to OIBs (in line with Hyppolito et al., 2014; Halama and Konrad-Schmolke, 2015), ruling out magmatic differentiation as an important process affecting the suite of studied samples. In order to investigate the presence of metasomatism, trace elements and chemographic analysis using the ACF diagram were designed considering classical basaltic and alteration mineral assemblages (***Fig. 4.3g*** and ***h; Fig. 4.4a***). As shown in the ACF projection (***Fig. 4.4a***), most of the non-spilitized/altered bulk compositions considered of the Infiernillo locality are compatible with a magmatic mineral

TABLE 1. ELECTRON PROBE MICROANALYSIS. MINERAL COMPOSITION AND CATIONS PER FORMULA UNIT IN THE BLUE-GREEN SCHISTS UNIT

Mineral group	Sample	Zone	SiO_2 (wt%)	TiO_2 (wt%)	Al_2O_3 (wt%)	Cr_2O_3 (wt%)	FeO (wt%)	MnO (wt%)	MgO (wt%)	CaO (wt%)	Na_2O (wt%)	K_2O (wt%)	Total (wt%)	*H_2O (wt%)	Si (a.p.f.u)	Al_{tot} (a.p.f.u)	Fe^{3+} (a.p.f.u)	Fe^{2+} (a.p.f.u)	Mg (a.p.f.u)	Ca (a.p.f.u)	Na (a.p.f.u)	K (a.p.f.u)	# (O - OH)
Amphibole	P17A	Blueschist matrix	55.35	0.32	2.44	0.12	16.98	0.31	12.22	7.12	3.21	0.08	98.15	2.07	7.95	0.41	0.29	1.75	2.62	1.10	0.89	0.01	22-2
	P17A	Blueschist Ab vein	56.81	0.06	6.69	0.00	16.05	0.23	9.40	1.74	6.49	0.03	97.49	2.10	8.00	1.11	0.57	1.31	1.97	0.26	1.77	0.00	22-2
	P17A	Blueschist vein	56.90	0.03	8.32	0.01	15.84	0.36	8.24	1.51	6.56	0.07	97.85	2.12	8.00	1.38	0.35	1.51	1.73	0.23	1.79	0.01	22-2
	P18.33	GS	57.61	0.10	6.75	0.04	15.66	0.20	9.89	1.92	6.49	0.04	98.70	2.13	8.00	1.10	0.54	1.28	2.05	0.29	1.75	0.00	22-2
	P18.33	BS	54.81	0.06	2.23	0.00	13.93	0.34	14.48	9.62	2.10	0.14	97.72	2.08	7.86	0.38	0.20	1.47	3.10	1.48	0.59	0.01	22-2
	P18.33	BS	56.98	0.02	1.23	0.00	12.69	0.39	15.64	10.44	1.42	0.06	98.88	2.12	8.04	0.20	0.00	1.50	3.29	1.58	0.39	0.01	22-2
	P18.33	BS	54.75	0.02	1.05	0.01	12.72	0.29	16.09	10.70	1.35	0.07	97.06	2.07	7.87	0.18	0.25	1.28	3.45	1.65	0.38	0.01	22-2
	P18.33	GS	55.57	0.09	5.64	0.02	16.46	0.14	10.05	2.20	6.27	0.05	96.48	2.07	7.96	0.95	0.55	1.42	2.15	0.34	1.74	0.00	22-2
	P18.33	GS	54.50	0.04	1.68	0.07	13.21	0.31	15.50	10.09	1.71	0.12	97.22	2.07	7.83	0.28	0.28	1.31	3.32	1.55	0.48	0.01	22-2
Chlorite	P18.33	GS	26.94	0.05	18.25	0.18	24.50	0.34	17.33	0.05	0.01	0.04	87.69	11.40	2.83	2.26	N.A.†	2.15	2.72	0.01	0.00	0.01	10-8
	P18.33	BS	26.96	0.01	17.71	0.06	24.21	0.35	17.24	0.19	0.07	0.04	86.84	11.29	2.86	2.22	N.A.†	2.15	2.73	0.02	0.01	0.01	10-8
Phengite	P18.33	BS	49.69	0.15	22.78	0.08	5.72	0.03	3.62	0.02	0.11	10.79	92.97	4.28	3.48	1.88	N.A.†	0.33	0.38	0.00	0.01	0.96	20-4
	P18.33	BS	50.39	0.10	23.14	0.20	4.55	0.00	4.25	0.02	0.13	10.59	93.38	4.34	3.48	1.88	N.A.†	0.26	0.44	0.00	0.02	0.93	20-4
	P18.33	GS	49.76	0.16	22.09	0.22	5.90	0.07	3.93	0.05	0.38	10.19	92.75	4.28	3.49	1.82	N.A.†	0.35	0.41	0.00	0.05	0.91	20-4
	P18.33	BS	50.99	0.06	23.87	0.13	3.23	0.02	4.00	0.01	0.13	11.01	93.44	4.37	3.50	1.93	N.A.†	0.19	0.41	0.00	0.02	0.96	20-4
	P18.33	GS	51.66	0.07	22.72	0.20	5.34	0.02	4.65	0.00	0.10	10.29	95.06	4.41	3.51	1.82	N.A.†	0.30	0.47	0.00	0.01	0.89	20-4
	P18.33	GS	49.89	0.11	22.41	0.21	3.96	0.01	4.06	0.03	0.13	10.64	91.46	4.26	3.51	1.86	N.A.†	0.23	0.43	0.00	0.02	0.96	20-4

Note: apfu—atoms per formula unit; tot—total; #(O – OH)—normalization defined in terms of O and OH relative to each mineral; BS—blueschist zone; GS—greenschist zone; Ab—albite; N.A.—not applicable

* = Calculated by stoichiometry.

TABLE 2. ESTIMATED SURFACE PROPORTIONS AT INFIERNILLO

Unit	Infiernillo absolute surface area (%)		
	Matrix	Albite veins	quartz+calcite veins
Blue-green schists	20.10	0.45	0.45
Dark phyllites	25.74	0.00	3.26
Orange metasediments	46.86	0.00	3.14
Sum	***92.70***	***0.45***	***6.85***

Note: Albite veins are neglected in the dark phyllites and orange metasediments because they are scarce in these units.

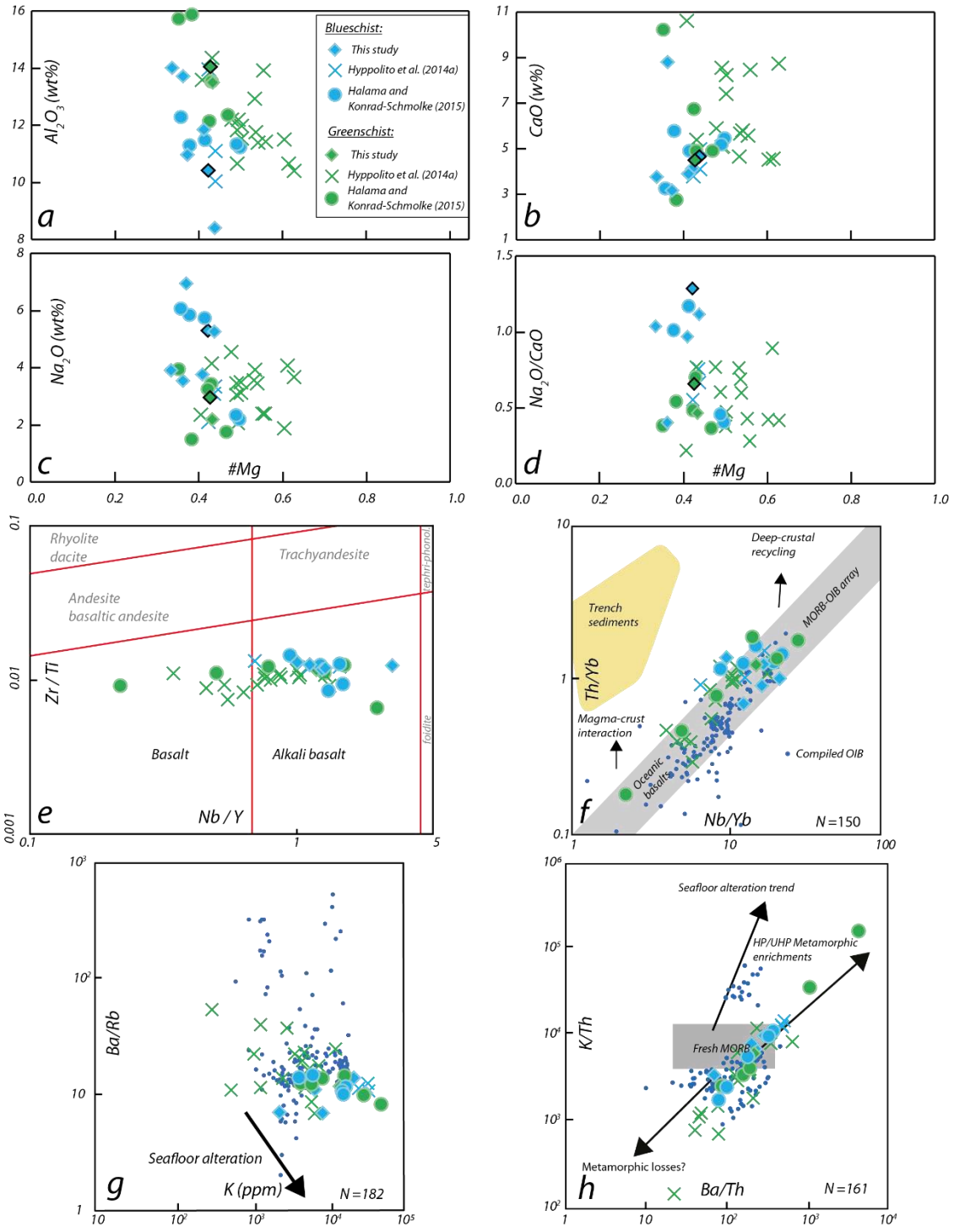

Figure 4.3. a to d: Major oxides Al_2O_3, CaO, Na_2O and Na/Ca ratio vs Mg# (a, b, c and d respectively). e. Zr/Ti versus Nb/Y diagram (Winchester and Floyd, 1977; modified from Pearce, 1996). f. Th/Yb vs. Nb/Yb diagram (Pearce, 2008). Most of the samples plot in the oceanic basalts field similar to compiled fresh OIBs. g. Ba/Rb vs K diagram showing the sea-floor alteration trend from Bebout (2007). h. K/Th vs Ba/Th diagram showing sea-floor alteration, HP/UHP metamorphic enrichments (metasomatic alteration according to Halama and Konrad-Schmolke, 2015) and metamorphic losses trends from Bebout (2007). OIB compositions from Galápagos and Hawaii compiled from the GeoRem database (http://georem.mpch-mainz.gwdg.de/).

assemblage composed of olivine (forsterite and fayalite) + clinopyroxene (augite) + orthopyroxene (enstatite and ferrosilite) + feldspar (plagioclase ± K-feldspar), similarly to fresh OIB compositions. However, part of the fields defined by the studied rocks and OIBs overlap the field of the sea-floor alteration assemblages (epidote + chlorite ± muscovite) hampering any conclusion about (cryptic) sea-floor metasomatism as an explanation for the geochemical variability of the studied suite of rocks, except for those samples that plot towards the high Al side, as indicated in ***Fig. 4.4a***. In addition, trace elements analysis using Ba/Rb vs K and K/Th vs Ba/Th ratios (***Fig. 4.3g*** and ***H***) show a clear correlation with compiled fresh OIB values instead of a sea-floor metasomatic trend. Nevertheless, two samples clearly follow a HP metasomatic enrichment trend (see also Halama and Konrad-Schmolke, 2015).

In addition to the ACF diagram, we show the composition of the studied rocks in the AFM diagram (***Fig. 4.4b***) in order to analyze the effect of bulk-rock FeO and MgO variations in the context of schematic phase relations expected at HP (e.g. Palin and White, 2015; ***Fig. 4.4b***). A clear trend can be distinguished, where (i) most of the blueschist samples plot within glaucophane-bearing assemblages and (ii) most of the greenschist samples plot in the field of chlorite + actinolite-bearing assemblages compatible with classical greenschist facies parageneses. Some greenschists that plot within glaucophane-bearing assemblages may indeed be considered as retrogressed blueschists in line with Halama and Konrad-Schmolke (2015). However, these authors have described the occurrence of glaucophane in all their analyzed greenschist samples, in agreement with the plotting of these compositions within the glaucophane-bearing assemblages.

4.5.3 Textures and Microstructures

4.5.3.1 The Dark Phyllites and Orange Metasediments: Matrix and Veins

Metasedimentary rocks from the Dark Phyllites and Orange Metasediments are essentially composed of phengite + quartz + organic matter + albite + chlorite ± titanite ± sulfides ± iron oxides and phengite + quartz + albite + stilpnomelane ± chlorite ± titanite ± sulfides ± iron oxides, respectively. Phengite grains defining the main foliation as well as folded crystals forming a crenulation cleavage S3 are present. These crystals are in apparent textural equilibrium with quartz and albite, although some plagioclase detrital remnants occur. Stilpnomelane and chlorite, which both growth post-kinematically, are abundant in the Orange Metasediments foliation together with iron oxides. Dark fringes of insoluble material are also present along the foliation, indicating that pressure solution deformation mechanisms were active during deformation. Noteworthy, carbonate phases are absent in the matrix of both units, even if they contain carbonate-bearing veins.

Representative vein textures can be seen in ***Fig. 4.5a*** to ***d***. Both, Dark Phyllites and Orange Metasediments veins are commonly sub-parallel to the main foliation and are composed mostly by blocky quartz and subordinate albite crystals that grow perpendicular to the host rock contact (***Fig. 4.5b*** and ***c***). Minerals in these veins show undulose extinction, grain boundary bulging and recrystallization, mostly in quartz, suggesting dislocation creep as an important deformation

mechanism. Collapse textures in the sense of Bons et al. (2012) were not observed. Inclusion tracks are abundant in quartz veins (***Fig. 4.5b***) and indicate several stages of re-opening (e.g. Ramsay, 1980).

Albite shows mostly brittle deformation with local kinking and incipient subgrain formation along grain boundaries (e.g. ***Fig. 4.5d***). Quartz infiltrates previous albite veins (***Fig. 4.5d***) and also occurs as ribbons cross-cutting previous quartz grains. Calcite is seen (i) subordinately related to quartz in veins following the main foliation and (ii) cross-cutting previous structures (***Fig. 4.5b***). Calcite also infiltrates along albite twins and occurs as late millimeter-sized veins together with chlorite and/or iron oxides.

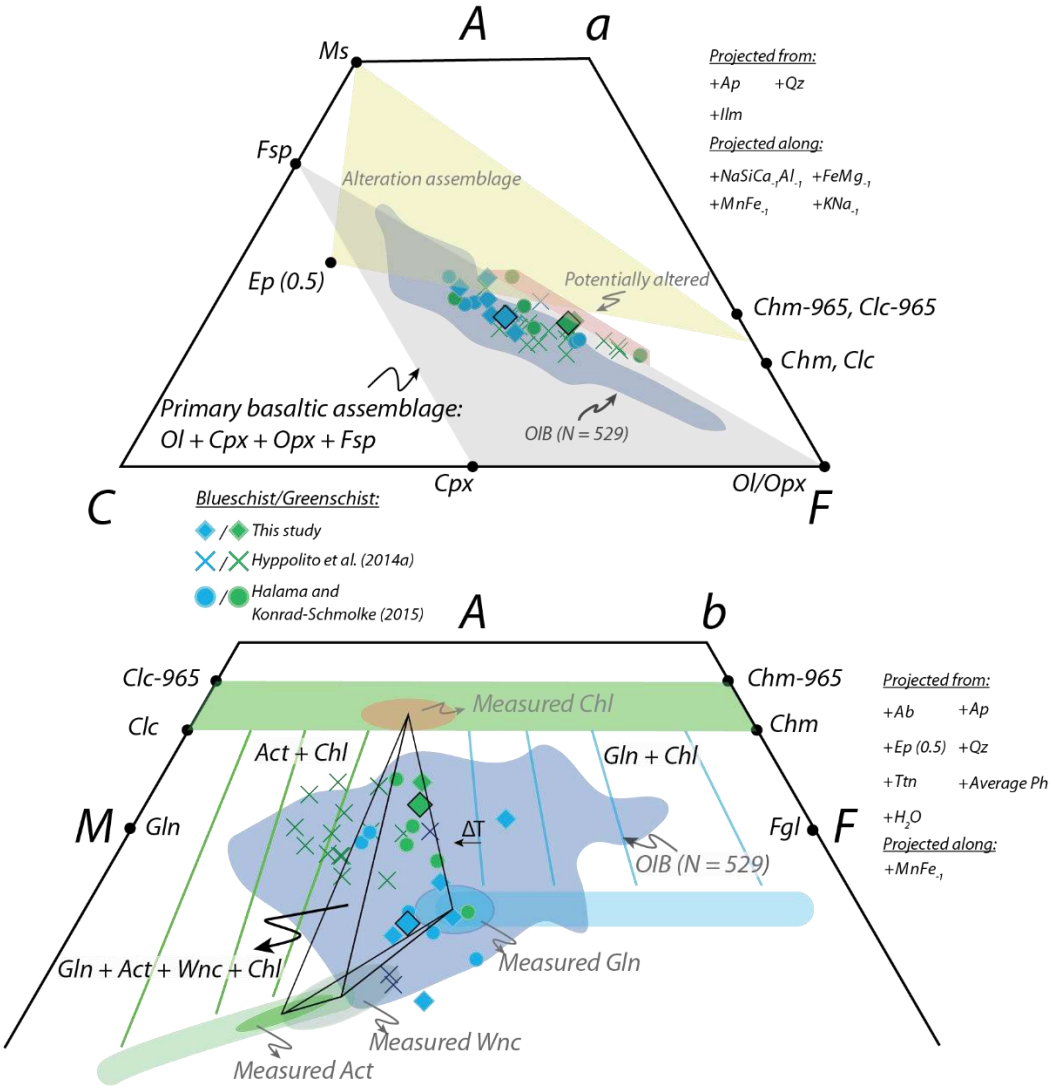

Figure 4.4. a. ACF projection. The basaltic assemblage corresponds to a typical basalt containing plagioclase, olivine, and pyroxene. The alteration assemblage corresponds to ocean-floor metamorphism/metasomatism forming chlorite, epidote and muscovite. b. AFM projection representing phase relationships of studied and reported blueschists and greenschists at the Infiernillo locality. The tie-triangle Gln + Act + Chl moves to the M apex upon temperature increase (modified from Spear, 1993). Chm- and Clc-965 according to the notation of Spear (1993). Ep (0.5) refers to epidote with 50% of pistacite component. OIB compositions from Juan Fernández, Galápagos and Hawaii compiled from the GeoRem database (http://georem.mpch-mainz.gwdg.de/). Lined symbols correspond to the BS and GS compositions calculated using EDS surface estimations.

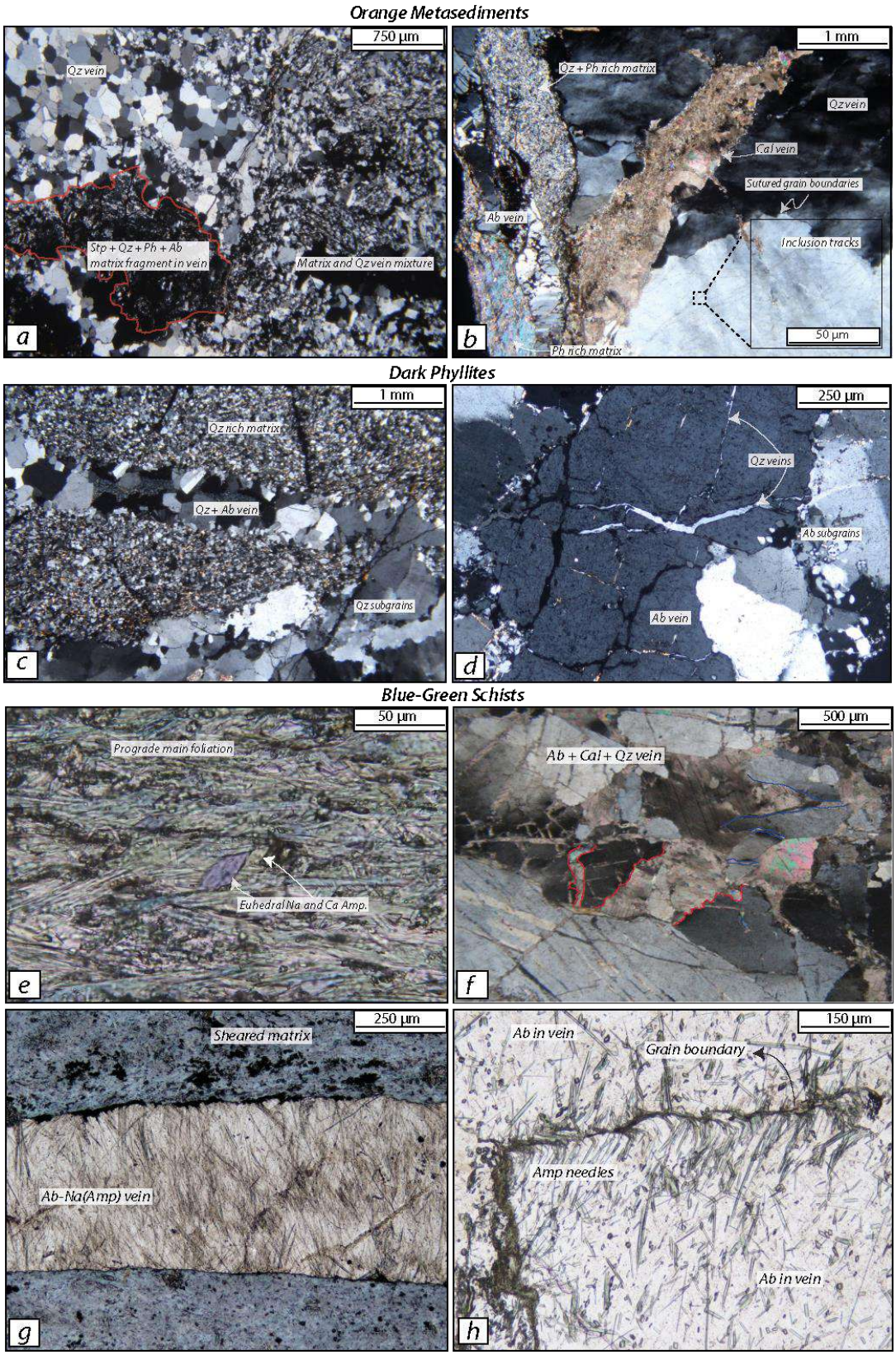

Figure 4.5. Optical photomicrographs of selected samples from the Orange Metasediments (a and b), Dark Phyllites (c and d) and Blue-Green Schists (e to h). a. Cross-polarized view of a stilpnomelane + quartz + phengite + albite matrix fragment

in a quartz vein. b. Cross-polarized view of a coarse-grained quartz vein cut by calcite (center and right part); note the inset showing inclusion tracks in the quartz vein and the phengite + quartz matrix transected by an albite vein oriented perpendicular to the contact with the host rock (lower left part). c. Cross-polarized view of a fine-grained matrix composed by quartz + phengite + albite being cut by coarse-grained quartz vein with subordinated albite; note the sub-perpendicular orientation of albite crystals growing from the vein contact towards the center of the vein. d. Cross-polarized view of an albite + quartz vein; note the irregular contacts and slight kinking of albite twins. e. General view of a blue-green schist (sample P18.33); note the blue and green colors of euhedral amphibole crystals occurring in sharp contact overgrowing an earlier prograde amphibole main foliation. f. Cross-polarized view of an albite + calcite + quartz vein; note the hydrofracture filled by calcite; red and blue contours represent grain boundaries likely representing a former albite crystal (one crystal for each color). g. Detailed view of contact relationships between the sheared matrix and albite + blue amphibole vein; note the orientation of blue amphibole needles perpendicular to the host rock. The greater amount of amphibole along vein walls is likely related to a diffusion-limited process as the source of Mg and Fe needed to grow amphibole in the albite vein is the matrix. h. Detailed view of albite grain contacts with blue-green amphibole growing perpendicular to it and sheared.

4.5.3.2 The Blue-Green Schists: Matrix

Blueschists and greenschists at the Infiernillo locality are medium to fine-grained rocks slightly affected by retrogression. In general, blueschists correspond to strongly foliated fine-grained metatuffs with abundant glaucophane (locally riebeckite) + winchite (locally barroisite) + actinolite + albite + chlorite + phengite ± titanite ± apatite and scarce quartz, epidote and sulfides. Few local relicts of pre-subduction hornblenditic amphibole are overgrown by actinolite mantles and glaucophane rims (***Fig. 4.6a***). Albite occurs in the matrix either overgrown by glaucophane (***Fig. 4.6b***) or lining the foliation in apparent equilibrium with phengite, glaucophane and winchite. The most abundant Ti-bearing phase in the foliation is rutile. However, titanite occurs in the vicinity of former plagioclase relicts, as a consequence of local calcium activity gradients on the rutile-titanite stability (Angiboust and Harlov, 2017). On the other hand, greenschists are mostly metatuffs, metalavas and metapillow lavas, the latter being weakly foliated in comparison to other rocks. Their mineral assemblage is mainly composed of actinolite + winchite + chlorite + albite + glaucophane + epidote + titanite and scarce sulfides and relict grains of igneous plagioclase and pyroxene. It is worth noting that either in blueschists and greenschists, carbonate minerals are almost absent. Phengite compositions are summarized in ***Fig. 4.7***. Here we refer to Na-amphibole as glaucophane, Na-Ca amphibole as winchite and Ca-amphibole as actinolite since other amphibole species are rather scarce (see compositions in ***Fig. 4.S4***).

To investigate the phase relationships and set the basis for a fluid production model, we have selected a blue-greenschist sample (sample P18.33; ***Fig. 4.5e***) which shows strong color contrasts at centimeter-scale from blue to green, suggesting straightforward distinctive mineral assemblages and compositions across the sample. The Blueschist Zone (BS) is characterized by fine grained glaucophane + winchite + titanite + albite ± actinolite ± phengite ± chlorite ± apatite ± iron oxides and sulfides, defining the penetrative main foliation (***Fig. 4.S1j*** and ***k***). Actinolite is in sharp contact with, as well as in thin overgrowing rims of earlier glaucophane. The Greenschist Zone (GS) is

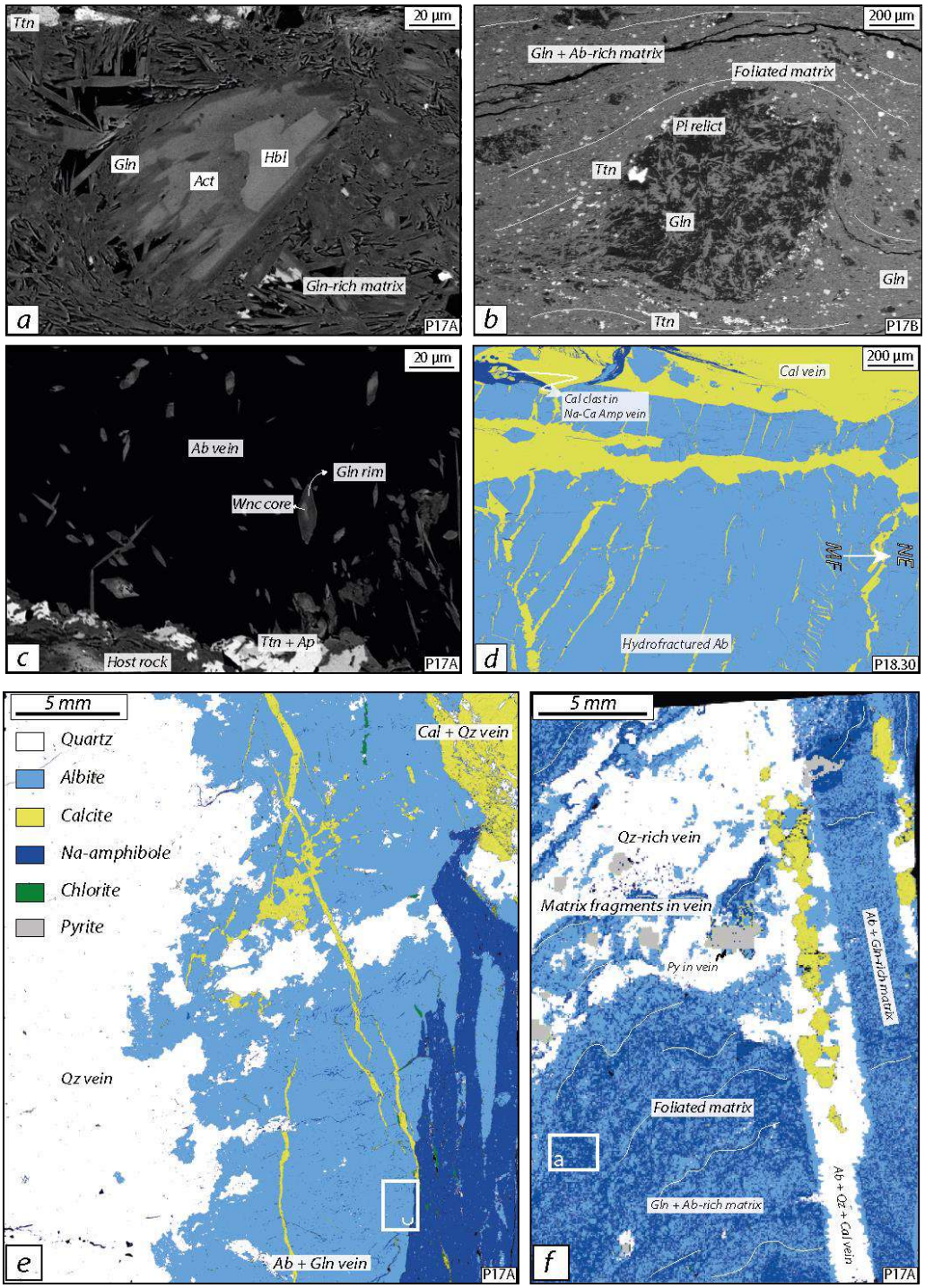

Figure 4.6. Blue-Green Schists back scattered electron images (a to c). a. Relict of hornblenditic amphibole replaced by actinolite and rimmed by glaucophane during prograde metamorphism close to HP peak metamorphic conditions. b. Plagioclase relict partially replaced by glaucophane in a fine-grained matrix; note the close spatial relationship between titanite and the plagioclase relict. c. Albite vein with amphibole showing prograde zoning pattern (winchite core and glaucophane rim). High resolution EDS phase maps (d to f) d. Albite vein with calcite veinlets showing hydrofracturing texture; note the calcite fragment in a Na- to Na-Ca amphibole-rich vein. MF refers to the main foliation oriented to the northeast (NE). e Albite + quartz + calcite ± glaucophane vein; albite is oriented perpendicular to the vein wall; note the later quartz + calcite hydrofracture-like domain affecting the albite vein. f. Quartz vein parallel to the main foliation as hydrofracture fabric affecting the foliated glaucophane + albite-rich matrix; note the host rock fragments in the vein and the later blocky quartz + calcite + albite vein cross-cutting the previous quartz vein.

characterized by higher abundances of chlorite and phengite compared to the BS. Glaucophane here is less abundant and occurs as cores and as prismatic euhedral crystals in the matrix, unlike winchite and actinolite which are most abundant among amphiboles. Locally, glaucophane cores and actinolite rims are present.

Importantly, the absolute abundance of amphibole decreases towards the GS zone. A first generation of winchite grows parallel to the main foliation, followed by glaucophane and actinolite in sharp contact, overgrowing in perfectly euhedral prismatic habit earlier prograde winchite (***Fig. 4.5e***), reflecting a superimposed prograde metamorphic condition. Thus, the association between glaucophane and winchite is complex, growing in sharp contacts or one mutually rimming the other (e.g. glaucophane core and winchite rims and vice versa). Phengite in the BS and GS is rich in celadonitic component (***Fig. 4.7***), with Si= 3.48 - 3.63 (a.p.f.u); Mg# = 0.53 - 0.69 and very low Na (0.01 - 0.05 a.p.f.u). The minor differences in phengite compositions between the BS and GS zones (***Fig. 4.7***) and the fact that no major retrogression-related textures occurs suggest almost complete preservation of the transitional greenschist-blueschist facies metamorphism.

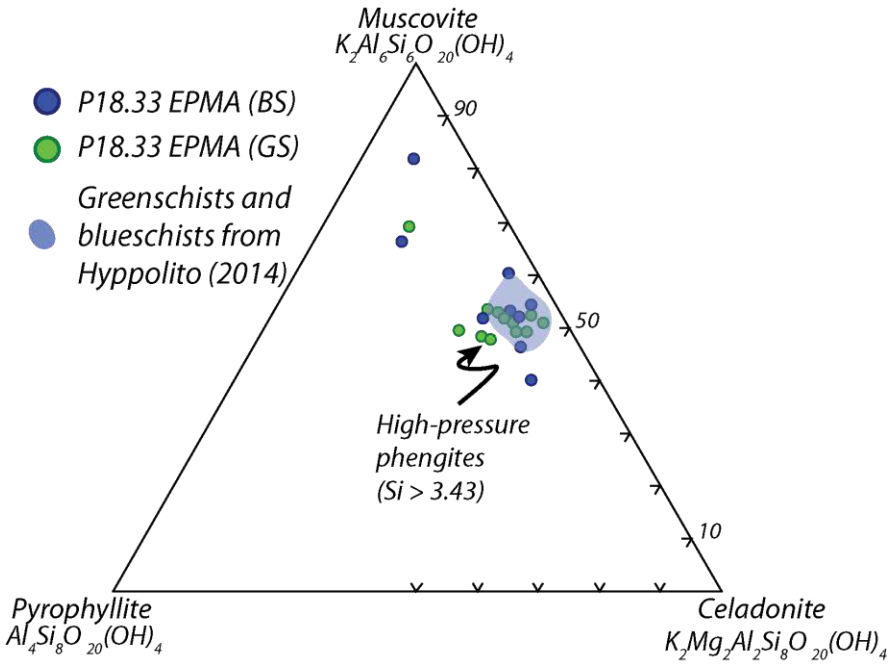

Figure 4.7. Triangular plot for phengite compositions in the Blue-Green Schists.

Phase abundances and compositional variations between centimeter-scale BS and GS intercalations are clearly appreciated in high-resolution X-Ray maps obtained in three zones from sample P18.33 (***Fig. 4.2c; Fig. 4.8***) as well as with the transect of SEM surface compositional estimates (***Fig. 4.8e***). As mentioned above, the selected sample P18.33 shows a clear difference in color from blue to green (***Fig. 4.8a***) reflecting variations in mineral abundances (***Fig. 4.8b*** to ***d***). The left section (BS) clearly shows higher proportions of glaucophane and albite (***Fig. 4.8b***). Towards the GS, slightly less albite and markedly more chlorite, actinolite-winchite, titanite and phengite proportions are observed (***Fig.***

4.8b to ***d***, respectively), together with a larger grain size and an increase in the calcic component in amphibole. Note that the relative amount of amphibole in the GS zone is lower compared to the BS. Towards the GS zone, the foliation style changes from a very continuous and homogeneous pattern to an anastomosing-like fabric, probably due to a greater abundance of phyllosilicates (***Fig. 4.S1i*** and ***m***).

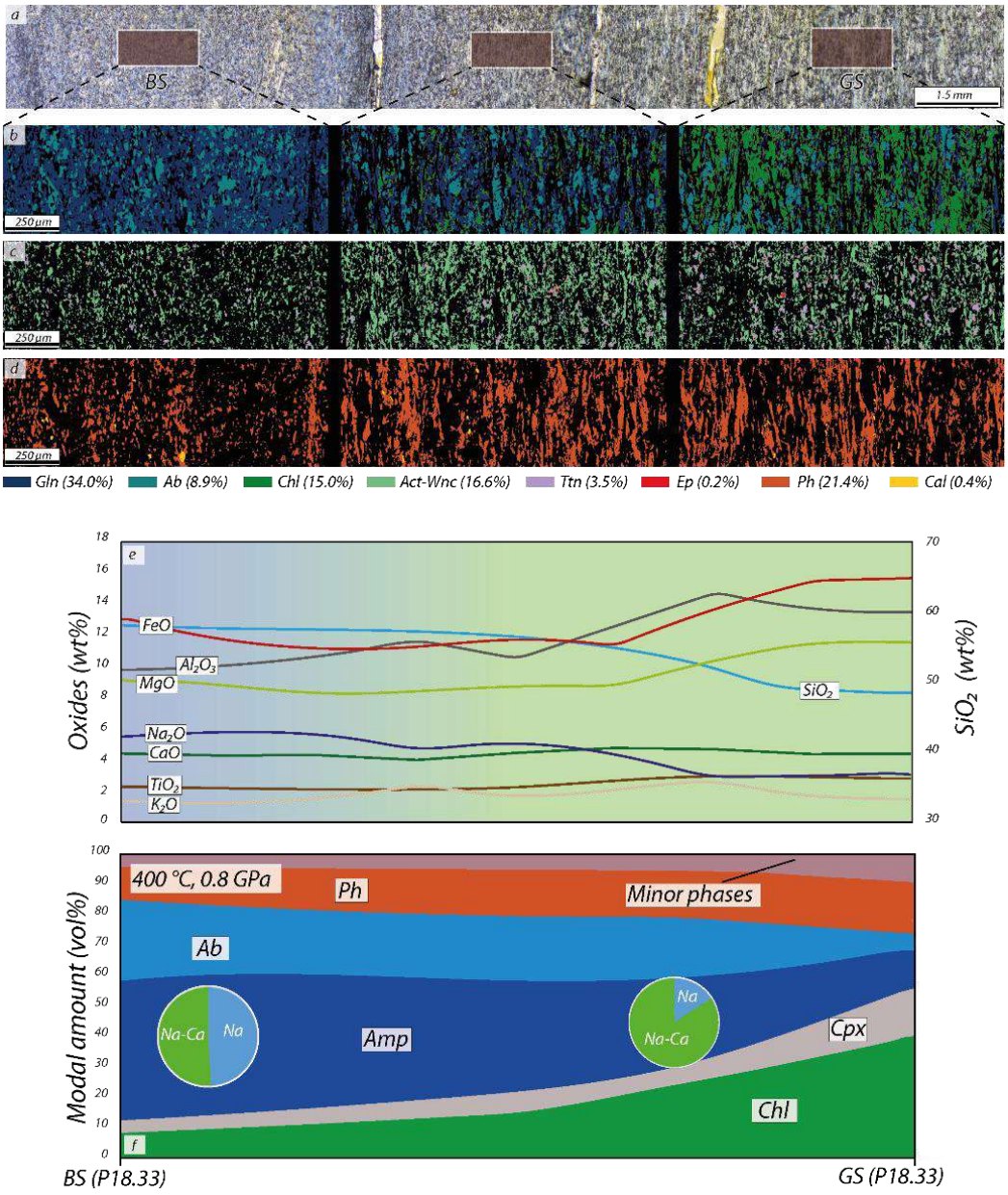

Figure 4.8. X-Ray maps-based masks of three different zones from a single thin section of the blueschist-greenschist sample P18.33. a. Image showing the location and size of each X-Ray map. b to d. Phase distribution and abundance images of glaucophane + albite + chlorite, actinolite-winchite + epidote + titanite and phengite + calcite, respectively (image created with DWImager software). e. Compositional diagram showing variation in major oxides (wt%) along a EDS surface estimation transect from the BS towards GS zone. f. Thermodynamically calculated phase abundance diagram at 400 °C and 0.80 GPa. Chemical composition variations (horizontal axis) were calculated for mixed BS-GS compositions. The pie charts show amphibole composition ratios; note that the calcic component in amphibole increases towards GS compositions. Minor phases include mostly quartz and titanite, among others.

The changes observed in the surface estimate composition transect (***Fig. 4.8e***) are characterized by a SiO_2 and Na_2O decrease (c. 10.6 and 2.3 wt% respectively) and an FeO, MgO, TiO and Al_2O_3 increase (2.9, 2.7, 2.8 and 4 wt% respectively), reflecting the modal increase of chlorite, phengite, titanite and actinolite, from the BS towards the GS section. CaO and K_2O content show almost no variation. On the other hand, none of the studied vein margins exhibit selvages that could witness local elemental mobility (e.g. see the sharp matrix margin on ***Fig. 4.6f***).

To address the effect of chemical bulk compositions variations at peak conditions (0.80 GPa and 400 °C, see Hyppolito, 2014), we developed a thermodynamic model for mixed BS-GS compositions (***Fig. 4.8f***). The calculation shows that major phase changes between BS and GS are characterized by the increase of phengite and chlorite abundances, and an important decrease in the absolute amount of amphibole and albite. The relative amount of the calcic component in amphibole strongly increases (see pie charts ***Fig. 4.8f***), in agreement with petrological analyses. Thermodynamic modelling, in line with petrographic observations (***Fig. 4.S1j*** to ***m***) and petrological analysis, thus confirms the importance of bulk-rock differences on the paragenesis.

4.5.3.3 The Blue-Green Schists: Veins

In this section, we describe the petrology of the previously defined vein types (see Structure and Distribution of Vein Networks section). Veins transposed and parallel to the main foliation (first and second sets) are composed of coarse-grained albite + quartz + fine-grained glaucophane/winchite (***Fig. 4.5g*** and ***h; Fig. 4.6c*** and ***e***) and subordinated titanite, apatite and iron sulfides. Albite crystals grew mostly perpendicular to the vein walls and show evidence of bending, subgrain formation and recrystallization. Albite veins elongated parallel to the S2 fabric are also present (***Fig. 4.6d***). These veins exhibit inclusion tracks sub-perpendicular to the elongation orientation and are sharply crosscut by later calcite veins, with evidence for hydrofracturing. In addition, abundant coarse-grained quartz + calcite ± fine-grained winchite and actinolite (***Fig. 4.5f; Fig. 4.6c, e*** and ***f***) occurs oriented according to the previous albite veins with evidence of hydrofracturing also affecting the host rock (e.g. ***Fig. 4.5g; Fig. 4.6d*** to ***f; Fig. 4.S1i***). The third vein set, with no clear cross-cutting relationship with respect to previously mentioned veins, is filled by quartz + calcite + albite of minor importance in terms of size and abundance (e.g. ***Fig. 4.6f***). Note that calcite vein fragments in winchite-rich veins are present (***Fig. 4.6d***). Finally, a late chlorite ± calcite vein set occurs cutting all previous vein sets (***Fig. 4.6e***), showing almost no evidence of deformation.

Amphibole in albite veins shows compositions similar to the matrix, with winchite cores and (volumetrically minor) glaucophane rims and vice versa (***Fig. 4.6c***). Hydrofracture fabrics can be seen in former albite veins and host rock (e.g. ***Fig. 4.5f; Fig. 4.6d*** to ***f; Fig. 4.S1i***). Like in metasediments, solid and fluid inclusions tracks are abundant in quartz. Calcite crystals show strong mechanical twinning. Quartz presents undulose extinction, subgrains and strong recrystallisation, evidencing recovery and crystal-plastic deformation processes. The homogeneous orientation of amphibole needles in vein sets are commonly sub-perpendicular to the walls of the host-rock (***Fig. 4.5g, h***). Albite grain boundaries in veins are rimmed with winchite needles that grew perpendicular

to the crystal margin (***Fig. 4.5h***). A summary of mineral occurrences in veins and matrix is presented in ***Fig. 4.9***.

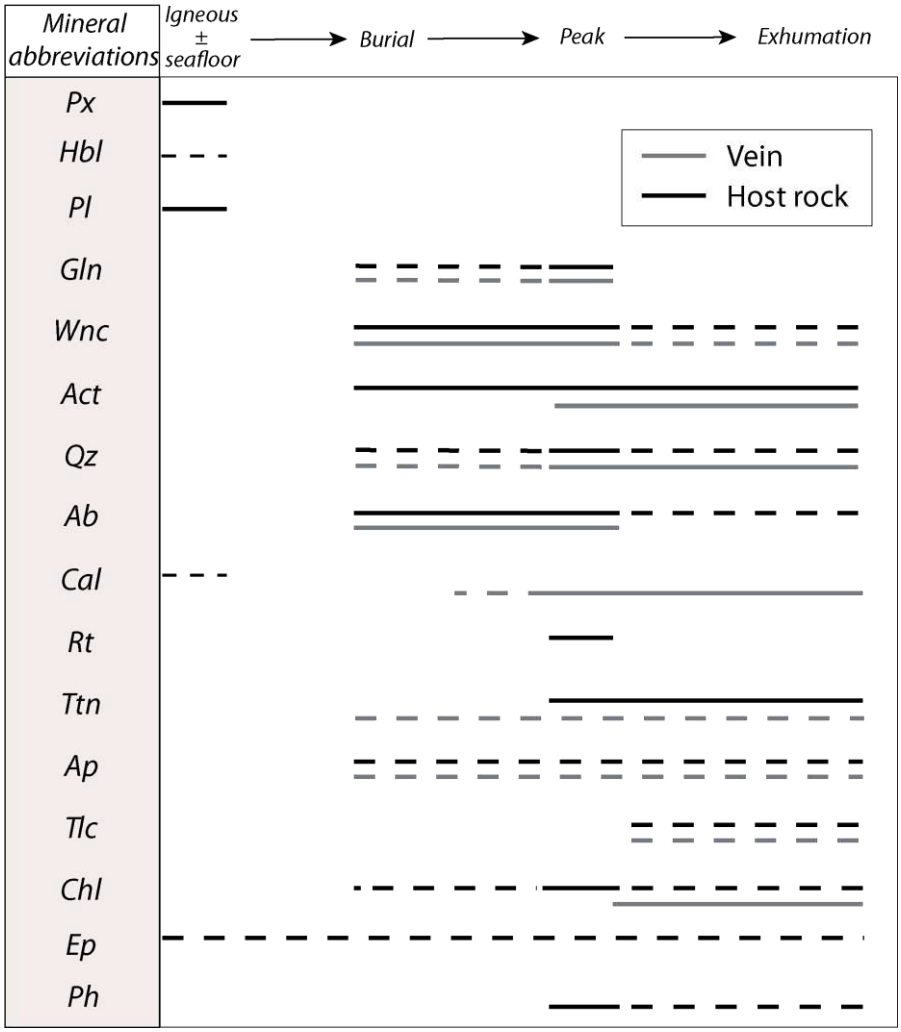

Figure 4.9. Diagram summarizing the mineralogical evolution of the Blue-Green Schists matrix and veins. Dashed line indicates uncertainty in the mineral formation stage.

4.5.4 Dehydration Models for Infiernillo Rocks

In order to estimate the fluid released by the metamorphic sequence of Infiernillo during burial, we developed a two-step dehydration model. The first step considers the fluid production at the very early stage of burial based on commonly reported mineral assemblages in the range between 0 °C - 0.01 GPa to 250 °C - 0.50 GPa. This approach has been chosen as the pseudosection modelling technique is not well suited for very low-grade conditions (e.g. < 250 °C). The second step corresponds to the thermodynamically calculated H_2O (wt%) released in the range of 250 °C - 0.50 GPa to 400 °C - 0.80 GPa using the Perple_X software. The sum of the fluid budget calculated for this two-step dehydration model corresponds to the total amount of H_2O (wt%) released up to peak conditions.

4.5.4.1 "Synthetic Minerals" Modelling from 0 to 250 °C

To construct dehydration curves on the range from 0 to 250 °C (***Fig. 4.10a***) we assume theoretical mineral and abundances present along the prograde path (***Table S4***). From this approach, H_2O contents (wt%) in minerals are considered together with H_2O contained in the porosity of the studied compositions. For further details on calculation procedure, see **Appendix 1** (see also a similar approach in Peacock, 1993). For the BS and GS compositions, an average of 25 % of porosity (e.g. Whitmarsh, 1978; Carlson and Herrick, 1990) is assumed to be filled by pure H_2O (***Fig. 4.10a***). This porosity value dramatically decreases to values close to 0 % in the first 3 km of burial (e.g. Whitmarsh, 1978; Carlson and Herrick, 1990). Here a linear reduction of porosity is assumed, and the final value was set to 1 %, in the same order of magnitude as calculated by Peacock et al. (2011) (see also Hyndman, 1988) for an over-pressurized subducting slab. For the Dark Phyllites and Orange Metasediments, porosity values selected were 28 and 38 % respectively, (extrapolated from Magara, 1980) and a value of 1 % was also assumed to be maintained up to peak conditions (***Fig. 4.10a***).

The main trends for the BS and GS compositions consist in a decrease of relict Ca-amphibole (hornblenditic), clinopyroxene, zeolite and clay minerals and an increase of actinolite, clinochlore and albite (Supplementary ***Table 4***). The H_2O contents for the two compositions dramatically decrease at the very early stage (***Fig. 4.10a***), due to porosity collapse, followed by the consumption of clay minerals, zeolites and stilpnomelane, releasing an average of c. 8.0 wt% of H_2O during burial.

For the Dark Phyllites and Orange Metasediments, the major changes consist in a decrease of smectite abundance and formation of illite, while quartz content is almost constant. H_2O contents for the two compositions dramatically decrease at the very early stage (***Fig. 4.10a***), due to porosity collapse, followed by the nearly complete consumption of clays, releasing c. 11.9 and 14.2 wt% of H_2O respectively.

Note that for every step of this calculation we made sure that the synthetic assemblage had a bulk composition sufficiently close to the actual rock composition (i.e. < 8 wt% difference for SiO_2, < 6 wt% for Al_2O_3, < 3 wt% for FeO, < 2 wt% for MgO, < 2 wt% for Na_2O and K_2O), assuming no or

only very minor mass transfer of major elements during the prograde burial metamorphism (apart from H_2O).

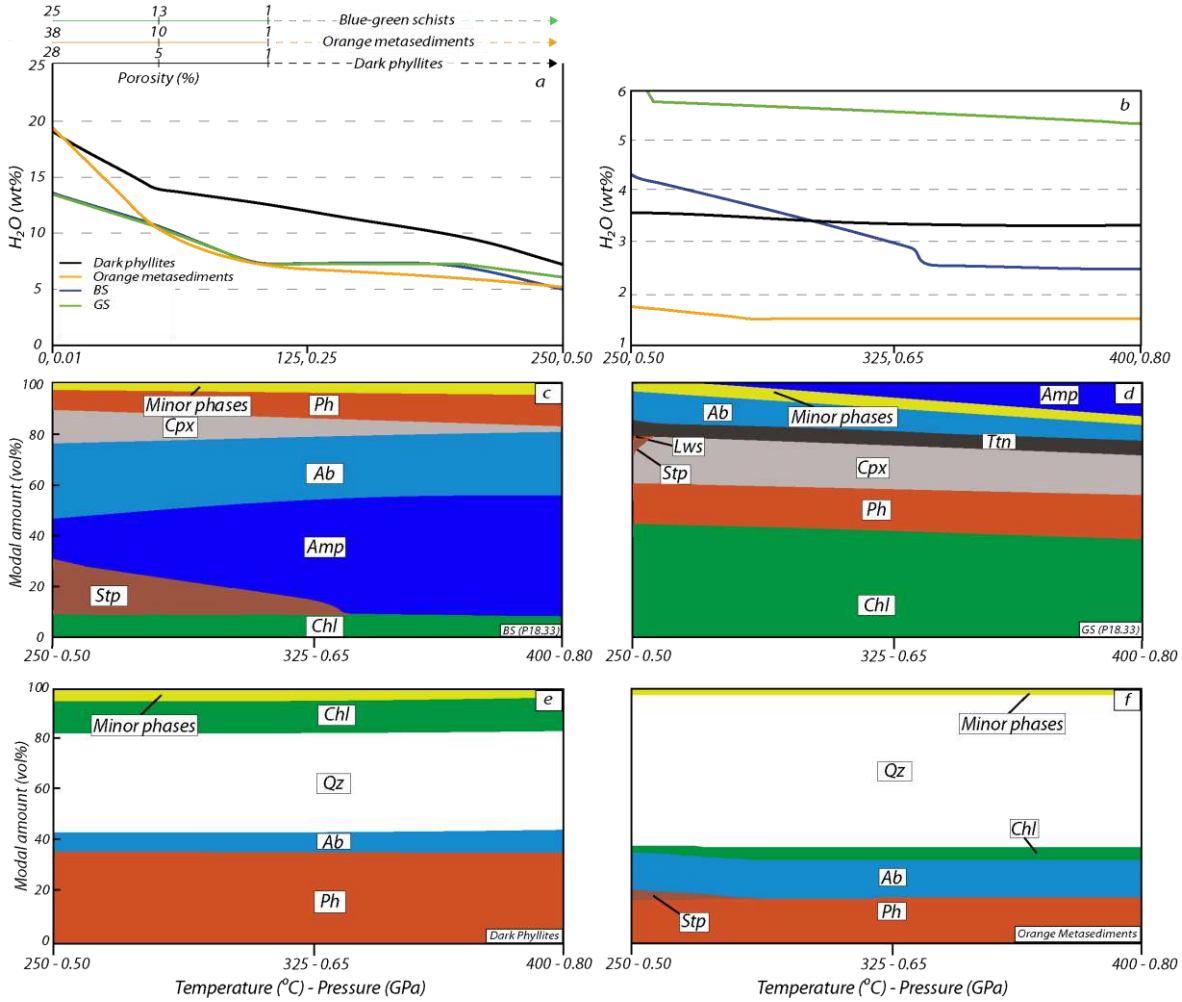

Figure 4.10. "Synthetic mineral" models and thermodynamically calculated H_2O contents and phase abundance diagrams. a. "Synthetic mineral" calculated H_2O content curves from 0 °C - 0.01 GPa to 250 °C - 0.50 GPa, showing fluid released during burial of the selected Blue-Green Schists, Dark Phyllites and Orange Metasediments compositions. Top arrows represent the variation in porosity values considered for each composition. Considered synthetic minerals taken from natural mineral assemblages reported by Thompson and Humphris (1977) and Cho et al. (1986) for the Blue-Green Schists and Worden and Morad (2003) for the Dark Phyllites and Orange Metasediments. Densities are assumed to be constant through the path: 1, 2.9 g/cm^3 and 2.4 g/cm^3 for water, oceanic basalt and shale and sandstone, respectively. b. Thermodynamically calculated H_2O-fluid content curves from 250 °C - 0.50 GPa to 400 °C to 0.80 GPa showing the fluid released from the selected Blue-Green Schists, Dark Phyllites and Orange Metasediments compositions. c to f. Thermodynamically calculated phase amounts for BS (Blue-Green Schists), GS (Blue-Green Schists), Dark Phyllites and Orange Metasediments, respectively. In all diagrams, the x axis corresponds to Temperature (ºC) - Pressure (GPa).

4.5.4.2 Thermodynamically Calculated Models from 250 to 400 °C

Thermodynamic modelling for the BS and GS compositions, in the range between 250 °C - 0.50 GPa to 400 °C - 0.80 GPa, predicts relatively similar trends of dewatering (***Fig. 4.10b***) with slightly different mineralogical changes. Dehydration in the Blue-Green Schists compositions is characterized by the consumption of stilpnomelane (***Fig. 4.10c*** and ***d***) and to a lesser extent lawsonite and chlorite (***Fig. 4.10d***).

Thermodynamic modelling for the Dark Phyllites and Orange Metasediments show almost no dehydration in the considered P-T window (***Fig. 4.10b, e*** and ***f***). In the case of Orange Metasediments, stilpnomelane is fully consumed at the beginning of the path (***Fig. 4.10f***), followed by little to no prograde paragenetic evolution with increasing depth.

Considering both the "synthetic minerals" and the thermodynamically calculated models, the total H_2O released during burial up to peak conditions for the BS and GS compositions is 10.5 and 8.3 wt%, respectively, yielding an average of c. 9.4 wt% of fluid. The total fluid released from the Dark Phyllites and Orange Metasediments during burial is c. 12.0 and 14.4 wt%, respectively.

It is difficult to quantify the uncertainties associated with the low-temperature (0 - 250 °C) part of the model, since it is impossible to precisely ascertain the proportions of the considered minerals during the early stages of the subduction path and the porosity of the initial material. As the amount of interstitial pore fluid was certainly high as expected for tuffaceous and sedimentary protoliths, we consider the high porosity values considered in our calculations (25-38 vol.%) as realistic upper bounds (e.g. Magara, 1980; Carlson and Herrick, 1990). In addition, thermodynamic modelling results should also be taken with care due to (i) the strong heterogeneity of the sedimentary material forming the units and (ii) the relatively high uncertainty of solid solution thermodynamic properties at low-temperature conditions. Last, it should be also mentioned that a slight disagreement exists in the prograde evolution of metavolcanic units, as a minor amount of clinopyroxene (***Fig. 4.8f***) is thermodynamically predicted but not observed in the studied natural samples.

4.6 Discussion

Petrological and microstructural investigations have revealed that evidence for HP metamorphism (including high-Si phengite and sodic amphibole) is ubiquitously found in all the units forming the Infiernillo sequence. The tectonic history and microstructural imprint left by the burial-exhumation trajectory in Infiernillo rocks is also identical in all the lithologies encountered on the coastal exposure. Altogether, these observations suggest that (i) the entire package now visible on the shore experienced HP-LT metamorphic conditions and (ii) most of the imbrication of the different lithotypes occurred during burial-related shearing, before peak metamorphism. It is therefore straightforward that Infiernillo exposures represent a key natural laboratory to study fluid production, fluid-rock interaction and subduction-related deformation within and at the downdip end of the seismogenic zone at maximum depths in the range of 25 to 30 km.

4.6.1 Blueschist and Greenschist Controlling factors

In a previous study, Halama and Konrad-Schmolke (2015) proposed that the layering of Infiernillo metavolcanics is commonly related to layer-parallel fluid transport that caused selective retrogression resulting in the blueschist and greenschist intercalations seen in the field (***Fig. 4.2c***). In their model, the retrograde greenschist facies overprint would have stabilized winchitic/actinolitic amphibole at 0.40 ± 0.10 GPa, after generalized peak glaucophane-bearing assemblages. The amphibole zoning pattern observed here in the Blue-Green Schist matrices and the apparent textural equilibrium between glaucophane and actinolite (e.g. ***Fig. 4.5e***) confirm that most of the greenschist facies domains are not the result of a retrogressive metamorphism. In addition, phengite compositions show little variations (***Fig. 4.7***), also pointing to a very limited greenschist overprint, in agreement with Willner (2005). The ACF projection (***Fig. 4.4a***) shows that the elemental variations in most of the greenschists and blueschists at Infiernillo locality, can well be explained by primary magmatic paragenesis. Mobile and immobile major and trace element analysis (***Fig. 4.3g*** and ***h***) support this statement suggesting that sea-floor metasomatism played a minor role and that fresh OIBs compositions correlate well with Infiernillo Blue-Green Schists. However, sea-floor fluid circulation evidently affected, at least locally, the rock volume as evidenced by the formation of rims around metapillows (***Fig. 4.2b***). X-Ray maps and SEM surface estimates (***Fig. 4.8***) show a clear trend of bulk-rock composition from the BS to the GS zone, resulting in variable amounts of glaucophane, actinolite, chlorite and phengite. The AFM projection analysis (***Fig. 4.4b***) shows that geochemical differences between BS and GS compositions (***Fig. 4.3a*** to ***d***) enhance the formation of glaucophane-bearing and actinolite-bearing rocks, respectively. The slightly higher Al proportions in the GS zone makes this composition favorable to form chlorite instead of glaucophane, while the opposite scenario is favorable for the BS composition which actually plots closer to the glaucophane apex, in agreement with petrological observations. It is important to note that OIB compositions fall in the actinolite + chlorite (± winchite) and glaucophane + chlorite (± winchite ± actinolite) fields, supporting the formation of both blueschist and greenschist parageneses at the same P-T conditions. Thereby, most samples indicate that major-element bulk composition correlates with the observed mineral paragenesis. Since the Mg# is the major factor controlling bulk-rock heterogeneities, we conclude

that Infiernillo greenschists and blueschists are both stable at the same peak P-T conditions, and that important differences in the bulk-rock Mg# as well as local Al, Ca and Na variations led to different paragenesis resulting in the millimeter-scale intercalation seen in the field at the transitional greenschist-blueschist facies (e.g. ***Fig. 4.2c***).

This conclusion is partially in agreement with Dungan et al. (1983), who proposed that the Fe/Mg ratio together with the absolute amount of FeO_{total} determine the occurrence of blueschists and greenschists, the latter parameter being higher in blueschists. Here we observe that the absolute amount of FeO_{total} in our blueschists compositions is actually lower compared to the greenschists. Thus, we propose that the Fe/Mg ratio is a more important controlling factor than the absolute amount of FeO_{total}. These observations are in line with thermodynamic modelling results demonstrating that the observed phase assemblages of BS and GS can be reproduced at fixed P-T conditions (***Fig. 4.8f***). We therefore conclude that the controlling factors resulting in blue-green layers in the Infiernillo exposure, i.e., different amphibole compositions at peak conditions and the variable amount of phases, can be mainly explained by geochemical variability previous to the HP stage due to: (i) primary differences in the protolith composition likely related with igneous heterogeneities and to a lesser extent (ii) hydrothermal effects of sea-floor fluids. However, some greenschists that plot in the glaucophane + actinolite + winchite + chlorite field (***Fig. 4.4b***) may represent retrogressed blueschists in agreement with samples that clearly show the HP metasomatic metamorphic enrichments trends illustrated in ***Fig. 4.3h*** (as suggested by Halama and Konrad-Schmolke, 2015; see also Hyppolito, 2014).

4.6.2 Prograde Veining and Fluid Production Model

4.6.2.1 Formation and Deformation of Veins

Natural observations in metamorphosed altered oceanic volcanic rocks have identified, among other reactions, analcime dehydration as an important fluid-producing reaction (e.g. Coombs, 1960):

$$\text{analcime } (NaAlSi_2O_6 \cdot H_2O) + \text{quartz} = \text{albite } (NaAlSi_3O_8) + H_2O$$

According to this reaction, prograde analcime breakdown may enable the formation of the widespread albite veins identified in this study. In addition, the breakdown of calcic zeolites (e.g. laumontite, wairakite, heulandite) may also contribute with large amounts of fluids. The observation of prograde zoning in albite vein amphibole suggest that these veins formed early during the burial history (i.e. before the blueschist facies overprint). We postulate that the texturally early albite veins visible in Infiernillo metavolcanics formed during zeolite facies mineral breakdown at temperatures below 200 °C (***Fig. 4.11a***; according to the experimental data from Liou, 1971; see also Fyfe et al., 1978; Spear, 1993). In other words, internally-derived Na-rich fluids can easily explain the texturally earliest albite veins extensively observed in Infiernillo Blue-Green Schists (***Fig. 4.11***). Some other vein sets, mainly filled by quartz, also may have formed as a result of burial-related mineral dehydration and compaction (***Fig. 4.11a*** inset 1). Synchronously, shear stresses favored orientation and re-orientation (transposition) parallel to the developing main foliation (***Fig. 4.11a*** inset 1 and 2). In addition, quartz

+ calcite veins also show winchite and actinolite. Besides, the presence of calcite fragments in winchite-bearing veins help us to constrain their occurrence during burial, likely near to peak conditions prior to exhumation (***Fig. 4.6d***). Approaching the HP stage, a supra-lithostatic pore fluid pressure environment enabled the fracturing followed by the precipitation of quartz + calcite ± albite as shown by (i) the hydrofracturing of the former albite veins (e.g. ***Fig. 4.5d*** and ***f; Fig. 4.6d*** to ***f; Fig. 4.11a*** inset 2) and by (ii) the crosscutting of the host rock by newly-formed vein sets (***Fig. 4.S1i***). Once the imbricated slices of the subducted material were basally accreted and incorporated in the deep duplex (e.g. Richter et al., 2007), the veined sequence of Infiernillo became isolated from the fluid-rich subduction interface region, thus preventing new inputs from the plate interface region.

Elongated amphibole needles occur perpendicular to grain boundaries inside and along the margins of albite-rich veins (***Fig. 4.5g*** and ***h***). We note that the long axis of the needles is, in most cases, perpendicular to the main foliation of the host. It is proposed here that the orientation of the principal compressive stress was parallel to the direction of vein amphibole needles during near-peak burial conditions (see also Moore et al., 2019 for another example). This stress orientation is kinematically compatible with the basal accretion process and ongoing nappe stacking on the interface (Richter et al., 2007). Additional re-orientation and deformation occurred during duplex exhumation as shown by the S3 fabrics.

4.6.2.2 Assessment of the Fluid Budget

Here we evaluate whether external fluid input is needed to justify the great abundance of veins observed in the Infiernillo sequence. Our fluid production model predicts an average of c. 9.4, 12.0 and 14.4 wt% of H_2O liberated from the Blue-Green Schists, Dark Phyllites and Orange Metasediments, respectively. Thus, to precipitate 0.45 vol.% of albite and 6.85 vol.% of quartz veins (not considering calcite; surface % values veins are shown in ***Table 2***), from a rock volume of 100 m^3 (0.45 m^3 of albite and 6.85 m^3 of quartz veins), solubilities of c. 50.2 wt% for quartz and c. 3.3 wt% for albite are needed (for further explanations see **Appendix 2**; note that albite is considered in the calculation only in the Blue-Green Schists as it is volumetrically rather abundant in this rock type). In agreement with our results, experimental studies have demonstrated that at P-T conditions above 0.9 GPa - 500 ºC and under pure H_2O compositions, albite solubilities in H_2O fluid are in the same order of magnitude than those calculated here (e.g. c. 2.5 wt%; Shmulovich et al., 2001). However, quartz solubilities are still one order of magnitude lower compared to our results (e.g. c. 1 to 4 wt%; Newton and Manning, 2000; Shmulovich et al., 2001).

It is known that chemical gradients may redistribute silica through diffusion mechanisms (Thompson, 1959; Korzhinskii, 1970). This process has been considered of minor importance in terms of mass transport in regional metamorphic environments where classical works have shown that solute diffusion through a standing fluid will take more than 200 years to reach the same transport distance than via fluid advection (e.g. Fletcher and Hoffman, 1974; Ruttern 1976; Etheridge et al., 1984). On the other hand, several authors have proposed, based on $\delta^{18}O$ and $\delta^{13}C$, that fluid-hosted diffusion may enhance silica (and carbonate) elemental mobility allowing the formation of calcite and quartz

veins (Cartwright et al., 1994; Henry et al., 1996; Cartwright and Barnicoat 1999). However, the lack of elemental depletion adjacent to the host/vein contact, identified only in few cases (Yardley, 1986; Cartwright and Barnicoat, 1999), suggests that silica mobility occurred through distances in the order of decimeters to meters under steady-state conditions (Cartwright and Buick, 2000). In addition, this process also requires large amounts of fluids (Etheridge et al., 1983). Since transient, near-lithostatic pore fluid pressure conditions and fracturing likely occur in a time span ranging from hours to days (e.g. Husen and Kissling, 2001; Frank et al., 2015), it is difficult to envision how the great amounts of quartz veins in the studied locality may have formed only via diffusion-related processes. In addition, the Infiernillo exposures lack evidence indicating substantial internal silica redistribution (e.g. massive and abundant solution seams, silica content or paragenetic changes approaching the veins). Therefore, we propose here that external fluids rich in quartz and calcite components (see for example ***Fig. 4.6***) were injected into to the system through strongly channelized pathways near-peak burial conditions (e.g. Cartwright and Barnicoat, 1999; Miller et al., 2000; Breeding and Ague, 2002; Lewerentz et al., 2017; Jaeckel et al., 2018; ***Fig. 4.11***). An external origin of CO_2 in the fluid phase infiltrating the studied vein sets is confirmed by the lack of calcite in the matrix material from all studied lithologies (e.g. ***Fig. 4.8d***). The CO_2 required to form calcite veins may come from decarbonation reactions which would take place at greater depths than that of Infiernillo peak metamorphism along the subduction channel (Cook-Kollars et al., 2014; Ague and Nicolescu. 2014; Menzel et al., 2020).

4.6.2.1 Nature and Mechanisms of Fluid-Rock Interaction Processes

Fluid release due to metamorphic dehydration reactions when crustal rocks enter the blueschist-eclogite facies transition (between 40 and 70 km depending on the P-T gradient) are known to be responsible for very high pore fluid pressures regions in the subduction environment (Audet et al., 2009; Fagereng and Diener, 2011; Saffer and Tobin, 2011). We have shown that the pervasive vein networks observed in Infiernillo rocks are the protracted result of (i) shallow prograde veining related to porosity collapse and early dehydration reactions along the interface before entering the slow-slip region (< 250 °C; ***Fig. 4.11***) and (ii) lower blueschist facies hydrofracturing due to external influx, as the relatively flat crustal dehydration pattern does not argue for massive local production in the 250 - 400 °C window (***Fig. 4.10b; Fig. 4.11***). By which physical mechanism did the external fluids enter the crustal sequence of Infiernillo causing hydrofracturing on their way?

It has been proposed that fluids under near-lithostatic pressures can travel upwards away from the reaction zone, either as “porosity waves” (Connolly, 1997) or along major sheared domains (Kawano et al., 2011; Angiboust et al., 2014). Heat may also be advected along with fluids resulting in a local perturbation of the geothermal gradient (e.g. Vrolijk et al., 1988; Spinelli and Wang, 2008; Harris et al., 2013). Studies of low-frequency earthquakes propose that metamorphic fluids may be trapped due to permeability anisotropies, implying weakening of the fault (Audet et al., 2009; Peacock et al., 2011; Frank et al., 2015). According to this model, during slow-slip events, along-fault permeability

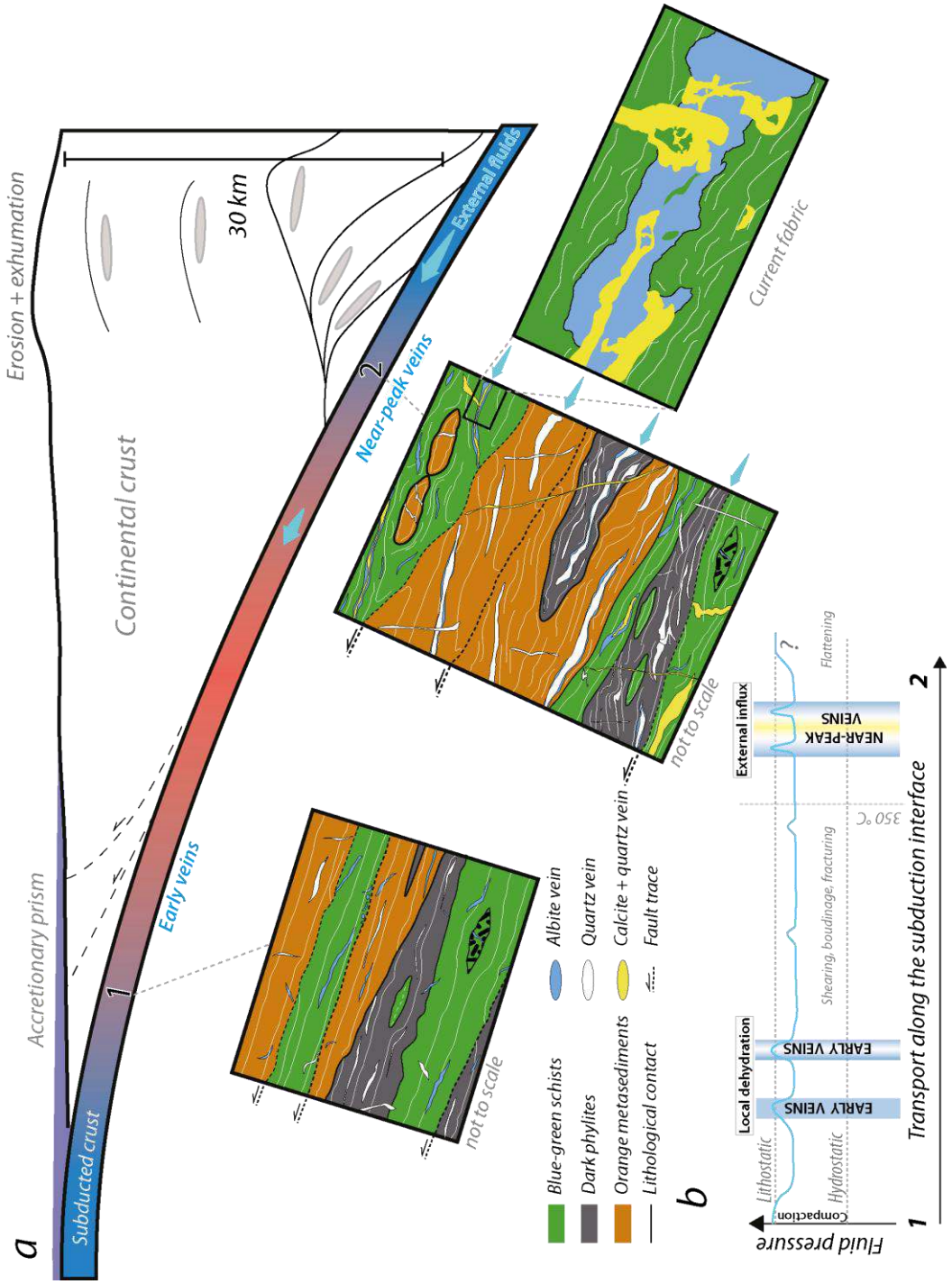

Figure 4.11. Subduction zone sketch illustrating vein formation and evolution of Infiernillo rocks. 1. During early stages of subduction, the entire sequence underwent compaction and porosity collapse causing a massive release of fluids, cracking and vein-filling (with random orientations) together with hydrofracture-like fabrics commonly sub-parallel to the main rock structure (see also Moore et al., 1995). 2. Further down during prograde burial (at seismogenic zone depths, in red), large amounts of fluids moving as pulses enhanced hydrofracturing (represented by the blue arrow), mainly through previous veins but also affecting the host rock and precipitating mostly quartz and calcite (as shown by albite and host rock fragments in veins). Additionally, boudinaged Orange Metasediments were wrapped in a Blue-Green Schists matrix developed close to peak conditions. b. Diagram showing fluid pressure distribution and deformation processes along the burial path (1 to 2) inspired from Saffer and Tobin (2011). Grey ovals are plotted in order to track the exhumation path. Duplex exhumation scheme modified from Willner (2005).

increases due to the creation of an inter-connected network of "reactivated" structures, resulting in high pore fluid pressure pulses that travel updip through the subduction interface at velocities on the order of 1 km/day (Radiguet et al., 2011; Frank et al., 2015). Interestingly, most deep hydrofractures at Infiernillo locality exhibit multiple stages of opening as suggested by the presence of crack-seal bands (e.g. Ramsay, 1980) and sequential mineral precipitation events (e.g. ***Fig. 4.5b; Fig. 4.6d*** to ***f***). Based on textural/fabric relationships, we infer that previous vein networks represent preferential mechanical weaknesses that enable external infiltration (e.g. Bons et al., 2012; Frank et al., 2015). Once opened, the veins enable fast influx of high pore fluid pulses triggering further hydrofracturing, a drop of the fault zone friction coefficient and ultimately the shearing of the metamorphic sequence (***Fig. 4.11***). It is commonly accepted that in active subduction systems slow slip events and ETS would be triggered in such fluid-saturated environments, characterized by high V_p/V_s ratios (Wang et al., 2006; Audet et al., 2009). This mechanism supports the idea that forces acting in the same direction of fluid motion, parallel to the subduction interface, may result in dilatational features (Shapiro et al., 2018). Nevertheless, the presence of (i) burial-related oblique (ptygmatic) veins cutting and being cut by veins oriented parallel to the main foliation, and (ii) amphibole needles oriented perpendicular to the vein margins suggest that the orientation of the least principal compressive stress (σ_3) must be in fact variable with time, switching between sub-parallel to sub-vertical on the subduction interface fault (e.g. Meneghini and Moore, 2007; Ujiie et al., 2018; Cerchiari et al., 2020). The apparent diversity of deformation patterns affecting the rocks along the subduction interface can likely be reconciled considering the evolution of the stress regime at the seismic cycle timescale (e.g. Magee & Zoback, 1993).

Last, we postulate that several distinct pulses contributed to the final state recorded in the exposure, as evidenced from crack-seal textures and cross-cutting relationships in the studied hydrofracture events (e.g. ***Fig. 4.5b; Fig. 4.6d*** to ***f***; Ramsay, 1980; Bachmann et al., 2009; Cerchiari et al., 2020). To precisely evaluate the amount of material deposited after a single pulse event, further fluid-rock experimental work is needed to refine (i) our understanding of the kinetics of fluid precipitation in vein systems and (ii) the quantification of the physico-chemical parameters acting during vein-filling processes. This information will help better constrain fluid transport dynamics in the ETS region and hence improve our understanding of the rheological properties of the plate interface as well as megathrust rupture nucleation processes.

4.7 Conclusions

Field and analytical results reveal that the Infiernillo sequence (central Chile) corresponds to a several hundreds of meter-thick stack of trench sediments and accreted oceanic material affected by multiple veining stages. Our investigation suggests that chemical and mineralogical differences in the protolith composition are the key factors controlling the millimeter to centimeter-scale occurrence of interlayered blueschist and greenschist, instead of selective retrogression due to late fluid influx. Additionally, our observations and results show that most of the veins present at the Infiernillo locality were formed during prograde burial towards peak conditions, from the contribution of three likely sources: (i) fluids expelled during initial compaction, (ii) fluids originated from metamorphic dehydration reactions and (iii) external deeply-generated fluid sources. Based on our calculations and observations, we propose that near-lithostatic pore pressure pulses supply the additional input of fluids necessary to justify the great amount of veins at the Infiernillo locality. These results shed light on fluid-rock interaction and over-pressurized fluid mobility at the base of the seismogenic zone as documented by seismological studies reporting high V_p/V_s segments as well as episodic tremor and slip events.

ACKNOWLEDGMENTS

Thaïs Hyppolito is acknowledged for sharing her knowledge about local geology. Anne Verlaguet, Hugues Raimbourg and James Connolly are also acknowledged for insightful discussions on fluid-rock metamorphic processes. Ralf Halama and two anonymous reviewers are warmly acknowledged for insightful comments. Mauricio Calderón, Francisco Fuentes and the Earth Sciences department from Universidad Andrés Bello are thanked for their technical assistance. Aitor Cambeses acknowledges the research grant provided by the Alexander von Humboldt Foundation for a post-doctoral fellowship at Bochum. This work has been funded by an IDEX grant #16C538 to S.A. The University of Granada is acknowledged for partial funding. Part of this work was also supported by the TelluS Program of CNRS/INSU. This is IPGP contribution #40xx. GSA Data Repository item 201Xxxx, including pseudosections, field pictures, microphotographs and supplementary data, is available online at www.geosociety.org/pubs/ft20XX.htm, or on request from editing@geosociety.org or Documents Secretary, GSA, P.O. Box 9140, Boulder, CO 80301, USA.

4.8 Supplementary information

4.8.1 "Synthetic Minerals" Model

Theoretical end-member mineral compositions for the Blue-Green Schists BS and GS compositions are: Ca-amphibole (relict hornblende), actinolite, albite, analcime (zeolite), montmorillonite, clinochlore (chlorite), muscovite, stilpnomelane, quartz, clinopyroxene (relict augite), iron oxide and prehnite (e.g. Cho et al., 1986; Thompson and Humphris, 1977). The theoretical minerals considered for the Dark Phyllites and Orange Metasediments are: kaolinite, berthierine, montmorillonite, clinochlore, albite, quartz, dickite, illite and stilpnomelane (e.g. Worden and Morad, 2003). Mineral proportions vary thorough the path from 0 to 250 °C (every 50 °C). The H_2O (wt%) content in each step corresponds to the sum of the H_2O (wt%) in each mineral multiplied by its volume abundance (assuming mineral densities as selected for each type of rock). In addition, we considered the fluid contained in porosity, from which we fixed the values detailed in ***Fig. 4.10a***. Density values as mentioned in the caption of ***Fig. 4.10***.

The next step is to sum thermodynamically calculated water released to the "synthetic minerals" calculated water released. Finally, the average between BS and GS compositions are considered as representative for the Blue-Green Schists, together with Dark Phyllites and Orange Metasediments compositions. The mineral proportions considered and H_2O released are shown in ***Table S4***.

4.8.2 Solubility Calculations

For solubility calculations an initial volume of 100 m^3 is considered, where 6.85 volume % ($6.85x10^6$ cm^3) corresponds to quartz and 0.45 volume % ($0.45x10^6$ cm^3) to albite veins, giving 92.3 volume % ($92.3x10^6$ cm^3) of host rock matrix, which is normalized to 100%. The next step is to multiply the volume values by density, which was calculated after the thermodynamic modelling considering the Blue-Green Schists, Orange Metasediments and Dark Phyllites compositions (c. 2.80 g/cm^3; see ***Table 2***). The new values correspond to the mass of matrix, quartz and albite in grams. Using the H_2O (in wt%) values calculated after thermodynamic and ¨synthetic minerals¨ modeling, the mass of H_2O liberated from the matrix can be calculated multiplying the weighted percentage fraction by the mass of rock of each of the three units (W_{Lib}, calculated from thermodynamic and "synthetical minerals" modeling). Finally, the solubility can be calculated dividing the mass of quartz and/or albite with the mass of water liberated. The H_2O needed (W_{Ned}) is calculated multiplying the H_2O liberated by the mass of quartz present in the beach exposures and dividing by the mass of quartz that would precipitate from the fixed solubility value (0.3 wt% for quartz, extrapolated from Anderson and Burnham, 1965) To precipitate the amount of quartz present in veins (c. $17.8x10^6$ g), c. $59.4x10^8$ g of water is necessary, in other words; 167 times more fluid than what has been produced by dehydration during burial must be released (W_{Ned}/W_{Lib}). Analogue calculations were made for albite but considering a solubility value of 0.25 wt% (extrapolated from Currie, 1968).

4.8.3 Figures and Tables

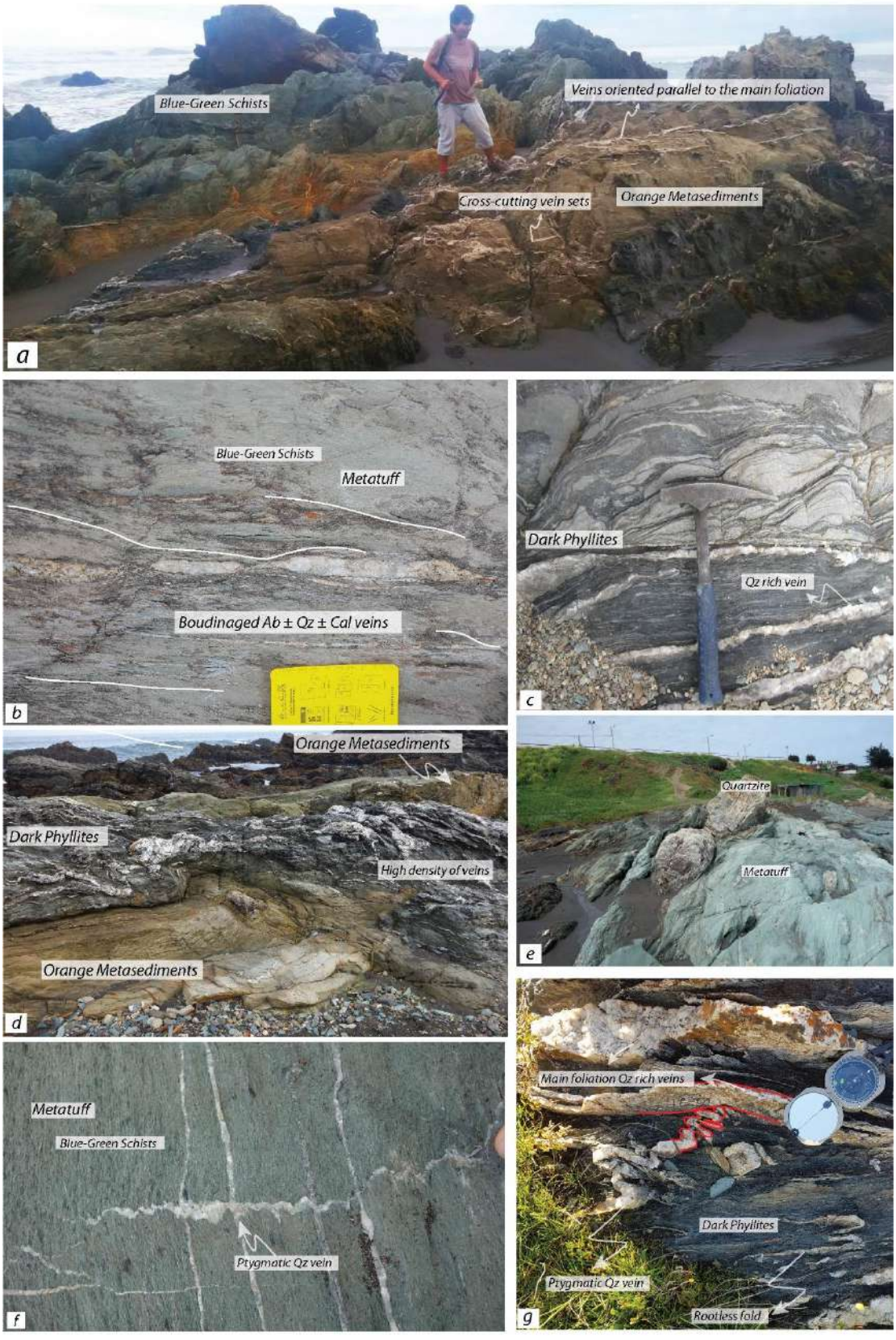

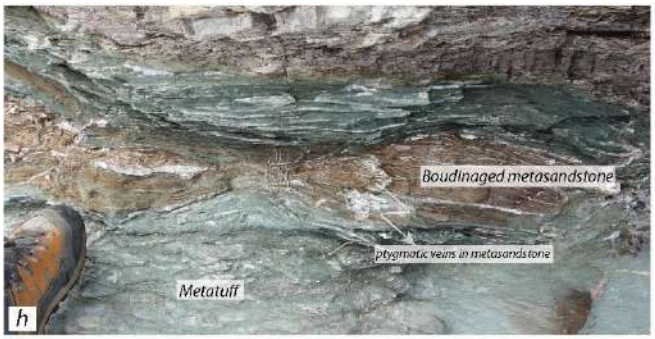
Boudinaged metasandstone
ptygmatic veins in metasandstone
Metatuff
h


Blue-Green Schists
chaotic vein network
Host rock fragment in vein
i

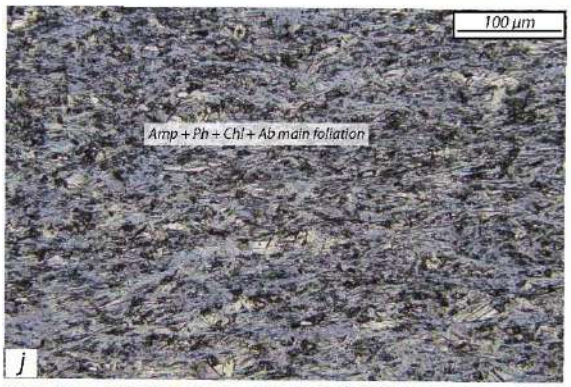
100 µm
Amp + Ph + Chl + Ab main foliation
j

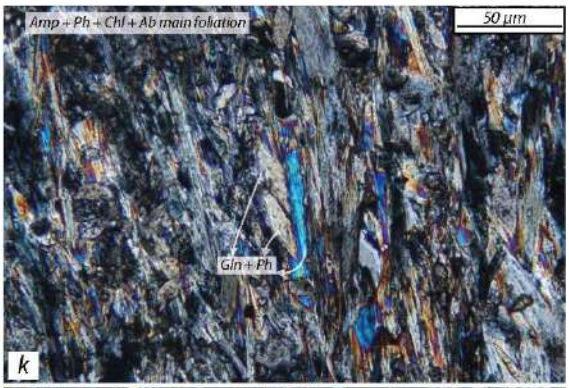
Amp + Ph + Chl + Ab main foliation
50 µm
Gln + Ph
k


100 µm
Amp + Chl + Ph + Ab main foliation
l

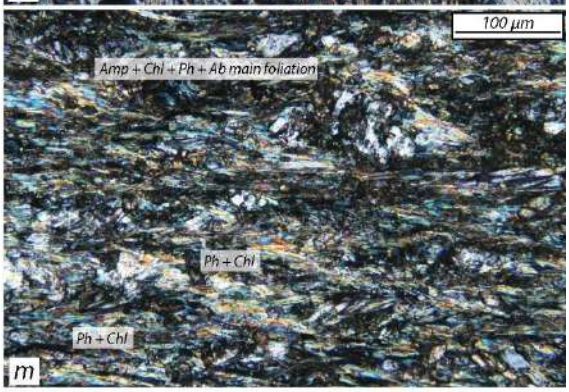
100 µm
Amp + Chl + Ph + Ab main foliation
Ph + Chl
Ph + Chl
m


Main foliation Qz-rich vein
Cutting Qz-rich vein
Dark Phyllites
n

Figure 4.S1. Additional field pictures and photomicrographs. a. Orange Metasediments general view of a layer with abundant quartz-rich veins. b. Centimeter-wide boudinaged albite ± quartz ± calcite vein in a metatuff matrix. c. Two different lithologies within the Dark Phyllites; note the greater abundance of veins in the lower part of the picture. d. Dark Phyllites intercalated between Orange Metasediments; note the greater abundance of veins in the Dark Phyllites. e. Metavolcanic rocks belonging to the Blue-Green Schists wrapping around boudinaged quartzite blocks from the Orange Metasediments. The veins are fragmented at the tip of the sigmoid. f. Ptygmatic quartz vein in a metatuff transecting veins parallel to the main foliation, thus suggesting a subduction-related metamorphic origin. The fold axis is parallel to the main foliation. g. Quartz vein parallel to the main foliation cutting an oblique ptygmatic quartz vein, the latter with an axial plane of folding parallel to the main foliation. h. Boudinaged Orange Metasediments wrapped in a metatuff matrix; note the occurrence of oblique ptygmatic quartz vein in metasandstone boudins with an axial plane of folding parallel to the main foliation and stretching direction. i. High density and chaotic calcite vein network in the Blue-Green Schists; note the tens of centimeter-sized matrix fragments in the calcite vein. j. General view of the BS zone (sample P18.33) showing the prograde to peak main foliation composed by amphibole, phengite, chlorite and albite. k. Cross-polarized detailed view of the BS (sample P18.33) main foliation; note the sharp contacts between glaucophane and phengite in textural equilibrium. l and m. General and cross-polarized view of the GS zone (sample P18.33) respectively; note the higher proportions of chlorite and phengite and lower proportions of amphibole relative to the BS zone. n. Oblique quartz vein cutting a quartz-rich vein oriented according to the main foliation; note the folding orientation coherent with the S2 fabric.

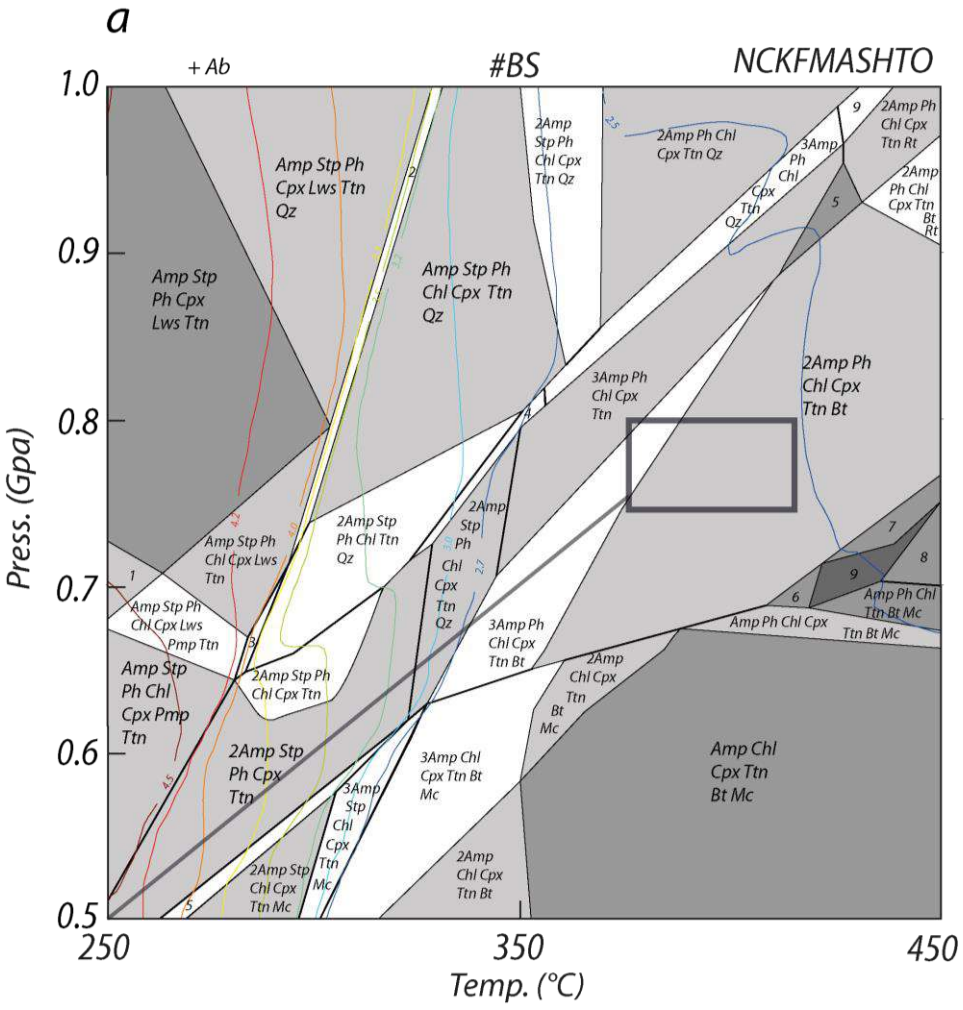

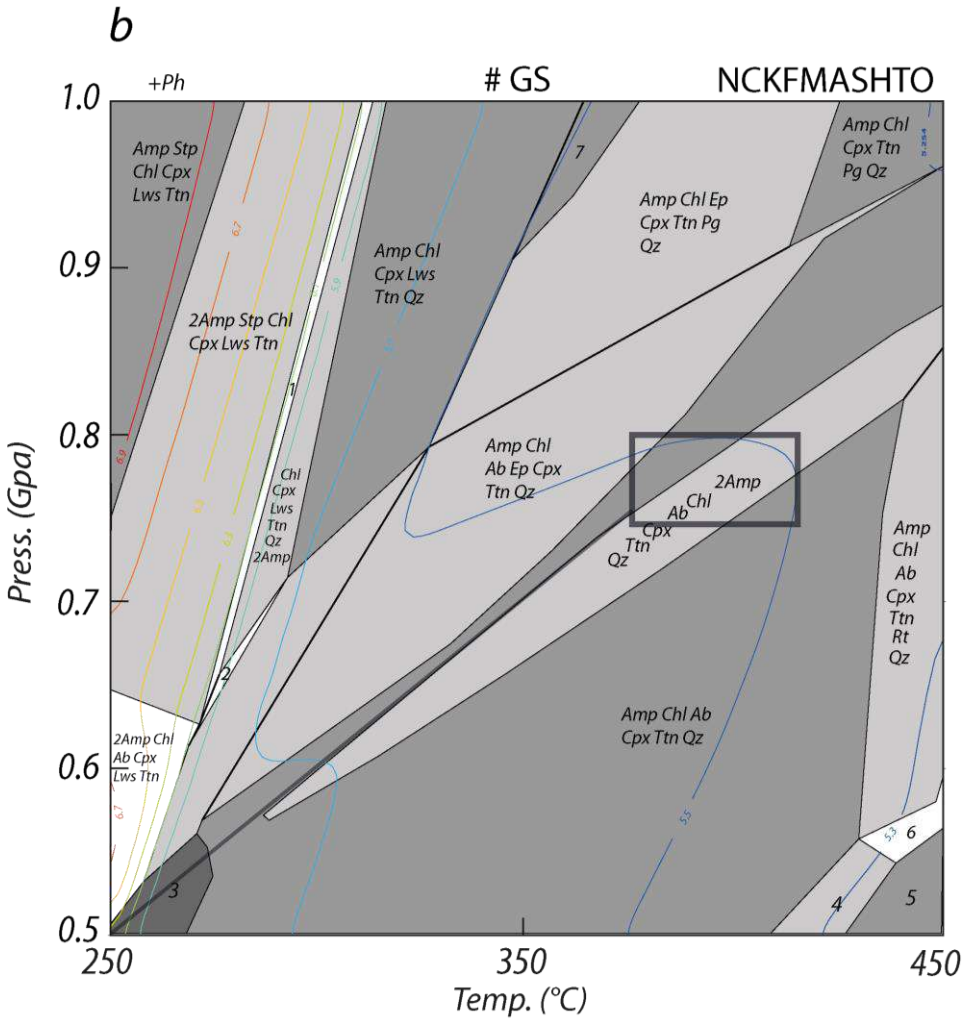

1. 2Amp Stp Chl Cpx Lws Ttn Qz
2. 2Amp Chl Ab Cpx Lws Ttn Qz
3. Chl Ab Cpx Ttn Qz
4. Amp Chl Ab Cpx Ttn Qz Hem
5. Amp Chl Ab Cpx Ttn Mt
6. Amp Chl Ab Cpx Ttn Rt Qz Hm
7. Amp Chl Ep Cpx Ttn Qz

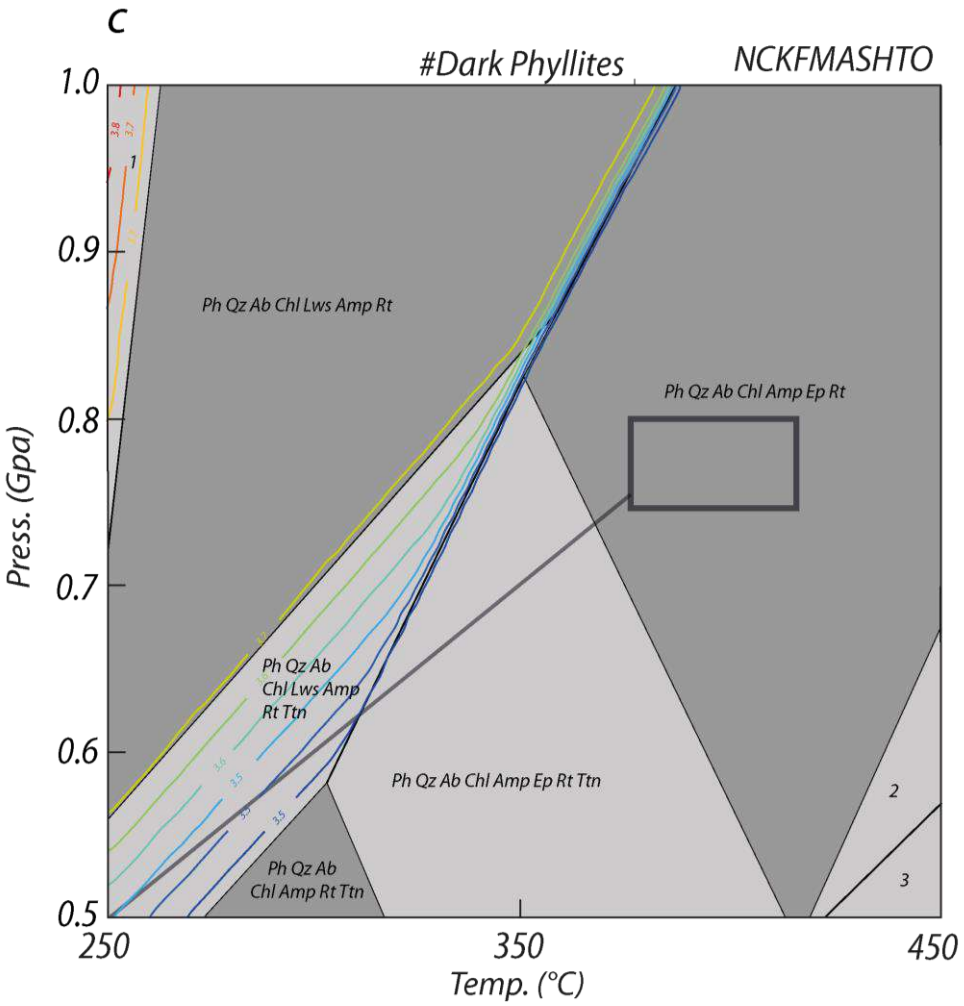

1. Ph Ab Qz Chl Stp Lws Amp Rt
2. Ph Ab Qz Chl Amp Ep Rt Mag
3. Ph Ab Qz Chl Ep Rt Ttn Mag

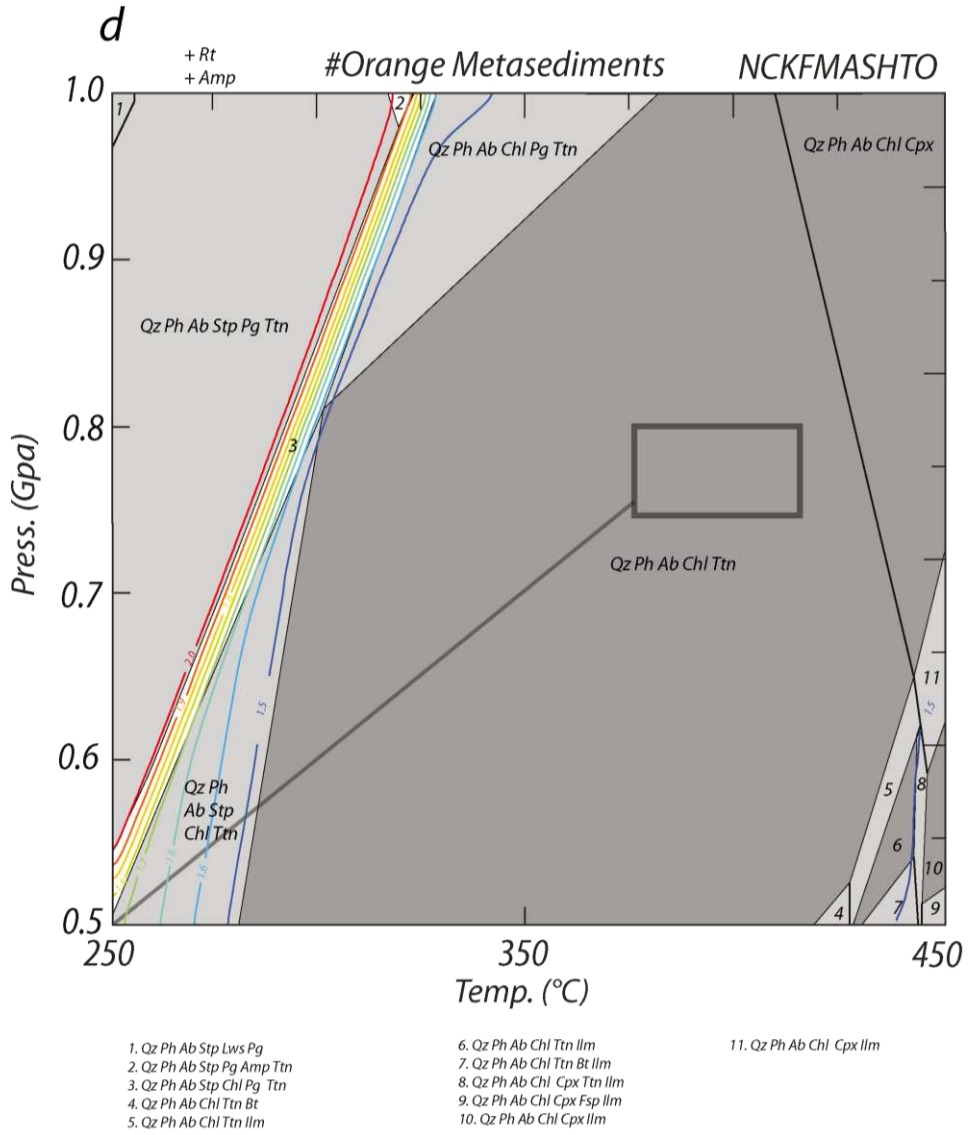

Figure 4.S2. a to d. Pseudosections of the BS, GS, Dark Phyllites and Orange Metasediments, respectively. H_2O isopleths in wt% are shown.

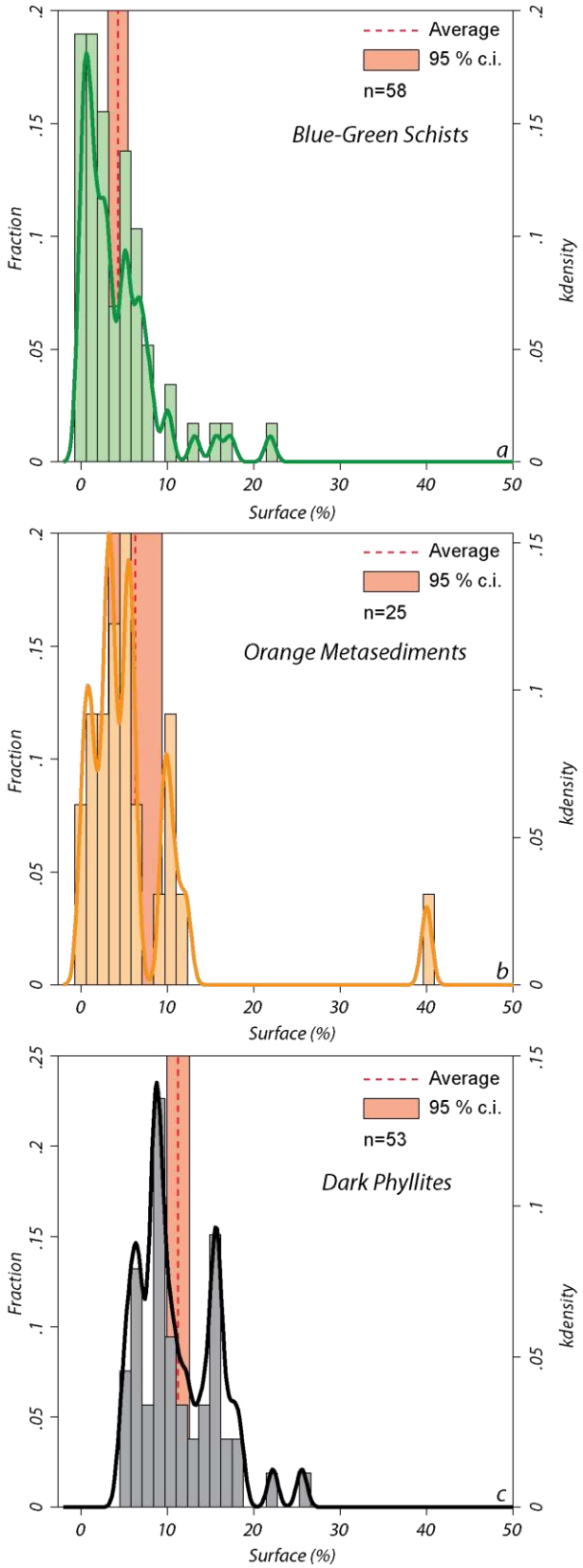

Figure 4.S3. a to c. Histograms of calculated vein abundance showing the mean values and the confidence interval for the Blue-Green Schists, Orange Metasediments and Dark Phyllites, respectively.

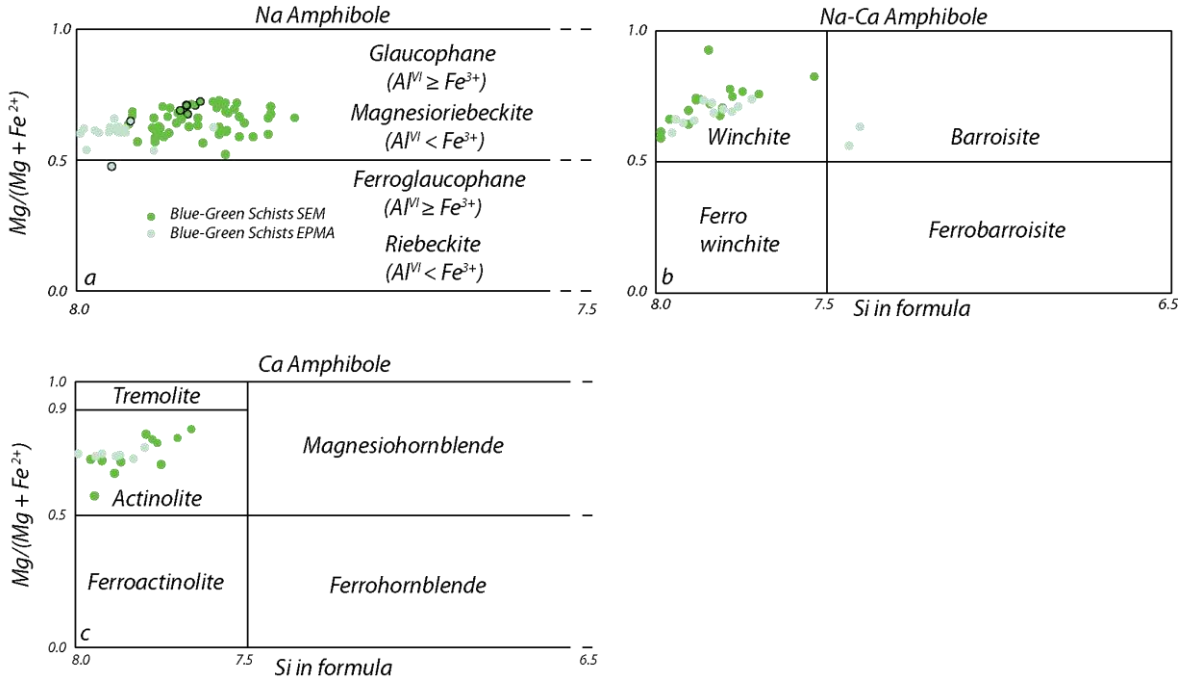

Figure 4.S4. Na amphibole composition (lined symbols correspond to amphibole with $Al^{VI} < Fe^{3+}$). b. Na-Ca amphibole composition. c. Ca amphibole composition. d. Amphibole classification diagrams after Leake et al. (1997). Lined symbols correspond to amphibole with $Al^{VI} < Fe^{3+}$.

TABLE S1. WHOLE ROCK GEOCHEMISTRY RESULTS

Sample	Classification	Method	SiO_2 (wt%)	TiO_2 (wt%)	Al_2O_3 (wt%)	FeO(T) (wt%)	MnO (wt%)	MgO (wt%)	CaO (wt%)	Na_2O (wt%)	K_2O (wt%)	P_2O_5 (wt%)	L.O.I (wt%)	TOTAL (wt%)	Ba (ppm)	Rb (ppm)	Sr (ppm)	Y (ppm)	Zr (ppm)
P18.39	BS	XRF	49.16	3.45	13.84	11.68	0.13	5.86	3.73	3.88	2.75	0.50	3.83	98.81	887	63	53	23	245
P18.40	BS	XRF	53.00	2.05	11.67	10.38	0.15	7.24	3.83	3.72	3.95	0.19	2.44	98.62	1041	100	36	22	158
P18.43A	BS	XRF	54.20	1.93	8.24	11.44	0.13	8.90	4.59	5.14	0.86	0.21	2.23	97.87	221	20	40	15	134
P18.43B	GS	XRF	40.80	3.43	13.15	13.38	0.18	10.22	4.58	2.15	1.83	0.44	7.36	97.52	505	43	53	25	237
P18.44B	BS	XRF	45.70	1.91	13.38	12.28	0.15	6.98	8.58	3.48	1.09	0.38	3.80	97.73	208	30	296	18	142
P18.45	BS	XRF	58.60	1.38	10.78	9.36	0.10	5.52	3.12	6.84	0.30	0.17	2.13	98.30	48	7	42	7	102
PI-17-AC-1	Orange Metasediment	XRF	75.12	0.55	11.79	3.20	0.03	1.05	0.25	2.79	2.19	0.14	1.65	98.76	318	48	12	14	138
PI-17-AC-6	Orange Metasediment	XRF	71.96	0.64	10.88	5.48	0.15	1.30	0.22	1.36	3.66	0.14	2.81	98.60	1604	141	16	16	89
PI-17-AC-6B	Orange Metasediment	XRF	88.93	0.19	3.85	1.84	0.11	0.33	0.09	1.45	0.45	0.04	0.79	98.05	339	20	11	8	40
PI-17-AC-4	Dark phyllite	XRF	69.24	0.68	13.75	5.40	0.04	1.54	0.25	0.57	3.99	0.16	3.20	98.82	293	87	15	14	126
PI-17-AC-P11A	Dark phyllite	XRF	61.55	0.70	17.33	7.13	0.24	1.99	0.51	1.19	4.44	0.13	3.65	98.86	562	97	14	8	107
PI-17-AC-P11B	Dark phyllite	XRF	58.71	0.82	18.45	7.34	0.09	2.55	0.71	1.52	4.29	0.18	4.11	98.75	167	46	14	11	128
P18.33	BS	SEM	57.04	1.42	10.42	11.7	*N.D	8.56	4.12	5.30	1.44	*N.D	*N.D	100	*N.D	*N.D	*N.D	*N.D	*N.D
P18.33	GS	SEM	47.39	2.89	14.05	15.1	*N.D	11.23	4.5	2.97	1.87	*N.D	*N.D	100	*N.D	*N.D	*N.D	*N.D	*N.D

*N.D= Not determined

Nb (ppm)	Th (ppm)	Pb (ppm)	Ga (ppm)	Zn (ppm)	Cu (ppm)	Ni (ppm)	V (ppm)	Cr (ppm)	Hf (ppm)	Cs (ppm)	Sc (ppm)	Ta (ppm)	Co (ppm)	Be (ppm)	La (ppm)	Ce (ppm)	Pr (ppm)	Nd (ppm)	Sm (ppm)	Eu (ppm)	Gd (ppm)	Tb (ppm)	Dy (ppm)	Ho (ppm)	Er (ppm)	Tm (ppm)	Yb (ppm)	Lu (ppm)
29	2.2	0.0	22	170	50	80	339	20	5.9	3.0	21.0	2.6	39	2.0	27.2	61.4	8.1	35.4	7.9	2.93	7.07	1.05	5.34	0.87	2.19	0.29	1.68	0.22
22	3.2	1.0	16	9	116	10	213	267	4.0	3.9	0.0	1.7	62	1.0	18.0	47.4	5.4	21.9	5.5	1.85	5.46	0.89	5.13	0.94	2.49	0.36	2.25	0.32
18	1.0	0.5	14	14	29	27	273	342	2.9	0.6	0.0	0.9	60	2.0	10.8	24.1	3.6	13.3	4.0	1.25	4.09	0.56	3.33	0.49	1.38	0.17	1.07	0.13
29	2.4	0.7	25	108	74	177	294	499	5.5	1.5	0.0	2.0	68	2.0	25.6	57.0	8.1	35.0	8.3	2.74	7.93	1.05	5.44	0.90	2.28	0.27	1.88	0.24
20	1.1	0.3	17	72	78	115	248	328	3.4	0.9	0.0	1.7	73	<1	16.0	31.7	4.9	21.7	5.2	1.50	5.20	0.66	3.57	0.65	1.81	0.22	1.54	0.16
15	0.7	0.5	9	26	39	56	210	246	2.9	0.3	0.0	1.7	88	2.0	4.4	12.6	1.8	7.1	2.0	0.52	1.75	0.25	1.44	0.25	0.80	0.09	0.67	0.10
8	4.0	11.4	13	52	9	15	59	53	3.7	3.2	6.6	0.7	7	1.7	18.3	45.9	4.3	16.7	3.3	0.65	2.60	0.39	2.38	0.46	1.23	0.20	1.36	0.21
9	6.1	49.7	15	80	61	60	120	140	2.3	5.2	13.4	0.8	43	2.0	18.7	48.9	4.7	18.6	3.8	0.48	3.11	0.48	2.80	0.59	1.56	0.26	1.64	0.27
3	3.3	6.7	4	31	23	20	23	39	1.1	1.0	5.8	0.3	44	0.5	9.9	22.2	2.1	8.0	1.7	0.28	1.43	0.23	1.28	0.29	0.81	0.13	0.90	0.14
9	6.0	12.4	17	78	18	39	111	100	3.4	5.4	7.7	0.8	11	2.5	23.7	50.9	5.6	21.6	4.1	0.83	3.18	0.47	2.61	0.52	1.42	0.23	1.38	0.22
11	4.5	9.6	22	94	73	52	147	86	2.9	4.9	9.4	1.0	22	3.0	15.1	41.7	3.7	14.3	2.8	0.46	2.11	0.31	1.42	0.31	0.89	0.16	1.02	0.19
14	4.8	18.3	21	94	27	33	129	88	3.5	3.4	7.2	1.2	15	3.1	24.8	53.7	6.3	24.3	4.5	0.82	3.10	0.42	2.02	0.44	1.22	0.21	1.31	0.22
*N.D	*N.D	*N.D	*N.D	*N.D	*N.D	*N.D	*N.D	*N.D	*N.D	*N.D	*N.D	*N.D	*N.D	*N.D	*N.D	*N.D	*N.D	*N.D	*N.D	*N.D	*N.D	*N.D	*N.D	*N.D	*N.D	*N.D	*N.D	*N.D
*N.D	*N.D	*N.D	*N.D	*N.D	*N.D	*N.D	*N.D	*N.D	*N.D	*N.D	*N.D	*N.D	*N.D	*N.D	*N.D	*N.D	*N.D	*N.D	*N.D	*N.D	*N.D	*N.D	*N.D	*N.D	*N.D	*N.D	*N.D	*N.D

TABLE S2. BULK ROCK COMPOSITIONS USED FOR THERMODYNAMIC CALCULATIONS

Composition	SiO_2 (wt%)	TiO_2 (wt%)	Al_2O_3 (wt%)	FeO (wt%)	Fe_2O_3 (wt%)	MgO (wt%)	CaO (wt%)	Na_2O (wt%)	K_2O (wt%)	sum (wt%)
BS (P18.33)	56.87	1.41	10.39	8.56	3.41	8.53	4.10	5.29	1.43	100.00
GS (P18.33)	47.20	2.88	13.99	11.04	4.40	11.19	4.48	2.96	1.87	100.00
Dark Phyllites	66.14	0.77	17.3	6.87	0.69	2.13	0.51	1.15	4.44	100.00
Orange Metasediments	81.47	0.48	9.15	3.27	0.40	0.93	0.19	1.93	2.18	100.00

TABLE S3. SURFACE MEASUREMENTS AND STATISTICAL ANALYSIS

Unit	Surface (%)	Surface Cm^2
Blue-Green Schists	17.27	1225
Blue-Green Schists	7.93	1369
Blue-Green Schists	0.47	875
Blue-Green Schists	0.08	22500
Blue-Green Schists	0.07	10000
Blue-Green Schists	0.07	22500
Blue-Green Schists	10.08	12000
Blue-Green Schists	21.89	5600
Blue-Green Schists	13.16	378
Blue-Green Schists	4.84	3760
Blue-Green Schists	6.73	2950
Blue-Green Schists	3.35	3612
Blue-Green Schists	5.32	840
Blue-Green Schists	3.21	248
Blue-Green Schists	5.11	735
Blue-Green Schists	1.23	828
Blue-Green Schists	0.81	1127
Blue-Green Schists	9.95	759
Blue-Green Schists	5.4	851
Blue-Green Schists	7.01	520
Blue-Green Schists	15.66	3102
Blue-Green Schists	8.19	1120
Blue-Green Schists	0.24	738
Blue-Green Schists	5.15	16388
Blue-Green Schists	2.84	13160
Blue-Green Schists	6.4	2451
Blue-Green Schists	4.78	2736
Blue-Green Schists	2.9	520
Blue-Green Schists	7.02	374
Blue-Green Schists	5.14	3298
Blue-Green Schists	3	2100
Blue-Green Schists	0.1	11000
Blue-Green Schists	1.51	255
Blue-Green Schists	1.87	350
Blue-Green Schists	6.65	2408
Blue-Green Schists	7.74	705
Blue-Green Schists	0.66	3760
Blue-Green Schists	0.15	1700
Blue-Green Schists	1.31	3096
Blue-Green Schists	1.08	228
Blue-Green Schists	2.35	72
Blue-Green Schists	1.22	1150
Blue-Green Schists	0.54	2911
Blue-Green Schists	3.8	2738
Blue-Green Schists	0.56	216
Blue-Green Schists	0.23	192
Blue-Green Schists	1.44	5005
Blue-Green Schists	2.33	399
Blue-Green Schists	4.29	799
Blue-Green Schists	2.82	7569
Blue-Green Schists	0.54	625
Blue-Green Schists	0.69	792
Blue-Green Schists	2.29	22290
Blue-Green Schists	5.48	6027
Blue-Green Schists	1.33	20643
Blue-Green Schists	6.52	39362
Blue-Green Schists	3.13	12513

Unit		All data			95 % Conf Interval	
	Variable	Data points	Mean	Error	Min	Max
Green	%	58	4.28	1.18	3.10	5.46
Green	Cm^2	58	5114.66	2011.43	3100.74	7128.57
Orange	%	25	6.29	3.12	3.07	9.51
Orange	Cm^2	25	13542.24	6208.38	7135.51	19948.97
Black	%	53	11.23	1.27	9.95	12.51
Black	Cm^2	53	27786.96	18688.55	9036.30	46537.62

Blue-Green Schists	2.25	11181
Orange Metasediments	2.29	5564
Orange Metasediments	2.97	910
Orange Metasediments	3.2	2492
Orange Metasediments	3.62	1421
Orange Metasediments	10.09	26331
Orange Metasediments	3.59	11193
Orange Metasediments	6.28	41580
Orange Metasediments	5.37	14356
Orange Metasediments	0.93	1764
Orange Metasediments	1	2601
Orange Metasediments	40.01	40397
Orange Metasediments	5.59	17514
Orange Metasediments	4.59	2450
Orange Metasediments	5.28	18000
Orange Metasediments	5.94	3500
Orange Metasediments	0.12	1200
Orange Metasediments	0.33	1312
Orange Metasediments	3	3000
Orange Metasediments	9.8	2000
Orange Metasediments	3.51	187
Orange Metasediments	9.52	189
Orange Metasediments	5.53	30218
Orange Metasediments	10.98	35098
Orange Metasediments	12.19	25654
Orange Metasediments	1.42	49625
Dark Phyllites	15.99	2116
Dark Phyllites	15.61	2736
Dark Phyllites	13.8	12740
Dark Phyllites	9.41	6192
Dark Phyllites	8.6	8480
Dark Phyllites	10.73	11639
Dark Phyllites	8.46	15004
Dark Phyllites	15.38	9409
Dark Phyllites	15.6	1443
Dark Phyllites	18.49	1225
Dark Phyllites	25.56	14274
Dark Phyllites	16.15	10058
Dark Phyllites	17.46	480000
Dark Phyllites	16.03	9999
Dark Phyllites	15.63	1225
Dark Phyllites	17.09	1296
Dark Phyllites	10.77	3136
Dark Phyllites	9.31	2800
Dark Phyllites	7.18	3481
Dark Phyllites	5.42	2601
Dark Phyllites	9.67	2288
Dark Phyllites	8.6	18252
Dark Phyllites	6.85	874
Dark Phyllites	22.2	1026
Dark Phyllites	14.8	1938
Dark Phyllites	6.01	5250
Dark Phyllites	4.62	100696
Dark Phyllites	8.52	42436
Dark Phyllites	14.24	26162
Dark Phyllites	8.96	6396
Dark Phyllites	9.15	101528
Dark Phyllites	8.33	14884
Dark Phyllites	11.41	14884
Dark Phyllites	5	14884
Dark Phyllites	13.27	5625
Dark Phyllites	11.87	6400
Dark Phyllites	6.88	3969
Dark Phyllites	8.78	80172
Dark Phyllites	9.71	19044
Dark Phyllites	8.43	5005
Dark Phyllites	5.35	43681
Dark Phyllites	12.27	27889
Dark Phyllites	5.91	3600
Dark Phyllites	7.74	3721
Dark Phyllites	6.49	9928
Dark Phyllites	15.09	91824.257
Dark Phyllites	6.51	28855
Dark Phyllites	18.13	25183
Dark Phyllites	8.53	23917
Dark Phyllites	12.44	43509
Dark Phyllites	10.62	15110
Dark Phyllites	6.17	50431
Dark Phyllites	10.11	33494

TABLE S4. SYNTHETIC MINERALS MODEL : PROPORTIONS AND WATER RELEASED

	BS		GS			Dark Unit		Orange Unit	
Mineral/Temperature	0°C	250°C	0°C	250°C		0°C	250°C	0°C	250°C
Hornblende	24.0	1.0	24.0	2.0	Kaolinite	11.8	1.0	9.0	0.0
Actinolite	0.0	23.0	0.0	20.0	Berthierine	4.7	7.4	7.0	0.0
Albite	12.0	20.0	12.0	15.0	Montmorillonite	19.6	0.0	10.0	0.0
Fe oxide	1.6	1.5	1.6	1.6	Albite	7.1	5.4	6.5	10.0
Analcime	16.0	8.0	12.0	10.4	Quartz	29.8	35.0	50.0	50.0
Montmorillonite	6.4	0.0	6.4	0.0	Dickite	9.4	5.0	5.0	0.0
Clinochlore	20.0	20.0	20.0	30.2	Clinochlore	7.8	7.0	0.0	0.0
Muscovite	2.4	10.0	6.4	12.4	Illite	2.7	32.6	6.0	33.0
Quartz	10.4	8.0	10.4	3.0	Stipnomelane	7.1	7.1	6.5	7.0
Augite	3.2	3.0	3.2	0.0					
Stilpnomelane	4.0	5.5	4.0	1.0					
Prehnite	0.0	0.0	0.0	4.0					
H_2O in minerals + porosity (wt %)	13.6	5.0	13.5	6.1		19.1	7.2	19.4	5.2
H_2O released (wt. %) from 0 to 250 °C	8.6		7.4			11.9		14.2	
Thermodynamically calculated H_2O (wt. %)released	1.9		0.9			0.1		0.2	
Total H_2O released (wt. %) for each Unit from 0 to 400 °C	9.4					12.0		14.4	

5. Episodic hydrofracturing and large-scale flushing along deep subduction interfaces: Implications for fluid transfer and carbon recycling (Zagros orogen, southeastern Iran)

Muñoz-Montecinos et al. (2021)

Episodic hydrofracturing and large-scale flushing along deep subduction interfaces: Implications for fluid transfer and carbon recycling (Zagros orogen, southeastern Iran)

Jesús Muñoz-Montecinos[1,2], Samuel Angiboust[1], Antonio Garcia-Casco[2,3], Johannes Glodny[4], Gray Bebout[5]

[1] Université de Paris, Institut de physique du globe de Paris, CNRS, F-75005 Paris, France, jesus.munozmontecinos@gmail.com; angiboust@ipgp.fr

[2] Department of Mineralogy and Petrology, Faculty of Sciences, University of Granada, Campus Fuentenueva s/n, 18002 Granada, Spain, agcasco@ugr.es

[3] Instituto Andaluz de Ciencias de la Tierra, CSIC-Universidad de Granada, 18100 Armilla, Granada, Spain

[4] GFZ German Research Centre for Geosciences, Telegrafenberg, 14473 Potsdam, Germany. glodnyj@gfz-potsdam.de

[5] Department of Earth and Environmental Sciences, Lehigh University, Bethlehem, PA 18015, USA. geb0@lehigh.edu

Published in: Chemical Geology Volume 571, 20 June 2021, 120173

Reference: Muñoz-Montecinos, J., Angiboust, S., Garcia-Casco, A., Glodny, J., & Bebout, G. (2021). Episodic hydrofracturing and large-scale flushing along deep subduction interfaces: Implications for fluid transfer and carbon recycling (Zagros Orogen, southeastern Iran). Chemical Geology, 571, 120173.

DOI: https://doi.org/10.1016/j.chemgeo.2021.120173

Journal Impact Factor (IF): 4.015

WoS Quartile: Q1 (GEOCHEMISTRY and GEOPHYSICS)

ABSTRACT

We investigate the late Cretaceous blueschist-facies (480 °C-1.8 GPa) segment of the Zagros suture zone, a well-preserved block-in-matrix paleo-subduction channel. We aim to determine the relative chronology, conditions of deformation, and potential fluid sources and processes associated with the widespread occurrence of lawsonite + clinopyroxene + glaucophane veins and aragonite-bearing hydraulic breccias. We use a multi-scale approach methodology to provide new insights into deep fluid flow mechanisms as well as to constrain possible sinks of CO_2-bearing fluids in the subducting slab. Petrological analyses suggest that silicate-rich vein systems began precipitating during early burial and evolved with ongoing burial and shearing-related deformation in the blueschist-facies, while most carbonate-rich veins and hydrofractures formed at near-peak *P-T* conditions. In situ LA-ICP-MS trace element analyses reveal that: (i) individual silicate host-vein pairs have similar REE signatures, reflecting local-scale fluid-mediated element redistribution, (ii) carbonate-bearing veins and metasediments also have similar trace element signatures and (iii) lawsonite in blueschist-hosted veins exhibit REE enrichments along their rims, suggesting an increasing contribution of metasedimentary-derived fluids upon approaching peak *P-T*. Carbonate O-C isotope compositions of the veins and metasedimentary rocks range from +13.6 to +17.9‰ ($\delta^{18}O_{VSMOW}$) and -1.0 to +3.1‰ ($\delta^{13}C_{VPDB}$), demonstrating metasedimentary-derived fluid sources related to large-scale H_2O homogenization with far-traveled mafic- ultramafic-derived fluids. Sr-Nd isotopic ratios in carbonate veins and the adjacent host resemble their host composition indicating that host rock-buffered isotopic homogenization occurred between the infiltrating fluids and the rock matrix, possibly during episodic porous flow. Thermodynamic modeling predicts that decarbonation via fluid-assisted reactions is inefficient at blueschist-facies and that carbon release likely occurs deeper along the subduction interface (i.e., at eclogite-facies). We propose that deeply produced H_2O-rich fluids interacted with the carbonate-bearing lithologies along the subduction interface facilitating fluid-mediated decarbonation and further fluid transport as hydraulic pulses (e.g., porosity waves) that traveled at the kilometer-scale parallel to the subduction interface, (i) contributing to the isotopic homogenization herein observed and (ii) triggering episodic hydrofracturing in the lawsonite-blueschist-facies (≈50-60km depth). Veinsets in exhumed subducted rocks hence provide a unique opportunity to understand fluid-rock interaction processes in the region at which episodic tremor and slow slip events phenomena occur.

Keywords: *Blueschist; Fluid-rock interaction; Hydrofracturing; Fluid pulses; Prograde veins; Peak aragonite veins; Subduction zones*

5.1 Introduction

Subduction zones represent the major volatile and mass transfer pathway into the mantle affecting its physicochemical properties such as melting temperature and rheology, among others (e.g., Poli and Schmidt, 1995; Stern, 2002). Along the subduction interface, H_2O-CO_2-fluids (hereafter referred to as COH fluids) generated by metamorphic devolatilization reactions have been considered a key factor controlling the slab-mantle coupling state, seismicity, arc magmatism and, eventually, building forearc topography (e.g., Hacker at al., 2003; Grove et al., 2006; van Keken et al., 2011; Menant et al., 2019). An important amount of fluid is expelled at shallow depths in the outer forearc due to porosity collapse and clay breakdown (Byrne and Fisher, 1990; Saffer and Tobin, 2011). At greater depths, most of the water (OH and/or H_2O) bound in hydrous minerals (e.g., lawsonite, chlorite, micas, amphibole and serpentine; Poli and Schmidt, 1995; Zheng and Hermann, 2014) will eventually be released during prograde metamorphism, especially at the blueschist-eclogite transition (Hacker, 2008). However, in cold subduction environments, considerable amounts of water can be retained to greater depths in the mantle (van Keken et al., 2011; Padrón-Navarta and Hermann, 2017; Kempf and Hermann, 2018).

The most obvious evidence for COH-bearing fluid-rock interactions in subduction zones is the occurrence of complex vein systems in both the subducting interface-channel and the overlying forearc (e.g., Philippot and Selverstone, 1991; Bebout and Barton, 1993; Spandler et al., 2011; Angiboust et al., 2020), which provide valuable information regarding fluid-rock interactions (e.g., Molina et al., 2004; Zack and John, 2007; Spandler et al., 2008; van der Straaten et al., 2012; Taetz et al., 2016), fluid pathways and chemistry (e.g., Scambelluri and Philippot 2001; Spandler et al., 2003; Angiboust et al., 2017), and pressure-temperature (P-T) conditions of fluid circulation (Vrolijk et al 1988; Raimbourg et al., 2018). Understanding whether fluids are locally derived or far-travelled has long been a matter of debate (Philippot and Kienast, 1989; Widmer and Thompson, 2001; Piccoli et al., 2018). While the former scenario considers closed-system mass transfer from the adjacent host rock towards a fracture that serves as the sink for solute precipitation (e.g., Nadeau et al., 1993; Hermann et al., 2006; Spandler and Hermann, 2006), the opposite requires open-system advective mass-transfer over meter- to kilometer-scale pathways before precipitation (Vrolijk et al., 1988; Breeding and Ague, 2002; Spandler et al., 2011; Angiboust et al., 2014). Both types of processes have been inferred based on trace element and isotopic studies (e.g., Nelson, 1995; Spandler et al., 2003; Bebout, 2007; Putnis and Austrheim, 2010; Schwarzenbach et al., 2018). Recently, it has been shown that important element transport may occur in the form of amorphous, alkali-Al-Si-rich materials via depolymerization of crystals along grain boundaries and lattices defects, and repolymerization of the amorphous phase in favorable domains, the latter facilitating nucleation and growth of crystals (Konrad-Schmolke et al., 2018). Another consequence of fluid-rock interaction is the formation of totally obliterated/hybridized lithologies such as jadeitites, omphacitites, lawsonitites or metasomatic rinds, particularly in mélange zones (e.g., Harlow and Sorensen, 2004; Vitale Brovarone et al., 2014; Bebout and Penniston-Dorland, 2016). When intense metasomatism occurs, the original geochemical signature is overprinted, resulting in hybrid lithologies (Spandler et al., 2008; Bebout and Penniston-

Dorland, 2016), selvages around vein margins (Spandler and Hermann, 2006; John et al., 2008; Beinlich et al., 2010; Taetz et al., 2016) or selective retrogression (van der Straaten et al., 2008).

In subduction-zone metamorphic rocks, C occurs in oxidized form (e.g., calcite, aragonite and dolomite) and as reduced organic matter (e.g., graphite, diamond, hydrocarbons) and is abundant in subducted oceanic sediments, ophicalcites and hybridized mafic/ultramafic lithologies. Studies attempting to characterize high pressure-low temperature (HP-LT) rock carbonation processes demonstrate that C dissolution and further precipitation in the subduction interface is an important manifestation of fluid-rock interactions allowing the formation of metasomatic carbonate-bearing lithologies with direct implications on the global C subduction budget (Piccoli et al., 2016; Scambelluri et al., 2016). On the other hand, thermodynamic calculations and natural occurrences demonstrate that decarbonation is important if the C-bearing rocks are pervasively infiltrated and equilibrated by H_2O-rich fluids (Collins et al., 2015; Ague and Nicolescu, 2014; Vitale Brovarone et al., 2018; Vitale Brovarone et al., 2020). Thus, a comprehensive vision of fluid-rock interaction products is required to characterize the full spectrum of fluid flow and carbonation-decarbonation processes in the subduction interface at depths (Oliver and Bons, 2001; Spandler and Hermann, 2006). While most of these studies focused on silicate-bearing veins and carbonate-bearing host rock, only a few have investigated carbonate-bearing metamorphic veins (e.g., Piccoli et al., 2016, 2018; Vitale Brovarone et al., 2018).

We herein investigate the HP-LT blueschist-facies segment of the Zagros suture exposed in the Soghan region (Iran; ***Fig.5.1A***), aiming at providing a comprehensive vision on fluid-rock interaction processes as well as mechanisms of fluid circulation taking place at different scales in cool subduction environments, a tectonic setting where a variety of slow earthquake processes are inferred to occur in active margins (e.g., Peng and Gomberg, 2010). In this field-based work, we employ a broad spectrum of petro-geochemical techniques to constrain timing and relative pressure-temperature (P-T) conditions of veining and to determine: (i) likely fluid sources and the degree of mixing and (ii) the petrophysical mechanisms involved in fluid flow at blueschist-facies depths. Finally, our results are integrated into a multiscale, petro-tectonic model that enables characterizing the variety of fluid flow patterns inferred to have been occurred in Seghin rocks, shedding light onto poorly-resolved processes of active subduction systems.

5.2 Geological setting

In the Zagros Orogen (southern Iran), rare remnants of the long-lived subduction (c. 180 to 35 Ma) which ended with the closure of the Neotethys ocean and the subsequent collision between Eurasia and Arabia plates, are exposed. The ophiolitic material comprising this suture is commonly referred to in the literature as “colored mélange” (Delaloye and Desmons, 1980; Agard et al., 2006 and references therein). Subduction was accompanied by abundant magmatic activity in the Eurasian plate, as recorded in the Sanandaj-Sirjan zone and the Urumieh-Dokhtar volcanic associations (***Fig.5.1A***). In the Hajiabad-Esfandagheh region, witnesses of this long-lasting subduction history crop out. We focus here on the northern Soghan region which comprises stacks of variably

metamorphosed rocks showing blueschist-facies mineral associations tectonically overlaid by the unmetamorphosed Sanandaj-Sirjan zone (Agard et al., 2006; Arfania and Shahriari, 2009). This subduction-related complex is rather unaffected by the collisional imprint and is made of three tectonic units exposed now as a large anticline tectonic window (Agard et al., 2006; Angiboust et al., 2016).

The uppermost Ashin complex is composed of a metasedimentary, metavolcanic and ultramafic lithological association. The lower part is locally composed of ultramafic lithologies (harzburgites and dunites) along the contact with the Seghin complex (***Fig.5.1B***) and exhibits a serpentinization gradient towards the inner part of the Ashin complex (Angiboust et al., 2016). Thermobarometric and geochronological investigations yielded peak amphibolite-facies conditions in the range of 500-600 °C and 0.9-1.2 GPa during middle Cretaceous (Ghasemi et al., 2002; Agard et al., 2006; Angiboust et al., 2016) followed by a blueschist-facies overprint of late Cretaceous age (500 °C at c. 1.3 GPa; Angiboust et al., 2016). In contrast, the Siah-Kuh unit (mapped as "colored mélange") consists of a large coherent ocean-derived massif dominated by pelagic and platform sediments, metamafic rocks and minor serpentinites (Sabzehei, 1974) interpreted as a subducted seamount (Bonnet et al., 2020b) presumably formed in a supra-subduction environment related to arc volcanism above the Neotethys in the range of 87 to 77 Ma (Moghadam et al., 2013; Bonnet et al., 2020a). The subduction-related metamorphic imprint occurred at peak conditions of 200-300 °C and 0.5-0.9 GPa in the lower blueschist-facies field (Bonnet et al., 2020b). The Siah-Kuh seamount was probably the latest unit of this nappe-stack to enter the subduction zone and to become accreted to the Iranian margin (Angiboust et al., 2016).

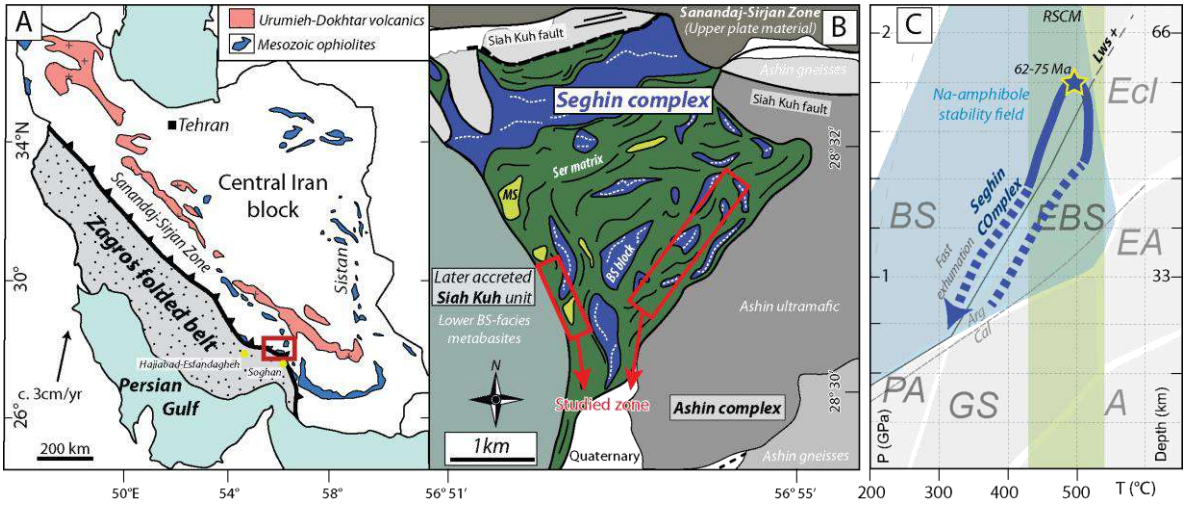

Figure 5.1. A. Geological map of Southeastern Iran showing the main regional structural features (modified from Angiboust et al., 2016). B. Geological map of the Soghan region with emphasis on the Seghin and adjacent units (modified from Angiboust et al., 2016). C. Pressure-Temperature (P-T) diagram showing the P-T path followed by the Seghin complex and Raman spectroscopy of carbonaceous material (RSCM) results after Angiboust et al. (2016). The metamorphic grid is after Evans (1990). A—amphibolite-facies; BS—blueschist-facies; EBS—epidote blueschist-facies; EA—epidote amphibolite-facies; Ecl—eclogite-facies; GS—greenschist-facies; PA—pumpellyite actinolite-facies; MS—metasediment; BS—blueschist; Ser—serpentinite.

The present study focuses on the blueschist-facies Seghin complex which is sandwiched between the Siah-Kuh and the Ashin complexes and that is characterized by abundant blueschists and minor metasedimentary blocks wrapped by an antigorite-rich serpentinite matrix (Sabzehei, 1974; Angiboust et al., 2016). Petrologically, the blueschists are composed of extremely well-preserved mineral assemblages containing HP-LT index minerals such as lawsonite, aragonite, glaucophane and omphacite (Sabzehei, 1974; Agard et al., 2006; Angiboust et al., 2016). Thermobarometric results and Rb-Sr multimineral ages yield peak P-T conditions around 430-530 °C and 1.6-1.8 GPa at c. 62-75 Ma (***Fig.5.1C***; Agard et al., 2006; Angiboust et al., 2016), in line with P-T estimates from a jadeitite body exposed along the Ashin-Seghin contact (Oberhänsli et al., 2006). No detailed studies attempting to characterize the vein-filling material, including crystallization sequence of the HP-LT mineral assemblages mentioned above, have been carried out in the Seghin complex so far.

Altogether, the metamorphic complexes exposed in the Soghan region represent three tectonic slices of material that underwent contrasted metamorphic histories during long-term accretion and tectonic transport along the Zagros subduction interface (Agard et al., 2006; Angiboust et al., 2016; Bonnet et al., 2020b). P-T-t reconstruction demonstrate that these three slices record the cooling of the Zagros subduction thermal gradient from c. 17 °C/km at c. 95 Ma down to c. 7 °C/km at 65 Ma (Angiboust et al., 2016).

5.3 Field observations

5.3.1 Lithological associations in the Seghin complex

The Seghin complex is mostly composed of foliated meter to hectometer-sized blueschist blocks wrapped by a serpentinite matrix (***Figs.5.2A*** and ***B***). The main foliation strikes ENE to NE and is gently to moderately dipping in the sheared serpentinite matrix while sub-vertical in the foliated blueschist blocks. The most abundant lithology (≈70 vol.%) corresponds to the serpentinite matrix which is essentially composed of blueish-greenish massive antigorite (Angiboust et al., 2016) with no relics of the original ultramafic protolith. The interface between blueschist blocks and the serpentinite matrix is generally sharp (***Fig.5.3A***), but minor centimeter-wide greenish transitional rinds locally occur. The blueschists consist of strongly foliated lenses of metatuffs and metalavas (***Figs.5.3B*** and ***D***) representing approximately a quarter of the entire unit (≈25 vol.%). Pillows and hyaloclastite structures have not been documented in the Seghin complex. Evidence for the HP-LT metamorphism can be seen by the ubiquitous presence of coarse-grained Na-amphibole, lawsonite and Na-Ca clinopyroxene. Meter-sized clinopyroxenite pods, which are volumetrically rare, occur wrapped by the serpentinite matrix (***Fig.5.3C***) or in the outer edge of blueschist blocks (***Fig.5.3B***). Metasedimentary material (≈5 vol.%), including metapelites, graphitic schists, calcschists and marbles increase in abundance towards the base of the complex in particular near the contact with the Siah-Kuh massif (***Fig.5.1B***). These rocks are well-foliated and fine-grained, except for impure marbles which are apparently devoid of foliation. In addition, interlayered metapelitic micaschist (devoid of carbonates) and blueschist blocks support the idea that the former and the latter underwent the same prograde P-T path.

5.3.2 Vein systems characteristics

All the lithologies exposed in the Seghin complex contain relatively high amounts of veins. Here we emphasize on representative textural and mineralogical relationships between veins and their host lithologies. For the sake of simplicity, we have defined two types of veins: veins composed mostly by silicate phases (***Fig.5.3D***) and those which contain abundant carbonates (***Figs.5.3C, E*** and ***F***).

Tens of centimeter-wide blueschist-hosted silicate-rich veins are composed of coarse-grained lawsonite, Na-amphibole, Na-clinopyroxene, quartz, albite and less abundantly phengite and apatite. These veins are either sheared along the main foliation fabric (***Fig.5.3D***) or crosscut the host matrix. Generally, up to tens of centimeter-wide carbonate-bearing veins occur as hydraulic breccias crosscutting the host rock and the previous silicate-rich veins (***Fig.5.3E***). Structural patterns such as mineral precipitation within hollows, cavities or pillow core-to-edge heterogeneities that may provide information regarding seafloor hydrothermal activity were not observed.

Serpentinite-hosted veins occur pervasively and are essentially composed of strained carbonate phases (***Fig.5.3F***). In a similar way, clinopyroxenite-hosted veins are composed by carbonates and develop hydraulic breccia-like structures (***Fig.5.3C***) with no traces of further deformation. The macro- to meso-scale textural relationships between host rock and veins are summarized in the schematic representation from ***Fig.5.2C***. Based on processing of more than 100 high-resolution field pictures with ImageJ software, covering areas ranging from c. 1 to 30 m^2 (several hundreds of m^2 were scanned), supported with field measurements, we estimate that the entire Seghin complex is composed of c. 8 surf.% of veins, from which, approximately 7 surf.% corresponds to carbonate-bearing veins (assuming that serpentinite-hosted veins are exclusively filled by carbonates; see the boxplot of ***Fig.5.2C***) while the remaining 1 surf.% is made of silicate-rich veins. Estimates of vein proportions higher than the mean mostly correspond to veins in serpentinites while the lower proportions are for blueschist-hosted veins. The metasediment-hosted veins are not considered in these calculations due to their minor abundance relative to the Seghin complex-scale. In further volume calculations (see discussion section) an infinite projection of the vein planes in the dip direction is assumed; thus, transformation from surface to volume is straightforward. These estimates help constraining fluid-rock interaction processes, as discussed below.

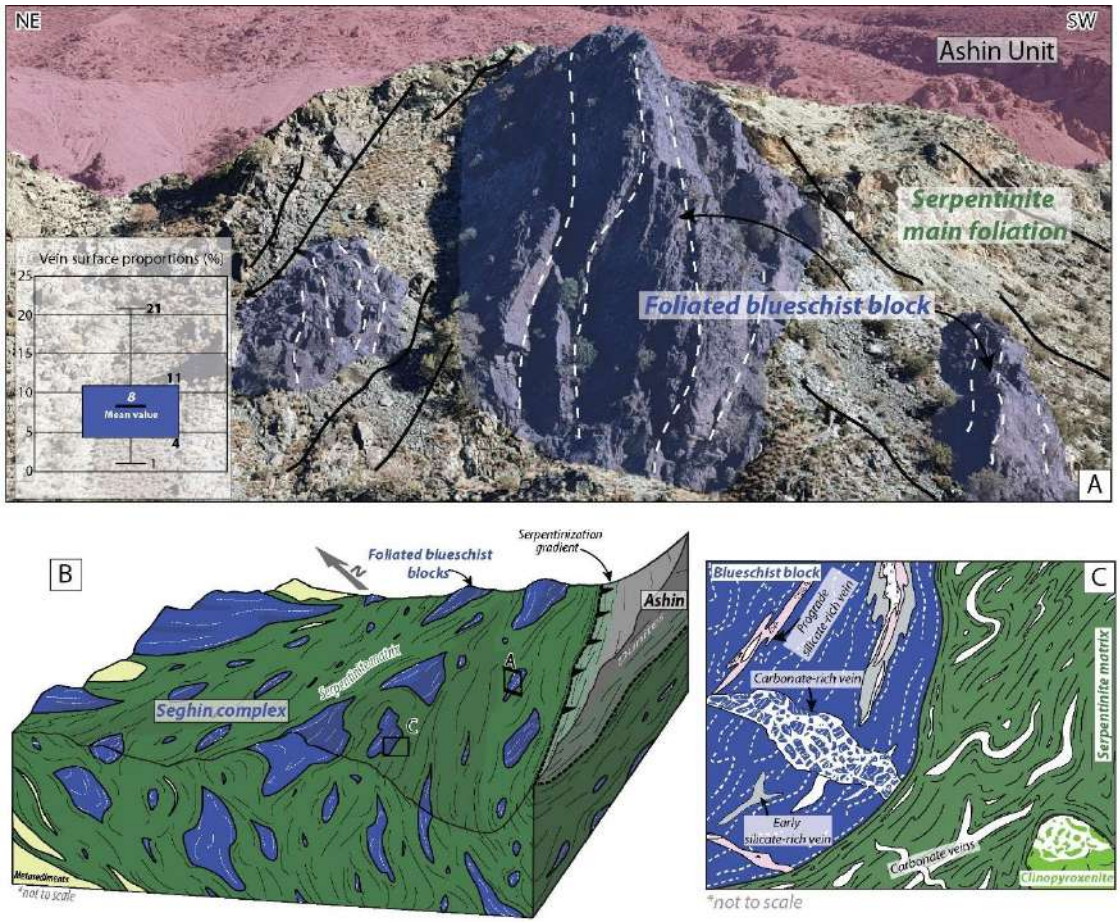

Figure 5.2. A. General view of the block-in-matrix fabric from the Seghin complex. The box plot depicts calculated vein surface proportions at the scale of the Seghin complex. The obtained mean value corresponds to the total proportion of veins. Approximately 7 surf%. of the veins are filled by carbonates. B. Simplified sketch of the Seghin complex structure and block distribution. C. Vein-host relationships. Note the viscously deformed serpentinite-hosted veins while brittle deformation dominates in the blueschist blocks.

5.4 Analytical methods

5.4.1 Scanning electron microscope, electron probe microanalyzer and cathodoluminescence optical microscopy

Electron probe microanalyses (EPMA) were performed at Sorbonne Université and GFZ Potsdam with a CAMECA SX-Five and a JEOL-JXA 8230 instruments, respectively, under common analytical conditions (15 kV, 20 nA, wavelength-dispersive spectroscopy mode) using a 2 to 5 µm beam diameter. Standards used for the calibration were the following: orthoclase (Al, Si, K), fluorite (F), rutile (Ti), Cr_2O_3 (Cr), wollastonite (Ca), albite (Na), MgO (Mg), Fe_2O_3 (Fe) and rhodonite (Mn). For representative analyses of major phases, the reader is referred to ***Table 1***. Elemental X-ray maps were obtained with the CAMECA SX-Five instrument applying the ZAF correction and with a scanning electron microscope (SEM) Zeiss model Evo MA10 at the Institut de Physique du Globe de Paris using internal calibration standards. The resulting X-ray maps were treated with DWImager software (Garcia-Casco, 2007). A barycentric quaternary Al_2O_3'-CaO'-FeO'-Na_2O' (ACFN) diagram

was designed using CSpace software by means of algebraic methods (Torres-Roldán et al., 2000) after projection of chemical compositions of mineral phases and exchange vectors necessary to condense the 11-dimensional composition space (c.f., Spear, 1993). Cathodoluminescence image mosaics were acquired with a Cathodyne (NEWTEC) machine coupled to an optical microscope operated at 18 kV and 120 µA plasma with an exposure time of 2 second per image.

Amphibole and pyroxene nomenclature, structural formulae and Fe^{3+} calculations are based on the recommendations of Leake et al. (1997) and Morimoto (1988), respectively. White mica structural formula was normalized to 11 equivalent oxygens assuming Fe^{2+} total in octahedral sites. Mineral compositions are given in atoms per formula unit (a.p.f.u). The $Mg/(Mg+Fe^{2+})$ ratio is abbreviated as XMg. Mineral abbreviations are from Whitney and Evans (2010).

5.4.2 Whole rock geochemistry, X-ray diffraction, electron backscatter diffraction and Raman spectroscopy

Representative samples of the main lithotypes (5 marbles, 3 metasediments, 5 serpentinites, 8 blueschists and 3 clinopyroxenites) were crushed and pulverized for major and trace element determinations performed by X-ray fluorescence (XRF) and inductively coupled plasma mass spectroscopy (ICP-MS) at Centre for Scientific Instrumentation of the University of Granada (CIC-UGR). For XRF analyses, the samples were melted using a lithium tetraborate fusion flux. Typical analytical precision is better than ± 1.5 % for an analyte concentration of 10 wt.%. Zirconium concentrations have been measured using the same analytical method. Trace elements were determined by Inductively Coupled Plasma-Mass Spectrometry (ICP-MS) after HNO^3 + HF digestion of 0.1 g of pulverized material in a Teflon-lined vessel at 180 °C for 30 min, evaporation to dryness and subsequent dissolution in 100 ml of 4 vol.% HNO^3; the precision was better than ± 2% for analyte concentrations of >50 ppm and ± 5 % for analyte concentrations of >5 ppm. The results are presented in ***Table S1***.

Powder X-ray diffraction analyses (XRD) were performed in representative blueschist and serpentinite-related vein samples using a Panalytical Empyrean X-ray diffractometer at Université de Paris, with Cu Kα radiation and equipped with a multi-channel "PIXcel" detector, in the angular range 5°-70° with a step size of 0.0131° and a 60 s time per step of 60s.

In order to characterize the spatial distribution of different carbonate species and discriminate between aragonite and calcite, we have performed electron backscatter diffraction (EBSD) and Raman spectroscopy measurements (see ***Figs. 5.S1***). EBSD data has been acquired at the Laboratoire de géologie of Ecole Normale Supérieure Paris (ENS) on a ZEISS SIGMA Field Emission Gun SEM equipped with and Nordlys Nano (Oxford instruments) detector. EBSD maps were acquired with the following parameters: 15 keV acceleration voltage, 5 nA of beam current and aperture of 120 µm, standard inclination of 70° and working distance of 14 mm, acquisition rate of 100 Hz and a step size of 4 and 3 µm for the serpentinite and marble maps, respectively. The Raman spectra were also acquired at ENS Paris using a Renishaw InVia Raman spectrometer and processed with the Peakfit©

software. Along this paper, we refer to specific carbonate species (e.g., aragonite or calcite) only if demonstrated by any of the analytical techniques herein used. On the other hand, the general term carbonate is used.

5.4.3 Mineral trace element analysis

In situ trace-element analyses were obtained at CIC-UGR using a Laser Ablation Quadrupole Inductively Coupled Plasma-Mass Spectrometer (LA-ICP-MS). The system is composed of a 213-nm Merchantek Nd-YAG laser coupled to an Agilent 7500 ICP mass spectrometer. Ablation was carried out in a He atmosphere, and the laser beam was adjusted to produce 30 μm diameter ablation spots. Before measuring, spots were pre-ablated for 15 seconds with a laser fluence of 2.5 Jcm^{-2}, then ablated for 60 seconds with a laser fluence of 7.5 Jcm^{-2}. A blank, measured in the same conditions but with zero laser energy, preceded every measurement. The resulting counts were subtracted from the sample signals. The stage was automated to move 5 μm every 20 s to increase sensitivity and avoid fractionation as the laser scavenges the ablation crater. As an external standard, we used the NIST-610 glass, measured every six spots for drift corrections, and at the beginning and the end of each analytical session. Note that linearity between signal intensity and concentration is regularly checked and generally maintained. As an internal standard, we used silicon. Data reduction was done using an in-house LA-ICP-MS data evaluation software written in STATA™ programming language at CIC-UGR. For each measurement, the software plots every replicate of each element against time, looking for spikes indicating microinclusions. If so, the affected replicates are excluded from the analyses. Precision calculated based on NIST-610 replicates was about ±5 % (relative) and the detection limit is c. 0.01 ppm for most elements (see Bea et al., 1996 for more details).

5.4.4 O-C and Sr-Nd isotope analysis

Carbonate phases in 32 veins from all lithotypes as well as 5 carbonate-bearing metasedimentary materials were analyzed for O-C isotopic characteristics. The vein material was mechanically separated from its host rock and then pulverized in an agate mortar. A similar procedure was followed in the preparation of the analyzed host rock lithologies avoiding any vein material. $\delta^{13}C$ and $\delta^{18}O$ isotope values were obtained after collecting the CO_2 released from the reaction of carbonate with 100% phosphoric acid (0.2 mL) followed by purification on a glass extraction line in dual-inlet mode (McCrea, 1950) before analysis on a Finnigan Mat 252 mass spectrometer at Lehigh University. For monitoring and data correction, internal standards and the international standard NBS-19 were routinely measured. Measured $\delta^{13}C$ and $\delta^{18}O$ resulted in 1σ uncertainties of 0.05 and 0.18‰, respectively. $\delta^{13}C$ and $\delta^{18}O$ values are relative to VPDB and VSMOW, respectively.

For Sr-Nd isotope analysis, 36 samples (20 carbonate, 16 silicate veins) were selected for Rb-Sr and 17 samples (8 carbonate, 9 silicate veins) for Sm-Nd determinations. Carbonate minerals from veins were separated and purified by hand-picking or microdrilling after careful removal of weathered parts of the samples. Crushed whole rock material was also carefully selected avoiding potentially altered fragments. Up to 100 mg of carbonate-bearing material (veins and host metasediments) and 200 mg of carbonate-free material (blueschists, clinopyroxenites and serpentinites) were spiked with adequate

amounts of ^{87}Rb, ^{84}Sr, ^{149}Sm and ^{150}Nd and carefully digested in a mixture of HF-HNO_3 (5:1). After evaporation to dryness, the fluoride salts were converted to chlorides using 6N HCl. Rb, Sr, Sm and Nd were then separated and purified by cation-exchange techniques. Isotopic data were acquired on a Thermo Fisher Scientific TRITON multi-collector thermal ionization mass spectrometer (TIMS) at GFZ Potsdam. Rb was measured in static multicollection mode, whereas Sr, Sm and Nd isotopic compositions were determined using dynamic multicollection. Sr reference material NBS 987 and Nd reference material JNdi-1 gave $^{87}Sr/^{86}Sr = 0.710229\pm16$ (2σ, n = 6) and $^{143}Nd/^{144}Nd= 0.512092\pm8$ (2σ, n = 3), respectively.

5.4.5 Thermodynamic modeling

In order to gain information on phase relations, devolatilization trends and fluid compositions, we performed thermodynamic calculations with the Perple_X software version 6.8.9 (Connolly, 2005; Connolly and Galvez, 2018). For pseudosection modeling, the selected chemical systems consist of a representative blueschist (sample SO1833; Na_2O-CaO-K_2O-FeO-MgO-MnO-Al_2O_3-SiO_2-H_2O-TiO_2-O_2), a serpentinite (sample SO1869; CaO-FeO-MgO-Al_2O_3-SiO_2-H_2O-O_2), a metapelite (Na_2O-CaO-K_2O-FeO-MgO-Al_2O_3-SiO_2-H_2O-CO_2-O_2), a calcschist (Na_2O-CaO-K_2O-FeO-MgO-Al_2O_3-SiO_2-H_2O-CO_2-O_2) and a marble (Sample SO1853; Na_2O-CaO-K_2O-FeO-MgO-Al_2O_3-SiO_2-CO_2). The metapelite and calcschist compositions were taken from similar rocks from the Alpine Schistes Lustrés since CO_2 was calculated by Epstein et al. (2020; SL99-12C and SL99-40C, respectively). CO_2 abundance in the marble composition has been calculated assuming all CaO bounded in aragonite/calcite since these are the only Ca-bearing phases present in the rock. All the pseudosections have been calculated in the range of 250 °C to 700°C from 0.2 to 2.8 GPa. In addition, blueschist and serpentinite calculations were performed under water-saturated conditions. For mineral solutions and aqueous fluids, the thermodynamic database (hp62ver.dat) from Holland and Powell (2011) complemented with the CORK equation of state from Holland and Powell (1998) for generic hybrid molecular fluids in COH-bearing systems (e.g., metapelite and calcschist) were used. Chemical compositions and solid-solution models used in each calculation are summarized in ***Table 2*** and ***S2***, respectively. A Fe^{2+}/Fe^{3+} ratio of 0.8 has been fixed according to Massonne and Willner (2008).

Infiltration-driven devolatilization calculations were developed considering the three carbonate-bearing metasediments (metapelite, calcschist and marble) in the system Na-Ca-K-Fe-Mg-Al-Si-H-C-O for the metapelite and calcschist while Na was not contemplated in the marble chemical system (Ca-Fe-Mg-Al-Si-H-C-O). We have applied the Deep Earth Water (DEW) aqueous thermodynamic dataset (DEW19HP622ver_elements.dat version 11 of December, 2019 in Perple_X; Huang and Sverjensky, 2019) complemented by the Holland and Powell (2011) database. We computed the lagged forward-calculated speciation algorithm which allow us to quantitatively estimate the effects of infiltration-driven devolatilization via equilibrium calculations between solids and an infiltrating fluid, emphasizing decarbonation processes; the method is detailed in Connolly and Galvez (2018; see also Menzel et al., 2019). The iterative infiltration-devolatilization has been modeled by incremental addition of 0.1 mol of H_2O to 1 kg of metapelite, calcschist and marble, respectively,

followed by fractionation of the infiltrated fluid at 480 °C and 1.8 GPa. Thus, the chemical composition of the fractionated fluid as well as the residual whole rock varies as more fluid is infiltrated and fractionated outwards the system.

TABLE 1. Selected electron probe microanalyses mineral composition and cations per formula unit in the Seghin complex

Mineral group	Lithology	Zone	SiO_2 (wt%)	TiO_2 (wt%)	Al_2O_3 (wt%)	Cr_2O_3 (wt%)	FeO (wt%)	MnO (wt%)	MgO (wt%)	CaO (wt%)	Na_2O (wt%)	K_2O (wt%)	Total (wt%)	$^{*}H_2O$ (wt%)	Si (a.p.f.u)	Ti (a.p.f.u)	Al_{tot} (a.p.f.u)	Fe^{3+} (a.p.f.u)	Fe^{2+} (a.p.f.u)	Mg (a.p.f.u)	Ca (a.p.f.u)	Na (a.p.f.u)	K (a.p.f.u)	XMg	# (O - OH)
Phengite	Metabasite	Host	53.41	0.03	22.86	0.00	3.14	0.06	4.43	0.28	0.05	11.68	95.93	4.48	3.58	0.00	1.80	N.A.†	0.18	0.44	0.02	0.01	1.00	0.72	20-4
	Metabasite	Host	54.80	0.11	19.14	0.00	3.75	0.12	5.56	0.11	0.35	10.32	94.25	4.42	3.72	0.01	1.53	N.A.†	0.21	0.56	0.01	0.05	0.89	0.73	20-4
	Metabasite	Vein	54.21	0.02	23.04	0.01	2.77	0.03	4.61	0.03	0.10	11.01	95.83	4.51	3.60	0.00	1.80	N.A.†	0.15	0.46	0.00	0.01	0.93	0.75	20-4
	Metabasite	Vein	54.77	0.02	21.02	0.00	4.04	0.04	4.73	0.01	0.07	10.82	95.51	4.47	3.67	0.00	1.66	N.A.†	0.23	0.47	0.00	0.01	0.93	0.68	20-4
	Metapelite	Host	50.93	0.06	26.51	N.A.†	3.03	0.08	2.95	0.01	0.23	10.56	94.36	4.43	3.44	0.00	2.11	N.A.†	0.17	0.30	0.00	0.03	0.91	0.63	20-4
	Calcschist	Host	50.82	0.09	26.44	0.09	3.54	0.03	3.04	0.00	0.22	10.63	94.90	4.44	3.43	0.00	2.10	N.A.†	0.20	0.31	0.00	0.03	0.91	0.60	20-4
	Marble	Host	53.05	0.09	24.33	0.74	2.00	0.04	4.71	0.02	0.17	10.42	95.56	4.51	3.52	0.00	1.90	N.A.†	0.11	0.47	0.00	0.02	0.88	0.81	20-4
Amphibole	Metabasite	Host	55.96	0.00	3.34	0.00	23.75	0.41	6.34	1.07	6.36	0.02	97.25	2.02	8.07	0.00	0.57	1.33	1.53	1.36	0.17	1.78	0.00	0.47	22-2
	Metabasite	Host	57.18	0.13	5.54	0.01	17.60	0.31	9.20	0.83	6.56	0.13	97.48	2.09	8.04	0.01	0.92	0.89	1.18	1.93	0.12	1.79	0.02	0.62	22-2
	Metabasite	Vein	57.44	0.00	9.46	0.00	13.94	0.14	9.00	0.33	7.15	0.02	97.48	2.14	7.99	0.00	1.55	0.35	1.27	1.87	0.05	1.93	0.00	0.60	22-2
	Metabasite	Vein	57.39	0.03	3.39	0.05	19.50	0.08	9.37	0.98	6.49	0.00	97.29	2.07	8.08	0.00	0.56	1.34	0.96	1.97	0.15	1.77	0.00	0.67	22-2
	Metabasite	Host	38.80	0.26	30.85	0.01	1.03	0.02	0.00	17.53	0.00	0.05	88.53	11.40	2.04	0.01	1.91	0.00	N.A.†	0.00	0.99	0.00	0.00	N.A.†	7-2
Lawsonite	Metabasite	Vein	37.77	0.01	32.37	0.00	0.83	0.00	0.00	17.30	0.02	0.00	88.30	11.39	1.98	0.00	2.00	0.04	N.A.†	0.00	0.97	0.00	0.00	N.A.†	7-2
	Metabasite	Vein	37.09	0.35	26.56	0.03	6.40	0.06	0.01	17.24	0.01	0.03	87.76	10.91	2.00	0.01	1.69	0.29	N.A.†	0.00	1.00	0.00	0.00	N.A.†	7-2
	Metapelite	Host	39.03	0.00	31.94	0.26	0.02	0.00	17.25	0.00	0.00	0.00	88.50	11.48	2.05	0.00	1.97	0.00	N.A.†	0.00	0.97	0.00	0.00	N.A.†	7-2
	Metabasite	Host	55.89	0.05	5.06	0.04	13.42	0.23	6.66	12.06	7.21	0.04	100.66	0.00	2.03	0.00	0.22	0.23	0.18	0.36	0.47	0.51	0.00	2.06	6-0
	Metabasite	Host	53.85	0.16	9.95	0.00	17.21	0.04	1.17	2.15	12.62	0.00	97.14	0.00	1.98	0.00	0.43	0.49	0.04	0.06	0.08	0.90	0.00	1.82	6-0
Clinopyroxene	Metabasite	Vein	54.98	0.11	7.35	0.03	17.17	0.13	2.65	5.09	11.18	0.00	98.68	0.00	2.01	0.00	0.32	0.45	0.08	0.14	0.20	0.79	0.00	1.81	6-0
	Cpte	Host	54.18	0.29	4.80	0.04	15.82	0.25	5.59	11.07	8.05	0.02	100.12	0.00	1.98	0.01	0.21	0.38	0.10	0.30	0.43	0.57	0.00	3.03	6-0
	Cpte	Host	54.33	0.07	0.35	0.00	6.53	0.61	13.89	25.86	0.36	0.04	102.03	0.00	1.98	0.00	0.02	0.05	0.14	0.75	1.01	0.03	0.00	5.23	6-0
	Cpte	Host	53.46	0.02	3.27	0.07	9.56	0.46	10.49	20.40	2.76	0.13	100.61	0.00	1.97	0.00	0.14	0.13	0.17	0.57	0.80	0.20	0.01	3.43	6-0
	Cpte	Host	53.99	0.00	5.49	0.01	10.33	0.39	8.41	15.89	5.55	0.00	100.06	0.00	1.97	0.00	0.24	0.22	0.09	0.46	0.62	0.39	0.00	4.86	6-0

* = Calculated by stoichiometry.
N.A.† = Not applicable

TABLE 2. Chemical compositions considered for thermodynamic modeling

Oxide	Pseudosection modelling (wt%)						Deep Earth Water modelling (mole/kg)				
	Metabasite	Serpentinite	Metapelite	Calcschist	Marble		Element	Metapelite	Calcschist	Marble	
SiO_2	50.98	47.49	49.82	46.67	13.85		Si	8.29	7.77	2.31	
TiO_2	2.14	-	-	-	-			-	-	-	
Al_2O_3	13.81	1.36	24.3	14.27	0.05 #		Al	4.77	2.8	0.01	
Fe_2O_3	2.85	2.86	0.72	0.52				-	-	-	
FeO	10.24	4.29	5.82	4.19	0.19		Fe*	0.9	0.65	0.03	
MnO	0.2	-	-	-	-			-	-	-	
MgO	6.26	42.72	3.55	3.12	0.29		Mg	0.88	0.77	0.07	
CaO	8.83	1.28	2.21	13.99	47.95		Ca	0.39	2.49	8.55	
Na_2O	4.21	-	0.49	1.09	-		Na	0.16	0.35	-	
K_2O	0.49	-	6.36	2.01	0.03		K	1.35	0.43	0.01	
H_2O	Saturated	Saturated	5.03	3.7	0.01		H_2	2.79	2.06	0.01	
CO_2	-	-	1.70	10.45	37.62		C	0.39	2.37	8.55	
							O_2	15.14	15.44	15.19	

= Value adjusted to take into account detrital components * = Total Fe

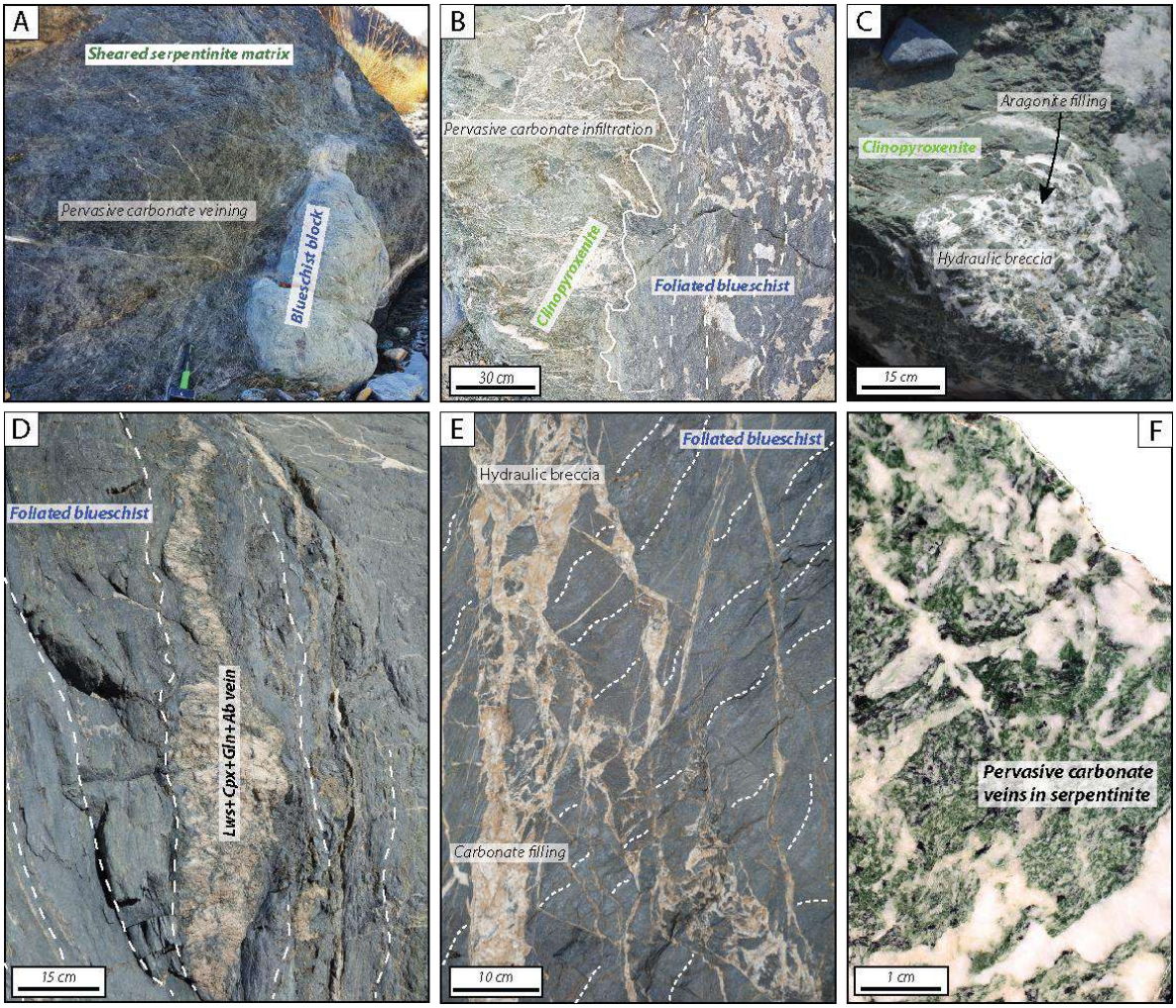

Figure 5.3. Representative photographs of outcrops and polished slabs showing vein and lithological features. A. Meso-scale block-in-matrix fabric characterized by a serpentinite matrix wrapping foliated blueschist blocks. Note pervasive carbonate veining at the centimeter-scale. B. Irregular contact relationship between foliated blueschist and clinopyroxenite, the latter occupying the outer part of the block. Carbonate veins are abundant in the clinopyroxenite region. C. Aragonite-filled hydraulic breccia in a massive clinopyroxenite. D. Centimeter-wide lawsonite + clinopyroxene + glaucophane + albite vein parallel to the main foliation opened as an extensional fracture. E. Hydraulic breccia in a foliated blueschist. Note how the fluid infiltrated mostly oblique to the main foliation but also subparallel to it while fragments show no traces of rotation. F. Polished slab of highly strained and pervasive carbonate veins in serpentinite.

5.5 Petrological characterization and mineral chemistry

5.5.1 Host rock

5.5.1.1 Serpentinites

Their mineralogy is characterized by abundant antigorite (>90 vol.%), magnetite and minor magnesite and chlorite, the latter commonly surrounding coarse-grained magnetite crystals. No evidence for talc or secondary olivine is observed in studied samples while no relicts of the previous protolith, including chromian spinel, have been found in the Seghin complex (Angiboust et al., 2016).

5.5.1.2 Metapelites, calcschists and marbles

Representative metapelites correspond to well-foliated lawsonite-bearing micaschists with abundant carbonaceous material and subordinate titanite and carbonate phases (***Fig.5.4A***). This lithotype represents a minute portion of the Seghin complex. The main foliation is defined by the ubiquitous presence of intermixed chlorite + phengite layers with quartz and organic matter. Si in phengite crystals lining the foliation range between 3.3 to 3.4 a.p.f.u (***Fig.5.5A***). Millimeter to centimeter-sized lawsonite crystals are iron-poor (***Fig.5.5B***), include abundant rotated organic matter trails, and are boudinaged according to the stretching S-surface in the mylonitic S-C fabrics.

Calcschist samples consist of subidiomorphic coarse-grained aggregates of carbonates + quartz + albite interlayered with phengite + chlorite + titanite bands, the sheet silicates defining the main foliation (***Fig.5.4B***). Phengite crystals are characterized by Si ranging between 3.23 to 3.43 a.p.f.u (***Fig.5.5A***). Carbonate grains are subhedral to anhedral (≈15 vol.%; ***Fig.5.4B***) and occurs in irregular contact with other silicate phases. Albite grains are anhedral and show strongly irregular contacts as well as truncated crystal surfaces (e.g., ***Fig.5.4B***).

Marble lithologies are characterized by abundant aragonite that represents more than 90 vol.% (***Figure 5.S1J***) with minor albite, chlorite, quartz and phengite. Aragonite is fine-grained (***Fig.5.4C***) with a rather pure chemical composition. Calcite is subordinately present as late thin veinlets (***Figure 5.S1J***). Similarly, albite consists of tiny detrital crystals that preserves the polysynthetic twining with no traces of internal deformation. Phengite is more abundant than chlorite, the former being richer in Si with values up to 3.52 a.p.f.u compared to those in the metapelites and calcschists (***Fig.5.5A***). Phengite occurs as intermixed layers or as single flakes in apparent equilibrium with, or as strain caps around truncated aragonite grains (***Fig.5.4C***).

5.5.1.3 Blueschists

Blueschists from the Seghin complex are lithologically heterogenous at the meter-scale. The main textural characteristic corresponds to a well-developed foliation slightly overprinted by an incipient crenulation cleavage better developed in less competent metatuffs. The foliation is defined by well-preserved coarse to fine-grained crystals of Na-amphibole + lawsonite + epidote + aegirine-augite + quartz + phengite + titanite (e.g., ***Figs.5.4E, H*** and ***J***). Epidote occurs as (i) inclusions in lawsonite grains, (ii) in the matrix as a prograde phase and (iii) replacing lawsonite as a retrograde phase. Earlier stages of prograde metamorphism are recorded as Ca-amphibole cores and epidote + quartz + albite

inclusions in lawsonite. It is important to note that carbonates were systematically not observed in the host blueschists.

Locally, the main foliation grades towards an anastomosing mylonitic fabric with visible dark-seams fringes, often associated with lawsonite porphyroblasts and the fine-grained glaucophane matrix around in the form of strain caps (***Fig.5.4J***). Pyrite grains are decorated by quartz strain shadows while other rigid phases show fractures healed by the same phase or sealed by glaucophane and/or quartz (***Fig.5.S1A***).

Phengite crystals are homogeneous, rich in celadonite component, with Si ranging from 3.55 to 3.72 (a.p.f.u) showing almost ideal Tschermak substitution (***Fig.5.5A***). The main type of amphibole corresponds to the sodic variety, which represent approximately half of the host blueschist volume. Its composition varies mostly from glaucophane to magnesio-riebeckite (locally ferro-glaucophane and riebeckite) with XMg up to 0.62 whereas strong $Fe^{3+}/(Fe^{3+}+Al)$ variations probably reflect local compositional heterogeneities (***Fig.5.5C***). These chemical variations are shown in ***Fig.5.6A*** where strong oscillatory zoning is observed at the single-grain scale. In this work, we refer to Na-amphibole as glaucophane both in the host rock blueschists and related veins. Fe^{3+} in lawsonite is commonly lower than 0.1 a.p.f.u but few crystals show values higher than 0.2 a.p.f.u, while Cr is very low (up to 0.004 a.p.f.u; ***Fig.5.5B***). Epidote in apparent textural equilibrium with glaucophane is essentially pistacite with molar proportions around XPs=0.18-0.21 (with $XPs=Fe^{3+}/(Fe^{3+}+Al)$). Na- and Na-Ca clinopyroxene are widely variable in compositions, ranging mostly between omphacite, aegirine-augite and aegirine ($Jd_{42-2}Aeg_{62-10}Quad_{59-9}$; ***Fig.5.5D***). Rare, sub-millimetric garnet crystals show irregular and sinuous zoning patterns characterized by higher grossular and lower pyrope contents towards their rims (***Fig.5.S1B***).

5.5.1.1 Clinopyroxenites

This rock type forms massive aggregates of deep greenish-darkish clinopyroxene showing extensive chemical variations characterized by a first generation of diopside ($Jd_{11-1}Aeg_{11-2}Quad_{97-80}$; ***Fig.5.5D***) crosscut by a second ($Jd_{15-6}Aeg_{21-18}Quad_{76-67}$) and a third generation of Na-Fe^{3+}-richer aegirine to omphacite ($Jd_{21-9}Aeg_{35-19}Quad_{62-49}$; ***Fig.5.5D***). Glaucophane occurs in apparent equilibrium with or replacing the third generation of Na-richer clinopyroxene crystals. Texturally, the first diopside generation seems to have been infiltrated by fluids along cracks sealed by gradually Na-Al-Fe^{3+}-richer clinopyroxene crystals (***Fig.5.5E***). Minor titanite is also present in apparent equilibrium with the early diopside generation.

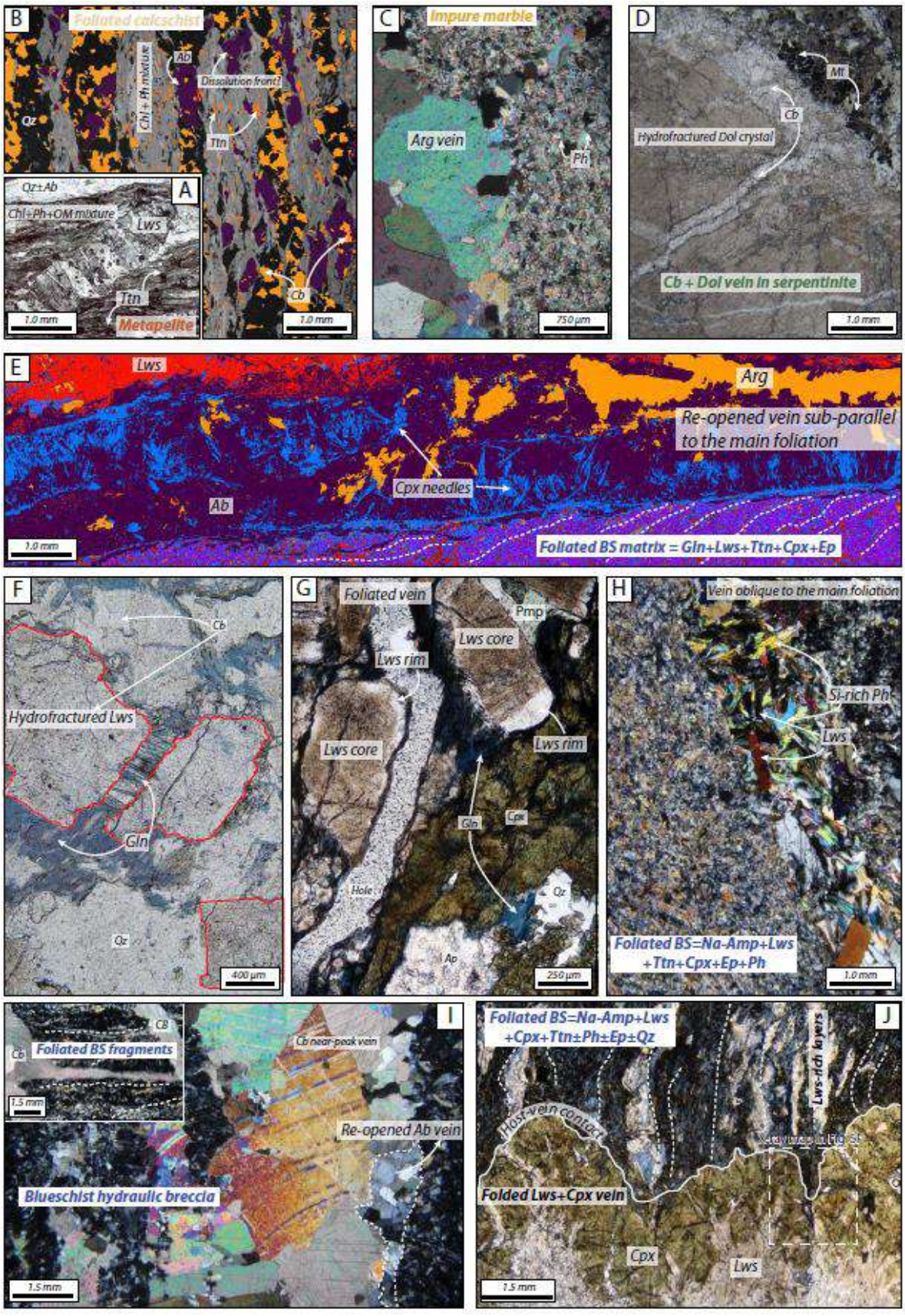
B
Foliated calcschist
Chl+Ph mixture
Ab
Dissolution front?
Qz
Ttn
Qz+Ab
A
Chl+Ph+OM mixture
Lws
Ttn
Metapelite
1.0 mm
Cb
1.0 mm
C
Impure marble
Arg vein
Ph
750 µm
D
Mt
Cb
Hydrofractured Dol crystal
Cb + Dol vein in serpentinite
1.0 mm
E
Lws
Arg
Re-opened vein sub-parallel to the main foliation
Cpx needles
Ab
1.0 mm
Foliated BS matrix = Gln+Lws+Ttn+Cpx+Ep
F
Cb
Hydrofractured Lws
Gln
Qz
400 µm
G
Foliated vein
Pmp
Lws core
Lws rim
Lws core
Lws rim
Gln
Cpx
Hole
Qz
Ap
250 µm
H
Vein oblique to the main foliation
Si-rich Ph
Lws
Foliated BS=Na-Amp+Lws +Ttn+Cpx+Ep+Ph
1.0 mm
I
CB
Cb
Foliated BS fragments
1.5 mm
Cb near-peak vein
Re-opened Ab vein
Blueschist hydraulic breccia
1.5 mm
J
Foliated BS=Na-Amp+Lws +Cpx+Ttn±Ph±Ep±Qz
Lws-rich layers
Host-vein contact
Folded Lws+Cpx vein
Cpx
Lws
1.5 mm

Figure 5.4. Optical polarized-light photomicrographs (A, C, D, F to J) and images of masks of selected phases based on high-resolution energy-dispersive X-ray (EDS) spectroscopy maps (B and E). A. General view of a foliated metapelite with millimeter-sized lawsonite porphyroblasts. B. Mask image with BSE background showing the main mineral assemblages and textures in a selected calcschist. The carbonates represent approximately the 15 vol.% of the rock as calculated with DWImager software. C. Cross-polarized view of contact relationships among an aragonite vein and its impure marble host. Truncated grains decorated with silica-rich phengite; strain caps indicate active pressure-solution at HP conditions. D. General view of hydrofractured dolomite crystals filled by carbonates. E. Mask image of a blueschist-hosted vein elongated sub-parallel to the main foliation. Several events of veining are visible implying episodic re-opening. Note: (i) the orientation of albite and clinopyroxene grains elongated perpendicular to the vein walls, (ii) clinopyroxene lining the vein edges surrounding what represents an earlier stage of veining, (iii) lawsonite at the internal part of the vein precipitated after aragonite. F. General view of a lawsonite + quartz + glaucophane sheared vein. The central lawsonite crystal has been hydrofractured and infiltrated by blade-shaped glaucophane in a "stitch-like" texture suggesting precipitation in fluid-filled open cracks. Note that glaucophane occupies an interstitial space between quartz and aragonite, implying that both minerals are related to the same infiltration event. G. Detailed view of a sheared vein. Lawsonite crystals are clearly zoned with dusty cores surrounded by clean rims. In addition, glaucophane is located in interstitial position between lawsonite and clinopyroxene suggesting a latter infiltration event. H. Cross-polarized view of a foliated phengite-bearing blueschist and cross-cutting vein. I. Cross-polarized view of a carbonate-filled hydraulic breccia. Note the remnants of a previous albite vein that indicates vein re-opening. The inset shows an enlarged field of view where the pattern of fracturing resembles an orthorhombic geometry. J. General view of a representative clinopyroxene-lawsonite vein hosted in a foliated blueschist. The vein is folded according to the main foliation. Lawsonite-rich layers occur in the foliated blueschist, while dark seams characterize the glaucophane-rich domains indicating that dissolution mainly affected the latter phase. The dashed square corresponds to the mapped area in Fig.5F. BS—blueschist; CM—carbonaceous material.

5.5.2 Vein systems

In this section we first describe the blueschist -hosted silicate-rich veins followed by carbonate-rich veins in all the studied lithotypes. Blueschist -hosted veins are characterized by lawsonite + Na-amphibole + Na-clinopyroxene + albite + phengite + quartz ± pumpellyite ± apatite. In general, the mineralogy of blueschist hosts and veins is similar, except for the lack of epidote in the vein domains. Submillimeter to millimeter-long albite crystals occur either as deformed or prismatic grains growing from the host contact towards the vein (syntaxial growth in Bons et al., 2012; ***Fig.5.4E***). In apparently pristine grains, abundant solid inclusion trails are observed aligned parallel to the host-vein margin (***Fig.5.6B***). These oscillations are locally crosscut by a later albite veining generation (***Fig.5.6B***). Clinopyroxene needles and aggregates occur inside and along albite crystals following their elongation or lining the host-vein contact (***Fig.5.4E***; see Munoz-Montecinos et al., 2020 for a similar example). Coarse-grained crystals in veins exhibit chemical zoning patterns characterized by Ca-richer aegirine-augite ($Jd_{8-2}Aeg_{49-32}Quad_{62-44}$; see green oval in ***Fig.5.5D***) patches located inwards of large Na-Al richer crystals ($Jd_{32-7}Aeg_{57-29}Quad_{65-18}$; ***Figs.5.4G, 5.5D*** and ***E***). Ferric iron content among the two different aegirine-augite families is relatively similar being slightly higher in the Na-Al richer group. Lawsonite is distributed in the host-vein contact showing syntaxial growth patterns, associated with clinopyroxene (e.g., ***Fig.5.5F***) or as prismatic crystals in the vein domain after albite veining (e.g., ***Fig.5.4E***). In these veins, multiple remnants of the host-vein walls are commonly documented aligned subparallel to the pristine host rock (***Fig.5.6C***). Their mineral composition is similar to that of lawsonite in the host rock, with Fe^{3+} commonly up to 0.1 a.p.f.u but clustering in the range of 0.0 to 0.05 a.p.f.u (***Fig.5.5C***). Lawsonite, which is commonly texturally zoned (***Fig.5.4G***), displays no systematic major element variations. In addition, lawsonite grains are deformed in a brittle fashion and bended developing incipient ondulose extinction with fractures filled by quartz, carbonates and blade-shaped glaucophane, resembling a "stitch-like" texture (***Fig.5.4F***). Elongated

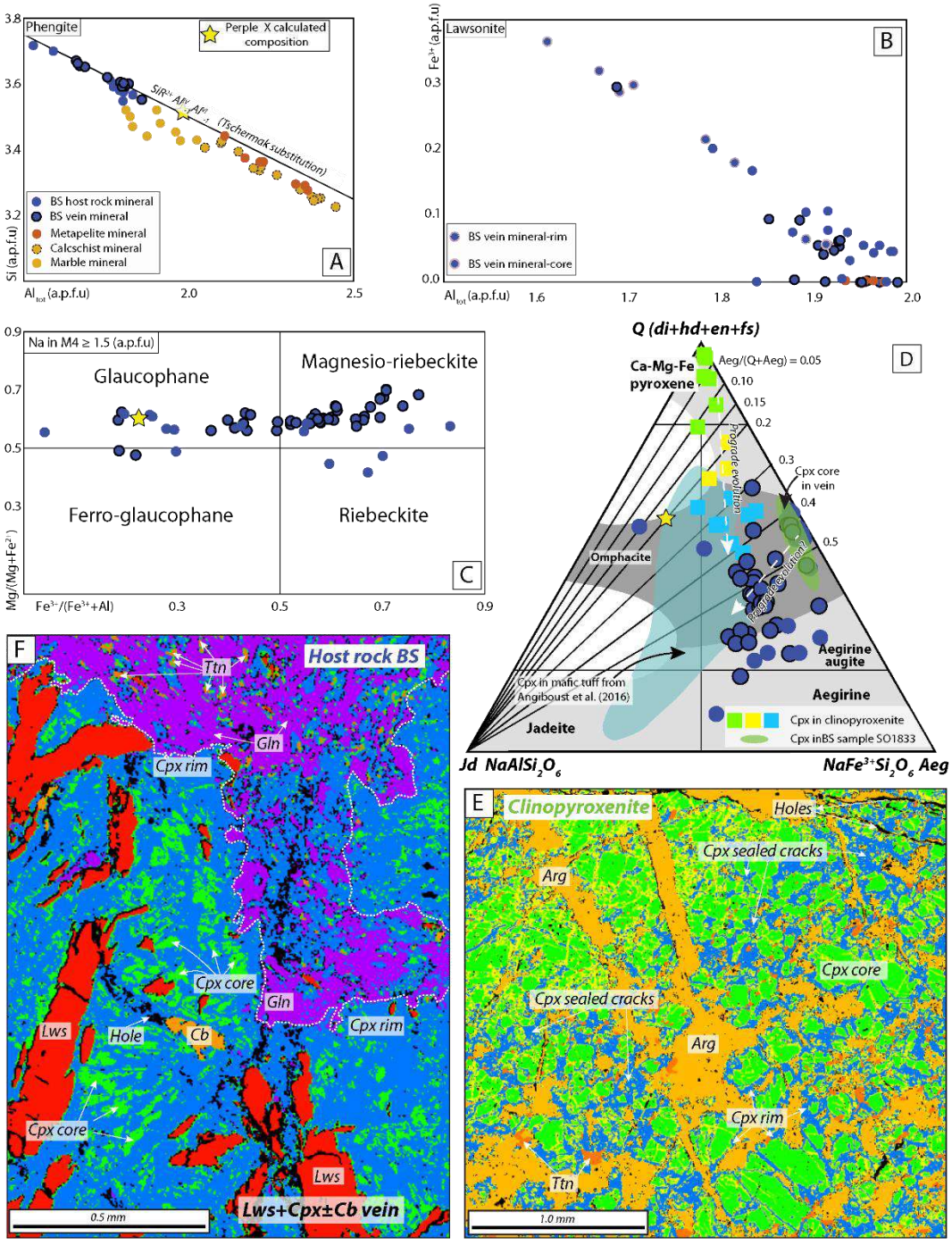

Figure 5.5. A. Si versus Al in phengite from the variety of lithologies. For comparison, the ideal Tschermak substitution trend is shown. B. Diagram depicting Fe^{3+} vs total Al variations in lawsonite. C. Sodic-amphibole classification diagram (Leake et al., 1997). D. Ternary classification diagram for clinopyroxene (after Morimoto, 1988). White regions correspond to calculated solvus gaps at 500 °C (Green et al., 2007). Some of the data has been extracted from the quantified EPMA X-ray map in panel F. In panels A, B and F, the yellow star represents the compositions of minerals calculated with Perple_X at 480 °C and 1.8 GPa. Phase masks images based on a High-resolution EPMA X-ray map (E and F). E. Clinopyroxenite sample (SO1825) where three generations of clinopyroxene are visible, represented by Ca-rich cores, Na-rich rims and healed cracks with the highest Na. F. Blueschist sample (SO1833) emphasizing the vein-host contact. Note the patchy zoning in clinopyroxene, with the internal part richer in Ca and the external richer in Na (green oval and single points in panel D, respectively). Lawsonite overprints the Ca-rich clinopyroxene and is in textural equilibrium with aegirine-augite. BS—blueschist

phengite laths are present mostly at the host-vein contact (***Fig.5.4H***) and subordinately as idiomorphic flakes in the vein domain. Neither chemical zoning (Si ranging between 3.55 to 3.67 a.p.f.u; ***Fig.5.5A***) nor deformation traces have been observed. Na-amphibole ranges commonly from very fine-grained needle aggregates to coarse-grained euhedral crystals. It occurs (i) in apparent textural equilibrium with lawsonite and clinopyroxene, (ii) precipitated through fractured lawsonite and clinopyroxene grains (***Figs.5.4F*** and ***G***) and (iii) crosscutting quartz + carbonate veins (e.g., ***Fig.5.S1C***). Magnesio-riebeckite is the most common Na-amphibole in the vein domain, but glaucophane is abundant and ferro-glaucophane is present (***Fig.5.5C***) with XMg and $Fe^{3+}/(Fe^{3+}+Al)$ ranging between 0.47 to 0.70 and 0.19 to 0.78, respectively. Ca-amphibole, namely actinolite, has been observed in few grains as cores.

Carbonate-bearing veins are characterized by abundant aragonite/calcite + quartz + albite, confirmed by powder XRD, Raman spectra and EBSD analyses (***Fig.5.S1D, 5.S1E, 5.S1G*** and ***5.S1I*** to ***5.S1K***). Textural observations, such as: calcite coronas around aragonite and fine-grained aragonite remnants surrounded by calcite (***Figs. 5.S1D, 5.S1G, 5.S1H, 5.S1I*** and ***5.S1K***), suggest that major back transformation from aragonite to calcite occurred in a very heterogeneous fashion, likely during exhumation (see Maekawa et al., 1995 for an example from dragged pristine metabasite blueschist-facies fragments). Thus, most carbonate veins are herein considered as former aragonite-bearing veins. In blueschists, these carbonate veins hydrofractured the host rock as well as the previous silicate-rich veins (e.g., ***Figs.5.3E, 5.4E, F*** and ***I***) with no clear evidence of further shearing, although viscous deformation is locally observed in few carbonates filling boudinaged lawsonite grains. Quartz is commonly associated with carbonates in apparent textural equilibrium. Carbonate veining is locally associated with or crosscut by glaucophane and lawsonite veins (e.g., ***Fig.5.4E***), pointing to HP conditions of formation. Retrograde chlorite + pumpellyite + calcite veins occur crosscutting all the previous structures. The prograde metamorphic evolution of blueschist-hosted vein systems is summarized in ***Fig. 5.7***.

In metasediments, carbonate-bearing veins occur mostly transecting the main foliation and are composed of aragonite/calcite with minor albite (e.g., ***Fig.5.4C*****;** see also ***Fig.5.S1J***). In serpentinites, they are composed of aragonite, calcite and dolomite (***Fig.5.S1F, 5.S1H*** and ***5.S1I***). The EBSD map from ***Fig.5.S1K*** shows that aragonite occurs as heterogeneous patches surrounded by calcite, in a similar way as observed in carbonate-bearing blueschist veins. In serpentinites, infiltration was pervasive (***Fig.5.3F***) allowing for several hydrofracturing stages, as determined by crosscutting relationships affecting coarse-grained dolomite (and other carbonates) and magnetite crystals (***Figs.5.4D*** and ***5.S1F***). These veins have been viscously deformed and sheared according to the matrix main fabric, but a cataclastic imprint is widespread. Clinopyroxenite-hosted carbonate-bearing veins are similar to those hosted in metasediments, also exhibiting minor amounts of quartz and albite. In this case, hydraulic breccia texture is clearly developed through massive clinopyroxene filled mostly by aragonite (***Fig.5.5E***). In addition, glaucophane and clinopyroxene seem to grow in replacement of former carbonate or as vein-filling materials cutting through aragonite.

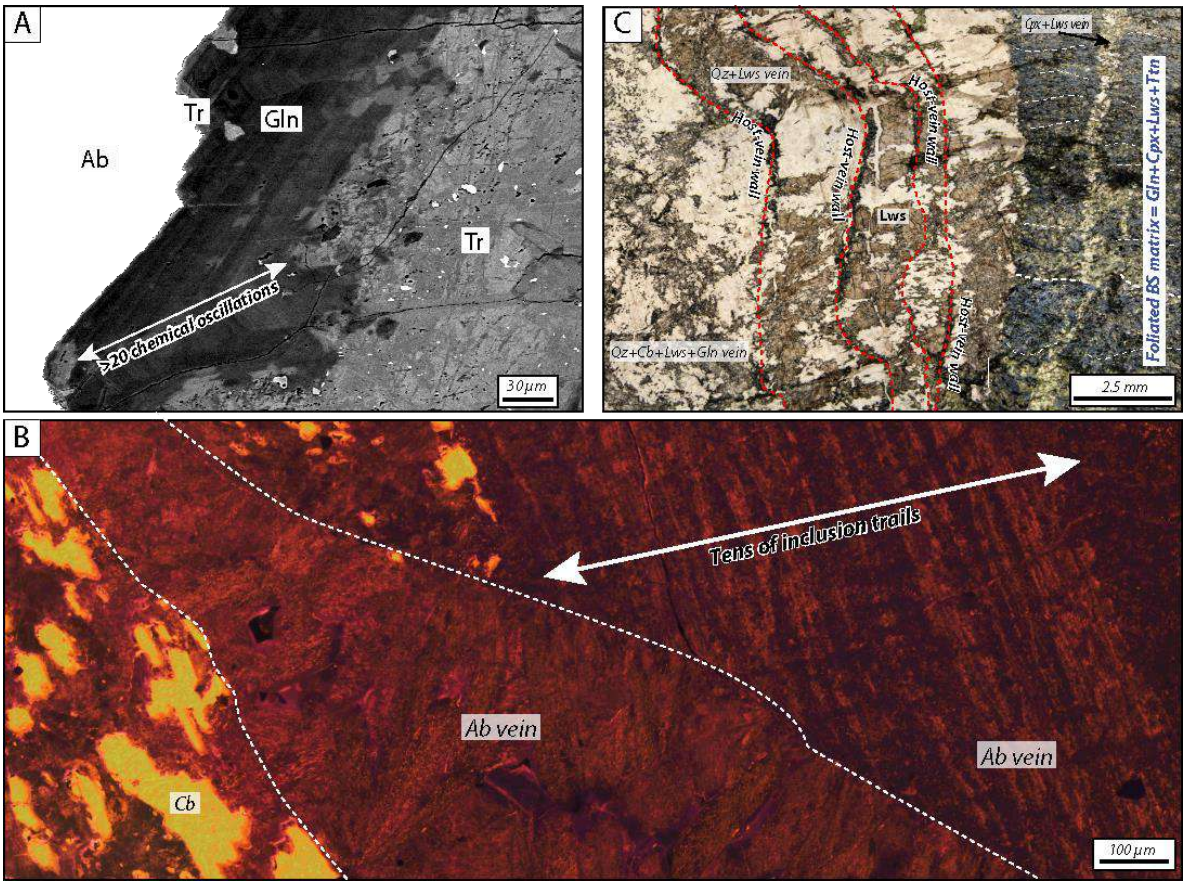

Figure 5.6. A. Backscattered electron image of an amphibole crystal from a blueschist sample showing a tremolite core surrounded by a glaucophane rim, the latter exhibiting several and sharp oscillatory chemical variations. B. Cathodoluminescence image of an albite + carbonate vein domain showing several inclusion trails. Note that albite grains in these veins are elongated perpendicular to the host blueschist-vein margin suggesting repeated vein opening followed by sealing (e.g., Ramsay, 1980). C. Optical polarized-light photomicrograph of a blueschist host and its vein. Several former vein-host walls are observed. In the vein domains, lawsonite is oriented perpendicular to the host-vein contact. Note that towards the vein center (left part of the image), carbonate minerals become abundant while clinopyroxene is absent.

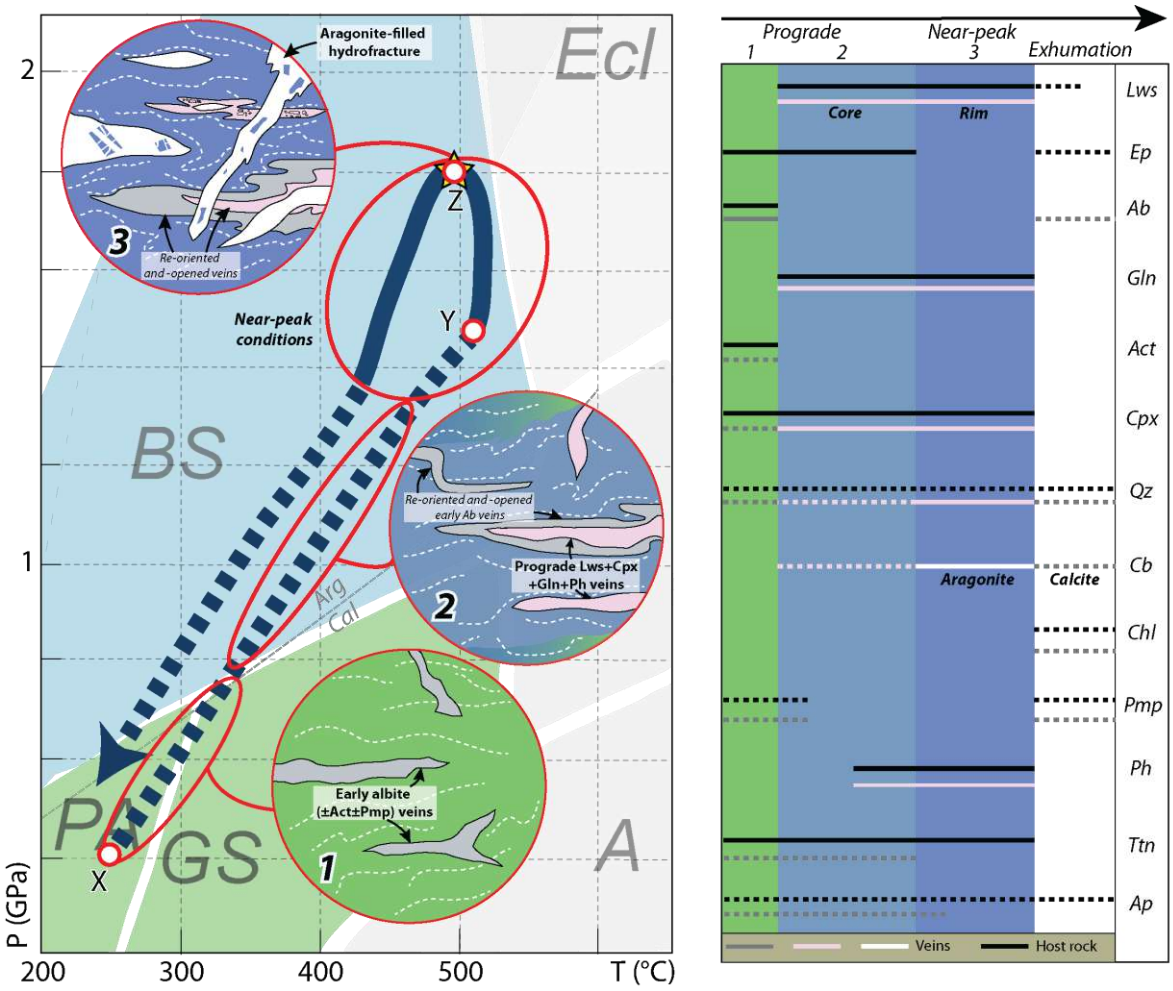

Figure 5.7. Sketch summarizing the metamorphic evolution trend for the blueschist host and for the various veining events. The dashed lines in the mineral occurrence table reflect the uncertainty in formation stage. (1) early veining in the prograde metamafic lithologies characterized by the formation of albite-rich veins transecting or following the prograde foliation, (2) prograde veining that resulted in the precipitation of lawsonite + Na-clinopyroxene + glaucophane + phengite and shearing of all the veinsets and (3) near-peak aragonite infiltration and formation of hydraulic breccias. Before carbonate-related hydrofracturing, most silicate-rich veins were sheared (re-oriented) or deformed according to the main fabric.

5.6 Whole Rock Geochemistry: Host Rocks

Major and immobile trace element geochemistry confirms that metatuffs and metalavas are basaltic in composition (***Fig.5.8A***) with SiO_2, Na_2O and K_2O values ranging between 42.7 to 48.5, 2.8 to 4.0 and 0.02 to 0.46 (wt%), respectively, whilst Th/Yb vs Nb/Yb (***Fig.5.8B***) indicate good correlation with MORB-OIB array similar to metavolcanic lithologies from the adjacent Siah-Kuh unit (Bonnet et al., 2020a). Clinopyroxenite immobile trace element patterns correlate well with the basaltic field close to the EMORB from Sun and McDonough (1989; ***Fig.5.8A***) but considerably higher Th/Yb ratios suggest that they cannot be considered as pristine metamafic rocks (***Fig.5.8B***).

Considering the blueschist trend as reference, the spider diagram from ***Fig.5.8C*** indicates that clinopyroxenite samples contain similar trace element compositions with relative depletion in Large Ion Lithophile Elements (LILEs) and slight enrichment in Light Rare Earth Elements (LREEs). The

marble and serpentinite compositions are up to c. 100 times more depleted in LILEs, High Field Strength Elements (HFSEs) and Heavy Rare Earth Elements (HREEs), but they differ in the Mantle Rock Forming Elements (MRFE) which are depleted in marbles and enriched in serpentinites, except for Cu and Zn. The metasediments show strong enrichments in LILEs, and LREEs and a depletion in HREEs.

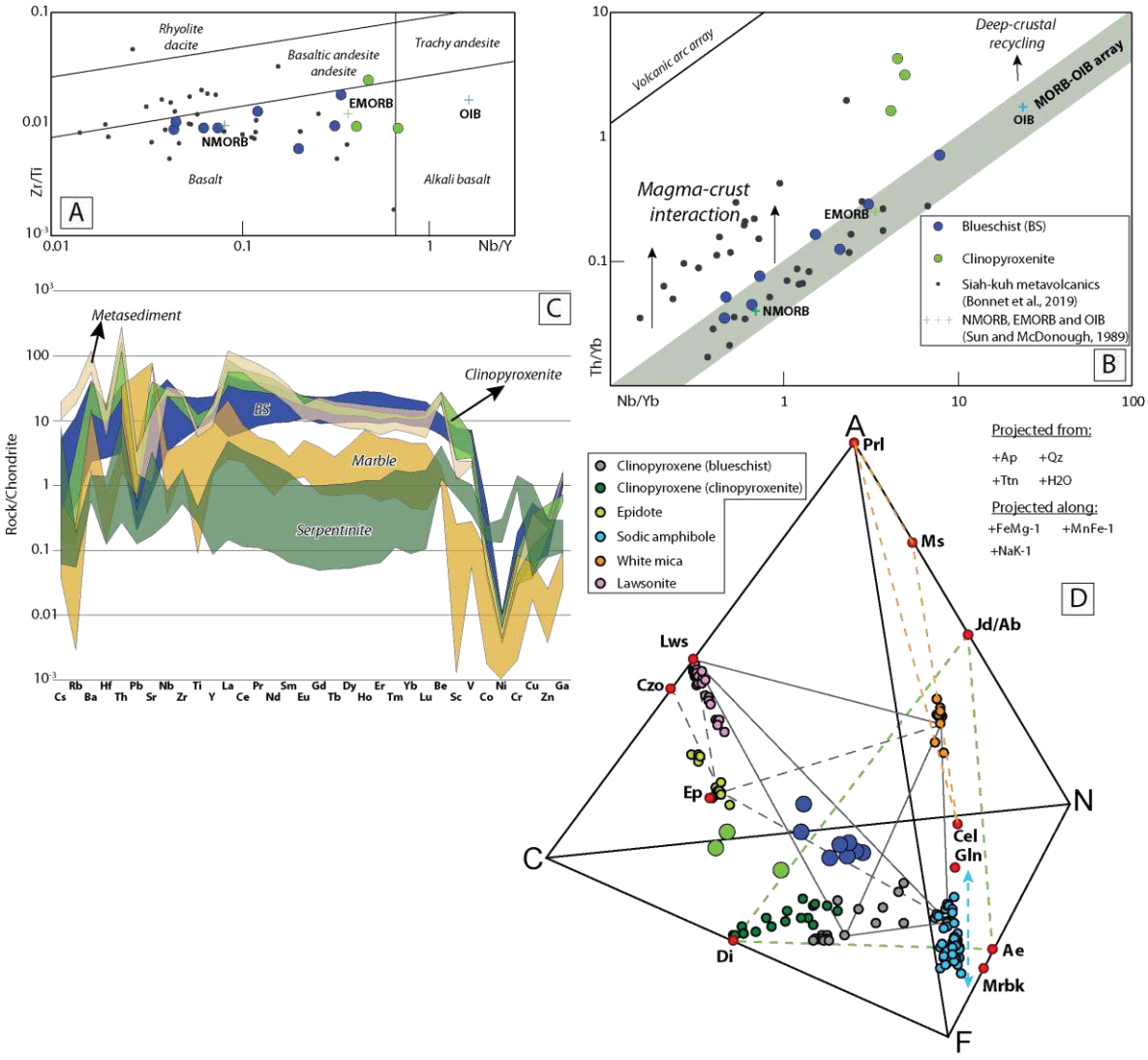

Figure 5.8. Whole rock geochemical analyses for the Seghin lithologies. For comparison, NMORB, EMORB and OIB compositions from Sun and McDonough (1989) and metavolcanic samples from the Siah-Kuh unit from Bonnet et al. (2020a) are shown, as specified in each figure. A. Nb/Y vs Zr/Ti discrimination diagram (from Pearce, 1996). Note that blueschists and clinopyroxenites plot in the basalt field. B. Th/Yb vs Nb/Yb diagram (from Pearce, 2008). Note that all blueschist samples plot in the MORB-OIB array while clinopyroxenites plot towards considerably higher Th/Yb ratios. C. Spider diagram of trace elements normalized to the chondrite from Taylor and McLennan (1985). D. ACFN tetrahedral diagram projected from the phases and exchange vectors as indicated. Note that white micas are rich in the celadonitic component and Fe^{3+} is not considered for simplicity.

In order to schematically represent phase relationships among clinopyroxenites and blueschists host rocks, we analyzed the major elements compositional space through an ACFN projection designed for our case study. As shown in the chemographic diagram from ***Fig.5.8D***, the blueschist compositions at peak conditions can be represented by a mineral assemblage characterized by lawsonite + phengite + clinopyroxene (aegirine-augite) + glaucophane (see black polygon from ***Fig.5.8D***). In samples where epidote and lawsonite are both stable at peak conditions, the polygon could be defined by intersecting tie-lines connecting the lawsonite + epidote + phengite + clinopyroxene (aegirine-augite) + Na-amphibole mineral assemblage. Such intersections would not necessarily imply univariant reaction relationships as long as the composition space is condensed along exchange vectors. Clinopyroxenite lithologies plot outside the polygon and, in one case, the bulk composition plots over the tie-line connecting the Jd(-Ab)-Di end members in agreement with the observed mineral paragenesis.

5.7 Mineral Trace Element Chemistry

The trace element results presented hereafter were acquired avoiding any appreciable mineral inclusions and are shown in ***Figs.5.9A*** to ***E***. A representative batch of analyses is offered in the supplementary material (***Table S3***). Analyzed amphibole crystals correspond to relatively homogenous blueschist-facies glaucophane-magnesioriebeckite grains. In the blueschists, amphibole REE patterns (***Fig.5.9A***) are similar to the chondritic abundance pattern (c.f., Taylor and McLennan, 1985). The only noticeable deflection from the trend is a slight negative Eu anomaly. However, this element is often below the instrumental detection limits in the studied samples. In addition, Cs/Rb ratios are considerably variable with values ranging from c. 0.005 to 0.05 while Ba/Rb proportions are fairly constant (c. 8; ***Fig.5.9E***). An overall identical signature is seen in vein-filling Na-amphibole crystals although no obvious Eu anomaly is observed and Cs/Rb ratios are, in general, slightly lower.

Host rock aegirine-augite and omphacite crystals show a slight enrichment in LREEs relative to HREEs as also noticed in vein clinopyroxene (***Fig.5.9B***). No Cr enrichments are herein observed as documented in other Na-clinopyroxene-bearing veins systems from elsewhere (See ***Table S3***; e.g., Spandler et al., 2011). Phengite analyses were particularly challenging due to its small grain size, especially in the host blueschists and marbles. In the latter, the resulting measurements were not satisfying and consequently discarded from the dataset. In all studied lithologies, phengite is the main carrier of Cs, Rb, and Ba and contains subchondritic REE concentrations, as already documented in previous studies (e.g., Zack et al., 2001; John et al., 2008). Phengite grains hosted in calcschists are the most enriched in Cs and Ba relative to Rb, plotting within the oceanic sediments field from ***Fig.5.9E***. In contrast, metapelite- and blueschist-hosted phengite crystals are the most depleted in Cs and Ba relative to Rb while vein-filling phengite grains are intermediate but closer in composition to those hosted in calcschist lithologies.

Medium to coarse-grained lawsonite crystals were carefully selected to avoid inclusions. In blueschist-hosted lawsonite, LREE and HREE concentrations are higher than chondritic abundances, and define a nearly flat pattern (***Fig.5.9C***). Th, U and Pb concentrations are in average 0.85, 0.38 and

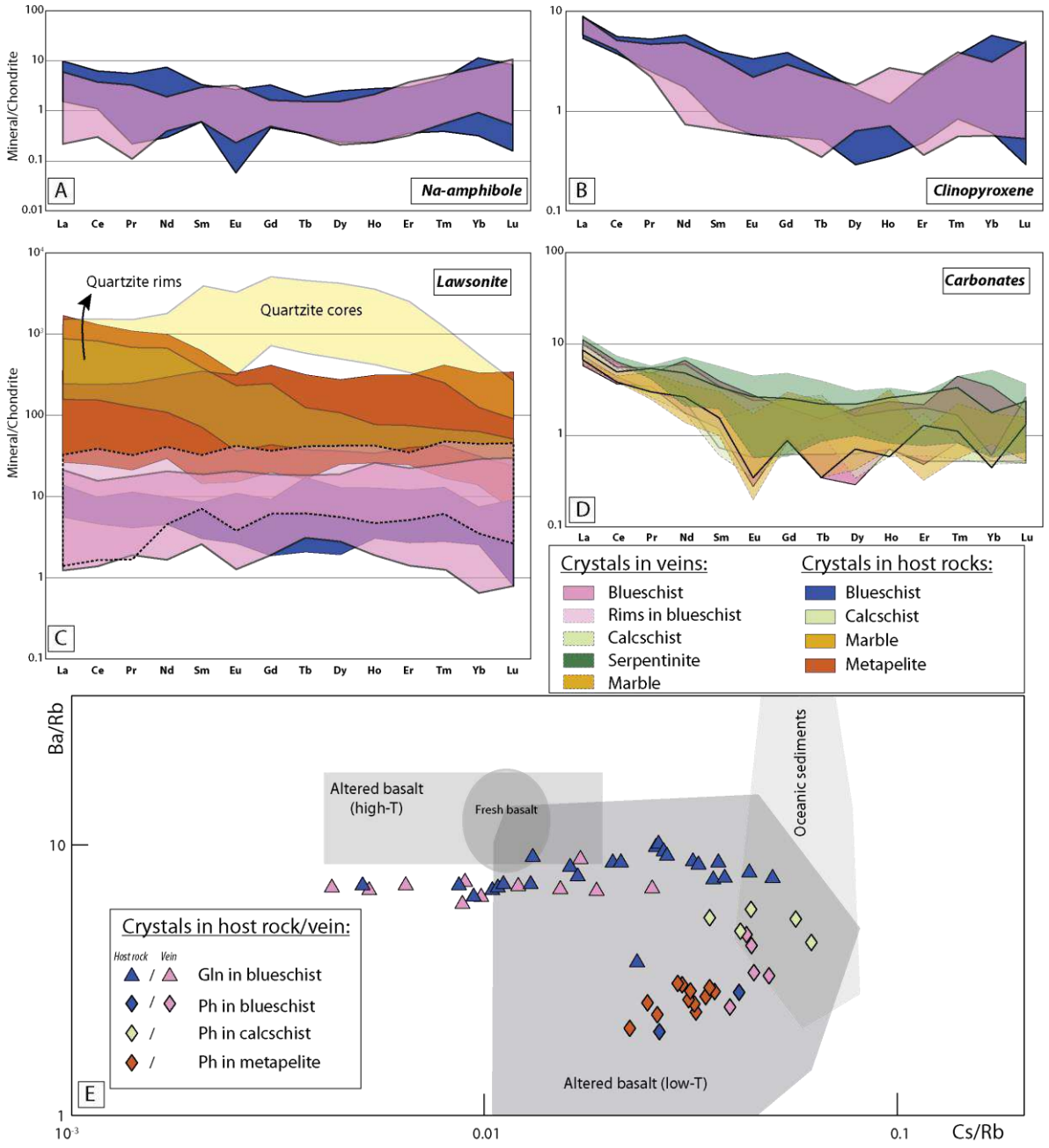

Figure 5.9. A to D. Trace element compositions from in-situ LA-ICP-MS measurements in host and vein amphibole, clinopyroxene, lawsonite and carbonates normalized to the chondritic element abundances (c.f., Taylor and McLennan, 1985). For comparison, In-situ LA-ICP-MS analyses in lawsonite cores and rims from a lawsonite-eclogite facies impure quartzite (Tavşanlı metamorphic belt, Turkey; Martin et al., 2014) are shown in panel C. E. Cs/Rb versus Ba/Rb diagram for different amphibole and phengite crystals in host rocks and vein domains. The relevant basaltic and oceanic sediment fields are from Zack et al. (2001 and references therein).

4.02 ppm. In contrast, lawsonite grains hosted in metapelites are much more enriched in these elements with values as high as 146, 25.1 and 10.5 ppm, respectively. In addition, all the REEs are strongly enriched relative to the blueschist-hosted lawsonite grains reaching abundances up to 1000 times higher than chondritic (***Fig.5.9C***; see also ***Table S3***). Lawsonite in veins consists of coarse-grained grains often showing core-rim patterns together with homogeneous (unzoned) grains. Since

the chemical composition of cores and homogeneous crystals is almost identical, both are referred to as lawsonite cores. In a broad sense, host rock and vein lawsonite cores show similar trends, but vein crystals are noticeably richer in REEs (***Fig.5.9C***). Interestingly, rims from vein lawsonite crystals show a similar pattern with even higher LREEs and HREEs concentrations than cores and host rock grains (***Fig.5.9C***). Apatite data were obtained only for grains of the vein assemblages due to its larger-grain size compared to the host rock crystals. Apatite shows LREE concentrations similar to Na-amphibole and clinopyroxene, but lower relative to lawsonite in veins. In contrast, similar HREE abundances compared to rims of lawsonite crystals in veins are noticed (***Table S3***). Anomalies in mantle rock-forming elements are not observed. Overall, the carbonate REE trends among different lithologies and domains (host rock or vein) are identical (***Fig.5.9D***) with higher LREE concentrations compared to HREEs.

5.8 O-C and Sr-Nd isotopes

$\delta^{18}O$ vs $\delta^{13}C$ and $^{87}Sr/^{86}Sr$ vs $^{143}Nd/^{144}Nd$ isotopic ratios from carbonate veins and host rock are presented in ***Fig.5.10*** and ***Table 3***. Carbonate veins in blueschists, clinopyroxenites and serpentinites show $\delta^{18}O$ ratios ranging between +14.1 to +17.3, +13.6 to +17.7 and +13.9 to +19.6‰, respectively (***Fig.5.10A***). Similarly, host marbles and metasediments $\delta^{18}O$ ratios vary between +15.3 and +17.9‰. Carbonate $\delta^{13}C$ values for blueschist, clinopyroxenite and serpentinite veins and host metasediments range from -1.0 to +1.7, -0.2 to +2.1, -0.6 to +3.1 and -0.9 to +2‰, respectively.

$^{87}Sr/^{86}Sr_i$ (calculated for t_i = 70 Ma) ratios in host blueschists are relatively homogeneous, ranging between 0.70460 to 0.70549 (***Fig.5.10B*** and ***Table 3***). Serpentinites show a broader distribution of initial Sr isotopic ratios, between 0.70517 and 0.70792, while clinopyroxenites are enriched in radiogenic Sr compared to blueschists ($^{87}Sr/^{86}Sr_i$ = 0.70616 and 0.70662). Metapelite sample SO1407 is the most radiogenic, with an $^{87}Sr/^{86}Sr_i$ as high as 0.71113, comparable to GLOSS I, GLOSS II and Makran trench-filling sediments (see Plank, 2014). The one calcschist analyzed has a relatively low $^{87}Sr/^{86}Sr_i$ (0.70597) similar to that of impure marble sample SO1836 ($^{87}Sr/^{86}Sr_i$ = 0.70610) while the marble sample SO1847 has a more radiogenic ratio ($^{87}Sr/^{86}Sr_i$ = 0.70768) comparable to that of seawater at 70 to 75 Ma. Carbonate veins hosted in blueschists, serpentinites, clinopyroxenites and a calcschist show a narrow range of $^{87}Sr/^{86}Sr_i$ ratios between 0.70501 to 0.70694 with one more radiogenic value considered as an outlier.

Nd isotope ratios are clearly distinguishable among different lithologies (***Figs.5.10B*** and ***D*** and ***Table 3***). $^{143}Nd/^{144}Nd_i$ in blueschists range between 0.512956 to 0.512958, falling in the field for island arcs, whereas the serpentinite sample has a less radiogenic composition ($^{143}Nd/^{144}Nd_i$ = 0.512572). Clinopyroxenite Nd isotopic ratios range from 0.512346 to 0.512769. Four measured metasediments have similar $^{143}Nd/^{144}Nd_i$, with the less radiogenic sample being a metapelite ($^{143}Nd/^{144}Nd_i$ = 0.512185) and the ratios of the calcschist and marble spanning from 0.512215 to 0.512243. Blueschist-hosted carbonate veins overlap the blueschist host field with $^{143}Nd/^{144}Nd_i$ ranging from 0.512965 to 0.512969. Similar to the host clinopyroxenites, its carbonate veins span a wide $^{143}Nd/^{144}Nd_i$ range (0.512327 to 0.512615) while the range of ratios in serpentinite-hosted veins is

slightly narrower ($^{143}Nd/^{144}Nd_i$ from 0.512600 to 0.512757). Finally, the measured calcschist-hosted vein is intermediate in $^{143}Nd/^{144}Nd_i$ (0.512272) between the ratios for the more radiogenic clinopyroxenite-hosted vein and host metapelite.

TABLE 3. Sr-Nd and O-C isotopic results

Sample	Lithology	Zone	Rb (ppm)	Sr (ppm)	Sm (ppm)	Nd (ppm)	$^{87}Sr/^{86}Sr_m$	$\pm2\sigma_m$ (%)*10-4	$^{87}Rb/^{86}Sr$	$\pm2\sigma$ (%)	$^{143}Nd/^{144}Nd_m$	$\pm2\sigma_m$ (%)*10-4	$^{147}Sm/^{144}Nd$	$^{87}Sr/^{86}Sr_i$ (70 Ma)	$^{143}Nd/^{144}Nd_i$ (70 Ma)	$\delta^{18}O$ (VSMOW)	$\delta^{13}C$ (VPDB)
SO1508d	Metabasite	Vein	-	-	-	-	-	-	-	-	-	-	-	-	-	17.3	0.3
SO1816	Metabasite	Vein	-	-	-	-	-	-	-	-	-	-	-	-	-	16.5	1.1
SO1818	Metabasite	Vein	0.03	1268	-	-	0.706610	16	0.00006	1.06	-	-	-	0.706610	-	16.5	-0.5
SO1821a	Metabasite	Host	6.76	102	-	-	0.705298	15	0.192	0.34	-	-	-	0.705109	-	-	-
SO1821a	Metabasite	Vein	0.00	23.6	-	-	0.705674	15	0.00033	31.9	-	-	-	0.705674	-	14.1	1.5
SO1821b	Metabasite	Vein	-	-	-	-	-	-	-	-	-	-	-	-	-	15.3	0.8
SO1822	Metabasite	Vein	-	-	-	-	-	-	-	-	-	-	-	-	-	15.9	-1.0
SO1823	Metabasite	Host	4.39	43.3	-	-	0.705777	17	0.293	0.29	-	-	-	0.705489	-	-	-
SO1823	Metabasite	Vein	0.01	976	-	-	0.705386	9	0.00002	15.0	-	-	-	0.705386	-	15.5	1.7
SO1826	Metabasite	Vein	-	-	-	-	-	-	-	-	-	-	-	-	-	15.9	2.0
SO1830	Metabasite	Vein	-	-	-	-	-	-	-	-	-	-	-	-	-	16.4	1.1
SO1831	Metabasite	Vein	0.07	424	-	-	0.705750	12	0.00048	1.55	-	-	-	0.705750	-	14.3	0.8
SO1832	Metabasite	Vein	0.04	604	0.11	0.38	0.705396	16	0.00018	1.69	0.513053	31	0.183	0.705396	0.512969	16.6	1.7
SO1832	Metabasite	Host	13.0	86.8	4.63	13.17	0.705459	28	0.433	0.32	0.513054	7	0.2126	0.705033	0.512956	-	-
SO1834	Metabasite	Vein	-	-	-	-	-	-	-	-	-	-	-	-	-	15.6	1.1
SO1842	Metabasite	Host	0.02	22.8	-	-	0.705120	22	0.00275	20.2	-	-	-	0.705117	-	-	-
SO1846	Metabasite	Host	9.35	286	6.97	19.17	0.705003	14	0.0945	0.29	0.513059	12	0.22	0.704910	0.512958	-	-
SO1846	Metabasite	Vein	0.71	41.9	1.19	3.17	0.705124	24	0.0487	1.06	0.513069	12	0.2265	0.705076	0.512965	15.8	1.4
SO1867	Metabasite	Vein	0.01	930	-	-	0.706842	20	0.00004	2.7	-	-	-	0.706842	-	-	-
SO1868	Metabasite	Vein	0.01	922	-	-	0.705952	13	0.00002	4.4	-	-	-	0.705952	-	15.0	1.2
SO1874	Metabasite	Host	32.1	30.2	-	-	0.707640	18	3.08	0.15	-	-	-	0.704605	-	-	-
SO1874	Metabasite	Vein	0.08	1077	-	-	0.705540	18	0.00022	2.76	-	-	-	0.705540	-	15.8	0.2
SO1876	Metabasite	Vein	-	-	-	-	-	-	-	-	-	-	-	-	-	16.1	-0.3
SO1881	Metabasite	Vein	0.00	1220	0.40	0.64	0.705011	14	0.00001	11.5	0.513099	28	0.3751	0.705011	0.512926	16.6	1.0
SO1824b	Cpxte	Vein	-	-	-	-	-	-	-	-	-	-	-	-	-	13.6	0.1
SO1825	Cpxte	Host	0.53	41.6	2.66	8.98	0.706201	40	0.0368	0.4	0.512851	7	0.1791	0.706165	0.512769	-	-
SO1825	Cpxte	Vein	0.02	2183	0.55	1.11	0.706311	21	0.00002	1.93	0.512751	16	0.2963	0.706311	0.512615	14.2	2.0
SO1838	Cpxte	Vein	-	-	-	-	-	-	-	-	-	-	-	-	-	16.9	-0.2
SO1840	Cpxte	Host	0.08	21.5	4.30	18.34	0.706627	20	0.0109	0.7	0.512411	18	0.1416	0.706616	0.512346	-	-
SO1840	Cpxte	Vein	0.00	1699	0.33	0.71	0.706717	26	0.0000	6.6	0.512456	19	0.2795	0.706717	0.512327	15.1	2.1
SO1850	Cpxte	Vein	-	-	-	-	-	-	-	-	-	-	-	-	-	17.7	0.0
SO1407	Metapelite	Host	60.1	13.1	3.02	15.96	0.724201	14	13.3	0.21	0.512238	8	0.1145	0.711125	0.512185	-	-
SO1852	Calcschist	Host	50.3	115	3.86	19.14	0.707219	14	1.27	0.18	0.512272	15	0.1219	0.705969	0.512216	-	-
SO1852	Calcschist	Vein	0.09	396	2.07	10.16	0.706941	13	0.00067	0.79	0.512329	10	0.123	0.706940	0.512272	17.9	0.9
SO1836	Marble	Host	0.00	707	2.24	10.32	0.706103	36	0.00001	26.2	0.512303	7	0.1311	0.706103	0.512243	15.3	2.0
SO1847	Marble	Host	1.46	919	0.83	4.46	0.707683	6	0.00459	0.77	0.512267	18	0.1123	0.707678	0.512215	16.3	0.2
SO1849	Marble	Host	-	-	-	-	-	-	-	-	-	-	-	-	-	16.0	-0.9
SO1867	Marble	Host	-	-	-	-	-	-	-	-	-	-	-	-	-	16.1	-0.5
SO1813	Serpentinite	Vein	-	-	-	-	-	-	-	-	-	-	-	-	-	16.7	1.7
SO1820	Serpentinite	Host	7.27	15.3	-	-	0.707540	18	1.38	0.19	-	-	-	0.706185	-	-	-
SO1820	Serpentinite	Vein	0.32	1198	-	-	0.706127	14	0.00078	0.39	-	-	-	0.706126	-	14.6	2.0
SO1837	Serpentinite	Host	0.02	0.68	0.04	0.19	0.707368	42	0.0831	1.46	0.512631	48	0.1289	0.707286	0.512572	-	-
SO1837	Serpentinite	Vein	0.01	3703	0.07	0.39	0.706449	15	0.00000	5.31	0.512649	58	0.1063	0.706449	0.512600	13.9	1.6
SO1839	Serpentinite	Host	0.16	1.33	-	-	0.708256	29	0.341	0.41	-	-	-	0.707921	-	-	-
SO1839	Serpentinite	Vein	0.01	667	-	-	0.708174	14	0.00003	6.05	-	-	-	0.708174	-	15.1	1.4
SO1844	Serpentinite	Vein	-	-	-	-	-	-	-	-	-	-	-	-	-	19.6	-0.2
SO1845	Serpentinite	Vein	-	-	-	-	-	-	-	-	-	-	-	-	-	15.2	-0.6
SO1869	Serpentinite	Vein	-	-	-	-	-	-	-	-	-	-	-	-	-	15.4	3.1
SO1880	Serpentinite	Vein	0.01	2238	0.08	0.26	0.705621	8	0.00001	2.56	0.512848	119	0.1968	0.705621	0.512757	15.3	1.3
SO1882	Serpentinite	Vein	0.00	967	-	-	0.706410	15	0.00001	24.1	-	-	-	0.706410	-	15.3	1.5

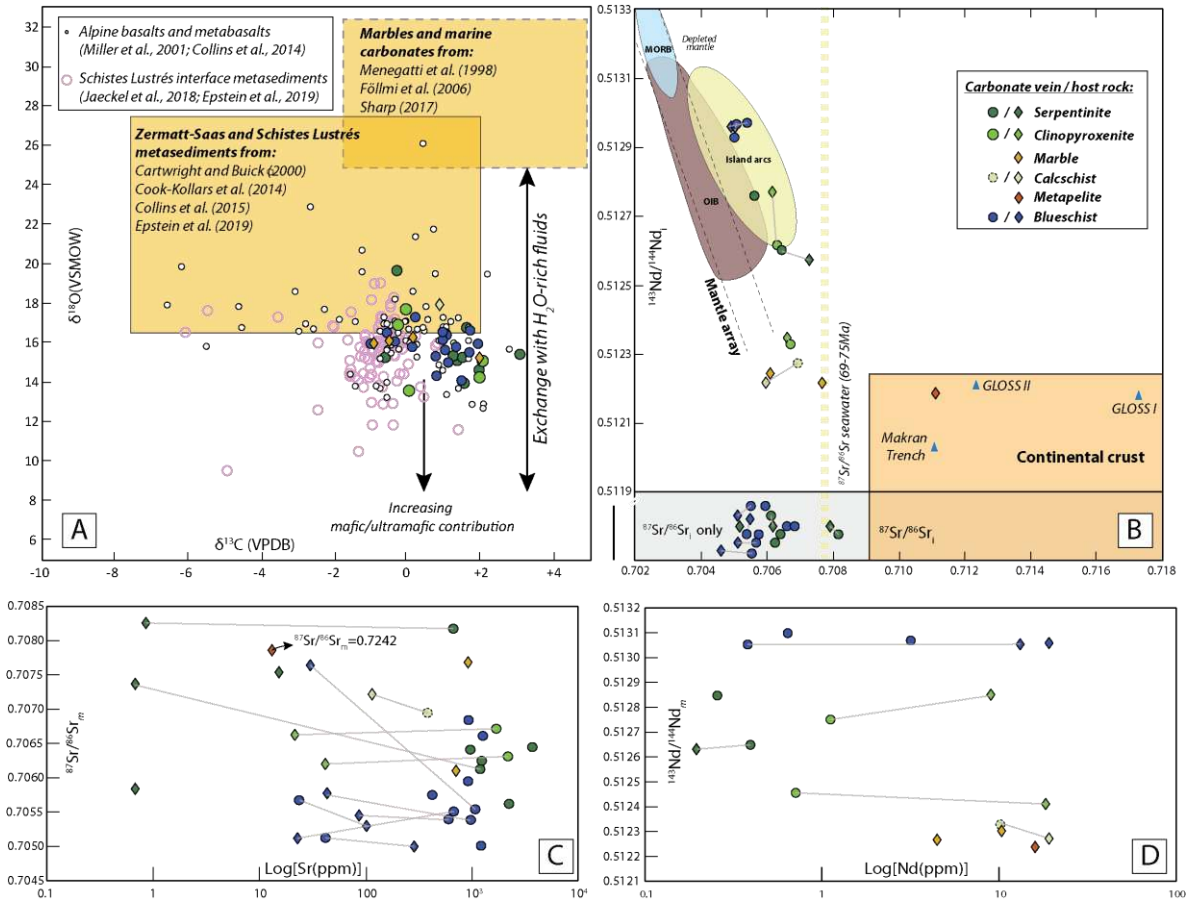

Figure 5.10. A. $\delta^{18}O$ vs $\delta^{13}C$ plot of measured carbonate-bearing veins and metasedimentary host rocks. For comparison, data from Alpine mafic and metasedimentary rocks and pristine marine carbonates are shown. B. Initial $^{87}Sr/^{86}Sr_i$ vs $^{143}Nd/^{144}Nd_i$ plot of carbonate veins and host rocks. Late Cretaceous $^{87}Sr/^{86}Sr$ ratios from Hess et al. (1986). Mantle array after DePaolo and Wasserburg (1979). For comparison, the global subducting sediment (GLOSS) values as well as trench-filling sediments from the Makran trench from Plank (2014) are shown. C-D. Measured $^{87}Sr/^{86}Sr_m$ vs Sr and $^{143}Nd/^{144}Nd_m$ vs Nd concentration diagrams, respectively. The tie-line links host-vein pairs.

5.9 Thermodynamic Modeling

The scope of this section is to gain information in terms of water and carbon devolatilization processes that may account for the fluid budget needed for veining and mineral precipitation. Here, we have modeled a representative blueschist, serpentinite, marble, metapelite and calcschist (***Figs.5.11*** and ***5.12***): the first two lithologies will allow addressing the fluid budget in terms of prograde dehydration since they represent ≈95 vol.% of the Seghin complex, while the metasedimentary material serves as a proxy to understand infiltration-reaction-fractionation decarbonation processes on a thermodynamic perspective.

Modeled phase relationships and devolatilization trends are shown in ***Fig.5.11*** and the resulting pseudosections in ***Fig.5.S2***. At peak P-T conditions, the pseudosection for a representative blueschist (***Fig.5.11A***) predicts a mineral assemblage dominated by glaucophane, clinopyroxene and lawsonite making >75 vol.% of the bulk assemblage, plus minor garnet, chlorite, phengite and titanite (see pie-charts in ***Fig.5.11A***). These predictions are in relatively good agreement with petrological

observations. Garnet proportions are overestimated, although rare crystals have been reported in other studied Seghin blueschist samples (***Fig.5.S1B***; see also Angiboust et al., 2016). Calculated XMg in glaucophane is c. 0.6, while Si in phengite is c. 3.5 (***Figs.5.5A*** and ***C***). However, predicted clinopyroxene composition is richer in the omphacitic component relative to the measured grains (***Fig.5.5D***).

The serpentinite model predicts that c. 80 and 13 vol.% of serpentine and chlorite are stable at peak conditions, in agreement with thin section estimates. The antigorite-out reaction is predicted to begin at c. 610 °C (***Fig.5.11A***), being rather insensitive to pressure. A minor discrepancy of our model is the presence of minor prograde olivine formation (<3 vol.%; resulting from the brucite + antigorite reaction) while olivine has not been preserved in the observed paragenesis, leading to a mild H_2O-release overestimation (along the X-Y segment).

To quantify H_2O release during burial and peak metamorphism, we consider the P-T path illustrated in ***Fig.5.11A***, where the segment X-Y represents the prograde burial while Y-Z is the isothermal pressure increase stage that culminates in the HP-LT peak metamorphic stage. The segment Y-Y' corresponds to the burial path of the Seghin slab, i.e., of subducted non-accreted rock packages at the time of accretion of the Seghin complex (see Angiboust et al., 2016).

The prograde X-Y path (***Fig.5.11A***) yields a total H_2O release from the modeled blueschist, serpentinite, metapelite and calcschist of c. 2.4 (1.33), 0.8 (0.44), 0.4 (0.22) and 2.3 (1.27; H_2O wt% and moles of H_2O/kg of rock), respectively (***Fig.5.11B***). In the blueschist, prograde H_2O-releasing reactions are characterized by the consumption of stilpnomelane, pumpellyite and partially chlorite and the formation of large amounts of amphibole and some epidote. Serpentinite dehydration involves the breakdown of brucite, while minor stilpnomelane and chlorite consumption characterizes dehydration in the metasediments. During the isothermal pressure increase (segment Y-Z), all models (except for the serpentinite) predict that H_2O is needed to form the natural parageneses. Thus, the formation of lawsonite after epidote represents the most important product of re-hydration towards the HP metamorphic stage requiring c. 0.8 wt% of H_2O. Total serpentine consumption will occur at c. 630 °C (eclogite-facies conditions; point Y' in ***Fig.5.11A***) releasing c. 9.0 wt% of H_2O (5.00 moles of H_2O/kg of rock; Y-Y' path) contemporaneously with the eclogitization of the blueschist composition at the same P-T conditions, involving the formation of a garnet + omphacite + phengite assemblage and releasing c. 2.0 wt% H_2O (1.11 moles of H_2O/kg of rock; Y-Y' path). The modeled metasedimentary material shows relatively minor dehydration at the end of the Y-Y' path, but, due to their volumetrically low abundance, metasediments have a negligible effect on the total water budget. Thus, at eclogite facies-conditions (point Y'), a subducted rock package, similar to the entire Seghin complex, may have released 7.1 wt% of H_2O (3.94 moles of H_2O/kg of rock).

Metapelite and calcschist pseudosection modeling demonstrates that minor decarbonation can occur at higher temperatures or under a hot subduction gradient (***Figs.5.11C*** and ***D***) whereas the modeled impure marble composition yields virtually no CO_2 release in the P-T window of interest (***Figs.5.S2C***

to ***5.S2E***). Since decarbonation cannot occur without infiltration of an externally-sourced H_2O-rich fluid, we have applied an infiltration-driven devolatilization model assuming pure H_2O as the infiltrating fluid. This assumption is realistic for relatively low temperature subduction zone fluids which are characterized by low amounts of dissolved components (e.g., Connolly and Galvez, 2018; Menzel et al., 2019). The P-T conditions selected correspond to those of the highest-pressure stage (480 °C–1.8 GPa; star in ***Fig.5.11A***).

Infiltration-driven decarbonation modeling show that metapelite decarbonation trend is characterized by the total consumption of dolomite, releasing up to 0.38 moles of C (***Fig.5.12A***). In addition, partial dissolution of quartz, clinopyroxene and white mica (***Fig.5.12A***) accounts for Si, and minor Fe, Na, K, Mg and Al mass loss from the initial rock mass (***Fig.5.12D***). Calcschist decarbonation is characterized by the total dissolution of dolomite first, followed by aragonite (***Fig.5.12B***), releasing c. 2.35 moles of C (***Fig.5.12E***). Similar amounts of Si, Al, Fe, Mg and Na compared to those in metapelite are potentially lost (***Fig.5.12E***). Note that lawsonite in calcschist is totally consumed in the modeled fluid-rock interaction process while garnet forms after the infiltration of c. 33 moles of H_2O/kg of rock. Strikingly different trends resulted after marble infiltration-devolatilization modeling. In this case, high amounts of H_2O are needed to account for element loss, with Si being the element most efficiently mobilized followed by C and Ca (***Fig.5.12F***). The infiltration-devolatilization models predict that c. 5, 49 and 390 moles of infiltrating H_2O are necessary to decarbonate one kilogram of metapelite, calcschist and marble, respectively (***Figs.5.12D*** to ***F***).

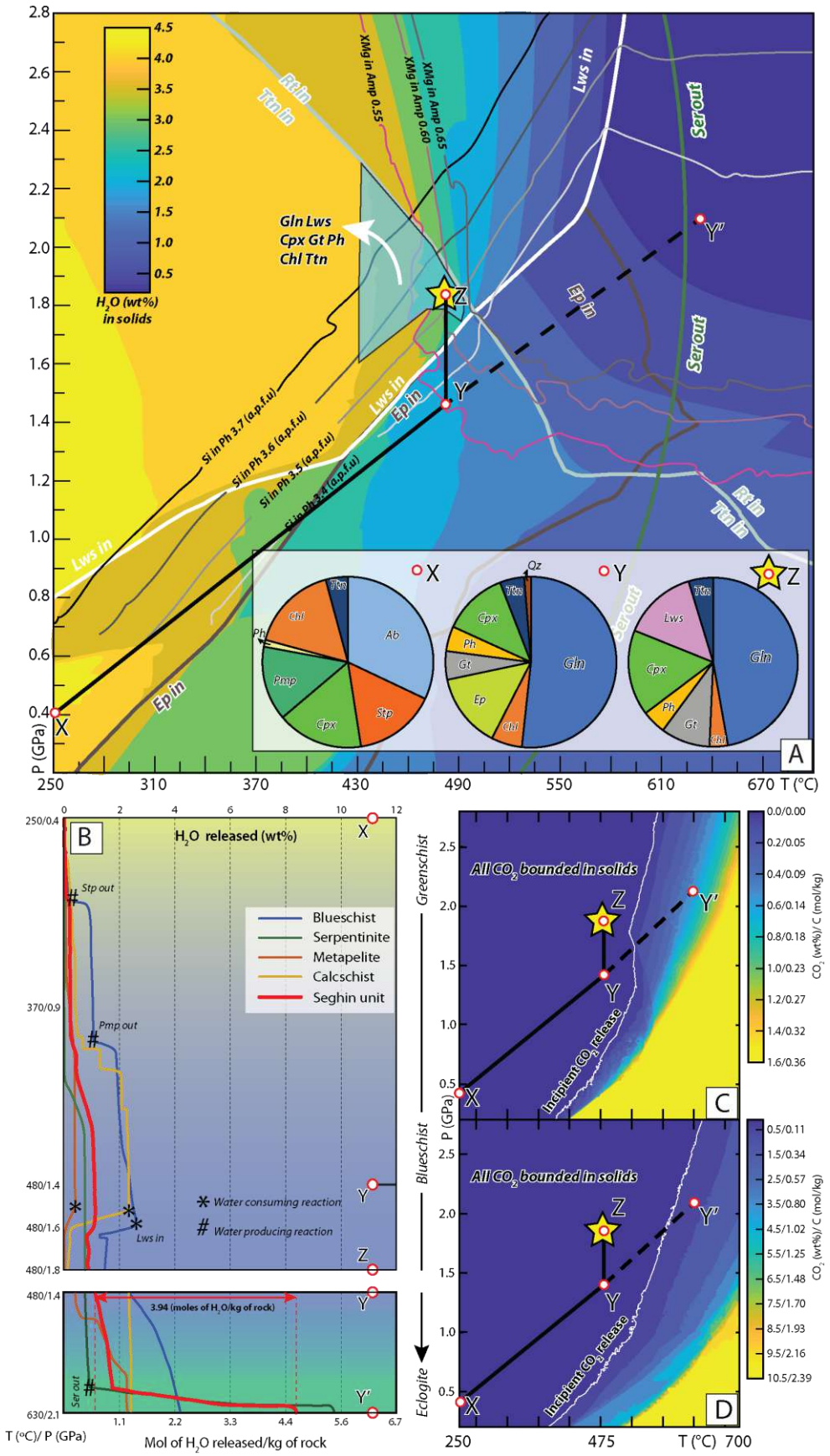
H2O (wt%) in solids
4.5
4.0
3.5
3.0
2.5
2.0
1.5
1.0
0.5
Gln Lws Cpx Gt Ph Chl Ttn
Rt in
Ttn in
XMg in Amp 0.55
XMg in Amp 0.60
XMg in Amp 0.65
Lws in
Ser out
Ep in
Si in Ph 3.7 (a.p.f.u)
Si in Ph 3.6 (a.p.f.u)
Si in Ph 3.5 (a.p.f.u)
Si in Ph 3.4 (a.p.f.u)
X
Y
Z
Y'
Ab
Stp
Cpx
Pmp
Chl
Ttn
Ph
Ep
Gln
Gt
Qz
Lws
A
P (GPa)
T (°C)
B
H2O released (wt%)
Stp out
Pmp out
Lws in
Blueschist
Serpentinite
Metapelite
Calcschist
Seghin unit
Water consuming reaction
Water producing reaction
3.94 (moles of H2O/kg of rock)
T (°C)/ P (GPa)
Mol of H2O released/kg of rock
Greenschist
Blueschist
Eclogite
All CO2 bounded in solids
Incipient CO2 release
C
D
CO2 (wt%)/ C (mol/kg)

Figure 5.11. A. Partial pseudosection for the blueschist sample SO1833 (see Table 2; the complete pseudosections can be seen in Fig.5.S2) showing the stability field that matches the assumed peak P-T conditions of 480 °C at 1.8 GPa (yellow star) as calculated by Angiboust et al. (2016). The colored background shows the amount of H_2O (wt%) in solids. XMg in amphibole and Si (a.p.f.u) in phengite at the P-T conditions of interest are shown. The antigorite-out reaction curve has been extracted from the pseudosection calculated for the serpentinite composition (Fig.5.S2B). The thick line from X to Y (250 °C at 0.4GPa and 480 °C at 1.4 GPa, respectively), represents the prograde path of the modelled rock. The path from Y to Z (480 °C at 1.4 GPa and 480 °C at 1.8 GPa, respectively) represents the isothermal pressure increase as recorded by these rocks (Angiboust et al., 2016). The thick dashed line (Y to Y') corresponds to a hypothetical P-T path at which the rock packages similar to Seghin complex may have been buried during subduction under a steady thermal gradient. Note that the prograde path X-Y-Z has been extracted from Angiboust et al. (2016). Pie-charts show modes (in vol.%) at X, Y and Z. B. H_2O released along the P-T path from all modeled composition and a weighted average for the entire Seghin complex. C-D. Isopleths of CO_2 released from metapelite and the calcschist compositions (Table 2), respectively. Results from the impure marble composition are not shown since no decarbonation is predicted in the P-T window.

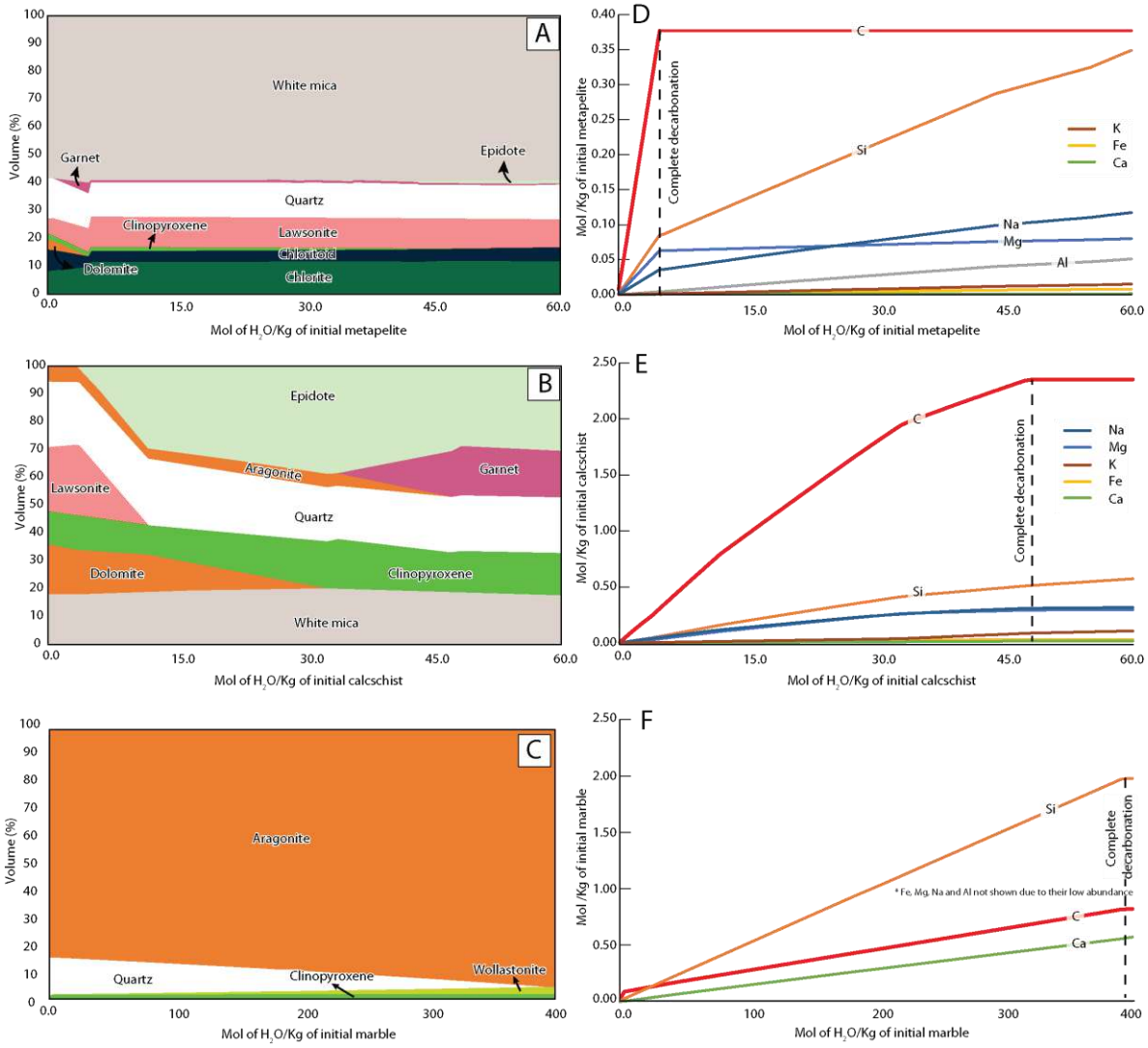

Figure 5.12. Infiltration-driven devolatilization results at 480 °C and 1.8 GPa. (A to C) Phase proportions and mass loss (D to F) for the metapelite, calcschist and marble compositions, respectively.

5.10 Discussion

Petrological and field-based characterization reveal that the Seghin complex exhibits a block-in-matrix fabric that shares similarities with other tectonic mélanges reported worldwide such as in Cuba or on Santa Catalina Island (e.g., Garcia-Casco et al., 2006; Grove and Bebout, 1995). The great abundance of serpentinite material relative to blueschist blocks as well as the cold conditions recorded by peak mineral assemblages from the Seghin complex are strikingly similar to features observed in the Franciscan Complex (e.g., Cloos, 1986). Such characteristics have been correlated to modern, non-accretionary Mariana-type subduction settings, where serpentinite-dominated subduction channels, including blueschists, occur (e.g., Maekawa et al., 2004 and references therein). Thus, the Seghin complex represents a pristine window onto HP-LT serpentinized subduction interfaces-channels (Angiboust et al., 2016), allowing an assessment of deep-forearc fluid pathways and fluid-rock interactions.

5.10.1 Mineralogical evolution of veins and host rock

Previous studies on metamorphic veining and fluid-source identification mostly focused on the outcrop scale (e.g., Cartwright and Buick, 2000; Scambelluri and Philippot, 2001; Spandler et al., 2011; Taetz et al., 2016). We emphasize here the importance of undertaking "metamorphic complex-scale" studies since assessing vein volume as well as the spatial distribution of vein structures is critical to accurately image deep fluid pathways.

Bulk major, trace element and Sr-Nd isotopic analyses demonstrate that the studied blueschists can be classified as oceanic material (***Fig.5.8A*** and ***B***). It is known that during seafloor metasomatism, spilitilization, among several other processes, may modify the chemical composition of the volcanic and plutonic protoliths (e.g., Narebski et al., 1986). Zeolite-facies minerals, namely zeolites, commonly form in cavities or fractures after seafloor fluid circulation (e.g., Maekawa et al., 1995). These minerals will eventually break down during early prograde metamorphism. For instance, Na-bearing zeolites such as analcime will break down into albite, releasing large amounts of H_2O (Spear, 1993). Other types of Ca-bearing zeolites (e.g., laumontite, wairakite) and clays also dehydrate during shallow burial at temperatures below 200 °C (Spear, 1993). Textural and mineralogical investigations suggest that the earliest stages of veining are characterized by repeated albite (and subordinate pumpellyite and actinolite) precipitation (***Fig.5.6B*** and ***5.7***). These veins are interpreted as representing former hydrofractures commonly oriented sub-parallel to, or transecting the main fabric (c.f., Moore et al., 1995). Their formation implies that overpressurized pore fluid conditions were attained during early subduction stages (Saffer and Tobin, 2011; Muñoz-Montecinos et al., 2020). It has been shown earlier that similar features formed by direct precipitation from seafloor hydrothermal fluids can locally survive subsequent subduction deformation (e.g., Vitale Brovarone et al., 2018). However, (i) the lack of diagnostic volcanic-derived features (such as pillows and volcanic breccia structures in lava flows) and (ii) the absence of key minerals such as Fe-rich epidote and chlorite (Humphris and Thompson, 1978) as well as high temperature pargasite or magnesiohornblende overgrown by actinolite and glaucophane in the early stages of veining or in structural domains such

as inter-pillow spaces (as seen in Alpine Corsica; Vitale Brovarone et al., 2018 and Central Chile; Muñoz-Montecinos et al., 2020), indicate that these veins were most likely not derived from direct seafloor alteration. In any case, early structural features are scarcely preserved in the Seghin complex due to overprinting during ongoing metamorphism and deformation.

Further during prograde burial in the blueschist-facies, a larger variety of silicate-rich veins started to precipitate and re-equilibrate, as testified by the presence of zoned lawsonite, aegirine-augite, glaucophane, as well as Si-rich phengite (***Fig.5.5***). A similar mineralogical evolution is observed in the blueschist host adjacent to the veins except for prograde epidote which is present only in the former. The inferred counterclockwise P-T path and observed mineral parageneses suggest that the Seghin blueschists likely underwent rehydration at near-peak conditions in order to account for the pervasive crystallization of lawsonite after prograde dehydration (***Fig.5.11A***). These observations are in line with pseudosection modeling which predicts that the addition of c. 1 wt% of H_2O is needed to stabilize c. 14 vol.% of lawsonite (***Figs.5.11A*** and ***B***). These statements are supported by the presence of epidote inclusions in lawsonite and epidote disequilibrium textures with respect to the peak mineral assemblage. Alternatively, a fluid with high CO_2 activity would also favor stabilization of prograde epidote rather than lawsonite. Nevertheless, titanite, a mineral much less stable at high CO_2 activities than lawsonite, is widespread in the studied blueschists ruling out this possibility (e.g., Vitale Brovarone et al., 2018).

It seems clear that bulk rock geochemical variations played a role in lawsonite stability (e.g., Maruyama and Liu, 1988; Maekawa et al., 1995) allowing this mineral to form in the veins during burial while epidote was still theoretically stable in the host mafic rock. Similar conclusions were drawn by Martin et al. (2014) who proposed that in such lawsonite-rich domains (e.g., veins; Whitney et al., 2020), a chemical system such as CASH (CASH-like in Martin et al., 2014) expands the lawsonite stability field towards higher temperatures. These observations better constrain the prograde metamorphic evolution which likely took place under a subduction thermal gradient in the vicinity of the band defining the lawsonite-epidote transition area (e.g., ***Fig.5.11A***). Nevertheless, some lithologies preserve (see ***Fig.5.8D***), in apparent textural equilibrium, the epidote-lawsonite mineral assemblage supporting the hypothesis that local geochemical heterogeneities critically influence the location of the main water-producing reactions in mafic systems (e.g., Maekawa et al., 1995; Massonne and Willner, 2008; Vitale Brovarone and Beyssac, 2014).

Our findings reveal that clinopyroxene range from diopside towards jadeitic-omphacitic compositions in both blueschists and clinopyroxenites (***Fig.5.5D***). Jadeite-rich clinopyroxene would be expected to eventually evolve to omphacite with increasing metamorphic grade (Maruyama and Liu, 1988). At peak P-T conditions, the most abundant pyroxene is aegirine-augite while the same variety, but Na-Al-poorer, characterizes the early prograde evolution (***Figs.5.5D*** to ***F***). Such type of clinopyroxene is considered as the Fe^{3+}-rich analogue of omphacite in rocks containing abundant Fe^{3+} at eclogite-facies conditions (e.g., Flores et al., 2015). The occurrence of virtually the same types of clinopyroxene, including a similar prograde zoning in veins and hosts, in addition to the prograde

formation of aegirine-augite in the form of healed cracks (***Fig.5.5E***), suggests that such Fe^{3+}(-Al-Na)-rich conditions (relatively oxidizing) were also occurring in the fluid phase from which the clinopyroxene precipitated, confirming a joint chemical evolution for both the host rock and the fluids. Na-amphibole also show strong Fe^{3+} variations (***Fig.5.5C***) with $Fe^{3+}/(Fe^{3+}+Al)$ commonly ranging from 0.0 to 0.7 at the thin section scale (***Fig.5.5C***). Due to the textural characteristics of the zoning pattern as well as the good agreement between measured and thermodynamically predicted amphibole XMg (***Figs.5.5C*** and ***5.11A***), we consider Fe^{3+} variations as an indication of local chemical heterogeneities (e.g., oxygen fugacity variations) rather than changes in P-T conditions (Spear, 1993).

The exchange of Fe^{3+} and Al in lawsonite has been considered as an indicator of metamorphic grade (Maruyama and Liu 1988; Maekawa et al 1995; Vitale Brovarone et al., 2014). Maekawa et al. (1995) and Maruyama and Liu (1988) suggested that Fe^{3+} is preferentially incorporated in lawsonite in low-grade blueschists with values as high as 0.13 a.p.f.u., while Vitale Brovarone et al (2014) favored the opposite scenario. Our petrological investigations show that lawsonite preserved in veins and blueschists exhibit Fe^{3+} contents ranging mostly between 0.00 to 0.05 a.p.f.u. (locally reaching up to 0.36 in one sample: ***Fig.5.5B*** and ***Table 1***). Clinopyroxene and amphibole, in apparent textural equilibrium with lawsonite, indicate that this paragenesis formed and evolved in an Fe^{3+}-rich chemical system in both the host and the fluid phase. We conclude that even in such Fe^{3+}-rich environments, lawsonite does not preferentially incorporate Fe^{3+} upon increasing metamorphic grade, in agreement with Maruyama and Liu. (1988) and Maekawa et al. (1995). In summary, most well-preserved vein systems formed in the blueschist-facies and chemically evolved approaching peak metamorphic conditions in a system resulting from the interplay between burial-related deformation and fluid-rock interaction processes.

5.10.2 The structural record of fluid-rock interactions

Correlation of petrological features (***Fig.5.7***) with the deformation history is critical to constrain deformation regimes associated with the various fluid-rock interaction stages (e.g., Fisher and Brantley, 1992; Franz et al., 2001). Most veins formed during burial have been affected by a mixture of brittle-viscous deformation patterns as evidenced by the brecciated nature of lawsonite and albite grains while weaker phases such as quartz deformed in a viscous manner (***Figs.5.3F, 5.4F*** and ***J***). During burial-related shearing, the initially oblique veins were largely transposed or folded according to the main fabric as illustrated in ***Fig.5.7*** (see Wassmann and Stöckhert, 2012; Munoz-Montecinos et al., 2020 for examples). Crosscutting relationships indicate that carbonate-bearing fluids also infiltrated earlier-formed silicate-rich veins (***Figs.5.4E, F*** and ***I***), suggesting that vein domains likely represent zones of preferential weaknesses in the rock volume (e.g., Philippot and Selverstone, 1991; Zack and John, 2007; Spandler et al., 2011; Taetz et al., 2016). At near-peak P-T conditions, several CO_2-bearing fluid-rock interaction events triggered hydrofracturing, affecting the entire Seghin complex as suggested by crosscutting and textural relationships well visible in mafic blocks (***Figs.5.3*** and ***5.13***). We cannot exclude that some of the texturally earliest features formed by seafloor alteration as suggested, for instance, by Vitale Brovarone et al. (2018) for lawsonite-eclogite-facies

former seafloor material from Alpine Corsica (France). Nevertheless, it is worth noting that such features are preserved there in non-deformed metabasites only. In the Seghin complex, the intense shearing that affected the silicate-rich veins and the host blueschists does not affect the aragonite-bearing hydraulic breccias, thus confirming a prograde veining origin rather than a hypothetic precipitation at the seafloor.

The host serpentinites, pervasively deformed in a viscous manner, contain abundant dolomite-rich domains that underwent hydrofracturing and brecciation throughout burial likely in the blueschist-facies (***Fig.5.3G***; see Cannaò et al., 2020 for similar examples). It is inferred that this prevalent hydrofracturing pattern, widespread in the Seghin complex, likely occurred through the incoming of CO_2-bearing fluids during and/or just after the blueschists detached from the subducting slab and incorporated into the serpentinite matrix as strong slivers (e.g., Guillot et al., 2009). We note that most hydraulic breccia fragments are devoid of post-brecciation shearing. If hydrofracturing had occurred while the Seghin-forming material was still mechanically coherent with the downgoing slab (i.e., before detachment in the sense of Agard et al., 2018) or if the aragonite-bearing breccias had formed as syn-sedimentary deposits in an oceanic basin environment (e.g., Marroni and Pandolfi, 2007; Festa et al., 2015), most carbonate-filled hydraulic breccias would have been parallelized and the clasts would have rotated during fabric formation and prograde- or detachment-related deformation (Spandler and Hermann, 2006; Angiboust et al., 2011). We hence conclude that the fluid-rock interaction event that was responsible for the massive hydrofracturing visible among Seghin lithologies occurred while the blocks were floating in a serpentinite-rich environment as shown in the present-day configuration (***Fig.5.2***).

5.10.3 Constraining fluid sources for silicate- and carbonate-bearing veining events

Trace element abundance in vein-filling minerals depends on mineral-fluid partition coefficients, which in turn depend on (i) mineral chemistry and structure (e.g., stable mineral assemblage) and (ii) the composition of the fluids from which veins precipitate (John et al., 2008; El Korh et al., 2009; Spandler et al., 2011). In the host rock, a Eu anomaly observed in glaucophane may represent an inherited feature due to preferential incorporation in plagioclase during early igneous stages (Ague, 2003; Carson and Ague 2008) or in lawsonite related to HP metamorphism (Ague, 2003; Vitale Brovarone et al., 2014; Ague, 2017). Van der Straaten et al. (2008) showed that glaucophane may eventually incorporate Co and Ni if abundant in the fluid phase while the same behavior has been documented for Cr in Na-clinopyroxene (Spandler et al., 2011). The studied amphibole and clinopyroxene crystals are not appreciably enriched in these elements, suggesting that the fluids from which these phases precipitated were not particularly rich in Cr, Ni and Co. Clinopyroxene host-vein pairs also contain similar amounts of trace elements, specially REEs (***Fig.5.9B*** and ***Table S3***). Thus, we speculate that amphibole and clinopyroxene crystals in veins were mostly locally-derived involving mass transfer from the blueschist host towards the infiltrating fluids and subsequent mineral precipitation (Oliver and Bons, 2001; Spandler and Hermann, 2006; John et al., 2008; Putnis and Austrheim, 2012). These statements should be taken with caution since previous studies have shown

that fluids produced at the blueschist-eclogite-facies transition are characterized by low REE and HFSE concentrations (John et al., 2008; El Kohr et al., 2009), making fluid source discriminations based on trace element concentrations difficult to evaluate.

Transport of fluid-mobile elements (e.g., LILE) is expected even at low fluid-rock ratios (Zack et al., 2001). In Na-amphibole, it has been shown that minor fluid-rock interactions may produce considerable mobilization of Cs and Ba (e.g., from 024 to 0.006 ppm and 12 to 2 ppm, respectively) while Rb remains virtually unchanged (Zack et al., 2001). The identical Ba/Rb ratios measured in Seghin Na-amphibole from host and vein domains and slightly higher Cs/Rb values in host amphibole grains (***Fig.5.9E***) suggest that fluid-rock ratios were likely very low at least during single amphibole-precipitating stages. On the other hand, both Cs/Rb and Ba/Rb ratios are identical in host and vein clinopyroxene crystals, preventing any trend interpretation (***Table S3***). In blueschists and metapelites, phengite is the major host of LILEs and is thought to record Cs/Rb and Ba/Rb ratios of the host protolith even at eclogite-facies conditions (Zack et al., 2001; see also El Korh et al., 2009). In Seghin lithologies, different Cs/Rb and Ba/Rb values between metapelite and calcschist-hosted phengite crystals (higher in the host calcschist) may be associated with the nature of the protolith, the latter strongly influenced by seawater Ba and Cs enrichments (see below). Phengite in the host blueschist and veins also differ, the latter showing higher Ba/Rb and Cs/Rb ratios close to calcschist phengite values, while the former is consistent with a slightly altered basaltic lithology (***Fig.5.9E***). These observations together with previous investigations (Zack et al., 2001) show that phengite crystals in veins are chemically comparable to those formed from metasedimentary sources and thus, an external origin is likely (Breeding et al., 2004; van der Straaten et al., 2008; Martin et al., 2014). Although further in the discussion we show, based on lawsonite trace element patterns and thermodynamic modeling, that a metasedimentary source is feasible, we cannot rule out that local mobilization of LILEs from the host towards phengite-bearing veins occurred in specific places, as documented for instance in Tianshan, China (John et al., 2008).

Lawsonite trace element compositions display a wide range of values among different domains (***Fig.5.9C***). The most notable differences arise from the higher REEs concentrations in vein lawsonite crystals while fairly constant in the host blueschist. It is also worth noting that all lawsonite crystals are not particularly enriched in Co, Ni and Cr (see ***Table S3***). Martin et al. (2014) documented enrichments in Th, U, Pb and REEs in lawsonite grains measured in an eclogite-facies quartzite (Dabie-Sulu, China) in good agreement with analyzed metapelite grains from the Seghin complex. Vein lawsonite crystals are richer in REEs compared to those in the host blueschist, with an increasing REEs content towards the rims (***Fig.5.9C***). In the host blueschist, it is likely that epidote scavenged REEs together with lawsonite during prograde metamorphism. On the other hand, vein-filling lawsonite likely precipitated in equilibrium with apatite, the latter also competing to uptake REEs, specially HREEs (***Table S3***). Thus, we interpret the lawsonite cores trend as reflecting locally-derived fluid sources that likely equilibrated with the host material during advection of material towards the vein before precipitation (e.g., Spandler and Hermann, 2006; John et al., 2008; Spandler et al., 2011).

During latter stages of metamorphism, enrichments in REEs, as observed in lawsonite rims, are compatible with an external, likely metasedimentary-derived contribution in the fluid phase from which the rims precipitated (Martin et al., 2014; Vitale Brovarone et al., 2014). This is in line with the modeled isothermal compression stage previous to attainment of peak-P conditions indicating that rocks consumed H_2O, hence preventing internal H_2O-fluid production at this stage (***Fig.5.11A***). In conclusion, most silicates in veins (amphibole, clinopyroxene and lawsonite cores) can be attributed to mostly locally-derived fluid sources, while the composition of phengite and lawsonite rims rather supports an external origin of metasedimentary affinity (e.g., Spandler and Hermann, 2006).

Enrichments in Mg, Co, Ni and Cr in minerals from eclogites and blueschists have been interpreted as the result of an external, serpentinite-derived, fluid contribution (van der Straaten et al., 2008; Spandler et al., 2011; Angiboust et al., 2014), most likely produced by antigorite breakdown in the eclogite-facies or fluid equilibration within serpentinites (Trommsdorff et al., 1998; Van de Straaten et al., 2008; Ferrando et al., 2009; Spandler et al., 2011). Our studied host-vein pairs are not enriched in Co, Ni and Cr, while these elements, especially Ni and Cr, are enriched in the analysed serpentinite material (***Table S3***). In addition, no evidence of Mg addition has been found (Van der Straaten et al., 2008; Angiboust et al., 2014). Therefore, a serpentinite-derived fluid imprint cannot be clearly identified in the studied prograde blueschist-facies veining.

The $\delta^{18}O$ vs $\delta^{13}C$ isotopic ratios from carbonate veins are very restricted, ranging mostly between +14 to +18‰ and -1 to +3‰, respectively (***Fig.5.10A***), essentially identical to those of the metasedimentary material (+15 to +16‰ and -1 to +2‰, respectively). Overall, the measured O isotopic signature does not reflect that of marine carbonates and, in the case of the host calcschist and marbles, it cannot be considered pristine since fresh marine carbonates cluster in the range of +25 to +32‰ (see the field in ***Fig.5.10A***). In the Alps, a number of authors have demonstrated that carbonate-bearing metasediments have been affected by regional-scale $\delta^{18}O$ equilibration lowering its value from c. +29‰ to values as low as +12‰ while their original $\delta^{13}C$ remained relatively unaffected (-2 to +2‰; Cartwright and Barnicoat, 1999; Miller and Cartwright, 2000; Cook-Kollars et al., 2014; Jaeckel et al., 2018; Epstein et al., 2020). Jaeckel et al. (2018) demonstrated that, along Dent Blanche paleosubduction interfaces in the Italian and Swiss Alps, non-pristine $\delta^{18}O$ ratios between +18 to +22‰, observed regionally in the Schistes Lustres, were overprinted by metasomatism resulting in values as low as +12‰. To accomplish this shift, infiltration through channelized pathways (such as a subduction interface) by mafic/ultramafic-derived H_2O-rich fluids with $\delta^{18}O$ between +8.5 and +10.5‰ was proposed by those authors. We similarly interpret the vein- and metasediment-measured $\delta^{18}O$ values obtained in this study as reflecting the interaction of mafic/ultramafic-derived low-$\delta^{18}O$ H_2O-rich fluids with metasedimentary material at near-peak conditions, while largely preserving their pristine marine-related $\delta^{13}C$. Vein $\delta^{18}O$ and $\delta^{13}C$ are also similar to values for Alpine metabasalts (see ***Fig.5.10A***). However, the systematic lack of carbonate phases in the host blueschists allows us to discard these lithologies as a likely C source (although fluid $\delta^{18}O$ values may have been buffered by the host). Thus, we consider the forming-fluids from which most carbonate-bearing veins precipitated

as largely metasedimentary-derived after infiltration by H_2O-rich fluids and synchronous $\delta^{18}O$ re-equilibration. The virtually identical carbonate trace element abundances in the metasedimentary hosts and veins support this scenario (***Fig.5.9D***).

An alternative C source is carbonaceous matter (Zheng et al., 2000; van der Straaten et al., 2012; Vitale Brovarone et al., 2020) which is locally observed in the rare metapelites. Vitale Brovarone et al. (2020) showed that during blueschist-facies fluid-rock interactions, carbonaceous materials can also be dissolved, contributing light $\delta^{13}C$ to veins with values lower than -12‰ (Spandler et al., 2008; Vitale Brovarone et al., 2020). It appears that the C-bearing veins studied here show no obvious isotopic signatures of carbonaceous material.

Sr-Nd isotope ratios of blueschists overlap with the island arc field in ***Fig.5.10B*** while a few Sr isotopic ratios are slightly higher than those of the mantle array. Thus, blueschist ratios are considered as mostly pristine whereas few samples with an apparent shift (see data with $^{87}Sr/^{86}Sr_i$ only and $^{87}Sr/^{86}Sr_m$ in ***Figs.5.10B*** and ***D***) may be explained by the interaction with pre-subduction or metamorphic seawater-derived fluids which imprint a signature more radiogenic than that of pristine oceanic basalts (e.g., van der Straaten et al., 2012). Due to the very low Sr and Nd concentrations in serpentinites (***Figs.5.10C*** and ***D***), their Sr-Nd isotopic ratios are easily affected by any infiltrating fluid with significant concentrations of these elements. Still, their Nd isotope signatures are fairly mantle-influenced, but samples containing the most radiogenic Sr isotopic ratios clearly argue in favor of variable metasomatic imprints with highly radiogenic fluids such as seawater or metasedimentary-derived fluids (van der Straaten et al., 2008; van der Straaten et al., 2012). In clinopyroxenites, Sr and Nd concentrations are comparable to those of the blueschists (***Figs.5.10C*** and ***D***) while the two analyzed samples show contrasting Sr-Nd isotopic ratios: one plots in the Island arc field while the other is less radiogenic in Nd with values similar to those in the metasediments (***Fig.5.10B***). These isotopic signatures, together with their petrological characteristics and immobile trace element ratios (***Figs.5.8B*** and ***D***) suggest that clinopyroxenites correspond to strongly metasomatized mafic volcanic material affected by metasedimentary-derived fluid infiltration during subduction. The calcschist and marble samples plotting near the Sr seawater band indicate a fairly pristine oceanic origin (***Fig.5.10B***). The metapelite sample is the highest in $^{87}Sr/^{86}Sr$ and the lowest in $^{143}Nd/^{144}Nd$, characteristic of continent-derived trench-fill sediments (e.g., Plank, 2014). Overall, the Sr-Nd isotopic ratios reflect pristine signatures corresponding to those of continent-derived metasediments, seawater-buffered marbles, unaltered oceanic mafic rocks and mantle-influenced serpentinites, allowing to suggest that the Seghin complex is composed of an amalgamation of scraped-off slab-top material, mixed within plate interface serpentinites (e.g., Guillot et al., 2009). The occurrence of abundant metatuffs rather than metalavas, the lack of gabbros and the occurrence of metasediments interlayered with blueschists support this scenario. It is not possible to determine whether the serpentinite surrounding the mafic blocks was rather derived from the downgoing plate or instead from the overlying mantle wedge.

The Sr-Nd isotopic signatures of carbonate-filled hydraulic breccias and hydrofractures (e.g., ***Figs.5.3C, D, F, 5.4C, D, E*** and ***I***) closely resemble those of their nearby host (***Fig.5.10B***). Thus, Sr-Nd systematics do not indicate clear evidence for seafloor alteration in the studied blueschists and carbonate-bearing veins, supporting the inferred scenario where most veins and host rock features were produced and evolved during subduction. A first, straightforward explanation, is that the related fluids are locally-derived (e.g., Nadeau et al., 1993; Cartwright and Barnicoat, 1999; Spandler and Hermann, 2006; Hermann et al., 2006; Taetz et al., 2016). This hypothesis, which involves mass-transfer at the local scale either by dissolution-precipitation or decarbonation (Putnis and Austrheim, 2012) is at odds with petrological, structural and geochemical evidences, including (i) the occurrence of these veins as hydraulic breccias and hydrofractures, implying vast amounts of advected fluids, (ii) crosscutting relationships where the hydraulic breccias sharply transect the strongly foliated fabrics of the hosts, (iii) the systematic absence of carbonates in the matrix of Seghin complex lithologies -except in the metasediments- and (iv) virtually identical O-C isotopic signatures in veins and metasediments. Alternatively, we propose that these veins are the result of large-scale and pervasive fluid infiltration into the Seghin complex. Such fluid-rock interaction events may have enhanced decarbonation from metasedimentary materials (Connolly and Galvez, 2018; Menzel et al., 2019), also imprinting its characteristic O-C isotopic signature. Furthermore, the fluids were expelled from the decarbonation front and infiltrated mafic/ultramafic rocks where local rock-vein homogenization occurred (Glodny et al., 2003; Glodny et al., 2008; Halama et al., 2011) before vein precipitation of carbonate phases.

Pressure-solution processes enhance redistribution of material at the local scale (Bell and Cuff, 1989). Stöckhert et al. (1999) showed that aragonite from HP-LT terranes can be dissolved and re-precipitated, in crystallographic continuity, as sub-mm-sized grains. Our petro-geochemical study demonstrates that this process was unequivocally active during prograde-peak metamorphism as evidenced by textural relationships and local Sr-Nd isotopic homogenization between host and adjacent veins which certainly involved dissolution of host rock material in the presence of fluids and further precipitation as veins. However, we do not envision a scenario where steady-state pressure-solution creep alone may result in sudden pore fluid pressure highs and further formation of hydraulic breccias. We stress that episodic advection of material is a feasible process to form the observed features (e.g., Oliver and Bons, 2001; Spandler et al., 2011). Consequently, fluid infiltration, reaction and further advection of material are key processes to redistribute CO_2 at large scales.

5.10.4 Insights into fluid-assisted decarbonation processes along the subduction interface

Down to subarc depths or beyond, prograde decarbonation in cool subduction environments is largely inefficient without considering the effect of an infiltrating H_2O-rich fluid (John et al., 2008; Ague and Nicolescu, 2014; Cook-Kollars et al., 2014; Gorce et al., 2019). Our thermodynamic modeling shows that a carbonate-rich rock cannot considerably decarbonate by increasing P-T alone (e.g., see metapelite and calcschist pseudosections in ***Figs.5.11C*** and ***D***; Ague and Nicolescu, 2014). In addition, the fluid-assisted decarbonation models show that the largest and smallest amounts of H_2O needed for decarbonation are for marble and metapelite, respectively, while the largest amount of C is released by a calcschist composition undergoing moderate fluid influx (***Figs.5.12D, E*** and ***F***). It is thus clear that varying amounts of C can be released via fluid-assisted decarbonation during burial in the blueschist-facies, with a greater efficiency in lithologies containing intermediate amounts of CO_2 such as calcschists. Similar conclusions were reached by Groppo et al. (2017) who, through a detailed thermodynamic modeling approach, have demonstrated that calcsilicate rocks release large amounts of CO_2 during prograde medium- to high-grade metamorphism in the Himalayan orogen. In the latter case, however, fluid-driven decarbonation reactions have not been invoked since the considered thermal gradient is far higher than in a cold subduction environment where decarbonation reactions are thermally enhanced.

The estimated 7 vol.% of carbonate veins in the whole Seghin complex contrasts with the low abundance (c. <5 vol.%) of metasediments. Considering a hypothetical volume of rock with a mass of 20 kg, from which 1 kg corresponds to metasediments, a total of c. 0.17 kg of C are required to form all the carbonate veins observed in the field, a value c. 6 times greater than what could be potentially decarbonated from the most suited composition (namely the calcschists; ***Fig.5.12E***). Although these rough estimates assume that veins are continuous in the dip direction and the density of solid material is constant, they indicate that -at least for the Seghin complex - full decarbonation from the now exposed lithological proportions cannot account for the amount of carbonate veining that occurred during blueschist-facies metamorphism (less than 0.002 kg of C/kg of rock is released along the Y-Y' dashed line in ***Fig.5.11C*** and ***D***). Hence, in order to reconcile all evidences, infiltration at near-peak conditions of deeply produced COH-rich fluids is needed (e.g., Piccoli et al., 2016), adding to the COH-bearing fluids generated by the fluid-assisted decarbonation of the metasediments exposed in the Seghin complex. This idea is supported by textural and crosscutting relationships of the veins as well as their O-C isotopic signature, interpreted here as the result of large-scale H_2O-rich fluid homogenization between externally, mafic/ultramafic-derived fluids and metasediments. H_2O-rich fluid infiltration in blueschists is also needed along the compression stage in order to achieve the observed mineral assemblage (***Fig.5.11A***). This deep dehydration pulse is theoretically expected to occur as subducted equivalents of the Seghin complex enter the eclogite-facies (***Fig.5.11B***).

These statements have direct implications regarding C mobility and recycling processes along the subduction channel. In line with thermodynamic modeling, it is proposed that C is stored as aragonite

veins (***Fig.5.3H***) that would subsequently be transported to greater depths. A pure aragonite vein can hence be locally considered as a "pseudo marble" system, enlarging its stability possibly at subarc depths and beyond in cold subduction environments (Canil and Scarfe, 1990; Molina and Poli, 2000; Franzolin et al., 2011; Piccoli et al., 2016), in a structural domain where fluid-assisted decarbonation would be rather inefficient (e.g., ***Fig.5.12F***). This new sink for C-bearing fluids should be considered in further subduction decarbonation mass balance studies.

Besides C, other major elements such as Si, Na, Mg, Al, Ca and K (***Figs.5.12D*** to ***F***) may have been potentially mobilized at large scales, thus explaining the aragonite + quartz association and the occurrence of phengite and lawsonite in some of the vein sets (e.g., Manning, 2004, Menzel et al., 2019).

5.10.5 Towards an integrated view of small- to large-scale fluid-rock interaction processes

The observed petrofabrics reveal active dissolution-precipitation creep during burial and dehydration, enabling dissolution of minerals and re-precipitation at the local scale. In addition, the occurrence of (i) euhedral inclusion-free millimeter-sized grains, (ii) sharp boundaries between fragmented grains, (iii) healed fractures of Na-rich pyroxene crystals in crystallographic continuity (e.g., ***Fig.5.5E***) and (iv) sealed lawsonite grains by "stitch like" glaucophane and quartz (***Fig.5.4F***), suggest that minerals nucleated epitaxially and precipitated in fluid-filled open cracks (Oliver and Bons, 2001; Spandler and Hermann, 2006; Wassmann and Stöckhert, 2012). Thus, we propose that fluid-pressure build up and subsequent pressure gradients, due to ongoing metamorphism, enhanced the development of an interconnected network of porosity and further propagation in localized fractures and/or microfractures that ultimately permitted fluid transport, solution-precipitation creep, and mobility of solutes (e.g., Etheridge et al., 1983; Yardley, 1986; Oliver and Bons 2001; Plümper et al., 2014). The finding of multiple veining events forming both silicate- and carbonate-dominated veins, combined with repeated vein re-opening, indicates that fluid pressures were transiently near- to supra-lithostatic (Etheridge et al., 1984; Spandler and Hermann, 2006; Saffer and Tobin, 2011; Munoz-Montecinos et al., 2020). In addition, the occurrence of (i) lawsonite-rich layers observed in blueschists (***Fig.5.4j***; e.g., Vitale Brovarone and Beyssac, 2014), (ii) ≈20 µm-wide Ca-richer overgrowths (***Fig.5.S1F***) in rare blueschist garnets (likely as a consequence of Ca mobility in the fluid phase), (iii) strong glaucophane oscillatory zoning patterns in host blueschists (***Fig.5.6A***; e.g., Yardley et al., 1991), (iv) truncated crystal surfaces and dissolution seams ubiquitously found in most lithologies (e.g., ***Fig.5.4B*** and ***J***), (v) pervasive serpentinite carbonation textures (***Fig.5.3G***; e.g., see subduction-related ophicarbonates in Cannaò et al., 2020), (vi) several solid inclusion trails in veins (***Fig.5.6B***), (vii) lawsonite-bearing veins lined by a series of relicted host-vein walls (***Fig.5.6C***) and (viii) strikingly similar O-C and Sr-Nd isotopic signatures between host rock and veins, suggest that fluid infiltration occurred episodically resulting possibly from a combination of pervasive porous and fracture-controlled, channelized flows (***Fig.5.13***; e.g., Oliver, 1996; Skelton et al., 2000).

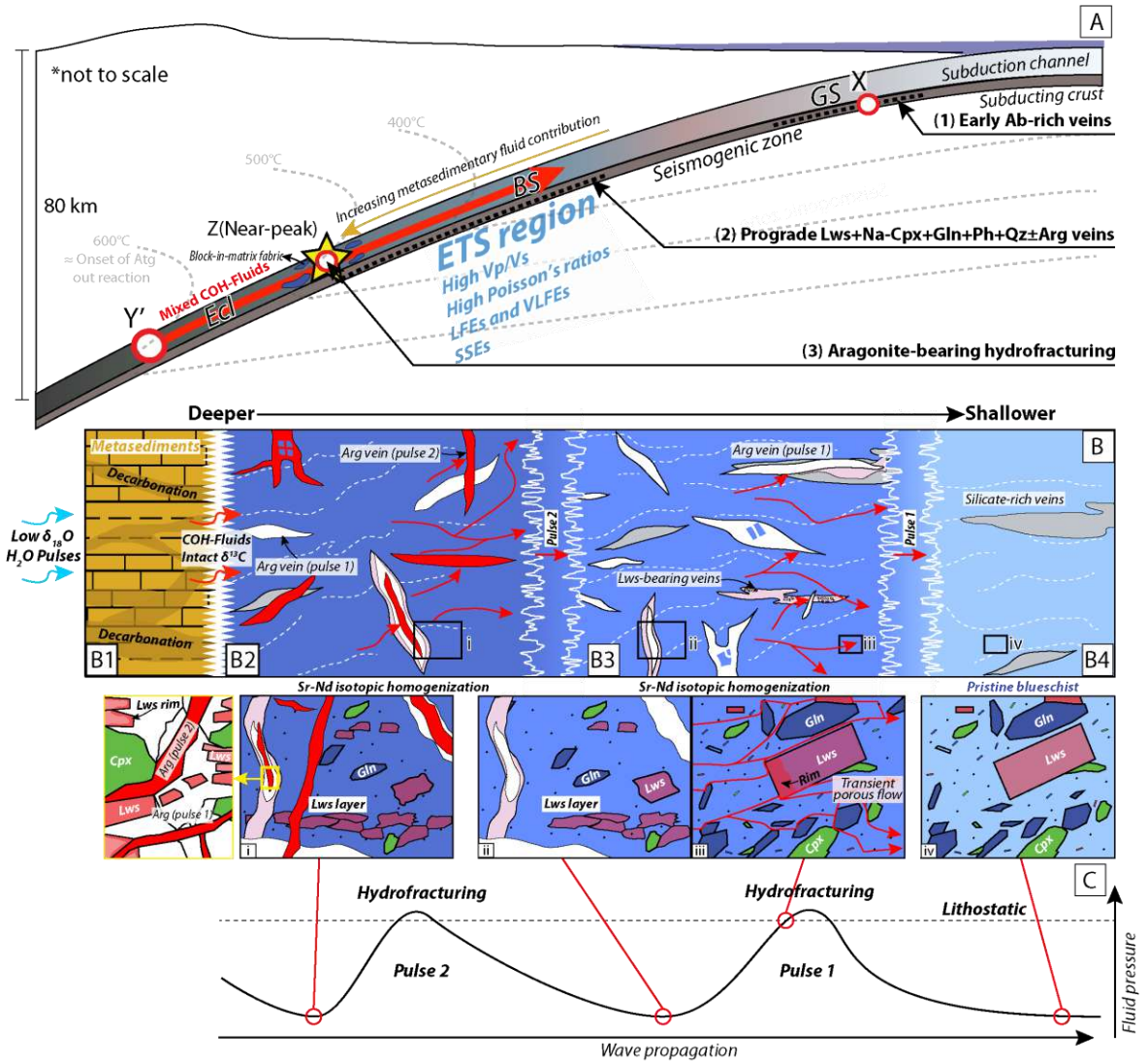

Figure 5.13. A. Subduction zone sketch illustrating relevant veining events and processes. Capital letters refer to the metamorphic segments outlined in Fig.5.11 while stages 1, 2 and 3 correspond to those from Fig.5.7. B. Conceptual model (not to scale) showing the infiltration of two successive fluid pulses (and associated hydrofracturing) traveling towards the right side of the panel. The left panel (B1) illustrates the episodic infiltration of deeply-produced H_2O-fluids into metasedimentary lithologies located upwards from the devolatilization front (Y' in panel A) and/or at Seghin complex depths, followed by decarbonation. The resulting COH-fluids were injected into blueschist lithologies and serpentinites as fluid pulses. Panel B2 shows a scenario where the rock volume has been affected by the passage of two porosity waves. The left section has been compacted (after veining) while the right section is undergoing hydrofracturing. The panel B3 shows a similar scheme to B2 but after/during the passage of a single porosity wave while B4 represents a pristine rock free of any deep fluid-pulse event (i.e., before interaction with moving fluid). The subpanels (i) and (ii) represent the stages of viscous compaction (fluid pressure below lithostatic) after hydrofracturing due to the passage of two and one fluid pulses, respectively. Note the yellow inset in the subpanel (i) depicting the resulting vein texture. The subpanel (iii) illustrates fluid infiltration emphasizing fluid circulation as porous flow allowing rock-buffered Sr-Nd isotopic homogenization during flow before hydrofracturing. Note that this process is expected to have occurred at all stages before fracturing and further veining. The subpanel (iv) is a scheme highlighting the pristine texture of the blueschist host before external fluid influx. The different sizes of the subpanel insets in panel B illustrate scale variations. C. Scheme representing fluid pulses propagation with respect to fluid pressure. Note that hydrofracturing occur only when the fluid pressure is near to lithostatic while fluid expulsion is related to compaction represented by the region of lower fluid pressure.

Assuming that similar, non-accreted rock packages were continuously subducted along the Y to Y' segment of ***Fig.5.11A***, all modeled lithologies are expected to strongly dehydrate upon entrance in the eclogite field (***Fig.5.11B***), in agreement with high Vp/Vs regions imaged along the Mariana margin analogue at depths between 70 and 120 km and interpreted as a consequence of slab dehydration processes (e.g., Barklage et al., 2015). Thus, we propose that deep H2O-rich fluids, expelled from deeply subducted mafic and ultramafic rocks, possibly interacted with the neighboring metasediments, but also along their way upwards along the interface (***Fig.5.13B***; e.g., Spandler et al., 2011). In consequence, the resulting fluid-rock interactions facilitated fluid-mediated decarbonation accompanying large-scale flushing of metasedimentary rocks (***Fig.5.13A***) and further infiltration-precipitation in the Seghin complex at near-peak-P-T burial depths (***Fig.5.13B***). We speculate that these fluid rock-interaction processes occurred as hydraulic pulses (Nur and Walder, 1992) whose physical mechanism could be analogue to the concept of upward-travelling porosity waves (Connolly and Podladchikov, 2004), possibly related to the continuous fluid production of downgoing plate rocks entering the eclogite-facies. This hypothesis is based on the physical formulation of fluid flow driven by transient, near-lithostatic, pressure gradients towards the region of lower pressure and is characterized by an overpressurized head, where hydrofracturing can occur, leaving behind a crammed tail (Connolly, 2010). This process possibly facilitated mass-transfer (Tian and Ague, 2014; Jordan et al., 2018) likely allowing for Sr-Nd isotopic homogenization between the host and the fluid (in the order of few years according to Beinlich et al., 2020; ***Figs.5.13B*** and ***C***), leading to geochemical fingerprints that can be otherwise regarded as the result of closed-system mass transfer if first-order petro-structural observations are not integrated.

In this regard, the subduction megathrust has been considered as a shear zone capable of channelizing and redistributing fluids upwards along the subduction interface (Van der Straaten et al 2008; Frank et al., 2015). In line with geophysical observations, transient overpressures may trigger Vp/Vs variations during episodic tremor and slip (ETS) as expected for a fault-valve behavior (Gosselin et al., 2020). We infer that external fluid contributions increase towards greater depths, supporting the idea that such transient processes would become more significant with increasing depths (e.g., Angiboust et al., 2014; Taetz et al., 2018). Therefore, the generation of episodic overpressuring, hydrofracturing and subsequent porosity waves transport upwards along the plate interface (Sibson, 1990; Connolly and Podladchikov, 2004; Connolly, 2010; Gosselin et al., 2020) seems a plausible mechanism to explain episodic hydrofracturing in the Seghin complex, at least for the inferred externally-derived fluids (***Fig.5.13***). We conclude that the Seghin complex represents a frozen-in plate interface setting that records a protracted sequence of fluid-rock interaction events that occurred at depths of up to 55 km, i.e., in a setting where low frequency earthquakes (LFEs) and ETSs are reported in active subduction margins such as central Mexico (Frank et al., 2015), New Zealand (Wallace and Eberhart-Phillips, 2013) or Northern Chile (Klein et al., 2018). Taetz et al. (2018) calculated that the infiltration of externally-derived fluids and further equilibration took place in c. 1 to 4 months whereas Skarbek and Rempel (2016) demonstrated that porosity wave successions are temporally comparable with ETS recurrences in the same way as other regional-scale fluid-rock

interaction processes (Beinlich et al., 2020). Similar suggestions were raised for a HP-LT terrain buried at 25-30 km at incipient blueschist-facies conditions in central Chile (Muñoz-Montecinos et al., 2020). In this case, however, the hydrofractures and the vein abundances are far smaller. We suspect that the infiltration of hydraulic pulses and further veining as described here is a process that occurs to a greater extent at greater depths (Seghin complex depths up to c. 55 km) than in the shallower Chilean example. One reason could be due to the magnitude of porosity waves, higher in the deeper setting and vanishing towards shallower (likely more brittle -and thus more permeable-) conditions. Future geophysical studies should investigate whether seismic source properties for deep ETSs and LFEs can be satisfactorily explained by fluid-rock interaction processes (e.g., Shapiro et al., 2018) such as those observed in the Seghin complex. Exhumed metamorphic complexes can undoubtedly provide key insights onto the variety of deformation mechanisms in the slow earthquake region of the plate interface (e.g., Behr and Burgmann, 2021) and therefore represent a crucial proxy for improving our understanding of the rheological properties of the slab as well as its possible control on the genesis of megathrust earthquakes (Obara and Kato, 2016).

5.11 Conclusions

Field, petrological, and geochemical studies reveal that the vein systems exposed in the blueschist-facies Seghin complex are the result of a protracted sequence of veining and other fluid-rock interactions. The earliest vein occurrences are characterized by the precipitation of albite and minor actinolite and pumpellyite after sub-greenchist-facies mineral break down. This set of veins evolved during burial, allowing the formation of prograde blueschist-facies mineral assemblages and serving as zones of preferential weaknesses for further fluid circulation. During early stages of prograde veining, the main fluid phase involved and mineral precipitation was probably internally-derived, with the protolith of the host blueschists being the most likely fluid source. During further burial, an external metasedimentary fluid source became important. Latter, at near-peak P-T conditions, externally-derived COH-fluids were injected into the system as high-pressure fluid pulses above the lithostatic threshold, causing massive hydrofracturing of all Seghin complex rocks. Although geochemical and isotopic approaches suggest that the likely source for CO_2-bearing fluids is likely the metasediments, thermodynamic modeling demonstrate that fluid-mediated decarbonation and dehydration are far more efficient C mobilization processes at deeper conditions and higher temperatures than what is actually recorded by the Seghin complex. We thus conclude that deeply, externally-generated fluid pulses were able to travel upwards -likely as hydraulic pulses or porosity waves- along a kilometer-scale pathway, namely the subduction interface, triggering the veining observed in Seghin complex rocks in the 50-60 km depth range, where high Vp/Vs ratios and episodic tremor and slip events are monitored along active subduction margins.

ACKNOWLEDGMENTS

Philippe Agard, Zeynab Gharamohammadi, Ali Kananian and Jafar Omrani are warmly acknowledged for logistical assistance. Olga Cazalla, Fernando Bea, Oona Appelt, Michel Fialin, Nicolas Rividi, Aitor Cambeses, Fabián VIllares, Sophie Nowak and Aniès Zeboudj are thanked for support and patience during analytical and sample preparation sessions. We thank Damien Deldicque for his assistance with Raman spectroscopy and EBSD measurements. Hughes Raimbourg, Isabelle Martinez, Gabe Epstein, Manuel Menzel and James Connolly are also acknowledged for stimulating discussions regarding fluid-rock interaction processes. The editor Balz Kamber and two anonymous reviewers are warmly acknowledged for accurate and insightful discussions helping to greatly improve this manuscript. Funding for the oxygen and carbon isotope analyses came from National Science Foundation grant EAR-1119264 (to GEB). This work has been funded by an Initiative D'EXcellence (IDEX) grant 16C538 and the TelluS Program of CNRS/INSU to S.A. Partial funding was also provided by the University of Granada at CIC. The German Academic Exchange Service (DAAD) is acknowledged for a mobility grant provided to JMM. This study contributes to the IdEx Université de Paris ANR-18-IDEX-0001. This is IPGP contribution #4207".

5.12 Supplementary information

5.12.1 Figures and Tables

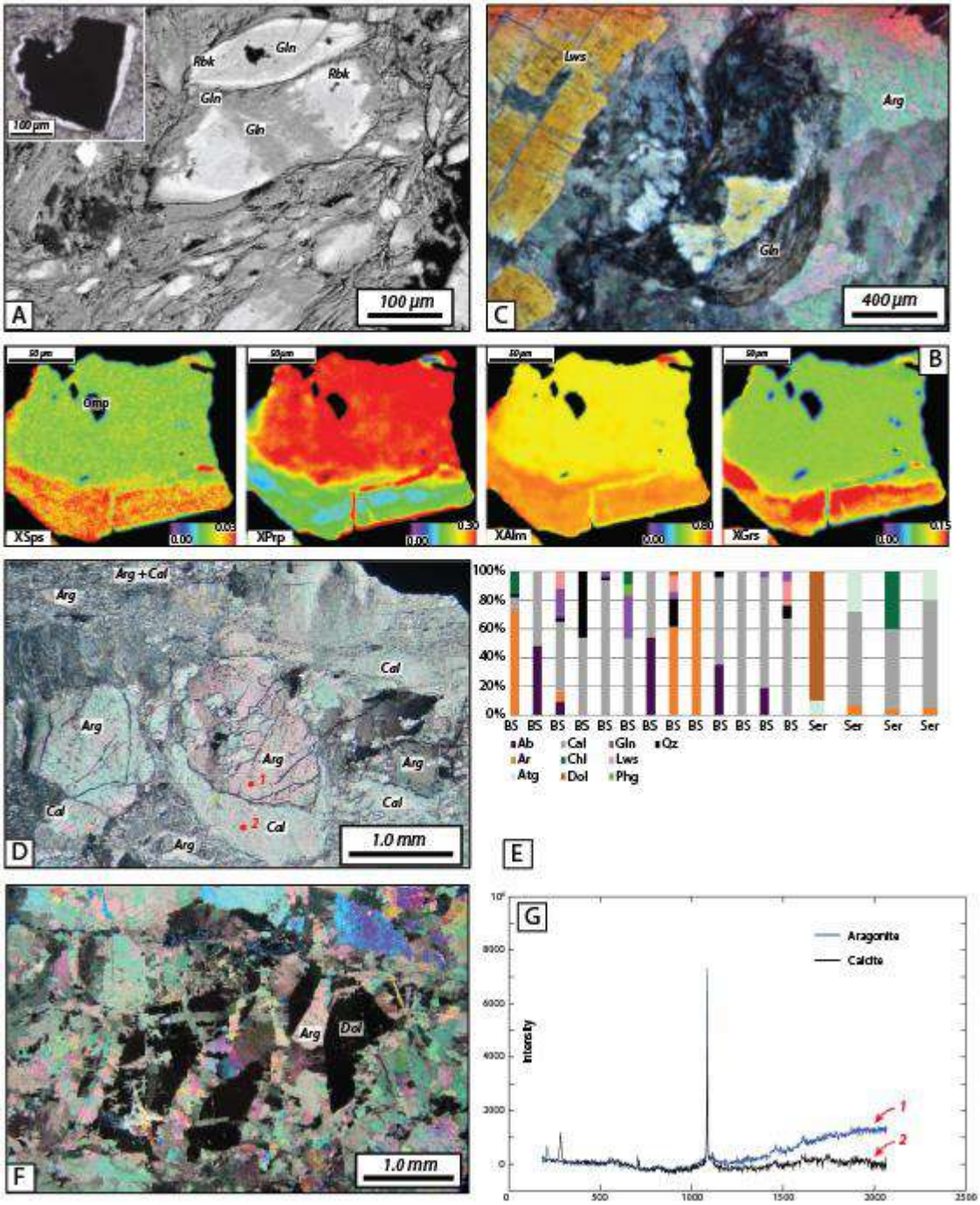

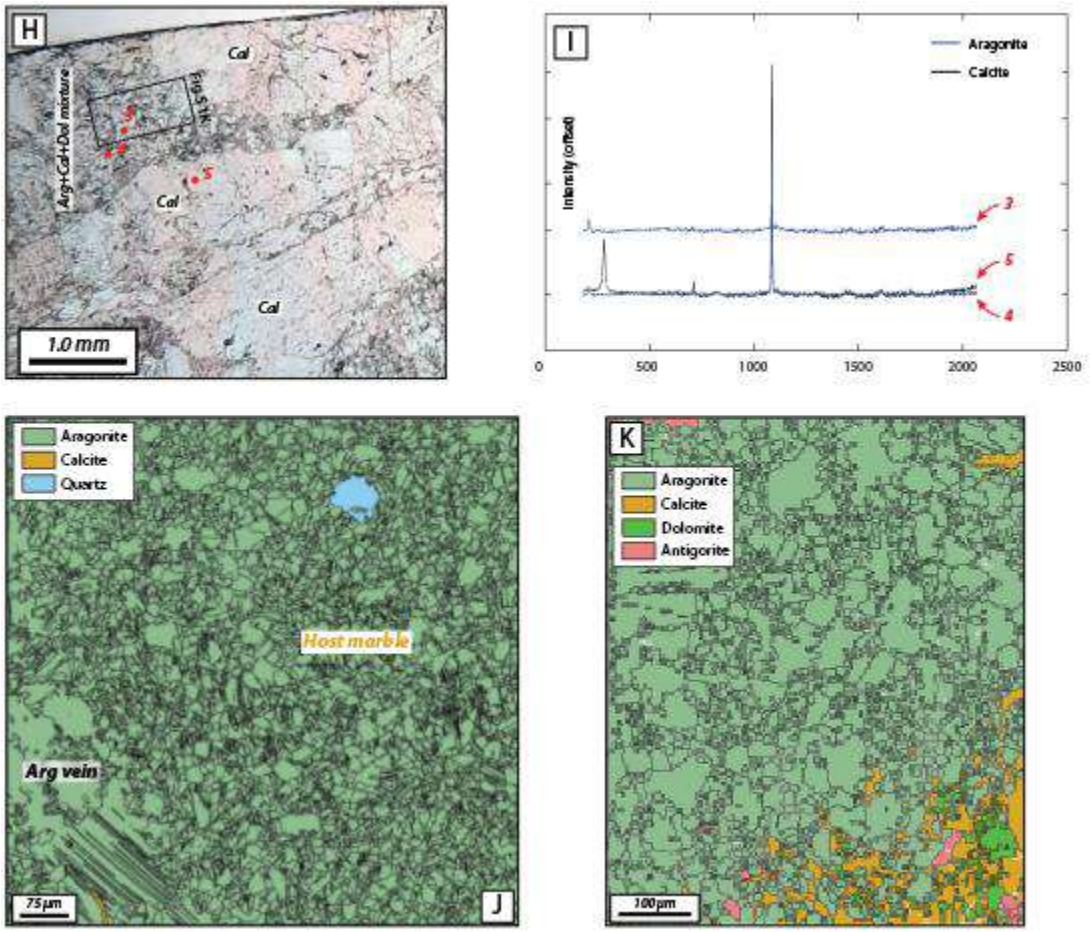

Figure 5.S1. A. Backscattered electron image of a representative blueschist sample highlighting microtextures of Na-amphibole and pyrite. Note the occurrence of glaucophane-sealed cracks, replacing riebeckite (and Mg-riebeckite). B. X-ray map showing compositional variations in garnet. The rim is richer in grossular relative to the core which is richer in pyrope. C. Optical polarized-light photomicrograph (cross-polarized view) showing cross cutting relationships in a carbonate + lawsonite + glaucophane vein. Note that glaucophane occurs in interstitial position denoting a later stage of fluid infiltration through carbonates and lawsonite. D. Optical polarized-light photomicrograph (cross-polarized view) depicting polymorphic replacement texture between calcite after aragonite. Note the multiple aragonite/calcite vein generations in which calcite coronas around aragonite occur. The numbers correspond to Raman spectra from Panel G. E. XRD results from carbonate-rich veins in blueschists and serpentinites. F. Optical polarized-light photomicrograph (cross-polarized view) of a representative serpentinite-hosted carbonate-rich vein. In this view, several generations of fibrous aragonite can be seen mutually cross cutting each other as well as dolomite. G. Representative Raman spectra for aragonite and calcite in a carbonate-filled former hydrofracture. H. Optical polarized-light photomicrograph of carbonates in a serpentinite-hosted vein. The numbers correspond to Raman spectra from panel I. I. Representative Raman spectra for aragonite and calcite in a serpentinite carbonate vein. J and K. EBSD maps showing phase distributions in a marble and a serpentinite-hosted vein, respectively. The maps were generated after EBSD data processing with the MTEX software (Bachmann et al., 2010) .

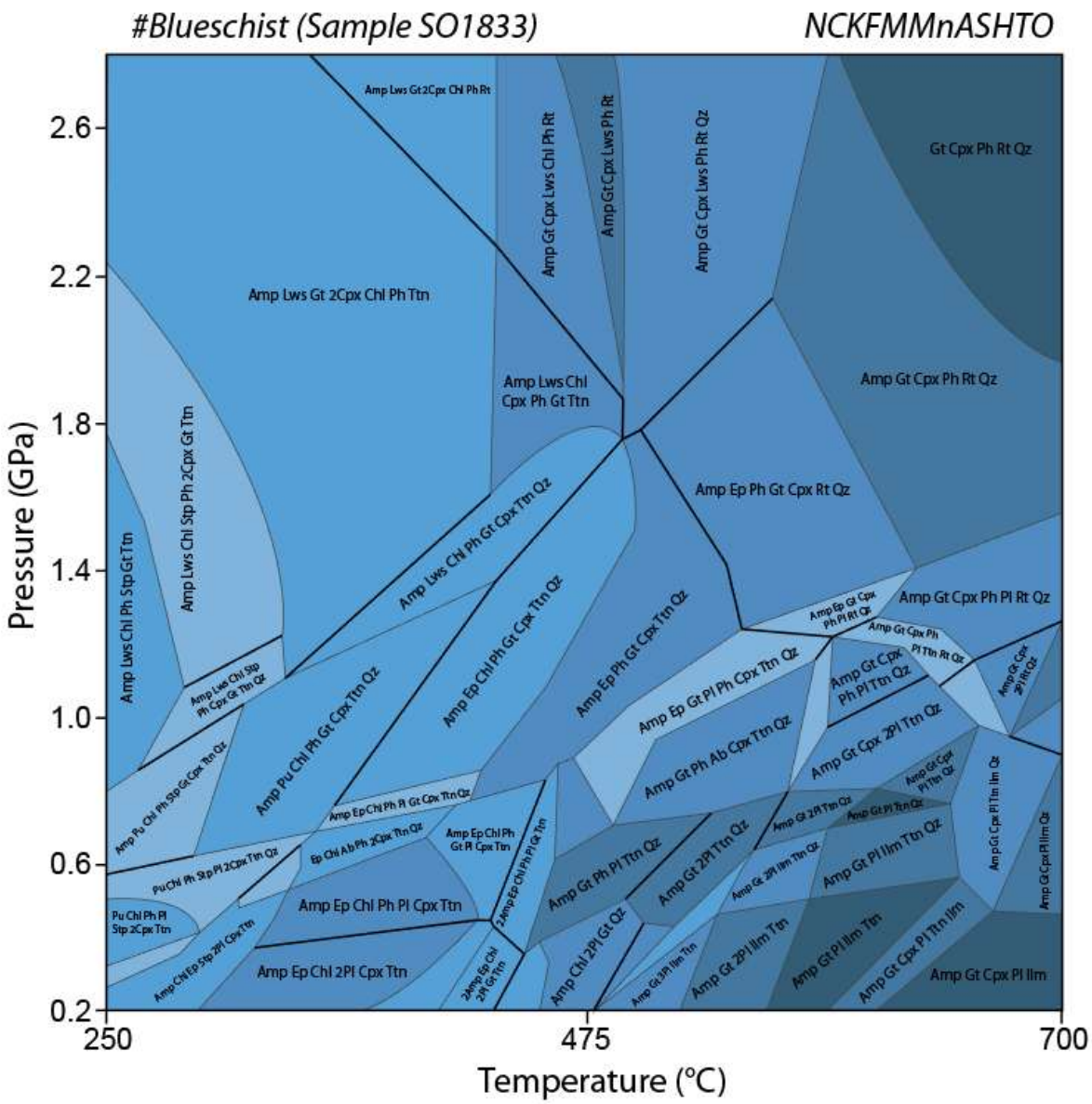
#Blueschist (Sample SO1833)
NCKFMMnASHTO
Pressure (GPa)
Temperature (°C)
2.6
2.2
1.8
1.4
1.0
0.6
0.2
250
475
700
Amp Lws Gt 2Cpx Chl Ph Rt
Amp Gt Cpx Lws Chl Ph Rt
Amp Gt Cpx Lws Ph Rt
Amp Gt Cpx Lws Ph Rt Qz
Gt Cpx Ph Rt Qz
Amp Lws Gt 2Cpx Chl Ph Ttn
Amp Lws Chl Cpx Ph Gt Ttn
Amp Gt Cpx Ph Rt Qz
Amp Lws Chl Stp Ph 2Cpx Gt Ttn
Amp Lws Chl Ph Stp Gt Ttn
Amp Lws Chl Ph Gt Cpx Ttn Qz
Amp Ep Ph Gt Cpx Rt Qz
Amp Ep Chl Ph Gt Cpx Ttn Qz
Amp Ep Ph Gt Cpx Ttn Qz
Amp Gt Cpx Ph Pl Rt Qz
Amp Pu Chl Ph Gt Cpx Ttn Qz
Amp Ep Gt Pl Ph Cpx Ttn Qz
Amp Gt Ph Ab Cpx Ttn Qz
Amp Gt Cpx Pl Ttn Qz
Amp Ep Chl Ph Pl Gt Cpx Ttn Qz
Amp Gt Ph Pl Ttn Qz
Amp Gt 2Pl Ttn Qz
Amp Gt Pl Ilm Ttn Qz
Amp Ep Chl Ph Pl Cpx Ttn
Amp Ep Chl 2Pl Cpx Ttn
Amp Chl 2Pl Gt Qz
Amp Gt 2Pl Ilm Ttn
Amp Gt Pl Ilm Ttn
Amp Gt Cpx Pl Ttn Ilm
Amp Gt Cpx Pl Ilm
Pu Chl Ph Pl Stp 2Cpx Ttn

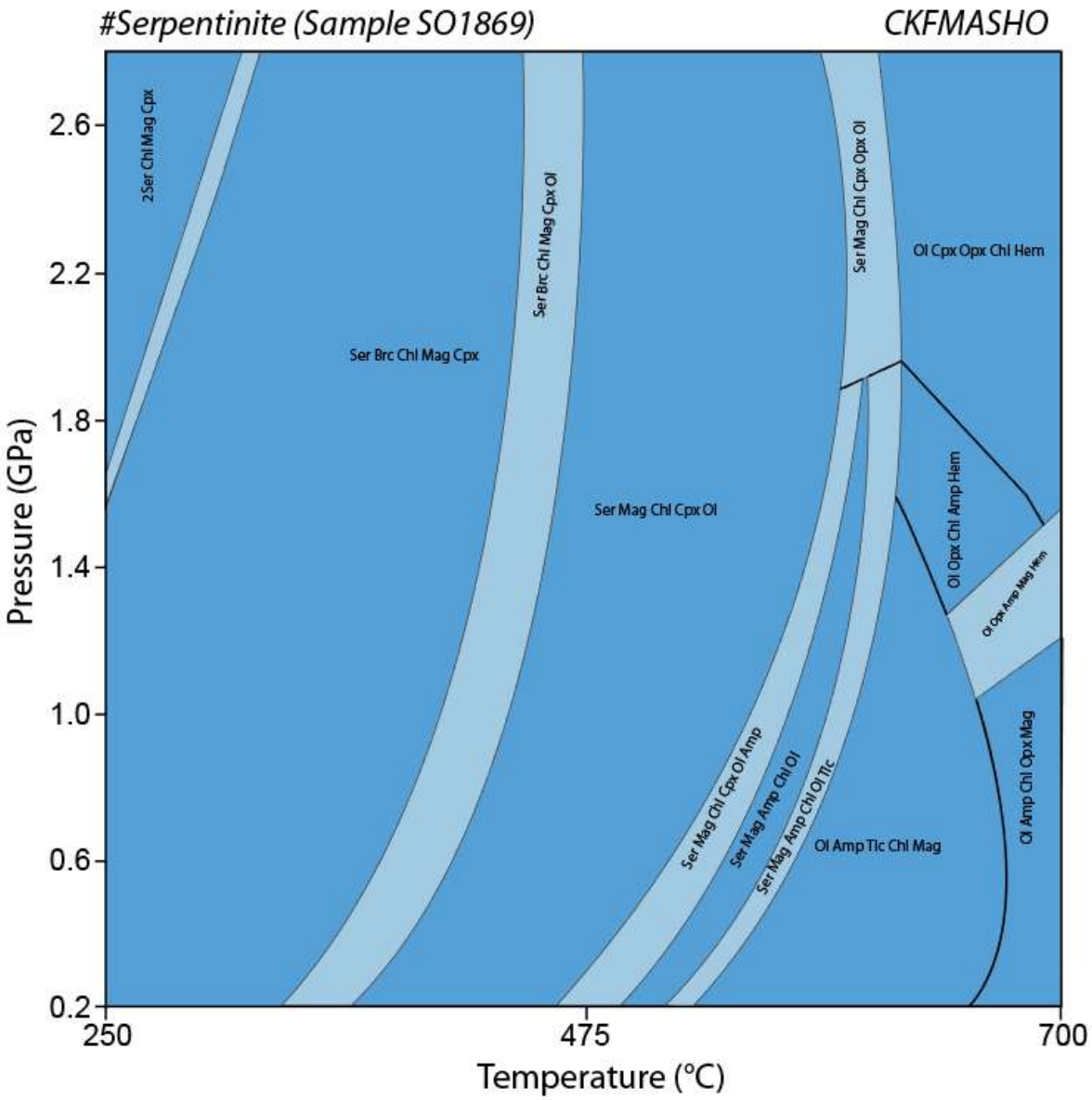
#Serpentinite (Sample SO1869)
CKFMASHO
2Ser Chl Mag Cpx
Ser Brc Chl Mag Cpx
Ser Brc Chl Mag Cpx Ol
Ser Mag Chl Cpx Ol
Ser Mag Chl Cpx Opx Ol
Ol Cpx Opx Chl Hem
Ol Opx Chl Amp Hem
Ol Cpx Amp Mag Hem
Ol Amp Chl Opx Mag
Ser Mag Chl Cpx Ol Amp
Ser Mag Amp Chl Ol
Ser Mag Amp Chl Ol Tlc
Ol Amp Tlc Chl Mag
Pressure (GPa)
2.6
2.2
1.8
1.4
1.0
0.6
0.2
250
475
700
Temperature (°C)

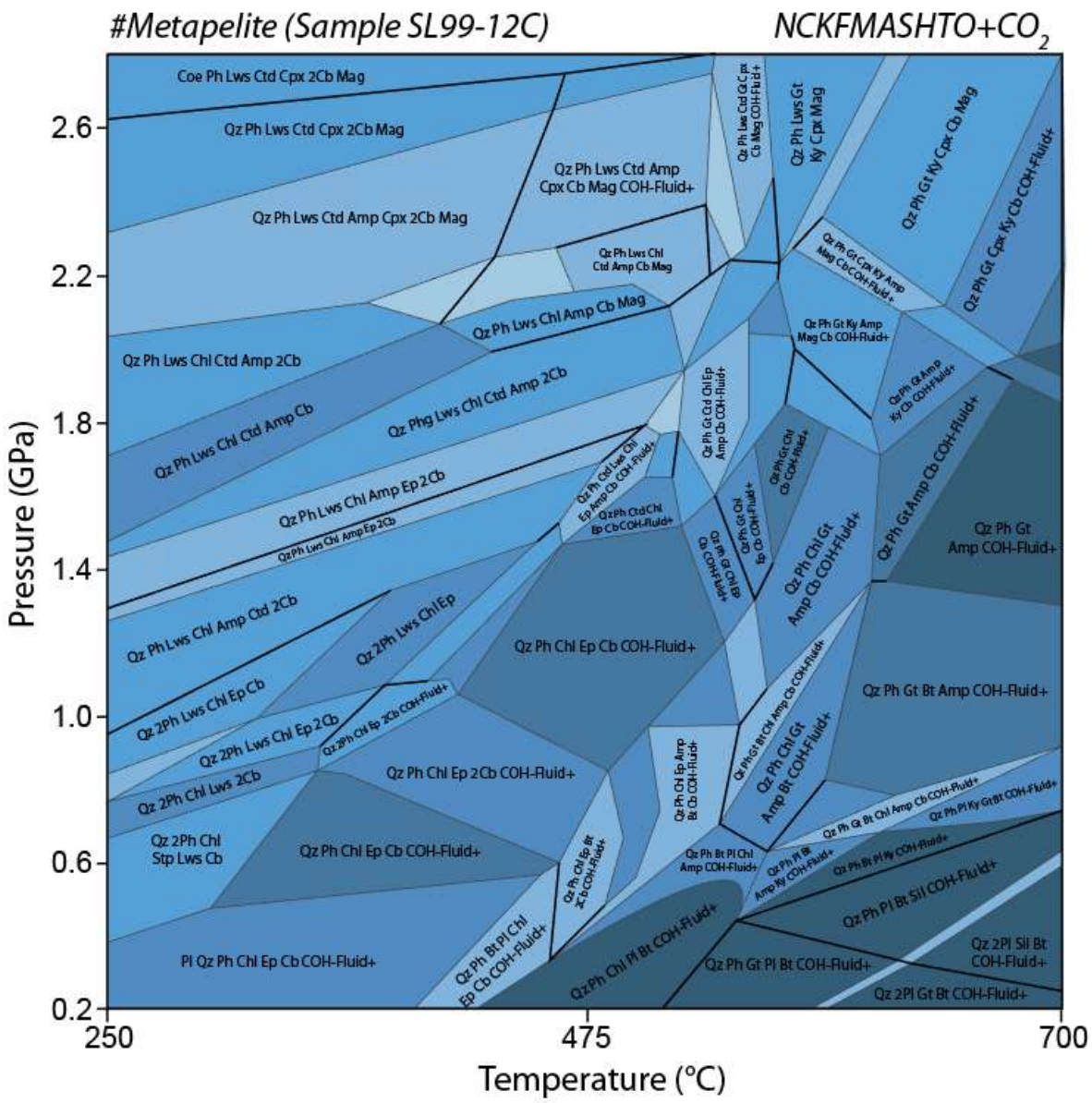
#Metapelite (Sample SL99-12C)
NCKFMASHTO+CO2
Coe Ph Lws Ctd Cpx 2Cb Mag
Qz Ph Lws Ctd Cpx 2Cb Mag
Qz Ph Lws Ctd Amp Cpx 2Cb Mag
Qz Ph Lws Ctd Amp Cpx Cb Mag COH-Fluid+
Qz Ph Lws Chl Ctd Amp Cb Mag
Qz Ph Lws Chl Amp Cb Mag
Qz Ph Lws Chl Ctd Amp 2Cb
Qz Ph Lws Chl Ctd Amp Cb
Qz Phg Lws Chl Ctd Amp 2Cb
Qz Ph Lws Chl Amp Ep 2Cb
Qz Ph Lws Chl Amp Ctd 2Cb
Qz 2Ph Lws Chl Ep
Qz 2Ph Lws Chl Ep Cb
Qz 2Ph Lws Chl Ep 2Cb
Qz 2Ph Chl Lws 2Cb
Qz 2Ph Chl Stp Lws Cb
Qz Ph Chl Ep Cb COH-Fluid+
Qz Ph Chl Ep 2Cb COH-Fluid+
Pl Qz Ph Chl Ep Cb COH-Fluid+
Qz Ph Chl Gt Amp Cb COH-Fluid+
Qz Ph Gt Amp Cb COH-Fluid+
Qz Ph Gt Amp COH-Fluid+
Qz Ph Gt Bt Amp COH-Fluid+
Qz Ph Chl Gt Amp Bt COH-Fluid+
Qz Ph Gt Cpx Ky Cb COH-Fluid+
Qz Ph Gt Ky Cpx Cb Mag
Qz Ph Lws Gt Ky Cpx Mag
Qz Ph Gt Ky Amp Mag Cb COH-Fluid+
Qz Ph Pl Bt Sil COH-Fluid+
Qz 2Pl Sil Bt COH-Fluid+
Qz Ph Gt Pl Bt COH-Fluid+
Qz 2Pl Gt Bt COH-Fluid+
Qz Ph Chl Pl Bt COH-Fluid+
Qz Ph Bt Pl Chl Ep Cb COH-Fluid+
Pressure (GPa)
Temperature (°C)
0.2
0.6
1.0
1.4
1.8
2.2
2.6
250
475
700

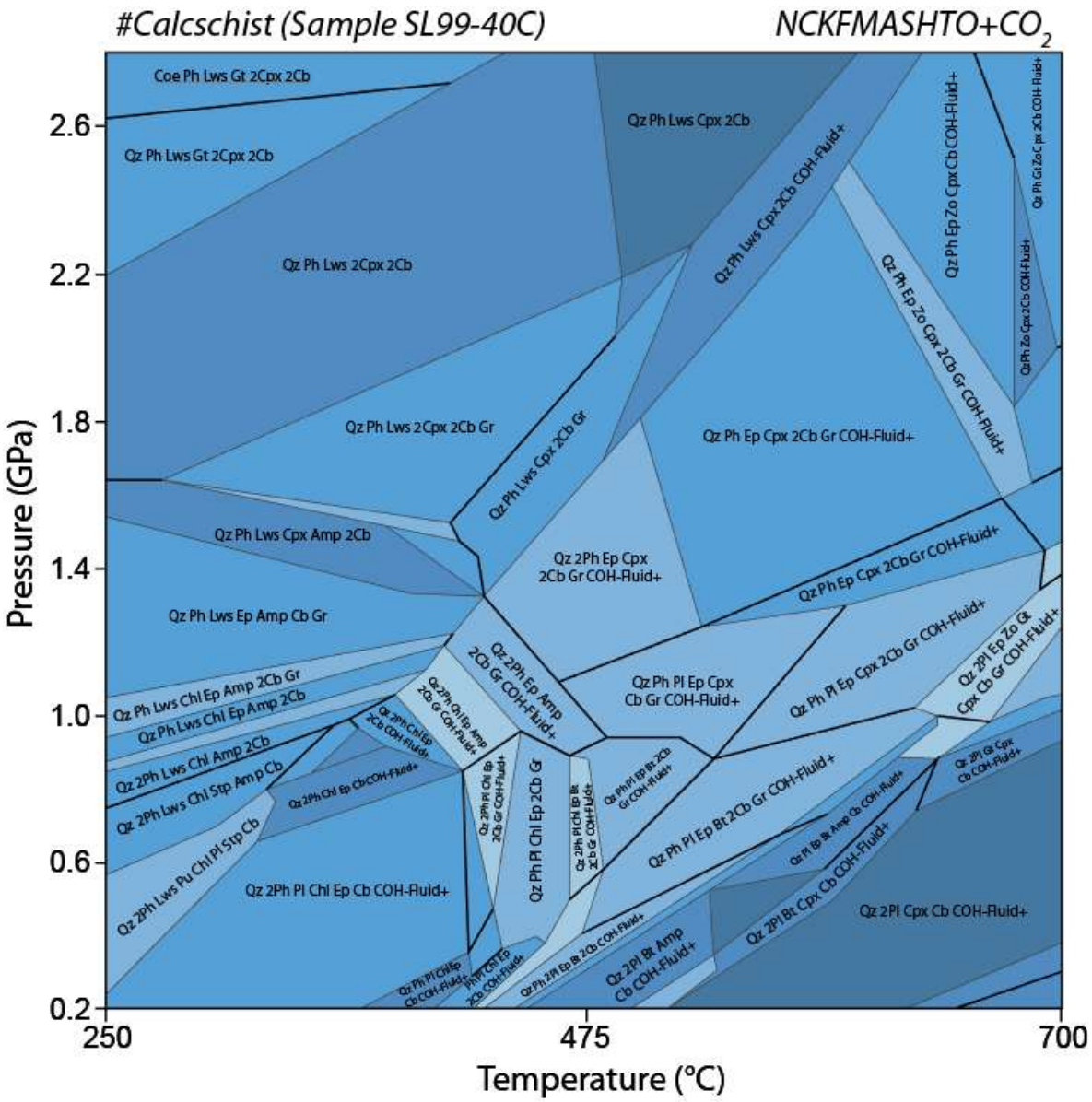
#Calcschist (Sample SL99-40C)
NCKFMASHTO+CO2
Coe Ph Lws Gt 2Cpx 2Cb
Qz Ph Lws Gt 2Cpx 2Cb
Qz Ph Lws Cpx 2Cb
Qz Ph Lws Cpx 2Cb COH-Fluid+
Qz Ph Ep Zo Cpx Cb COH-Fluid+
Qz Ph Lws 2Cpx 2Cb
Qz Ph Lws 2 Cpx 2Cb Gr
Qz Ph Lws Cpx 2Cb Gr
Qz Ph Ep Cpx 2Cb Gr COH-Fluid+
Qz Ph Ep Zo Cpx 2Cb Gr COH-Fluid+
Qz Ph Lws Cpx Amp 2Cb
Qz 2Ph Ep Cpx 2Cb Gr COH-Fluid+
Qz Ph Lws Ep Amp Cb Gr
Qz Ph Lws Chl Ep Amp 2Cb Gr
Qz Ph Lws Chl Ep Amp 2Cb
Qz 2Ph Ep Amp 2Cb Gr COH-Fluid+
Qz Ph Pl Ep Cpx Cb Gr COH-Fluid+
Qz Ph Pl Ep Cpx 2Cb Gr COH-Fluid+
Qz 2Ph Lws Chl Amp 2Cb
Qz 2Ph Lws Chl Stp Amp Cb
Qz 2Ph Chl Ep Cb COH-Fluid+
Qz 2Ph Lws Pu Chl Pl Stp Cb
Qz 2Ph Pl Chl Ep Cb COH-Fluid+
Qz Ph Pl Chl Ep 2Cb Gr
Qz Ph Pl Ep Bt 2Cb Gr COH-Fluid+
Qz 2Pl Cpx Cb COH-Fluid+
Qz 2Pl Bt Amp Cb COH-Fluid+
Qz 2Pl Bt Cpx Cb COH-Fluid+
Pressure (GPa)
2.6
2.2
1.8
1.4
1.0
0.6
0.2
250
475
700
Temperature (°C)

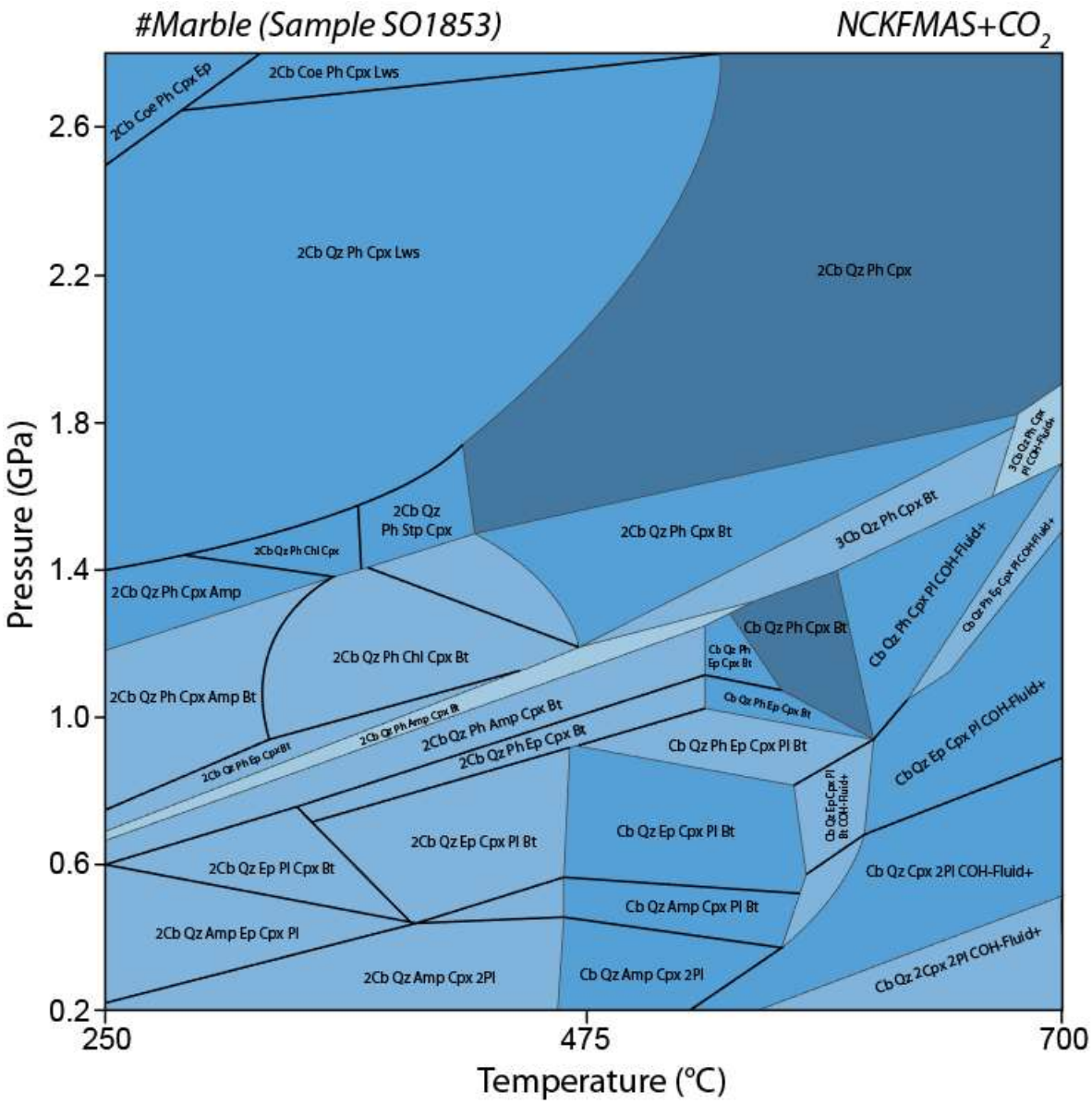

Figure 5.S2. Pseudosections for all modeled compositions. A. Blueschist. B. Serpentinite. C. Metapelite. D. Calcschist. E. Marble

6. Lawsonite veins record fluid overpressures and brittle creep in the subduction slow earthquake region

Muñoz-Montecinos et al. (in preparation)

Lawsonite veins record fluid overpressures and brittle creep in the subduction slow earthquake region

Jesús Muñoz-Montecinos[1,2], Samuel Angiboust[1], Antonio Garcia-Casco[2,3]

[1] Université de Paris, Institut de physique du globe de Paris, CNRS, F-75005 Paris, France, jesus.munozmontecinos@gmail.com; angiboust@ipgp.fr

[2] Department of Mineralogy and Petrology, Faculty of Sciences, University of Granada, Campus Fuentenueva s/n, 18002 Granada, Spain, agcasco@ugr.es

[3] Instituto Andaluz de Ciencias de la Tierra, CSIC-Universidad de Granada, 18100 Armilla, Granada, Spain

Paper in preparation

ABSTRACT

Geophysical investigations aiming at understanding the complex feedbacks between inferred overpressures and processes belonging to the subduction slow earthquakes family have made significant progress over the last 25 years. However, a significant scientific gap in validating this knowledge from a geological point of view exists. In order to provide a new light on this phenomenology, we herein investigate an exhumed high pressure-low temperature metamorphic complex that exposes rocks that experienced lawsonite-blueschist-facies metamorphism compatible with the slow earthquake region downdip the base of the seismogenic zone. The studied locality (Zagros suture, southeaster Iran) is a tectonic mélange comprising up to hectometre-sized blueschist blocks wrapped by a serpentinite matrix. The mafic lithologies exhibit brecciated lawsonite, Na-amphibole, Na-Ca clinopyroxene and quartz veins hosted in variably foliated cataclastic (and ultracataclastic) blueschists. Fine-scale micro-textural characterization of the host and vein systems reveals that brittle creep, together with pressure solution processes, were the dominant deformation mechanisms during lawsonite-blueschist facies metamorphism. Elements such as titanium, high field strength elements and chromium are markedly enriched in the ultracataclasites host-vein margin as well as in Na-amphibole-titanite shear bands filling or wrapping brecciated lawsonite-vein clasts. These features support a scenario where an externally-derived fluid source accompanies and predates brittle creep. According to this model, episodic injection of fluid pulses triggered weakening of the subduction interface and subsequent slow slip.

Keywords: *Subduction zones; Blueschist; Lawsonite vein; Fluid pulses; Ultracataclasite; Slow earthquakes*

6.1 Introduction

The recent discovery of episodic tremor and slip (ETS) gave rise to numerous studies aiming at explaining the transient nature of slow slip at depths below the seismogenic zone (25-60 km; e.g., Rogers and Dragert, 2003, Lay et al., 2012; Ujiie et al., 2018; Behr and Burgmann, 2021). ETS are typified as aseismic slow slip events (SSEs) and non-volcanic tremor swarms of very low- and low-frequency earthquakes (VLFEs and LFEs, respectively), and are commonly associated with high Vp/Vs ratios interpreted as reflecting near- to supra-lithostatic pore fluid pressures along the plate interface (Audet et al 2009; Frank et al., 2015; Gosselin et al., 2020). Both processes form part of the so-called slow earthquakes family, where SSEs are characterized by displacements, rupture dimensions, slip velocities and stress drops in the order of 10^{-3}-10^{-1} m, 10^{4} m, 10^{-8} m/s and 1-100 kPa, respectively, while the same parameters characterizing LFEs are approximately 10^{-5}-10^{-4} m, $<10^{3}$ m, 10^{-4}-10^{-3} m/s and 1-10 kPa, respectively (Shelly et al., 2006; Ide et al., 2007; Bostock et al., 2015; Frank et al., 2015; Thomas et al., 2016; Michel et al., 2019; see also Behr and Bürgmann, 2020 and Oncken et al., in press).

Recent experimental and field-based geological studies have attempted to characterize the dominant deformation mechanisms during deep SSEs and LFEs via inferring a match between transient deformational and geophysically-observed properties (Fagereng et al., 2011; Angiboust et al., 2015; Goswami and Barbot, 2018; Kotowski and Behr, 2019). Thus, the transient nature of SSEs and LFEs is thought to be somehow recorded in subducted (now exhumed) metamorphic rocks, which must be distinguished from the pervasive diffusion creep fabrics considered to accommodate the background strain rates imposed by plate convergence (c. $10^{-12}s^{-1}$; Wassmann and Stöckhert, 2012; Platt et al., 2018). Some of these fabrics include (i) distributed viscous flow in a weak matrix coeval with brittle deformation of blocks enhanced by viscosity contrasts (Fagereng and Sibson, 2010; Fagereng et al., 2014 (GRL); Behr et al., 2018; Kotowski and Behr, 2019), (ii) veins exhibiting evidence of re-opening and re-precipitation (crack-seal structures; Ramsay, 1980; Fagereng et al., 2010; Ujiie et al., 2018; **Chapter 4**), (iii) localized slip allowing the formation of cataclasites and further grain size-sensitive diffusion creep (Angiboust et al., 2015; Fabbri et al., 2020) and (iv) reaction-induced rheological weakening allowing the transition from distributed viscous flow to localized brittle deformation (Tarling et al., 2019). In most cases, these mechanisms require the presence of fluids at near-lithostatic conditions in order to promote brittle deformation upon decreasing the effective normal stresses acting on the shear zone or serving as a transport medium for dissolved solutes during fluid-assisted diffusion creep.

Despite the importance of fluids in promoting LFEs and SSEs, very little is known about their sources (Taetz et al., 2016; **Chapter 5**), fluid pathways (Raimbourg et al., 2018) and the fate of their precipitation products (e.g., veins). Recent investigations have shown that brittle creep (e.g., Brantut et al., 2012) associated with extensional veining occurring at near-lithostatic fluid pressure conditions can well explain the instrumentally inferred strain rates spectrum of deep ETS, SSEs and LFEs, among other phenomena (e.g., ***Figure 6.1***; see Oncken et al., in press). However, due to the fine-

grained nature of these fault products and the presence of large amounts of fluids, both enhancing pressure-solution creep, such features are largely erased from the rock record (e.g., Angiboust et al., 2015). The study of metamorphic veins, which represent fossilized products of fluids once circulating along and across the subducting interface, provides a unique opportunity to illuminate deformation mechanisms as their fabrics are commonly better preserved than in the surrounding host. We herein provide the first field-based structural investigation on lawsonite-glaucophane-bearing metamorphic veins hosted in blueschists from the Zagros suture (Seghin complex; for further details regarding the location of the studied locality and its architecture, the reader is referred to **Chapters 5** and **7**). Previous petrological studies on these vein systems demonstrate that mineral precipitation started early during prograde burial and evolved towards peak metamorphic conditions (see **Chapter 5**). However, detailed observations aiming at characterizing the deformation mechanisms affecting these veins – which certainly entered the ETSs region during their metamorphic history – are up to date lacking. This **Chapter** presents a preliminary high-resolution, meso- to micro-scale characterization of the vein networks exposed in the Seghin complex in order to provide new light on the deformation mechanisms recorded by these vein systems during their prograde evolution in the ETS region – a key part of the puzzle to be discussed in greater detail in the discussion section of this thesis (**Chapter 8**).

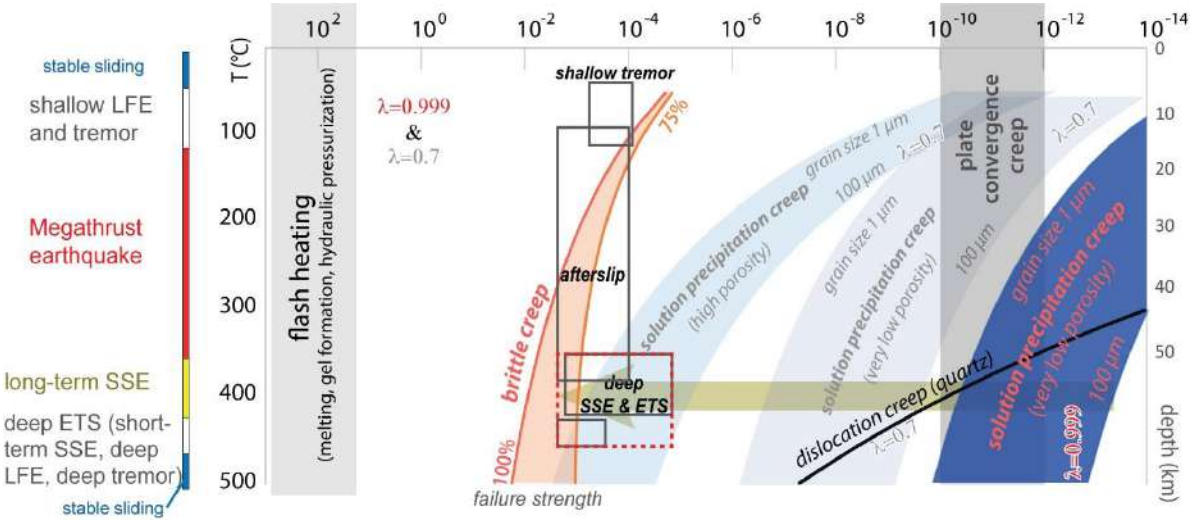

Figure 6.1. Deformation mechanism as a function of strain rate and temperature (at a particular subduction thermal gradient) under pore-pressure ratio ranging from 0.7 to 0.999. Pressure-solution creep flow laws are depicted for a range of porosities and grain sizes. For brittle creep, stresses are assumed to be at the 100% and 75% of the peak strength (where 100% corresponds to the failure limit). For further details, the reader is referred to Oncken et al. (in press).

6.2 Geological background

The long-lived subduction below Eurasia and ensuing collision with the Arabian plate (Lower Cretaceous-Eocene) resulted in the closure of the Neotethys ocean exposed now as exhumed ophiolitic units in the Zagros suture zone (Gansser, 1955; Stöcklin, 1968; Berberian and King, 1981; McCall, 1997; Agard et al., 2006). In the Soghan region, in Iran, the unique remnants of this paleo-subduction event are exposed as a tectonic stack of variably metamorphosed metamorphic complexes. In this contribution, we focus on the Seghin complex, a tectonic sliver whose architecture is characterized by a block-in-matrix fabric where up to hectometre-sized lawsonite-bearing blueschist blocks are surround by a dominant antigorite-rich serpentinite matrix. Thermobarometric constraints on blueschist host materials yielded a range of peak burial conditions spanning the upper blueschist-facies (1.5-1.8 GPa at c. 400-520 ºC; Agard et al., 2006; Oberhänsli et al., 2007; Angiboust et al., 2016) dated at 62-75 Ma, with some blocks displaying a lower blueschist-facies overprint (0.6-1.0 GPa; 230-300 ºC, **Chapter 7**). Hence, the Seghin mélange likely resulted from the gathering of blocks during basal accretion and/or detachment of an oceanic sliver (against the serpentinized subcontinental mantle) and further return flow along a subduction channel. Its study thus enables understanding deformation processes along the plate interface from the deep slow earthquakes window to the shallower seismogenic region (**Chapters 5** and **7**).

6.3 Conditions of veining and meso-scale observations

In the mafic lithologies, three main veining stages are recognized (see ***Figure 5.7***): (1) early albite-rich precipitation events possibly associated with breakdown of subgreenschist- to greenschist-facies mineral assemblages, (2) prograde to near-peak blueschist-facies veining characterized by abundant lawsonite as well as Na-amphibole (glaucophane to riebeckite), Na-Ca-clinopyroxene (aegirine-augite), quartz, titanite, apatite, phengite and aragonite and (3) a near-peak stage of massive formation of aragonite-bearing hydraulic breccias together with lawsonite, Na-amphibole and Na-Ca clinopyroxene. We herein focus on the second vein sets since they formed and evolved within the slow earthquake region (see ***Figure 5.7***) and show widespread and unreported shear fabrics (see below). The vein-precipitating fluids have been interpreted as a combination of internally-produced, e.g., prograde dehydration of the rock volume, and externally-derived sources (mixed mafic/ultramafic- and metasedimentary-derived; see **Chapter 5**).

Lawsonite-rich veins occur generally oriented parallel to the main foliation as well as crosscutting at c. 30 to 60° in sets of conjugated structures (see upper-hemisphere equal-area stereoplots from ***Figures 6.2A*** and ***B***) and perpendicular to the main foliation. In most cases, pristine vein domains were subsequently sheared and deformed resulting in heavily transposed networks up to the point of intense brecciation, whereas cataclastic fabrics characterize the host blueschists (***Figure 6.2A***). In addition, extensional vein networks evolve towards localized shear bands crosscutting the main fabric of the blueschist host, in which drag folds are observed in the shear bands near the host margins (***Figure 6.S1A***). Pristine veins exhibit clear evidence of extensional fracturing and precipitation in a syntaxial mode (e.g., see Bons et al., 2012), and are characterized by centimetre-sized tabular

lawsonite crystals while adjacent domains display strained sigmoidal, disrupted and brecciated lawsonite clasts as well as Na-amphibole and quartz fringes (***Figure 6.2B***). Similar structures are observed in the vein margins where, locally, a mixture of the cataclastic blueschist host and vein fragments is present. Other veins exhibit highly strained centimetre-sized sigmoidal lawsonite clasts in a matrix of heavily micro-brecciated lawsonite fragments associated with quartz and Na-amphibole (***Figure 6.2C***). In this case, reconstruction of former lawsonite grains is not possible, indicating substantial shearing and strain. The adjacent host is constituted by a cataclastic blueschist matrix which, interestingly, shows a gradient of grain size comminution: a cataclastic blueschist evolves towards a heavily pulverized ultracataclasite in the host-vein contact (***Figures 6.2C*** and ***S1B***). In the XY plane (with respect to the finite strain ellipsoid) of the latter domain, Na-amphibole-coated slickenlines are observed (***Figure S1C***).

6.4 Methods

6.4.1 Scanning electron microscopy, electron probe microanalyzer, back-scattered diffraction and Cathodoluminescence

Scanning electron microscopy (SEM) has been carried out on a Zeiss Evo MA10 machine at the Institut de Physique du Globe de Paris operated at an acceleration voltage of 15 kV using internal calibration standards. Electron probe microanalyses (EPMA) were performed at Sorbonne Université (CAMPARIS) with a CAMECA SX-Five instrument. Analytical conditions used for X-ray mapping (wavelength-dispersive spectroscopy mode; WDS) were 25 kV, 247 nA, a dwell time of 130 ms/pixel and 3 µm pixel size. The PAP correction was applied for quantifying map data in terms of wt% oxides, including for measuring low concentrations elements as for Ti and Cr in lawsonite. Standards used for calibration were Fe_2O_3 (Fe), $MnTiO_3$ (Mn, Ti), diopside (Mg, Si), Cr_2O_3 (Cr), orthoclase (Al, K), anorthite (Ca) and albite (Na). The resulting composition maps and X-ray maps acquired with the SEM (energy-dispersive spectroscopy mode) instrument were further processed with DWImager software (Garcia-Casco, 2007). For details regarding mineral compositions, formula recalculations and mineral classification, the reader is referred to **Chapter 5**. Mineral abbreviations are from Whitney and Evans (2010).

Electron backscattered diffraction analyses (EBSD) were performed on a Carl Zeiss Auriga SMT field emission SEM equipped with an Oxford Instruments detectors (EDS and EBSD) using AZTEC Synergy (Energy and HKL) software at the Center of Scientific Instrumentation of the University of Granada (CIC-UGR). Samples used for EBSD measurements have been double polished with a diamond powder (0.25 µm grain size) using a colloidal silica suspension media at the Department of Mineralogy and Petrology of the University of Granada. The SEM has been operated using 20 kV acceleration voltage with an aperture of 60 µm and a working distance of 15 mm. Coated thin sections were taped with conductive adhesive copper and tilted at 70° with respect to the incoming electron beam. Kikuchi bands indexing correspond to 8 to 12 bands of detection and step sizes of 2 to 0.4 µm for ***Figures 5A, B*** and ***C***, respectively. Post data processing of the maps, generation of pole figures

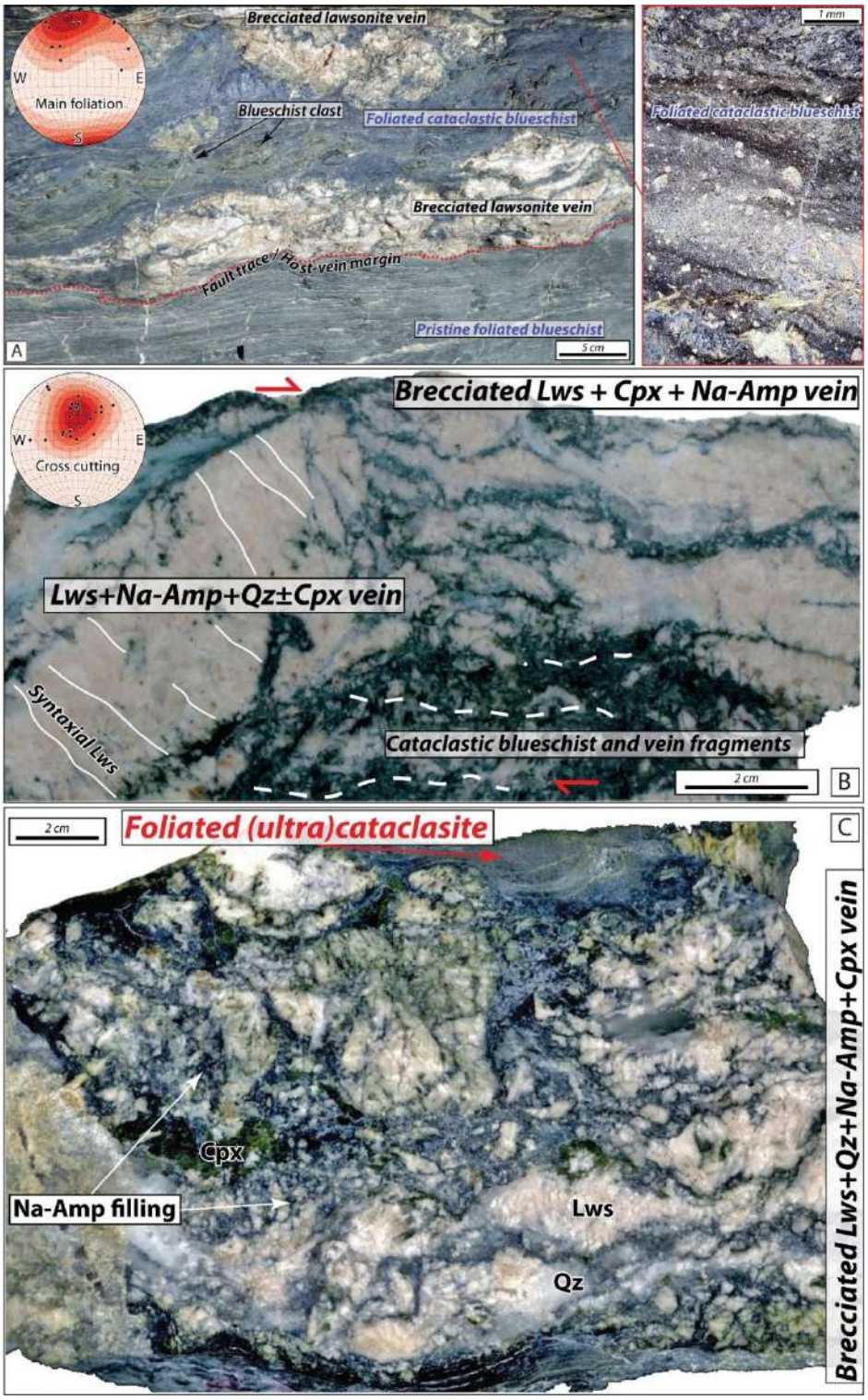

Figure 6.2. A. Field view of a pristine foliated blueschist and adjacent heavily brecciated lawsonite vein. Note the sigmoidal morphologies of the lawsonite clasts as well as the occurrence of blueschist clasts within the cataclastic foliated blueschist domain. The inset aims at illustrating the cataclastic nature of the blueschist host. B. Polished hand specimen of a lawsonite-rich vein. The lawsonite vein structure is heterogeneous ranging from almost pristine to the left hand to brecciated to the right hand of the image. C. Polished hand specimen of a heavily sheared lawsonite-rich vein showing a more heterogenous grain size distribution and irregular clast shapes that makes fragment reconstruction impossible. Note the occurrence of a foliated ultracataclasite at the host-vein margin. Na-Amp – Na-amphibole

and noise reduction has been performed using MTEX software (Bachmann et al., 2010; Bachmann et al., 2011). Cathodoluminescence (CL) mosaic images were constructed after stitching several photomicrographs (acquisition time of 11 seconds per image) taken with a Cathodyne (NEWTEC) machine at the Institut de Physique du Globe de Paris equipped with an automated stage and operated at 14 kV and a 120 µA argon plasma.

6.4.2 In situ trace element analyses

In situ Laser Ablation Quadrupole Inductively Coupled Plasma-Mass Spectrometer (LA-ICP-MS) analyses were performed at CIC-UGR, using a 213-nm Merchantek Nd-YAG laser coupled to an Agilent 7500 ICP mass spectrometer in a He atmosphere and the beam fixed to a diameter of 100 µm in raster mode through a 500 µm across-foliation distance, covering a surface of 500x100 µm per data point. Preceding each measurement, the spots were pre-ablated for 15 seconds with a laser fluence of 2.5 Jcm^{-2} followed by further ablation during 60 seconds with a laser fluence of 7.5 Jcm^{-2}. Similarly, a blank was measured with the same conditions but with zero laser energy; the resulting counts were subtracted from the signals. The stage was programed to move 5 µm every 20 seconds to increase sensitivity and avoid fractionation due to laser scavenging and cratering effects. The NIST-610 glass, used as external standard, was measured every six spots for drift corrections at the beginning and end of each analytical session. Note that linearity between signal intensity and concentration is regularly checked and generally maintained, while silicon is used as an internal standard. Data reduction was done using an in-house LA-ICP-MS data evaluation software. Precision calculated based on NIST-610 replicates was about ±5% (relative) and the detection limit is c. 0.01 ppm for most elements. The resulting analyses from several transects starting from the cataclastic blueschist matrix towards the ultracataclasite in the vein-host contact, as illustrated in ***Figure 6.3A***, are shown in ***Figures 6.6A*** and ***B***, normalized to an average of eight pristine blueschist compositions obtained through X-ray fluorescence analysis (see **Chapter 5**).

6.5 Microstructures, textures and fabrics

Brecciated lawsonite veins and adjacent ultracataclasites exhibit diffuse and curvy slip surface margins, while the contact between the ultracataclasite and its cataclastic blueschist host is sharper and curvy-planar (***Figure 6.3A***). Host cataclastic blueschists correspond to medium to fine-grained foliated lawsonite, epidote and Na-amphibole schists with variable amounts of Na-Ca clinopyroxene, chlorite, titanite, apatite and zircon (for a detailed characterization of non-cataclastic host rocks materials the reader is referred to **Chapter 5**). An obvious comminution gradient increasing towards the vein margins is shown in ***Figure 6.3A***, characterized by comminution down to the submicrometric scale and not resolvable with optical microscopic observations. The ultracataclasite consists of major amounts of Na-amphibole and titanite (***Figure 6.4A***) and subordinate amounts of lawsonite and epidote. It is important to note that epidote is only found as very rare clasts in the ultracataclasites near the vein margins while ultracataclastic domains within veins are epidote-free. Epidote from the cataclastic blueschist shows evidence of brittle fracturing and further grain rotation. It is commonly possible to reconstruct the previous shape of former crystals (e.g., ***Figures 6.S1D, E*** and ***F***),

indicating pulling-apart and strain up to the millimetre-scale. Epidote concentrates into layers which are intimately associated with Na-amphibole and chlorite (***Figure 6.S1D***), the latter phases generally as dark layers or strain shadows around epidote grains and likely representing pressure-solution seams. Lawsonite grains, aligned along the main foliation, exhibit oriented Na-amphibole and epidote inclusion trails that define a previous foliation misoriented at low angle with respect to the main foliation (***Figure 6.S1D***). They also bear evidence that indicates brittle deformation such as pulled-apart grains.

The brecciated veins are generally constituted of coarse-grained lawsonite grains associated with quartz and Na-amphibole together with minor clinopyroxene (***Figures 6.3B*** and ***S1H***). Na-amphibole and titanite stripes commonly wrap lawsonite fragments or occur along interstitial interclast spaces. Indeed, the distribution of some Na-amphibole through lawsonite interclast spaces resembles hydraulic breccia structures (***Figure 6.4B***). When possible, reconstruction of former lawsonite grains – now fragmented – indicates that pulling-apart and strain range from few millimetres to few centimetres. However, a large part of grains does not show recognizable precursor crystal morphologies due to shearing. Lawsonite crystals bear undulose extinction and subordinated twining and bending. Na-amphibole in lawsonite-rich veins are mostly distributed into extremely fine-grained bands (e.g., ***Figures 6.3B*** and ***C***) or as euhedral undeformed crystals filling interclast spaces (***Figure 6.S1G***), the later clearly indicating precipitation into fluid filled cavities (see also **Chapter 5**). In the former case, it was not possible to determine Na-amphibole optical properties owing to its extremely fine-grained nature whereas in the latter, undulose extinction is not observed. Similarly, lawsonite also tends to concentrate into shear bands of heavily fragmented grains (e.g., ***Figure 6.5A***), while Na-amphibole crystals are always smaller than lawsonite.

Pristine and comminuted Na-amphibole needles are observed (***Figure 6.3C***) as if they had flowed or injected through paths surrounding or infiltrating fragmented grains. Indeed, some veins within the veins are deflected when facing coarse-grained lawsonite crystals (***Figure 6.S1K***). The Na-amphibole bands exhibit textures characterized by highly sigmoidal Na-amphibole clasts surrounded by submicrometric Na-amphibole fragments and/or crystals (***Figures 6.3D*** and ***E***). Similar textures are displayed by titanite crystals associated within the Na-amphibole bands. Na-amphibole bands, especially near lawsonite crystals, exhibit widespread dissolution seam fringes indicating pressure-solution creep fabrics (e.g., ***Figure 6.3F***).

Lawsonite exhibit intriguing zoning patterns characterized by “dusty” brownish regions under the optical microscope which are apparently partly dissolved. These regions are commonly surrounded by translucent or “clean” lawsonite. Both lawsonite types are locally surrounded by tiny euhedral lawsonite prisms which also occupy the interclast space (***Figure 6.3F***). The zoning pattern among “dusty” and “clean” lawsonite coincides with the titanium distribution of lawsonite grains, with “dusty” regions corresponding to Ti+Fe-richer and Al-poor domains. The amount of titanium and

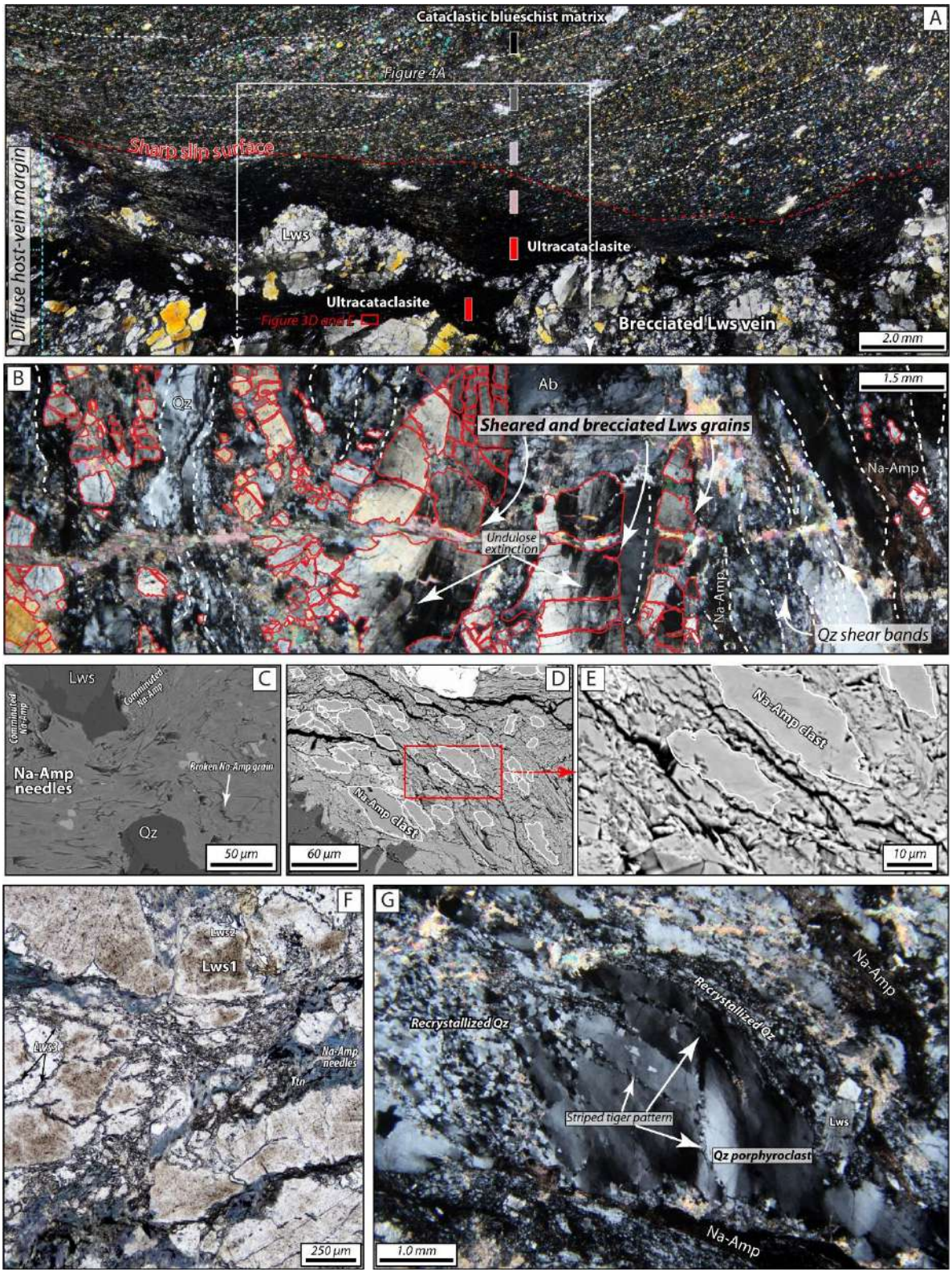

Figure 6.3. Optical polarized-light photomicrographs (A, B, F and G) and backscattered electron images (BSE; C, D and E) of representative cataclastic blueschist and vein breccias. Cross-polarized view of a lawsonite-rich vein breccia and adjacent Na-amphibole- and epidote-rich cataclastic blueschist host. A strong grain size comminution gradient can be noticed towards the vein. The coloured rectangles illustrate the distance and geometry of the measured LA-ICP-MS surfaces

represented in Figure 6.6. We highlight that the measured surfaces were distributed across the foliation at roughly similar distances from the vein margin. B. Cross-polarized view of the representative structure of a lawsonite-rich vein breccia. C. SEM image of a Na-amphibole band from the vein breccia. D. SEM image of a Na-amphibole band from a lawsonite vein breccia corresponding to the margin between a large lawsonite porphyroclast and a Na-amphibole band. Note the occurrence of sigmoidal Na-amphibole clasts surrounded by an ultracomminuted submicrometric Na-amphibole matrix. The location of this image is depicted in the inset from panel A. E. Detail from panel D. F. General view of different generations of lawsonite crystals and Na-amphibole needles from a vein breccia. G. Microstructures of quartz in a vein breccia.

iron in lawsonite are anomalously high, up to the weight percent TiO_2 and FeO level (***Figures 6.4B*** and ***6.S1I***). The patterns are very uneven, ranging from (1) very sharp boundaries within a single grain, (2) patchy zoning, (3) concentric zoning to (4) healed fractures (see arrows in ***Figure 6.4B***). Similarly, Na-Ca clinopyroxene display patchy-like zoning patterns containing weight percent TiO_2 level towards its cores (***Figure 6.S1J***). Note that titanium enrichments are not clearly associated with regions containing high amounts of vein titanite (***Figure 6.4B***), indicating that lawsonite and clinopyroxene zoning patterns predates the preserved "last" stage of titanite and Na-amphibole veining. In addition, the lawsonite breccia matrix is enriched in chromium showing values up to the weight percent Cr_2O_3 level (***Figure 6.4C***). Lawsonite is also zoned – although very weakly – in chromium (corresponding to low aluminum regions), with values up to c. 0.25 Cr_2O_3 wt%, while clinopyroxene Cr_2O_3 does not show any obvious zoning pattern but reaches up to c. 0.3 wt% (***Figures 6.S1I*** and ***J***). The matrix regions richest in chromium corresponds to bands extremely enriched in titanite (***Figure 6.4C***).

Quartz exhibits complex textural-structural relationships. First, core-and-mantle structures define quartz porphyroclasts surrounded by fine-grained dynamically recrystallized aggregates (***Figure 6.3G***). Optical, SEM and EBSD results show quartz grain sizes ranging from microns up to few centimetres in recrystallized grains and porphyroclasts, respectively (e.g., ***Figures 6.3G*** and ***6.5B***). Based on microscale observations, a limit grain size diameter of 100 μm has been selected to discriminate recrystallized grains from porphyroclasts. The range from 15 to 50 μm is the most representative for most recrystallized grains (***Figure 6.S2A***). This threshold limit allows proper displaying of pole figures information (see below) aiming at investigating the orientation of recrystallized crystals without interference of clasts. Most grains exhibit irregular and sutured grain boundaries while bulging and rotated subgrains are distinguished. Undulose extinction is well visible among all porphyroclasts whereas it is developed to a lesser extent in finer grains. Stripes of quartz grains (referred to as stripped tiger pattern) crosscutting and misoriented with respect to larger porphyroclasts are common (***Figure 6.3G***). In addition, bands of heavily recrystallized quartz grains wrapping around lawsonite fragments are widespread (***Figure 6.3B***). CL imaging (***Figure 6.S1L***) reveals similar textures characterized by shades of red and dark redish color exhibiting stripes of sigmoidal quartz crystals within a porphyroclast. The Z axis EBSD orientation map (with X the maximum strain orientation of the strain ellipsoid; ***Figure 6.5B***) reveals a preferential – although somehow weak – crystallographic preferred orientation (CPO) of the quartz c axis ([0001]) along the brecciated shear vein at relatively high angles with respect to the stretching orientation. These observations are confirmed after examination of the <c> and <a> ([11-20]) axes pole figures (***Figure***

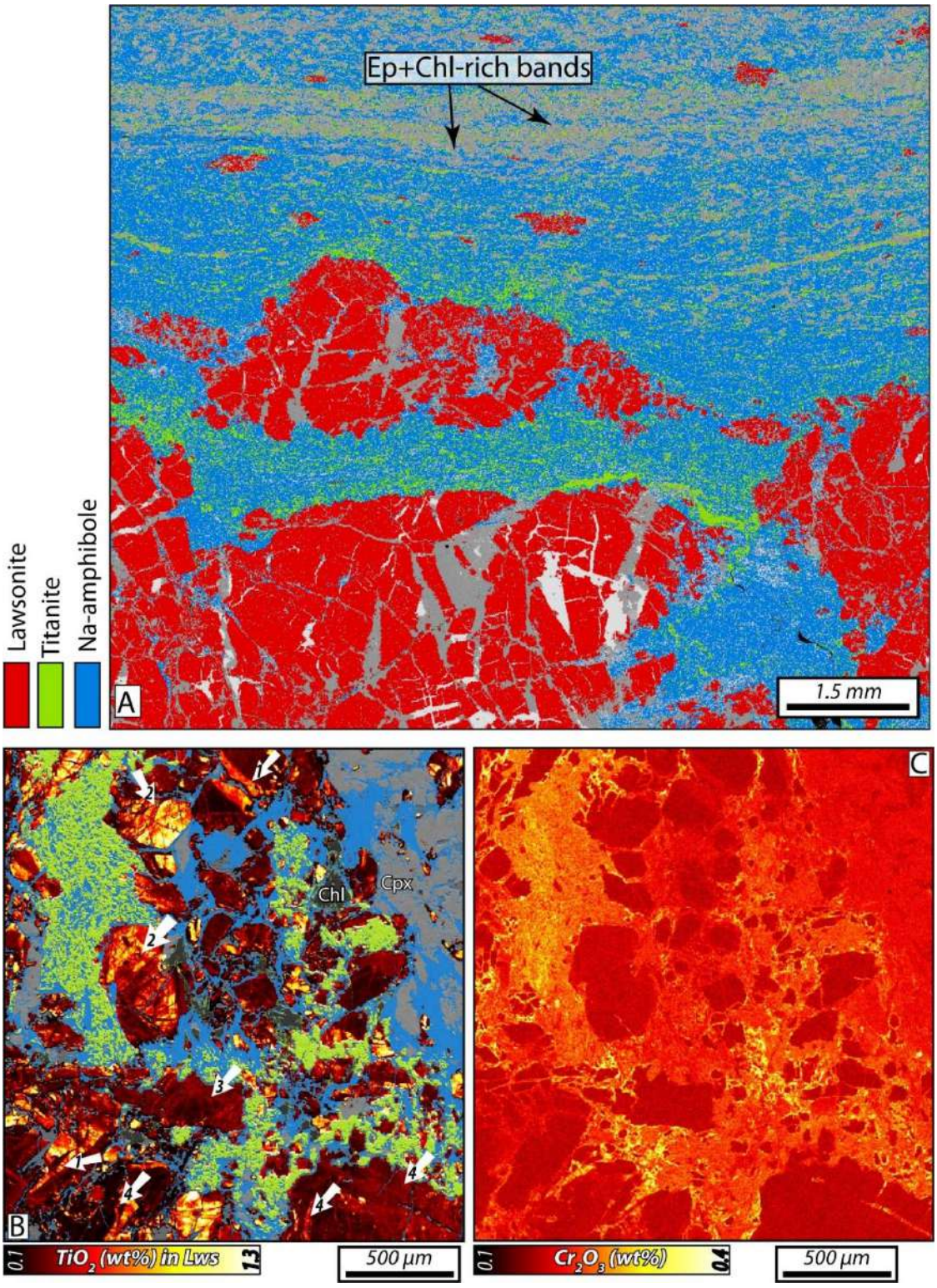

Figure 6.4. A. Selected phases based on high-resolution EDS X-ray maps from the cataclastic blueschist host and vein margin. B. Selected phases based on high-resolution WDS maps with the corresponding BSE image in the background (not selected phases) from a lawsonite-rich vein breccia. Key code as in panel A. TiO_2 in wt% is shown for lawsonite. Arrows 1 – sharp chemical zoning boundaries along fragmented grains; Arrows 2 – Patchy zoning; Arrows 3 – concentric zoning; Arrows 4 – healed cracks. C. high-resolution WDS map from the same lawsonite-rich vein breccia as in B depicting the distribution of Cr_2O_3 (wt%). Note that the higher amounts of chromium oxide are mostly coincident with titanite.

6.5C) depicting weak maxima at c. 60° with respect to the stretching lineation and contained in the foliation plane (perpendicular to the stretching orientation), respectively. Note that <c> axes also exhibit a girdle oblique to the foliation and stretching directions.

EBSD mapping in Na-amphibole from an almost pure monophase domain around a large lawsonite clast reveals a clear CPO with respect to the X axis of the finite strain ellipsoid (***Figure 6.5D***). In this case, a <c> ([001]) axis CPO is evident and confirmed by pole figures analysis (***Figure 6.5E***). In addition, the [100] and [010] are oriented nearly perpendicular and contained into the foliation plane, respectively, highlighting a strong SL-type Na-amphibole fabric (see Cao et al., 2014). This fabric, however, is apparently crosscut by a tiny shear band as illustrated in ***Figure 6.5D***. There, several grains are teared apart and show offsets up to the point of fragmentation. Grains that were not fragmented do not show significant internal crystal misorientation (***Figure 6.S2C***), whereas either undeformed and non-misoriented Na-amphibole crystals crosscut the fault trace as illustrated in ***Figures 6.5D*** and ***6.S2C***. Note that pulled-apart grains, with a stretching orientation according to the overall shape preferred orientation, are also observed. Larger, highly misoriented Na-amphibole grains are frequently surrounded by apparently strain-free finer crystals (***Figure 6.S2C***), possibly representing recrystallized Na-amphibole grains. In the case of lawsonite, a CPO is observed (***Figure 6.S2E***) characterized by fragmented grains that coincide with the orientation of its coarser-grained counterparts, resulting in pole figures displaying several maxima (sub) parallel to the stretching orientation and contained in the foliation plane. In addition, lawsonite crystals are not significantly misoriented, with the higher misorientation angles matching regions of twins or undulous extinction (***Figure 6.S2D***).

6.6 Rock trace elements geochemistry

The geochemical signatures of different domains from the cataclastic blueschist matrix towards the ultracataclasites (see colour code in ***Figure 6.3A***) has been investigated through LA-ICP-MS measurements in raster mode (see methods section for further details). This approach enables studying highly heterogeneous samples with domains that cannot be resolved using classical whole rock geochemical analyses. However, the obtained results can be regarded as whole rock analyses of the selected domains that reflect chemical trend variations rather than accurate absolute values due to mineral heterogeneities that affect trace element abundances.

Rare Earth Element (REE) patterns along the transect are presented in ***Figure 6.6A***. As expected, the cataclastic blueschist matrix, up to few centimetres away from the ultracataclasites, contains virtually identical trace element abundances compared to those of the averaged pristine blueschists samples (see **Chapter 5**). Towards the ultracataclasite-vein margin, a two-orders of magnitude depletion in light rare earth elements (LREEs) is evidenced, while the concentration of heavy rare earth elements (HREE) are essentially identical in all domains (the subtle enrichment relative to average blueschist is within error). High field strength element (HFSE; Zr-Ta-Nb-Ti) and chromium concentrations

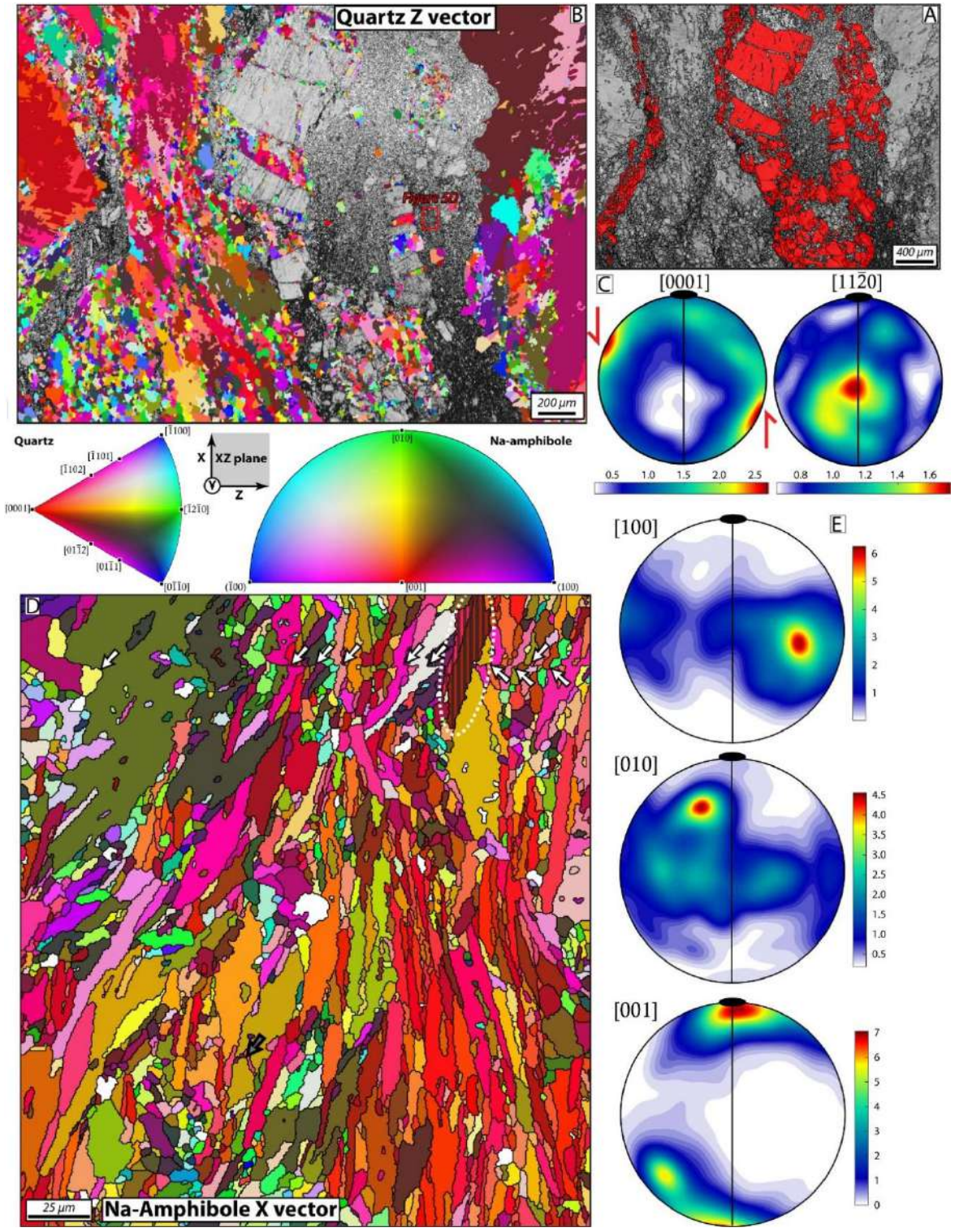

Figure 6.5. A. EBSD phase map of lawsonite above a band contrast image background. Orientation maps (B and D) colored according to the inverse pole figure (IPF) key for quartz and Na-amphibole, respectively, showing a shape preferred orientation parallel to the X axis direction of the finite strain ellipsoid (i.e., stretching orientation). For consistency with chemical data, Na-amphibole nomenclature is written in the figure and further EBSD data analysis, however, the indexed phase corresponds to glaucophane. Pole figure diagrams represented in an upper hemisphere equal-area projection for quartz and Na-amphibole (C and E, respectively). The bold black line and the oval represents the foliation plane and the lineation direction, respectively. Contours are multiples of uniform density distributions (the number of grains is 5322 and

1507 for quartz and Na-amphibole, respectively). B. View corresponding to the Z axis of the finite strain ellipsoid. C. Pole figure for [0001] and [11 -2 0] quartz crystallographic axis for grains equal or smaller than 100 µm, considered to represent recrystallized crystals. D. View corresponding to the X axis of the finite strain ellipsoid. The location of this map is depicted in panel B. The white arrows aim at representing a fault trace crosscutting clear offset crystals while the grey arrow points to a pulled-apart grain. Texturized crystals (enclosed by a white dashed oval) highlight Na-amphibole crystals crosscutting the fault. E. Pole figure for [100], [010] and [001] Na-amphibole crystallographic axis.

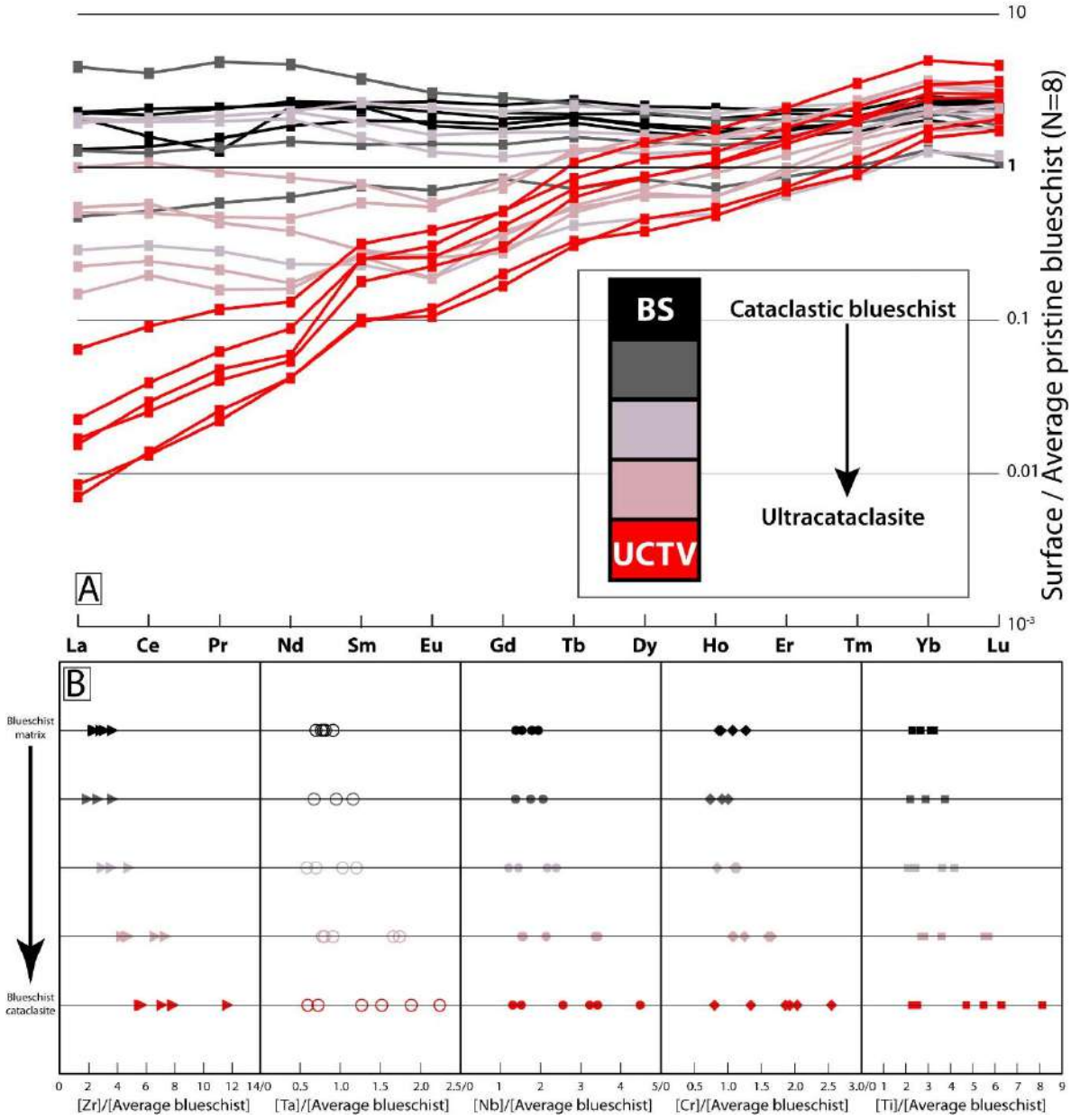

Figure 6.6. A. In situ LA-ICP-MS Rare Earth Elements composition diagram of surfaces from the blueschist cataclastic matrix towards the ultracataclasite vein margin normalized to average pristine (i.e., non-cataclased) blueschist compositions from Chapter 5. The color code aims at illustrating the distance of surface measurement with respect to the vein margin (as also illustrated in Figure 6.3A). B. Zr, Ta, Nb, Cr and Ti concentration diagrams versus relative distance for the same transect using the color code from panel A and Figure 6.3A.

relative to average blueschist standard are depicted in ***Figure 6.6B***. Similar trends as those depicted for LREE can be noticed: HFSEs and chromium concentrations are enriched from 2.2 up to 12 times for Ta and Zr, respectively. As noted for the HREE, the concentrations of HFSE in the cataclastic blueschist matrix are, in most cases, slightly higher than the pristine blueschist standard. This may be due to a real enrichment of the cataclastic blueschist matrix which is still capturing the metasomatic effects of circulating fluids (see below) or due to slight imprecisions among the used instrumental methods.

6.7 Discussion

In this section, we discuss the structural records and geochemical fingerprints of the studied cataclastic lithologies and veins in the frame of processes occurring in the rocks under investigation, without considering a wide vision of fluid flow and tectonic processes. The integration of this data into a broader perspective, including constraints regarding slow earthquake processes, is discussed in the **Chapter 8** of this manuscript.

6.7.1 Interpretation of the observed textures and fabrics in the light of fluid flow

Exhaustive inspection of meso-scale field outcrops as well as hand specimens demonstrate that shearing affected to various extent the herein studied lithologies and structures (e.g., ***Figure 6.2***). First, we note that cataclastic blueschists are intimately associated with brecciated vein domains. Indeed, the distribution of these cataclastic fabrics is not necessarily symmetrical as, for example, depicted in ***Figures 6.2A*** and ***6.S1A*** where sharp shear band margins widen or thicken along strike. In addition, shear bands commonly develop in regions that were affected by an earlier stage of hydrofracturing and subsequent evolution into localized shear bands. These insights suggest that hydrofracturing and/or fluid overpressures likely precede or were contemporaneous with shearing.

In the cataclastic blueschist host, brittle creep is witnessed by the occurrence of comminuted and/or fragmented stiff mineral phases such as epidote (e.g., Park et al., 2020) and/or lawsonite in a weaker Na-amphibole-rich matrix (e.g., ***Figures 6.S1D*** to ***F***; Teyssier et al., 2010). In addition, the obvious and prominent grain size reduction towards the ultracataclasites (***Figures 6.3A*** and ***6.S1B***) is another firm evidence that allows demonstrating a brittle nature. Furthermore, the finding of slickenlines coated with Na-amphibole crystals (***Figure 6.S1C***) contained in the XY plane of the vein-host margin and with a lineation parallel to the stretching orientation of the brecciated veins, is consistent with brittle deformation in the blueschist-facies under the same stress field that induced vein brecciation. In addition, widespread pressure-solution creep fabrics characterized by dissolution of matter around rigid objects, such as epidote (e.g., ***Figures 6.S1E*** to ***G***) and lawsonite (e.g., **Chapter 5**), and precipitation of chlorite and Na-amphibole, indicate overprinting deformation mechanisms operating at different rates: faster brittle creep is followed (or preceded) by slower pressure-solution creep (e.g., Wassmann and Stöckhert, 2012; Angiboust et al., 2015; Oncken et al., in press). These arguments thus suggest that brittle creep, pressure-solution (and to a lesser extent dislocation creep) mechanisms occur in the vein and its surroundings at maximum depths of c. 55 km compatible with slow earthquake processes.

In brecciated vein networks, the occurrence of minerals with contrasting viscosity results in far more complex patterns. It should be noted that brecciation intensity is highly heterogeneous, ranging from almost non-brecciated veins, such as those studied in **Chapter 5**, to heavily brecciated ones where the original extensional (opening) structures have been completely obliterated (e.g., ***Figure 6.2C***). Lawsonite crystals show widespread and obvious evidence demonstrating brittle creep as the main deformation mechanism. Even though lawsonite grains are commonly pulled-apart or boudinaged and stretched over millimeter- to few centimeter-scales (e.g., ***Figure 6.3B***), some other lawsonite grains have been completely obliterated by extensive fragment disruption (***Figure 6.2C***). Moreover, millimeter-wide shear bands of heavily comminuted lawsonite points to localized deformation within the vein domains (***Figure 6.5A***). CPO in lawsonite is typically observed in material derived from single crystals (e.g., ***Figures 6.5A*** and ***6.S2E***). The lack of observation indicating significant viscous deformation mechanisms allow speculating that the main deformation mechanism of lawsonite is rigid body rotation (e.g., Teyssier et al., 2010; Cao et al., 2014) and brittle creep.

Quartz wrapping lawsonite porphyroclasts show evidence that suggests viscous creep deformation mechanism such as: (i) irregular and serrated grain boundaries, (ii) subgrains and grain boundary migration, (iii) undulose extinction and (iv) a core-in-mantle structure (e.g., Stipp et al., 2002). In addition, shear bands containing recrystallized quartz grains, which are often found crosscutting quartz porphyroclasts, support this hypothesis. These observations are sustained by a clear, although slightly weak, quartz CPO (***Figure 6.5C***). Interestingly, the quartz <c> axis maxima are oriented oblique to the overall stretching lineation of the analyzed vein, which may provide evidence for a non-coaxial and highly heterogeneous stress field acting during viscous flow. Indeed, the anastomosing fabrics of the vein domains may be consistent with local stress variations, as for example, due to rheological or viscosity heterogeneities. This pattern reminds contexts where rigid objects are surrounded by a weak flowing matrix, as for example in mélanges (e.g., Yamato et al., 2019; Beall et al., 2019; Ioannidi et al., 2021). Previous detailed investigations on quartz microstructures suggest that the striped tiger structures, commonly observed herein in quartz, may result from strain hardening processes associated with a misoriented slip system with respect to the acting stress field (likely the <a> prism; Kjøll et al., 2015). After an initial stage of dislocation creep, the accumulation of dislocations may ultimately result in intra-granular fractures and micro-gouges (Stünitz et al., 2003) followed by subsequent dislocation creep. Although further investigations would better constrain this phenomenon in the herein studied veins, the finding of roughly similar structures in quartz (as supported by the finding of pervasive micro-fracturing in quartz CL images; ***Figure 6.S1L***), in addition to widespread brittle structures in other minerals, allow speculating that similar processes of strain hardening may have resulted in brittle deformation of quartz.

Na-amphibole-rich bands and veins within lawsonite vein breccias systematically crosscut all other silicate minerals (i.e., lawsonite, quartz, clinopyroxene, Na-amphibole, see **Chapter 5**) except chlorite. In any case, pressure-solution creep affecting Na-amphibole but also lawsonite is widespread. Fine-scale observations allow identifying: (i) Na-amphibole porphyroclasts surrounded

by a sub-micrometric Na-amphibole-rich matrix (***Figures 6.3D*** and ***E***), (ii) broken and fragmented Na-amphibole needles (***Figure 6.3C***) and (iii) micro-faults with appreciable offset crosscutting Na-amphibole crystals overgrowths by newly-formed Na-amphibole (***Figure 6.5D***). These observations allow concluding that a brittle creep deformation mechanism was also active in Na-amphibole vein crystals. In fact, it could be hypothesized that the extremely fine-grained nature of Na-amphibole bands in veins resulted from shearing and ultracomminution of former Na-amphibole veins (e.g., see texture in ***Figure 6.4B***). The texture depicted by misorientation maps (***Figure 6.S2C***) characterized by larger misoriented grains surrounded by finer non-misoriented grains suggests some degree of dislocation creep (see Kotowski and Behr, 2019). These statements are supported by EBSD results depicting a strong CPO defining a SL-type fabric. This CPO is commonly reported in glaucophane (e.g., Bezacier et al., 2010; Cao et al., 2014) and is consistent with the activation of the [001]{hk0} slip system (Reynard et al., 1989) and a plain strain regime. Nevertheless, Ildefonse et al. (1990) have shown that similar fabrics also develop due to rigid body ration. Thus, further fine-scale characterization is needed to accurately determine the CPO-forming deformation mechanisms observed in glaucophane-bearing veins.

6.7.2 Interpretation of geochemical fingerprints

The intimate association between shear veins and foliated ultracataclasites (e.g., ***Figure 6.2C***) offers a unique opportunity to illuminate the complex feedbacks between cataclasis and fluid flow since ultracomminuted host-vein margins, as well as comminuted vein domains, represent regions of enhanced metasomatism due to a larger reactive surface area (e.g., Lai et al., 2015). Once altered and cemented (likely at short timescales; e.g., Kay et al., 2006), recovery or even strengthening of the formerly comminuted domain is enhanced via dissolution-precipitation processes (Giger et al., 2008; **Chapter 7**). These statements are supported here by the occurrence of a blueschist-facies foliation and widespread pressure-solution creep fabrics in the cataclastic blueschist as well as within the vein networks (***Figures 6.3A, F, 6.S1E*** and ***F***). Metasomatic effects are identified in both, the brecciated lawsonite veins and in ultracataclastic host domains. In the veins, fluid-rock interaction is revealed by mineralogical and chemical anomalies that can neither be explained by internal fluid production nor by mechanical wearing. The modal proportions of minerals forming brecciated veins and adjacent pristine extensional domains cannot be envisioned by internal fragmentation alone. For example, the pristine lawsonite-rich domains shown in ***Figure 6.2B*** contains substantially less Na-amphibole and quartz compared to its respective brecciated analogue domain, suggesting mineral-forming events or mechanical mixing with host material. Similar arguments have been made for (ultra) cataclasites from shallower seismogenic regions interpreted as representing open-system behavior (Meneghini et al., 2010). Several studied veins contain anomalously high amounts of titanite in close association with Na-amphibole bands (e.g., ***Figure 6.4B***). Interestingly, lawsonite zoning patterns also show very uneven enrichments in titanium and iron. It is beyond the scope of this investigation to expand on crystallographic or chemical processes controlling the distribution of zoning patterns (for such details see Vitale Brovarone et al., 2014). Nevertheless, the occurrence of titanium-rich healed cracks, oscillatory and patchy zoning patterns as well as sharp chemical boundaries may indicate that titanium

enrichments occurred (i) in several events (episodically) and (ii) from a fluid phase in an open system (see Vitale Brovarone et al., 2014). Weak zoning patterns in chromium, which are decoupled from titanium enrichments in the same crystals, (***Figures 6.4C*** and ***6.S1I***) are also indicative for an external fluid source infiltrating the fault zone.

In situ trace elements analysis in the ultracataclasites shows strong depletions in LREEs while HFSEs and chromium are enriched compared to the host cataclastic blueschist. It is well known that LREEs are preferentially incorporated into epidote and lawsonite in blueschist lithologies (e.g., Tribuzio et al., 1996). Since the studied blueschist host is epidote-rich, it is a likely possibility that the absence of epidote and the low amounts of lawsonite in ultracataclasites can account for this anomaly. There is no reason to expect that a mechanical process would have preferentially mobilized epidote from the ultracataclasite. However, it is likely that mechanical wearing enhanced metasomatism in the fine-grained products of the host-vein margins boosting fluid-assisted chemical reactions, ultimately scavenging/leaching epidote, and thus taking along considerable amounts of LREEs. Although the herein proposed feedbacks between ultra (cataclasites) and metasomatism in the blueschist-facies field have never been reported so far, preferential scavenging of trace elements around veins is a rather common process in high pressure environments (e.g., John et al., 2008). However, in **Chapter 5** we have shown LREEs enrichments in lawsonite rims ("clean" zones described herein) relative to the cores ("dusty") in unbrecciated lawsonite-bearing veins from the Shegin complex. Thus, we speculate that, in addition to an inferred metasedimentary contribution for these LREEs enrichments, re-deposition of ultracataclasite-mobilized LREEs may account for some of the rimwards lawsonite enrichments reported in **Chapter 5** implying transport distances greater than the meter-scale.

The vein breccia matrix around large clasts exhibits interesting chromium anomalies that correlate with titanite distribution. It should be noted that common Ti-bearing phases such as titanite and rutile do not contain appreciable amounts of chromium, unless the crystallizing environment is particularly enriched in this element (in this case, the fluid; Spandler et al., 2011; Angiboust et al., 2014). HFSEs are also related to the high abundance of titanite, which is in turn only possible if considering precipitation from a titanium-rich fluid. HFSEs are commonly regarded as highly immobile, although it appears that they can be well mobilized under certain conditions (Ague, 2017; see **Chapter 8** for discussions on this issue). None of the lithologies forming the Seghin complex are rich enough in HFSE to justify high concentrations of these elements in ultracataclasites (see **Chapter 5**). Thus, internal fluid production, even at the scale of the entire metamorphic complex is unlikely. Similar HFSE enrichments have been documented in the Tianshan belt, China. There, Gao et al. (2007) documented rutile-bearing veins anomalously rich in Ti-Nb-Ta. The authors suggest that the transformation of titanite into rutile during the blueschist-to-eclogite transition, associated with the breakdown of H_2O-bearing minerals, results in massive fluid release and further mobilization of former titanite components into vein systems at the pluri-meter-scale – but probably at much larger distances. Similar conclusions regarding titanium mobility have been raised by Sorensen and Grossman (1989) in the Catalina Schists amphibolites and by Cárdenas-Párraga et al (in press) in

fluid-related jadeitite forming processes in a mantle wedge setting. In addition, Lucassen et al (2011) suggested that high HFSE contents in titanite may allow distinguishing titanite from a former rutile-related precursor. The authors also inferred transport distances of at least several tens of centimetres. Based on these investigations, we conclude that the fluids resulting in titanite crystallization and HFSE enrichments were externally-derived and sourced downdip near the blueschist-to-eclogite transition (e.g., Gao et al., 2007). Zirconium, also noticeably enriched in ultracataclasites, is compatible with titanium-bearing phases (Brenan et al., 1994). The anomalously high amounts of Zr in ultracataclasites suggests that (i) fluids were particularly enriched in Zr and (ii) zircon did not crystallize during deep titanite breakdown, otherwise Zr would have been sequestrated into it (Gao et al., 2007). Similarly, the observed chromium enrichments also require and external fluid source, most likely serpentinite/peridotite-derived (e.g., Angiboust et al., 2014). Spandler et al. (2011; see also Angiboust et al., 2014) demonstrated that chromium-enrichments in rutile could develop in cold subduction environments if infiltrated by antigorite breakdown fluids at eclogite-facies depths. Therefore, the episodic injection of overpressurized fluids from a deeper source, possibly from blueschist-facies mineral assemblage breakdown, (Frank et al., 2015; **Chapter 5**) is inferred to have contributed to the mechanical weakening promoting shearing and brittle creep in the deep slow earthquake source region.

6.8 Conclusions

The approach undertaken here allows us to characterize textures, fabrics and geochemical trends which have never been reported elsewhere so far. The occurrence of stunning lawsonite vein breccias and associated host-vein margins in the studied locality from the Seghin complex, Zagros suture, resulted from the complex interplay between brittle and viscous deformation under a fluid-saturated environment. The cataclastic blueschist matrix shows an increasing comminution gradient towards the host-vein margin, where ultracomminution led to the formation of ultracataclasites associated with brittle creep. These deformation events were overprinted by widespread pressure-solution fabrics and probably minor dislocation creep. Similar deformation patterns are observed in adjacent lawsonite-Na-amphibole-Na-Ca-clinopyroxene-quartz veins. Lawsonite and Na-amphibole show clear evidence of brittle deformation and creep and both phases were significantly overprinted by further pressure-solution creep, while Na-amphibole bands (including clasts) exhibit mild evidence of crystal plasticity. Quartz, on the other hand, shows clear evidence of dislocation creep; however, a brittle precursory event can be inferred. Anomalously high amounts of titanite and, consequently, Ti-Nb-Ta-Zr, in the ultracataclasites and some vein domains is firm evidence suggesting an externally-derived fluid contribution, likely from a deep-seated mafic source at the blueschist-to-eclogite transition. Furthermore, chromium enrichments can be related to the release of fluid at depth after antigorite-decomposition in subducting serpentinites. We hence conclude that brittle creep processes occurring in the subduction slow earthquake region were triggered by the injection of externally-derived fluid pulses. As shown here, the exhaustive study of blueschist-facies metamorphic vein networks offers a novel avenue to illuminate complex fluid-rock and tectonic interactions in the frame of slow earthquakes processes.

Acknowledgments

Philippe Agard, Zeynab Gharamohammadi, Ali Kananian and Jafar Omrani are warmly acknowledged for logistical and field assistance. Olga Cazalla, Alicia González, Jesus Montes, Nicolas Rividi and Coline Hopquin are thanked for support and patience during analytical and sample preparation sessions. This work has been funded by an Initiative D'EXcellence (IDEX) grant 16C538 and the TelluS Program of CNRS/INSU to S.A. Partial funding was also provided by the University of Granada at CIC.

6.9 Supplementary information

6.9.1 Figures

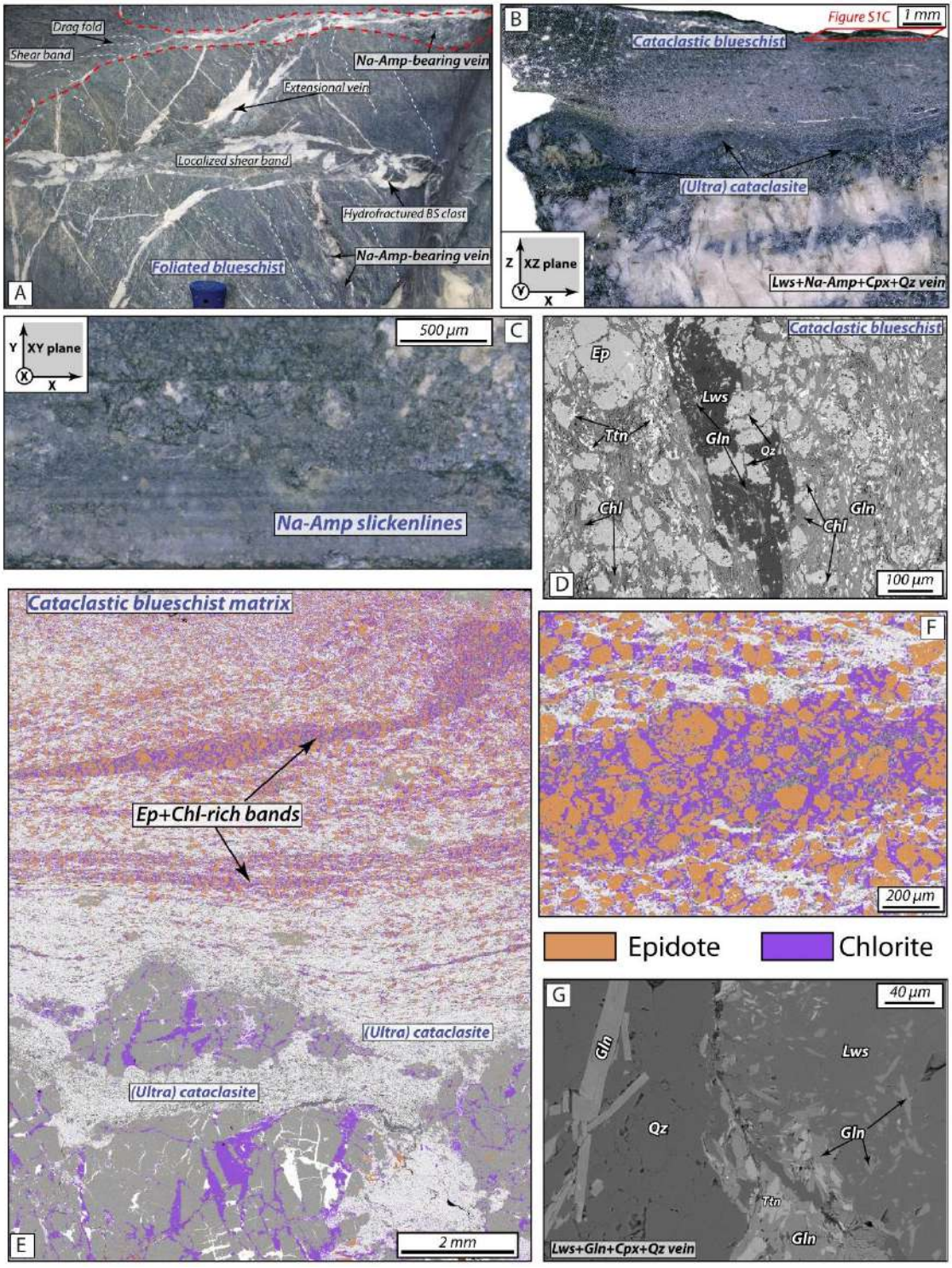

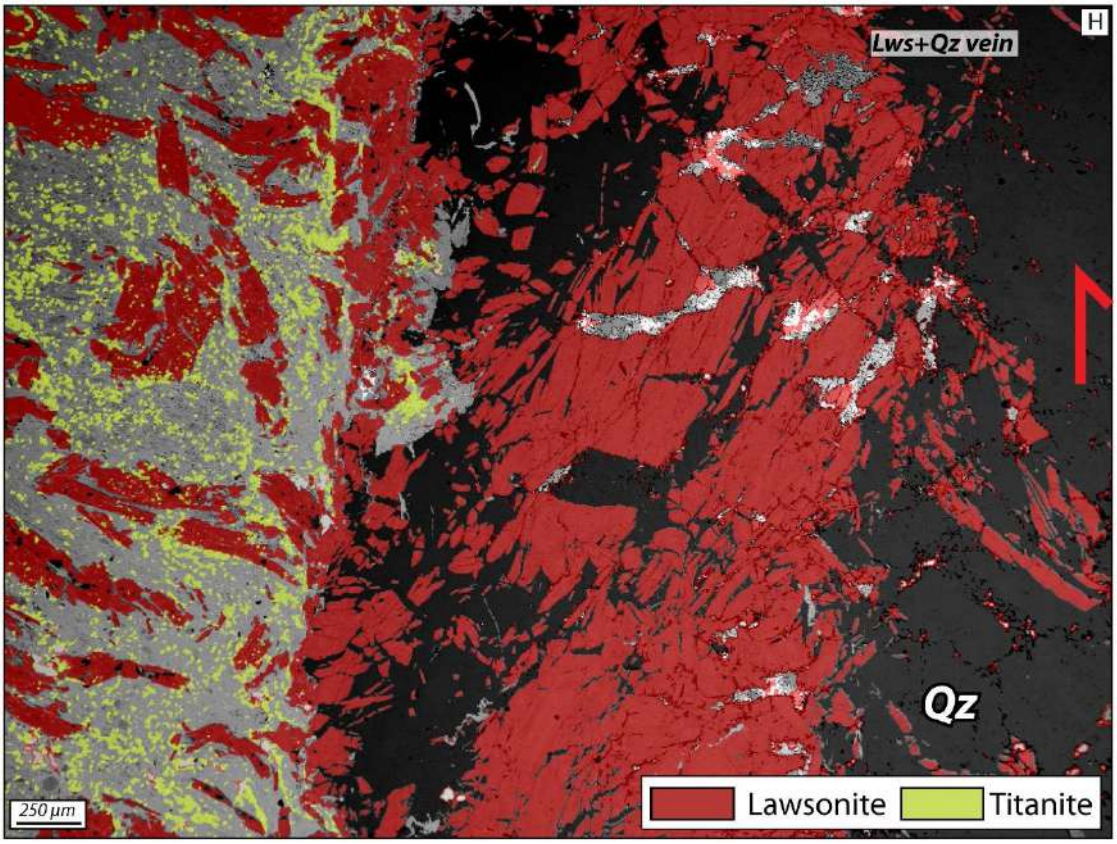
H
Lws+Qz vein
Qz
250 µm
Lawsonite
Titanite

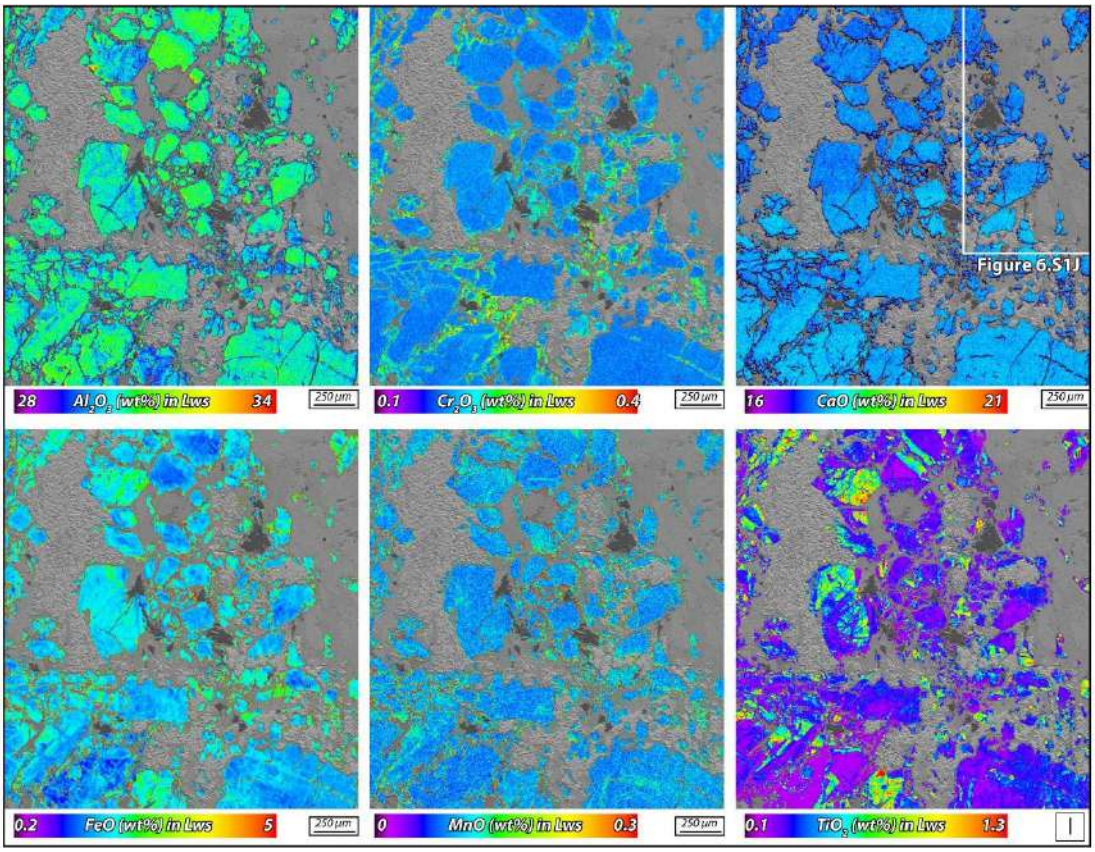
Figure 6.S1J
28 Al2O3 (wt%) in Lws 34
250 µm
0.1 Cr2O3 (wt%) in Lws 0.4
250 µm
16 CaO (wt%) in Lws 21
250 µm
0.2 FeO (wt%) in Lws 5
250 µm
0 MnO (wt%) in Lws 0.3
250 µm
0.1 TiO2 (wt%) in lws 1.3

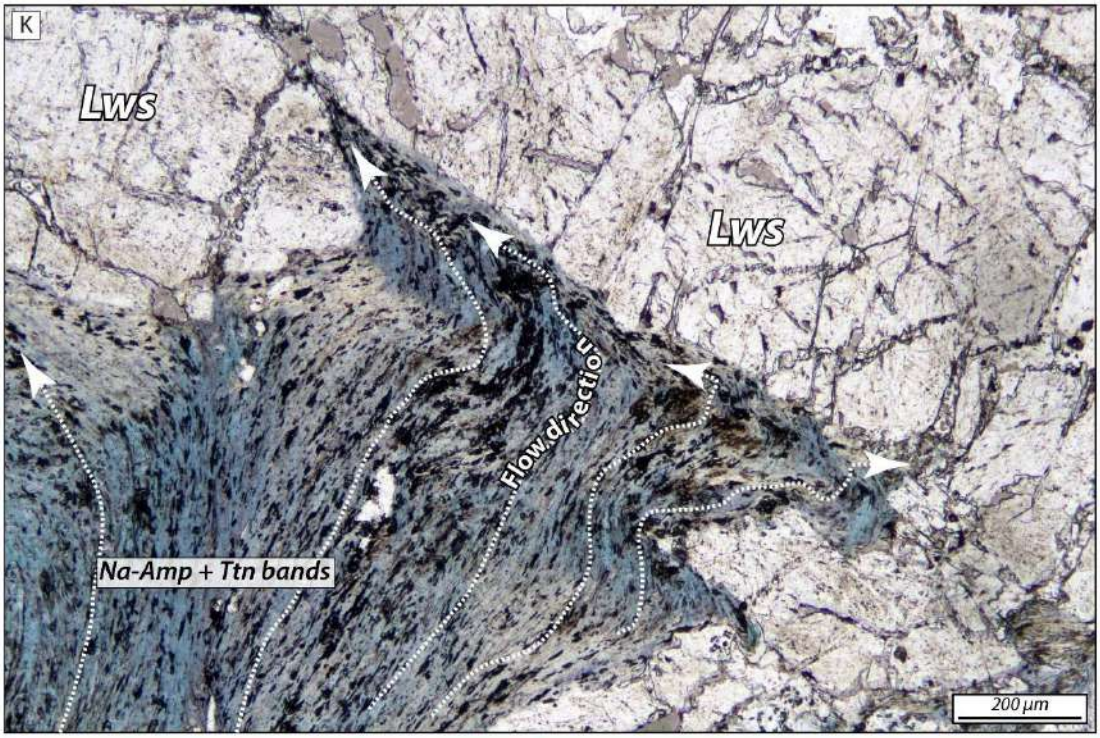
K
Lws
Lws
Flow direction
Na-Amp + Ttn bands
200 µm

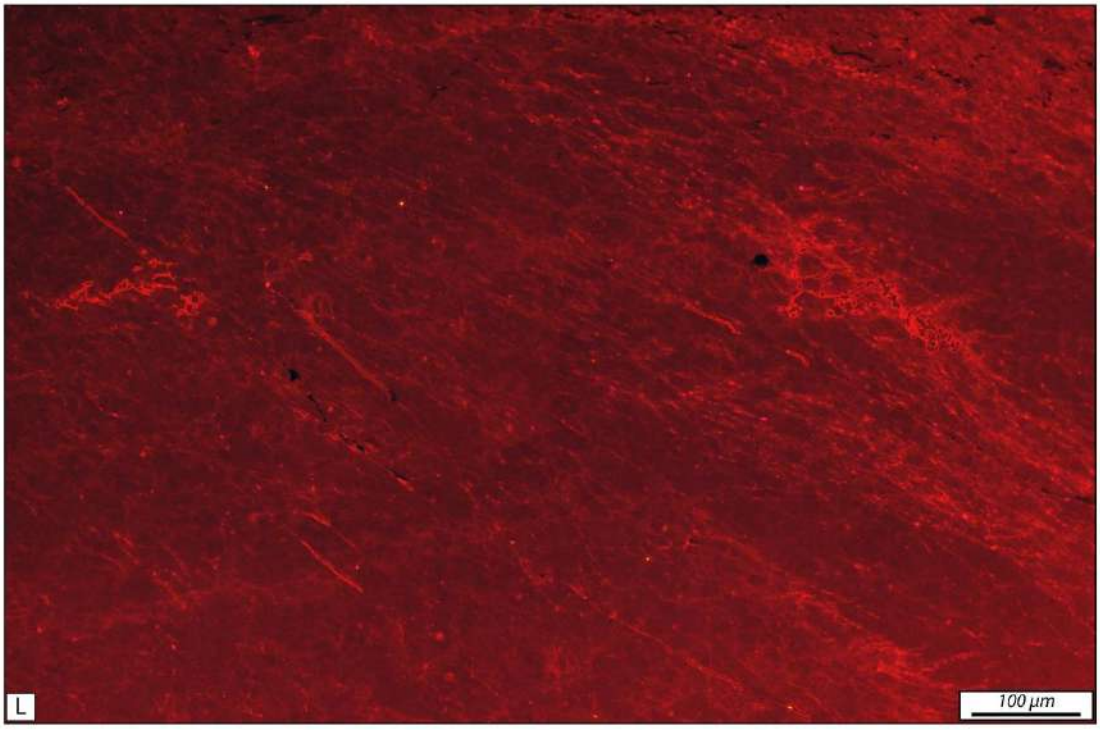
L
100 µm

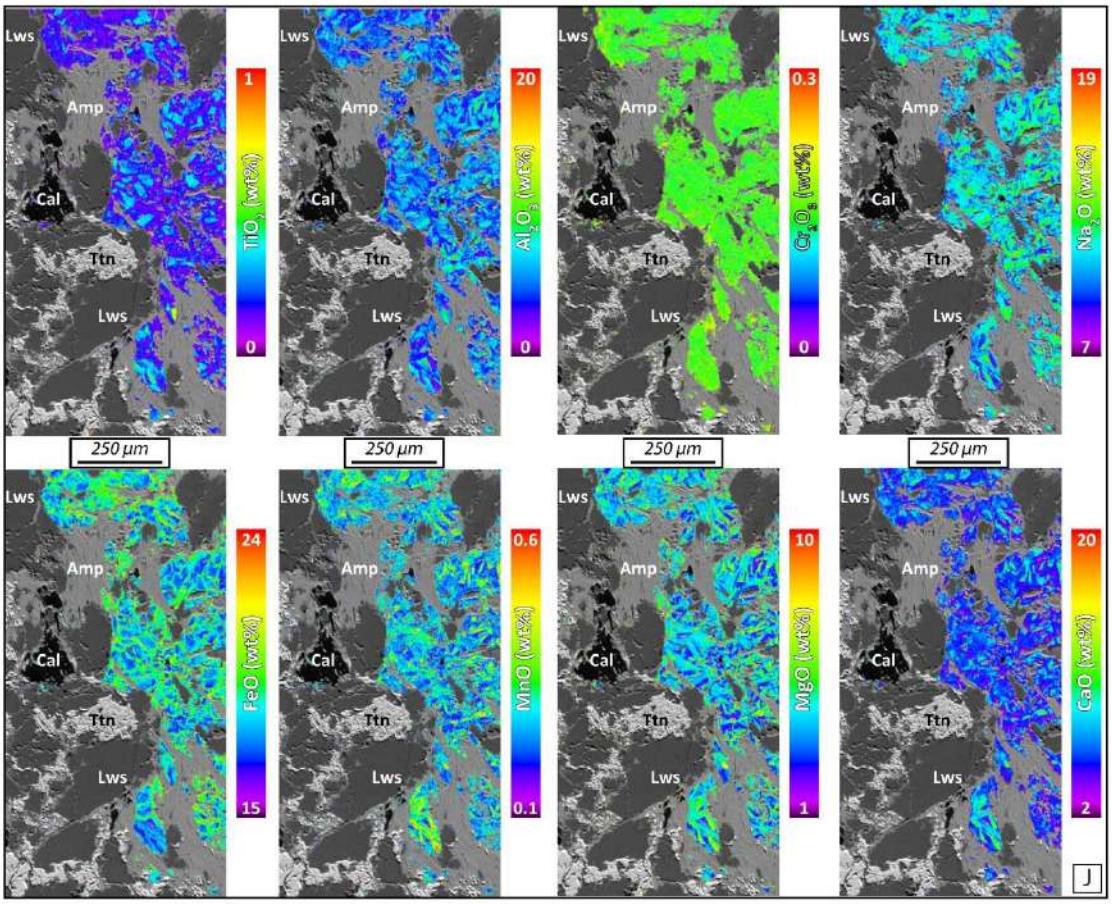

Figure 6.S1. Additional meso-scale (A, B and C), BSE (D and G), EDS (E, F and H), WDS (I and J; lawsonite and clinopyroxene, respectively) X-ray maps images, (K) photomicrographs and (L) CL mosaic images depicting the variety of encountered fabrics highlighting, in most cases, the occurrence of brittle and viscous features in the blueschist-facies and related chemical fingerprints.

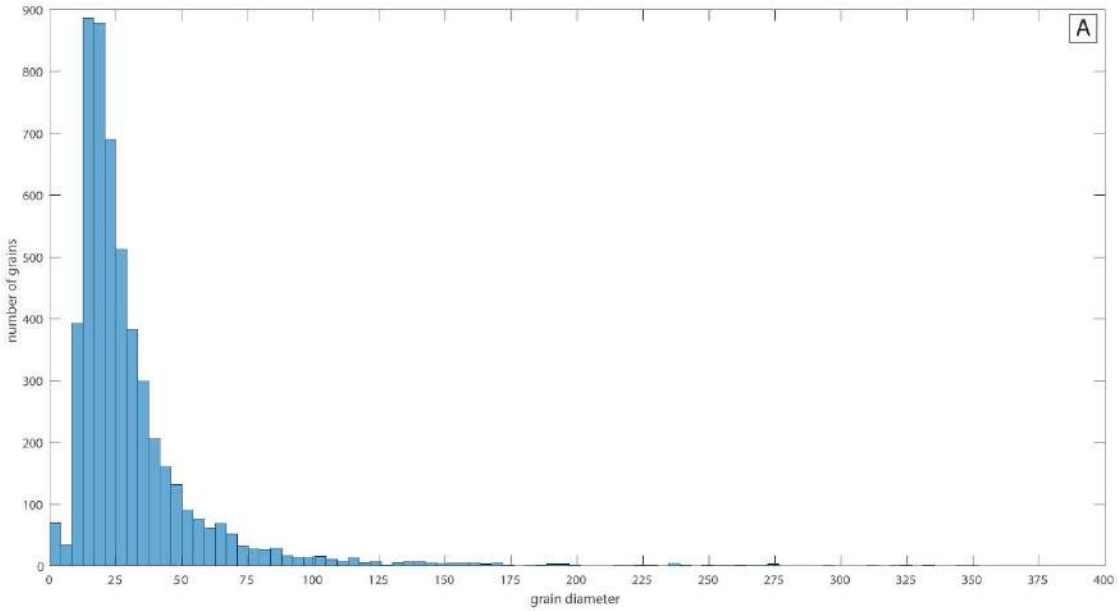
A
number of grains
grain diameter
0
100
200
300
400
500
600
700
800
900
0
25
50
75
100
125
150
175
200
225
250
275
300
325
350
375
400

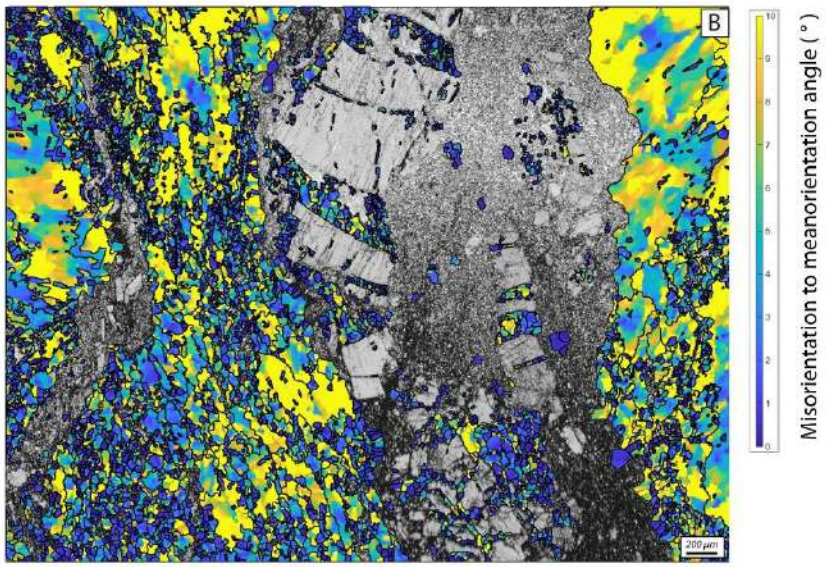
B
200 µm
Misorientation to meanorientation angle (°)

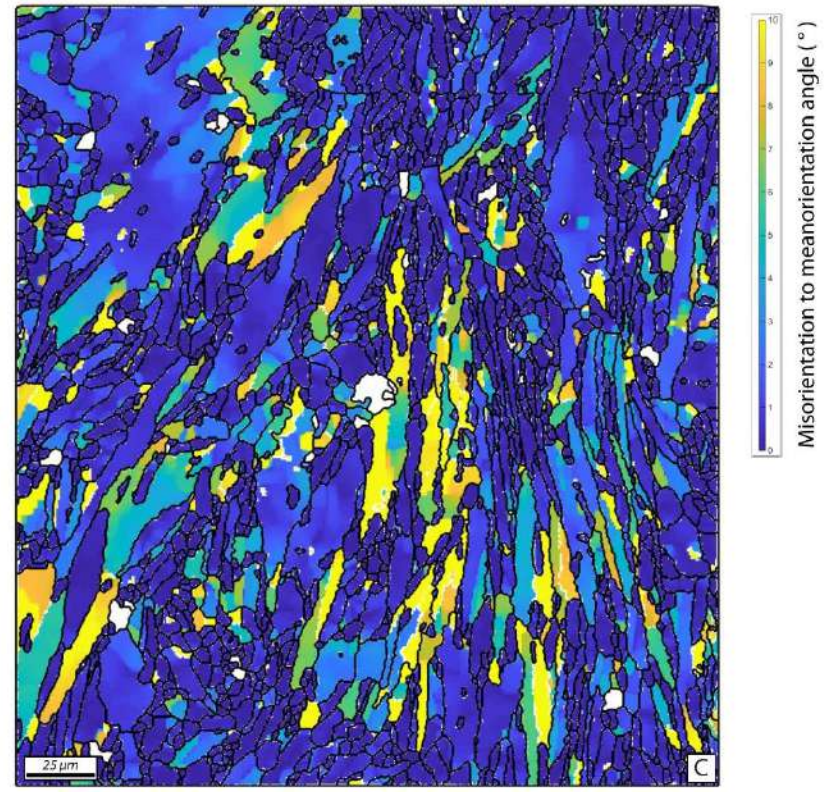
25 µm
C
Misorientation to meanorientation angle (°)

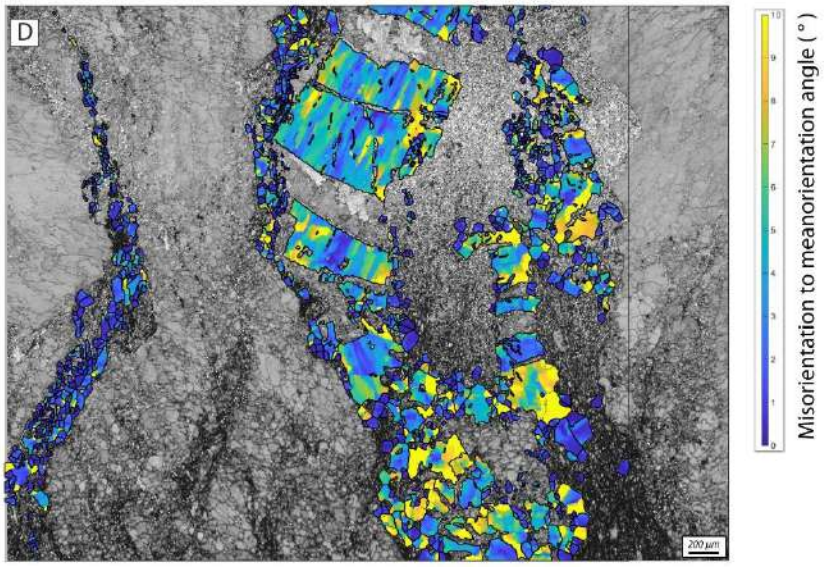
D
200 µm
Misorientation to meanorientation angle (°)

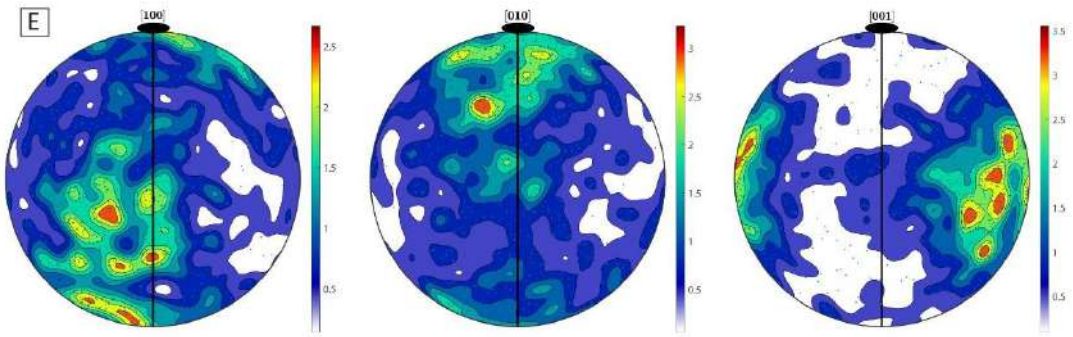

Figure 6.S2: Additional EBSD data for a representative lawsonite vein breccia and a Na-amphibole stripe. A. Histogram depicting quartz grain diameters. B to C. Misorientation to mean orientation maps for quartz, Na-amphibole and lawsonite. D. Pole figure for [100], [010] and [001] lawsonite crystallographic axis. Each data point represents the mean orientation of a crystal (one point per grain; 1116 lawsonite grains).

7. Blueschist-facies paleo-earthquakes in a serpentinite channel (Zagros suture, Iran) enlighten seismogenesis in Mariana-type subduction margins

Muñoz-Montecinos et al. (2021)

Blueschist-facies paleo-earthquakes in a serpentinite channel (Zagros suture, Iran) enlighten seismogenesis in Mariana-type subduction margins

Jesús Muñoz-Montecinos[1,2], Samuel Angiboust[1], Antonio Garcia-Casco[2,3]

[1] Université de Paris, Institut de physique du globe de Paris, CNRS, F-75005 Paris, France, jesus.munozmontecinos@gmail.com; angiboust@ipgp.fr

[2] Department of Mineralogy and Petrology, Faculty of Sciences, University of Granada, Campus Fuentenueva s/n, 18002 Granada, Spain, agcasco@ugr.es

[3] Instituto Andaluz de Ciencias de la Tierra, CSIC-Universidad de Granada, 18100 Armilla, Granada, Spain

Published in: Earth and Planetary Science Letters Volume 573, 20 November 2021, 117135

Reference: Muñoz-Montecinos, J., Angiboust, S., & Garcia-Casco, A. (2021). Blueschist-facies paleo-earthquakes in a serpentinite channel (Zagros suture, Iran) enlighten seismogenesis in Mariana-type subduction margins. Earth and Planetary Science Letters, 573, 117135.

DOI: https://doi.org/10.1016/j.epsl.2021.117135

Journal Impact Factor (IF): 5.255

WoS Quartile: Q1 (GEOCHEMISTRY and GEOPHYSICS)

ABSTRACT

The architecture and pressure-temperature conditions reached by a Cretaceous block-in-matrix serpentinite mélange exposed in the Zagros suture resemble those imaged in the active Mariana subduction zone. There, large magnitude-earthquakes (Mw>9) have never been recorded but smaller events – of poorly-constrained physical origin – in the range Mw~3-6 are widespread. Field and petro-structural constraints led to a first report of blueschist-facies seismic fault-related rocks in the Zagros serpentinite mélange, including breccias, foliated cataclasites and ultracataclasites; all observed within a foliated mafic metatuffaceous block embedded in serpentinite schists. Fine-scale petrological characterization of ultrafine-grained, fluidized cataclastic material reveals the presence of newly-formed glaucophane, lawsonite, phengite, albite and pumpellyite, an assemblage inferred (based on thermodynamic modelling) to have crystallized in the lower lawsonite-blueschist facies at ~0.6-1.0 GPa and 230-300 °C. Extensional veins containing similar mineral assemblages are observed crosscutting the aforementioned rocks but are also identified as comminuted fragments in all fault-related lithologies. Crosscutting relationships among the multiple generations of fluidized ultracataclasites and brecciated blueschists suggest that episodic faulting and hydrofracturing were contemporaneous processes at ~20-35 km depth, i.e., at similar conditions as reported for metabasalts expelled by Mariana serpentinite mud volcanoes. Mechanical modelling confirms that the studied fault-related features can only have formed under nearly lithostatic pore fluid pressure conditions, maintaining the system in a critically unstable regime that promoted recurrent seis-mic faulting, as monitored in the Mariana seismogenic zone. These fluids are likely associated with externally and deeply-generated fluid pulses that may have reached the seismogenic window, imprinting a Ta-Th-Nb-HREEs-enriched trace element signature. This new faulted blueschist occurrence highlights the physical nature and the mechanical processes operating within fluid-saturated fault zones in the serpentinized subduction channel.

Keywords: *Mariana-type margins; Blueschists; Earthquakes; Paleo-earthquakes; Ultracataclasites; Zagros suture*

7.1 Introduction

Mariana-type subduction settings are believed to represent the “aseismic”, non-accretionary end-member where moderate-magnitude seismicity is widespread but no large megathrust earth-quakes (Mw>9.0) are so far reported (e.g. Emry et al., 2011and references therein). This absence was explained by Hyndman et al. (1997) who suggested that a highly serpentinized mantle – thought to promote aseismic creep – intersects the plate inter- face at shallow depths inhibiting earthquake nucleation. Recently, Emry et al. (2011) and Eimer et al. (2020) challenged this hypothesis demonstrating that the seismogenic region of the Mari-ana subduction zone spans the depth range 10 to 60 km along a highly serpentinized region of the plate interface (Fryer et al., 2020), demonstrating that brittle deformation is actively occurring there. Emry et al. (2011) emphasized that the lack of large earthquakes along the Mariana margin is produced by frictional strength heterogeneities of the megathrust possibly associated with sub-ducting roughness, fluid overpressuring and serpentinization of the forearc mantle. In addition to moderate magnitude megathrust earthquakes, extensional seismicity is commonly observed in the outer rise region in the vicinity of the trench (Eimer et al., 2020) or as tensional normal-faulting in the subducting slab (Emry et al., 2011), possibly associated with gravitational slab pull and roll-back.

On a petrological perspective, rock fragments dredged from serpentinite mud volcanoes in the Mariana forearc preserve mineral paragenesis indicating lower blueschist-facies metamorphism (~150-250 °C at 0.5-0.6 GPa; Maekawa et al., 1993). Recent discoveries demonstrate that some of the blueschist fragments may have been buried to greater depths of ~50 km (590 °C at 1.6 GPa) before being exhumed (Tamblyn et al., 2019). These rock clasts were brought back to the surface through channel flow and serpentinite mud volcanism which is thought to be triggered by slab devolatilization and subsequent fluid flow along normal faults in the forearc (Fryer et al., 2020). These observations suggest that the Mariana forearc is extensively serpentinized and the ascent of fluidized serpentinite material (protrusion) and rare blueschist fragments is due to diapiric buoyancy forces associated with deep re-turn flow in an extensional regime (Maekawa et al., 2004). On-land fossilized analogues to Mariana-type serpentinite channel are exceptionally preserved in HP-LT suture zones where “mélanges” exhibit blueschist-facies metavolcanic (and metasedimentary) blocks wrapped by a serpentinite matrix. Some key localities correspond to the Franciscan complex (California, United States; Cloos, 1986; Grove and Bebout, 1995), the Kamuikotan belt (Hokkaido, Japan; Maekawa et al., 2004) and the herein studied Seghin complex (Soghan region, Iran; Muñoz-Montecinos et al., 2021).

Although most of the worldwide observed earthquake activity is reported in subduction zones (e.g., Scholz and Campos, 2012), evidence for localized slip at seismic rates from exhumed high pressure-low temperature (HP-LT) metamorphic complexes is extremely scarce (e.g., Austrheim and Andersen, 2004; John and Schenk, 2006). In the blueschist-facies, it is expected that the mechanical behaviour of the subducting slab is transitional between conditionally stable aseismic creep and unstable stick-slip faulting (Austrheim and Andersen, 2004; Behr and Platt, 2013; Angiboust et al.,

2015). Evidence for seismic faulting includes the formation of pseudotachylytes and/or fault gouges which are commonly found in dry crystalline rocks (Sibson and Toy, 2006; Bonnet et al., 2019). Recent studies arguing for pseudotachylyte formation in water-saturated fault zones demonstrate the presence of fluids during frictional melting/sliding processes (Meneghini et al., 2010; Menant et al., 2018), but the fluid-rock mechanical feedbacks during seismic slip remain to be better documented (Rowe et al., 2005; Di Toro et al., 2009; Fagereng et al., 2018). Even if elevated pore fluid pressures reduce the effective normal stresses promoting brittle faulting and inhibiting the formation of frictional melts (thermal pressurization and lubrication; Rice, 2006; Di Toro et al., 2009), the low shear stresses expected in subduction settings (e.g., Dielforder et al., 2020) suggest that the occurrence of fluidized fault gouges (e.g., fluidized ultracataclasites) are likely more representative of earthquakes in these environments (e.g., Ujiie et al., 2007; Meneghini et al., 2010).

We herein present a first report of fluidized fault rocks (cataclasites and ultracataclasites) interpreted to represent blueschist-facies paleo-earthquakes in mafic blueschists discovered in the Zagros suture (Seghin complex); a HP-LT mélange composed of blueschist blocks wrapped by a serpentinite matrix which presumably formed in a Mariana-type paleo-subduction margin (Muñoz-Montecinos et al., 2021). This work addresses water-saturated frictional sliding processes combining petro-structural observations with mechanical modelling and compares the observed structural features with what is currently being imaged and dredged in the active Mariana subduction margin.

7.2 Geological context of the Seghin complex

7.2.1 Regional background

The Soghan region exhibits the unique HP-LT remnants of the paleo-subduction zone between Eurasia and Arabia plates (Lower Cretaceous-Eocene) exposed now in the Zagros suture (***Fig.7.1A***; Delaloye and Desmons, 1980; Agard et al., 2006 and references therein). In this region, the uppermost Ashin complex represents a paleo-accretionary system (comprising ultramafic domains) metamorphosed at amphibolite-facies conditions during middle Cretaceous times, followed by blueschist-facies overprinting (Angiboust et al., 2016). While the lowermost Siah-Kuh massif has been characterized as a former seamount subducted down to lower blueschist-facies conditions during Upper Cretaceous times (Bonnet et al., 2019, 2020). We focus here on the Seghin complex (***Fig.7.1B***), a km-thick tectonic sliver structurally sandwiched between the Ashin and Siah-Kuh complexes, composed of blueschist blocks embedded in a serpentinite matrix. Peak metamorphic conditions of 1.5-1.8 GPa (~430-530◦C; ***Fig.7.1C***) at ~62-75 Ma are recorded by some of the mafic blocks (Sabzehei, 1974; Angiboust et al., 2016). Overall, petrological investigations demonstrate that the tectonic slices exposed in the Soghan region record contrasted P-T-time metamorphic paths documenting the cooling of the subduction thermal gradient from ~17 down to 7 °C/km from ~95 to 65 Ma (Angiboust et al., 2016; ***Fig.7.1C***).

7.2.2 Geology of the Seghin complex

The Seghin complex is composed of a moderately dipping antigorite-rich ultramafic schistose matrix wrapping stiffer, metre to hectometre-sized, blueschist tuffaceous blocks showing a sub-vertical main foliation striking ENE-NE (***Fig.7.1B***; see also Sabzehei, 1974). In the serpentinites, no remnant of the ultramafic protolith is observed while the lithological contacts with the blueschist blocks are generally sharp and devoid of blackwall rinds. The blueschist blocks are mainly fine-grained glaucophane-, lawsonite-and jadeitic-omphacitic clinopyroxene-bearing rocks (Angiboust et al., 2016). The same index phases are present in prograde, centimetre-wide metamorphic veins that follow or crosscut the main foliation, while aragonite occurs as vein-filling material in hydraulic breccias. It is worth mentioning that these veins are highly strained due to burial-related shearing according to the main foliation (Muñoz-Montecinos et al., 2021). Minor metasedimentary material is present as isolated blocks or interlayered within blueschists, mostly in the basal part of the Seghin complex.

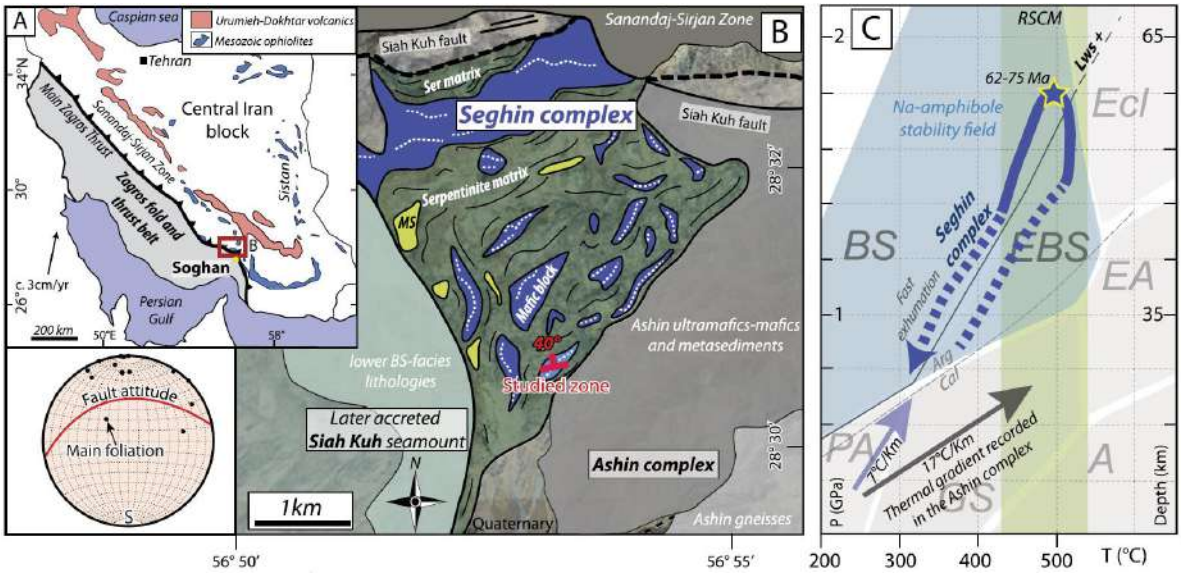

Figure 7.1. A. Regional geological map of southeastern Iran showing major geological features (modified from Angiboust et al., 2016). B. Local geological map of the Soghan region emphasising the Seghin complex fabric (modified from Angiboust et al., 2016). The lower hemisphere equal area stereographic projection depicts main foliation and studied fault attitudes. C. Pressure-Temperature (P-T) diagram showing the path followed by the upper blueschist-facies blocks from the Seghin complex together with Raman spectroscopy of carbonaceous material (RSCM) temperatures (after Angiboust et al., 2016). Peak conditions for the adjacent Ashin complex as well as inferred subduction thermal gradients are shown for comparison. For further details regarding phase stabilities and facies subdivision the reader is referred to Evans (1990) and Angiboust et al. (2016). MS—metasediment; Ser—serpentinite; BS—blueschist; A—amphibolite-facies; BS—blueschist-facies; EBS—epidote blueschist-facies; EA—epidote amphibolite-facies; Ecl—eclogite-facies; GS—greenschist-facies; PA—pumpellyite actinolite-facies. Mineral abbreviations used along this paper are: Ab—albite; Act—actinolite; Amp—amphibole; Cal—calcite; Cb—carbonate; Chl—chlorite; Chm—chamosite; Clc—clinochlore; Cpx—clinopyroxene; Ep—epidote; Fac—ferro-actinolite; Gln—glaucophane; Jd—jadeite; Lws—lawsonite; Or—orthoclase; Pmp—pumpellyite; Ph—phengite; Py—pyrite; Qz—quartz; Ttn—titanite.

7.3 Field observations on fault-related rocks

In the studied area (***Fig.7.1A***), an elongated block of blueschist occurs in direct and sharp contact with the surrounding antigorite schist matrix (***Fig.7.2A*** and ***B***). The latter also enclosing further dismembered blueschist fragments and showing cataclastic fabrics such as reworked serpentinite and vein fragments in the foliated serpentinite matrix (***Fig. 7.S1A***). These brittle networks are difficult to follow at several metres scale, due to the strong weathering of the soft serpentinite. A brittle fault zone (up to 4 m-wide but variable along strike) crosscuts at high angle the studied well-foliated hectometre-sized blueschist block from the mélange (***Fig.7.2A, C*** and ***7.S1B***). In the damage zone of this fault network, the most common lithology is a chaotic blueschist breccia including unsorted, up to tens of centimetre-wide angular to rounded blueschist and vein fragments enclosed in a very fine-grained foliated cataclastic matrix (***Fig.7.2D*** and ***E***). A precise localization of the fault core was not possible. Brittle deformation was accompanied by extensive grain fragment rotation as evidenced by the mismatch between foliated fragments and their respective counterparts (e.g., ***Fig.7.2E***). The slip boundaries between pristine and brecciated blueschists are sharp and subplanar (e.g., ***Fig.7.2C*** and ***7.S1C***), while brecciation intensity increases towards a discontinuously exposed fault core. At the meso-scale, shearing-related brecciation appears to be post-dated by further ductile shearing as evidenced by the development of a foliation within the matrix surrounding fragments. Extensional veins containing albite, glaucophane, lawsonite, phengite and pumpellyite crosscut pristine non-brecciated blueschist domains (e.g., ***Fig. 7.S1C***). Remnants from the same vein set are also found as breccia clasts within adjacent brecciated domains (***Fig.7.2E*** and ***7.S1C***). Unlike higher grade prograde blueschist-facies veins showing shearing-related deformation parallel to the main foliation (Muñoz-Montecinos et al., 2021), the veins reported in this study developed as purely extensional structures devoid of vis-cous features.

Cohesive, ultrafine-grained zones with a darkish satin appearance (hereafter referred to as ultracataclastic veins) are associated with brecciated blueschists within the central region of the fault zone. These veins, that resemble pseudotachylytes (e.g., Lin, 2007), crosscut the host blueschist (***Fig.7.2F***) and more commonly the breccias as thin injection (<5 mm-wide) or fault veins (<3 cm-wide), the latter with planar slip boundaries (***Fig.7.2F, 7.3A, B*** and ***C***). Several layers of fault-related material commonly exhibit flow textures and streaks (***Fig.7.3B*** and ***C***). Note that reworked ultracataclastic veins are observed as fragments in the brecciated domains (***Fig.7.3A***).

7.4 Microstructures and mineral chemistry

Petrographic observations and petro-geochemical analyses, including thermodynamic modelling, on ultracataclastic veins, brecciated blueschists and extensional vein material have been per formed using (i) scanning electron microscope in back-scattered (SEM-BSE) and energy dispersive X-ray spectroscopy (EDS; including X-ray maps and estimates of the chemical composition of large scanned surfaces) modes, (ii) electron probe microanalyzer (EPMA; including defocused beam surface estimates), (iii) powder X-Ray diffractometry (XRD), (iv) in situ laser ablation-inductively coupled plasma-mass spectrometer (LA-ICP-MS) and (v) Perple_X software (version 6.8.9). Details of the analytical techniques, parameters and software used are outlined in the supplementary material.

Micro-scale observations show that the fault breccia is com-posed of blueschist clasts and extensional vein fragments (***Fig.7.4A***) enclosed in a very fine-grained foliated comminuted matrix (mostly <30 μm in diameter; ***Fig. 7.S2A*** and ***7.S2B***). The blueschist clast morphologies are subangular, containing mainly glaucophane (locally exhibiting actinolitic cores and/or rims) and pumpellyite (>50 vol.%) and minor lawsonite, phengite, chlorite, winchite, titanite and albite. The same mineralogy is present in the pristine foliated host blueschists and in the comminuted matrix, but chlorite and winchite are absent in the latter (***Fig.7.4B***). In addition, Si-rich phengite (up to 3.7 a.p.f.u.; ***Fig.7.5A***), glaucophane and albite fringes occur in the interclast breccia matrix (***Fig.7.4A***). Such features are not observed in the blueschist host, which is mostly devoid of phengite and albite, indicating that the phase assemblage distributions cannot be envisioned by clast comminution alone, but involved the formation of new minerals. Note that structurally similar foliated cataclasites and blueschist breccias have been observed upstream in other high grade blocks, that contain abundant lawsonite and clinopyroxene and only very minor pumpellyite. In the studied locality, carbonate- and silicate-rich lawsonite-bearing vein fragments and vugs occur, the latter characterized by highly rounded and irregular morphologies apparently devoid of cataclastic imprint, likely representing crystallized fluid-filled cavities present during comminution (***Fig.7.4C***). Glaucophane-lawsonite-phengite-bearing albite-rich vein clasts, identical in mineralogy to the aforementioned extensional veins, also occur in the fault breccias beside blueschist clasts. The contact between the brecciated blueschist domains and the ultracataclastic veins is sharp and clean (***Fig.7.3D*** and ***7.4A***).

The ultracataclastic veins consist of several layers of dark-shaded regions (hereafter referred to as Brown and Black regions, respectively; see ***Fig.7.3D***) separated by sharp, subplanar slip boundaries (***Fig.7.3B*** and ***D***). Flow textures and streaks of alternating Black and Brown ultracataclastic vein materials are distinguishable and oriented subparallel to the slip surfaces crosscutting the brecciated blueschist domains. In general, the Black regions are located in the host-vein margins whereas the Brown layers are concentrated in the central part of the veins (***Fig.7.3B*** and ***D***), the latter being commonly intruded by the former. The Brown regions are dominated by micrometreto submicrometer-sized pumpellyite and glaucophane, the latter partly replaced by actinolite and phengite are found as newly formed grains that overgrow the ultracomminuted matrix and cement

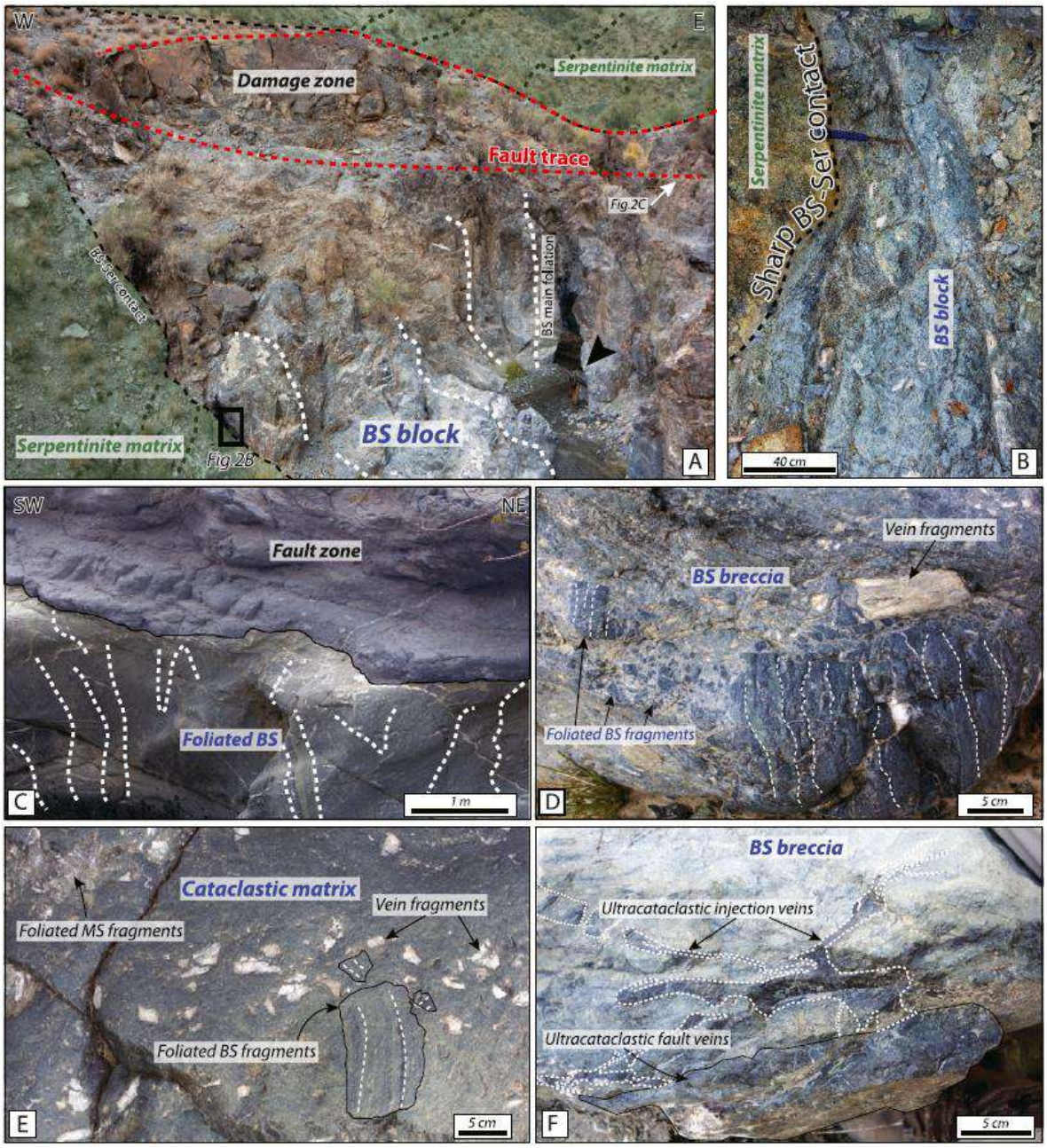

Figure 7.2. Field pictures of the investigated fault zone from the Seghin complex. A. General view of the studied blueschist block surrounded by serpentinite matrix. Note the fault features in the upper part of the image and the width (≤4 m) of the well-preserved fault zone. Black arrow pointing to a geologist for scale. B. Detailed view of the sharp blueschist block-serpentinite matrix contact. C. Crosscutting relationships between the fault zone and the pristine foliated blueschist block. Note how the fault crosscuts at high angle the main blueschist foliation. D. Blueschist breccia. E. Blueschist chaotic breccia showing highly angular and foliated blueschist, albite-glaucophane-phengite-bearing vein and metasedimentary fragments. F. Ultracataclastic injection and fault vein structures in a blueschist breccia. BS—blueschist; MS—metasediments.

interstices between larger fragmented grains. Irregular albite aggregates and clasts from former vein material are often associated with strain caps and shadows, the latter containing anhedral to euhedral fine- to very fine-grained glaucophane and pumpellyite (***Fig.7.3D*** and ***7.4D***). In addition, some

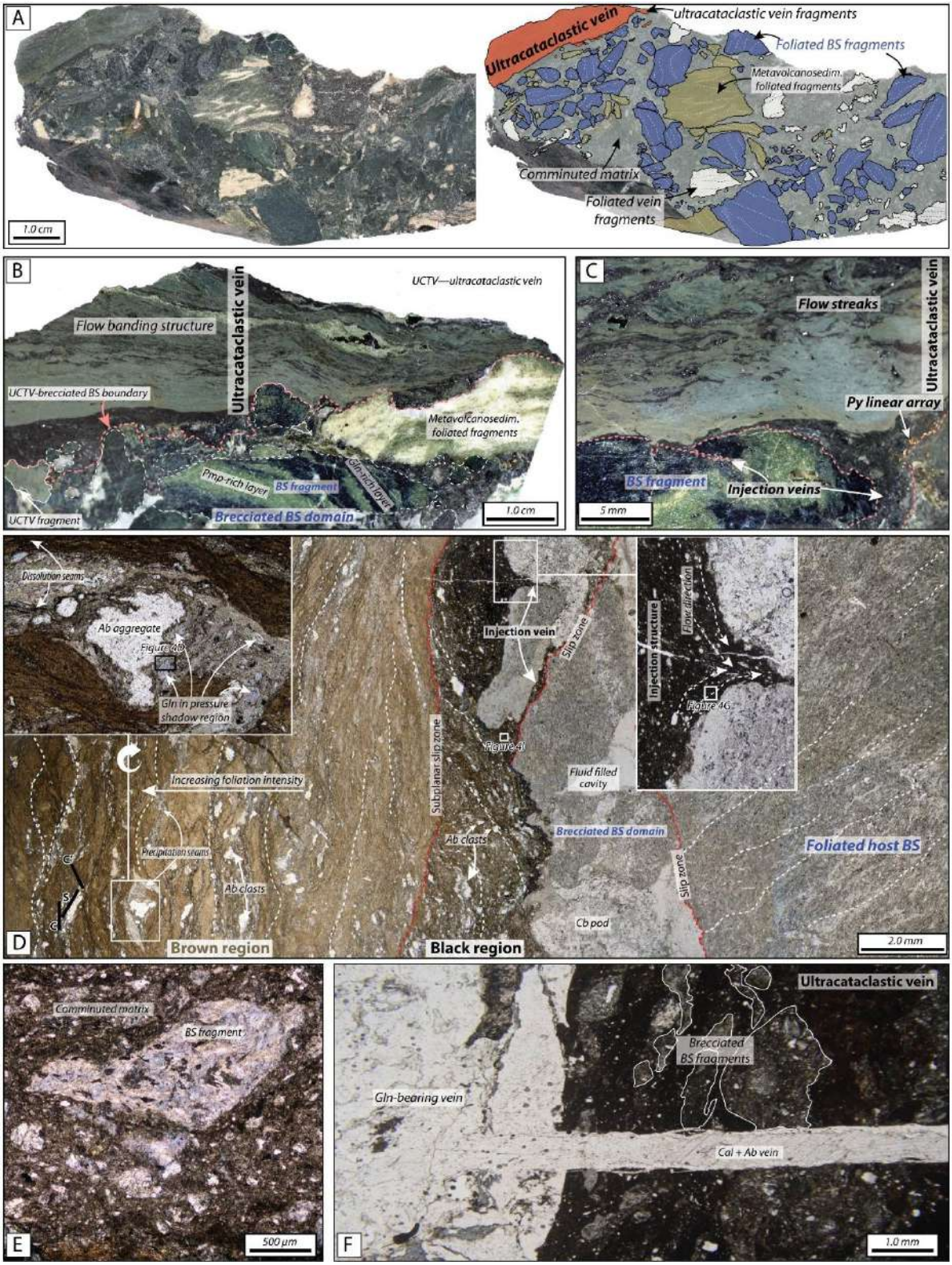

Figure 7.3. Polished rock slab pictures (A to C) and thin section views (D to F) of representative samples from the Seghin complex fault zone. A. Complex brecciated blueschist showing a variety of fragments and a crosscutting ultracataclastic vein; reworked fragments of the ultracataclastic vein are also present as clasts in the breccia. The right-hand panel is a schematic representation emphasizing relevant features. Note that millimetres-wide ultracataclastic vein fragments have

been reworked and incorporated in the brecciated region. B. Picture highlighting the ultracataclastic vein-breccia contact and related surrounding features. C. Detailed picture of the ultracataclastic injection vein fabrics. Flow streaks of fault gouge materials as well as linear arrays of sulfides are visible. D. photomicrograph showing representative structural features of a brecciated blueschist and an ultracataclastic vein. Note the presence of (i) different layers of fault gouge material, (ii) mylonitic deformation, including S-C-C' fabrics, within the Brown regions, (iii) black dissolution and pale green precipitation seams, (iv) sharp slip boundaries between fault gouge material and against the brecciated domain, (v) injection and flow textures, (vi) albite-glaucophane-phengite (±lawsonite)-bearing vein fragments, (vii) sharp slip surfaces between brecciated and pristine blueschist and (viii) a pristine foliated blueschist host. E. Blueschist fragments incorporated into an ultracataclastic vein. F. Albite-glaucophane-phengite-bearing extensional vein crosscutting an ultracataclastic vein. Metavolcanosedim.—metavolcanosedimentary; UCTV—ultracataclastic vein. (For interpretation of the colours in the figure, the reader is referred to the web version of this article.)

mineral fragments can also be present in the pressure shadow regions. These viscous patterns are better developed towards the internal region of the ultracataclastic veins where S-C-C' fabrics are present (e.g., ***Fig.7.3D***). Rare rounded and sub-elongated vugs containing pumpellyite, albite, glaucophane and lawsonite are observed (***Fig.7.4E***). Such domains may also represent minerals precipitated in fluid-filled pockets from former free fluids present during cataclasis. Note that lawsonite in the Brown region matrix has not been detected using X-ray diffraction techniques (***Fig. 7.S3C***), although it has been rarely observed in vugs.

In Black regions (***Fig.7.3D***), millimetres-wide injection structures occur infiltrating the brecciated blueschist domains and developing flow structures composed of (i) submicrometre, irresolvable material, (ii) ultracomminuted or embayed glaucophane, lawsonite, albite, phengite, pumpellyite and titanite fragments (***Fig.7.4H, 7.S2D*** and ***E***), (iii) millimetres-wide albite-rich vein clasts similar to those observed in the host blueschist breccias, (iv) millimetres- to micrometres-wide albite crystals or aggregates in the matrix, commonly associated with newly formed, post-comminution anhedral to euhedral glaucophane, lawsonite and Si-rich phengite (3.5 to 3.7 a.p.f.u.; ***Fig.7.4F, G, 7.5A*** and ***7.S2C***) and (v) lawsonite overgrowths along fractured albite grains and/or albite cleavages as well as replacement of lawsonite by albite (***Fig.7.4G*** and ***I***). These mineral occurrences were confirmed by X-ray diffraction analysis as shown in ***Fig. 7.S3B***. We note that newly formed glaucophane shows retrograde features such as actinolite rims and pumpellyite needles (***Fig.7.S2D***). These faulting-related textures (including the breccia matrix) have been affected by subsequent viscous deformation and development of a foliation (e.g., ***Fig.7.3D, 7.S2A*** and ***7.S2B***). Millimetres-wide blueschist breccia and pristine blueschist fragments can be seen incorporated in the ultracataclastic veins (***Fig.7.3E*** and ***F***). The brecciated domains of the damage zone are in sharp and subplanar contact with the pristine well-foliated blueschists as well as with the ultracataclastic veins (***Fig.7.3D***). Last, some post-faulting extensional glaucophane- and (Si-rich) phengite-bearing, albite-rich veins crosscut all the forementioned fault-related features (***Fig.7.3F***).

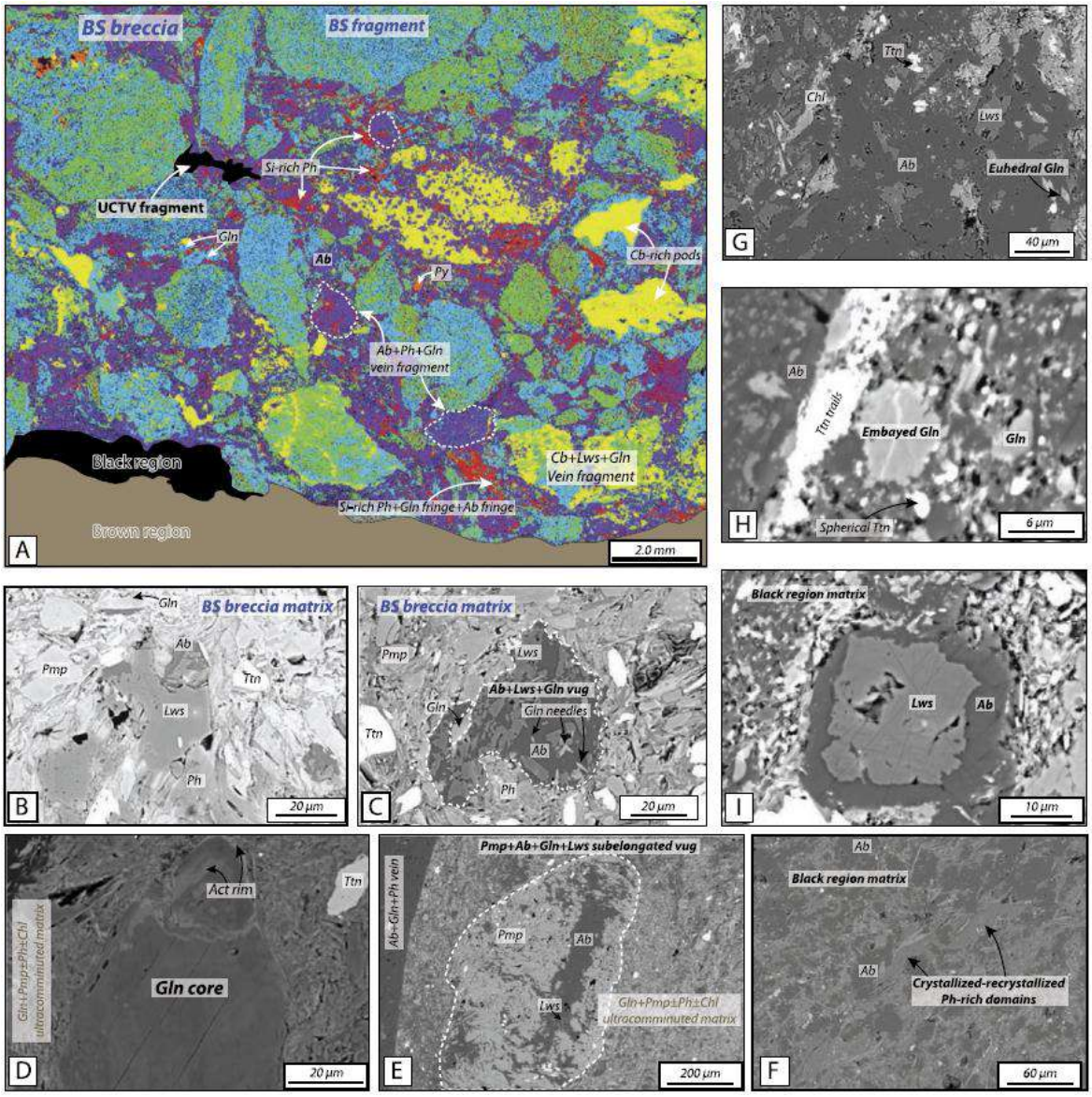

Figure 7.4. A. Map image of selected phases from a blueschist breccia based on energy-dispersive X-ray (EDS) spectroscopy. The bottom part of the image has been masked out since the grain size is extremely fine and mineral identification is not possible at the ultracomminuted scale of the ultracataclastic veins. Note the presence of (i) a variety of clasts characterized by subrounded and subspherical morphologies, (ii) fringes filled by albite and Si-rich phengite, (iii) vein fragments (delineated by dashed white lines) and (iv) vugs that lack cataclastic imprints. Electron backscattered images (B to I). B. Image showing the ultracomminuted interclast matrix in the blueschist breccia. Note the highly angular crystal morphology. C. Subrounded vug filled by albite, lawsonite and glaucophane needles surrounded by ultracomminuted material. D. Pressure shadow domain from the Brown region around an albite aggregate as depicted in Fig.7.3D. E. Elongated and rounded pumpellyite, albite and lawsonite vug in the Brown region. Note that pumpellyite crystals are elongated perpendicular to the margins (towards the centre of the vug; syntaxial growth) while albite and lawsonite are almost exclusively occurring in the vug centre. F. Black region microdomain composed mainly of newly formed or recrystallized albite and phengite. G. Black region microdomain composed of newly formed or recrystallized albite, glaucophane, pumpellyite, lawsonite and chlorite. H. Embayed and ultracomminuted glaucophane grains and titanite trails immersed in an albite matrix from the Black region. I. Replacement texture of a lawsonite grain rimmed by albite in the ultracomminuted Black region. (For interpretation of the colours in the figure, the reader is referred to the web version of this article.)

7.5 Geochemistry

Composition-space analysis of SEM and EPMA surface chemical estimates show that Brown regions compositions are comparable to those of pristine blueschist samples and breccia fragments (***Fig.7.5B***). The ACFN projection indicates that Brown region bulk compositions can well be explained by an assemblage dominated by pumpellyite and Na-amphibole with minor phengite and chlorite (brown tie-tetrahedron in ***Fig.7.5B***). On the other hand, the composition of the Black regions is clearly displaced towards albite, reflecting enrichments in Al_2O_3 and Na_2O components, and can be explained by the lawsonite-glaucophane-albite-phengite mineral assemblage (grey tie-tetrahedron in ***Fig.7.5B***), in agreement with the observed parageneses.

Rasterized LA-ICP-MS results on the different studied domains are shown in the spider diagram from ***Fig.7.5C***, normalized to the averaged pristine blueschists and host fragments (hereafter referred to as average blueschist). The Brown regions trace element patterns are characterized by negative anomalies in Rb, Tl and in most Light Rare Earth Elements (LREEs), whereas elements such as Ta, Th, Sr, Nb, Y, Cu, P and Heavy Rare Earth Elements (HREEs) are enriched relative to the host pristine and brecciated blueschists. Unexpectedly, somewhat different trends are observed in the trace element patterns from the Black regions. The most important anomalies correspond to markedly higher contents of Cs, Rb, Ta, Th, U, Nb, Cu and P relative to the average blueschist.

7.6 Discussion

7.6.1 P-T conditions of faulting

Field and petrological characterization (this study), together with previous thermometric results (Agard et al., 2006; Angiboust et al., 2016), indicate that the Seghin complex formed by the gathering of lenses with resolvable P-T differences (~150 °C and several kilobars) in a serpentinite channel. The fault zone and the host blueschist investigated here reveal the occurrence of lawsonite blueschist-facies mineral associations characterized by glaucophane, pumpellyite, lawsonite, Si-rich phengite and albite.

P-T conditions of faulting are evaluated through thermodynamic modelling in two domains corresponding to the Black and Brown regions. This approach is assumed to be valid in the host blueschist since the pumpellyite and glaucophane-rich domain compositions are virtually identical to that of the Brown regions (e.g., ***Fig.7.5B***). The chemical compositions were acquired after averaging defocused beam surface estimates in the system Na_2O-CaO-K_2O-FeO-MgO-Al_2O_3-SiO_2-H_2O-O_2 (***Table S2***). Both pseudosections were computed in the range 200 to 500 °C and 0.2 to 1.5 GPa under water-saturated conditions. Selected solid solution models are summarized in ***Table S3***. For the following pseudosection analysis, we only consider observed and measured mineral assemblages and their mineralogical and chemical composition of newly formed/recrystallized domains. The purpose of this approach is to roughly constrain ambient P-T conditions of faulting rather than potential – although unlikely – flash heating temperatures reached during fast slip. In the Black regions, natural mineral occurrences and abundances are in relatively good agreement with the calculated field

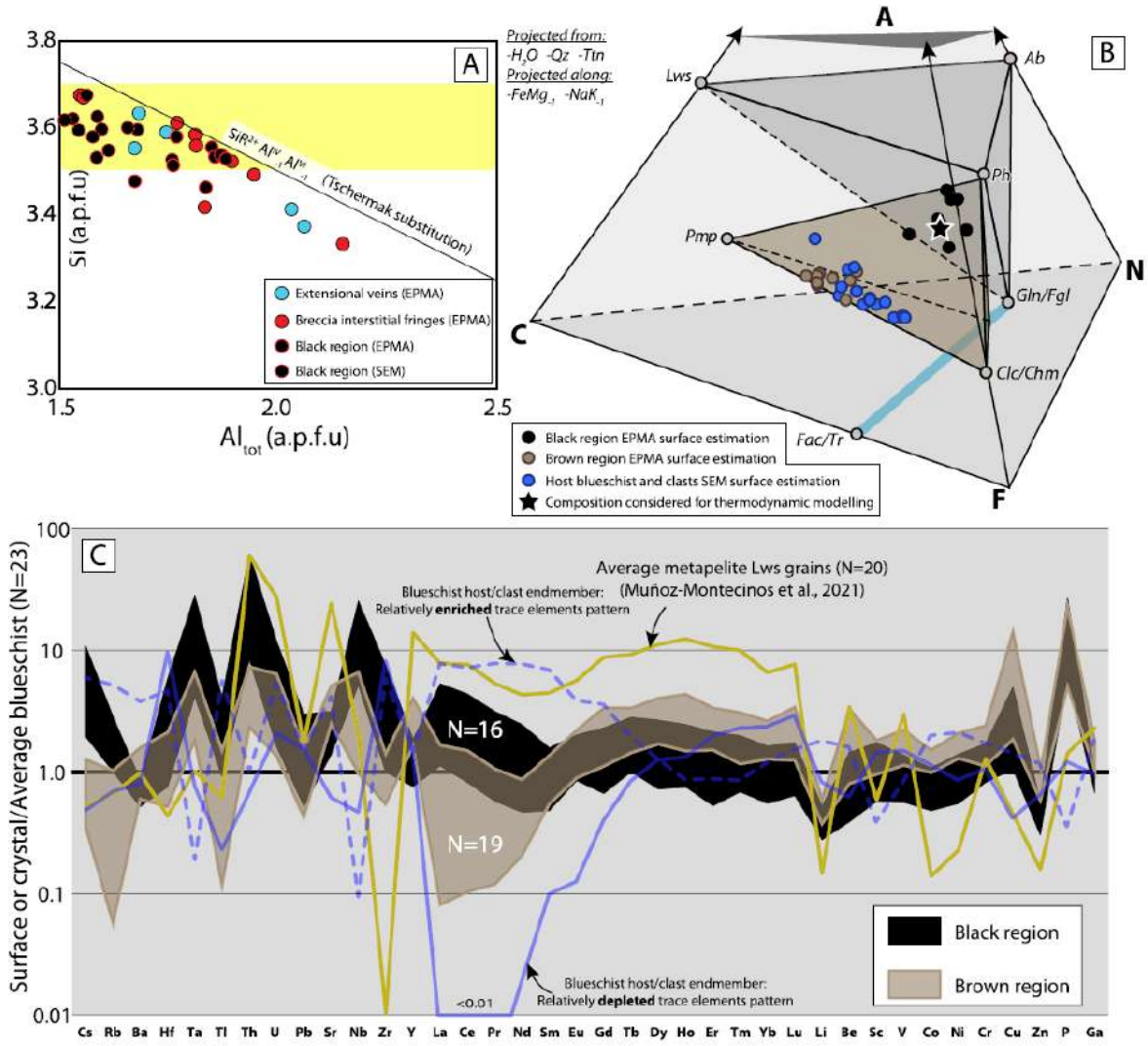

Figure 7.5. A. Altot (a.p.f.u.) vs. Si (a.p.f.u.) in phengite from the Black regions, extensional albite-rich veins and breccia interclast fringes. SEM analyses with the best stoichiometric formula were selected. B. ACFN tetrahedral diagram projected from the phases and exchange vectors indicated. The chemical compositions used in this study were estimated by EPMA and SEM surface analysis (see methods section for details). This methodology is notably advantageous in highly heterogeneous rocks. Note that neither albite nor lawsonite are considered in the Brown region assemblage since these phases are derived from comminution or represent isolated vugs domains, respectively. C. In situ LA-ICP-MS trace element composition diagram of Black and Brown regions from ultracataclastic veins normalized to average pristine blueschists/clasts. The latter is obtained after averaging the results from the studied samples: SO1877 and SO1877.1. In addition, an average of 20 analysed metapelite-hosted lawsonite crystals from Muñoz-Montecinos et al. (2021) are shown for comparison and assumed to represent a metasedimentary signature since they are the main carriers of REEs, Th, U and Sr in such rocks. The bold and dashed blue patterns represent highly enriched and depleted blueschists host and clast endmembers. The number of analyses for each domain is 23, 16 and 19 for the blueschists, Black and Brown regions, respectively. (For interpretation of the colours in the figure, the reader is referred to the web version of this article.)

predicting major amounts of albite and Na-amphibole together with moderate lawsonite, phengite (~70 vol.%; see ***Fig.7.6*** for details), clinopyroxene and minor quartz. Glaucophane composition predicted in the pseudosection is analogue to measured compositions of Na-amphibole (***Table S1***). Calculated Si-in-phengite isopleths intersect the best-fit field as shown in ***Fig.7.6***, in agreement with measured crystals (see ***Fig.7.5A*** and ***Table S1***). In addition, the occurrence of lawsonite and albite

and the lack of peak pumpellyite and actinolite in the Black regions, allow us to infer faulting conditions in the range of 0.6-1.0 GPa and 230-300 °C (lower blueschist-facies). A retrograde stage associated with final exhumation is characterized by the occurrence of thin actinolite rims around glaucophane and pumpellyite aggregates (± albite) which likely took place below the Na-Amp-in curve, in the pumpellyite stability field (***Fig.7.6***). A similar approach applied in the Brown regions domain yields similar faulting metamorphic conditions in the range 0.6-1.0 GPa and 280-300 °C (***Fig. 7.S3A***).

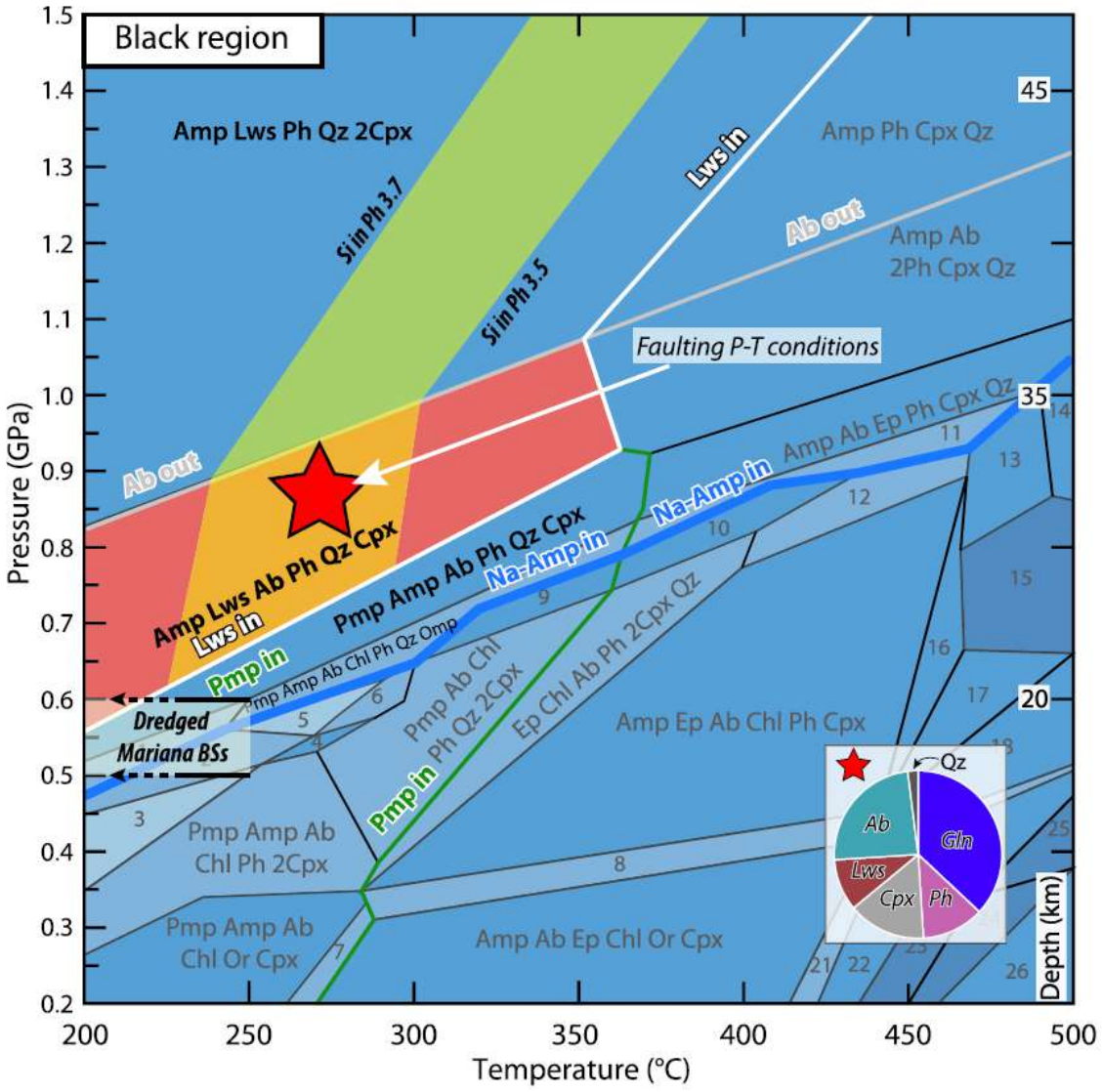

Figure 7.6. Pseudosection for the Black regions composition. The red fields highlight the best-fitting mineral assemblages and abundances. The yellow area corresponds to Si-in-phengite isopleths of 3.5 to 3.7 (see Fig.7.5A). Pie-chart shows mineral modes (in vol.%) at the P-T conditions indicated by the red star. However, the actual faulting conditions are depicted by the intersection between Si in phengite isopleths and the red field. Dredged Mariana blueschist field represents inferred P-T conditions from Maekawa et al. (1993). Relevant reaction curves are marked as thick coloured lines. Parageneses in the fields marked with numbers are detailed in a table in Fig.7.S3.

This approach is subject to uncertainties inherent to the former ultracataclastic processes, namely, the mixing of material that is originally not in thermodynamic equilibrium. Nevertheless, as stated previously, our calculations consider microdomains in which apparently newly formed (or recrystallized) grains occur implying – at least – local equilibrium. In addition, our thermo-dynamic calculations predict the occurrence of peak clinopyroxene and minor quartz which were not observed in the natural samples. This discrepancy may derive from slight imprecision in effective bulk composition, but other factors such as uncertainties in the solution models, fluid composition and/or oxygen fugacity may also have an effect. In the host blueschist, the occurrence of minor amounts of lawsonite may indicate slightly higher peak pressure conditions or little imprecision in the modelled bulk composition. Overall, the relatively good agreement between observed and predicted mineral paragenesis (e.g., Evans, 1990) confirms the relative robustness of the inferred P-T conditions for the fault rocks.

In addition to pseudosection modelling, inferred HP-LT conditions of faulting are supported by (i) the presence of Si-rich phengite and glaucophane as fringes and lawsonite-bearing vugs in the matrix of blueschist breccias (interpreted as minerals precipitated from HP fluids in fault zone porosity), (ii) the growth of newly formed, euhedral glaucophane and lawsonite in ultracataclastic vein fluid-filled vugs and (iii) mutually crosscutting-reworking relationships between faulting-related ultracataclastic veins and glaucophane-phengite-bearing extensional veins. The resulting P-T conditions are interpreted as the crystallization and/or recrystallization of the fluidized fault gouge material right after seismic sliding (see below) in the lower blueschist-facies. Such features were progressively obliterated by ongoing viscous shearing (e.g., Lin, 2007) as evidenced by the occurrence of solution seams and pressure shadows filled by glaucophane and pumpellyite, indicating HP-LT conditions during dissolution-precipitation processes. Thus, brittle faulting, extensional hydrofracturing and viscous creep all coevally occurred in the depth range 20-35 km, as illustrated in ***Figs.7.7*** and ***7.8***.

7.6.2 Deciphering deformation and fluid circulation processes

Close spatial associations between ultracataclastic veins and brecciated blueschists (***Fig.7.2B***) and the occurrence of reworked ultracataclastic vein fragments in breccias, witness for an episodic nature of faulting resulting in the formation of a large palette of rock fabrics and structures. The intrusive character of ultracataclastic veins, as well as the occurrence of flow and injection fabrics are features known in pseudotachylytes and fluidized ultracataclasites reported in other paleo-subduction environments (e.g., Rowe et al., 2005; Meneghini et al., 2010). Whichever the case, fast, seismically-generated events seem the best candidates to account for such structures (Rice, 2006; Ujiie et al., 2007; Lin, 2011; Rowe and Griffith, 2015). Although X-ray diffraction patterns and microscopic observations show that ultracomminuted crystalline material is the main constituent of the ultracataclastic veins, the shape of their diffraction base lines at low angles (***Fig. 7.S3B*** and ***S3C***) together with the presence of (i) embayed grains, (ii) pyrite and Ti-oxides trails and (iii) elongated and rounded fluid-filled vugs similar to amygdules (***Fig.7.3C, 7.4E, 4G, 4H*** and ***7.S2E***), may indicate that some melt could have formed during frictional sliding (Magloughlin and Spray, 1992; Rowe et

al., 2005; Lin, 2007; Meneghini et al., 2010). Recently, similar features have been observed in shallower environments and interpreted as former melt products (pseudotachylytes; see Ujiie et al., 2021). However, we cannot unequivocally establish that a frictional melt has been once present in the studied fault zone.

The ultracomminuted material appears to have behaved as a fluidized fluid-solid system capable of forming complex flow and injection structures (e.g., Ujiie et al., 2007). Lin (2011) reported strikingly similar structures and inferred that fluidized ultracataclasite formation resulted from a recent (2008) Mw 7.9 earthquake, emphasising coseismic shearing as a mechanism capable of fluidization and injection of fine-grained material virtually devoid of frictional melts. Mutual crosscutting relationships among several ultracataclasite domains indicate synchronous formation during similar seismic events (e.g., Rowe et al., 2005; Lin, 2011).

Sharp slip surfaces, including injection structures approaching the brecciated blueschist host (e.g., ***Fig.7.3A*** to ***D***), demonstrate that fault propagation generally proceeds towards the host breccia and blueschist domains rather than via fast reshearing of the previously-generated ultracataclasite (e.g., Collettini et al., 2009). This statement is supported by contrasted major and trace element signatures among Black and Brown regions indicating different sources (***Fig.7.5B*** and ***C***). It is thus inferred that brecciated blueschist domains are mechanically weaker than fault core lithologies, provided that fault gouge interstices become cemented at short timescales (e.g., Kay et al., 2006; e.g., ***Fig.7.3D*** and ***7.4D***). This possibility is supported by experimental investigations showing that incremental slip in a fault zone results in progressive fault gouge strengthening (Ujiie et al., 2009). These observations demonstrate that fluid-assisted cementation of the ultracomminuted matrix could potentially have occurred during interseismic periods associated with viscous creep (e.g., Lin, 2007; Di Toro et al., 2009). In addition, crosscutting relationships of pristine extensional or fragmented veins filled by HP-LT mineral assemblages, as well as the presence of similar mineral paragenesis filling vugs and fringes along the brecciated matrix, demonstrate that hydrofracturing and high pore fluid pressure conditions were also cyclically attained and temporally compatible with a sequence of seismic faulting events.

The composition of the Brown regions is similar to pristine blueschists and blueschist fragments, while the Black regions are substantially shifted towards the albite endmember (***Fig.7.5B***). These contrasted compositions indicate that the Brown regions were produced by ultracomminution of the host blueschist and breccia while Black regions incorporated considerable amounts of albite vein component. Textural evidence demonstrating that albite clasts are more abundant in the Black regions also reflects this discrepancy (e.g., Lin, 2007). Nevertheless, trace element analyses show marked anomalies among the different ultracataclastic vein domains relative to the average blueschist standard pointing to similar metasomatic processes affecting both domains. Thus, the observed shift cannot be explained solely by mechanical mixing and homogenization of fault zone material (***Fig.7.5C***).

Strong Cs and Rb negative anomalies in the Brown regions while the same elements are abundant in the Black regions reflect relative depletions and enrichments in phengite, the main Large Ion Lithophile Elements carrier in the system (***Fig.7.5C***). In both domains, substantial Nb and Ta positive anomalies are observed relative to the host breccias and pristine blueschists. Th and HREEs enrichments are also observed in the Brown and Black regions relative to the average and two blueschist compositions selected for comparison (***Fig.7.5C***). These two compositions correspond to analyses containing the highest and the lowest amount of trace element abundances allowing to detect true enrichments (or depletions) that cannot be explained by ultracomminution of the host materials. Thus, strong Ta, Th, Nb and HREEs positive anomalies require an external source to match the values measured in the ultracataclastic vein domains. It is worth noticing that measured albite vein crystals show Ta, Th, Nb and REEs abundances commonly below 0.1 ppm and cannot be considered as the source of any anomaly.

Similar Ta and Nb (and Ti) anomalies have been reported in metasomatic eclogite lithologies from the Tianshan (China) and attributed to titanite dissolution during blueschist to eclogite-facies dehydration reactions and further long distance transport before precipitation as veins (Gao et al., 2007). Considerable positive P anomalies are also observed in the Brown and Black regions likely reflecting exceptionally high amounts of apatite relative to the host blueschists. Similarly, Cu is also enriched only in the Brown and Black regions possibly associated with the presence of higher amounts of Cu-bearing phases such as chalcopyrite. In addition, strong Th and HREEs (and LREEs) positive anomalies are noticed in metapelite lawsonite crystals from the Seghin complex, the latter serving as a proxy of a metasedimentary-derived signature (Muñoz-Montecinos et al., 2021; see average metapelite lawsonite grains in ***Fig.7.5C***). Therefore, it is stated that the observed trace element anomalies (Ta, Th, Nb, HREEs, Cu and P) represent a fingerprint of externally-derived mixed metamorphic fluid contributions associated with open-system behaviour during fluid circulation as reported in other subduction settings (Gao et al., 2007; Meneghini et al., 2010; Muñoz-Montecinos et al., 2020). Externally-derived fluid infiltration has been proposed by Muñoz-Montecinos et al. (2021). The authors concluded that metasedimentary and mafic/ultramafic-derived fluids were injected in the Seghin complex during prograde burial to near-peak conditions in the form of upwards traveling fluid pulses (e.g., Frank et al., 2015). These pulses were possibly associated with deep-seated metamorphic reactions taking place at greater depths than Seghin upper blueschists peak conditions (Muñoz-Montecinos et al., 2021). In contrast, the inferred fluid-rock interactions in the studied fault zone occurred at lower blueschist-facies conditions, once the Seghin complex was constituted as an uprising serpentinite mélange emplaced at seismogenic depths at near 35 km depth. Thus, deeply-generated fluids may have travelled upwards along the subduction interface channel and reached the seismogenic region where active fluid circulation through the different fault domains and seismic cycle stages occurred (e.g., Angiboust et al., 2014).

7.6.3 Modelling fluid – stress feedbacks in a blueschist-facies fault zone

To explain the episodic nature of the inferred brittle-viscous deformation events, a failure mode diagram considering pore fluid pressure vs. stress state variations has been constructed following the procedure detailed in Cox (2010; see caption from ***Fig.7.7*** for details). In this diagram, fluid pressure is represented by the pore fluid factor λ_f (P_f/σ_v) and the stress state by the differential stress σ_1-σ_3 (in MPa), where P_f is the fluid pressure and σ_v the vertical stress. In order to compare our structural observations with modern subduction analogues, we assume a stress drop (difference of stress state after and before an earthquake) of 10 MPa, as inferred for mean thrust earthquakes from active subduction settings such as in Hikurangi and Mariana (Abercrombie et al., 2017; Bird, 1978). A lower stress drop of 5 MPa is also depicted for comparison. These values may represent upper boundaries since Coulomb wedge theory applied in active subduction margins re-quires a very weak megathrust to maintain force balance close to an equilibrium state, underscoring the role of overpressurized fluids (see below; e.g., Dielforder et al., 2020).

Our mechanical model reveals that the observed fabrics can be explained by stress and pore fluid pressure fluctuations (***Fig.7.7A***). Assuming a brecciated blueschist as a starting point (i.e., after a hydrofracturing event), seismic faulting will potentially occur once λ_f vs.σ_1-σ_3 reach the brittle faulting failure envelope from ***Fig.7.7A*** (point 1). At these conditions, pore fluid pressure must be high, near to lithostatic, to promote seismic faulting and explain the observed ultracataclasite injections crosscutting the host blueschists and breccias (***Fig.7.7B1***). This brittle event is followed by poroelastic relaxation and fluid drainage, as a consequence of syn-faulting permeability increase, allowing λ_f and σ_1-σ_3 to drop until reaching point 2 (***Fig.7.7A***; Cox, 2010, see also Sibson, 2013). During inter-seismic periods, fluid-present viscous deformation occurs as evidenced by the observed fabrics associated with pressure-solution processes, possibly strengthening the fault gouge previously generated (***Fig.7.7B2***). Recovery of low $\partial\lambda_f/\partial(\sigma_1$-$\sigma_3)$, likely associated with sealing-induced permeability reduction and tectonic loading, allows for λ_f and σ_1-σ_3 build up until reaching the failure envelope at point 1 again. This triggers a new earthquake, as evidenced by the injection of newly formed ultracataclasites and brecciation in the margins of the faulting region (***Fig.7.7B3***). Thus, seismic faulting-viscous creep cyclicity requires that fluid pressure must remain high, nearing the lithostatic threshold (e.g., Angiboust et al., 2015). This scenario is evidenced by the presence of fluidized fabrics as well as by the occurrence of vugs and fringes filled by HP-LT minerals interpreted as former fluid-filled cavities. Besides faulting activity, cyclic hydrofracturing is also testified by mutually crosscutting occurrences of extensional veins (e.g., ***Fig.7.3F***) and their brecciation (e.g., ***Fig.7.2E, 7.3D, 7.4A*** and ***7.S1C***). Note that this process is possible only if a high $\partial\lambda_f/\partial(\sigma_1$-$\sigma_3)$ buildup occurs. To accomplish for these sudden pore fluid pressure highs, in situ dehydration of metabasaltic material or injection of external fluids are possible candidates. The former case is very unlikely since at these conditions, materials forming the Seghin complex were on their way upwards in the serpentinite subduction channel and water-consuming reactions are expected (Muñoz-Montecinos et al., 2021). We herein favour the latter case, where highly pressurized fluids originating from deep-seated dehydration reactions, infiltrate the Seghin complex sequence allowing for reaching again

near-lithostatic λ_f (point 3 in ***Fig.7.7A***), promoting hydrofracturing, veining and subsequent pore fluid pressure drop (***Fig.7.7B4***).

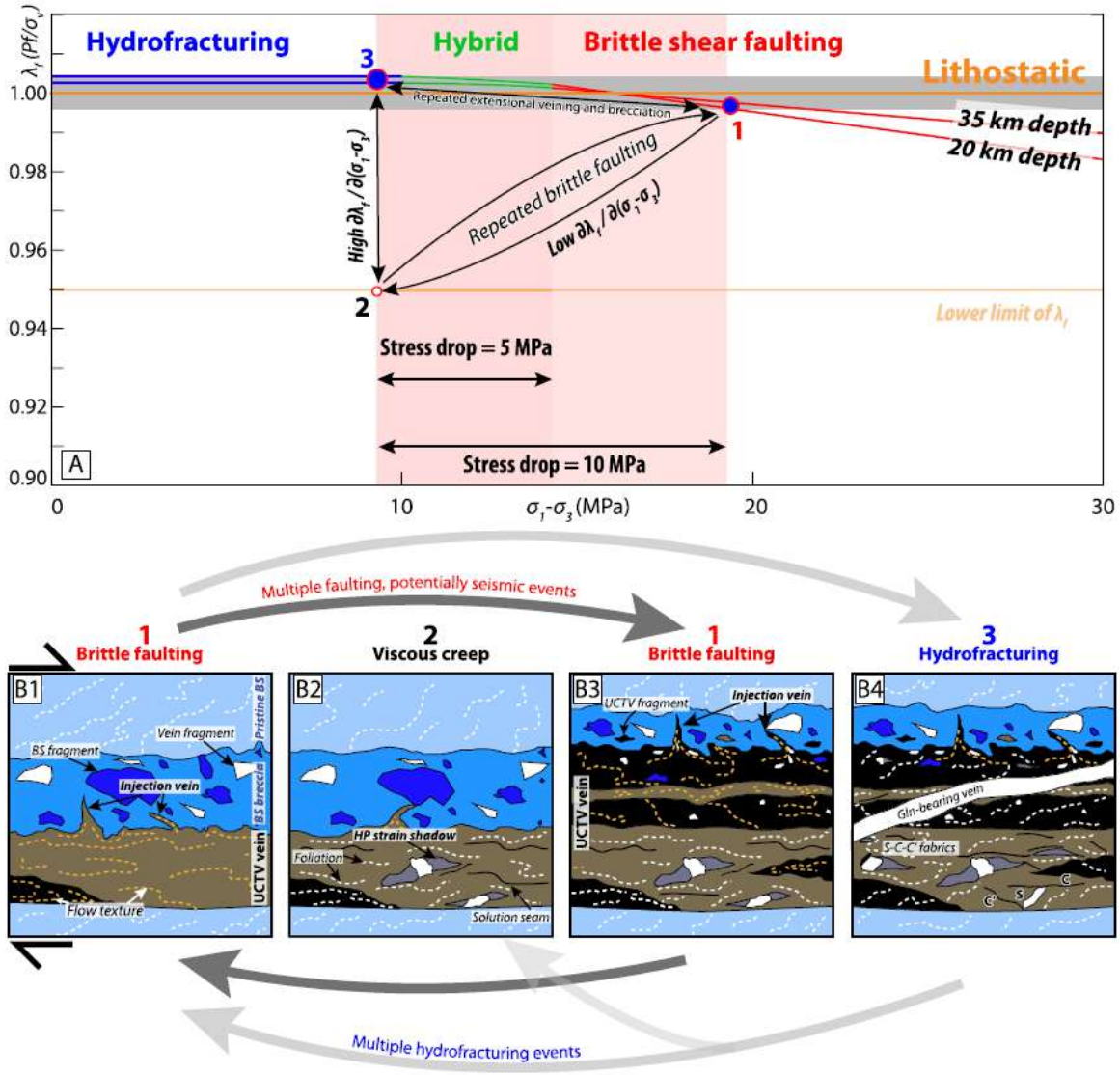

Figure 7.7. Structural and mechanical evolution sketches of fault rock fabrics from the Seghin complex. A. λ_f vs.σ_1-$\sigma_3$diagram for the compressional regime state calculated for 20 and 35 km depths, corresponding to inferred faulting P-T conditions. An Andersonian stress state is assumed where for a compressional setting $\sigma_v=\sigma_3$, whereas for an extensional regime $\sigma_v=\sigma_1$. For the sake of simplicity, only the compressional regime is shown (see discussion section for details). The failure envelopes were constructed following the mathematical formulation detailed in Cox (2010). The points 1, 2 and 3 correspond to λ_f vs.σ_1-$\sigma_3$states as shown in panel A where brittle faulting, viscous deformation and hydrofracturing are expected, respectively. The position of these points were chosen based on observed rock fabrics and considering a likely stress drop of 10 MPa (see text for further details). The parameters used are density=3000 g/cm^3; gravity acceleration=9.8 m/s^2; friction coefficient=0.45; tensile strength of a blueschist (basaltic) rock mass=2.5 MPa; Cohesion=5.2 MPa. The lower limit of λ_f corresponds to the minimum value calculated in Angiboust et al. (2015) and is based on exhumed subduction-related petrofabrics inferred to have formed at blueschist-facies depths. Justification and references regarding parameter selection are given in the Supplementary Material. B1 to B4. Fabric evolution sketches associated with λ_f vs.σ_1-σ_3 variations. The thick bold black and grey arrows aim at representing cyclicity in the different events. Note that after any hydrofracturing event at point 3 (e.g., panel B4) the λ_f vs.σ_1-σ_3 path may potentially evolve directly towards point 1 or 2 (or any intermediate state between point 2 and 3) before subsequent stress recovery and reaching point 1 once again (or another hydrofracturing event). (For interpretation of the colours in the figure, the reader is referred to the web version of this article.)

7.6.4 A window onto Mariana-type subduction-related seismicity?

Investigations in dredged blueschist fragments from the Mari-ana subduction zone yield upper to lower blueschist-facies peak metamorphic conditions (Tamblyn et al., 2019 and Maekawa et al., 1993, respectively), comparable to those recorded by some of the peak blueschist blocks and the fault zone herein investigated, respectively. Thus, our findings demonstrate that the Seghin com-plex can be considered as a world-class, on-land analogue to the current seismogenic window of the Mariana margin (Maekawa et al., 2004; Fryer et al., 2020; Muñoz-Montecinos et al., 2021). In this tectonic configuration, active seismicity is characterized mostly by small-and moderate-magnitude earthquakes (e.g., Eimer et al., 2020) whereas Mw>7events are scarce (Emry et al., 2011). Focal mechanisms inferred from well-resolved moderate-magnitude earthquakes (Mw 4.9-5.8), show that most seismic activity is associated with thrusting near the subduction interface channel (Emry et al., 2011; ***Fig.7.8***). These and other lower magnitude events cluster at depths in the ranges 10 to 30 km and 45 to 60 km (Emry et al., 2011; Eimer et al., 2020), well within the calculated 20 to 35 km depths estimated for Seghin complex paleo-earthquakes.

A Mw~5earthquake requires a rupture area in the order of 10 km^2 and a total slip of few tens of centimetres (Sibson, 1989). The spatial dimensions of the Seghin complex, including the occurrence of several hectometre-sized blueschist blocks enclosed in a serpentinite matrix, are compatible with measured moderate-magnitude earthquake source properties. Using structural and kinematic observations, it was neither possible to state whether the studied fault system was reverse or normal nor whether faulting events also affected the serpentinite matrix around or other mafic blocks. Note, however, that our main conclusions regarding episodic faulting and fluid pressure cyclicity would remain mostly unchanged if the studied features were produced by normal faulting. Moreover, we suspect that the fault may have propagated through the serpentinite matrix around since localized deformation in the form of cataclastic fabrics were also observed therein and in other HP blocks (e.g., Muñoz-Montecinos et al., 2021; ***Fig.7.8*** and ***7.S1A***). Experimental results on serpentinites and serpentinite gouge materials show that these fabrics may result from localized seismic slip interspersed with distributed stable creep (Reinen, 2000). In addition, it has been shown that transient changes on pore fluid pressures and/or slip velocities may trigger the mechanical transition from velocity-strengthening to velocity-weakening behaviour, thus promoting transient unstable slip (Moore et al., 1997; Reinen, 2000; Proctor et al., 2014). Lower magnitude earthquakes (e.g., Mw ~4) would also be associated with the rupture of single hectometre-sized blocks, also in line with Mariana-type seismicity.

The episodic nature of fluid pressure and stress build up is a compelling evidence for a seismogenic zone alternating between low and high $\partial\lambda_f/\partial(\sigma_1-\sigma_3)$ regimes (***Fig.7.7***). These variations are interpreted here as short-term seismicity recurrence (Emry et al., 2011) switching with longer-term, transient fluid circulation along the subduction channel as highly pressurized fluid pulses (Frank et al., 2015). Muñoz-Montecinos et al. (2021) suggest that fluid pressure build-up intensities are higher at greater

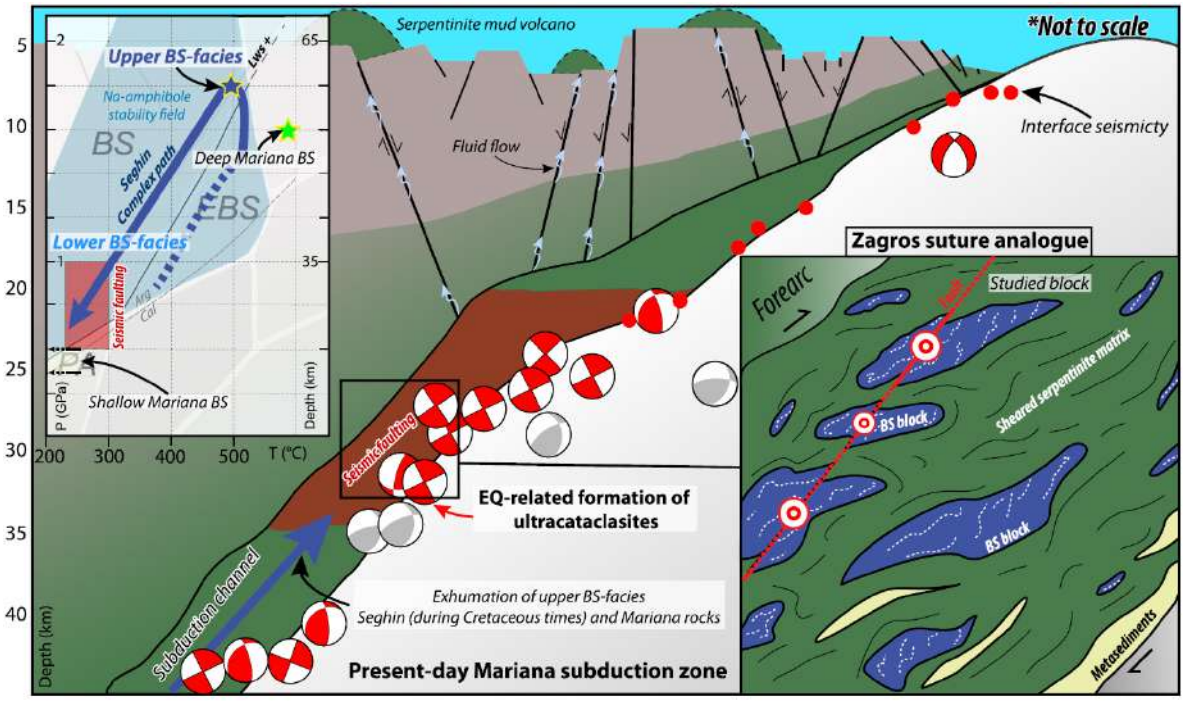

Figure 7.8. Subduction sketch (modified from Fryer et al., 2020) and relocated focal mechanisms (red for thrusting and grey for extension; within errors) from 2003-2004 moderate magnitude earthquakes (Emry et al., 2011). The red dots represent well-resolved earthquake locations inferred as representing the subduction interface (after Oakley et al., 2008). The inset is a schematic representation of how the subduction channel (not to scale) would look like using the Seghin complex as an exhumed analogue. Note the fault trace cutting across blocks and the serpentinite matrix. Dark blue colour represents higher grade blueschist blocks (e.g., Angiboust et al., 2016; Muñoz-Montecinos et al., 2021). The red region in the subduction channel depicts calculated faulting depths for the Seghin complex, while the lower blueschist field corresponds to conditions inferred for recent blueschist-facies metamorphism by Maekawa et al. (1993). The P-T inset compiles relevant metamorphic (Maekawa et al., 1993; Angiboust et al., 2016; Tamblyn et al., 2019) and faulting conditions (this study). EQ—earthquake. (For interpretation of the colours in the figure, the reader is referred to the web version of this article.)

depths, where massive hydrofracturing occurred in the mafic blocks near the eclogite-to-blueschist transition, vanishing at shallower conditions (see also Muñoz-Montecinos et al., 2020). These statements correlate well with high V_p/V_s ratios imaged in the Mariana setting in the depth range of 70 to 120 km (eclogite-facies depths), interpreted as slab dehydration processes (Barklage et al., 2015). Interestingly, high V_p/V_s conditions were also imaged in the depth window between 20 to 30 km (Barklage et al., 2015), suggesting that high pore fluid pressure conditions are also attained in the seismogenic region. On a rheological perspective, Wang et al. (2020) suggested that the scarcity of aftershocks in the shallow mantle wedge corner after the Maule megathrust earthquake (Mw8.8; Chile) is due to the velocity-strengthening behaviour of lizardite/chrysotile while the deeper occurrence of antigorite-rich patches allow for downdip aftershock generation. Wang et al. (2020) emphasize that a similar rheological behaviour is expected in settings where buoyant serpentinite-rich subduction channels are able to flow updip, such as in Mariana-type margins. The proposition of Wang et al. (2020) supports the herein suggested scenario where earthquakes may have propagated through the foliated antigorite-rich matrix (see also Tarling et al., 2018).

In Mariana-type margins, two hypotheses are commonly invoked to explain the lack of large-scale earthquakes (see Emry et al., 2011 and references therein for more details). In the first instance, it has been proposed that a weak serpentinized mantle – commonly thought to behave as a velocity-strengthening material – is capable of inhibiting earthquake nucleation (Hyndman et al., 1997). The other hypothesis invokes a weak coupling state of the plate interface due to very low normal stresses (e.g., Scholz and Campos, 2012). Our field-based investigation demonstrates that earthquakes may well occur within a highly serpentinized subduction channel in agreement with geophysical observations (e.g., Emry et al., 2011). In addition, our structural-mechanical inferences suggest that near- to supra-lithostatic fluid pressure conditions (***Fig.7.7***) are a prerequisite to maintain the system in a critically unstable mechanical regime, capable of promoting seismicity in the Mariana and other similar subduction margins such as the Izu-Bonin, Hikurangi, South Tonga and Kermadec (see for instance the Mw=8.1earthquake that occurred at c. 20 km depth in the Kermadec subduction on March 4th, 2021; see also Scholz and Campos, 2012; ***Fig.7.8***). Therefore, we conclude that local fluid pressure highs promote seismic faulting in some patches (e.g., the studied blocks and their surroundings), while adjacent regions at lower fluid pressure conditions will potentially behave aseismically arresting earthquake nucleation and/or propagation (Scholz and Campos, 2012; Wang et al., 2020). Even though similar cataclastic fabrics are not reported so far (to our knowledge) in other similar localities (e.g., Franciscan complex), we speculate that such seismic-related features must have widely occurred but were in most cases overprinted due to exhumation-related metamorphism and deformation or, remain to be recognized in the geological record.

7.7 Conclusions

Our investigations demonstrate that the Seghin complex represents an extremely well-preserved fragment of a paleosubduction channel that likely evolved into a tectonic setting analogue to modern Mariana-type margins, where large-scale return flow enables the exhumation of HP-LT metamorphic rocks from depths of ~55 km up to the inferred seismogenic region near 25 km depth. We herein document the finding of a several meters-wide fault zone, comprising a variety of fabrics, including some produced by blueschist-facies paleo-earthquakes. Combining structural features with a mechanical modelling approach, we show that (i) stress accumulation must proceed faster than pore fluid pressure build-up in order to trigger moderate-magnitude seismicity and (ii) pore fluid pressure build-ups should be faster relative to stress build-up to explain the observed hydrofracturing pattern at seismogenic depths. In both cases, fluid pressure must be maintained at near-lithostatic values in order to explain the investigated rock fabrics, as indicated by high V_p/V_s ratios in the seismogenic region of the Mariana margin. Enrichments in Ta, Th, Nb, and HREEs indicate that external, possibly deep-seated fluids were capable of maintaining pore fluid pressures at critically high levels in order to trigger the inferred mechanical instabilities. Thus, the Seghin fault system provides an unprecedented opportunity to document the complex feedbacks between fluctuating pore fluid pressures and stress evolution in active Mariana-type subduction settings and help refining our understanding of earthquake-related processes in serpentinized subduction channels.

Acknowledgments

Zeynab Gharamohammadi, Ali Kananian, Philippe Agard and Ja-far Omrani are acknowledged for logistical assistance. Olga Cazalla, Laura Crespo and Miguel Angel Hidalgo Laguna are acknowledged for their technical support at Centre of Scientific Instrumentation, University of Granada. We are very grateful to Sophie Nowak for further support during XRD analytical sessions. Onno Oncken is warmly thanked for insightful discussions and support regarding mechanical earthquake-related processes. Hugues Raimbourg and Isabelle Martinez are also acknowledged for exciting discussions and suggestions regarding fluid-rock interaction processes. The editorial handling by Alexander Webb is very much appreciated. Whitney Behr and Volker Schenk are warmly acknowledged for detailed and constructive reviews, but also for their stimulating words that helped improving this work. This project has been funded by an Initiative D'EXcellence (IDEX) grant 16C538 and the TelluS Program of CNRS/INSU to S.A. Partial funding was also provided by the University of Granada at CIC.

7.8 Supplementary information

7.8.1 Analytical methods

Ten representative brecciated and faulted blueschist samples were selected and prepared for polished thin sections from which two samples (SO1877 and SO1878) have been studied in greater detail. Electron probe microanalyses (EPMA) were performed at the University of Granada with a CAMECA SX-100, using a 1 µm to defocused 30 µm beam diameter in order to acquire representative chemical surface estimates on the ultracataclastic veins. This methodology (surface scans) has been broadly applied in previous studies of fault-related rocks (see Lin, 2007 and Angiboust et al., 2015). The machine was operated at 15 kV and 15 to 20 nA beam current (wavelength-dispersive spectroscopy mode). Standards used for calibration were: albite (Na), periclase (Mg), SiO_2 (Si), Al_2O_3 (Al), sanidine (K), Fe_2O_3 (Fe), $MnTiO_3$ (Mn), Cr_2O_3 (Cr), diopside (Ca) and TiO_2 (Ti). Representative mineral phase analyses are offered in ***Table S1***. Elemental X-Ray maps were obtained with a scanning electron microscope (SEM) Zeiss model Evo MA10 at the Institut de Physique du Globe de Paris using internal calibration standards. The resulting X-Ray maps were treated with DWImager software (Garcia-Casco, 2007). In addition, surface chemical estimates (up to 6 mm2) of the host blueschists and clasts, were also acquired with the SEM instrument. A barycentric quaternary Al_2O_3'-CaO'-FeO'-Na_2O' (ACFN; ***Fig. 7.5B***) diagram was designed using CSpace software by means of algebraic methods (Torres-Roldán et al., 2000) after projection of chemical compositions of mineral phases and exchange vectors necessary to condense the 9-dimensional composition space. Amphibole structural formulae and Fe^{3+} were calculated following the procedure outlined in Leake et al. (1997). White mica structural formula was normalized to 11 equivalent oxygens assuming Fe^{2+} total in octahedral sites. Mineral compositions are given in atoms per formula unit (a.p.f.u; ***Table S1***). Thermodynamic calculations have been performed using the Perple_X software (version 6.8.9; Connolly, 2005) considering the internally consistent database from Holland and Powell (2011; hp62ver.dat in Perple_X). The considered chemical system for the Black region corresponds to nine averaged surface estimates (***Fig.7.5B***) from two samples, while for the Brown region the same number of averaged areas in the same samples has been used. Chemical comparisons among the samples (***Fig.7.5B***) show that this approach is appropriate due to their bulk major element similarities. Last, the strong similarities among the Brown regions and blueschist compositions allow applying the thermodynamic model developed for the Brown region in the blueschist compositions (see discussion section).

In situ trace element analyses were obtained at Center of Scientific Instrumentation of University of Granada using a Laser Ablation Quadrupole Inductively Coupled Plasma-Mass Spectrometer (LA-ICP-MS). The system is composed of a 213-nm Merchantek Nd-YAG laser coupled to an Agilent 7500 ICP mass spectrometer. The laser ablation has been performed in a He atmosphere and the beam was fixed to a diameter of 30 µm in raster mode. Prior to each measurement, spots were pre-ablated for 15 seconds with a laser fluence of 2.5 Jcm^{-2} followed by further ablation during 60 seconds with a laser fluence of 7.5 Jcm^{-2}. Preceding each measurement, a blank has been measured in the same conditions but with zero laser energy and the resulting counts subtracted from the signals. The stage

is automated to move 5 µm every 20 seconds to increase sensitivity and avoid fractionation due to laser scavenging and ablation cratering effects. The NIST-610 glass, measured every six spots for drift corrections, and at the beginning and the end of each analytical session, has been used as external standard. Note that linearity between signal intensity and concentration is regularly checked and generally maintained. While as an internal standard, we used silicon. Data reduction was done using an in-house LA-ICP-MS data evaluation software. Precision calculated based on NIST-610 replicates was about ±5% (relative) and the detection limit is c. 0.01 ppm for most elements (see Bea et al., 1996 for more details). The resulting analyses shown in ***Fig.7.5C*** and ***Table S4*** have been acquired in two thin section samples (SO1877 and SO1877.1) from the same specimen.

Powder X-ray diffraction analyses (XRD) were performed in representative Brown and Black region samples after mechanical extraction with a microdrilling device using a Panalytical Empyrean X-ray diffractometer at Université de Paris, with Cu Kα radiation and equipped with a multi-channel "PIXcel" detector, in the angular range 5°-70° with a step size of 0.0131° and a 60 seconds time per step of 60 seconds. Two representative diffraction patterns are shown in ***Fig.7.S3B*** and ***7.S3C***.

7.8.2 Pore fluid pressure factor vs differential stress model parameters

The selected density value (3000 g/cm^3) has been calculated with Perple_X software for a metabasaltic composition at blueschist-facies conditions. The friction coefficient (0.45) corresponds to the maximum values obtained experimentally by Okazaki and Hirth (2020) for an amphibole-rich mafic schist at high pressure conditions from 0.75 to 1.5 GPa, conditions and compositions similar as those inferred from our analyses. The tensile strength (T) has been extracted from Schultz (1995) who obtained maximum values of 2.5 MPa for a basaltic rock mass while the cohesion has been calculated using the simple empirical formulation from Secor (1965) as 2.083*T. Similar values in the range of 0.6-6.0 MPa were obtained by Schultz (1995).

7.8.3 Supplementary figures and tables

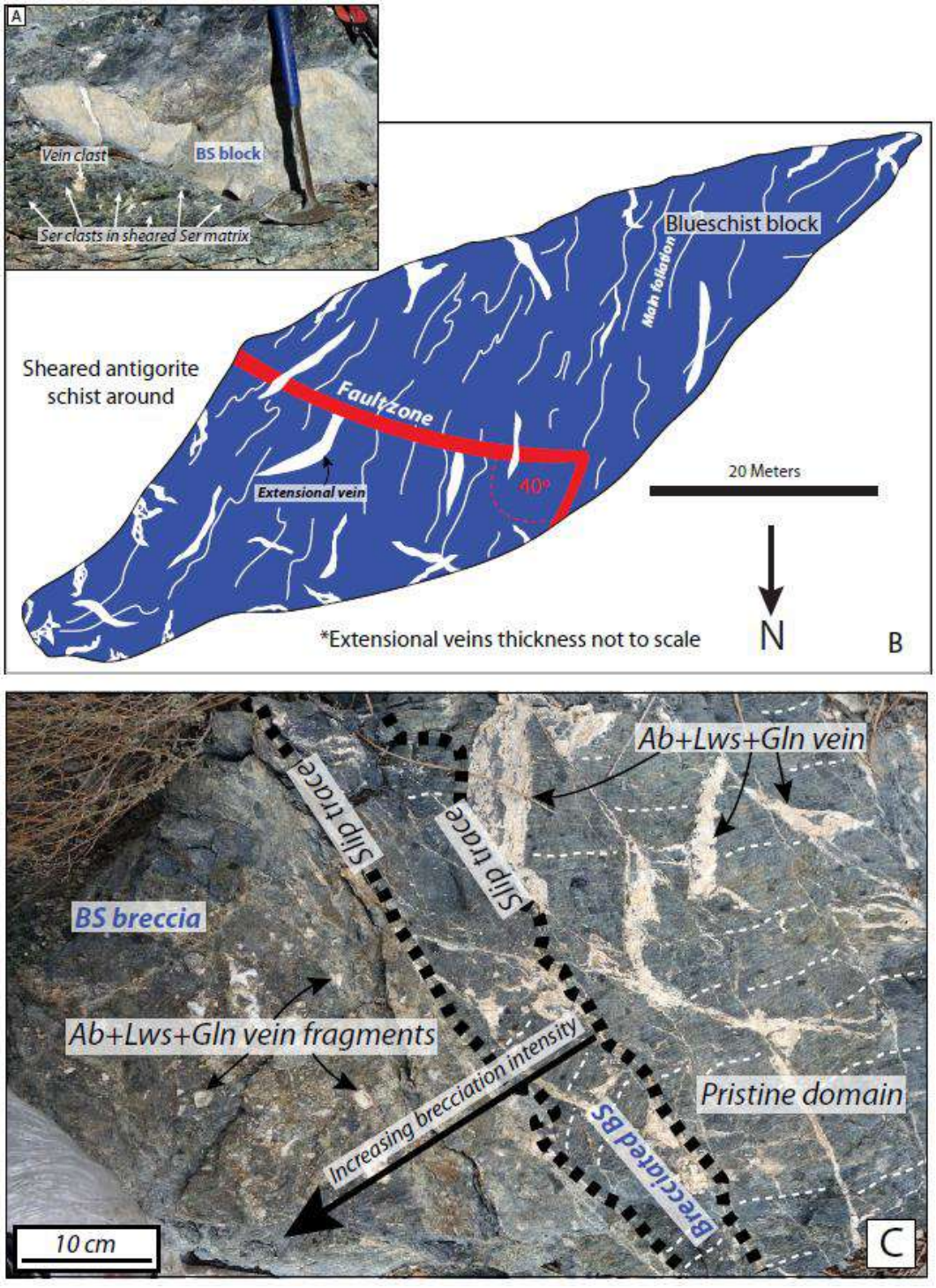

Figure 7.S1. A. Field picture of the serpentinite matrix surrounding a blueschist block. Note the occurrence of clasts in the foliated serpentinite. B. Schematic geometrical representation of the studied blueschist block. C. Field view of a blueschist block showing a pristine foliated domain affected by intense albite-lawsonite-glaucophane-bearing extensional veining that is sharply crosscut by slip surfaces where the brecciation degree is greater towards the left hand. Note the presence of angular vein fragments.

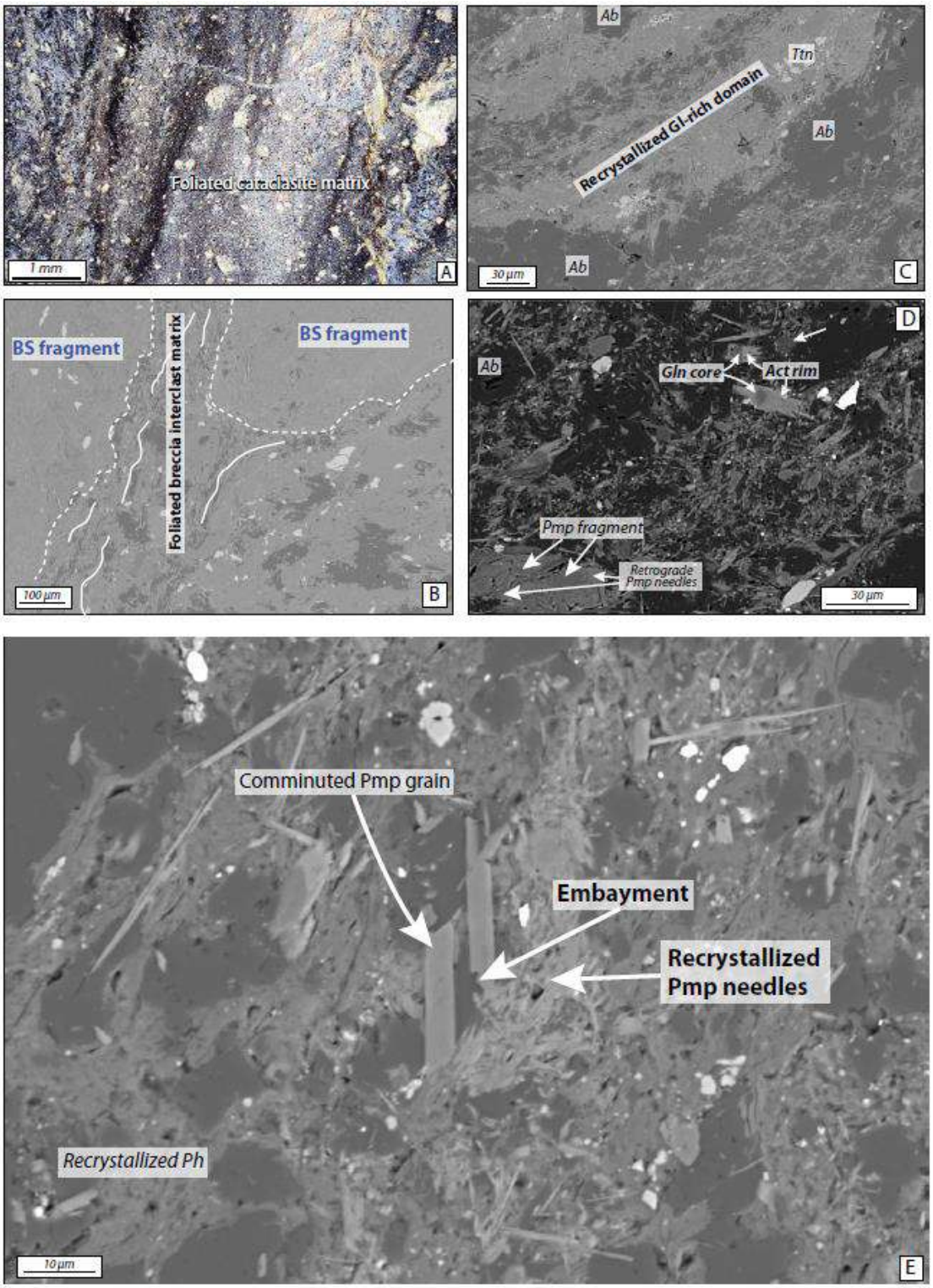

Figure 7.S2. A. Optical polarized-light photomicrograph of a blueschist-facies foliated cataclasite in another fault zone adjacent to the studied block (cross-polarized view). B. BSE image of a brecciated blueschist highlighting the foliated interclast matrix fabric. C. BSE image of a highly recrystallized glaucophane-rich domain in the Black region. D. BSE image of the ultracomminuted material from the Black region. E. BSE image of the Black region showing embayed fragments and newly formed retrograde pumpellyite.

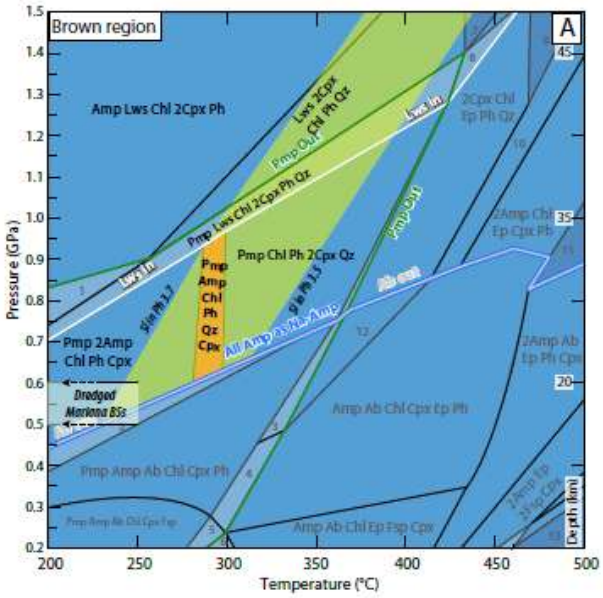

Black region pseudosection fields:

1 Amp Pu Ab Ph Mstp Qz Cpx
2 2Amp Pu Ab Chl Ph Cpx
3 2Amp Pu Ab Chl Ph 2Cpx
4 Amp Pu Ab Chl Ph Cpx
5 2Amp Pu Ab Chl Ph Qz Cpx
6 Amp Pu Ab Chl Ph Qz Cpx
7 Amp Pu Ab Chl Ep Fsp Cpx
8 Amp Ab Chl Ep Ph Fsp Cpx
9 Pu Ab Chl Ph Qz Cpx
10 Chl Ep Ab Ph Qz Cpx
11 2Amp Chl Ep Ab Ph Cpx
12 Amp Chl Ab Ph Qz Cpx
13 2Amp Ep Ab Ph Cpx
14 2Amp Ab Ph Qz Cpx
15 2Amp Ab Ph Cpx
16 2Amp Chl Ab Ph Cpx
17 2Amp Ab Ph Cpx Bt
18 2Amp Ab Ph Fsp Bt
19 2Amp Chl Ab Ph Fsp Bt
20 2Amp Chl Ab Ph Fsp
21 2Amp Ab Chl Ep Fsp Bt
22 2Amp Ab Chl Ep Fsp
23 2Amp Ab Chl Fsp
24 2Amp Ab Chl 2Fsp
25 2Amp Cb Chl Qz Fsp
26 2Amp Chl Ab 2Fsp Bt

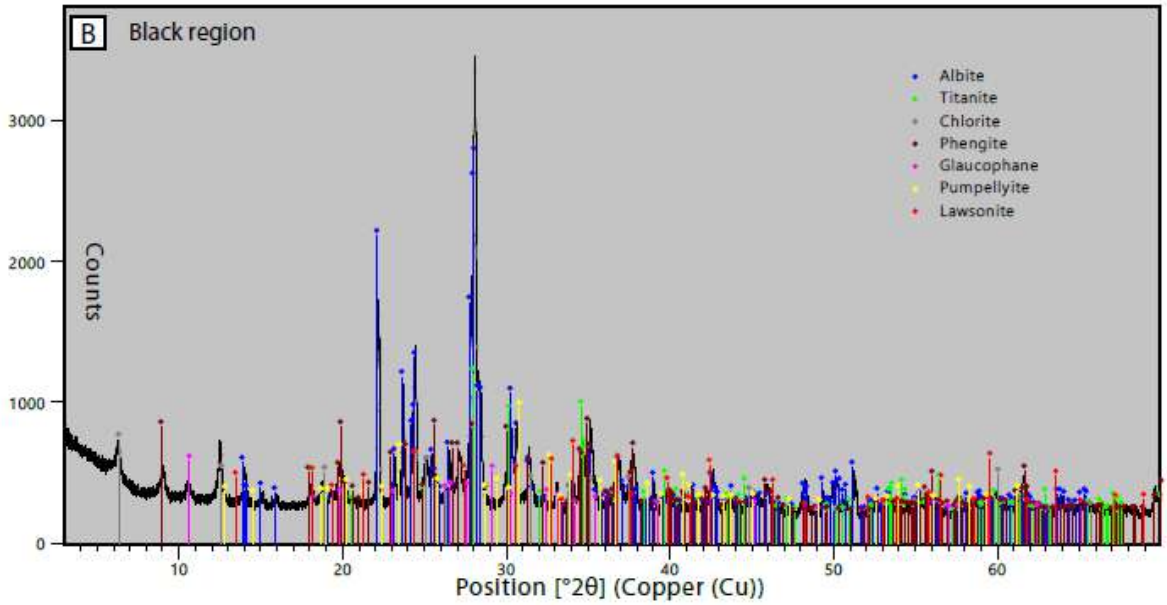

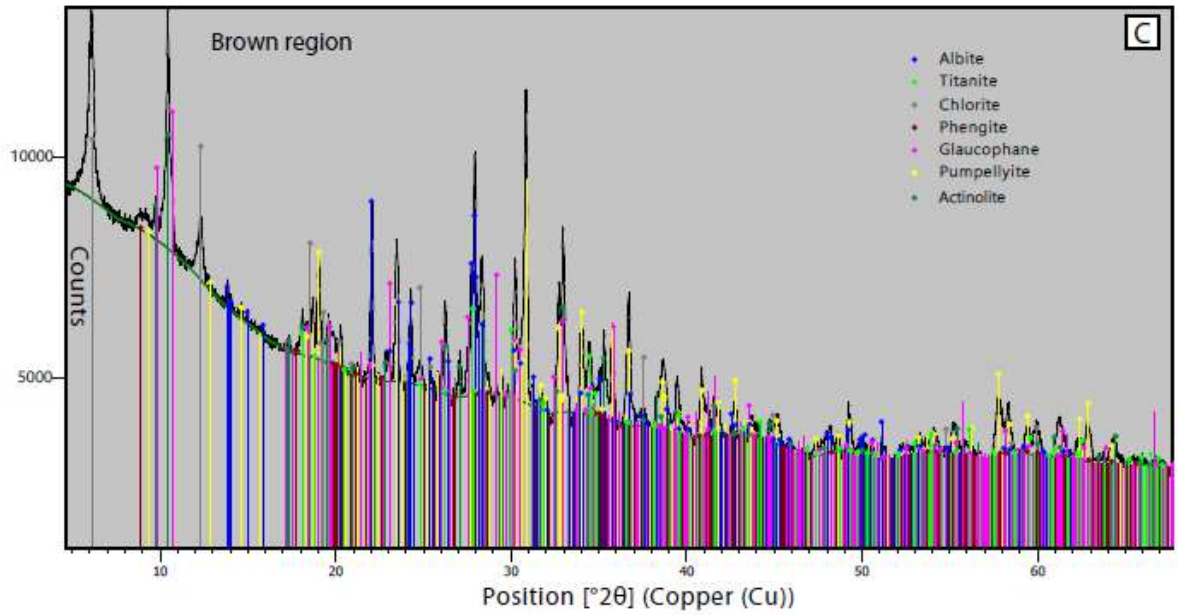

Figure 7.S3. A. Pseudosection of the Brown region composition. B. Powder X-Ray diffraction spectra of a representative Black region from an ultracataclastic vein.

TABLE S1. SELECTED ELECTRON PROBE MICROANALYSIS MINERAL COMPOSITION AND CATIONS PER FORMULA UNIT IN THE SEGHIN COMPLEX

Mineral	Zone	Observation	SiO_2 (wt%)	TiO_2 (wt%)	Al_2O_3 (wt%)	Cr_2O_3 (wt%)	FeO (wt%)	MnO (wt%)	MgO (wt%)	CaO (wt%)	Na_2O (wt%)	K_2O (wt%)	Total (wt%)	Si (a.p.f.u)	Ti (a.p.f.u)	Al_{tot} (a.p.f.u)	Fe^{3+} (a.p.f.u)	Fe^{2+} (a.p.f.u)	Mg (a.p.f.u)	Ca (a.p.f.u)	Na (a.p.f.u)	K (a.p.f.u)	XMg	$Fe^{3+}/(Fe^{3+}Al)$
Glaucophane	Black region		57.93	0.26	8.42	0.01	13.76	0.05	9.66	2.26	6.07	0.29	98.71	8.02	0.03	1.37	0.17	1.42	1.99	0.33	1.63	0.05	0.58	0.11
Glaucophane	Black region	Core	58.03	0.07	10.14	0.02	11.66	0.13	9.38	0.67	7.17	0.06	97.33	8.02	0.01	1.65	0.22	1.12	1.93	0.10	1.92	0.01	0.63	0.12
Actinolite	Black region	Rim	53.45	0.20	2.14	0.00	14.98	0.56	13.16	10.61	1.33	0.54	96.98	7.84	0.02	0.37	0.06	1.78	2.88	1.67	0.38	0.05	0.62	0.14
Glaucophane	Brown region		57.18	0.12	9.72	0.01	12.17	0.07	9.38	0.67	7.22	0.03	96.56	8.00	0.01	1.60	0.21	1.22	1.96	0.10	1.96	0.00	0.62	0.11
Pumpellyite	Brown region		37.81	0.37	24.80	0.09	3.14	0.47	3.50	21.96	0.24	0.12	92.52	3.03	0.02	2.34	0.00	0.21	0.42	1.89	0.04	0.01	0.67	0.00
Pumpellyite	Black region		38.74	0.58	23.04	0.22	4.72	0.15	3.44	21.19	0.31	0.10	92.50	3.13	0.04	2.19	0.00	0.32	0.41	1.83	0.05	0.01	0.56	0.00
Phengite	Black region		53.59	0.02	20.93	0.00	5.05	0.01	6.34	0.00	0.12	9.30	95.35	3.60	0.00	1.66	N.A.†	0.28	0.63	0.00	0.02	0.80	0.69	N.A.†
Glaucophane	Vein		56.02	0.01	6.73	0.01	14.66	0.49	9.86	2.29	6.20	0.07	96.34	7.99	0.00	1.13	0.42	1.32	2.10	0.35	1.71	0.01	0.61	0.27
Glaucophane	Vein		56.18	0.04	7.20	0.14	16.09	0.26	8.56	0.57	7.21	0.03	96.27	8.00	0.00	1.21	0.60	1.32	1.82	0.09	1.99	0.01	0.58	0.33
Phengite	Vein		49.18	0.11	25.50	0.03	5.01	0.07	3.81	0.03	0.32	10.19	94.26	3.37	0.01	2.06	N.A.†	0.29	0.39	0.00	0.04	0.89	0.58	N.A.†
Phengite	Vein		53.15	0.01	21.94	0.05	3.07	0.09	5.65	0.03	0.05	10.40	94.42	3.59	0.00	1.75	N.A.†	0.17	0.57	0.00	0.01	0.90	0.58	N.A.†
Glaucophane	Blueschist		58.17	0.03	8.96	0.00	11.43	0.06	10.43	1.33	6.68	0.02	97.11	8.03	0.00	1.46	0.37	0.95	2.15	0.20	1.79	0.00	0.69	0.20
Glaucophane	Blueschist		57.03	0.05	9.01	0.00	12.87	0.06	10.20	0.89	7.44	0.03	97.60	7.95	0.01	1.48	0.21	1.29	2.12	0.13	2.01	0.00	0.62	0.12
Winchite	Blueschist		56.50	0.06	5.67	0.02	13.35	0.13	11.71	4.21	5.03	0.09	96.78	7.99	0.01	0.95	0.36	1.22	2.47	0.64	1.38	0.01	0.67	0.27
Phengite	Blueschist		53.48	0.02	25.00	0.05	1.88	0.04	4.92	0.74	0.07	10.90	97.12	3.50	0.00	1.93	N.A.†	0.10	0.48	0.05	0.01	0.91	0.82	N.A.†
Phengite	Blueschist		52.82	0.02	19.45	0.08	5.10	0.07	8.29	0.23	0.02	9.29	95.38	3.56	0.00	1.55	N.A.†	0.29	0.83	0.02	0.00	0.80	0.74	N.A.†
Pumpellyite	Blueschist		38.41	0.07	23.00	0.08	5.18	0.27	4.25	20.77	0.43	0.03	92.50	3.08	0.00	2.18	0.00	0.35	0.51	1.79	0.07	0.00	0.59	0.00

* = Calculated by stoichiometry.

N.A.† = Not applicable

TABLE S2. CHEMICAL COMPOSITIONS CONSIDERED FOR THERMODYNAMIC MODELLING

	Pseudosection modelling (wt%)	
Oxide	Black region (N*=9)	Brown region (N*=9)
SiO_2	59.3	46.5
Al_2O_3	16.1	17.3
Fe_2O_3	1.3	2.2
FeO	4.6	8.0
MgO	5.3	8.3
CaO	4.5	14.4
Na_2O	6.8	1.8
K_2O	1.3	0.3
H_2O	Saturated	Saturated

N* = Number of averaged surface estimates

TABLE S3. SUMMARY OF SOLID-SOLUTION MODELS USED IN THERMODYNAMIC MODELLING

Mineral	Solid solution model	Reference
Amphibole	cAmph(G)	Green et al. (2016)
Clinopyroxene	Omph(GHP)	Green et al. (2007)
Chlorite	Chl(W)	White et al. (2014)
Epidote	Ep(HP11)	Holland and Powell (2011)
Garnet	Gt(W)	White et al. (2014)
White mica	Mica(W)	White et al. (2014)

TABLE S4. LA-ICP-MS RESULTS I

	Sample	SO1877.1	SO1877.1	SO1877.1	SO1877.1	SO1877.1	SO1877.1	SO1877.1	SO1877.1	SO1877.1	SO1877.1	SO1877.1	SO1877	SO1877	SO1877	SO1877	SO1877	SO1877	SO1877	SO1877	SO1877	SO1877
	Lithology/region	Host	Host	Host	Host	Host	Host	Host	Host	Host	Clast	Clast	Clast	Clast	Clast	Clast	Host	Host	Host	Host	Host	Black
	PointId	77cuad5-1	77cuad5-2	77cuad4-1	77cuad4-2	77cuad3-1	77cuad3-2	77cuad3-3	77cuad1-1	77cuad1-2	77cuad1-3	77cuad2-1	77cuad2-2	77cuad2-3	77cuad4-1	77cuad4-2	77cuad3-1	77cuad3-2	77cuad3-3	77cuad5-1	77cuad5-2	77cuad1-1	77cuad1-2	77cuad1-3	77d-1	77d-2
Cs	(ppm)	0.09	0.02	0.13	0.32	0.34	0.19	0.04	0.55	3.14	4.78	0.1	0.07	0.15	0.89	0.39	0.25	2.35	0.49	2.26	1.28	0.29	0.18	0.19	1.57	3.63
Rb	(ppm)	0.14	0.11	5.75	5.08	5.16	4.19	0.15	19.4	107	113	0.35	0.32	0.23	21.6	15.1	3.51	77.3	11.8	70.6	39.3	1.17	0.19	0.27	23.1	62.3
Ba	(ppm)	11.2	8.67	17.8	22	21.6	21.4	5.83	33.2	173	165	6.41	5.74	5.99	56.7	34.9	14.6	104	26	154.3	96.6	4.8	3.86	5.66	22.5	29.9
Hf	(ppm)	*B.D.L	0.12	0.16	0.95	1.79	0.31	*B.D.L	0.9	2.76	8.78	0.27	0.18	0.35	0.61	18.2	2.07	4.69	0.3	0.39	0.32	0.19	*B.D.L	0.11	1.42	4.34
Ta	(ppm)	0.16	*B.D.L	0.22	*B.D.L	0.14	1.09	*B.D.L	0.03	0.23	0.02	0.02	*B.D.L	*B.D.L	*B.D.L	0.08	0.04	0.03	0.02	0.14	0.2	*B.D.L	*B.D.L	*B.D.L	0.52	0.75
Tl	(ppm)	*B.D.L	*B.D.L	0.08	0.07	0.03	0.04	*B.D.L	0.03	0.24	0.49	*B.D.L	0.02	*B.D.L	0.15	0.02	0.09	0.4	*B.D.L	0.26	0.08	*B.D.L	*B.D.L	*B.D.L	0.18	0.24
Th	(ppm)	0.1	0.13	0.43	0.73	5.52	0.2	0.03	0.36	0.18	0.57	0.64	*B.D.L	*B.D.L	0.26	0.38	0.19	2.63	0.11	0.19	0.03	0.23	*B.D.L	*B.D.L	4.58	7.39
U	(ppm)	0.17	0.11	0.18	0.62	1.04	0.35	0.04	0.17	0.23	1.71	0.06	0.05	0.09	0.15	0.67	0.17	0.89	0.11	0.1	0.13	0.08	0.1	0.15	0.68	1.83
Pb	(ppm)	3.55	2.47	4.83	4.19	5.38	6.52	3.4	0.95	2.34	4.93	1.52	1.63	2.63	3.15	4.95	3.98	6.66	1.92	2.04	2.67	1.45	1.17	1.51	2.62	14
Sr	(ppm)	8.68	6.21	8.24	11.7	25.7	10.6	6.16	8.33	9.19	49.6	10.4	5.65	4.85	6.12	7.34	9.08	41.6	7.42	9.27	9.1	6.19	6.49	6	21.6	20
Nb	(ppm)	4.3	0.91	4.03	0.03	6.03	16.8	*B.D.L	0.27	0.82	0.17	0.02	0.04	0.06	0.11	0.84	0.28	2.04	0.07	0.26	4.1	0.09	0.02	*B.D.L	10.9	13.6
Zr	(ppm)	3.21	24.9	12.8	66.1	79	3.94	2.62	9.21	27	323	10.9	2.33	7.48	4.91	452	151	67.8	3.52	7.52	3.99	2.35	3.36	2.41	55.4	158
Y	(ppm)	21.5	15.8	31.6	30.9	22.7	30.6	1.36	17.5	32.2	25.5	4.12	0.78	1	24	26.7	16	25.7	11.9	34.4	26.2	0.33	0.55	0.52	21.2	13.2
La	(ppm)	0.29	0.41	0.7	11.2	77	0.28	0.05	0.09	0.14	111	27.9	0.01	0.04	1.59	0.1	0.27	96.2	0.03	0.16	0.16	0.12	0.03	0.45	16	19.3
Ce	(ppm)	0.69	0.51	2.46	28.5	186	0.86	0.04	0.26	0.64	229	56.9	0.05	0.27	3.26	0.18	0.49	225	0.31	0.43	0.26	0.06	0.03	0.48	26.2	38
Pr	(ppm)	0.16	0.05	0.22	4.03	32.6	0.16	*B.D.L	0.06	0.14	43.9	9.54	*B.D.L	0.03	0.37	0.02	0.08	38.1	0.13	0.07	0.08	*B.D.L	0.1	0.03	3.25	5.54
Nd	(ppm)	0.91	0.79	3.35	22.6	164	1.22	*B.D.L	0.59	1.17	241	51.1	*B.D.L	0.34	3.27	0.6	0.86	222	1.56	1.34	0.75	*B.D.L	*B.D.L	0.24	14.6	23
Sm	(ppm)	1.96	1.07	1.37	5.94	41.6	2.66	*B.D.L	0.59	1.82	48.1	10.7	0.07	0.2	1.29	0.69	0.81	38.4	1.05	1.2	0.75	*B.D.L	0.15	0.14	3.76	3.51
Eu	(ppm)	0.78	0.51	2.05	2.38	13.1	1.68	0.04	0.44	1.09	6.15	1.08	*B.D.L	0.02	0.25	0.2	0.27	4.16	0.31	0.94	0.96	0.06	*B.D.L	0.03	1.48	1.07
Gd	(ppm)	2.07	3.19	0.76	6.28	17.4	4.12	0.25	1.65	3.63	14.5	5	*B.D.L	2.23	1.62	1.62	1.52	19.6	0.76	2.42	3.58	*B.D.L	1.69	0.85	3.92	3.25
Tb	(ppm)	0.41	0.26	0.94	1.07	1.46	0.97	0.01	0.5	0.83	1.11	0.5	0.03	*B.D.L	0.26	0.48	0.44	1.44	0.32	0.85	0.75	0.08	0.24	0.12	0.59	0.59
Dy	(ppm)	3.4	1.88	4.21	7.27	5.47	5.92	0.16	2.61	6.33	4.03	1.86	0.06	0.22	3.03	4	2.01	6.79	2.81	5.84	4.84	0.09	0.11	*B.D.L	4.37	3.37
Ho	(ppm)	0.7	0.48	1.6	1.34	0.71	1.32	0.13	0.51	1.58	0.61	0.23	0.02	0.03	0.82	0.93	0.58	1.1	0.44	1.73	1.32	*B.D.L	0.03	*B.D.L	0.77	0.67
Er	(ppm)	2.95	1.62	3.82	3.62	2.22	4.29	0.12	2.29	4.03	1.85	0.54	0.41	0.06	3.25	4.16	1.88	2.88	1.83	3.11	3.27	0.21	*B.D.L	*B.D.L	1.47	1.11
Tm	(ppm)	0.21	0.15	0.19	0.5	0.37	0.8	0.04	0.39	0.45	0.25	0.03	0.02	0.03	0.55	0.67	0.25	0.34	0.21	0.68	0.53	0.05	*B.D.L	*B.D.L	0.21	0.27
Yb	(ppm)	2.44	2.26	4.74	3.98	2.64	6.74	0.13	3.16	4.11	3.33	0.88	0.51	0.27	5.11	6.56	2.18	3.88	1.52	5.49	3.4	0.11	0.29	0.13	1.67	1.68
Lu	(ppm)	0.47	0.34	0.52	0.22	0.2	1.13	0.03	0.21	0.36	0.53	0.04	0.03	0.06	0.72	1	0.22	0.36	0.3	0.73	0.36	0.03	0.07	*B.D.L	0.41	0.22
Li	(ppm)	25.2	27.2	31.3	27.1	23.4	13.9	22.5	21.5	23.5	43.3	22.6	21.3	23.7	25.6	19.9	19.4	28.7	20.9	20.2	23.6	22.5	22.8	22.33	7.13	10.8
Be	(ppm)	1	0.43	1.38	2.45	0.89	0.5	1.1	0.93	0.82	1.44	0.15	0.26	1.57	*B.D.L	0.56	0.52	0.88	1.5	1.39	0.96	0.86	0.68	0.41	1	0.33
Sc	(ppm)	67.1	85.8	18.1	19.6	43.8	39.7	53.3	79.2	11.7	18.2	45.8	15.22	58.4	38.8	67.1	73.3	37.1	104	13.1	141	13.9	14.6	16.5	42.9	29.6
V	(ppm)	263	270	464	478	322	372	52.9	232	332	219	164	130	191	439	393	261	268	197	482	274	75.2	71.4	75.8	279	157
Co	(ppm)	28	26.3	31.3	28.3	29.8	22.9	26	46.7	47.4	83.7	45	41.6	42.4	56.2	48.1	47.7	62.3	44.1	45.3	45	39.7	39.8	39.4	26.7	24
Ni	(ppm)	176.2	174	226	193	144	129	131	171	177	292	76.4	58.1	80.3	142	119	127	187	115.1	130	122	68.7	77.8	67.3	117	100
Cr	(ppm)	261	430	1103	773	627	672	103	458	548	711	80.5	6.95	68.4	465	437	693	477	306	707	424	311	38.9	40.8	512	338
Cu	(ppm)	75.3	20.4	27.5	26.3	31.9	27.2	67.8	21.2	15.8	32.3	12.7	16.8	12.8	9.96	9.38	12.5	20.8	11.4	13.5	19.9	10.6	10.3	11.2	60.9	60.8
Zn	(ppm)	366	359	470	396	315	237	360	158	145	245	105	121	124	154	135	138	216	123	117	127	124	134	131	85.2	117
P	(ppm)	6.54	7.2	18.2	22.6	22.8	14.4	8.06	12.2	12.3	6.35	20.6	16.8	11.9	12.1	21.7	25.3	36.2	66.2	22.2	2.46	15.3	21.2	8.03	218	232
Ga	(ppm)	20.3	13.9	29.5	29.4	19.6	19.2	5.94	14.8	29.9	31.1	8.23	7.9	7.44	19.7	16.6	13.6	31.6	13.7	28.8	16.9	5.51	5.38	5.62	14.5	11.8

*B.D.L = Below detectio

N FAULT ZONE BRECCIATED BLUESCHISTS

SO1877	SO1877	SO1877	SO1877	SO1877.1	SO1877.1	SO1877.1	SO1877.1	SO1877.1	SO1877.1	SO1877.1	SO1877.1	SO1877.1	SO1877.1	SO1877	SO1877	SO1877	SO1877	SO1877	SO1877	SO1877	SO1877	SO1877	SO1877	SO1877	SO1877	SO1877	SO1877	SO1877.1	SO1877.1	SO1877.1	SO1877.1	SO1877.1
Black	Black	Black	Black	Black	Black	Black	Black	Black	Black	Black	Black	Black	Black	Brown	Brown	Brown	Brown	Brown	Brown	Brown	Brown	Brown	Brown	Brown	Brown	Brown	Brown	Brown	Brown	Brown	Brown	Brown
77d-3	77d-4	77d-5	77d-6	771a-4	771a-6	771a-5	771a-3	771a-2	771a-1	771b-1	771b-2	771d-1	771d-2	77a-5	77a-4	77a-3	77a-2	77-a1	77b-3	77b-4	77b-1	77b-2	77c-1	77c-2	77c-3	77c-4	77c-5	771c-1	771c-2	771e-1	771f-1	771f-2
2.91	1.95	1.84	2.48	4.61	5.6	5.73	5.07	3.48	3.24	8.74	6.32	2.62	3.38	1.02	0.53	0.83	0.74	0.52	0.51	0.63	0.97	0.64	0.8	0.65	0.72	0.95	1.02	0.9	0.28	0.34	0.88	0.91
39.9	25.5	21.9	35.6	57.5	21.9	38.4	30.6	36.9	29.1	48.4	45.1	45.4	68.9	4.25	5.91	11	10.8	4.23	4.76	10.1	21.4	6.84	11.01	6.12	6.49	9.37	9.65	22.3	2.35	1.55	5.02	1.24
24.6	37.3	24.1	30.3	40.7	32.1	40.8	33.5	36.9	25.5	33.5	34.5	29.1	36.6	36.3	37	37.7	34	41.2	39.7	31.3	26	26.4	45.7	58	47.7	46.6	51.4	52.7	56.4	44.9	68.8	55.5
1.53	3.8	2.96	1.47	1.94	8.66	4.31	11	8.95	2.73	3.24	4.59	1.88	7.45	1.63	0.97	1.61	2.26	3.97	8.69	2.05	1.48	1.98	2.45	1.9	2.2	1.51	1.64	1.83	3.37	1.36	1.61	2.16
0.44	1	0.71	0.81	0.97	2.99	2.37	1.99	1.59	1.28	1.79	1.65	0.96	1.25	0.19	0.28	0.45	0.43	0.27	0.33	0.4	0.33	0.19	0.61	0.38	0.37	0.69	0.61	0.4	0.38	0.03	0.22	0.22
0.28	0.23	0.14	0.28	0.36	0.13	0.31	0.18	0.22	0.08	0.27	0.28	0.21	0.21	0.06	0.09	0.11	0.11	0.05	0.01	0.1	0.12	0.02	0.09	0.11	0.07	0.07	0.23	0.13	*B.D.L	0.06	0.06	*B.D.L
2.3	13.1	4.69	7.17	4.96	34.9	18	20.4	22.2	8.59	16.9	14.8	5.19	7.9	2.25	1.81	2.44	2.14	3.16	2.62	2.96	2.42	1.95	3.41	4.24	2.39	4.05	2.91	4.1	3.94	1.51	2.13	1.3
0.52	1.52	0.82	0.86	1.2	3.82	1.89	1.99	1.68	1.19	2.22	2.23	0.69	1.87	0.64	0.7	0.91	1.35	1.21	2.12	1.04	1.24	0.8	1.01	2.04	1.11	1.19	1.21	1.48	1.63	0.72	0.76	0.43
3.44	12.1	1.68	2.75	3.61	9.61	4.55	3.07	3.22	3.55	2.14	2.24	3.48	2.64	10	2.16	2.49	2.18	2.52	2.1	2.03	4.84	3.66	3.19	28.9	3.64	4.99	3.86	3.06	1.56	1.36	2.19	2.21
16.7	27	19.8	27.2	21.1	37.5	27.3	26.5	27.1	21.1	23.9	26.5	17.8	21.6	38.3	33.3	34.4	34.2	40.2	38.9	29.6	31	30.6	40.6	51.8	40.8	47.3	40.9	47.5	50.5	45.5	61.1	55.7
9.33	17.6	11.2	14.4	14.4	45.7	31.9	37.1	28.1	21.2	24.3	25.4	14.2	15.8	5.54	5.17	7.57	7.57	6.57	6.34	7.37	7.21	7.64	8.97	10.7	8.92	11.8	8.94	8.33	10.5	1.73	5.17	4.98
75.4	131	120	107	67.4	291	199	418	139	89.1	127	153	183	352	49.0	49.5	60.2	53.7	64.9	150	52.2	56.9	36.6	63.4	65.3	67.4	72.4	65.1	51.1	77.3	29.9	43.6	108
14	30.2	19.3	25.3	19.8	50.6	33.4	33.7	32.3	22.5	29	29.6	15.7	19.2	43.7	37.4	41.3	38.3	50.6	46.8	35.3	28.5	34.1	55.3	70.8	57.8	61.1	59.9	58.7	62.1	43.1	57.9	51.1
6.89	49.2	47.6	76	8.31	111	76.9	43.4	70.2	21.9	57.9	72.9	5.47	15.5	2.64	2.73	8.66	4.29	10.5	3.46	2.04	16.4	6.98	17.1	14.9	3.53	23.6	4.36	7.56	9.12	1.15	3.16	1.15
11.9	92.8	96.8	130	15.7	198	134	77.3	140	40.6	106	120	13.7	28.8	6.17	6.17	19.4	11.2	23.9	7.89	4.96	29.8	11.3	34.2	30.7	7.5	47.8	12.0	11.2	20.5	3.3	6.3	4.12
1.85	10.9	10.3	15.9	2.19	25.2	15.4	9.72	17.7	5.01	11.6	13.2	2	3.63	0.96	1.11	2.4	1.89	2.87	1.39	0.88	3.36	1.3	5.28	3.81	1.55	5.97	2.27	2.01	2.73	0.67	1.68	0.91
6.11	42.5	42.4	62.8	9.51	106	63.8	47.2	76.7	22.5	45.2	55.2	9.83	16.9	7.45	7.29	11.2	12.9	14.5	10.2	6.39	13.6	8.55	23.5	18.0	12.7	26.9	16.4	10.4	16.4	9.22	11.8	9.91
1.22	8.31	6.9	8.57	3.44	15.8	9.59	8.73	11	3.35	9.16	8.67	3.48	3.39	4.57	3.8	4.72	4.75	6.83	5.3	3.74	3.92	3.81	8.82	9.48	5.3	8.70	8.75	6.94	7.54	4.56	5.48	4.39
1.05	2.47	1.79	2.29	1.35	4.59	2.22	2.56	3.2	1.49	2.71	2.25	0.88	1.11	2	1.47	1.83	1.63	2.47	1.97	1.76	1.83	1.42	2.47	3.51	3.37	3.14	3.03	2.35	2.7	1.87	3.28	1.94
2.16	8.95	3.44	4.64	2.69	12	6.9	9.34	6.82	5.16	7.34	7.65	1.7	2.21	5.97	4.99	4.61	5.44	8.25	4.48	7.11	4.52	5.58	7.8	13.7	8.94	8.18	8.29	6.8	6.71	8.07	9.29	7.13
0.62	1.04	0.57	0.78	0.59	1.6	0.76	1.61	1.4	0.82	1.08	1.11	0.48	0.35	0.91	1.09	1.13	0.93	1.52	1.32	0.89	0.82	0.92	0.99	1.73	1.22	1.91	1.61	1.42	1.41	0.91	1.57	1.1
2.29	5.9	4.38	5.81	3.35	12.4	7.63	8.45	6.59	4.34	6.6	6.02	3.69	3.95	7.16	5.4	7.3	6.82	7.78	8.5	5.44	5.37	5.72	9.26	12.9	9.61	10	10.6	10.4	10.7	6.47	8.31	6.57
0.53	1.1	0.68	1.25	0.68	2.11	1.73	1.33	1.47	0.86	1.36	1.74	0.73	0.77	1.6	1.42	1.59	1.56	1.89	1.77	1.37	1.05	1.54	1.81	3.07	2.04	2.35	2.37	2.03	2.61	1.99	2.14	2.14
1.12	4.39	1.85	3.17	1.28	5.11	4.5	3.37	3.94	2.16	2.25	3.56	2.02	2.05	4.03	4.08	4.93	3.65	5.71	5.15	3.56	3.19	3.89	6.66	7.08	6.73	5.97	6.68	6.18	5.77	4.63	5.7	5.76
0.37	0.35	0.31	0.46	0.3	0.84	0.58	0.46	0.54	0.2	0.47	0.35	0.32	0.46	0.58	0.48	0.86	0.66	0.61	0.8	0.57	0.34	0.51	0.74	0.9	0.79	0.90	0.6	0.68	0.44	0.73	0.66	0.73
1.53	2.51	1.81	2.52	2.21	6.34	3.21	3.89	4.53	1.77	3.05	2.62	1.6	3.17	4.6	3.55	4.48	4.63	5.88	4.75	4.1	3.54	5.11	5.7	7.3	5.43	5.26	7.23	7.17	7.03	5.47	5.7	5.12
0.14	0.33	0.31	0.43	0.32	0.83	0.5	0.5	0.48	0.45	0.53	0.6	0.25	0.38	0.51	0.51	0.63	0.66	0.83	0.82	0.6	0.43	0.54	0.72	0.83	0.75	1.07	1.18	0.88	0.82	0.76	0.9	0.49
9.68	8.14	6.65	8.4	11.6	9.72	11.5	9.36	10.1	9.08	11.7	12.5	8.68	12.5	9.5	9.02	10.1	9.73	10.8	12.5	9.91	10.6	9.53	10.8	11.7	10.7	11.6	11.3	13.9	12.2	13.3	12.4	14.5
0.15	0.99	0.81	0.58	0.35	0.85	*B.D.L	0.86	0.92	1.3	2.21	0.56	0.66	0.26	0.91	0.75	0.72	1.12	1.41	1.74	1.06	1.41	*B.D.L	1.21	1.39	1.89	1.43	1.03	2.98	0.27	0.79	1	2.37
27	44.8	34.2	38.9	29.6	81.4	68	52.6	62.6	45.8	46.9	55.6	38.7	39.1	61.1	52.3	62	58.3	58.4	59	64.6	44.7	50.4	72.6	82.9	73.6	76.5	79.9	72.3	76.1	61.2	85.4	72.8
147	280	202	236	182	360	300	243	329	216	251	309	180	238	420	391	427	387	459	468	391	298	341	464	584	521	496	545	511	551	454	580	468
25.6	33.4	20.2	24.3	36.2	37.5	39.9	30.6	38.2	34.6	42.1	45.3	31.8	35.9	48.1	42.5	44.6	42.2	45.3	52.2	42.3	42.4	40.7	46.7	50.2	44.8	50.5	162	54.8	41.5	43.7	63.7	62.8
114	123	76.1	105	184	144	173	140	170	154	170	194	141	153	202	196	194	195	197	230	179	187	184	204	230	217	217	283	280	289	258.4	239	258
356	550	386.1	480	399	703	669	520	624	406	501	613	400	481	621	634	659	681	688	703	589	460	516.8	751	992	840	779	916	787	856	489.6	772	676
29.5	67.8	41.6	40.8	76	80.5	86.4	90.3	112	65.2	23.7	76.6	47	54.1	202	114	124	119	132	115	90.8	103	83.1	76.1	151	142	85.2	323	220	21.7	21.8	41.9	155
76.6	83	63.1	75.6	138	106	107	102	115	91.3	104	118	81.4	88.3	141	144	168	244	205	154	122	140	148	138	131	125.4	164	147	136	135	139	128	164
266	287	105	486	422	405	136	282	245	287	455	182	502	1268	167	217	404	140	392	212	154	89.4	136	131	176.5	153	156	134	374	238	116	151	162
11.5	16.5	14.9	17.03	15.2	16.9	15.3	12.8	16.1	14.4	16	16.3	9.63	11.6	22.2	19.9	20.6	21.2	23.5	24.3	17.7	18.4	18.3	23.8	24.7	22.1	25.9	25.2	31.6	27.7	29.9	30.3	26.4

limits

8. Discussion and conclusions

8.1 Fluid producing reactions and further constraints on the origin of fluids at blueschist-facies conditions and beyond

Historically, there has been some debate about the definition, or even the existence, of the blueschist-facies mineral paragenesis (e.g., Turner, 1981) not so commonly preserved in metamafic lithologies. However, blueschists in orogenic belts and suture zones are key evidence for the existence of a paleo-subduction environment (e.g., Ernst, 1973). Blueschists offer visually impressive mineral assemblages, with the following most diagnostic index phases indicating a high pressure-low temperature metamorphism: glaucophane, lawsonite, omphacitic-jadeitic clinopyroxene, phengite, pumpellyite and aragonite. These phases occur in varying modal abundances and are accompanied by significant to minor amounts of epidote, chlorite, quartz, actinolite, albite, paragonite, stilpnomelane and garnet. Notably, most of these minerals contain considerable amounts of water ranging from c. 1.7 to 11.5 wt% of H_2O. Thus, an altered oceanic metabasite contains around 2 and 6 wt% of H_2O in the epidote and lawsonite blueschist-facies, respectively, before dehydration upon entering the eclogite-facies during subduction (e.g., Peacock, 1993). An oceanic basaltic lithology is transformed into a blueschist upon progress of multivariant reactions that can be described roughly in two different ways. For a "warm" subduction gradient, a metabasite will transform into blueschist via the breakdown of a greenschist-facies assemblage. This can be described as:

$$\text{Actinolite} + \text{Chlorite} + \text{Albite} = \text{Glaucophane} + \text{Zoisite (or epidote)} + \text{Quartz} + H_2O \quad (8.1)$$

For a colder thermal gradient, the process may be described as:

$$\text{Actinolite} + \text{Chlorite} + \text{Albite} + \text{Quartz} = \text{Glaucophane} + \text{Lawsonite} + \text{Paragonite} + H_2O \quad (8.2)$$

(actinolite generally disappears from the assemblages after reaction progress). In situations where a blueschist is formed due to the breakdown of a prehnite-pumpellyite-facies lithology, the main reactions are characterized as follow:

$$\text{Prehnite} + \text{Calcite} + \text{Albite} + \text{Chlorite} = \text{Glaucophane} + \text{Lawsonite} + \text{Zoisite} + H_2O + CO_2 \quad (8.3)$$

and

$$\text{Pumpellyite} + \text{Chlorite} + \text{Albite} + \text{Quartz} = \text{Glaucophane} + \text{Lawsonite (or Epidote)} + H_2O \pm \text{Paragonite} \quad (8.4)$$

It should be noted that dehydration of a rock volume cannot proceed until the amount of H_2O required to satisfy a certain mineral assemblage at a given P-T condition is less than the pre-reaction bulk H_2O content of a rock. Thus, under H_2O-saturated conditions rocks will eventually release H_2O. At undersaturated conditions, the minerals may be characterized by a fully metamorphic (minerals are

stable and react but H_2O saturation is not reached) or not fully metamorphic (a magmatic metastable assemblage is preserved) assemblage. The H_2O distribution within the oceanic crust is heterogenous even at the millimeter-scale. Under this perspective, rocks containing the greater amounts of H_2O are expected to devolatilize earlier, while those water-deficient remain metastable until reaching higher temperatures. Consequently, fluid-undersaturated rocks eventually undergo hydration if they are infiltrated by external fluids produced at deeper levels or adjacent to dehydrating lithologies (e.g., Bebout, 1991; Peacock, 1993). In this regard, H_2O-undersaturated rocks behave as sinks for free H_2O-rich fluids. The subduction thermal gradient will also have a strong impact on the location of the water-releasing reactions (van Keken et al., 2011; ***Figure 2.6***). In cold subduction environments, a lawsonite blueschist retains c. 6 wt% of H_2O until reaching the eclogite transition. The transformation of a blueschist into an eclogite is accompanied by massive H_2O release via crossing the upper boundary of the lawsonite blueschist-facies field:

$$\text{Glaucophane} + \text{Lawsonite} = \text{Omphacite} + \text{Garnet} + \text{Quartz} + H_2O \quad (8.5)$$

or, in warmer environments, as following:

$$\text{Glaucophane} + \text{Clinozoisite} = \text{Omphacite} + \text{Garnet} + \text{Quartz} + H_2O \quad (8.6)$$

Note that the reactions above contain the solid solutions omphacite and garnet for simplicity; however, the corresponding reactions have been deduced considering end-members in the NCMASH system (Evans, 1990), thus, including jadeite + diopside and pyrope, instead of omphacite and garnet, respectively, can also be regarded as a correct procedure. Potassium is not considered in the above set of reactions; however, phengite, the most common K-bearing phase in mafic systems, can well be stable under blueschist and eclogite-facies conditions.

In Seghin and Infiernillo blueschists (**Chapters 4** and **5**), the early stages of veining are characterized by internal fluid production (dehydration), while external sources are inferred at near-peak conditions. In the metamafic lithologies, early albite veins, thought to have precipitated from zeolite or clays breakdown (see below), were followed by further internally-derived veining; precipitating glaucophane and winchite at Infiernillo whereas lawsonite, glaucophane and clinopyroxene formed at Seghin. Depending on the bulk rock composition, reactions 8.1, 8.2, 8.3 and 8.4 are likely candidates to account for the earlier stages of blueschist-facies veining. At Infiernillo locality, lawsonite is absent but glaucophane is abundant. In consequence, a reaction of the types 8.1 and 8.4 were the main responsible for internal fluid production and further glaucophane veining. These statements are supported by thermodynamic modelling which predicts the following set of prograde (250-0.5 to 400°C-0.8 GPa) reactions: Chl + Ab + Ttn + Qz -> Act + Chl + Ab + Ttn + Qz -> Wnc + Gln + Chl + Ab + Ttn + Qz (see pseudosection from ***Figure 4.S2B***). Note that neither chlorite nor albite are fully consumed during reaction progress, but their volumetric abundance decreases. In addition, glaucophane has been observed lining albite vein-host walls or as needles replacing albite along grain boundaries (e.g., ***Figures 4.5G*** and ***H***). An explanation for these textures is that a reaction

involving partial consumption of chlorite and albite, facilitated by strong differences in Fe-Mg chemical potential between the chlorite-bearing host and the albite vein, enhanced diffusion and, in consequence, glaucophane precipitation associated with H_2O production.

In Seghin, all the four reactions mentioned above are possible. Yet, some arguments can be made for roughly constraining the most likely fluid producing reactions for the early stages of blueschist-facies veining. Actinolite is widely observed as cores within amphibole grains and rare pumpellyite grains are present, while lawsonite and zoisite (or epidote) are rarely observed in apparent textural equilibrium. This texture favors type 8.1, 8.2 and 8.4 reactions, although it does not discard reaction 8.3. Among reactions 8.1, 8.2 and 8.4, it is not possible to accurately establish which was the most important fluid-producing reaction in the early stages of veining, as the prograde path falls along the transition band between the epidote- and lawsonite-blueschist-facies. For a prograde trajectory along the epidote-blueschist-facies (250-0.4 to 480°C-1.4 GPa; ***Figure 8.1A***), thermodynamic modelling predicts the consumption of pumpellyite, albite and chlorite (partially) to give rise to an assemblage dominated by epidote + glaucophane + white mica + chlorite + quartz + clinopyroxene as well as minor garnet and titanite. On the other hand, a prograde path along the lawsonite-blueschist-facies involves the breakdown and the formation of similar phases but resulting in a lawsonite-bearing assemblage instead of epidote (***Figure 8.1B***). Consequently, it is likely that the most important H_2O-producing reaction during prograde epidote- and lawsonite-blueschist-facies metamorphism was of the type 8.4. In this scenario, a slight variation in the bulk rock composition (or subduction thermal gradient) would allow the formation of one or the other mineral assemblage (including variations in major elements and in oxygen fugacity). Interestingly, albite in veins is lined and apparently replaced by Na-Ca clinopyroxene. Similar to the case of Infiernillo, this texture may be explained by strong gradients in the Fe-Mg chemical potential from the host towards the vein. In this case, associated with a reaction of the type of albite = clinopyroxene + quartz, but considering a Fe-Mg-bearing phase on the reactant side. A point of particular interest is the absence of epidote in the vein while it is present in the host and, instead, lawsonite occur. In **Chapter 5**, we have concluded that this is due to a compositional effect as the vein system will be dominated by O, Ca, Al, Si, H, Na and to a lesser extent Fe and Mg, extending the stability field of lawsonite towards higher temperatures and suppressing that of epidote (e.g., Martin et al., 2014). These veining events are followed by rehydration stages at near-peak conditions, as suggested by lawsonite overgrowths after epidote in the blueschists and as predicted using thermodynamic modelling (***Figure 5.11***). Peacock (1993) suggested that this scenario is possible under the presence of deep-seated, externally-derived fluids (see **Chapter 5** for further details).

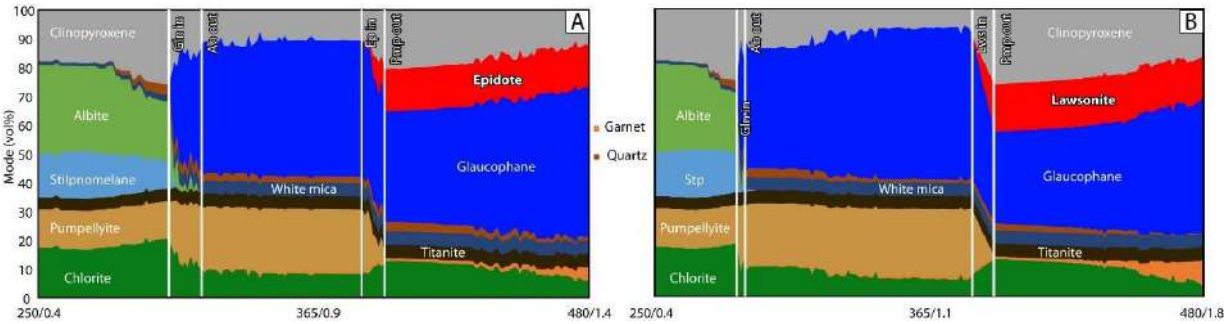

Figure 8.1. Modes (vol%) for a given P-T path characteristic of an (A) epidote-blueschist-facies and a (B) lawsonite-blueschist-facies metamorphism for a basaltic blueschist composition (see the modeled blueschist from Chapter 5). The appearance or disappearance of relevant minerals is highlighted. For illustrative purposes, the epidote- to lawsonite-blueschist-facies transition has been obtained after varying the subduction thermal gradient slope in the pseudosection P-T space, however, similar effects are expected considering bulk rock chemical variations.

In **Chapters 6** and **7**, we report intriguing Ti enrichments materialized in (i) anomalously high amounts of titanite in the vein domains (titanite + Na-amphibole bands in ***Figure 6.4B***), (ii) gradual titanite enrichments towards ultracataclastic host-vein margins (e.g., ***Figure 6.4A***) and (iii) titanite-rich ultracataclastic veins from the fault-related rocks (e.g., **Chapter 7**). Other Ti-related elements such as Zr, Ta and Nb, as well as Cr, are also enriched, accordingly. Furthermore, LREEs are notably depleted approaching the vein margins. In titanite, REEs, Y, Sr, U, Th and Pb may eventually substitute Ca in the corresponding structural site. While HFSEs such as Nb, Ta, Zr and W substitute Ti in the octahedral position (Ribbe, 1980). The incorporation of very high amounts of some of these elements (e.g., up to 16 and 9 wt% of Nb_2O_5 and ZrO_2; Liferovich and Mitchell, 2005) into titanite is controlled by its availability, enlightening the nature of the fluids from which titanite precipitated. In addition, Ti-rich phases (rutile and titanite) are the main carriers of HFSEs in subducted mafic lithologies (e.g., Zack et al., 2002).

Setting a hypothesis for this issue is challenging since, to my knowledge, somehow comparable chemical signatures have only been reported in the Tianshan (China; Gao et al., 2007) and Tromsø (Norway; Lucassen et al., 2010; 2011) eclogites. In the Tianshan, up to tens of meters-long transport veins bearing coarse-grained rutile as well as segregation veins and adjacent host eclogites were documented. Trace and major elements analyses show depletions in Ti, Nb, Ta, LILEs and HREEs from the eclogite host towards the segregations, interpreted as the breakdown of titanite associated with rutile-forming reactions occurring in the blueschist-to-eclogite transition (reactions 8.5, 8.6 and 8.7).

$$\text{Clinozoisite (or } \mathbf{Lawsonite}) + \mathbf{Titanite} = \text{Garnet} + \mathbf{Rutile} + SiO_2 + H_2O \quad (8.7)$$

In addition, similar chemical variations are reported in garnet rims and omphacite cores from the host eclogite, confirming a joint element mobilization towards the segregation vein. In the latter domain, the HFSEs were preferentially incorporated into centimeter-sized rutile crystals. It is inferred that Ti-Nb-Ta mobilization processes occurred at least at the decametre-scale, perhaps even at larger scales in strongly "channelized" pathways through hydrofractures and the shear zone (e.g., Zack and John,

2007). The exact mechanisms enhancing mobility of such "immobile" elements are unknown. However, Gao et al. (2007) hypothesized that F-Na-Al-Si polymers in solution (e.g., Manning, 2004; John et al., 2008; Antignano and Manning, 2008) have enhanced rutile, and consequently Ti-Nb-Ta solubilities allowing transport at the several tens of meters scale. In addition, an increase in CO_2 activities in C-O-H fluids would allow rutile precipitation (Ayers and Watson, 1993), leading to the incorporation of Ti-Nb-Ta within rutile crystals depleting the fluids in these elements. Somewhat similar conclusions were drawn by Lucassen et al. (2011) at Tromsø, where titanite grains, produced by rutile dissolution associated with eclogite retrogression, record fluid-assisted mobilization of HFSEs into titanite. Combining trace elements along with $^{87}Sr/^{86}Sr$ analyses, the authors concluded that centimeter-sized titanite crystals in veins and titanite aggregates around rutile formed under a mixture of rock-buffered porous flow and fracture-enhanced channelized flow similar to the mixed channelized-porous flow model (porosity waves) proposed in **Chapter 5**.

It is clear that elements such as Ti-Nb-Ta and others are indeed mobile under certain conditions related to titanite or rutile breakdown and/or precipitation, especially in the vicinity of the blueschist-to-eclogite transition. **Therefore, I propose that the Ti-Nb-Ta (-Zr) enrichments detected towards ultracataclasites in the host-vein margins, as well as the high amounts of titanite in the vein stripes, represent metasomatic fingerprints of the influx of externally-derived fluids sourced from the blueschist-to-eclogite transition occurring at greater depths**. Note that the in-situ LA-ICP-MS results are from rasterized surfaces (500x100 μm) from fine- to extremely fine-grained materials and, identification of the exact mineral chemistry of trace elements was not possible. However, the high amounts of titanite detected optically and through X-ray mapping (e.g., ***Figures 6.4A*** and ***B***), as well as the lack of rutile and normal (trace) amounts of zircon in all studied Seghin blueschists, allows to propose titanite as the main HFSEs-bearing phase. In addition, LREEs depletion towards the host-vein margins (e.g., ***Figure 6.6A***) point to selective leaching of these elements from the bulk rock (e.g., John et al., 2008), possibly associated with preferential dissolution of epidote, while the HREEs remained largely unaltered or buffered by the addition of titanite instead of epidote (see **Chapter 6**).

Motivated by these findings, I have reprocessed the Infiernillo X-ray maps presented in **Chapter 4** from an albite + glaucophane vein and a putative blueschist host (see ***Figures 4.6E, F*** and ***8.2***). The updated X-ray map displays the distribution of titanite throughout a large part of the thin section. There, an extremely fine-grained glaucophane-rich domain occurs as a clast within the albite + glaucophane vein, the former containing significantly higher amounts of titanite compared to other foliated blueschist domains. This titanite-rich domain differs in mineralogy compared to the foliated blueschist host; notably, glaucophane is much more abundant and fine-grained in the former while the latter is richer in albite. **Thus, I hypothesize that this glaucophane-titanite-rich "clast" represents a former (ultra?) cataclasite derived from the comminution of a blueschist host**. This statement is based on the striking similarities between the clast and Seghin cataclasites investigated in **Chapter 6**. Oddly, the foliation of the cataclastic domain from Infiernillo (***Figure 8.2***) is

perpendicular to that of the foliated blueschist host, but in agreement with the vein strike. Indeed, syntaxial crystal grow of albite and glaucophane seems to have nucleated from the inferred cataclastic domain, suggesting that comminution was followed by further veining in the prograde path. Unfortunately, the hand specimen has been accidentally broken during thin section preparation and adequate microstructural inspection of the host-vein margin is not possible.

The blueschist-to-eclogite transition occurring at deeper conditions implies Ti-Nb-Ta-Zr mobilization at least at the kilometres-scale (e.g., John et al., 2012). As noted above, transport of HFSEs is enhanced under a typical albitic aqueous fluid rich in F^-. To this point, it is inferred that fluids are typical Na-Al-Si solutions together with certain amounts of Fe-Mg-Ca (**Chapter 5**). Furthermore, I note that CO_2 (and Ca) activities are quite variable, as carbonate-veining events are usually associated with silicate-rich veining events. Moreover, it is likely that under conditions where CO_2 activities are low, rutile solubilities increase (e.g., Ayers and Watson, 1993; Gao et al., 2007), but mixing with CO_2-rich fluids enhanced precipitation of rutile, titanite and other Ti-rich minerals (and quartz; e.g., Wood and Walther, 1986; Gieré, 1990; Vitale Brovarone et al., 2018). It is suggested that CO_2-bearing fluids are generated after the interaction of H_2O-rich fluids with CO_2-bearing lithologies (e.g., calcschists) and further CO_2-dissolution (see **Chapter 5** for details). A similar process could have been responsible for external CO_2 fluid infiltration into the Infiernillo complex, since an external CO_2 source has also been inferred therein. **The interaction site is thought to be seated near the dehydration front (blueschist-to-eclogite transition)**. There, tremendous and continuous amounts of free H_2O are available to interact with nearby and distal lithologies on their way upwards along the subduction channel (e.g., Hacker et al., 2008; Padrón-Navarta et al., 2011). Although H_2O-fluid mediated decarbonation was probably produced by the flushing of mainly ultramafic-, but also mafic-derived fluids, **the mobilization of HFSEs and subsequent titanite-precipitating metasomatism clearly points to a mafic influence** – at least for some of the fluid pulses. Thus, it is expected that low amounts of CO_2 allow H_2O activity to increase up to critical levels enhancing transport and episodic precipitation of titanite at further shallower conditions.

The influx of mixed mafic-and sediment-derived fluids is evident, in agreement with low $\delta^{18}O$ values (compared to higher fresh marine carbonate $\delta^{18}O$ values of c. +30) measured in carbonate veins and host metasediments. However, these low $\delta^{18}O$ values (+17.9 to +13.9) are also compatible with H_2O mixing with an ultramafic-derived input (Jaeckel et al., 2018); not clearly identified in **Chapter 5**. The in-situ LA-ICP-MS analytical routines presented in **Chapter 6** shed a new light on this likely fluid source. First, we note that Cr concentrations gradually increase towards the ultracataclasite-vein margins, with values up to 2.6 times higher than with respect to the pristine blueschist host (e.g., ***Figure 6.6B***). Cr is commonly incorporated into titanite and/or rutile when hosted in metabasites (e.g., Zack et al., 2004) or infiltrated by an external Cr-rich fluid, as documented in rutile crystals from the Monviso (Spandler et al., 2011). Second, “trace elements” X-ray mapping in a brecciated lawsonite vein reveals Cr-“rich” regions (up to the weight percent level) in the vein breccia matrix as well as in lawsonite grain margins, in the latter domain apparently cementing some lawsonite

fragments (***Figure 6.S1I***). **Therefore, it is inferred that Cr enrichments represent the fingerprints of ultramafic-derived fluid sources associated with the breakdown of Cr-bearing minerals such as Cr-spinel or antigorite, as documented elsewhere** (van der Straaten et al., 2008; Spandler et al., 2011; Angiboust et al., 2014). **Thus, after careful inspection of lawsonite** (and clinopyroxene; see **Chapter 6**) **zoning patterns together with trace elements, isotopic and textural analyses** (see also **Chapter 5**), **it is possible to associate some of the major vein-forming fluid pulses to the subduction metamorphic history of these rocks as indicated in *Figures 8.3A*** to ***C***.

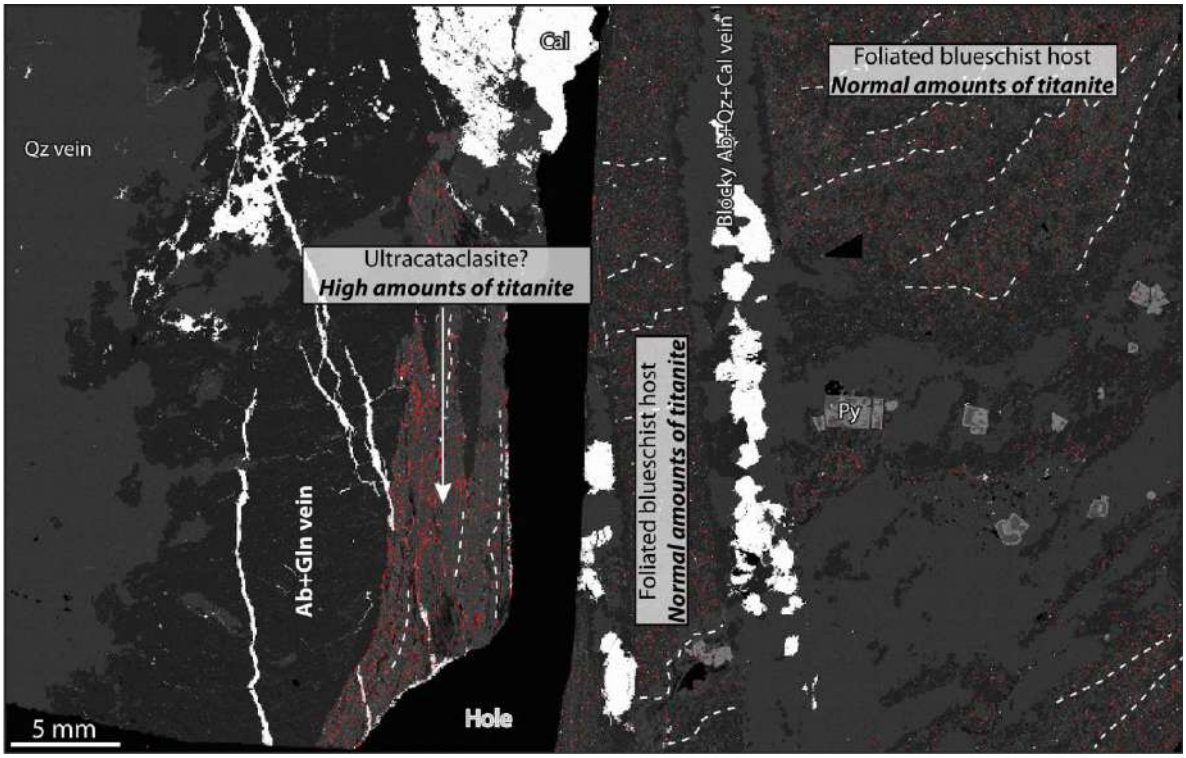

Figure 8.2. X-ray map (EDS) from the host-vein system investigated in Chapter 4 (see Figures 4.6E and F). Masked titanite (red) is displayed over a BSE background.

Even though antigorite breakdown at c. 650 °C eventually releases tremendous amounts of H_2O (c. 10 wt%; Padrón-Navarta et al., 2013), the structural position of the ultramafic lithologies during the prograde path and at deeper eclogite-facies conditions is undetermined. In other words, it is unknown to which extent serpentinite-derived fluids from the subcontinental or oceanic mantle were able to flow across the lithosphere to reach the highly permeable subduction channel and subsequent fluid flow (e.g., Kawano et al., 2011). In summary, this investigation allowed to detect the fingerprints of the three most common types of fluid sources: metasedimentary, mafic and ultramafic, reflecting complex fluid interactions in the megathrust shear zone. Last, I noted that some chemical anomalies, namely Ti, Nb and Ta enrichments were detected in the fault rocks studied in **Chapter 7**, while high amounts of titanite, likely associated with HFSE enrichments, are also observed in the Infiernillo sequence. The anomalies documented in **Chapter 7** are interpreted as the product of a externally-derived fluid contribution evolved from a mafic source. In contrast, these structures were produced

at shallower seismogenic depths (c. 30 km), and a scenario of larger-scale fluid circulation has been proposed (see below), **thus strengthening the representativeness of this signal along a range of depths and thermal gradients in subduction environments**.

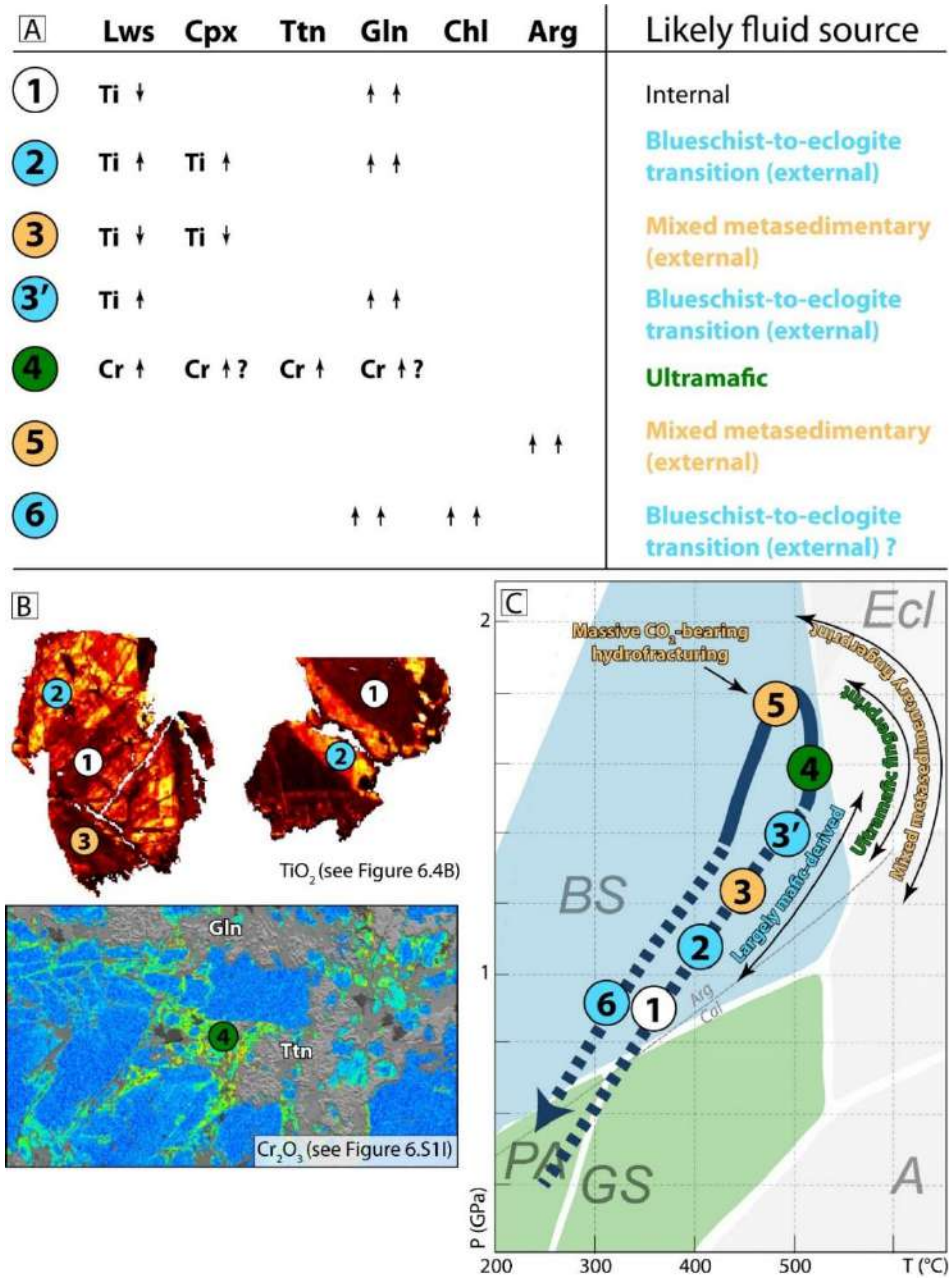

Figure 8.3. Summary and illustrative sketch of some of the main veining stages, fluid sources, mineralogical and chemical fingerprints relative to the inferred metamorphic path followed by the Seghin complex. A. Summary table of mineral chemical fingerprints detected in the lawsonite vein breccia samples studied in Chapter 6 complemented with some of the main observations from Chapter 5 (i.e., stages 3 and 5). The likely fluid sources for each stage are also depicted. B. Illustrative selected mapped crystals and areas from Figures 6.4B and 6.4SI linking a textural mineralogical pattern with respect to the relative conditions of fluid circulation and precipitation. C. P-T diagram depicting the veining stages inferred from Chapters 5 and 6, as also illustrated in panels A and B. The synthesis among the patterns shown here using the Seghin complex as example, are at some extent also valid for the Infiernillo complex since similar features were also observed there. Nevertheless, an ultramafic fluid contribution has not yet been detected in the latter.

8.2 Further considerations on carbon recycling

Large-scale fluid circulation is associated with fluid-mediated decarbonation reactions and further CO_2 flushing enhanced by the influx of H_2O-rich fluids through carbonate-bearing metasediments, in agreement with low $\delta^{18}O$ values and pristine marine carbonate $\delta^{13}C$ values in the range of +3.1 to -1.0. Our thermodynamic modelling approach demonstrates that prograde decarbonation in any of the Seghin CO_2-bearing lithologies is largely inefficient without considering the effects of H_2O infiltration and reaction (e.g., ***Figures 5.11C*** and ***D***; see also Ague and Nicolescu, 2014). Extrapolation of this model to the thermal gradient that characterizes Infiernillo metamorphism, i.e., c. 15 °C/km, and assuming that CO_2-bearing lithologies (e.g., marbles, calcschists and metapelites) would have constituted part of the subducting sequence, it is obtained that significantly higher amounts of CO_2 could potentially be released from a metapelite and calcschists, while a marble would still remain unaffected. In detail, a metapelite and a calcschist largely decarbonate releasing up to 1.6 wt% of CO_2 (0.36 mol of C/kg of rock) and 5.5 wt% of CO_2 (1.25 mol of C/kg of rock), respectively, within the epidote-blueschist-facies (c. 45 km depth) in the vicinity of the albite-epidote-amphibolite-facies. **These results confirm that in colder Seghin-like environments, decarbonation is only possible if an H_2O-rich fluid infiltrates, whereas under warmer Infiernillo-like conditions, CO_2-producing reactions do not require fluid-mediated decarbonation to proceed** (e.g., Gorce et al., 2019). In any case, there is still the need for a free fluid phase to allows for large-scale transportation and infiltration at warm conditions, as recorded by the Infiernillo sequence. Indeed, the hydrological state of the subduction zone is a key parameter driving decarbonation (e.g., Gorce et al., 2019; Stewart and Ague, 2020). Thus, if CO_2-bearing lithologies are subducted under an Infiernillo-like thermal gradient, decarbonation and further mobilization would be enhanced in the presence of fluids; even at conditions shallower than a hypothetical epidote-blueschist- or eclogite-facies metamorphism characteristic of "warm" thermal gradients (e.g., van Keken et al., 2018).

Carbonate vein abundance calculations are in the range of c. 0.5 to to 7 vol% for the Infiernillo and Seghin localities, respectively. Using open-system thermodynamic modelling, we have obtained that a calcschist, the most suitable lithology for decarbonation (see also Groppo et al., 2017), releases c. 28.2 g of C/kg of calcschist (2.35 mol of C/Kg of calcschist) after the infiltration of 49 mol of H_2O/kg of calcschist. Since no carbonate-bearing lithologies are exposed at Infiernillo locality (except for the veins), the following discussion considers the modelled lithologies and vein abundances from Seghin as representative for comparison with other subduction environments.

In this thesis (**Chapter 5**) we have deduced that widespread hydraulic breccias and former hydrofractures resulted from the infiltration of CO_2-bearing fluids. Thermodynamic calculations (e.g., ***Figure 5.11***) and previous experimental investigations have demonstrated that a carbonate-rich vein, considered as analogue to a marble-like system, is stable to conditions beyond subarc depths (e.g., Molina and Poli 2000; Franzolin et al., 2011). Consequently, free CO_2 produced by decarbonation at depths is potentially recycled and reprecipitated throughout the subducting slab creating a "pure"

carbonate domain (a vein) prone to sink into the mantle. In other words, devolatilized CO_2 and further outgassing calculations should consider this effect.

It is unexpected how contrasting are the conclusions regarding the viability of carbon to sink in the mantle or to be released at the forearc from subarc depths. Theoretical and petrological investigations indicate values ranging from 0% to more than 80% of carbon outgassed towards Earth's surface (e.g., Dasgupta and Hirschmann, 2010; Kelemen and Manning, 2015; Gorce et al., 2019). For comparison, I use a mathematical formulation devoted to estimate the amount of CO_2 needed to precipitate the observed vein volume using the estimates obtained for the Seghin complex, in the frame of a global point of view (e.g., Collins et al., 2015; Menzel et al., 2020; Stewart and Ague, 2020; Epstein et al., 2021).

In the following formulation (***Figure 8.4A***), I assume: (i) a perfectly tabular geometry for the subduction interface of length equal to the global trench length (L = $4.45*10^7$ m; Jarrard, 2003), (ii) width calculated from the hypothenuse length of a subduction zone dipping 60 ° in the 55 to 25 depth range (a 30 km window assuming to represent the ETS region), (iii) thickness of 300 m following Stewart and Ague (2020), (iv) a density of 3000 kg/m^3 to represent the whole rock column (including aragonite veins; aragonite density = 2930 kg/m^3) and (v) a carbonate vein abundance of 7 vol%. The first step is to calculate the subducting rock volume representing the interface, the region where fluids are most likely flowing through. Using simple trigonometry, it is derived that c. $3.95*10^{14}$ m^3 of rocks are contained in the proposed tabular body of dimensions 300 m x $4.45*10^7$ m x 25980 m, giving a total mass of $1.182*10^{18}$ kg; assuming a 7 vol% of veins, c. $9.9.*10^6$ Mt of C are needed to precipitate the amount of veins. These values are c. $1.2*10^5$ times larger than the total carbon input **per year** into the global subduction factory (i.e., altered oceanic crust + metasediments + altered peridotites = 82 ± 14 Mt/yr; see Plank and Manning, 2019); thus, c. $1.2*10^5$ years of carbon release and further re-precipitation in the subducting slab would be required to explain the observed vein abundances. Note that the estimates from Plank and Manning (2019) consider the input from organic and inorganic C independently. However, it has been shown that more than 80% of carbon is present as carbonate minerals (Bebout, 2007) and, for simplicity, considerations on organic carbon are neglected.

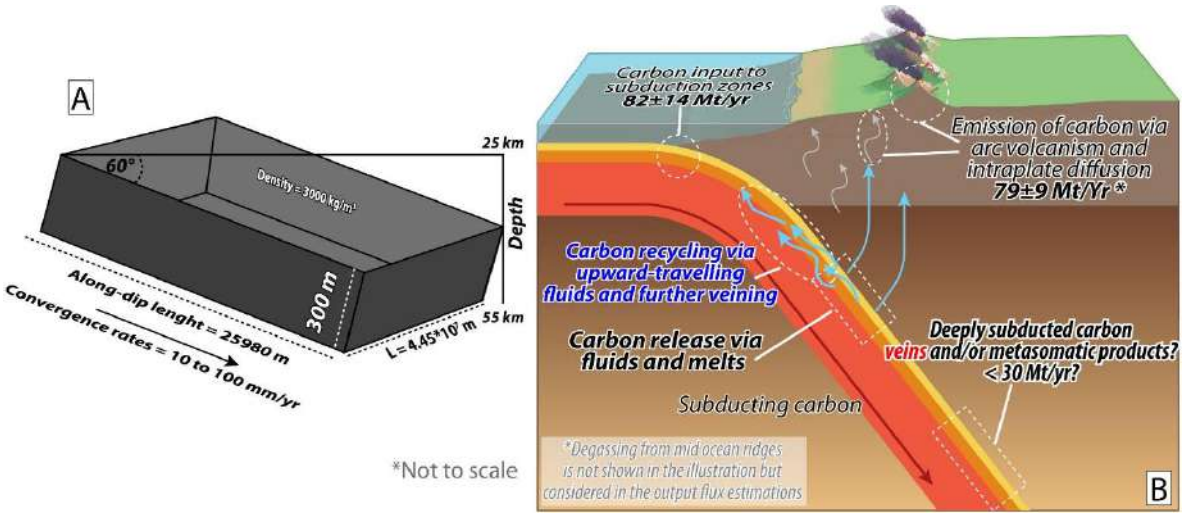

Figure 8.4. A. Sketch depicting the model formulation proposed in section 8.2. B. Illustration of a subduction margin constraining inputs and outputs of the carbon cycle modified from Plank and Manning (2019). The arrows symbolize decarbonation reactions and carbon transport through upward-travelling fluids and melts.

Of course, my intention is not to say that all carbon subducted in 120.000 years is (i) released from the subducting slab, (ii) able to flow upwards along the subduction interface and (iii) re-precipitate in the form of carbonate veins or hydraulic breccias. Indeed, if considering plate convergence velocities in the range of 10 to 100 mm/yr (e.g., Schellart, 2005), the along-dip length of our model tabular interface would be covered in $2.6*10^5$ to $2.6*10^6$ years in the depth range 25 to 55 km (25.98 km assuming a dipping angle of 60°). Thus, our model subduction interface will require 0.26 to 2.6 Myrs to subduct to conditions beyond the blueschist-facies. In consequence, the subducting tabular body would have a residence time of c. 2.2 to 22 times longer than that required for vein precipitation and hydrofracturing. Assuming that the carbon input and further decarbonation are constant along the envisaged time window, it can be speculated that c. 4.6 % to 46 % of the global input C budget is required (i.e., 3.8 to 38 Mt/yr) in order to precipitate 7 vol% of carbonate veins.

Previous carbon output calculations have proposed values of c. 79 +/- 9 Mt/yr of total C degassing through mid ocean ridge volcanism, volcanic arcs and intraplate diffusion (Plank and Manning, 2019), leaving a difference of c. 3 to 26 Mt/yr (within uncertainty) available to sink into the deep mantle (see also Kelemen and Manning, 2015). These calculations are in conflict with petrological constraints from Dasgupta and Hirschman (2010), predicting values orders of magnitude greater for C fluxes into the deep mantle. As noted above, **my estimates in the range of 3.8 to 38 Mt/yr indicate that a significant fraction of the total carbon input is likely stored or recycled as highly thermodynamically stable veins (almost pure carbonate composition) into the mantle** – no or very minor decarbonation is predicted using closed and open system thermodynamic modelling at eclogite-facies conditions (see **Chapter 5**). These crude estimates should be regarded as highly inaccurate for a number of reasons: (i) the vein abundances in the Seghin complex are likely high (up to one order of magnitude) compared to other subduction terrains such as the shallower Infinierllo complex, possibly representing an upper boundary. (ii) I cannot say for sure that all veins precipitated

in the 25 to 55 km depth range. (iii) The exact amounts of subducting carbon are still poorly constrained and their fate – e.g., almost complete decarbonation at sub-arc depths (or shallower) vs. recycling of a large part of the total C budget into the mantle – is a matter of vivid debate (e.g., Dasgupta and Hirschman, 2010; Plank and Manning, 2019). (iv) The subduction angles (and velocities) worldwide are variable and the assumption of 60° is certainly not representative for all subduction zones worldwide (but in agreement for margins experiencing oceanic-continental and oceanic-oceanic subduction, i.e., in the range of 50 ± 20° and 70 ± 20°, respectively; see Lallemand et al., 2005). (v) The kinetics of carbonate fluid precipitation at the blueschist-facies conditions is, to the best of my knowledge, unknown and (vi) dissolution-precipitation creep processes affecting carbonate minerals along the subduction interface (e.g., Stöckhert et al., 1999; Epstein et al., 2020) are, so far, not considered in any study attempting to estimate global C fluxes.

Establishing a correlation between fluid pulses related to slow earthquake processes and the carbon budget in a particular subduction margin is even more challenging. The main uncertainty lies on the amounts and poorly constrained physicochemical properties of fluids circulating within each fluid pulse, such as: (i) the concentration of CO_2 in COH-fluids, which in turn depends on the lithologies being affected by decarbonation processes, (ii) the extent of fluid flow without reequilibration until reaching the precipitation front, (iii) the kinetics associated with carbonate precipitation (in the presence of highly variable fluid compositions as demonstrated in **Chapters 5** and **6**) and (iv) the solubilities of CO_2. In consequence, any constraint aiming at quantifying the amount of C in fluids within the frame of slow earthquake processes is not possible.

However, **the key message of this section is that carbonate-bearing metamorphic veins represent a significant route for refractory CO_2-bearing materials available to sink into the deep mantle**. In the frame of the global flux estimations of Plank and Manning (2019), **a c. 3 Mt/year (probably < 30 Mt/yr) difference between subducting and outgassing C fluxes can be regarded as significant reprecipitation of materials analogue to the herein studied veins or other metasomatic products** (e.g., metasomatic marbles from Piccoli et al., 2016; ***Figure 8.4B***).

8.3 Interplay between fluid flow and ongoing metamorphism

Upon increasing temperature and pressure, metamorphic rocks typically devolatilize, a process of particular interest for a number of reasons: fluid fluxes, overpressures and metasomatism critically control rock mechanics, mineralization (potentially associated with ore-forming processes) and the kinetics of further ongoing metamorphic reactions and deformation (e.g., Jamtveit and Austrheim, 2010). In a subduction environment (and elsewhere), the rocks affected by fluid fluxes are expected to be not only those undergoing devolatilization, but also the surrounding environment. If a pressure gradient exists, as for example due to the lithostatic load, fluids will flow upwards and laterally along a subduction interface, provided that permeabilities are high enough (e.g., Connolly, 1997; Ferry and Gerdes, 1998). The magnitude of fluid pressure is modulated by the rates of (i) fluid production/dehydration or injection, (ii) deformation and accommodation of the rock volume to the new fluid-present environment (e.g., dehydration-enhanced porosity formation) and (iii) drainage of the reacting rock associated with its permeability, which is ultimately modified in the megathrust by ongoing shearing (e.g., Etheridge et al., 1984; Connolly, 2010; Angiboust et al., 2014; Frank et al., 2015). If, for example, dehydration/injection rates are high enough so deformation cannot accommodate porosity nor create sufficiently permeable pathways, it is theoretically possible for fluid pressure to exceed the lithostatic pressure and cause hydrofracturing (see equations 2.2 and 2.5; Sibson, 1990). This phenomenon is expected to take place in a wide range of subduction environments, as inferred from high Vp/Vs and Poisson's ratios interpreted as nearly lithostatic overpressurized fluid conditions (Audet et al., 2009; Bostock, 2013; Gosselin et al., 2020). Another possibility is pore collapse (compaction) of the rock volume (e.g., Walder and Nur, 1984; Cox, 2007) as a response to densification at the expenses of the solid volume or viscous deformation; a process imaged through geophysical observations (Hetènyi et al., 2007; Bloch et al., 2018), isotopic analyses (e.g., Graham et al., 1998) and petrologic investigations (Malvoisin et al., 2020). Further in this section I will return to this idea in the framework of the studied metamorphic systems.

In literature, the definitions of the fluid flow modes are yet somewhat ambiguous. In the following analysis, I use a definition similar to that proposed in Ague (2014) who considers porous (or pervasive) flow to fluids migrating through an interconnected porosity network at the grain-scale or microcracks, and channelized (or focused) flow to fluxes preferentially through one or more high-permeability conduits. I note, however, that this definition is somehow inaccurate since, for instance, fluid flow along a subduction interface can be viewed as strongly channelized at the scale of the shear zone, but the mode of fluid flow may occur in a strongly pervasive way (e.g., Angiboust et al., 2014) – at least a large part of it. In nature, metamorphic fluid flow occurs most likely as a mixture of channelized and porous fluid flow (e.g., Rumble et al., 1991; Lucassen et al., 2011). Numerical modelling demonstrates that fluid transport within the crust occurs through Darcian flow until the matrix permeability is fluid-overfed, allowing for hydrofracturing to proceed (Sachau et al., 2015); thus, porous flow commonly precedes focused flow and hydrofracturing.

At a first sight, the occurrence of centimeters-wide extensional vein systems, as well as the presence of hydraulic breccias testifying for sudden high fluid pressure conditions under low differential stress, allow speculating that fluid flow is strongly channelized and focused within fractures. Indeed, this is certainly the case in the Seghin complex the Infiernillo sequence, and elsewhere (e.g., Vannucchi et al., 2010; Spandler et al., 2011 Angiboust et al., 2014). In addition, an episodic nature of veining, fracturing and healing have been also demonstrated and discussed in **Chapters 4** and **5**. The isotopic study undertaken in aragonite-bearing hydraulic breccias, carbonate-bearing metasediments along with blueschist and serpentinite hosts, exhibit patterns that are challenging to reconcile. On the one hand, the O-C isotopic signature of the carbonate veins from all lithotypes and host metasediments suggest a metasedimentary-derived source, but with the contribution of an external mafic/ultramafic-derived component (see above). On the other hand, the Sr-Nd isotopic signature of the host and related carbonate veins are virtually identical (***Figure 5.10B***). A first impression is that these two pairs of isotopic systems (i.e., O-C and Sr-Nd) are in conflict or all analyzed veins were internally-derived. As discussed in **Chapter 5**, the latter hypothesis can be discarded since petrological and structural observations do not support a scenario of internal CO_2 production and massive hydrofracturing, especially in a context of cold prograde subduction, which is progressively cooled down even further (Angiboust et al., 2016). Thus, it is concluded that our geochemical, petrological and structural observations can be reconciled in a model consisting of external fluid infiltration from a deep-seated source through a mixture of porous and channelized flows – explaining the Sr-Nd isotopic re-equilibration (rock-buffered) of the CO_2-bearing fluids and the mafic-ultramafic-influence on O-C isotopic signatures of metasediment-derived fluids. Hence, allowing fluids to travel along the interface and ultimately trigger hydraulic fracturing.

In one way or another, similar conclusions are proposed – at least for a potential porous-like fluid flow – using $\delta^{18}O$ analyses in quartz veins. For example, in a case interpreted as internally-produced fluids, Raimbourg et al (2015) have shown that the O isotopic composition of quartz in veins from the Shimanto belt (Japan) were likely buffered by their respective host rocks. A similar scenario has been drawn in the Namibian Damara belt by Fagereng et al. (2018). There, based on $\delta^{18}O$ analyses in quartz veins, the authors suggested that fluids resulting in vein precipitation at c. 470-550 °C were likely internally-derived. Even though their thermodynamic approach can be discussed (given amount of H_2O is needed), the authors speculate that chlorite breakdown was responsible for the formation of quartz veins, despite having no petrological arguments. Thus, the rule seems to indicate a local origin for the precipitation of quartz veins (see Mullis et al., 1994 for further examples; Cartwright and Barnicoat, 1999). I emphasize, however, that most of these studies are based on single isotopic systems, and an extensive petrologic characterization, including trace and major elements geochemistry, is lacking. A combination of these tools has proven to be the most robust approach aiming at distinguishing and elucidating potential fluid sources (e.g., van der Straaten et al., 2012). **Therefore, I suggest that models considering pervasive fluid flow through the rock matrix prior to hydrofracturing and veining should be taken in consideration before interpreting possible**

fluid sources and pathways along subduction zones (e.g., Lucassen et al., 2011) or any other geological context (e.g., Oliver et al., 1996).

A model combining porous and channelized flow in a deformable viscous media has been proposed more than three decades ago (Bailey, 1990; Spiegelman (1993). This model is referred to in the literature as "porosity waves" and most improvements have been acquired on theoretical and numerical basis. On a geological perspective, just one study offered field evidence for this process to date: Bouilhol et al. (2011) demonstrates that porosity waves have channelized and pervasively distributed melt. Nevertheless, no study has presented explicit evidence for this phenomenon in fluids (other than melts; Ague 2014) except for some preliminary investigations on subduction zone rocks (John et al., 2012). The porosity waves model is associated with a two-phase compaction-decompaction effect produced at conditions at which rocks can deform in a viscous manner (Connolly, 2010). When fluids are produced and/or injected into a rock volume, decompaction of the rock mass due to new porosity created under fluid-present conditions will occur. Subsequent compaction of the viscous matrix due to ongoing deformation will allow fluids to be squeezed out of the rock volume and further propagation of localized fluid pathways in fluid-saturated environments. This process is expected to occur in nature (i) in viscous rheologies, (ii) in a transient manner (e.g., Connolly and Podladchikov, 1998), (iii) surpassing up to 3 orders magnitude the background Darcian fluid flow rates (Räss et al., 2019) and (iv) transporting mass, i.e., they can imprint geochemical signatures indefinitely until facing a perturbation (Connolly and Podladchikov, 1998; Tian and Ague, 2014; Jordan et al., 2018). Interestingly, recent investigations have shown that porosity waves generated in overpressurized regions can travel at rates in the order of kilometers per day, being capable of triggering aseismic slip in a décollement environment (Joshi and Appold, 2017). Furthemore, Skarbek and Rampel (2016) simulated a metamorphic pile undergoing dehydration within the subduction interface and concluded that metamorphic dehydration allows the generation of overpressurized porosity waves transport along the slow slip region. Note that in their simulations, permeabilities in the range of $6.5x10^{-15}$ to $5x10^{-12}$ m^2 are a prerequisite for porosity waves to propagate at periods comparable to those of ETS.

I stress here that the Seghin (and Infiernillo) rocks meet many of the expected and/or possible fingerprints of porosity waves. Among them, those relating to viscous and transient deformational patterns, geochemical signatures suggesting mass transport at a variety of scales and the occurrence of vein systems that may represent the witnesses of the passage of these waves. In fact, upon close examination of the vein structures, **it can be speculated that some patterns resemble a sort of "dehydration" or "segregation" veinlets channelizing fluids into larger hydrofractures** (***Figures 8.5A*** to ***C***; see John et al., 2008). **Such structures would represent a frozen stage of fluid expulsion (compaction) from the rock volume and dilatation in the form of brittle fracturing**. Of course, these are vague speculations and much more research is needed before anything can be said in terms of potential geological records for this enigmatic process. It is worth noticing that the passage of porosity waves in subduction environments could be significantly associated with shear slip,

especially if overpressurized porosity waves are considered to enhance brittle or ductile shearing. To my knowledge, this complex feedback has not been studied so far, though some hypotheses can be drawn. Seghin and Infiernillo lithologies, including silicate-rich veins and host rock materials, exhibit widespread evidence for shearing and brecciation (***Figures 4.2F, 6.2*** and ***6.3***). On the other hand, the carbonate-bearing hydraulic breccias show no evidence of subsequent shearing. Indeed, some of these structures resembles percolation of fluids through porosity formed due to hydrofracturing and/or shearing in the vein (i.e., re-opened veins; ***Figure 6.4B***) and host domains (***Figures 8.5B*** and ***C***). Thus, it can be inferred that, at conditions where the differential stresses are "high" enough (see for example ***Figure 7.7***), the passage of a porosity wave may be interrupted before the lithostatic threshold (or the lithostatic pressure plus the tensile strength of the rock) of the rock volume is achieved, resulting in shearing rather than hydrofracturing (or mixed mode extensional-shear veins). Likewise, a porosity wave may lose its propagation capacity due to a shear-induced increase in permeability. In consequence, porosity waves propagation trains are strongly dependent on the seismic cycle; in the coseismic stage they would tend to vanish if a low or very-low frequency earthquake (or whatever type of brittle deformation occurs) is locally prone for rupturing (diminishing the effect of viscous deformation). Whereas, in the interseismic stage, or in patches where differential stresses are "low" (or in low viscosity regions; e.g., Kotowski and Behr, 2019), porosity waves can propagate without major rheological perturbations until reaching conditions where the rock matrix behavior is inevitably more brittle at, for example, shallower conditions (e.g., Infiernillo depths, see below).

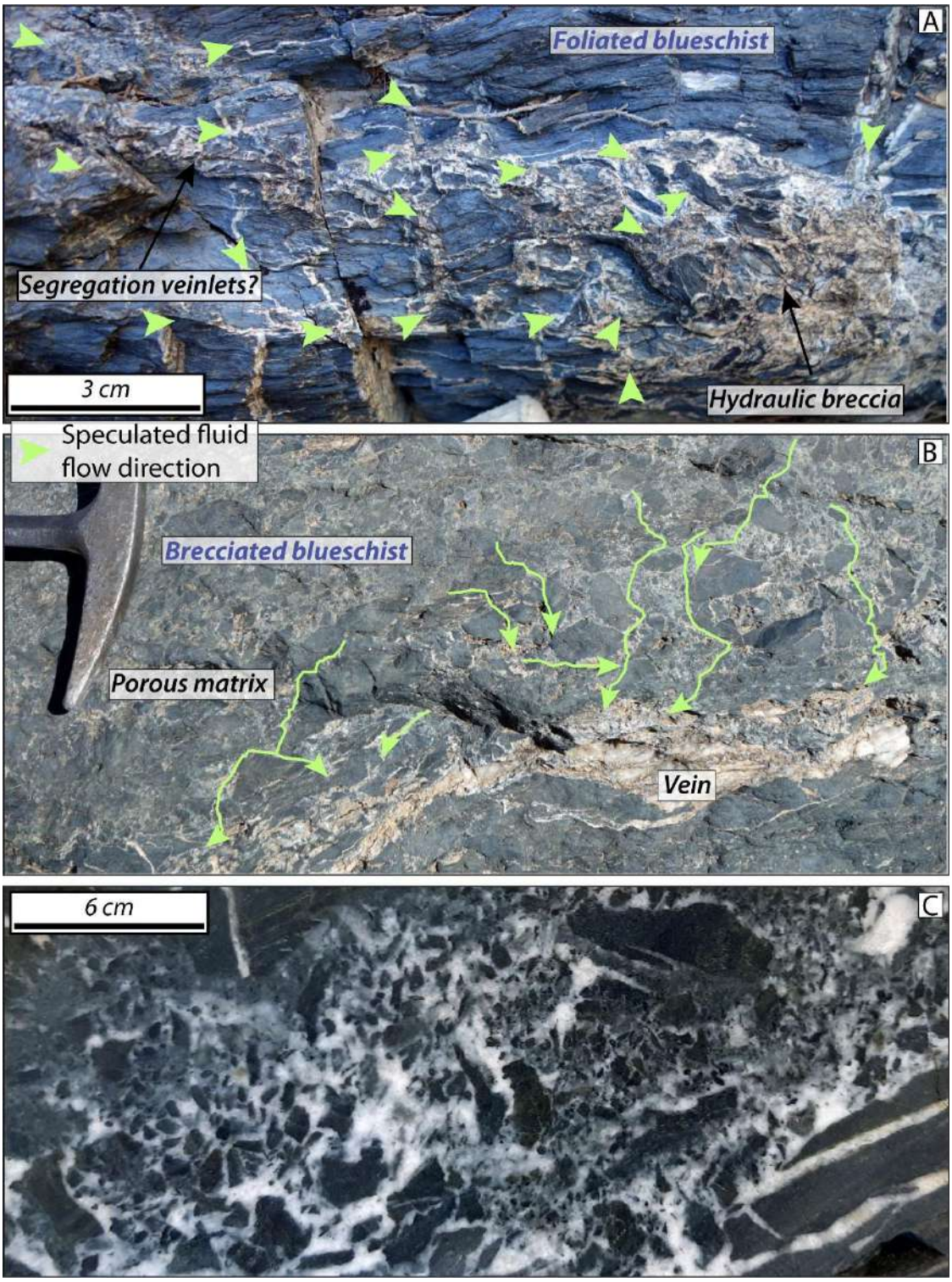

Figure 8.5. Field pictures of Seghin blueschists. A. Vein networks within a foliated blueschist host. The larger hydraulic breccia appears to be connected to the host rock by means of smaller veinlets. Such geometry is similar to "segregation" or "dehydration" veins documented elsewhere (e.g., John et al., 2008; Plumper et al., 2017). Note that the direction of fluid flow is speculative. B. Vein networks within a brecciated blueschist. A set of veinlets converge into a larger former extensional vein. In this case, the matrix is apparently highly porous as noted by the brecciated nature of the host and the abundance of a large number of tiny veinlets that seems to have flowed around clasts within the matrix. C. Polished hand specimen of a blueschist lithology potentially representing a frozen stage of the passage of a "porosity wave"

8.4 Fluid overpressures and slip: who controls whom? – a chicken-and-egg problem?

The potential relationship between veining and shearing as possible triggers (and records) of slow earthquake processes is of relatively novel scientific interest. Despite the mode of fluid flow, as discussed in section 8.3, it is still unclear whether (slow) slip occurs prior or subsequent to veining, or if fluid pressures near or above the lithostatic threshold are indeed a prerequisite to promote further shearing (e.g., Angiboust et al., 2012). I begin by emphasizing the occurrence of several multiple veining events that attest to the episodic nature of hydrofracturing at all stages along the subduction path in the herein studied localities. Shearing to the point of brecciation of the vein systems is also documented (e.g., ***Figure 4.2F*** and ***6.2***). **These observations indicate that, at some point, earlier events of extensional veining were followed by slip**. Moreover, similar veins, but witnessing for mixed extensional-shearing opening modes (e.g., shear veins from Fagereng et al., 2010; see ***Figures 4.6D*** and ***6.2B***), and extensional veins that precipitated originally oriented parallel to sub-parallel to the foliation, **point to (i) a very weak subduction interface, (ii) stresses varying during different stages of veining, potentially related to the seismic cycle** (e.g., Magee and Zoback, 1993; Cerchiari et al., 2020) **and (iii) shearing and fluid overpressures may have acted coevally.**

Further constraints are gained here through the study of lawsonite and lawsonite breccia veins (**Chapters 5** and **6**). In these networks, not only multiple events of veining, but also a strongly heterogenous fluid composition for the vein-forming stages are reported. Folded and sheared vein clinopyroxene crystals (e.g., ***Figure 5.4J, 5.5F*** and ***6.S1J***) and statically hydrofractured metasomatic rocks (i.e., clinopyroxenites), display similar clinopyroxene prograde zoning patterns (e.g., ***Figures 5.5.E*** and ***8.6***) **supporting a scenario where veining, shearing and metasomatism are intimately associated processes**. Even though shearing and metasomatism likely occurred during prograde burial, the exact timing of deformation with respect to fluid infiltration cannot be assessed with precision. In the lawsonite breccia veins, Ti zoning patterns and titanite enrichments associated with Na-amphibole stripes are challenging to interpret. In the former case, Ti zoning patterns follow an uneven trend; some grains display features resembling healed fractures and/or concentric zoning (see Garcia-Casco et al., 2002 and Angiboust et al., 2012 for examples in garnet crystals) while others show a patchy-like zoning along with sharp boundaries. In addition, some chemical patterns show as if the lawsonite clasts have been cemented, as for example indicated in Cr-richer regions among fragments (***Figure 6.S1I***), suggesting several veining and brecciation events of variable fluid compositions. Altogether, these patterns suggest that (i) lawsonite zoning occurred in several crystal growth events under an environment of varying chemical composition (e.g., ***Figure 8.3***), (ii) lawsonite crystal growth in veins and their zoning patterns were probably produced by incremental pulses of fluid infiltration and precipitation (e.g., crack-seal veins; Ramsay, 1980), (iii) fluid injection occurred through heterogeneous percolation/fluid pathways in re-opened vein systems and (iv) fluid infiltration is contemporaneous with some of the Ti enrichments as long as titanite precipitated in the same vein domains in the form of extremely-fine grained aggregates (or comminuted), in which Na-

amphibole witnesses neat evidences of brittle deformation (see below; see also ***Figures 3D, E*** and ***5D***).

These observations converge in that fluid overpressures are contemporaneous and subsequent to brittle shearing. These feedbacks have been somewhat addressed in the framework of rare eclogite-facies paleo-earthquakes, possibly representing a record of intermediate depth seismicity (e.g., Austrheim and Boundy, 1994), or in other lower grade shear zones representing conditions closer to the transition and seismogenic regions (e.g., Bachmann et al., 2009; Fagereng and Sibson, 2010; Ujiie et al., 2018). In central Zambia, John and Schenk (2006) reported the occurrence of pseudotachylytes and (ultra) cataclasites inferred to have formed and/or recrystallized in the eclogite-facies conditions. Textural relationships and petrological observations allowed the authors to illuminate the role of fluids associated with these fault-related rocks: (i) vein-forming hydrofracturing events took place after faulting and associated pseudotachylte formation, (ii) further vein precipitation continued during ongoing burial, (iii) veining occurred in multiple events of fluid injection and hydrofracturing, (iv) coupled brittle deformation (e.g., grain-size comminution) and reactive fluid flow enhanced obliteration of the precursor rock and mineral materials transforming the gabbroic protolith into an eclogite and (v) faulting was not preceded by veining but occurred contemporaneously to the injection of external fluids in a dry gabbroic rock – not due to dehydration embrittlement. Similar conclusions have been drawn for Alpine eclogite breccias from the Monviso metaophiolite (Angiboust et al., 2011; see also the study case presented in Andersen et al., 2014 for a slightly similar scenario in Alpine Corsica). There, eclogite breccia blocks containing mylonitic eclogite clasts occur wrapped by serpentinite schists. Brecciation, possibly associated with one or some intermediate-depth earthquake(s), affected the mylonitic subduction-related fabric creating an interclast matrix of occasionally fibrous eclogite materials, the latter devoid of further fabric development but wrapped within an eclogite-facies serpentinite foliation (e.g., Angiboust et al., 2012). Based on (i) the apparently dry nature of the therein studied Fe-Ti metagabros (< 0.5 wt% of H_2O) and (ii) clear evidences of an external fluid contribution, the authors concluded that dehydration embrittlement was not an important triggering mechanism for intermediate-depths brecciation (see also Locatelli et al., 2019).

Thus, as also concluded in the studies commented above dealing with eclogite-facies rocks from the Alps and Zambia, I suggest that a process of **dehydration embrittlement could not have generated by any chance the documented fluid overpressures** since (i) titanite in a blueschist composition, such as those measured in several specimens from this study, is expected to be stable along the prograde path (see the pseudoesections presented in ***Figures 4.S2A*** and ***5.S2A***), hampering titanium dissolution into a free fluid phase. In consequence, the observed Ti enrichments in lawsonite (and clinopyroxene) and the high abundance of titanite in veins and in the (ultra)cataclasites domains from the host-vein margins require and external source and (ii) at conditions accompanying veining – at least during a part of it – the blueschists were rehydrated or a lawsonite-rich assemblage is stable, preventing dehydration reactions. In addition, widespread evidence for reopening in Seghin and

Infiernillo veins, along with the apparent lack of cataclasites or ultracataclasites in regions of the host rock devoid of vein systems, **indicate that extensional veining must have precluded slip, serving as regions of preferential weaknesses** (see below).

Rheological contrasts can allow brittle or ductile deformation to concentrate in layers of higher viscosity or strength, as for example around eclogite blocks in a blueschist matrix (e.g., Behr et al., 2018) or veins within a blueschist host (Wassmann and Stöckher, 2012). In the former case, dislocation creep in glaucophane is believed to dominate distributed viscous creep coevally to brittle deformation of stiffer eclogite pods. In the latter, widespread pressure-solution creep is the inferred dominant deformation mechanism in a blueschist matrix containing veins that preferentially deformed by brittle and/or pressure-solution creep – dislocation creep is only locally observed in quartz aggregates. **These investigations allow us to suggest that the herein studied now brecciated lawsonite-, albite- and glaucophane-bearing veins (or other rigid objects) are effective high viscosity objects that allow concentrating localized deformation into discrete levels or zones of contrasted viscosity**. Based on our structural and microstructuraI observations, **I conclude that preferential brittle weaknesses in the form of vein structures – therefore former fluid overpressurized regions – likely allow promoting shearing within the slab in the blueschist-facies field within the ETS region**.

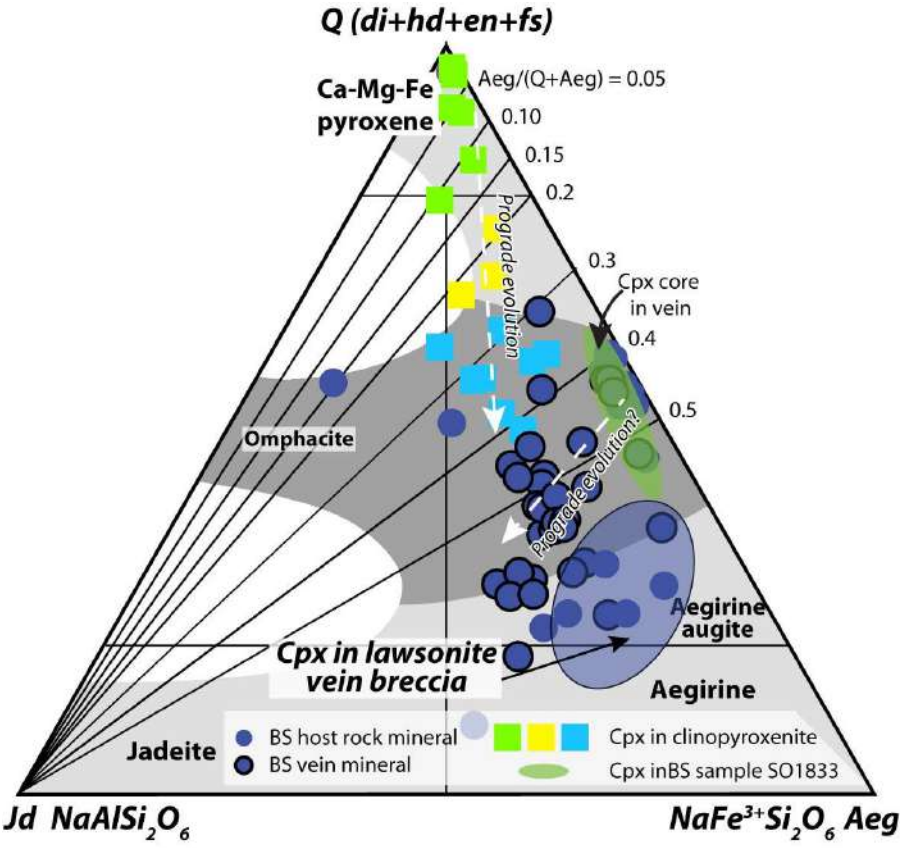

Figure 8.6. Ternary classification diagram for clinopyroxene (after Morimoto, 1988) including quantified data points extracted from the lawsonite vein breccia X-Ray maps shown in Chapter 6.

It is known that veins precipitated in open cavities commonly develop as syntaxial structures with the long axis of the precipitating minerals oriented perpendicular to the vein margin (e.g., Bons et al., 2012). To date, the slip systems dominating lawsonite glide are poorly constrained (e.g., Cámara et al., 2001). This is maybe due to the fact that lawsonite commonly deforms in a brittle manner and plastic deformation of this mineral is not relevant in subduction environments (e.g., Teyssier et al., 2010; Kim et al., 2015). In addition, at the peak temperature reached by the Infiernillo sequence, albite is also expected to deform in a brittle manner (Passchier and Trow, 2005). Nevertheless, crystal plasticity is locally observed in the aforementioned studies and here in the form of undulose extinction, bended crystals and twins. Recently, brittle deformation precluding viscous creep has been documented in quartz by means of EBSD-based microstructural analyses. In this context, strain hardening due to suitable oriented (or misoriented) lattice planes allowed brittle failure associated with the formation of shear microgouges and microfratures in tiger stripe-like patterns (e.g., Kjøll et al., 2015). I highlight those similar fabrics are observed in quartz from the herein studied veins (e.g., ***Figure 6.3G*** and ***6.S1L***; see **Chapter 6**) and that a brittle precursor is plausible, as is also suggested by the observed vein structures and breccias discussed here (see also below). **In consequence, similar strain hardening effects or slip due to favorable (or unfavorable) orientations of the lawsonite and albite long axes with respect to the conditions of the stress field, i.e., oblique to the orientation of crystals in veins, may represent another factor facilitating further brittle deformation after a precursory stage of extensional fracturing or quartz strain hardening**.

8.5 Comparison among the Infiernillo sequence and the Seghin mélange

At a first sight, one may think that the coherent sequence of Infiernillo is incomparable to the block-in-matrix tectonic mélange comprising the Seghin complex. This idea is supported by the abundance of serpentinites in the latter, absent in the former, and by the apparent warmer subduction thermal gradient recorded in the peak assemblage of Infiernillo complex, comparable to other localities such as the Dent Blanche (Roda and Zucali, 2008; Angiboust et al., 2014; Manzotti et al., 2020), south Tianshan (Gao et al., 1995), Qiangtang belt (Kapp et al., 2003), the Franciscan Complex (Ward Creek area, Brown, 1977; Maruyama et al., 1986), among others. Despite these gross differences, several aspects are remarkably comparable among them, including insights on their past geological history.

Petrologically, the Infiernillo sequence is characterized by a metamorphic peak within the transition from greenschist- to blueschist-facies (Hyppolito, 2014; this study). Thus, although glaucophane crystals (and Si-rich phengite) are well developed in some lithologies, the blueschist-facies metamorphism is rather obscured in other rock types. As demonstrated in this study, this is mainly due to local geochemical heterogeneities favoring the formation of a glaucophane-rich or glaucophane-absent mineral assemblages, the latter allowing the formation of chlorite and actinolite. If Infiernillo lithologies would have been buried to deeper conditions, comparable to those reached at peak temperature by the Seghin complex, i.e., 480 °C, the resulting peak metamorphic assemblage in the blueschist-facies would have been dominated by epidote (Evans, 1990). As shown in **Chapters 5** and **6**, this paragenesis is widespread in Seghin blueschists, besides lawsonite is also present in blueschist lithologies. In the Iranian case, our thermodynamic modelling approach (***Figure 5.11***) demonstrates that Seghin blueschists fall within a transitional band limiting the stability of epidote and lawsonite – remarkably during prograde burial – making the presence of these minerals a function of bulk rock compositional variations as detailed in **Chapter 5** (see Ao and Bhowmik, 2014 and Cetinkaplan, 2020 for a similar Neotethys context). **These observations indicate that both Seghin and Infiernillo metamorphic complexes subducted under a roughly comparable subduction thermal gradient and, hence, comparable physical conditions along the subduction interface in the transition ETS region**. Nevertheless, I speculate that a long-lasting residence in the subduction factory and further maturation of the subduction environment (i.e., cooling of the thermal regime upon continued subduction; e.g., Peacock, 1990b; Wang et al., 1995; Angiboust et al., 2016) allowed the Seghin complex to re-equilibrate its prograde epidote-blueschist-facies assemblage towards a lawsonite-bearing one, as indicated by the occurrence of lawsonite grains overgrowing a previous prograde fabric and earlier epidote grains (see **Chapter 5** and ***Figure 6.S1D***). Note that the prograde growth of lawsonite in veins was contemporaneous to the development of an epidote blueschist-facies assemblage in the host, due to a bulk compositional effect on mineral stabilities, as discussed above and in **Chapter 5** (e.g., Martin et al., 2014; this study).

It is yet unknown where and when the mélange fabric of the Seghin complex has been acquired. One line of research typically considers mélanges as depositional structures formed due to erosion and gravitational mas transport processes at the seafloor in the forearc-trench regions where formerly

subducted materials are exhumed, eroded, deposited and, eventually recycled back into the subduction factory (e.g., Wakabayashi, 2012; Festa et al., 2014; Bonnet et al., 2018). In these environments, the mélange structure is associated with sedimentary and vulcanosedimentary breccias, slope deposits, gravitational mass flows as well as abundant serpentinite-derived sediments and seafloor-related ophicarbonates (e.g., Lafay et al., 2017; Vitale Brovarone et al., 2018; Menzel et al., 2019). Another possibility is formation of a tectonic mélange in the subduction environment (Shreve and Cloos, 1986; Closs and Shreve, 1988a; b; Blanco-Quintero et al., 2011). There, the subducting coherent metamorphic sequence is dismembered forming a block-in-matrix fabric. Depending on the burial conditions at which this process occurs, it may take place in the interface with the serpentinized subcontinental mantle, allowing the incorporation of slab blocks within a serpentinite-rich matrix (e.g., Garcia-Casco et al., 2008).

Integrating field and petro-geochemical and structural observations, I can give a light on the timing of mélange formation relative to the subduction path. First, the Sr-Nd isotopic compositions of most mélange-forming lithologies (see ***Figure 5.10***) and veins, including hydraulic breccias, depart from an oceanic-derived signature, suggesting that carbonate precipitation did not occur directly from seawater. Similar conclusions are derived considering the $\delta^{18}O$ values from the studied veins and metasediments. Second, the Seghin mélange is composed of a mixture of blueschist blocks metamorphosed at quite similar P-T conditions within the lawsonite-blueschist field (Angiboust et al., 2016), in contrast to other settings (e.g., Franciscan complex) where the mélange resulted from a chaotic gathering of blocks in the subduction channel during the return flow of the buoyant serpentinite-rich mélange or as recycled sedimentary structures (Cowan and Page, 1975; Wakabayashi, 2012; Platt, 2014). Third, the near-peak aragonite-bearing hydraulic breccias are largely devoid of further shearing, except in the serpentinite matrix where the carbonate veins are largely deformed and transposed (see **Chapter 5**). These observations are compatible with nearly strain-free conditions in the mafic domains, as expected in a block-in-matrix fabric where rigid blocks (blueschists) are embedded within a weak matrix (serpentinites), the latter accommodating most of the distributed deformation (Behr et al., 2018; Beall et al., 2019). In addition, numerical simulations have shown that basal accretion generates the largest amount of strain along a subduction path right after detachment from the subducting slab (Menant et al., 2019). Thus, it is inferred that the hydraulic breccias precipitated right after basal accretion, otherwise the veins would have been largely transposed. **These observations suggest that the present-day mélange fabric of the Seghin complex has been acquired at near peak conditions during underplating against the subcontinental, serpentinized forearc mantle and subsequent return flow**. **Therefore, the prograde blueschist-facies metamorphic stage and related structures occurred within the ETS region while the Seghin mafic lithologies (and minor metasediments) were still part of a coherent subducting plate** (e.g., ***Figure 5.13***), in a similar way as the coherent Infiernillo sequence did. Thus, the Infiernillo sequence may be considered as a pristine witness of the architecture of the subducting slab offshore central Chile.

In terms of vein system structures and mineral assemblages, many similarities are also evident. All the vein systems described above precipitated episodically. At the studied localities, the early veining stages are characterized by the precipitation of albite (**Chapters 4** and **5**). This stage necessarily involved the breakdown of low-pressure and low-temperature minerals formed during seafloor alteration such as clays or zeolites in former fractures or other preferential domains (e.g., amigdules, cavities, joints, etc) upon increasing temperature during early burial (e.g., Ernst, 1972; Spear 1993). While metasedimentary lithologies underwent pore collapse and fluid expulsion releasing most of its water volume (e.g., Fisher and Brantley 1992; Fisher et al., 1995; Saffer and Wallace, 2011). In fact, the early formation of albite veins (± actinolite ± pumpellyite) seems to be widespread in subduction environments (e.g., Bebout, 1991). These veins are followed by further HP-LT mineral formation and re-equilibration. In the Chilean case, albite veins were followed by winchite and glaucophane-bearing veins, as well as dissolution-precipitation along contacts lined with these HP-LT mineral assemblages. In Seghin, the albite veins were followed by a far more complex mineralogy characterized by sequential glaucophane, lawsonite and aegirine-augite. Furthermore, transposition, shearing and brecciation of these veins have been documented in both settings (e.g., ***Figures 4.2, 6.2B*** and ***C***) and, according to crosscutting relationships and mineral assemblages, brecciation and slip must have occurred within the seismogenic and/or the ETS regions. **Clinopyroxene and Na-amphibole needles replacing and lining albite grains or along host-vein contacts (*Figures 8.7A, B* and *C*) represent a common evidence of fluid-assisted pressure-solution under HP-LT conditions following hydrofracturing and subsequent mineral precipitation** (e.g., Wassmann and Stöckhert, 2012).

The occurrence of quartz accompanying all the previous structures, specially at HP-LT conditions, is another intriguing common feature. This mineral is the only one showing obvious evidence of fabrics indicating dislocation creep, which, according to cathodoluminescence imaging and microtextural observations (e.g., **Chapter 6**), could have been deformed in a brittle manner prior (or postdating) to ductile creep (e.g., Kjøll et al., 2015; see below).

Carbonate filled hydraulic breccias are abundant in both complexes crosscutting earlier subduction-related structures. At Infiernillo, these veins were filled with calcite, while at Seghin they are composed of aragonite, in both localities intimately associated with quartz and, to a lesser extent, with other HP-LT minerals. It should be noted that the thermal gradient associated with the Carboniferous subduction event in the rears of Gondwanaland, as recorded by Infiernillo rocks, was “warm” enough to allow the formation of calcite rather than aragonite, the latter being widely observed in Seghin (e.g., Brown et al., 1962; Hacker et al., 2005). As discussed previously, the origin of the CO_2-bearing fluids from which these veins precipitated is related to fluid-mediated decarbonation from metasediments. In the case of Seghin, the fluids would have been produced at depths around 60 km, while at Infiernillo, the eclogite-facies boundary would have been crossed at shallower conditions around 45 km depth, as predicted for the modern Cascadia subduction margin analogue (Peacock et al., 2002; Preston et al., 2003). Interestingly, the explosive breccia structures (Jébrak, 1997) are less

developed and less abundant in Infiernillo than in the Seghin complex. This observation can be explained by considering the fluid flow mechanisms as a mixture of channelized porous flow (porosity waves or hydraulic pulses; e.g., Nur and Walder, 1984; Connolly, 2010) that develops due to the continuous fluid production in the eclogite-facies (see section 8.4). There, the fluids would have been expelled upwards along the subduction interface and, according to numerical simulations, an increase of the Darcian porous flow component would result in larger events of fluid expulsion while channelized fluid flow in a fracture-dominated system (e.g., de Riese et al., 2020). Furthemore, Connolly (2010) emphasized that if decompaction occurs during the passage of a porosity wave train associated with hydrofracturing, fluid flow would manifest in a highly channelized form and the porosity wave will vanish by subsequent brittle fracturing. **In consequence, volatiles originated at depth and ascending along the subduction interface were capable of causing massive hydrofracturing in Seghin and, to a lesser extent, in the Infiernillo complex due to rheological differences of the compacting-decompacting rock, being nearer to the fluid expulsion front at greater Seghin-like depths**. The lack of CO_2-bearing lithologies accessible for further fluid-mediated decarbonation or the inability of H_2O-rich fluids to enhance fluid-mediated decarbonation (e.g., little H_2O is released, or the released H_2O is not capable of interacting with the CO_2-bearing lithologies) can be considered as alternative explanations to justify the lower abundance of veins at Infiernillo.

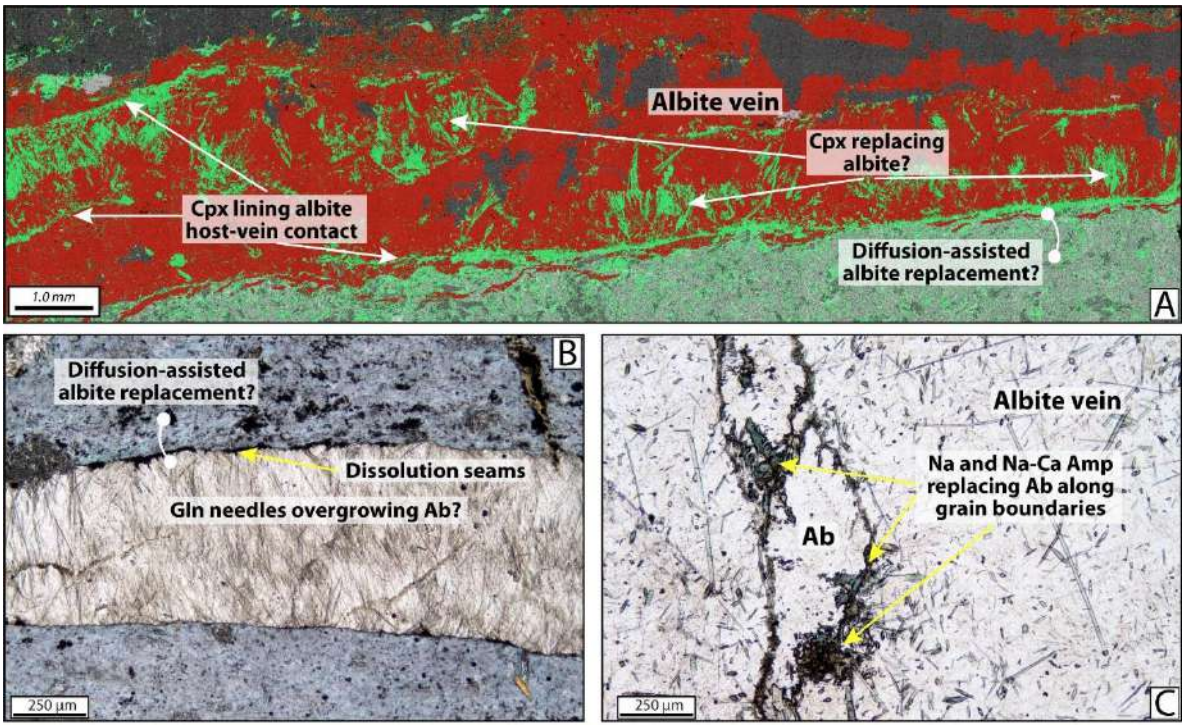

Figure 8.7. A. Mask image based on an EDS X-ray map of a vein and its blueschist host (see Figure 5.4E for further details). Note the apparent replacement texture characterized by clinopyroxene growth at the expenses of albite (and likely chlorite from the host), specially near the host-vein margins. B. Photomicrograph of an albite veins and a very-fined grained blueschist host emphasizing potential replacement of albite by glaucophane, specially at the host-vein margins. Photomicrograph of an albite vein depicting albite grain boundary contacts lined with Na- and Na-Ca amphibole grains. This texture is thought to have formed due to pressure solution along grain boundaries.

In summary, the herein studied localities show similarities that allow comparing deformation and fluid-rock interactions in the light of ETS-related processes, among which are the following: (1) roughly comparable conditions of metamorphism during the prograde burial (both complexes share a prograde P-T slope compatible with epidote-blueschist-facies metamorphism, however, Seghin records a colder trajectory). (2) A presumably similar architecture of the subducting slab, at least until near-peak conditions. (3) A protracted sequence of episodic and multiple veining events associated with burial-related shearing, including brittle creep within the slow earthquake region. (4) CO_2-bearing fluid infiltration crosscutting all the previous structures and fabrics.

8.6 Proposed rock records for some of the earthquake-related phenomena

As shown, brittle behavior and fluid-rock interaction products are similar in the deeper (colder) Seghin and shallower (warmer) Infiernillo complexes. Further research in other metamorphic complexes is necessary to allow extrapolating these features into a global comprehensive subduction model. **However, our investigations allow speculating that the studied structures and metasomatic products are representative of slow (and regular) earthquake processes in subduction environments**. Among the number of reported structures, **the most likely candidates associated with the slow earthquake phenomenon are vein breccias and its surrounding cataclastic blueschist host and ultracataclasites** (see **Chapter 6** and below). These structures are thought to have formed due to brittle creep, which may have been triggered by combination of stress amplification or rheological contrasts between the host and the vein (Beall et al., 2019; Kotowski and Behr, 2019) under high fluid pressure conditions, the latter being broadly present at all stages (see below).

To date, the deformation mechanisms governing different processes of the subduction megathrust are still poorly constrained. As noted above, studies suggest that a mixture of pressure-solution creep and brittle deformation may account for the background plate boundary strain rates and faster velocities (e.g., in the Alps: Bachmann et al., 2009; Angiboust et al., 2015; in the Franciscan complex: Wassmann and Stöckhert, 2012; 2013), while others indicate a power-law viscous dislocation creep mechanism together with brittle shearing (Syros Island: Behr et al., 2018; Kotowski and Behr, 2019). In any case, a brittle mechanism is broadly observed in the form of brittle veins and offsets of rigid blocks in a weaker matrix. **In the herein studied blueschists, metasediments and veins from Seghin and Infiernillo localities, evidence of pressure-solution creep is widespread in the full spectrum of grain sizes, while dislocation creep is restricted to quartz rich aggregates, layers or veins**. **Thus, this investigation supports a scenario where pressure-solution creep was the main deformation mechanism in the subduction environment**. However, the distance of the lithologies (here and elsewhere) relative to a fault core (or master fault) is critical. Rocks away from the main slip systems likely undergo strain at considerably lower rates, possibly explaining switches in the active deformation mechanisms, as for example, between Syros Island and the Franciscan, in virtually identical lithologies. This dichotomy can also be seen from a grain size perspective. In Syros Island, Kotowski and Behr (2019) documented grain sizes range from few hundreds of microns up to the milimeter-scale for glaucophane and epidote while in the Franciscan, Seghin, and Infiernillo complexes, grain sizes are commonly much finer, in the range of few hundreds to tens of microns. Since pressure-solution creep is grain size sensitive, finer-grained lithologies of identical composition are prone to pressure-solution creep while coarser rocks for other deformation mechanisms such as dislocation creep (e.g., Rutter, 1983; Behr and Platt, 2013).

Constitutive flow laws for pressure-solution creep are still poorly constrained and represent, indeed, a major scientific gap with relevant implications for understanding plate interface rheology (e.g., Wassmann and Stöckhert, 2013; Platt et al., 2018). For example, Fagereng and den Hartog (2017)

developed a microphysical model to investigate the importance of pressure-solution creep in accommodating deformation in a subduction environment. The authors concluded that aseismic frictional-viscous flow is the main deformation mechanism accommodating plate boundary rates via shearing along cleavage planes and pressure solution of rigid clasts. At temperatures above 100 °C, earthquakes are predicted to nucleate once the boundary conditions of the aseismic frictional-viscous system are disturbed: a local transition from velocity-strengthening to velocity-weaking is apparently required. **In the context of the studied structures, this transition could represent a switch from viscous pressure-solution creep to brittle creep.**

Recently, Oncken et al. (in press) used the constitutive flow laws for dislocation creep (Luan and Paterson, 1992), solution precipitation creep (high porosity: Niemeijer et al., 2002; low porosity: Rutter, 1983) and brittle creep (stress corrosion creep: Brantut et al., 2012), to determine maximum strain rates that can be recorded by these structures as observed in exposed shear zones (see ***Figure 6.1***). Their results suggest that the entire spectrum of plate convergence velocities and slow earthquakes could be accommodated by either pressure-solution creep (at high porosities only) and/or brittle creep. Nevertheless, pressure-solution creep is strongly dependent on the hydrologic state (i.e., pore fluid pressure) of the subduction environment while brittle creep is not. Thus, at differential stresses close to failure (100-75% to failure), brittle creep is predicted to accommodate the bulk of the instrumentally observed ETS processes. Therefore, in a broader perspective, Oncken et al. (in press) concluded that (i) pressure-solution creep may dominate in the early stages of the loading seismic cycle, (ii) brittle creep dominates at advanced stages of the seismic cycle and can be regarded as the main mechanism accommodating ETSs and (iii) the transition from pressure-solution to brittle creep is a complex interplay between increasing pore fluid pressures and shear stresses (see also **Chapter 7**).

Since cataclasite networks are expected to bring a light onto brittle creep as the main driving mechanism for deep slow earthquake processes, the documentation of these structures is critical. Yet, these structures have never been reported in blueschist-facies vein networks so far. In this regard, the lawsonite (and albite) vein breccias and adjacent blueschist foliated ultracataclasites and cataclasites studied here may represent a first report (***Figures 4.2F, 6.2, 6.3, 6.4*** and ***6.5***). **Both fabrics, as documented in Infiernillo and Seghin localities, show features that suggest events of brittle creep overprinted by pressure-solution fabrics** (see Rowe et al., 2011 for another example). In this context, the textures observed in some blueschist hosts may be re-interpreted as overprinting fabrics where initially riebekite-rich amphibole got fragmented or boudinaged and immediately healed by glaucophane, followed by or contemporaneous to comminution as evidenced by the finer-grained matrix around (***Figure 8.8***).

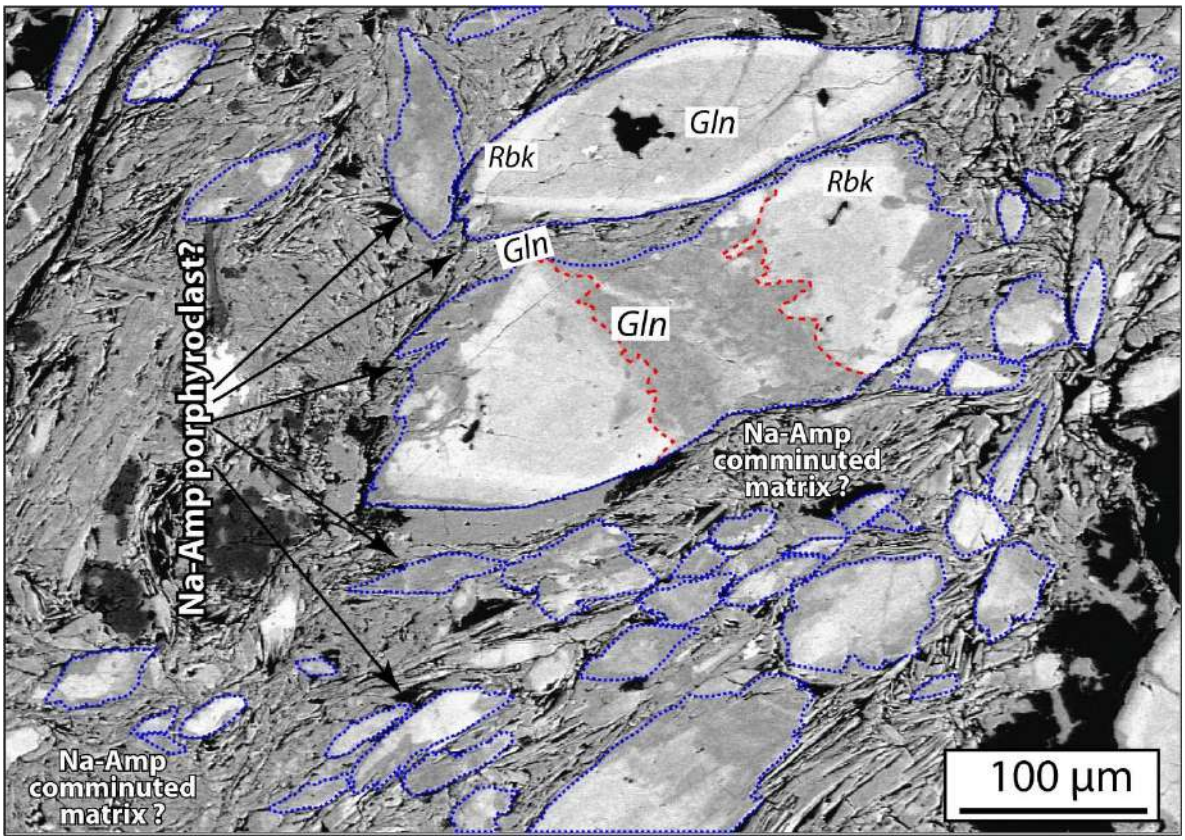

Figure 8.8. Backscattered electron image of a blueschist host (see also Figure 5.S1A). The textural zoning patterns indicate that an earlier generation of riebeckitic amphibole is replaced along grain boundaries and fractures (i.e., red dashed contour depicts a boudinaged crystal) by glaucophane. In addition, larger grains display a sigmoid and/or fragmented-like fabric (see blue dashed contours) surrounded by a fine- to very fine-grained glaucophane-rich matrix, re-interpreted here as ultracomminuted materials. The replacement of glaucophane by riebeckite possibly associated with ultracominution points to (i) high-pressure conditions for the cataclastic event and (ii) a fluid contribution richer in glaucophanitic component.

The vein breccias and (ultra)cataclastic blueschists likely formed at strain rates faster than background plate convergence rates but slower or equal to seismic slip velocities (including low- and very low-frequency earthquakes; e.g., Rowe et al., 2011; Fabbri et al., 2020). In the vein breccias, the cataclastic fabrics are characterized by coarse grained lawsonite or albite fragments (up to the centimeter-scale) transposed and/or sheared according to the main foliation. When possible, reconstruction of clasts indicates estimated offset in the range of millimeters to a few centimeters (e.g., ***Figure 4.2F*** and ***6.5A***). **The excellent match between clast orientations with respect to former non-brecciated crystals and identical precipitation products in dilatational sites allows suggesting that individual slip displacements, resulting in clasts pulling-apart and offsets, were in the same range**. **In addition, when clasts are bounded by euhedral glaucophane needles** (***Figure 5.4F***), **it is possibly to infer that: (i) shearing occurred at pore fluid pressures near the lithostatic threshold and (ii) precipitation occurred rapidly in single events and, in consequence, so was pulling-apart of clasts - at least at the millimeter-scale.** Veins displaying heavily brecciated and sigmoidal clasts witness for several slip events. **The observed clast sizes, clast-matrix ratios (higher than in ultracataclasites and Na-amphibole bands; see Chapter 6) as well as vein widths**

(from centimeters up to few tens of centimeters) and displacements (up to few centimeters), allow speculating that these structures deformed at subseismic strain rates, as do deep slow slip events (e.g., Ide et al., 2007; Fu and Freymuller, 2013; Bedford et al., 2013; Frank et al., 2015; see Behr and Bürgmann, 2021 and Oncken et al., in press for a review). In the present state of knowledge, the slipping area or rupture lengths of the veins could not be determined. These parameters are critical to evaluate the potential of vein networks to accommodate deformation induced by slow slips. For instance, by means of an extensive field-based investigation in the Syros Island, Kotowski and Behr (2019) demonstrated that the distribution and size of stiff heterogeneities, as well as observed displacements, allow proposing brittle deformation of stiff materials in a weaker matrix as a likely ETS-genic system. The authors also noted that eclogite pods are too small to account for any of the slow earthquake source properties. Alternatively, it is proposed that coalescence of slip into several blocks may account for ETSs (Behr et al., 2018).

In this thesis, documented vein systems are in the order of several centimeters-wide while localized shear bands exhibit thicknesses down to the micrometric-scale, matching well effective slipping thicknesses inferred through geophysical investigations (e.g., Oncken et al., in press). Assuming that the total vein length (up to few tens of meters) represents the length of the rupture during a slow slip, single veins in the order of tens of kilometers are required to match the inferred source properties. This scenario is unlikely since vein lengths in this range have not been documented. Thus, I speculate that coalescence of slip along several tens to hundreds of metamorphic veins could have accounted for slow slips (e.g., Kirkpatrick et al., 2021). Note that this hypothesis is somehow like the one proposed by Behr et al (2018), in the sense that metamorphic veins represent rheological heterogeneities capable of localizing slip within and around (see ***Figures 8.9A*** to ***C***). The premise of slip coalescence along several vein networks is in part supported by the orientation of the conjugated vein networks at high angles to the main foliation and the shear veins. The bulk of the vein network forming and deforming processes, i.e., extensional hydrofracturing and shearing may have acted synchronously, like in the "dilatational hydroshears" model from Fagereng et al (2010). This model aims at explaining the geometrical association between shear veins and hydrofractures orientated sub-parallel and at high angles with respect to the main foliation and the principal compressive stress. Thus, episodic shearing in pre-existing weak domains (Collettini et al., 2009) and heterogeneous rock volumes (e.g., Skarbek et al., 2012) is possible under the same stress field at low differential stresses, provided that material properties such as cohesion, tensile strength and friction coefficient are low enough. Yet, further extensive field-based investigations are essential to correlate vein networks geometry with tectonic stresses. Considering the great variability of materials, slow slip source properties and structures, it is likely that a combination of processes, lithologies and structures control the deep slow earthquake environment (Kirkpatrick et al., 2021).

Ultracataclasites occur as localized shear bands of localized deformation lining the host-vein interfaces. Sharper slip surfaces, extremely fine grain sizes, widths down to few hundreds of microns or less, and displacements at the micrometric-scale, match the instrumentally-derived

source properties for LFEs (e.g., Shelly et al., 2006; Ito et al., 2007; Bostock et al., 2015; Oncken et al., in press)**, allowing to propose blueschist-facies ultracataclasites as a potential fossilized record of seismic signals from deep slow earthquakes** (e.g., Angiboust et al., 2015). In this case, the required rupture lengths are at least two or three orders of magnitude longer than observed cataclastic host-vein systems. Similar to the aforementioned case of slow slips and vein breccias, it is likely that several, not only one ultracataclastic shear band, were active. Together with other geological objects, it is thus possible to reconcile source dimensions and lengths (e.g., Kirkpatrick et al., 2021; see ***Figures 8.10A*** and ***B*** for a synthesis of some of the main findings of this thesis).

The transition from background plate convergence rates to subseismic (slow slip) and seismic strain rates (LFEs and regular) is certainly associated with episodic fluid overpressures, as evidenced in the herein studied blueschist-facies localities (see also Angiboust et al., 2015; French et al., 2019). The effects of pore fluid pressure highs are to enhance frictional sliding via decreasing the strength of the shear zone (Okazaki and Katayama, 2015), driving strain rates towards faster velocities compatible with slow or regular earthquakes. Similarly, induced stress amplification due to the rheological diversity of the shear zone-forming materials has been proven to cause slip acceleration towards subseismic rates (Beall et al., 2019; see also Ioannidi et al., 2021). Strain hardening is another process capable of triggering frictional sliding, as documented in minerals deformed by crystal plasticity (i.e., dislocation tangling during dislocation creep; Kjøll et al., 2015). These processes are inferred to have contributed to the finite deformation of the vein breccias. Stress heterogeneities and high pore fluid pressures would have triggered brittle creep and transposition of veins formerly oriented at more favorable angles (i.e., oblique; see ***Figure 8.9B***) relative to other structures (considering a variable stress field in the forearc during the seismic cycle; Magee and Zoback, 1993; Sibson, 2013). In fact, the former orientation of extensional veins with respect to the stress field (e.g., during the seismic cycle; Cox, 2010) also affects the capability of veins to deform preferentially in a brittle manner associated with shearing (e.g., ***Figures 4.1C, 4.2F*** and ***6.2B***). Furthermore, veins, once transposed, developed an incipient brecciated fabric characterized by stiff lawsonite or albite clasts in a weaker quartz matrix. **In consequence, favorably-oriented structures for slipping (and to a lesser extent unfavorably-oriented ones), may have initially ruptured in a brittle manner due to a complex interplay between stress heterogeneities (amplification), strain hardening and fluid pressures**. **Once fractured, these transposed structures become preferential weaknesses capable of deforming under a stress field unfavorably-oriented for slipping** (e.g., Collettini et al., 2009; Fagereng et al., 2010; ***Figure 8.9C***). **Therefore, it is inferred that a combination of processes rather than fluid pressure highs alone is a prerequisite to trigger acceleration towards seismic and subseismic velocities.**

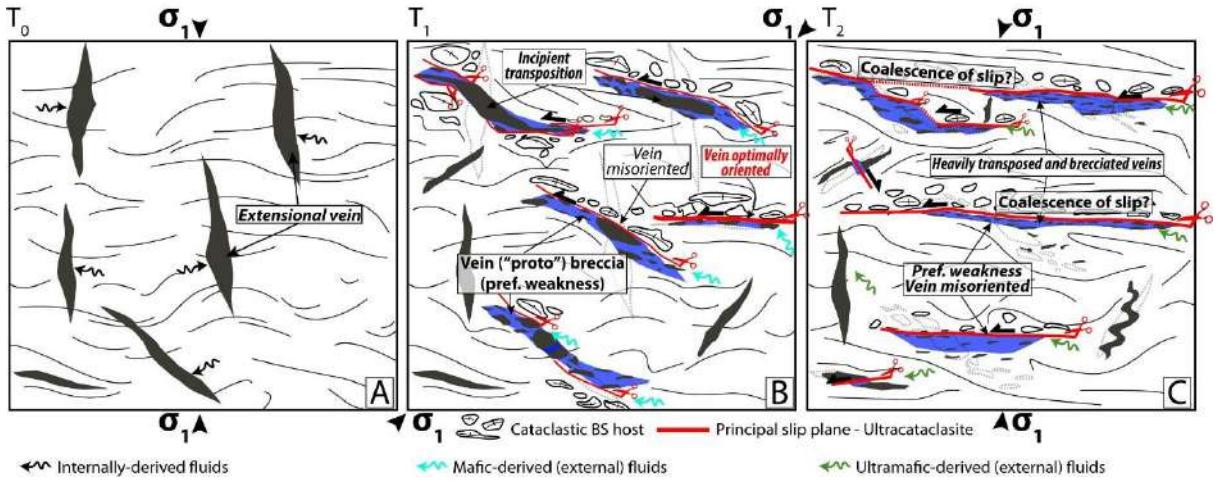

Figure 8.9. Conceptual illustration (not to scale) depicting some of the main vein-forming and -deforming processes associated with brecciated silicate-rich veins (i.e., albite- and lawsonite-rich veins from Infiernillo and Seghin) and their cataclastic host. I emphasize that this illustration is not intended to show a potential relation of the brecciated veins and cataclastic blueschist host with the seismic cycle related to large earthquakes, but rather to explain how the vein structures have deformed and interacted under a variable stress field, characteristic of the subduction forearc region (Magee and Zoback, 1993; Ide et al., 2011). A. At a stage T_0, the principal compressive stress is oriented subperpendicular to the main shear plane (i.e., the subduction interface). In this scenario, extensional fractures (i.e., hydrofractures) oriented (sub)parallel to the principal compressive stress and filled with high-pressure minerals, the latter precipitated in a syntaxial mode, will occur. B. Under these new prevailing conditions, veins oriented at c. 45° with respect to the main compressive stress will represent structural favorably-oriented discontinuities for slipping (see thick red line), while those oriented at higher angles are not. In either case, however, the veins represent preferential weaknesses in the rock volume. Therefore, it is likely that both favorably- and unfavorably-oriented veins can slip and be transposed, although favorably oriented veins are expected to form major slip planes. C. Further stress switching (i.e., at T_2 stage) would result in the formation of new veins, but also in shearing along already brecciated and transposed veins. In this case, unfavorably-oriented veins are capable of shearing, as they represent weaknesses associated with strain hardening processes (see main text). In addition, due to intense shearing and transposition, vein structures and related discontinuities can merge or connect into main slip planes. Fluid sources are depicted by colored arrows; for simplicity, the contribution of metasedimentary fluid is not depicted.

The brittle structures produced during a potential slow earthquake were largely overprinted by pressure-solution creep as evidenced by dissolution seams, interpenetrating crystals and dissolved grains (e.g., albite grains lined with amphibole and clinopyroxene needles: ***Figures 4G*** and ***H***; dissolved and reprecipitated lawsonite grains: ***Figure 6.3F***). Although pressure-solution creep is unlikely to accommodate any of the slow earthquake transients (Bos and Spiers, 2002; Oncken et al., in press), the herein documented structures and fabrics demonstrate that this process is essential to recover the fault strength (e.g., Kay et al., 2006; Giger et al., 2008; Rowe et al., 2011; Bernaudin and Gueydan, 2018; see **Chapter 7**), allowing recovery of the tectonic loading and fluid pressures, potentially promoting a new slow or regular earthquake. In this regard, metasomatism associated with an increase in permeability during fault-related damage is key to boost shear zone healing (Giger et al., 2008).

Titanium, HFSE and Cr anomalies, related to precipitation of titanite in ultracataclasites (e.g., Gao et al., 2007; see above), **indicate that slow earthquakes are triggered by – or at least associated with – the episodic injection of fluid pulses sourced downdip the deep slow earthquakes region**. In fact, this may be one of the reasons why slow earthquakes cannot be related to any particular dehydration metamorphic reaction (Peacock, 2009; Peng and Gomberg, 2010), despite some attempts to constrain a potential link (Condit et al., 2020). The occurrence of ultracataclasites (and vein shear bands) highly enriched in titanite appears to be a common feature in subduction zones, as they have been documented in the two localities investigated here. **Therefore, I propose that titanite (and possibly rutile) enrichments associated with (ultra) comminuted materials represent a "metasomatic" rock record witnessing for slip (seismic or subseismic) related to fluid injection in subduction interfaces**. This pattern is likely useful when seeking for deformation structures in rocks whose cataclastic fabrics have been erased during subsequent deformation – as in most cases. In fact, the fluidized ultracataclasites described in **Chapter 7** display similar titanite-enrichments (and HFSEs; ***Figure 7.5C***), suggesting that this "metasomatic" slip record can be expanded towards shallower conditions compatible with the seismogenic region.

The fault rocks structures reported in **Chapter 7** (i.e., fluidized ultracataclasites and blueschist breccias) and **Chapter 6** are sensibly different and have been interpreted as fossilized, regular (moderate magnitude) and low-frequency earthquakes (and slow slips), respectively. The distinction arises from the following structural criteria: (i) the ultracataclasites from **Chapter 7** crosscut the main foliation (***Figure 7.3A***), while those associated with slow earthquakes (sub) parallel to it, thus likely indicating lower stress drops for the latter, which is consistent with tremors (e.g., Fagereng et al., 2010). (ii) Ultracataclasites slip margins display sharp boundaries, but those from **Chapter 7** are sharper. (iii) Ultracataclasites from the shallower seismogenic region (**Chapter 7**) exhibit fluidized and injection structures (***Figures 7.3C*** and ***D***), typically produced during regular fast slips (e.g., Lin, 2011). (iv) The ultracataclasites black regions from **Chapter 7** were produced by the mechanical mixture of veins and blueschists, indicating slip at the several centimeters-scale (probably up to tens of centimeters), as also indicated by observable offsets among fragmented clasts in the damage zone breccias (e.g., ***Figure 7.2D*** and ***E***). (v) Ultracataclasites formed at regular earthquake velocities are in sharp slip contact with heavily brecciated blueschists, the latter also in sharp contact with respect to the pristine blueschist host (e.g., ***Figure 7.3D***) rather than displaying a grain size transition such as those related to LFEs. Altogether, these structures, especially the occurrence of injections and larger displacements, support formation during fast slip associated with a regular earthquake for the ultracataclasites from **Chapter 7** (e.g., Chester and Chester, 1988; Sibson, 2003; Rowe et al., 2005; Wesnousky, 2008), rather than a LFE of smaller magnitude and displacement (see **Chapter 6**; Shelly et al., 2006; Bostock et al., 2015; Kirkpatrick et al., 2021).

Hydraulic breccias formed via explosive hydrofracturing are the clearest geological evidence for supra-lithostatic fluid pressure conditions at depths within the Earth's lithosphere (Jébrak, 1997). Indeed, mass transport through hydrofracturing is a key process allowing, for example, fluid flow

from the slab towards the suprasubduction mantle (e.g., Fyfe et al., 1978; Davies, 1999; Padrón-Navarta et al., 2010; Angiboust et al., 2021). While transient fluid pressures highs are thought to play a first order role in controlling the occurrence of LFEs and other phenomena (e.g., Bons, 2001; Brown et al., 2005; Frank et al., 2015). The herein reported carbonate-rich hydraulic breccias precipitated at near-peak conditions and crosscut most previous structures. Our comparative analysis suggests that massive hydrofracturing occurs mostly towards greater depths approaching the blueschist-to eclogite transition (see above).

Recent seismological observations demonstrate that tremor (including LFEs; e.g., Shelly et al., 2006) distributions are heterogeneous along (and across) the slow earthquake source (Brudzinski and Allen, 2007; Rubinstein et al., 2009), being clustered at greater depths during major slow earthquakes and followed by migration upwards along the subduction interface (e.g., Obara, 2010; Frank et al., 2015). These patterns are compatible with a fault-valve mechanism as imaged in the Cascadia margin, representing fluid pressure fluctuations upwards along the interface (Gosselin et al., 2020). At shallower conditions, however, tremor signals appear to vanish (Frank et al., 2015). In addition, theoretical and numerical investigations have shown that transient LFE and tremor seismic signals can also be produced by fluid injection in the same direction of flow and associated hydrofracturing, and not only by shear slip (Bernaudin and Gueydan 2018; Shapiro et al., 2018; Farge et al., 2021).

With this theoretical and seismological background in mind, **I propose that the greater abundance of hydraulic breccias inferred to have precipitated towards the base of the ETS region represents a potential deep tremor source associated with hydrofracturing rather than shear slip**. This interpretation does not discard further hydrofracturing and tremor-like signals updip the deep slow earthquake source (c. <50 km depth; Frank et al., 2015; Gosselin et al., 2020). In fact, this is a likely possibility since the herein proposed model of upward travelling of porosity waves and rock-buffered chemical homogenization, ultimately requires hydrofracturing (e.g., Skarbek and Rempel, 2016). **Thus, the slow earthquake region – at least from a field-geology perspective – evolves alongdip from a shallower tremor-genic source characterized by localized slip and related ultracataclasites, towards a deeper region dominated by massive, tremor-genic hydrofracturing (*Figure 8.10A*)**. These speculations could explain the alongdip segmentation (10 km depth difference) observed in southwest Japan characterized by shallower episodic tremor bursts and deeper stable tremor activity, interpreted as weakening towards greater depths, possibly related to higher pore fluid pressure conditions or stable creep (Obara et al., 2010). Similar observations in Cascadia demonstrate that deep tremor bursts are not always associated with slip (or rarely), in agreement with theoretical investigations (McCausland et al., 2005; Kao et al., 2005; Shapiro et al., 2018). I conclude that exhumed subduction terranes record the protracted results of slow slips, tremors (including LFEs) and regular earthquakes during burial in the form of brecciated and ultracataclastic fabrics along preferential brittle weaknesses (for tremors and slow slips; e.g., *Figure 8.10B*). While approaching peak burial conditions, these fabrics are progressively overprinted by tremor-genic carbonate-filled hydrofractures. The near-peak massive hydraulic breccias are, in general, devoid of

further shearing and deformation. Thus, these hydraulic breccia-forming fluid overpressures could have weakened the interface up to the point of triggering slicing, mélange formation and detachment of the uppermost part of the subducting crust (e.g., Menant et al., 2019), marking the end of significant burial-related deformation.

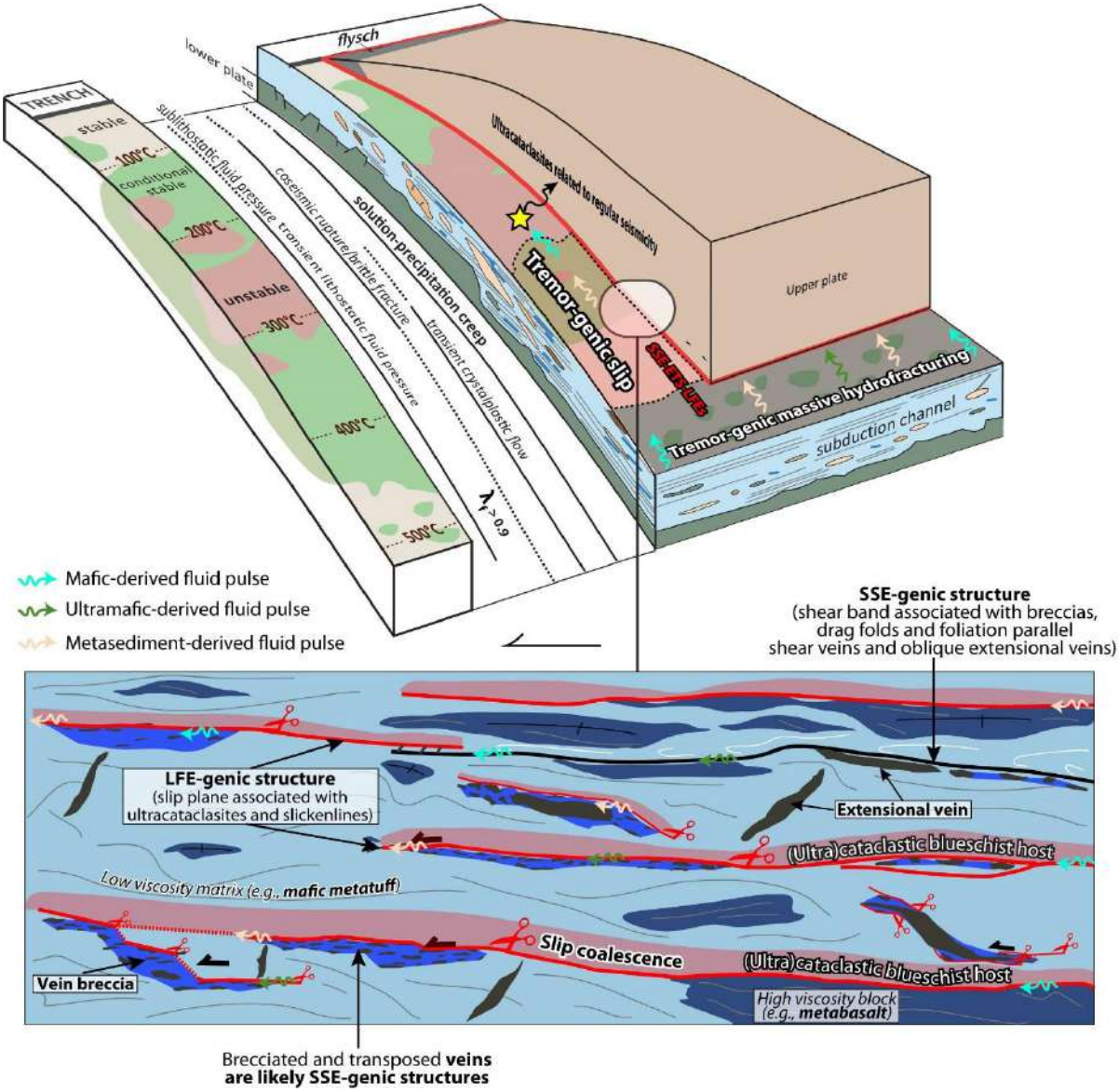

Figure 8.10. A. Illustration of a generic subduction environment depicting relevant deformation mechanisms, plate architecture and earthquakes (regular and slow) source properties (modified from Oncken et al., in press). B. Inset showing some relevant findings in the context of the deep slow earthquake source structures as inferred from previous investigations and this study (modified from Kirkpatrick et al., 2021). I emphasize that this sketch aims at illustrating general characteristics in the frame of vein systems and their potential relation to the slow earthquake region rather than providing a general picture (for such, the reader is referred to Kirkaptrick et al., 2021). Note that such structures are expected to be overprinted by CO_2-bearing fluid pulses within the "tremor-genic massive hydrofracturing" region.

8.7 Large-scale considerations

Tremors bursts migrating updip along the subduction interface reaches velocities in the order of 1 to 3600 kilometers per day (e.g., Shelly et al., 2007; Obara, 2010; Ghosh et al., 2010; Frank et al., 2015; Peng et al., 2015; Cruz-Atienza et al., 2018) and are thought to correlate with ETS initiation in a region of slightly contrasting physical properties as, for example, the contact between a weak and a weaker zone of the interface (Obara, 2010). In the model proposed above, **this transition could be viewed as a slightly stronger interface deforming via LFEs and slow slips which evolves towards a region where massive hydrofracturing generates tremor signals at depths**. The interval of tremor migration depths is in the range of 10 to 30 kilometers (e.g., Obara et al., 2010; Cruz-Atienza et al., 2018; Gosselin et al., 2020). A major outcome of this work is the discovery of common petro-geochemical signatures formed at both, the shallower seismogenic region and the deeper slow earthquakes source (an interval of c. 20 km depth and more along dip). Synthesizing the investigations carried out at Infiernillo and Seghin localities, I propose a scenario where metamorphic fluids produced in the blueschist-to-eclogite transition (with identifiable components from mafic, ultramafic and metasedimentary sources) are expulsed and able to travel updip along the subduction interface. **This model is in full agreement with seismological observations indicating fast tremor migration associated with overpressurised fluids** (e.g., Frank et al., 2015; Gosselin et al., 2020). Furthermore, Cruz-Atienza et al. (2018) suggested that tremor migration occurs as fast pore-pressure waves capable of travelling updip along the interface, ultimately triggering weaking of the shear zone and subsequent slip. Interestingly, the herein studied petro-geochemical signatures have been inferred to occur via the porosity waves model (e.g., Connolly, 2010), which is, to the best of my knowledge, similar to the pore-pressure waves of Cruz-Atienza et al. (2018). Indeed, these two models aim at explaining the same physical process from rheological (porosity waves) and seismological (pore-pressure waves) perspectives. **Therefore, large-scale circulation of fluid pulses along (and across) subduction interfaces is a key process controlling a large palette of seismological manifestations**. This thesis demonstrates that a number of fluid-rock interaction products can potentially be studied from a rock record perspective in the light of earthquake-related processes, opening new avenues for further research.

8.8 Perspectives for future research

8.8.1 Timing of fluid rock-interactions and further constraints on fluid chemistry

Dating metamorphic veins is key for refining our understanding of fluid-rock interaction processes in the frame of ongoing subduction. To assess the timing of fluid-rock interactions and overpressures associated with slow earthquakes processes, I propose using the vein-forming minerals as well as those precipitated in the cataclastic blueschists. Lawsonite, phengite and apatite from veins are potential targets for multi-mineral TIMS Lu-Hf or Rb-Sr geochronology (e.g., Mulcahy et al., 2009). In addition, U-Pb LA-MC-ICP-MS (e.g., Simonetti et al., 2006) or SHRIMP (Aleinikoff et al., 2002) dating of titanite will provide significant advances in constraining the timing of ultracataclastic and veining process. If a meaningful age is obtained, a paleo-slow earthquake may be dated.

The second part of this proposal involves combining trace elements in situ geochemistry as well as fluorine measurements (or other relevant elements) of the metasomatic products. These measurements are expected to be carried out using in situ LA-ICP-MS in mapping mode (for trace elements; in collaboration with Tom Raimondo at University of South Australia) and EPMA machines; as far as possible, equipped with a field emission gun (e.g., FE-EPMA at GFZ Potsdam). The aim of measuring these elements is two-fold. In the first place, measuring trace elements in mapping mode is a powerful tool to further constrain fluid-rock interaction processes and the relative timing of the expected pulses of fluids associated with a determined fluid source. For example, if chromium enrichments are found interspersed with HFSEs, it is possible to speculate about the episodic injection of ultramafic- and mafic-derived fluids. On the other hand, measuring elements such as fluorine may help at understanding the mechanisms of element complexation that allow large-scale mobilization of elements commonly considered as immobile, such as HFSEs (e.g., Gao et al., 2007).

8.8.2 Fluid mass balances: testing the porosity waves hypothesis

Another approach is to validate the model of rock-buffered fluid circulation proposed for the CO_2-bearing veins, inferred to have been sourced from metasediments after reaction with H_2O-rich fluids containing low $\delta^{18}O$ values. To do so, I propose to examinate the O-C, Sr-Nd as well as the Li isotopic signature of metamorphic terranes displaying similar veins such as the Seghin and Infiernillo localities. This study should be accompanied with detailed field structural measurements. In particular, vein abundances relative to the rock volume and careful inspection of geological objects (e.g., vugs) that may resemble fluid-filled porosity at depths (e.g., Angiboust and Raimondo, submitted). After having characterized the isotopic signatures, I expect to perform mass balance calculations and diffusion modelling in order to estimate: (i) the amount of fluids needed to homogenize the isotopic Sr-Nd compositions as measured in the vein systems and hosts (also for Rb-Sr isotopic system; e.g., Glodny et al., 2003), (ii) the extent of fluid-rock interactions in order to imprint a characteristic low $\delta^{18}O$ signature and to compare with the results obtained from the Deep Earth Water (DEW) thermodynamic modelling from **Chapter 5** and (iii) relative porosities and durations of fluid pulses. The last point is motivated by the interesting results from John et al. (2012).

This field-based petro-geochemical approach has the potential of providing further evidence that may witness for the passage of porosity waves and help at refining durations and physical processes behind it. Last, after having calculated mass fluxes and better constrained amounts of fluids needed for CO_2-related veining, I would attempt to constrain in a more accurate way the total C budget associated with each out of several events of veining associated with tremors and slow earthquakes.

8.8.3 Illuminating stress distributions and deformation mechanisms of slow earthquakes processes

After having identified the processes associated with veining and ultracataclasite-forming slips, it is critical to perform further high-resolution and systematic structural investigations of the ultracataclastic vein margins and associated veins. In this regard, I propose three main lines of research. First, the structural characterization of the ultracataclastic lithologies with respect to conjugated vein systems, which would allow estimating stress distributions and magnitudes associated with deep slow earthquake process, following a similar geometrical approach to the one used in Fagereng et al. (2010). Second, by measuring the widths and lengths (aspect ratios) of a large number of former hydrofractures, it would be possible to provide constrains for calibrating the numerical models for tectonic tremor generation associated with fluid overpressures, such as those from Shapiro et al. (2018) and Farge et al. (2021). Finally, an extensive microstructural study of the brecciated vein systems, the ultracataclasites and pristine blueschist host through a EBSD- and TEM-based investigation in order to characterize favourable and unfavourable crystallographic orientations of former extensional veins which commonly grow with the C axis perpendicular to the vein margins. Thus, it would be possible to address the mechanisms driving the earliest stages of vein brecciation and brittle creep, among which strain hardening or slip along unfavourable crystallographic planes with respect to the imposed stresses could have had significant effects. Furthermore, via comparing the orientation of the brecciated crystals with respect to former extensional veins, it is possible to develop a vorticity analysis (e.g., Teyssier et al., 2010) to better characterize the stress distributions during brittle creep. A transect starting from a pristine non-cataclastic foliated blueschist towards the ultracataclastic vein margins would contribute to illuminate the deformation mechanisms operating at background subduction slip rates and faster slow earthquake processes, and the transition towards faster rates. Last, integrating the three parts of this study would make it possible to provide further physical constraints on the studied structures, their possible relation to slow earthquake processes, and the relative timing of SSE and LFEs from a geological perspective. In addition, this investigation may help at validating vein breccias and ultracataclasites as possible records of SSEs and LFEs, respectively.

8.8.4 Petrophysical properties of the subducting slab

Many studies have attempted to characterize the elastic seismic properties of the subducting slab using representative eclogite and blueschist materials (e.g., Bascou et al., 2001; Bezacier et al., 2010; Worthington et al., 2013; Cao et al., 2014; Cossette et al., 2015; Ha et al., 2018). The methodology used in these approaches is based on measuring a large number of representative CPOs (via EBSD or

universal stage microscope, the latter technique used in older studies) and, through a mathematical formulation, convert them into elastic properties (e.g., Mainprice and Humbert, 1994; Mainprice et al., 2011). Thus, the seismic anisotropies are compared to the geometry of the subduction margin, the rock fabrics and instrumental seismological observations. Nonetheless, these studies can only be compared to the background conditions (and deformation fabrics) of the subduction zone, since the effects of cracks and porosities resulting from fluid pulses during slow earthquake processes are not taken into account. By performing a detailed EBSD-based investigation in the host and vein materials it would be possible to constraint the elastic transient effects of porosities and fractures using the AnisEulerSC software (Kim et al., 2020), devoted to modelling the seismic properties of polycrystalline aggregates with cracks, porosity and geometrical parameters. This approach is expected to be calibrated using field and microscopic data from host and vein materials (see Tewksbury-Christle and Behr, 2021 for a slightly similar approach in a warm and metasedimentary-dominated complex). In particular, estimating the shape, abundance and geometry of veins (former cracks) and cavities (former porosities) that may have been produced during slow earthquake processes. Thus, these calculations can be compared with the seismic properties imaged from the slow earthquake source and corroborate (or refute), from a geological approach, the widely accepted assumption that high Vp/Vs ratios are associated with fluid-filled porosity.

9. References

References and bibliography

Abercrombie, R., Poli, P., Bannister, S., 2017. Earthquake directivity, orientation, and stress drop within the subducting plate at the Hikurangi Margin, New Zealand. Journal of Geophysical Research: Solid Earth. 122(12), 10-176.

Agard, P., Omrani, J., Jolivet, L., and Mouthereau, F. (2005). Convergence history across Zagros (Iran): constraints from collisional and earlier deformation. International journal of earth sciences, 94(3), 401-419.

Agard, P., Monié, P., Gerber, W., Omrani, J., Molinaro, M., Meyer, B., Labrousse, L., Vrielynck, B., Jolivet, L., Yamato, P., 2006. Transient, synobduction exhumation of Zagros blueschists inferred from P-T, deformation, time, and kinematic constraints: Implications for Neotethyan wedge dynamics. Journal of Geophysical Research: Solid Earth. 111(B11).

Agard, P., Omrani, J., Jolivet, L., Whitechurch, H., Vrielynck, B., Spakman, W., Monié, P., Meyer, B., Wortel, R., 2011. Zagros orogeny: a subduction-dominated process. Geological Magazine. 148(5-6), 692-725.

Agard, P., Plunder, A., Angiboust, S., Bonnet, G., Ruh, J., 2018. The subduction plate interface: rock record and mechanical coupling (from long to short timescales). Lithos. 320, 537-566.

Agard, P., and Handy, M. R. (2021). Ocean subduction dynamics in the Alps. Elements: An International Magazine of Mineralogy, Geochemistry, and Petrology, 17(1), 9-16.

Ague, J., 2003. Fluid infiltration and transport of major, minor, and trace elements during regional metamorphism of carbonate rocks, Wepawaug Schist, Connecticut, USA. American Journal of Science. 303(9), 753-816.

Ague, J. J. (2014). 4.6. Fluid flow in the deep crust. The Crust, Treatise on Geochemistry (eds. HD Holland and KK Turekian, Second Edition), Elsevier-Pergamon, Oxford, 203-247.

Ague, J., Nicolescu, S., 2014. Carbon dioxide released from subduction zones by fluid-mediated reactions. Nature Geoscience. 7(5), 355-360.

Ague, J. J., 2017. Element mobility during regional metamorphism in crustal and subduction zone environments with a focus on the rare earth elements (REE). American Mineralogist, 102(9), 1796-1821.

Aguirre, L., Hervé, F., and Godoy, E., 1972, Distribution of metamorphic facies in Chile—An outline: Krystalinikum, v. 9, p. 7–19.

Alavi, M. (1994). Tectonics of the Zagros orogenic belt of Iran: new data and interpretations. Tectonophysics, 229(3-4), 211-238.

Aleinikoff, J. N., Wintsch, R. P., Fanning, C. M., and Dorais, M. J. (2002). U–Pb geochronology of zircon and polygenetic titanite from the Glastonbury Complex, Connecticut, USA: an integrated SEM, EMPA, TIMS, and SHRIMP study. Chemical Geology, 188(1-2), 125-147.

Andersen, T. B., Austrheim, H., Deseta, N., Silkoset, P., and Ashwal, L. D. (2014). Large subduction earthquakes along the fossil Moho in Alpine Corsica. Geology, 42(5), 395-398.

Anderson, E. M. (1951). The dynamics of faulting and dyke formation with applications to Britain. Oliver and Boyd.

Anderson, G.M., and Burnham, C.W., 1965, The solubility of quartz in super-critical water: American Journal of Science, v. 263, p. 494–511.

Anderson, D. L. (1975). Accelerated plate tectonics. Science, 187(4181), 1077-1079.

Angiboust, S., Agard, P., Raimbourg, H., Yamato, P., Huet, B., 2011. Subduction interface processes recorded by eclogite-facies shear zones (Monviso, W. Alps). Lithos. 127(1-2), 222-238.

Angiboust, S., Agard, P., Yamato, P., and Raimbourg, H. (2012). Eclogite breccias in a subducted ophiolite: A record of intermediate-depth earthquakes?. Geology, 40(8), 707-710.

Angiboust, S., Pettke, T., De Hoog, J. C., Caron, B., Oncken, O., 2014. Channelized fluid flow and eclogite-facies metasomatism along the subduction shear zone. Journal of petrology. 55(5), 883-916.

Angiboust, S., Kirsch, J., Oncken, O., Glodny, J., Monié, P., Rybacki, E., 2015. Probing the transition between seismically coupled and decoupled segments along an ancient subduction interface. Geochemistry, Geophysics, Geosystems. 16(6), 1905-1922.

Angiboust, S., Agard, P., Glodny, J., Omrani, J., Oncken, O., 2016. Zagros blueschists: Episodic underplating and long-lived cooling of a subduction zone. Earth and Planetary Science Letters. 443, 48-58.

Angiboust, S., Yamato, P., Hertgen, S., Hyppolito, T., Bebout, G. E., Morales, L., 2017. Fluid pathways and high-P metasomatism in a subducted continental slice (Mt. Emilius klippe, W. Alps). Journal of Metamorphic Geology. 35(5), 471-492.

Angiboust, S., and Harlov, D., 2017, Ilmenite breakdown and rutile-titanite stability in metagranitoids: Natural observations and experimental results: American Mineralogist, v. 102, p. 1696–1708.

Angiboust, S., Hyppolito, T., Glodny, J., Cambeses, A., Garcia-Casco, A., Calderón, M., and Juliani, C. (2017). Hot subduction in the middle Jurassic and partial melting of oceanic crust in Chilean Patagonia. Gondwana Research, 42, 104-125.

Angiboust, S., Cambeses, A., Hyppolito, T., Glodny, J., Monié, P., Calderón, M., and Juliani, C., 2018, A 100-my-long window onto mass-flow processes in the Patagonian Mesozoic subduction zone (Diego de Almagro Island, Chile): Geological Society of America Bulletin, v. 130, p. 1439–1456.

Angiboust, S., Glodny, J., Cambeses, A., Raimondo, T., Monié, P., Popov, M., Garcia-Casco, A., 2020. Drainage of Subduction Interface Fluids into the Fore-arc Mantle Evidenced by a Pristine Jadeitite Network (Polar Urals). Journal of Metamorphic Geology.

Angiboust, S., Muñoz-Montecinos, J., Cambeses, A., Raimondo, T., Deldicque, D., and Garcia-Casco, A. (2021). Jolts in the Jade factory: A route for subduction fluids and, their implications for mantle wedge seismicity. Earth-Science Reviews, 103720.

Antignano, A., and Manning, C. E. (2008). Rutile solubility in H_2O, H_2O–SiO_2, and H_2O–$NaAlSi_3O_8$ fluids at 0.7–2.0 GPa and 700–1000 C: implications for mobility of nominally insoluble elements. Chemical Geology, 255(1-2), 283-293.

Ao, A., and Bhowmik, S. K. (2014). Cold subduction of the Neotethys: the metamorphic record from finely banded lawsonite and epidote blueschists and associated metabasalts of the Nagaland Ophiolite Complex, India. Journal of Metamorphic Geology, 32(8), 829-860.

Arfania, R., Shahriari, S., 2009. Role of southeastern Sanandaj–Sirjan Zone in the tectonic evolution of Zagros Orogenic Belt, Iran. Island arc. 18(4), 555-576.

Arvin, M., and Robinson, P. T. (1994). The petrogenesis and tectonic setting of lavas from the Baft ophiolitic mélange, southwest of Kerman, Iran. Canadian Journal of Earth Sciences, 31(5), 824-834.

Arvin, M., Pan, Y., Dargahi, S., Malekizadeh, A., and Babaei, A. (2007). Petrochemistry of the Siah-Kuh granitoid stock southwest of Kerman, Iran: Implications for initiation of Neotethys subduction. Journal of Asian Earth Sciences, 30(3-4), 474-489.

Audet, P., Bostock, M.G., Christensen, N.I., and Peacock, S.M., 2009, Seismic evidence for overpressured subducted oceanic crust and megathrust fault sealing: Nature, v. 457, p. 76–78.

Audet, P., and Bürgmann, R. (2014). Possible control of subduction zone slow-earthquake periodicity by silica enrichment. Nature, 510(7505), 389-392.

Audet, P., and Kim, Y. (2016). Teleseismic constraints on the geological environment of deep episodic slow earthquakes in subduction zone forearcs: A review. Tectonophysics, 670, 1-15.

Austrheim, H., and Boundy, T. M. (1994). Pseudotachylytes generated during seismic faulting and eclogitization of the deep crust. Science, 265(5168), 82-83.

Austrheim, H., Andersen, T., 2004. Pseudotachylytes from Corsica: fossil earthquakes from a subduction complex. Terra nova. 16(4), 193-197.

Ayers, J. C., and Watson, E. B. (1993). Rutile solubility and mobility in supercritical aqueous fluids. Contributions to Mineralogy and Petrology, 114(3), 321-330.

Bach, W., and Früh-Green, G. L. (2010). Alteration of the oceanic lithosphere and implications for seafloor processes. Elements, 6(3), 173-178.

Bachmann, R., Oncken, O., Glodny, J., Seifert, W., Georgieva, V., and Sudo, M., 2009, Exposed plate interface in the European Alps reveals fabric styles and gradients related to an ancient seismogenic coupling zone: Journal of Geophysical Research, v. 114, B05402.

Bachmann, F., Hielscher, R., Schaeben, H., 2010. Texture analysis with MTEX–free and open source software toolbox. In Solid State Phenomena (Vol. 160, pp. 63-68). Trans Tech Publications Ltd.

Bachmann, F., Hielscher, R., and Schaeben, H. (2011). Grain detection from 2d and 3d EBSD data—Specification of the MTEX algorithm. Ultramicroscopy, 111(12), 1720-1733.

Bailey, R. C. (1990). Trapping of aqueous fluids in the deep crust. Geophysical Research Letters, 17(8), 1129-1132.

Barklage, M., Wiens, D. A., Conder, J. A., Pozgay, S., Shiobara, H., Sugioka, H., 2015. P and S velocity tomography of the M ariana subduction system from a combined land-sea seismic deployment. Geochemistry, Geophysics, Geosystems. 16(3), 681-704.

Barrientos, X., and Selverstone, J., 1993, Infiltration vs. thermal overprinting of epidote blueschists, Ile de Groix, France: Geology, v. 21, p. 69–72.

Barrier, E., and Vrielynck, B. (2008). Palaeotectonic map of the Middle East, Atlas of 14 maps, tectonosedimentary-palinspastic maps from Late Norian to Pliocene. Commission for the Geologic Map of the World (CCMW, CCGM), Paris, France.

Bascou, J., Barruol, G., Vauchez, A., Mainprice, D., and Egydio-Silva, M. (2001). EBSD-measured lattice-preferred orientations and seismic properties of eclogites. Tectonophysics, 342(1-2), 61-80.

Bassett, D., Sutherland, R., and Henrys, S. (2014). Slow wavespeeds and fluid overpressure in a region of shallow geodetic locking and slow slip, Hikurangi subduction margin, New Zealand. Earth and Planetary Science Letters, 389, 1-13.

Bassett, D., and Watts, A. B. (2015). Gravity anomalies, crustal structure, and seismicity at subduction zones: 2. Interrelationships between fore-arc structure and seismogenic behavior. Geochemistry, Geophysics, Geosystems, 16(5), 1541-1576.

Baziotis, I., and Mposkos, E., 2011, Origin of metabasites from upper tectonic unit of the Lavrion area (SE Attica, Greece): Geochemical implications for dual origin with distinct provenance of blueschist and greenschist's protoliths: Lithos, v. 126, p. 161–173.

Bea, F., 1996. Residence of REE, Y, Th and U in granites and crustal protoliths; implications for the chemistry of crustal melts. Journal of petrology. 37(3), 521-552.

Beall, A., Fagereng, Å., and Ellis, S. (2019). Strength of strained two-phase mixtures: Application to rapid creep and stress amplification in subduction zone mélange. Geophysical Research Letters, 46(1), 169-178.

Bebout, G. E., and Barton, M. D. (1989). Fluid flow and metasomatism in a subduction zone hydrothermal system: Catalina Schist terrane, California. Geology, 17(11), 976-980.

Bebout, G. E. (1991). Field-based evidence for devolatilization in subduction zones: implications for arc magmatism. Science, 251(4992), 413-416.

Bebout, G., Barton, M. D., 1993. Metasomatism during subduction: products and possible paths in the Catalina Schist, California. Chemical Geology. 108(1-4), 61-92.

Bebout, G., 2007. Metamorphic chemical geodynamics of subduction zones. Earth and Planetary Science Letters. 260(3-4), 373-393.

Bebout, G., Penniston-Dorland, S. C., 2016. Fluid and mass transfer at subduction interfaces—The field metamorphic record. Lithos. 240, 228-258.

Bedford, J., Moreno, M., Baez, J. C., Lange, D., Tilmann, F., Rosenau, M., ... and Vigny, C. (2013). A high-resolution, time-variable afterslip model for the 2010 Maule Mw= 8.8, Chile megathrust earthquake. Earth and Planetary Science Letters, 383, 26-36.

Behr, W., Platt, J., 2013. Rheological evolution of a Mediterranean subduction complex. Journal of Structural Geology. 54, 136-155.

Behr, W. M., and Platt, J. P. (2014). Brittle faults are weak, yet the ductile middle crust is strong: Implications for lithospheric mechanics. Geophysical Research Letters, 41(22), 8067-8075.

Behr, W. M., and Becker, T. W. (2018). Sediment control on subduction plate speeds. Earth and Planetary Science Letters, 502, 166-173.

Behr, W. M., Kotowski, A. J., and Ashley, K. T. (2018). Dehydration-induced rheological heterogeneity and the deep tremor source in warm subduction zones. Geology, 46(5), 475-478.

Behr, W. M., Bürgmann, R., 2021. What's down there? The structures, materials and environment of deep-seated slow slip and tremor. Philosophical Transactions of the Royal Society A, 379(2193), 20200218.

Beinlich, A., Klemd, R., John, T., Gao, J., 2010. Trace-element mobilization during Ca-metasomatism along a major fluid conduit: Eclogitization of blueschist as a consequence of fluid–rock interaction. Geochimica et Cosmochimica Acta, 74(6), 1892-1922.

Beinlich, A., John, T., Vrijmoed, J. C., Tominaga, M., Magna, T., Podladchikov, Y., 2020. Instantaneous rock transformations in the deep crust driven by reactive fluid flow. Nature Geoscience. 13(4), 307-311.

Bell, T. H., Cuff, C., 1989. Dissolution, solution transfer, diffusion versus fluid flow and volume loss during deformation/metamorphism. Journal of Metamorphic Geology. 7(4), 425-447.

Berberian, M., and King, G. C. P. (1981). Towards a paleogeography and tectonic evolution of Iran. Canadian journal of earth sciences, 18(2), 210-265.

Berberian, F., and Berberian, M. J. Z. H. K. H. G. E. (1981). Tectono-plutonic episodes in Iran. Zagros Hindu Kush Bernaudin, M., and Gueydan, F. (2018). Episodic tremor and slip explained by fluid-enhanced microfracturing and sealing. Geophysical Research Letters, 45(8), 3471-3480. Himalaya Geodynamic Evolution, 3, 5-32.

Beroza, G. C., and Mikumo, T. (1996). Short slip duration in dynamic rupture in the presence of heterogeneous fault properties. Journal of Geophysical Research: Solid Earth, 101(B10), 22449-22460.

Beroza, G. C., and Ide, S. (2011). Slow earthquakes and nonvolcanic tremor. Annual review of Earth and planetary sciences, 39, 271-296.

Bezacier, L., Reynard, B., Bass, J. D., Wang, J., and Mainprice, D. (2010). Elasticity of glaucophane, seismic velocities and anisotropy of the subducted oceanic crust. Tectonophysics, 494(3-4), 201-210.

Bickert, M., Cannat, M., Tommasi, A., Jammes, S., and Lavier, L. (2021). Strain Localization in the Root of Detachment Faults at a Melt-Starved Mid-Ocean Ridge: A Microstructural Study of Abyssal Peridotites From the Southwest Indian Ridge. Geochemistry, Geophysics, Geosystems, 22(5), e2020GC009434.

Bilek, S. L., Schwartz, S. Y., and DeShon, H. R. (2003). Control of seafloor roughness on earthquake rupture behavior. Geology, 31(5), 455-458.

Bird, P., 1978. Stress and temperature in subduction shear zones: Tonga and Mariana. Geophysical Journal International. 55(2), 411-434.

Bjørnerud, M. (2010). Rethinking conditions necessary for pseudotachylyte formation: Observations from the Otago schists, South Island, New Zealand. Tectonophysics, 490(1-2), 69-80.

Blanco-Quintero, I. F., García-Casco, A., and Gerya, T. V. (2011). Tectonic blocks in serpentinite mélange (eastern Cuba) reveal large-scale convective flow of the subduction channel. Geology, 39(1), 79-82.

Bloch, W., John, T., Kummerow, J., Salazar, P., Krüger, O. S., and Shapiro, S. A. (2018). Watching dehydration: Seismic indication for transient fluid pathways in the oceanic mantle of the subducting Nazca slab. Geochemistry, Geophysics, Geosystems, 19(9), 3189-3207.

Bonnet, G., Agard, P., Angiboust, S., Monie, P., Jentzer, M., Omrani, J., ... and Fournier, M. (2018). Tectonic slicing and mixing processes along the subduction interface: The Sistan example (Eastern Iran). Lithos, 310, 269-287.

Bonnet, G., Agard, P., Angiboust, S., Fournier, M., Omrani, J., 2019. No large earthquakes in fully exposed subducted seamount. Geology, 47(5), 407-410.

Bonnet, G., Agard, P., Whitechurch, H., Fournier, M., Angiboust, S., Caron, B., Omrani, J., 2020a. Fossil seamount in southeast Zagros records intraoceanic arc to back-arc transition: New constraints for the evolution of the Neotethys. Gondwana Research. 81, 423-444.

Bonnet, G., Agard, P., Angiboust, S., Monié, P., Fournier, M., Caron, B., Omrani, J., 2020b. Structure and metamorphism of a subducted seamount (Zagros suture, Southern Iran). Geosphere. 16(1), 62-81.

Bonorino, G. G. (1991). Late Paleozoic orogeny in the northwestern Gondwana continental margin, western Argentina and Chile. Journal of South American Earth Sciences, 4(1-2), 131-144.

Bons, P.D., 2001, The formation of large quartz veins by rapid ascent of fluids in mobile hydrofractures: Tectonophysics, v. 336, p. 1–17.

Bons, P., Elburg, M., Gomez-Rivas, E., 2012. A review of the formation of tectonic veins and their microstructures. Journal of Structural Geology. 43, 33-62.

Bos, B., and Spiers, C. J. (2002). Frictional-viscous flow of phyllosilicate-bearing fault rock: Microphysical model and implications for crustal strength profiles. Journal of Geophysical Research: Solid Earth, 107(B2), ECV-1.

Bostock, M. G., Royer, A. A., Hearn, E. H., and Peacock, S. M. (2012). Low frequency earthquakes below southern Vancouver Island. Geochemistry, Geophysics, Geosystems, 13(11).

Bostock, M. G. (2013). The Moho in subduction zones. Tectonophysics, 609, 547-557.

Bostock, M. G., Thomas, A. M., Savard, G., Chuang, L., and Rubin, A. M. (2015). Magnitudes and moment-duration scaling of low-frequency earthquakes beneath southern Vancouver Island. Journal of Geophysical Research: Solid Earth, 120(9), 6329-6350.

Bouilhol, P., Connolly, J. A., and Burg, J. P. (2011). Geological evidence and modeling of melt migration by porosity waves in the sub-arc mantle of Kohistan (Pakistan). Geology, 39(12), 1091-1094.

Brantut, N., Baud, P., Heap, M. J., and Meredith, P. G. (2012). Micromechanics of brittle creep in rocks. Journal of Geophysical Research: Solid Earth, 117(B8).

Breeding, C., Ague, J., 2002. Slab-derived fluids and quartz-vein formation in an accretionary prism, Otago Schist, New Zealand. Geology. 30(6), 499-502.

Breeding, C., Ague, J., Bröcker, M., 2004. Fluid–metasedimentary rock interactions in subduction-zone mélange: implications for the chemical composition of arc magmas. Geology. 32(12), 1041-1044.

Brenan, J. M., Shaw, H. F., Phinney, D. L., and Ryerson, F. J. (1994). Rutile-aqueous fluid partitioning of Nb, Ta, Hf, Zr, U and Th: implications for high field strength element depletions in island-arc basalts. Earth and Planetary Science Letters, 128(3-4), 327-339.

Brimhall, G. H., and Crerar, D. A. (1987). Minerals, Fluids and Melts.

Bröcker, M., 1990, Blueschist-to-greenschist transition in metabasites from Tinos Island, Cyclades, Greece: Compositional control or fluid infiltration?: Lithos, v. 25, p. 25–39.

Brown, W. H., Fyfe, W. S., and Turner, F. J. (1962). Aragonite in California glaucophane schists, and the kinetics of the aragonite—calcite transformation. Journal of Petrology, 3(3), 566-582.

Brown, E. H. (1977). Phase relations of Na-pyroxene in blueschists and eclogites of the Franciscan Formation, California, USA. Problems of Physicochemical Petrology, 7-20.

Brown, E., Wilson, D., Armstrong, R., and Harakal, J., 1982. Petrologic, structural, and age relations of serpentinite, amphibolite, and blueschist in the Shuksan Suite of the Iron Mountain–Gee Point area, North Cascades, Washington. Geological Society of America Bulletin. 93(11), 1087-1098.

Brown, K. M., Tryon, M. D., DeShon, H. R., Dorman, L. M., and Schwartz, S. Y. (2005). Correlated transient fluid pulsing and seismic tremor in the Costa Rica subduction zone. Earth and Planetary Science Letters, 238(1-2), 189-203.

Brudzinski, M. R., and Allen, R. M. (2007). Segmentation in episodic tremor and slip all along Cascadia. Geology, 35(10), 907-910.

Burg, J. P. (2018). Geology of the onshore Makran accretionary wedge: Synthesis and tectonic interpretation. Earth-Science Reviews, 185, 1210-1231.

Bürgmann, R. (2018). The geophysics, geology and mechanics of slow fault slip. Earth and Planetary Science Letters, 495, 112-134.

Busquets, P., Colombo, F., Heredia, N., de Porta, N. S., Fernández, L. R., and Marrón, J. Á. (2005). Age and tectonostratigraphic significance of the Upper Carboniferous series in the basement of the Andean Frontal Cordillera: Geodynamic implications. Tectonophysics, 399(1-4), 181-194.

Busquets, P., Méndez-Bedia, I., Gallastegui, G., Colombo, F., Cardó, R., Limarino, O., ... and Césari, S. N. (2013). The relationship between carbonate facies, volcanic rocks and plant remains in a late Palaeozoic lacustrine system (San Ignacio Fm, Frontal Cordillera, San Juan province, Argentina). International Journal of Earth Sciences, 102(5), 1271-1287.

Byrne, T., Fisher, D., 1990. Evidence for a weak and overpressured decollement beneath sediment-dominated accretionary prisms. Journal of Geophysical Research: Solid Earth. 95(B6), 9081-9097.

Cámara, F., Doukhan, J. C., and Carpenter, M. A. (2001). Lattice defects in lawsonite: a TEM investigation. Mineralogical Magazine, 65(1), 33-39.

Cannaò, E., Scambelluri, M., Bebout, G. E., Agostini, S., Pettke, T., Godard, M., and Crispini, L. (2020). Ophicarbonate evolution from seafloor to subduction and implications for deep-Earth C cycling. Chemical geology, 546, 119626.

Cannat, M. (1993). Emplacement of mantle rocks in the seafloor at mid-ocean ridges. Journal of Geophysical Research: Solid Earth, 98(B3), 4163-4172.

Canil, D., Scarfe, C. M., 1990. Phase relations in peridotite+ CO_2 systems to 12 GPa: implications for the origin of kimberlite and carbonate stability in the Earth's upper mantle. Journal of Geophysical Research: Solid Earth. 95(B10), 15805-15816.

Cao, Y., Jung, H., and Song, S. (2014). Microstructures and petro-fabrics of lawsonite blueschist in the North Qilian suture zone, NW China: Implications for seismic anisotropy of subducting oceanic crust. Tectonophysics, 628, 140-157.

Cao, Y., Du, J., Jung, H., Jung, S., Lee, J., Park, M., and Kim, J. (2021). Crystal preferred orientations, deformation mechanisms and seismic properties of high pressure metamorphic rocks from the Central Qiangtang metamorphic belt, Tibetan Plateau. Journal of Structural Geology, 145, 104309.

Cárdenas-Párraga, J., Garcia-Casco, A., Blanco-Quintero, I., Rojas-Agramonte, Y., Nuñez Cambra, K., Harlow, G (in press). A highly dynamic hot hydrothermal system in the subduction environment: Geochemistry and geochronology of jadeitite and associated rocks of the Sierra del Convento mélange (Eastern Cuba). American Journal of Science.

Carlson, R.L., and Herrick, C.N., 1990, Densities and porosities in the oceanic crust and their variations with depth and age: Journal of Geophysical Research, v. 95, p. 9153–9170.

Carson, C., Ague, J., 2008. Early Palaeozoic metasomatism of the Archaean Napier Complex, East Antarctica. Geological Society, London, Special Publications. 308(1), 283-316.

Cartwright, I., Power, W.L., Oliver, N.H.S., Valenta, R.K., and McLatchie, G.S., 1994, Fluid migration and vein formation during deformation and greenschist facies metamorphism at Ormiston Gorge, central Australia: Journal of Metamorphic Geology, v. 12, p. 373–386.

Cartwright, I., Barnicoat, A., 1999. Stable isotope geochemistry of Alpine ophiolites: a window to ocean-floor hydrothermal alteration and constraints on fluid–rock interaction during high-pressure metamorphism. International Journal of Earth Sciences. 88(2), 219-235.

Cartwright, I., Buick, I., 2000. Fluid generation, vein formation and the degree of fluid–rock interaction during decompression of high-pressure terranes: the Schistes Lustrés, Alpine Corsica, France. Journal of Metamorphic Geology. 18(6), 607-624.

Cerchiari, A., Remitti, F., Mittempergher, S., Festa, A., Lugli, F., and Cipriani, A. (2020). Cyclical variations of fluid sources and stress state in a shallow megathrust-zone mélange. Journal of the Geological Society, 177(3), 647-659.

Cetinkaplan, M. (2020). Epidote-lawsonite coexistence in blueschist-facies block from the Tavşanlı Zone-Turkey: petrological implications. Turkish Journal of Earth Sciences, 29(7), 1073-1099.

Chan, L. H., and Kastner, M. (2000). Lithium isotopic compositions of pore fluids and sediments in the Costa Rica subduction zone: implications for fluid processes and sediment contribution to the arc volcanoes. Earth and Planetary Science Letters, 183(1-2), 275-290.

Charrier, R. (1973). Interruptions of spreading and the compressive tectonic phases of the Meridional Andes. Earth and Planetary Science Letters, 20(2), 242-249.

Charrier, R. (1979). El Triásico en Chile y regiones adyacentes de Argentina: Una reconstrucción paleogeográfica y paleoclimática. Comunicaciones, Departamento de Geología, Universidad de Chile, Santiago, 26, 1-47.

Charrier, R., Pinto, L., and Rodríguez, M. P. (2007). Tectonostratigraphic evolution of the Andean Orogen in Chile. In The geology of Chile (pp. 21-114).

Charrier, R., Ramos, V. A., Tapia, F., and Sagripanti, L. (2015). Tectono-stratigraphic evolution of the Andean Orogen between 31 and 37 S (Chile and Western Argentina). Geological Society, London, Special Publications, 399(1), 13-61.

Chester, F. M., and Chester, J. S. (1998). Ultracataclasite structure and friction processes of the Punchbowl fault, San Andreas system, California. Tectonophysics, 295(1-2), 199-221.

ChO, M., Liou, J. G., and Maruyama, S. (1986). Transition from the zeolite to prehnite-pumpellyite facies in the Karmutsen metabasites, Vancouver Island, British Columbia. Journal of Petrology, 27(2), 467-494.

Cloos, M., 1986. Blueschists in the Franciscan Complex of California: Petrotectonic constraints on uplift mechanisms. In Blueschists and eclogites (Vol. 164, pp. 77-93). Geological Society of America Memoir.

Cloos, M., and Shreve, R. L. (1988a). Subduction-channel model of prism accretion, melange formation, sediment subduction, and subduction erosion at convergent plate margins: 1. Background and description. Pure and Applied Geophysics, 128(3), 455-500.

Cloos, M., and Shreve, R. L. (1988b). Subduction-channel model of prism accretion, melange formation, sediment subduction, and subduction erosion at convergent plate margins: 2. Implications and discussion. Pure and Applied Geophysics, 128(3), 501-545.

Cloos, M., and Shreve, R. L. (1996). Shear-zone thickness and the seismicity of Chilean-and Marianas-type subduction zones. Geology, 24(2), 107-110.

Coira, B., Davidson, J., Mpodozis, C., and Ramos, V. (1982). Tectonic and magmatic evolution of the Andes of northern Argentina and Chile. Earth-Science Reviews, 18(3-4), 303-332.

Collettini, C., Niemeijer, A., Viti, C., Marone, C., 2009. Fault zone fabric and fault weakness. Nature. 462(7275), 907-910.

Collettini, C., Niemeijer, A., Viti, C., Smith, S. A., and Marone, C. (2011). Fault structure, frictional properties and mixed-mode fault slip behavior. Earth and Planetary Science Letters, 311(3-4), 316-327.

Collins, N., Bebout, G., Angiboust, S., Agard, P., Scambelluri, M., Crispini, L., John, T., 2015. Subduction zone metamorphic pathway for deep carbon cycling: II. Evidence from HP/UHP metabasaltic rocks and ophicarbonates. Chemical Geology. 412, 132-150.

Condit, C. B., Guevara, V. E., Delph, J. R., and French, M. E. (2020). Slab dehydration in warm subduction zones at depths of episodic slip and tremor. Earth and Planetary Science Letters, 552, 116601.

Connolly, J. A. D. (1997). Devolatilization-generated fluid pressure and deformation-propagated fluid flow during prograde regional metamorphism. Journal of Geophysical Research: Solid Earth, 102(B8), 18149-18173.

Connolly, J. A. D., and Podladchikov, Y. Y. (1998). Compaction-driven fluid flow in viscoelastic rock. Geodinamica Acta, 11(2-3), 55-84.

Connolly, J., Podladchikov, Y., 2004. Fluid flow in compressive tectonic settings: Implications for midcrustal seismic reflectors and downward fluid migration. Journal of Geophysical Research: Solid Earth. 109(B4).

Connolly, J., 2005. Computation of phase equilibria by linear programming: a tool for geodynamic modeling and its application to subduction zone decarbonation. Earth and Planetary Science Letters. 236(1-2), 524-541.

Connolly, J., 2010. The mechanics of metamorphic fluid expulsion. Elements. 6(3), 165-172.

Connolly, J., Galvez, M., 2018. Electrolytic fluid speciation by Gibbs energy minimization and implications for subduction zone mass transfer. Earth and Planetary Science Letters. 501, 90-102.

Cook-Kollars, J., Bebout, G., Collins, N., Angiboust, S., Agard, P., 2014. Subduction zone metamorphic pathway for deep carbon cycling: I. Evidence from HP/UHP metasedimentary rocks, Italian Alps. Chemical Geology. 386, 31-48.

Coombs, D. S. (1960). Lower grade mineral facies in New Zealand. In Intern. Geol. Congress (pp. 339-351).

Cooper, F. J., Platt, J. P., and Anczkiewicz, R. (2011). Constraints on early Franciscan subduction rates from 2-D thermal modeling. Earth and Planetary Science Letters, 312(1-2), 69-79.

Cossette, E., Schneider, D., Audet, P., Grasemann, B., and Habler, G. (2015). Seismic properties and mineral crystallographic preferred orientations from EBSD data: Results from a crustal-scale detachment system, Aegean region. Tectonophysics, 651, 66-78.

Cowan, D. S., and Page, B. M. (1975). Recycled Franciscan material in Franciscan melange west of Paso Robles, California. Geological Society of America Bulletin, 86(8), 1089-1095.

Cox, S. F., and Etheridge, M. A. (1983). Crack-seal fibre growth mechanisms and their significance in the development of oriented layer silicate microstructures. Tectonophysics, 92(1-3), 147-170.

Cox, S. F. (1999). Deformational controls on the dynamics of fluid flow in mesothermal gold systems. Geological Society, London, Special Publications, 155(1), 123-140.

Cox, S. F. (2007). Structural and isotopic constraints on fluid flow regimes and fluid pathways during upper crustal deformation: an example from the Taemas area of the Lachlan Orogen, SE Australia. Journal of Geophysical Research: Solid Earth, 112(B8).

Cox, S., 2010. The application of failure mode diagrams for exploring the roles of fluid pressure and stress states in controlling styles of fracture-controlled permeability enhancement in faults and shear zones. Geofluids. 10(1-2), 217-233.

Cruz-Atienza, V. M., Villafuerte, C., and Bhat, H. S. (2018). Rapid tremor migration and pore-pressure waves in subduction zones. Nature communications, 9(1), 1-13.

Currie, K. L. (1968). On the solubility of albite in supercritical water in the range of 400 degrees to 600 degrees C and 750 to 3500 bars. American Journal of Science, 266(5), 321-341.

Dalla Salda, L. H., Dalziel, I. W., Cingolani, C. A., and Varela, R. (1992). Did the Taconic Appalachians continue into southern South America?. Geology, 20(12), 1059-1062.

Dasgupta, R., and Hirschmann, M. M. (2010). The deep carbon cycle and melting in Earth's interior. Earth and Planetary Science Letters, 298(1-2), 1-13.

Davies, J. H. (1999). The role of hydraulic fractures and intermediate-depth earthquakes in generating subduction-zone magmatism. Nature, 398(6723), 142-145.

DePaolo, D., Wasserburg, G., 1979. Petrogenetic mixing models and Nd-Sr isotopic patterns. Geochimica et Cosmochimica Acta. 43(4), 615-627.

Delaloye, M., Desmons, J., 1980. Ophiolites and mélange terranes in Iran: a geochronological study and its paleotectonic implications. Tectonophysics. 68(1-2), 83-111.

Den Hartog, S. A., and Spiers, C. J. (2014). A microphysical model for fault gouge friction applied to subduction megathrusts. Journal of Geophysical Research: Solid Earth, 119(2), 1510-1529.

de Riese, T., Bons, P. D., Gomez-Rivas, E., and Sachau, T. (2020). Interaction between Crustal-Scale Darcy and Hydrofracture Fluid Transport: A Numerical Study. Geofluids, 2020.

Dercourt, J., Zonenshain, L. P., Ricou, L. E., Kazmin, V. G., Le Pichon, X., Knipper, A. L., ... and Biju-Duval, B. (1986). Geological evolution of the Tethys belt from the Atlantic to the Pamirs since the Lias. Tectonophysics, 123(1-4), 241-315.

Dielforder, A., Vollstaedt, H., Vennemann, T., Berger, A., and Herwegh, M. (2015). Linking megathrust earthquakes to brittle deformation in a fossil accretionary complex. Nature Communications, 6(1), 1-10.

Dielforder, A., Hetzel, R., Oncken, O., 2020. Megathrust shear force controls mountain height at convergent plate margins. Nature. 582(7811), 225-229.

Dipple, G. M., and Ferry, J. M. (1992). Metasomatism and fluid flow in ductile fault zones. Contributions to Mineralogy and Petrology, 112(2), 149-164.

Di Toro, G., Goldsby, D. L., and Tullis, T. E. (2004). Friction falls towards zero in quartz rock as slip velocity approaches seismic rates. Nature, 427(6973), 436-439.

Di Toro, G., Pennacchioni, G., Nielsen, S., 2009. Pseudotachylytes and earthquake source mechanics. International geophysics. 94, 87-133.

Dragert, H., Wang, K., and James, T. S. (2001). A silent slip event on the deeper Cascadia subduction interface. Science, 292(5521), 1525-1528.

Dragovic, B., Angiboust, S., and Tappa, M. J. (2020). Petrochronological close-up on the thermal structure of a paleo-subduction zone (W. Alps). Earth and Planetary Science Letters, 547, 116446.

Dobson, D. P., Thomas, R. W., and Mitchell, T. M. (2018). Diffusion profiles around quartz clasts as indicators of the thermal history of pseudotachylytes. Geochemistry, Geophysics, Geosystems, 19(11), 4329-4341.

Dollinger, G., and Blacic, J. D. (1975). Deformation mechanisms in experimentally and naturally deformed amphiboles. Earth and Planetary Science Letters, 26(3), 409-416.

Dungan, M. A., Vance, J. A., and Blanchard, D. P. (1983). Geochemistry of the Shuksan greenschists and blueschists, North Cascades, Washington: variably fractionated and altered metabasalts of oceanic affinity. Contributions to Mineralogy and Petrology, 82(2-3), 131-146.

Eimer, M., Wiens, D., Cai, C., Lizarralde, D., Jasperson, H., 2020. Seismicity of the incoming plate and forearc near the Mariana Trench recorded by ocean bottom seismographs. Geochemistry, Geophysics, Geosystems. 21(4), e2020GC008953.

El Korh, A., Schmidt, S. T., Ulianov, A., and Potel, S., 2009. Trace element partitioning in HP–LT metamorphic assemblages during subduction-related metamorphism, Ile de Groix, France: a detailed LA-ICPMS study. Journal of Petrology, 50(6), 1107-1148.

Emry, E., Wiens, D., Shiobara, H., Sugioka, H., 2011. Seismogenic characteristics of the Northern Mariana shallow thrust zone from local array data. Geochemistry, Geophysics, Geosystems. 12(12).

Epstein, G., Bebout, G., Angiboust, S., Agard, P., 2020. Scales of fluid-rock interaction and carbon mobility in the deeply underplated and HP-Metamorphosed Schistes Lustrés, Western Alps. Lithos. 354, 105229.

Epstein, G. S., Bebout, G. E., and Angiboust, S. (2021). Fluid and mass transfer along transient subduction interfaces in a deep paleo-accretionary wedge (Western Alps). Chemical Geology, 559, 119920.

Ernst, W. G. (1972). Possible Permian oceanic crust and plate junction in central Shikoku, Japan. Tectonophysics, 15(3), 233-239.

Ernst, W. G. (1973). Blueschist metamorphism and PT regimes in active subduction zones. Tectonophysics, 17(3), 255-272.

Ernst, W. G. (1975). Systematics of large-scale tectonics and age progressions in Alpine and Circum-Pacific blueschist belts. Tectonophysics, 26(3-4), 229-246.

Ernst, W. G. (1990). Thermobarometric and fluid expulsion history of subduction zones. Journal of Geophysical Research: Solid Earth, 95(B6), 9047-9053.

Essene, E. J., and Fyfe, W. S. (1967). Omphacite in Californian metamorphic rocks. Contributions to Mineralogy and Petrology, 15(1), 1-23.

Etheridge, M. A., Wall, V. J., and Vernon, R. H.,1983, The role of the fluid phase during regional metamorphism and deformation. Journal of Metamorphic Geology, 1(3), 205-226.

Etheridge, M., Wall, V., Cox, S., Vernon, R., 1984. High fluid pressures during regional metamorphism and deformation: implications for mass transport and deformation mechanisms. Journal of Geophysical Research: Solid Earth. 89(B6), 4344-4358.

Evans, B. W., 1990. Phase relations of epidote-blueschists. Lithos. 25(1-3), 3-23.

Fabbri, O., Goldsby, D. L., Chester, F., Karpoff, A. M., Morvan, G., Ujiie, K., ... and Curewitz, D. (2020). Deformation structures from splay and décollement faults in the Nankai accretionary prism, SW Japan (IODP NanTroSEIZE Expedition 316): Evidence for slow and rapid slip in fault rocks. Geochemistry, Geophysics, Geosystems, 21(6), e2019GC008786.

Fagereng, Å., Remitti, F., and Sibson, R. H. (2010). Shear veins observed within anisotropic fabric at high angles to the maximum compressive stress. Nature Geoscience, 3(7), 482-485.

Fagereng, Å., and Sibson, R. H. (2010). Melange rheology and seismic style. Geology, 38(8), 751-754.

Fagereng, Å., and Diener, J. F. (2011). Non-volcanic tremor and discontinuous slab dehydration. Geophysical Research Letters, 38(15).

Fagereng, Å., and Toy, V. G. (2011). Geology of the earthquake source: an introduction. Geological Society, London, Special Publications, 359(1), 1-16.

Fagereng, Å., Hillary, G. W., and Diener, J. F. (2014). Brittle-viscous deformation, slow slip, and tremor. Geophysical Research Letters, 41(12), 4159-4167.

Fagereng, Å., and Den Hartog, S. A. (2017). Subduction megathrust creep governed by pressure solution and frictional–viscous flow. Nature Geoscience, 10(1), 51-57.

Fagereng, Å., Diener, J. F., Ellis, S., and Remitti, F. (2018). Fluid-related deformation processes at the up-and down-dip limits of the subduction thrust seismogenic zone: What do the rocks tell us (Vol. 534, pp. pp-1). Geol. Soc. Am. Spec. Pap.

Fagereng, Å., and Beall, A. (2021). Is complex fault zone behaviour a reflection of rheological heterogeneity?. Philosophical Transactions of the Royal Society A, 379(2193), 20190421.

Farge, G., Jaupart, C., and Shapiro, N. M. (2021). Episodicity and migration of low frequency earthquakes modeled with fast fluid pressure transients in the permeable subduction interface. Journal of Geophysical Research: Solid Earth, 126, e2021JB021894.

Ferrando, S., Frezzotti, M. L., Petrelli, M., Compagnoni, R., 2009. Metasomatism of continental crust during subduction: the UHP whiteschists from the Southern Dora-Maira Massif (Italian Western Alps). Journal of Metamorphic Geology. 27(9), 739-756.

Festa, A., Ogata, K., Pini, G. A., Dilek, Y., Codegone, G., 2015. Late Oligocene–early Miocene olistostromes (sedimentary mélanges) as tectono-stratigraphic constraints to the geodynamic evolution of the exhumed Ligurian accretionary complex (Northern Apennines, NW Italy). International Geology Review, 57(5-8), 540-562.

Ferry, J. M., and Gerdes, M. L. (1998). Chemically reactive fluid flow during metamorphism. Annual Review of Earth and Planetary Sciences, 26(1), 255-287.

Fisher, D. M., Brantley, S. L., 1992. Models of quartz overgrowth and vein formation: deformation and episodic fluid flow in an ancient subduction zone. Journal of Geophysical Research: Solid Earth, 97(B13), 20043-20061.

Fisher, D. M., Brantley, S. L., Everett, M., and Dzvonik, J. (1995). Cyclic fluid flow through a regionally extensive fracture network within the Kodiak accretionary prism. Journal of Geophysical Research: Solid Earth, 100(B7), 12881-12894.

Fisher, D. M., and Brantley, S. L. (2014). The role of silica redistribution in the evolution of slip instabilities along subduction interfaces: Constraints from the Kodiak accretionary complex, Alaska. Journal of Structural Geology, 69, 395-414.

Fletcher, R. C., and Hofmann, A. W. (1974). Simple models of diffusion and combined diffusion-infiltration metasomatism. In Geochemical transport and kinetics (Vol. 634, pp. 243-259). Carnegie Institution of Washington Washington, DC.

Flores, K., Skora, S., Martin, C., Harlow, G., Rodríguez, D., Baumgartner, P., 2015. Metamorphic history of riebeckite- and aegirine-augite-bearing high-pressure–low-temperature blocks within the Siuna Serpentinite Mélange, northeastern Nicaragua. International Geology Review. 57(5-8), 943-977.

Frank, W., Shapiro, N., Husker, A., Kostoglodov, V., Bhat, H., Campillo, M. 2015. Along-fault pore-pressure evolution during a slow-slip event in Guerrero, Mexico. Earth and Planetary Science Letters. 413, 135-143.

Franz, L., Romer, R. L., Klemd, R., Schmid, R., Oberhänsli, R., Wagner, T., Shuwen, D., 2001. Eclogite-facies quartz veins within metabasites of the Dabie Shan (eastern China): pressure-temperature-time-deformation path, composition of the fluid phase and fluid flow during exhumation of high-pressure rocks. Contributions to Mineralogy and Petrology, 141(3), 322-346.

Franzolin, E., Schmidt, M., Poli, S., 2011. Ternary Ca–Fe–Mg carbonates: subsolidus phase relations at 3.5 GPa and a thermodynamic solid solution model including order/disorder. Contributions to Mineralogy and Petrology. 161(2), 213-227.

Freed, A. M. (2005). Earthquake triggering by static, dynamic, and postseismic stress transfer. Annu. Rev. Earth Planet. Sci., 33, 335-367.

French, M. E., Hirth, G., and Okazaki, K. (2019). Fracture-induced pore fluid pressure weakening and dehydration of serpentinite. Tectonophysics, 767, 228168.

Föllmi, K., Godet, A., Bodin, S., Linder, P., 2006. Interactions between environmental change and shallow water carbonate buildup along the northern Tethyan margin and their impact on the Early Cretaceous carbon isotope record. Paleoceanography. 21(4).

Fondriest, M., Mecklenburgh, J., Passelegue, F. X., Artioli, G., Nestola, F., Spagnuolo, E., ... and Di Toro, G. (2020). Pseudotachylyte alteration and the rapid fade of earthquake scars from the geological record. Geophysical Research Letters, 47(22), e2020GL090020.

Forsythe, R. (1982). The late Palaeozoic to early Mesozoic evolution of southern South America: a plate tectonic interpretation. Journal of the Geological Society, 139(6), 671-682.

Fryer, P. (1996). Evolution of the Mariana convergent plate margin system. Reviews of Geophysics, 34(1), 89-125.

Fryer, P., Wheat, C. G., Williams, T., Kelley, C., Johnson, K., Ryan, J., ... and Pomponi, S. (2020). Mariana serpentinite mud volcanism exhumes subducted seamount materials: implications for the origin of life. Philosophical Transactions of the Royal Society A, 378(2165), 20180425.

Fu, Y., and Freymueller, J. T. (2013). Repeated large slow slip events at the southcentral Alaska subduction zone. Earth and Planetary Science Letters, 375, 303-311.

Fyfe, W. S., and Zardini, R. (1967). Metaconglomerate in the Franciscan formation near Pacheco Pass, California. American Journal of Science, 265(9), 819-830.

Fyfe, W.S., Price, N.J., and Thompson, A.B., 1978, Fluids in the Earth's Crust: Their Significance in Metamorphic, Tectonic and Chemical Transport Processes: New York, Elsevier Scientific, Developments in Geochemistry, v. 1, 401 p.

Gansser, A. (1955, June). 2. New Aspects of the Geology in Central Iran (Iran). In 4th World Petroleum Congress. OnePetro.

García-Casco, A., Torres-Roldán, R. L., Millán, G., Monié, P., and Schneider, J. (2002). Oscillatory zoning in eclogitic garnet and amphibole, Northern Serpentinite Melange, Cuba: a record of tectonic instability during subduction?. Journal of Metamorphic Geology, 20(6), 581-598.

Garcia-Casco, A., Torres-Roldán, L., Iturralde-Vinent, A., Millán, G., Cambra, K., Lázaro, C., Vega, A., 2006. High pressure metamorphism of ophiolites in Cuba. Geologica Acta: an international earth science journal. 4(1), 63-88.

Garcia-Casco, A., 2007. Magmatic paragonite in trondhjemites from the Sierra del Convento mélange, Cuba. American Mineralogist. 92, 1232-1237.

García-Casco, A., Lázaro, C., Rojas-Agramonte, Y., Kröner, A., Torres-Roldán, R. L., Núñez, K., ... and Blanco-Quintero, I. (2008). Partial melting and counterclockwise P–T path of subducted oceanic crust (Sierra del Convento mélange, Cuba). Journal of Petrology, 49(1), 129-161.

Gasc, J., Hilairet, N., Yu, T., Ferrand, T., Schubnel, A., and Wang, Y. (2017). Faulting of natural serpentinite: Implications for intermediate-depth seismicity. Earth and Planetary Science Letters, 474, 138-147.

Gao, J., He, G., Li, M., Xiao, X., Tang, Y., Wang, J., and Zhao, M. (1995). The mineralogy, petrology, metamorphic PTDt trajectory and exhumation mechanism of blueschists, south Tianshan, northwestern China. Tectonophysics, 250(1-3), 151-168.

Gao, J., and Klemd, R. (2001). Primary fluids entrapped at blueschist to eclogite transition: evidence from the Tianshan meta-subduction complex in northwestern China. Contributions to Mineralogy and Petrology, 142(1), 1-14.

Gao, J., John, T., Klemd, R., and Xiong, X. (2007). Mobilization of Ti–Nb–Ta during subduction: evidence from rutile-bearing dehydration segregations and veins hosted in eclogite, Tianshan, NW China. Geochimica et Cosmochimica Acta, 71(20), 4974-4996.

Ghasemi, H., Juteau, T., Bellon, H., Sabzehei, M., Whitechurch, H., Ricou, L., 2002. The mafic–ultramafic complex of Sikhoran (central Iran): a polygenetic ophiolite complex. Comptes Rendus Geoscience. 334(6), 431-438.

Ghosh, A., Vidale, J. E., Sweet, J. R., Creager, K. C., Wech, A. G., Houston, H., and Brodsky, E. E. (2010). Rapid, continuous streaking of tremor in Cascadia. Geochemistry, Geophysics, Geosystems, 11(12).

Giere, R. (1990). Hydrothermal mobility of Ti, Zr and REE: examples from the Bergell and Adamello contact aureoles (Italy). Terra nova, 2(1), 60-67.

Giger, S. B., Cox, S. F., and Tenthorey, E. (2008). Slip localization and fault weakening as a consequence of fault gouge strengthening—Insights from laboratory experiments. Earth and Planetary Science Letters, 276(1-2), 73-84.

Glodny, J., Austrheim, H., Molina, J., Rusin, A., Seward, D., 2003. Rb/Sr record of fluid-rock interaction in eclogites: The Marun-Keu complex, Polar Urals, Russia. Geochimica et Cosmochimica Acta. 67(22), 4353-4371.

Glodny, J., Lohrmann, J., Echtler, H., Gräfe, K., Seifert, W., Collao, S., and Figueroa, O. (2005). Internal dynamics of a paleoaccretionary wedge: insights from combined isotope tectonochronology and sandbox modelling of the South-Central Chilean forearc. Earth and Planetary Science Letters, 231(1-2), 23-39.

Glodny, J., Ring, U., and Kühn, A. (2008). Coeval high-pressure metamorphism, thrusting, strike-slip, and extensional shearing in the Tauern Window, Eastern Alps. Tectonics, 27(4).

Glodny, J., Kühn, A., Austrheim, H., 2008. Geochronology of fluid-induced eclogite and amphibolite facies metamorphic reactions in a subduction–collision system, Bergen Arcs, Norway. Contributions to Mineralogy and Petrology. 156(1), 27-48.

Godard, G., and van Roermund, H. L. (1995). Deformation-induced clinopyroxene fabrics from eclogites. Journal of Structural Geology, 17(10), 1425-1443.

Godoy, E. 1970. Estudio petrográfico del Granito de Constitución y su aureola de Metamorfismo. Me-moria de Título, Univ. Chile, Depto. Geol., 130 p. Santiago.

González-Bonorino, F. 1970. Series Metamórficas del Basamento Cristalino de la Cordillera de la Costa de Chile Central. Universidad de Chile, Departamento de Geología, Publicación No. 37, 81 p.

González-Bonorino, F., and Aguirre, L. (1970). Metamorphic facies series of the crystalline basement of Chile. Geologische Rundschau, 59(3), 979-994.

Gorce, J., Caddick, M., Bodnar, R., 2019. Thermodynamic constraints on carbonate stability and carbon volatility during subduction. Earth and Planetary Science Letters. 519, 213-222.

Gottschalk, M. (2007). Equations of state for complex fluids. Reviews in Mineralogy and Geochemistry, 65(1), 49-97.

Gosselin, J., Audet, P., Estève, C., McLellan, M., Mosher, S., Schaeffer, A., 2020. Seismic evidence for megathrust fault-valve behavior during episodic tremor and slip. Science advances. 6(4), eaay5174.

Goswami, A., and Barbot, S. (2018). Slow-slip events in semi-brittle serpentinite fault zones. Scientific reports, 8(1), 1-11.

Graham, C. M., Valley, J. W., Eiler, J. M., and Wada, H. (1998). Timescales and mechanisms of fluid infiltration in a marble: an ion microprobe study. Contributions to Mineralogy and Petrology, 132(4), 371-389.

Gratier, J. P., Renard, F., and Vial, B. (2014). Postseismic pressure solution creep: Evidence and time-dependent change from dynamic indenting experiments. Journal of Geophysical Research: Solid Earth, 119(4), 2764-2779.

Green, E., Holland, T., Powell, R., 2007. An order-disorder model for omphacitic pyroxenes in the system jadeite-diopside-hedenbergite-acmite, with applications to eclogitic rocks. American Mineralogist. 92(7), 1181-1189.

Green, E., White, R., Diener, J., Powell, R., Holland, T., Palin, R., 2016. Activity–composition relations for the calculation of partial melting equilibria in metabasic rocks. Journal of Metamorphic Geology. 34(9), 845-869.

Groppo, C., Rolfo, F., Castelli, D., Mosca, P., 2017. Metamorphic CO_2 production in collisional orogens: Petrological constraints from phase diagram modeling of Himalayan, scapolite-bearing, calc-silicate rocks in the NKC (F) MAS (T)-HC system. Journal of Petrology, 58(1), 53-83.

Grove, M., and Bebout, G. E. (1995). Cretaceous tectonic evolution of coastal southern California: insights from the Catalina Schist. Tectonics, 14(6), 1290-1308.

Grove, T., Chatterjee, N., Parman, S., Médard, E., 2006. The influence of H_2O on mantle wedge melting. Earth and Planetary Science Letters. 249(1-2), 74-89.

Guillot, S., Hattori, K., Agard, P., Schwartz, S., Vidal, O. 2009. Exhumation processes in oceanic and continental subduction contexts: a review. In Subduction zone geodynamics (pp. 175-205). Springer, Berlin, Heidelberg.

Guillot, S., and Hattori, K. (2013). Serpentinites: essential roles in geodynamics, arc volcanism, sustainable development, and the origin of life. Elements, 9(2), 95-98.

Ha, Y., Jung, H., and Raymond, L. A. (2019). Deformation fabrics of glaucophane schists and implications for seismic anisotropy: The importance of lattice preferred orientation of phengite. International Geology Review, 61(6), 720-737.

Halama, R., John, T., Herms, P., Hauff, F., Schenk, V., 2011. A stable (Li, O) and radiogenic (Sr, Nd) isotope perspective on metasomatic processes in a subducting slab. Chemical Geology. 281(3-4), 151-166.

Halama, R., Konrad-Schmolke, M., Sudo, M., Marschall, H. R., and Wiedenbeck, M. (2014). Effects of fluid–rock interaction on 40Ar/39Ar geochronology in high-pressure rocks (Sesia-Lanzo Zone, Western Alps). Geochimica et Cosmochimica Acta, 126, 475-494.

Halama, R., and Konrad-Schmolke, M. (2015). Retrograde metasomatic effects on phase assemblages in an interlayered blueschist–greenschist sequence (Coastal Cordillera, Chile). Lithos, 216, 31-47.

Hacker, B., Peacock, S., Abers, G., Holloway, S., 2003. Subduction factory 2. Are intermediate-depth earthquakes in subducting slabs linked to metamorphic dehydration reactions?. Journal of Geophysical Research: Solid Earth. 108(B1).

Hacker, B. R., Rubie, D. C., Kirby, S. H., and Bohlen, S. R. (2005). The calcite→ aragonite transformation in low-Mg marble: Equilibrium relations, transformation mechanisms, and rates. Journal of Geophysical Research: Solid Earth, 110(B3).

Hacker, B. R., 2008. H_2O subduction beyond arcs. Geochemistry, Geophysics, Geosystems. 9(3).

Hancock, P. L. (1985). Brittle microtectonics: principles and practice. Journal of structural geology, 7(3-4), 437-457.

Hardebeck, J. L., and Loveless, J. P. (2018). Creeping subduction zones are weaker than locked subduction zones. Nature Geoscience, 11(1), 60-64.

Healy, D., Reddy, S. M., Timms, N. E., Gray, E. M., and Brovarone, A. V. (2009). Trench-parallel fast axes of seismic anisotropy due to fluid-filled cracks in subducting slabs. Earth and Planetary Science Letters, 283(1-4), 75-86.

Harlow, G., Hemming, S., Lallemant, H., Sisson, V., Sorensen, S., 2004. Two high-pressure–low-temperature serpentinite-matrix mélange belts, Motagua fault zone, Guatemala: a record of Aptian and Maastrichtian collisions. Geology. 32(1), 17-20.

Harlow, G. E., and Sorena S. Sorensen. "Jade (nephrite and jadeitite) and serpentinite: metasomatic connections." International Geology Review 47.2 (2005): 113-146.

Harris, R., Yamano, M., Kinoshita, M., Spinelli, G., Hamamoto, H., and Ashi, J. (2013). A synthesis of heat flow determinations and thermal modeling along the Nankai Trough, Japan. Journal of Geophysical Research: Solid Earth, 118(6), 2687-2702.

Hayman, N. W., and Lavier, L. L. (2014). The geologic record of deep episodic tremor and slip. Geology, 42(3), 195-198.

Heaton, T. H. (1990). Evidence for and implications of self-healing pulses of slip in earthquake rupture. Physics of the Earth and Planetary Interiors, 64(1), 1-20.

Heinrich, C. A. (2007). Fluid-fluid interactions in magmatic-hydrothermal ore formation. Reviews in Mineralogy and Geochemistry, 65(1), 363-387.

Henry, C., Burkhard, M., and Goffe, B. (1996). Evolution of synmetamorphic veins and their wallrocks through a Western Alps transect: no evidence for large-scale fluid flow. Stable isotope, major-and trace-element systematics. Chemical Geology, 127(1-3), 81-109.

Heredia, N., García-Sansegundo, J., Gallastegui, G., Farias, P., Giacosa, R. E., Giambiagi, L. B., ... and Ramos, V. A. (2018). Review of the geodynamic evolution of the SW margin of Gondwana preserved in the Central Andes of Argentina and Chile (28°-38° S latitude). Journal of South American Earth Sciences, 87, 87-94.

Hermann, J., Spandler, C., Hack, A., Korsakov, A., 2006. Aqueous fluids and hydrous melts in high-pressure and ultra-high pressure rocks: implications for element transfer in subduction zones. Lithos. 92(3-4), 399-417.

Hervé, F., Munizaga, F., Godoy, E., and Aguirre, L. (1974). Late Paleozoic K/Ar ages of blueschists from Pichilemu, central Chile. Earth and Planetary Science Letters, 23(2), 261-264.

Hervé, F., Theile, R., and Parada, M. A. (1976). El basamento metamorfico del archipiélago de las Guaitecas, Aysen, Chile. In Actas I Congreso Geológico Chileno (Vol. 1, pp. B73-85).

Hervé, F. (1977). Petrology of the crystalline basement of the Nahuelbuta Mountains, south-central Chile. In: Ishikawa, T, and Aguirre, L. (eds) Comparative studies on the Geology of the Circum Pacific Orogenic Belt in Japan and Chile. Japan Society for the Promotion of Science, Tokyo, 1-51.

Hervé, F., Nelson, E., Kawashita, K., and Suárez, M. (1981). New isotopic ages and the timing of orogenic events in the Cordillera Darwin, southernmost Chilean Andes. Earth and Planetary Science Letters, 55(2), 257-265.

Hervé, F., Kawashita, K., Munizaga, F., and Bassei, M. (1984). Rb-Sr isotopic ages from late Palaeozoic metamorphic rocks of central Chile. Journal of the Geological Society, 141(5), 877-884.

Hervé, F. (1988). Late Paleozoic subduction and accretion in Southern Chile. Episodes Journal of International Geoscience, 11(3), 183-188.

Hervé, F., Faundez, V., Calderón, M., Massonne, H. J., and Willner, A. P. (2007). Metamorphic and plutonic basement complexes. In The Geology of Chile (pp. 5-19).

Herve, F., Calderón, M., Fanning, C. M., Pankhurst, R. J., and Godoy, E. (2013). Provenance variations in the Late Paleozoic accretionary complex of central Chile as indicated by detrital zircons. Gondwana Research, 23(3), 1122-1135.

Hervé, F., Fanning, C. M., Calderón, M., and Mpodozis, C. (2014). Early Permian to Late Triassic batholiths of the Chilean Frontal Cordillera (28°–31° S): SHRIMP U–Pb zircon ages and Lu–Hf and O isotope systematics. Lithos, 184, 436-446.

Hervé, F., Calderon, M., Fanning, C. M., Pankhurst, R. J., Fuentes, F., Rapela, C. W., ... and Marambio, C. (2016). Devonian magmatism in the accretionary complex of southern Chile. Journal of the Geological Society, 173(4), 587-602.

Hess, J., Bender, M., Schilling, J., 1986. Evolution of the ratio of strontium-87 to strontium-86 in seawater from Cretaceous to present. Science. 231(4741), 979-984.

Hetényi, G., Cattin, R., Brunet, F., Bollinger, L., Vergne, J., Nábělek, J. L., and Diament, M. (2007). Density distribution of the India plate beneath the Tibetan plateau: Geophysical and petrological constraints on the kinetics of lower-crustal eclogitization. Earth and Planetary Science Letters, 264(1-2), 226-244.

Heuret, A., Conrad, C. P., Funiciello, F., Lallemand, S., and Sandri, L. (2012). Relation between subduction megathrust earthquakes, trench sediment thickness and upper plate strain. Geophysical Research Letters, 39(5).

Hilairet, N., Daniel, I., and Reynard, B. (2006). Equation of state of antigorite, stability field of serpentines, and seismicity in subduction zones. Geophysical Research Letters, 33(2).

Hirauchi, K. I., Katayama, I., Uehara, S., Miyahara, M., and Takai, Y. (2010). Inhibition of subduction thrust earthquakes by low-temperature plastic flow in serpentine. Earth and Planetary Science Letters, 295(3-4), 349-357.

Hirth, G., Teyssier, C., and Dunlap, J. W. (2001). An evaluation of quartzite flow laws based on comparisons between experimentally and naturally deformed rocks. International Journal of Earth Sciences, 90(1), 77-87.

Holland, T., and Powell, R. (1996). Thermodynamics of order-disorder in minerals: II. Symmetric formalism applied to solid solutions. American Mineralogist, 81(11-12), 1425-1437.

Holland, T., Powell, R., 1998. An internally consistent thermodynamic data set for phases of petrological interest. Journal of metamorphic Geology. 16(3), 309-343.

Holland, T., and Powell, R. (2003). Activity–composition relations for phases in petrological calculations: an asymmetric multicomponent formulation. Contributions to Mineralogy and Petrology, 145(4), 492-501.

Holland, T., Powell, R., 2011. An improved and extended internally consistent thermodynamic dataset for phases of petrological interest, involving a new equation of state for solids. Journal of Metamorphic Geology. 29(3), 333-383.

Holness, M. B., and Graham, C. M. (1995). PTX effects on equilibrium carbonate-H_2O-CO_2-NaCl dihedral angles: constraints on carbonate permeability and the role of deformation during fluid infiltration. Contributions to Mineralogy and Petrology, 119(2-3), 301-313.

Holtkamp, S., and Brudzinski, M. R. (2010). Determination of slow slip episodes and strain accumulation along the Cascadia margin. Journal of Geophysical Research: Solid Earth, 115(B4).

Holyoke III, C. W., and Kronenberg, A. K. (2013). Reversible water weakening of quartz. Earth and Planetary Science Letters, 374, 185-190.

Huang, F., Sverjensky, D., 2019. Extended Deep Earth Water Model for predicting major element mantle metasomatism. Geochimica et Cosmochimica Acta. 254, 192-230.

Hubbert, M., and Rubey, W. W. (1959). Role of fluid pressure in mechanics of overthrust faulting: I. Mechanics of fluid-filled porous solids and its application to overthrust faulting. Geological Society of America Bulletin, 70(2), 115-166.

Hulme, S. M., Wheat, C. G., Fryer, P., and Mottl, M. J. (2010). Pore water chemistry of the Mariana serpentinite mud volcanoes: A window to the seismogenic zone. Geochemistry, Geophysics, Geosystems, 11(1).

Humphris, S. E., Thompson, G., 1978. Hydrothermal alteration of oceanic basalts by seawater. Geochimica et Cosmochimica Acta, 42(1), 107-125.

Husen, S., and Kissling, E. (2001). Postseismic fluid flow after the large subduction earthquake of Antofagasta, Chile. Geology, 29(9), 847-850.

Hyndman, R. D., Yamano, M., and Oleskevich, D. A. (1997). The seismogenic zone of subduction thrust faults. Island Arc, 6(3), 244-260.

Hyndman, R. D. (1988). Dipping seismic reflectors, electrically conductive zones, and trapped water in the crust over a subducting plate. Journal of Geophysical Research: Solid Earth, 93(B11), 13391-13405.

Hyndman, R. D., and Peacock, S. M. (2003). Serpentinization of the forearc mantle. Earth and Planetary Science Letters, 212(3-4), 417-432.

Hyppolito, T., Juliani, C., García-Casco, A., Meira, V. T., Bustamante, A., and Hervé, F. (2014a). The nature of the Palaeozoic oceanic basin at the southwestern margin of Gondwana and implications for the origin of the Chilenia terrane (Pichilemu region, central Chile). International Geology Review, 56(9), 1097-1121.

Hyppolito, T., García-Casco, A., Juliani, C., Meira, V. T., and Hall, C. (2014b). Late Paleozoic onset of subduction and exhumation at the western margin of Gondwana (Chilenia Terrane): Counterclockwise P–T paths and timing of metamorphism of deep-seated garnet–mica schist and amphibolite of Punta Sirena, Coastal Accretionary Complex, central Chile (34 S). Lithos, 206, 409-434.

Hyppolito, T.N., 2014, Metamorfismo y evolucion tectonica del cinturon pareado Permo-Carbonifero en la region de Pichilemu, cordillera de la costa de Chile central [Ph.D. thesis]: Sao Paulo, Granada, Universidade de Sao Paulo and Universidad de Granada, 358 p.

Hyppolito, T., Angiboust, S., Juliani, C., Glodny, J., Garcia-Casco, A., Calderón, M., Chopin, C., 2016. Eclogite-, amphibolite-and blueschist-facies rocks from Diego de Almagro Island (Patagonia): Episodic accretion and thermal evolution of the Chilean subduction interface during the Cretaceous. Lithos. 264, 422-440.

Ide, S., Beroza, G. C., Shelly, D. R., and Uchide, T. (2007). A scaling law for slow earthquakes. Nature, 447(7140), 76-79.

Ide, S., Baltay, A., and Beroza, G. C. (2011). Shallow dynamic overshoot and energetic deep rupture in the 2011 Mw 9.0 Tohoku-Oki earthquake. Science, 332(6036), 1426-1429.

Ikari, M. J., Saffer, D. M., and Marone, C. (2009). Frictional and hydrologic properties of clay-rich fault gouge. Journal of Geophysical Research: Solid Earth, 114(B5).

Ikari, M. J., and Kopf, A. J. (2017). Seismic potential of weak, near-surface faults revealed at plate tectonic slip rates. Science Advances, 3(11), e1701269.

Ildefonse, B., Lardeaux, J. M., and Caron, J. M. (1990). The behavior of shape preferred orientations in metamorphic rocks: amphiboles and jadeites from the Monte Mucrone area (Sesia-Lanzo zone, Italian Western Alps). Journal of Structural Geology, 12(8), 1005-1011.

Im, K., Saffer, D., Marone, C., and Avouac, J. P. (2020). Slip-rate-dependent friction as a universal mechanism for slow slip events. Nature Geoscience, 13(10), 705-710.

Ioannidi, P. I., Le Pourhiet, L., Agard, P., Angiboust, S., and Oncken, O. (2021). Effective rheology of a two-phase subduction shear zone: Insights from numerical simple shear experiments and implications for subduction zone interfaces. Earth and Planetary Science Letters, 566, 116913.

Ito, Y., Hino, R., Suzuki, S., and Kaneda, Y. (2015). Episodic tremor and slip near the Japan Trench prior to the 2011 Tohoku-Oki earthquake. Geophysical Research Letters, 42(6), 1725-1731.

Ito, Y., and Obara, K. (2006). Very low frequency earthquakes within accretionary prisms are very low stress-drop earthquakes. Geophysical Research Letters, 33(9).

Jaeckel, K., Bebout, G., Angiboust, S., 2018. Deformation-enhanced fluid and mass transfer along Western and Central Alps paleo-subduction interfaces: Significance for carbon cycling models. Geosphere. 14(6), 2355-2375.

Jahangiri, A. (2007). Post-collisional Miocene adakitic volcanism in NW Iran: geochemical and geodynamic implications. Journal of Asian Earth Sciences, 30(3-4), 433-447.

Jamtveit, B., and Austrheim, H. (2010). Metamorphism: the role of fluids. Elements, 6(3), 153-158.

Jara, J., Socquet, A., Marsan, D., and Bouchon, M. (2017). Long-term interactions between intermediate depth and shallow seismicity in North Chile subduction zone. Geophysical Research Letters, 44(18), 9283-9292.

Jarrard, R. D. (2003). Subduction fluxes of water, carbon dioxide, chlorine, and potassium. Geochemistry, Geophysics, Geosystems, 4(5).

Jébrak, M. (1997). Hydrothermal breccias in vein-type ore deposits: a review of mechanisms, morphology and size distribution. Ore geology reviews, 12(3), 111-134.

Jennings, E., Holland, T., 2015. A simple thermodynamic model for melting of peridotite in the system NCFMASOCr. Journal of Petrology. 56(5), 869-892.

John, T., and Schenk, V. (2006). Interrelations between intermediate-depth earthquakes and fluid flow within subducting oceanic plates: Constraints from eclogite facies pseudotachylytes. Geology, 34(7), 557-560.

John, T., Klemd, R., Gao, J., Garbe-Schoenberg, C., 2008. Trace-element mobilization in slabs due to non steady-state fluid–rock interaction: constraints from an eclogite-facies transport vein in blueschist (Tianshan, China). Lithos. 103(1-2), 1-24.

John, T., Gussone, N., Podladchikov, Y. Y., Bebout, G. E., Dohmen, R., Halama, R., ... and Seitz, H. M. (2012). Volcanic arcs fed by rapid pulsed fluid flow through subducting slabs. Nature Geoscience, 5(7), 489-492.

Jolivet, L., and Faccenna, C. (2000). Mediterranean extension and the Africa-Eurasia collision. Tectonics, 19(6), 1095-1106.

Jordan, J. S., Hesse, M. A., Rudge, J. F., 2018. On mass transport in porosity waves. Earth and Planetary Science Letters, 485, 65-78.

Joshi, A., and Appold, M. S. (2017). Numerical modeling of porosity waves in the Nankai accretionary wedge décollement, Japan: implications for aseismic slip. Hydrogeology Journal, 25(1), 249-264.

Kanamori, H., and Brodsky, E. E. (2004). The physics of earthquakes. Reports on Progress in Physics, 67(8), 1429.

Kaneko, L., Ide, S., and Nakano, M. (2018). Slow earthquakes in the microseism frequency band (0.1–1.0 Hz) off Kii Peninsula, Japan. Geophysical Research Letters, 45(6), 2618-2624.

Kao, H., Shan, S. J., Dragert, H., Rogers, G., Cassidy, J. F., and Ramachandran, K. (2005). A wide depth distribution of seismic tremors along the northern Cascadia margin. Nature, 436(7052), 841-844.

Kapp, P., Murphy, M. A., Yin, A., Harrison, T. M., Ding, L., and Guo, J. (2003). Mesozoic and Cenozoic tectonic evolution of the Shiquanhe area of western Tibet. Tectonics, 22(4).

Kastner, M., Elderfield, H., Jenkins, W. J., Gieskes, J. M., and Gamo, T. (1993). 32. Geochemnical and isotopic evidence for fluid flow in the western Nankai subduction zone Japan. In Proceedings of the Ocean Drilling Program. Sci Results (Vol. 131, pp. 397-413).

Kato, T. T., and Godoy, E. (1995). Petrogenesis and tectonic significance of Late Paleozoic coarse-crystalline blueschist and amphibolite boulders in the Coastal Range of Chile. International Geology Review, 37(11), 992-1006.

Kato, T. T., Sharp, W. D., and Godoy, E. (2008). Inception of a Devonian subduction zone along the southwestern Gondwana margin: 40Ar–39Ar dating of eclogite–amphibolite assemblages in blueschist boulders from the Coastal Range of Chile (41° S). Canadian Journal of Earth Sciences, 45(3), 337-351.

Kato, T. T., and Godoy, E. (2015). Middle to late Triassic mélange exhumation along a pre-Andean transpressional fault system: coastal Chile (26–42 S). International Geology Review, 57(5-8), 606-628.

Kay, M. A., Main, I. G., Elphick, S. C., and Ngwenya, B. T. (2006). Fault gouge diagenesis at shallow burial depth: Solution–precipitation reactions in well-sorted and poorly sorted powders of crushed sandstone. Earth and Planetary Science Letters, 243(3-4), 607-614.

Kawano, S., Katayama, I., and Okazaki, K. (2011). Permeability anisotropy of serpentinite and fluid pathways in a subduction zone. Geology, 39(10), 939-942.

Kelemen, P. B., and Manning, C. E. (2015). Reevaluating carbon fluxes in subduction zones, what goes down, mostly comes up. Proceedings of the National Academy of Sciences, 112(30), E3997-E4006.

Kempf, E. D., Hermann, J., 2018. Hydrogen incorporation and retention in metamorphic olivine during subduction: Implications for the deep water cycle. Geology, 46(6), 571-574.

Kempf, E. D., Hermann, J., Reusser, E., Baumgartner, L. P., and Lanari, P. (2020). The role of the antigorite+ brucite to olivine reaction in subducted serpentinites (Zermatt, Switzerland). Swiss journal of geosciences, 113(1), 1-36.

Keppler, R. (2018). Crystallographic preferred orientations in eclogites–A review. Journal of Structural Geology, 115, 284-296.

Kesler, S. E. (2005). Ore-forming fluids. Elements, 1(1), 13-18.

Kilian, R., Heilbronner, R., and Stünitz, H. (2011). Quartz grain size reduction in a granitoid rock and the transition from dislocation to diffusion creep. Journal of Structural Geology, 33(8), 1265-1284.

Kim, D., Katayama, I., Michibayashi, K., and Tsujimori, T. (2013). Rheological contrast between glaucophane and lawsonite in naturally deformed blueschist from D iablo R ange, C alifornia. Island Arc, 22(1), 63-73.

Kim, D., Katayama, I., Wallis, S., Michibayashi, K., Miyake, A., Seto, Y., and Azuma, S. (2015). Deformation microstructures of glaucophane and lawsonite in experimentally deformed blueschists: Implications for intermediate-depth intraplate earthquakes. Journal of Geophysical Research: Solid Earth, 120(2), 1229-1242.

Kim, E., Kim, Y., and Mainprice, D. (2020). AnisEulerSC: A MATLAB program combined with MTEX for modeling the anisotropic seismic properties of a polycrystalline aggregate with microcracks using self-consistent approximation. Computers and Geosciences, 145, 104589.

Kimura, G., Yamaguchi, A., Hojo, M., Kitamura, Y., Kameda, J., Ujiie, K., ... and Hina, S. (2012). Tectonic mélange as fault rock of subduction plate boundary. Tectonophysics, 568, 25-38.

Kirkpatrick, J. D., Shipton, Z. K., and Persano, C. (2009). Pseudotachylytes: Rarely generated, rarely preserved, or rarely reported?. Bulletin of the Seismological Society of America, 99(1), 382-388.

Kirkpatrick, J. D., Fagereng, Å., and Shelly, D. R. (2021). Geological constraints on the mechanisms of slow earthquakes. Nature Reviews Earth and Environment, 2(4), 285-301.

Kjøll, H. J., Viola, G., Menegon, L., and Sørensen, B. E. (2015). Brittle–viscous deformation of vein quartz under fluid-rich lower greenschist facies conditions. Solid Earth, 6(2), 681-699.

Klein, E., Duputel, Z., Zigone, D., Vigny, C., Boy, J., Doubre, C., Meneses, G., 2018. Deep transient slow slip detected by survey GPS in the region of Atacama, Chile. Geophysical research letters. 45(22), 12-263.

Ko, B., and Jung, H. (2015). Crystal preferred orientation of an amphibole experimentally deformed by simple shear. Nature communications, 6(1), 1-10.

Kopf, A., and Brown, K. M. (2003). Friction experiments on saturated sediments and their implications for the stress state of the Nankai and Barbados subduction thrusts. Marine Geology, 202(3-4), 193-210.

Konrad-Schmolke, M., Halama, R., Wirth, R., Thomen, A., Klitscher, N., Morales, L., Schreiber, A., Wilke, F. D., 2018. Mineral dissolution and reprecipitation mediated by an amorphous phase. Nature communications. 9(1), 1-9.

Korzhinskiĭ, D.S., 1970, Theory of Metasomatic Zoning [translated from Russian by Jean Agrell]: London, Clarendon Press, 162 p.

Kotowski, A. J., and Behr, W. M. (2019). Length scales and types of heterogeneities along the deep subduction interface: Insights from exhumed rocks on Syros Island, Greece. Geosphere, 15(4), 1038-1065.

Lafay, R., Baumgartner, L. P., Stephane, S., Suzanne, P., German, M. H., and Torsten, V. (2017). Petrologic and stable isotopic studies of a fossil hydrothermal system in ultramafic environment (Chenaillet ophicalcites, Western Alps, France): processes of carbonate cementation. Lithos, 294, 319-338.

Lagabrielle, Y., and Cannat, M. (1990). Alpine Jurassic ophiolites resemble the modern central Atlantic basement. Geology, 18(4), 319-322.

Lai, P., Moulton, K., and Krevor, S. (2015). Pore-scale heterogeneity in the mineral distribution and reactive surface area of porous rocks. Chemical Geology, 411, 260-273.

Lallemand, S. E., Schnürle, P., and Malavieille, J. (1994). Coulomb theory applied to accretionary and nonaccretionary wedges: Possible causes for tectonic erosion and/or frontal accretion. Journal of Geophysical Research: Solid Earth, 99(B6), 12033-12055.

Lallemand, S., Heuret, A., and Boutelier, D. (2005). On the relationships between slab dip, back-arc stress, upper plate absolute motion, and crustal nature in subduction zones. Geochemistry, Geophysics, Geosystems, 6(9).

Lamb, S. (2006). Shear stresses on megathrusts: Implications for mountain building behind subduction zones. Journal of Geophysical Research: Solid Earth, 111(B7).

Lay, T., Kanamori, H., Ammon, C. J., Koper, K. D., Hutko, A. R., Ye, L., ... and Rushing, T. M. (2012). Depth-varying rupture properties of subduction zone megathrust faults. Journal of Geophysical Research: Solid Earth, 117(B4).

Lay, T. (2015). The surge of great earthquakes from 2004 to 2014. Earth and Planetary Science Letters, 409, 133-146.

Leake, B., et al., 1997. Nomenclature of amphiboles; report of the Subcommittee on Amphiboles of the International Mineralogical Association Commission on new minerals and mineral names. Mineralogical magazine. 61(405), 295-310.

Lewerentz, A., Skelton, A. D., Linde, J. K., Nilsson, J., Möller, C., Crill, P. M., and Spicuzza, M. J. (2017). On the association between veining and index mineral distributions in Barrow's metamorphic zones, Glen Esk, Scotland. Journal of Petrology, 58(5), 885-907.

Li, J., Shillington, D. J., Saffer, D. M., Bécel, A., Nedimović, M. R., Kuehn, H., ... and Abers, G. A. (2018). Connections between subducted sediment, pore-fluid pressure, and earthquake behavior along the Alaska megathrust. Geology, 46(4), 299-302.

Liebscher, A. (2010). Aqueous fluids at elevated pressure and temperature. Geofluids, 10(1-2), 3-19.

Liferovich, R. P., and Mitchell, R. H. (2005). Composition and paragenesis of Na-, Nb-and Zr-bearing titanite from Khibina, Russia, and crystal-structure data for synthetic analogues. The Canadian Mineralogist, 43(2), 795-812.

Lin, J., and Stein, R. S. (2004). Stress triggering in thrust and subduction earthquakes and stress interaction between the southern San Andreas and nearby thrust and strike-slip faults. Journal of Geophysical Research: Solid Earth, 109(B2).

Lin, A. (2007). Fossil earthquakes: The formation and preservation of pseudotachylytes (Vol. 111). Springer.

Lin, A. (2011). Seismic slip recorded by fluidized ultracataclastic veins formed in a coseismic shear zone during the 2008 Mw 7.9 Wenchuan earthquake. Geology, 39(6), 547-550.

Liou, J.G., 1971, Analcime equilibria: Lithos, v. 4, p. 389–402.

Liou, J. G. (1971). P—T Stabilities of Laumontite, Wairakite, Lawsonite, and Related Minerals in the System CaAl2Si2O8-SiO2-H2O. Journal of petrology, 12(2), 379-411.

Locatelli, M., Verlaguet, A., Agard, P., Pettke, T., and Federico, L. (2019). Fluid pulses during stepwise brecciation at intermediate subduction depths (Monviso eclogites, W. Alps): First internally then externally sourced. Geochemistry, geophysics, geosystems, 20(11), 5285-5318.

Luan, F. C., and Paterson, M. S. (1992). Preparation and deformation of synthetic aggregates of quartz. Journal of Geophysical Research: Solid Earth, 97(B1), 301-320.

Lucassen, F., Trumbull, R., Franz, G., Creixell, C., Vásquez, P., Romer, R. L., and Figueroa, O. (2004). Distinguishing crustal recycling and juvenile additions at active continental margins: the Paleozoic to recent compositional evolution of the Chilean Pacific margin (36–41 S). Journal of South American Earth Sciences, 17(2), 103-119.

Lucassen, F., Dulski, P., Abart, R., Franz, G., Rhede, D., and Romer, R. L. (2010). Redistribution of HFSE elements during rutile replacement by titanite. Contributions to Mineralogy and Petrology, 160(2), 279-295.

Lucassen, F., Franz, G., Dulski, P., Romer, R. L., and Rhede, D. (2011). Element and Sr isotope signatures of titanite as indicator of variable fluid composition in hydrated eclogite. Lithos, 121(1-4), 12-24.

Lusk, A. D., and Platt, J. P. (2020). The Deep Structure and rheology of a plate boundary-scale shear zone: constraints from an exhumed Caledonian shear zone, NW Scotland. Lithosphere, 2020(1), 8824736.

Maekawa, H., Shozul, M., Ishll, T., Fryer, P., Pearce, J., 1993. Blueschist metamorphism in an active subduction zone. Nature. 364(6437), 520-523.

Maekawa, H., Fryer, P., Ozaki, A., 1995. Incipient blueschist-facies metamorphism in the active subduction zone beneath the Mariana forearc. Active Margins and Marginal Basins of the Western Pacific, Geophys. Monogr. Ser. 88, 281-289.

Maekawa, H., Yamamoto, K., Ueno, T., Osada, Y., Nogami, N., 2004. Significance of serpentinites and related rocks in the high-pressure metamorphic terranes, Circum-Pacific regions. International Geology Review. 46(5), 426-444.

Magara, K. (1980). Comparison of porosity-depth relationships of shale and sandstone. Journal of Petroleum Geology, 3(2), 175-185.

Magee, M. E., and Zoback, M. D. (1993). Evidence for a weak interplate thrust fault along the northern Japan subduction zone and implications for the mechanics of thrust faulting and fluid expulsion. Geology, 21(9), 809-812.

Magloughlin, J., Spray, J., 1992. Frictional melting processes and products in geological materials: introduction and discussion. Tectonophysics. 204(3-4), 197-204.

Magott, R., Fabbri, O., and Fournier, M. (2020). Seismically-induced serpentine dehydration as a possible mechanism of water release in subduction zones. Insights from the Alpine Corsica pseudotachylyte-bearing Monte Maggiore ophiolitic unit. Lithos, 362, 105474.

Mainprice, D., and Nicolas, A. (1989). Development of shape and lattice preferred orientations: application to the seismic anisotropy of the lower crust. Journal of Structural Geology, 11(1-2), 175-189.

Mainprice, D., and Humbert, M. (1994). Methods of calculating petrophysical properties from lattice preferred orientation data. Surveys in Geophysics, 15(5), 575-592.

Mainprice, D., Hielscher, R., and Schaeben, H. (2011). Calculating anisotropic physical properties from texture data using the MTEX open-source package. Geological Society, London, Special Publications, 360(1), 175-192.

Malvoisin, B., Austrheim, H., Hetényi, G., Reynes, J., Hermann, J., Baumgartner, L. P., and Podladchikov, Y. Y. (2020). Sustainable densification of the deep crust. Geology, 48(7), 673-677.

Manning, C., 2004. The chemistry of subduction-zone fluids. Earth and Planetary Science Letters. 223(1-2), 1-16.

Manzotti, P., Ballèvre, M., Pitra, P., Putlitz, B., Robyr, M., and Müntener, O. (2020). The growth of sodic amphibole at the greenschist-to blueschist-facies transition (Dent Blanche, Western Alps): bulk-rock chemical control and thermodynamic modelling. Journal of Petrology, 61(4), egaa044.

Marroni, M., Pandolfi, L., 2007. The architecture of an incipient oceanic basin: a tentative reconstruction of the Jurassic Liguria-Piemonte basin along the Northern Apennines–Alpine Corsica transect. International Journal of Earth Sciences, 96(6), 1059-1078.

Martin, L., Hermann, J., Gauthiez-Putallaz, L., Whitney, D., Vitale Brovarone, A., Fornash, K., Evans, N., 2014. Lawsonite geochemistry and stability–implication for trace element and water cycles in subduction zones. Journal of Metamorphic Geology. 32(5), 455-478.

Maruyama, S., Liou, J., 1988. Petrology of Franciscan metabasites along the jadeite-glaucophane type facies series, Cazadero, California. Journal of Petrology. 29(1), 1-37.

Massonne, H., Willner, A., 2008. Phase relations and dehydration behaviour of psammopelite and mid-ocean ridge basalt at very-low-grade to low-grade metamorphic conditions. European Journal of Mineralogy. 20(5), 867-879.

McCall, G. J. H., and Kidd, R. G. W. (1982). The Makran, Southeastern Iran: the anatomy of a convergent plate margin active from Cretaceous to Present. Geological Society, London, Special Publications, 10(1), 387-397.

McCall, G. J. H. (1997). The geotectonic history of the Makran and adjacent areas of southern Iran. Journal of Asian Earth Sciences, 15(6), 517-531.

McCausland, W., Malone, S., and Johnson, D. (2005). Temporal and spatial occurrence of deep non-volcanic tremor: From Washington to northern California. Geophysical Research Letters, 32(24).

McCrea, J., 1950. On the isotopic chemistry of carbonates and a paleotemperature scale. The Journal of Chemical Physics. 18(6), 849-857.

McQuarrie, N., and van Hinsbergen, D. J. (2013). Retrodeforming the Arabia-Eurasia collision zone: Age of collision versus magnitude of continental subduction. Geology, 41(3), 315-318.

Melgar, D., Crowell, B. W., Geng, J., Allen, R. M., Bock, Y., Riquelme, S., ... and Ganas, A. (2015). Earthquake magnitude calculation without saturation from the scaling of peak ground displacement. Geophysical Research Letters, 42(13), 5197-5205.

Melnick, D., Moreno, M., Quinteros, J., Baez, J. C., Deng, Z., Li, S., and Oncken, O. (2017). The super-interseismic phase of the megathrust earthquake cycle in Chile. Geophysical Research Letters, 44(2), 784-791.

Menant, A., Angiboust, S., Monie, P., Oncken, O., Guigner, J., 2018. Brittle deformation during Alpine basal accretion and the origin of seismicity nests above the subduction interface. Earth and Planetary Science Letters. 487, 84-93.

Menant, A., Angiboust, S., Gerya, T., 2019. Stress-driven fluid flow controls long-term megathrust strength and deep accretionary dynamics. Scientific reports. 9(1), 1-11.

Menegatti, A., Weissert, H., Brown, R., Tyson, R., Farrimond, P., Strasser, A., Caron, M., 1998. High-resolution δ13C stratigraphy through the early Aptian “Livello Selli” of the Alpine Tethys. Paleoceanography. 13(5), 530-545.

Meneghini, F., and Moore, J. C. (2007). Deformation and hydrofracture in a subduction thrust at seismogenic depths: The Rodeo Cove thrust zone, Marin Headlands, California. Geological Society of America Bulletin, 119(1-2), 174-183.

Meneghini, F., Di Toro, G., Rowe, C., Moore, J., Tsutsumi, A., Yamaguchi, A., 2010. Record of mega-earthquakes in subduction thrusts: The black fault rocks of Pasagshak Point (Kodiak Island, Alaska). GSA Bulletin. 122(7-8), 1280-1297.

Menzel, M. D., Garrido, C. J., López Sánchez-Vizcaíno, V., Hidas, K., and Marchesi, C. (2019). Subduction metamorphism of serpentinite-hosted carbonates beyond antigorite-serpentinite dehydration (Nevado-Filábride Complex, Spain). Journal of Metamorphic Geology, 37(5), 681-715.

Menzel, M., Garrido, C., Sánchez-Vizcaíno, L., 2020. Fluid-mediated carbon release from serpentinite-hosted carbonates during dehydration of antigorite-serpentinite in subduction zones. Earth and Planetary Science Letters. 531, 115964.

Michel, S., Gualandi, A., and Avouac, J. P. (2019). Similar scaling laws for earthquakes and Cascadia slow-slip events. Nature, 574(7779), 522-526.

Miller, J., Cartwright, I., 2000. Distinguishing between seafloor alteration and fluid flow during subduction using stable isotope geochemistry: examples from Tethyan ophiolites in the Western Alps. Journal of Metamorphic Geology. 18(5), 467-482.

Miller, J. A., Buick, I. S., and Cartwright, I. (2000). Textural implications of high-pressure fluid flow controlled by pre-subduction deformation and alteration patterns. Journal of Geochemical Exploration, 69, 551-555.

Miller, J., Cartwright, I., Buick, I., Barnicoat, A., 2001. An O-isotope profile through the HP–LT Corsican ophiolite, France and its implications for fluid flow during subduction. Chemical Geology. 178(1-4), 43-69.

Miyashiro, A. (1961). Evolution of metamorphic belts. Journal of petrology, 2(3), 277-311.

Moghadam, H. S., and Stern, R. J. (2011). Geodynamic evolution of Upper Cretaceous Zagros ophiolites: formation of oceanic lithosphere above a nascent subduction zone. Geological Magazine, 148(5-6), 762-801.

Moghadam, H., Corfu, F., Stern, R., 2013. U–Pb zircon ages of Late Cretaceous Nain–Dehshir ophiolites, central Iran. Journal of the Geological Society. 170(1), 175-184.

Moghadam, H., Bröcker, M., Griffin, W. L., Li, X. H., Chen, R. X., and O'Reilly, S. Y. (2017). Subduction, high-P metamorphism, and collision fingerprints in South Iran: Constraints from zircon U-Pb and mica Rb-Sr geochronology. Geochemistry, Geophysics, Geosystems, 18(1), 306-332.

Molina, J., Poli, S., 2000. Carbonate stability and fluid composition in subducted oceanic crust: an experimental study on H2O–CO2-bearing basalts. Earth and Planetary Science Letters. 176(3-4), 295-310.

Molina, J. F., Poli, S., Austrheim, H., Glodny, J., Rusin, A., 2004. Eclogite-facies vein systems in the Marun-Keu complex (Polar Urals, Russia): textural, chemical and thermal constraints for patterns of fluid flow in the lower crust. Contributions to Mineralogy and Petrology, 147(4), 484-504.

Molinaro, M., Leturmy, P., Guezou, J. C., Frizon de Lamotte, D., and Eshraghi, S. A. (2005). The structure and kinematics of the southeastern Zagros fold-thrust belt, Iran: From thin-skinned to thick-skinned tectonics. Tectonics, 24(3).

Monie, P., and Agard, P. (2009). Coeval blueschist exhumation along thousands of kilometers: Implications for subduction channel processes. Geochemistry, Geophysics, Geosystems, 10(7).

Moreno, M., Haberland, C., Oncken, O., Rietbrock, A., Angiboust, S., and Heidbach, O. (2014). Locking of the Chile subduction zone controlled by fluid pressure before the 2010 earthquake. Nature Geoscience, 7(4), 292-296.

Morimoto, N., 1988. Nomenclature of pyroxenes. Mineralogy and Petrology, 39(1). 55-76.

Moore, D. E., Liou, J. G., and King, B. S. (1981). Chemical modifications accompanying blueschist facies metamorphism of Franciscan conglomerates, Diablo Range, California. Chemical Geology, 33(1-4), 237-263.

Moore, J.C., Shipley, T.H., Goldberg, D., Ogawa, Y., Filice, F., Fisher, A., Jurado, M.-J., Moore, G.F., Rabaute, A., Yin, H., Zwart, G., Brückmann, W., Henry, P., Ashi, J., Blum, P., Meyer, A., Housen, B., Kastner, M., Labaume, P., Laier, T., Leitch, E.C., Maltman, A.J., Peacock, S., Steiger, T.H., Tobin, H.J., Underwood, M.B., Xu, Y., and Zheng, Y., 1995, Abnormal fluid pressures and fault-zone dilation in the Barbados accretionary prism: Evidence from logging while drilling: Geology, v. 23, p. 605–608

Moore, J.., et al., 1995. Abnormal fluid pressures and fault-zone dilation in the Barbados accretionary prism: Evidence from logging while drilling. Geology. 23(7), 605-608.

Moore, D., Lockner, D., Ma, S., Summers, R., Byerlee, J., 1997. Strengths of serpentinite gouges at elevated temperatures. Journal of Geophysical Research: Solid Earth. 102(B7), 14787-14801.

Moore, J., Beinlich, A., Austrheim, H., and Putnis, A. (2019). Stress orientation–dependent reactions during metamorphism. Geology, 47(2), 151-154.

Mouthereau, F., Tensi, J., Bellahsen, N., Lacombe, O., De Boisgrollier, T., and Kargar, S. (2007). Tertiary sequence of deformation in a thin-skinned/thick-skinned collision belt: The Zagros Folded Belt (Fars, Iran). Tectonics, 26(5).

Mpodozis, C., and Ramos, V. (1989). The Andes of Chile and Argentina. In: Ericksen, G, E., Cañas, M. T and Reinemund, K. A. (eds) Geology of the Andes and its Relation to Hydrocarbon and Energy Resources. Circum-Pacific Council for Energy and Hydrothermal Resources, American Association of Petroleum Geologists, Houston, Texas, Earth Science Series, 11, 59-90.

Mpodozis, C., and Kay, S. M. (1990). Provincias magmáticas ácidas y evolución tectónica de Gondwana: Andes chilenos (28-31 S). Andean Geology, 17(2), 153-180.

Muldashev, I. A., and Sobolev, S. V. (2020). What controls maximum magnitudes of giant subduction earthquakes?. Geochemistry, Geophysics, Geosystems, 21(9), e2020GC009145.

Mulcahy, S. R., King, R. L., and Vervoort, J. D. (2009). Lawsonite Lu-Hf geochronology: A new geochronometer for subduction zone processes. Geology, 37(11), 987-990.

Mullis, J., Dubessy, J., Poty, B., and O'Neil, J. (1994). Fluid regimes during late stages of a continental collision: Physical, chemical, and stable isotope measurements of fluid inclusions in fissure quartz from a geotraverse through the Central Alps, Switzerland. Geochimica et cosmochimica Acta, 58(10), 2239-2267.

Muñoz-Montecinos, J., Angiboust, S., Cambeses, A., Garcia-Casco, A., 2020. Multiple veining in a paleo–accretionary wedge: The metamorphic rock record of prograde dehydration and transient high pore-fluid pressures along the subduction interface (Western Series, central Chile). Geosphere. 16(3), 765-786.

Muñoz-Montecinos, J., Angiboust, S., Garcia-Casco, A., Glodny, J., Bebout, G., 2021. Episodic hydrofracturing and large-scale flushing along deep subduction interfaces: Implications for fluid transfer and carbon recycling (Zagros Orogen, southeastern Iran). Chemical Geology, 120173.

Nadeau, S., Philippot, P., and Pineau, F. (1993). Fluid inclusion and mineral isotopic compositions (HCO) in eclogitic rocks as tracers of local fluid migration during high-pressure metamorphism. Earth and Planetary Science Letters, 114(4), 431-448.

Nakano, M., Yabe, S., Sugioka, H., Shinohara, M., and Ide, S. (2019). Event size distribution of shallow tectonic tremor in the Nankai trough. Geophysical Research Letters, 46(11), 5828-5836.

Narebski, W., Dostal, J., Dupuy, C., 1986. Geochemical characteristics of Lower Paleozoic spilite-keratophyre series in the Western Sudetes (Poland): petrogenetic and tectonic implications. Neues Jahrbuch für Mineralogie, Abhandlungen. 155, 243-258.

Nelson, B. K., 1995. Fluid flow in subduction zones: evidence from Nd-and Sr-isotope variations in metabasalts of the Franciscan complex, California. Contributions to Mineralogy and Petrology. 119(2-3), 247-262.

Newton, R. C., and Manning, C. E. (2000). Quartz solubility in H_2O-NaCl and H_2O-CO_2 solutions at deep crust-upper mantle pressures and temperatures: 2–15 kbar and 500–900 C. Geochimica et Cosmochimica Acta, 64(17), 2993-3005.

Niemeijer, A. R., Spiers, C. J., and Bos, B. (2002). Compaction creep of quartz sand at 400–600 C: Experimental evidence for dissolution-controlled pressure solution. Earth and Planetary Science Letters, 195(3-4), 261-275.

Noda, A., Koge, H., Yamada, Y., Miyakawa, A., and Ashi, J. (2020). Subduction of trench-fill sediments beneath an accretionary wedge: Insights from sandbox analogue experiments. Geosphere, 16(4), 953-968.

Nur, A., Walder, J., 1992. Hydraulic pulses in the Earth's crust. In International Geophysics (Vol. 51, pp. 461-473). Academic Press.

Oakley, A., Taylor, B., Moore, G., 2008. Pacific Plate subduction beneath the central Mariana and Izu-Bonin fore arcs: New insights from an old margin. Geochemistry, Geophysics, Geosystems. 9(6).

Obara, K. (2002). Nonvolcanic deep tremor associated with subduction in southwest Japan. Science, 296(5573), 1679-1681.

Obara, K. (2010). Phenomenology of deep slow earthquake family in southwest Japan: Spatiotemporal characteristics and segmentation. Journal of Geophysical Research: Solid Earth, 115(B8).

Obara, K., Tanaka, S., Maeda, T., and Matsuzawa, T. (2010). Depth-dependent activity of non-volcanic tremor in southwest Japan. Geophysical Research Letters, 37(13).

Obara, K., Kato, A., 2016. Connecting slow earthquakes to huge earthquakes. Science. 353(6296), 253-257.

Oberhänsli, R., Bousquet, R., Moinzadeh, H., Moazzen, M., Arvin, M., 2007. The field of stability of blue jadeite: a new occurrence of jadeitite at Sorkhan, Iran, as a case study. The Canadian Mineralogist. 45(6), 1501-1509.

Okazaki, K., and Katayama, I. (2015). Slow stick slip of antigorite serpentinite under hydrothermal conditions as a possible mechanism for slow earthquakes. Geophysical Research Letters, 42(4), 1099-1104.

Okazaki, K., and Hirth, G. (2016). Dehydration of lawsonite could directly trigger earthquakes in subducting oceanic crust. Nature, 530(7588), 81-84.

Okazaki, K., Hirth, G., 2020. Deformation of mafic schists from subducted oceanic crust at high pressure and temperature conditions. Tectonophysics. 774, 228217.

Oliver, N., 1996. Review and classification of structural controls on fluid flow during regional metamorphism. Journal of Metamorphic Geology. 14(4), 477-492.

Oliver, N., Bons, P., 2001. Mechanisms of fluid flow and fluid–rock interaction in fossil metamorphic hydrothermal systems inferred from vein–wallrock patterns, geometry and microstructure. Geofluids. 1(2), 137-162.

Omrani, J., Agard, P., Whitechurch, H., Benoit, M., Prouteau, G., and Jolivet, L. (2008). Arc-magmatism and subduction history beneath the Zagros Mountains, Iran: a new report of adakites and geodynamic consequences. Lithos, 106(3-4), 380-398.

Oncken, O., Hindle, D., Kley, J., Elger, K., Victor, P., and Schemmann, K. (2006). Deformation of the central Andean upper plate system—Facts, fiction, and constraints for plateau models. In The Andes (pp. 3-27). Springer, Berlin, Heidelberg.

O'Neill, C., Jellinek, A. M., and Lenardic, A. (2007). Conditions for the onset of plate tectonics on terrestrial planets and moons. Earth and Planetary Science Letters, 261(1-2), 20-32.

Oohashi, K., Hirose, T., and Shimamoto, T. (2011). Shear-induced graphitization of carbonaceous materials during seismic fault motion: Experiments and possible implications for fault mechanics. Journal of Structural Geology, 33(6), 1122-1134.

Otsubo, M., Hardebeck, J. L., Miyakawa, A., Yamaguchi, A., and Kimura, G. (2020). Localized fluid discharge by tensile cracking during the post-seismic period in subduction zones. Scientific reports, 10(1), 1-8.

Owen, C. (1989). Magmatic differentiation and alteration in isofacial greenschists and blueschists, Shuksan Suite, Washington: Statistical analysis of major-element variation. Journal of Petrology, 30(3), 739-761.

Padrón-Navarta, J. A., Tommasi, A., Garrido, C. J., Sánchez-Vizcaíno, V. L., Gómez-Pugnaire, M. T., Jabaloy, A., and Vauchez, A. (2010). Fluid transfer into the wedge controlled by high-pressure hydrofracturing in the cold top-slab mantle. Earth and Planetary Science Letters, 297(1-2), 271-286.

Padrón-Navarta, J. A., Lopez Sanchez-Vizcaino, V., Garrido, C. J., and Gómez-Pugnaire, M. T. (2011). Metamorphic record of high-pressure dehydration of antigorite serpentinite to chlorite harzburgite in a subduction setting (Cerro del Almirez, Nevado–Filábride Complex, Southern Spain). Journal of Petrology, 52(10), 2047-2078.

Padrón-Navarta, J. A., Tommasi, A., Garrido, C. J., and Sánchez-Vizcaíno, V. L. (2012). Plastic deformation and development of antigorite crystal preferred orientation in high-pressure serpentinites. Earth and Planetary Science Letters, 349, 75-86.

Padrón-Navarta, A., Sánchez-Vizcaíno, L., Hermann, J., Connolly, J., Garrido, C., Gómez-Pugnaire, M., Marchesi, C., 2013. Tschermak's substitution in antigorite and consequences for phase relations and water liberation in high-grade serpentinites. Lithos. 178, 186-196.

Padrón-Navarta, J. A., Hermann, J., 2017. A subsolidus olivine water solubility equation for the Earth's upper mantle. Journal of Geophysical Research: Solid Earth, 122(12), 9862-9880.

Palazzin, G., Raimbourg, H., Famin, V., Jolivet, L., Kusaba, Y., and Yamaguchi, A. (2016). Deformation processes at the down-dip limit of the seismogenic zone: The example of Shimanto accretionary complex. Tectonophysics, 687, 28-43.

Palin, R. M., and White, R. W. (2016). Emergence of blueschists on Earth linked to secular changes in oceanic crust composition. Nature Geoscience, 9(1), 60-64.

Parada, M. A. (1990). Granitoid plutonism in central Chile and its geodynamic implications: a review. Plutonism from Antarctica to Alaska, 241, 51-66.

Park, Y., Jung, S., and Jung, H. (2020). Lattice Preferred Orientation and Deformation Microstructures of Glaucophane and Epidote in Experimentally Deformed Epidote Blueschist at High Pressure. Minerals, 10(9), 803.

Passchier, C. W. (1987). Stable positions of rigid objects in non-coaxial flow—a study in vorticity analysis. Journal of Structural Geology, 9(5-6), 679-690.

Passchier, C. W., and Trouw, R. A. (2005). Microtectonics. Springer Science and Business Media.

Paul, A., Hatzfeld, D., Kaviani, A., Tatar, M., and Péquegnat, C. (2010). Seismic imaging of the lithospheric structure of the Zagros mountain belt (Iran). Geological Society, London, Special Publications, 330(1), 5-18.

Peacock, S. A. (1990a). Fluid processes in subduction zones. Science, 248(4953), 329-337.

Peacock, S. M. (1990b). Numerical simulation of metamorphic pressure-temperature-time paths and fluid production in subducting slabs. Tectonics, 9(5), 1197-1211.

Peacock, S. M. (1993). The importance of blueschist→ eclogite dehydration reactions in subducting oceanic crust. Geological Society of America Bulletin, 105(5), 684-694.

Peacock, S. M. (1996). Thermal and petrologic structure of subduction zones. Subduction: top to bottom, 96, 119-133.

Peacock, S. M., and Wang, K. (1999). Seismic consequences of warm versus cool subduction metamorphism: Examples from southwest and northeast Japan. Science, 286(5441), 937-939.

Peacock, S. M., Wang, K., McMahon, A. M., Kirby, S., and Dunlop, S. (2002). Thermal structure and metamorphism of subducting oceanic crust: Insight into Cascadia intraslab earthquakes. The Cascadia Subduction Zone and Related Subduction Systems: Seismic Structure, Intraslab Earthquakes and Processes, and Earthquake Harzards, 2, 123-126.

Peacock, S. M. (2009). Thermal and metamorphic environment of subduction zone episodic tremor and slip. Journal of Geophysical Research: Solid Earth, 114(B8).

Peacock, S. M., Christensen, N. I., Bostock, M. G., and Audet, P. (2011). High pore pressures and porosity at 35 km depth in the Cascadia subduction zone. Geology, 39(5), 471-474.

Pearce, J., 1996. A user's guide to basalt discrimination diagrams. Trace element geochemistry of volcanic rocks: applications for massive sulphide exploration. Geological Association of Canada, Short Course Notes. 12(79), 113.

Pearce, J. A. (2008). Geochemical fingerprinting of oceanic basalts with applications to ophiolite classification and the search for Archean oceanic crust. Lithos, 100(1-4), 14-48.

Pec, M., Stünitz, H., Heilbronner, R., Drury, M., and de Capitani, C. (2012). Origin of pseudotachylites in slow creep experiments. Earth and Planetary Science Letters, 355, 299-310.

Peng, Z., Gomberg, J., 2010. An integrated perspective of the continuum between earthquakes and slow-slip phenomena. Nature Geoscience. 3(9), 599-607.

Peng, Z., Shelly, D. R., and Ellsworth, W. L. (2015). Delayed dynamic triggering of deep tremor along the Parkfield-Cholame section of the San Andreas Fault following the 2014 M6. 0 South Napa earthquake. Geophysical Research Letters, 42(19), 7916-7922.

Penniston-Dorland, S. C., Gorman, J. K., Bebout, G. E., Piccoli, P. M., and Walker, R. J. (2014). Reaction rind formation in the Catalina Schist: Deciphering a history of mechanical mixing and metasomatic alteration. Chemical Geology, 384, 47-61.

Philippon, M., Gueydan, F., Pitra, P., and Brun, J. P. (2013). Preservation of subduction-related prograde deformation in lawsonite pseudomorph-bearing rocks. Journal of Metamorphic Geology, 31(5), 571-583.

Philippot, P., Kienast, J. R., 1989. Chemical-microstructural changes in eclogite-facies shear zones (Monviso, Western Alps, north Italy) as indicators of strain history and the mechanism and scale of mass transfer. Lithos, 23(3), 179-200.

Philippot, P., Selverstone, J., 1991. Trace-element-rich brines in eclogitic veins: implications for fluid composition and transport during subduction. Contributions to Mineralogy and Petrology. 106(4), 417-430.

Phillips, N. J., Motohashi, G., Ujiie, K., and Rowe, C. D. (2020). Evidence of localized failure along altered basaltic blocks in tectonic mélange at the updip limit of the seismogenic zone: implications for the shallow slow earthquake source. Geochemistry, Geophysics, Geosystems, 21(7), e2019GC008839.

Piccoli, F., Vitale Brovarone, A., Beyssac, O., Martinez, I., Ague, J., Chaduteau, C., 2016. Carbonation by fluid–rock interactions at high-pressure conditions: implications for carbon cycling in subduction zones. Earth and Planetary Science Letters. 445, 146-159.

Piccoli, F., Brovarone, A. V., Ague, J. J., 2018. Field and petrological study of metasomatism and high-pressure carbonation from lawsonite eclogite-facies terrains, Alpine Corsica. Lithos, 304, 16-37.

Pimienta, L., Schubnel, A., Violay, M., Fortin, J., Guéguen, Y., and Lyon-Caen, H. (2018). Anomalous Vp/Vs ratios at seismic frequencies might evidence highly damaged rocks in subduction zones. Geophysical Research Letters, 45(22), 12-210.

Plank, T., 2014. The Chemical Composition of Subducting Sediments. In: Treatise on Geochemistry., ed. by Keeling, Ralph F. Elsevier, Amsterdam, pp. 607-629. 2. ed.

Plank, T., and Manning, C. E. (2019). Subducting carbon. Nature, 574(7778), 343-352.

Platt, J. P. (1986). Dynamics of orogenic wedges and the uplift of high-pressure metamorphic rocks. Geological society of America bulletin, 97(9), 1037-1053.

Platt, J. P., Leggett, J. K., and Alam, S. (1988). Slip vectors and fault mechanics in the Makran accretionary wedge, southwest Pakistan. Journal of Geophysical Research: Solid Earth, 93(B7), 7955-7973.

Platt, J. P. (2015). Origin of Franciscan blueschist-bearing mélange at San Simeon, central California coast. International Geology Review, 57(5-8), 843-853.

Platt, J. P., Behr, W. M., and Cooper, F. J. (2014). Metamorphic core complexes: windows into the mechanics and rheology of the crust. Journal of the Geological Society, 172(1), 9-27.

Platt, J. P., Xia, H., and Schmidt, W. L. (2018). Rheology and stress in subduction zones around the aseismic/seismic transition. Progress in Earth and Planetary Science, 5(1), 1-12.

Plaza-Faverola, A., Henrys, S., Pecher, I., Wallace, L., and Klaeschen, D. (2016). Splay fault branching from the H ikurangi subduction shear zone: Implications for slow slip and fluid flow. Geochemistry, Geophysics, Geosystems, 17(12), 5009-5023.

Plissart, G., González-Jiménez, J. M., Garrido, L. N., Colás, V., Berger, J., Monnier, C., ... and Padrón-Navarta, J. A. (2019). Tectono-metamorphic evolution of subduction channel serpentinites from South-Central Chile. Lithos, 336, 221-241.

Plümper, O., Beinlich, A., Bach, W., Janots, E., Austrheim, H., 2014. Garnets within geode-like serpentinite veins: Implications for element transport, hydrogen production and life-supporting environment formation. Geochimica et Cosmochimica Acta. 141, 454-471.

Poli, S., Schmidt, M., 1995. H2O transport and release in subduction zones: experimental constraints on basaltic and andesitic systems. Journal of Geophysical Research: Solid Earth. 100(B11), 22299-22314.

Powell, R., and Holland, T. (1999). Relating formulations of the thermodynamics of mineral solid solutions; activity modeling of pyroxenes, amphiboles, and micas. American Mineralogist, 84(1-2), 1-14.

Précigout, J., Prigent, C., Palasse, L., and Pochon, A. (2017). Water pumping in mantle shear zones. Nature Communications, 8(1), 1-10.

Preston, L. A., Creager, K. C., Crosson, R. S., Brocher, T. M., and Trehu, A. M. (2003). Intraslab earthquakes: Dehydration of the Cascadia slab. Science, 302(5648), 1197-1200.

Proctor, B., Mitchell, T., Hirth, G., Goldsby, D., Zorzi, F., Platt, J., Di Toro, G., 2014. Dynamic weakening of serpentinite gouges and bare surfaces at seismic slip rates. Journal of Geophysical Research: Solid Earth. 119(11), 8107-8131.

Proctor, B., and Hirth, G. (2016). “Ductile to brittle” transition in thermally stable antigorite gouge at mantle pressures. Journal of Geophysical Research: Solid Earth, 121(3), 1652-1663.

Putnis, A., Austrheim, H., 2010. Fluid-induced processes: metasomatism and metamorphism. Geofluids. 10(1-2), 254-269.

Putnis, A., Austrheim, H., 2012. Metasomatism and the Chemical Transformation of Rock. Lect. Notes Earth Sci. 141-170.

Radiguet, M., Cotton, F., Vergnolle, M., Campillo, M., Valette, B., Kostoglodov, V., and Cotte, N. (2011). Spatial and temporal evolution of a long term slow slip event: the 2006 Guerrero Slow Slip Event. Geophysical Journal International, 184(2), 816-828.

Raimbourg, H., Thiery, R., Vacelet, M., Ramboz, C., Cluzel, N., Le Trong, E., ... and Kimura, G. (2014). A new method of reconstituting the P–T conditions of fluid circulation in an accretionary prism (Shimanto, Japan) from microthermometry of methane-bearing aqueous inclusions. Geochimica et Cosmochimica Acta, 125, 96-109.

Raimbourg, H., Vacelet, M., Ramboz, C., Famin, V., Augier, R., Palazzin, G., ... and Kimura, G. (2015). Fluid circulation in the depths of accretionary prisms: an example of the Shimanto Belt, Kyushu, Japan. Tectonophysics, 655, 161-176.

Raimbourg, H., Famin, V., Palazzin, G., Mayoux, M., Jolivet, L., Ramboz, C., Yamaguchi, A., 2018. Fluid properties and dynamics along the seismogenic plate interface. Geosphere. 14(2), 469-491.

Raleigh, C. B., and Paterson, M. S. (1965). Experimental deformation of serpentinite and its tectonic implications. Journal of Geophysical Research, 70(16), 3965-3985.

Ramos, V. A., Jordan, T. E., Allmendinger, R. W., Mpodozis, C., Kay, S. M., Cortés, J. M., and Palma, M. (1986). Paleozoic terranes of the central Argentine-Chilean Andes. Tectonics, 5(6), 855-880.

Ramos, V. A. (1988). Late Proterozoic-early Paleozoic of South America-a collisional history. Episodes Journal of International Geoscience, 11(3), 168-174.

Ramos, V. A. (1994). Terranes of southern Gondwanaland and their control in the Andean structure (30–33 S latitude). In Tectonics of the Southern Central Andes (pp. 249-261). Springer, Berlin, Heidelberg.

Ramos, V. A. (2004). Cuyania, an exotic block to Gondwana: review of a historical success and the present problems. Gondwana Research, 7(4), 1009-1026.

Ramsay, J.,1980. The crack–seal mechanism of rock deformation. Nature. 284(5752), 135-139.

Rapela, C. W., Pankhurst, R. J., Casquet, C., Baldo, E., Saavedra, J., Galindo, C., and Fanning, C. M. (1998). The Pampean Orogeny of the southern proto-Andes: Cambrian continental collision in the Sierras de Córdoba. Geological Society, London, Special Publications, 142(1), 181-217.

Räss, L., Duretz, T., and Podladchikov, Y. Y. (2019). Resolving hydromechanical coupling in two and three dimensions: spontaneous channelling of porous fluids owing to decompaction weakening. Geophysical Journal International, 218(3), 1591-1616.

Reinen, L., 2000. Seismic and aseismic slip indicators in serpentinite gouge. Geology. 28(2), 135-138.

Renard, F., Dysthe, D., Feder, J., Bjørlykke, K., and Jamtveit, B. (2001). Enhanced pressure solution creep rates induced by clay particles: Experimental evidence in salt aggregates. Geophysical Research Letters, 28(7), 1295-1298.

Rempe, M., Smith, S. A., Ferri, F., Mitchell, T. M., and Di Toro, G. (2014). Clast-cortex aggregates in experimental and natural calcite-bearing fault zones. Journal of Structural Geology, 68, 142-157.

Reynard, B., Gillet, P., and Willaime, C. (1989). Deformation mechanisms in naturally deformed glaucophanes; a TEM and HREM study. European Journal of Mineralogy, 1(5), 611-624.

Reynard, B., Nakajima, J., and Kawakatsu, H. (2010). Earthquakes and plastic deformation of anhydrous slab mantle in double Wadati-Benioff zones. Geophysical Research Letters, 37(24).

Ribbe, P. H. (1980). Titanite (sphene). In Orthosilicates (pp. 137-154). De Gruyter.

Rice, J., 2006. Heating and weakening of faults during earthquake slip. Journal of Geophysical Research: Solid Earth. 111(B5).

Richter, P. P., Ring, U., Willner, A. P., and Leiss, B. (2007). Structural contacts in subduction complexes and their tectonic significance: the Late Palaeozoic coastal accretionary wedge of central Chile. Journal of the Geological Society, 164(1), 203-214.

Roda, M., and Zucali, M. (2008). Meso and microstructural evolution of the Mont Morion metaintrusive complex (Dent-Blanche nappe, Austroalpine domain, Valpelline, Western Italian Alps). BOLLETTINO-SOCIETA GEOLOGICA ITALIANA, 127(1), 105.

Rogers, G., and Dragert, H. (2003). Episodic tremor and slip on the Cascadia subduction zone: The chatter of silent slip. Science, 300(5627), 1942-1943.

Rondenay, S., Abers, G. A., and Van Keken, P. E. (2008). Seismic imaging of subduction zone metamorphism. Geology, 36(4), 275-278.

Rowe, C., Moore, J., Meneghini, F., McKeirnan, A., 2005. Large-scale pseudotachylytes and fluidized cataclasites from an ancient subduction thrust fault. Geology. 33(12), 937-940.

Rowe, C. D., Meneghini, F., and Moore, J. C. (2011). Textural record of the seismic cycle: strain-rate variation in an ancient subduction thrust. Geological Society, London, Special Publications, 359(1), 77-95.

Rowe, C., Griffith, W., 2015. Do faults preserve a record of seismic slip: A second opinion. Journal of Structural Geology. 78, 1-26.

Rubinstein, J. L., Shelly, D. R., and Ellsworth, W. L. (2009). Non-volcanic tremor: A window into the roots of fault zones. In New Frontiers in Integrated Solid Earth Sciences (pp. 287-314). Springer, Dordrecht.

Ruff, L. J. (1989). Do trench sediments affect great earthquake occurrence in subduction zones?. In Subduction Zones Part II (pp. 263-282). Birkhäuser Basel.

Rumble, D., and Spear, F. S. (1983). Oxygen-isotope equilibration and permeability enhancement during regional metamorphism. Journal of the Geological Society, 140(4), 619-628.

Rumble, D., Oliver, N. H. S., Ferry, J. M., and Hoering, T. C. (1991). Carbon and oxygen isotope geochemistry of chlorite-zone rocks of the Waterville limestone, Maine, USA. American Mineralogist, 76(5-6), 857-866.

Rutter, E. H. (1976). A discussion on natural strain and geological structure-the kinetics of rock deformation by pressure solution. Philosophical Transactions of the Royal Society of London. Series A, Mathematical and Physical Sciences, 283(1312), 203-219.

Rutter, E. H., and Elliott, D. (1976). The kinetics of rock deformation by pressure solution, Philos. Trans. R. Soc. London, A, 283, 43-54.

Rutter, E. H. (1983). Pressure solution in nature, theory and experiment. Journal of the Geological Society, 140(5), 725-740.

Sabzehei, M., 1974. Les Mélanges ophiolitiques de la région d'Esfandagheh (Iran méridional): étude pétrologique et structurale, interprétation dans le cadre iranien (Doctoral dissertation).

Sachau, T., Bons, P. D., and Gomez-Rivas, E. (2015). Transport efficiency and dynamics of hydraulic fracture networks. Frontiers in Physics, 3, 63.

Saffer, D., Tobin, H., 2011. Hydrogeology and mechanics of subduction zone forearcs: Fluid flow and pore pressure. Annual Review of Earth and Planetary Sciences. 39, 157-186.

Saffer, D. M., and Wallace, L. M. (2015). The frictional, hydrologic, metamorphic and thermal habitat of shallow slow earthquakes. Nature Geoscience, 8(8), 594-600.

Sato, A. M., Llambías, E. J., Basei, M. A., and Castro, C. E. (2015). Three stages in the Late Paleozoic to Triassic magmatism of southwestern Gondwana, and the relationships with the volcanogenic events in coeval basins. Journal of South American Earth Sciences, 63, 48-69.

Scambelluri, M., Philippot, P., 2001. Deep fluids in subduction zones. Lithos. 55(1-4), 213-227.

Scambelluri, M., Bebout, G., Belmonte, D., Gilio, M., Campomenosi, N., Collins, N., Crispini, L., 2016. Carbonation of subduction-zone serpentinite (high-pressure ophicarbonate; Ligurian Western Alps) and implications for the deep carbon cycling. Earth and Planetary Science Letters. 441, 155-166.

Scambelluri, M., Cannaò, E., and Gilio, M. (2019). The water and fluid-mobile element cycles during serpentinite subduction. A review. European Journal of Mineralogy, 31(3), 405-428.

Schellart, W. P., and Rawlinson, N. (2013). Global correlations between maximum magnitudes of subduction zone interface thrust earthquakes and physical parameters of subduction zones. Physics of the Earth and Planetary Interiors, 225, 41-67.

Schmidt, M. W., and Poli, S. (1998). Experimentally based water budgets for dehydrating slabs and consequences for arc magma generation. Earth and Planetary Science Letters, 163(1-4), 361-379.

Scholz, C., Campos, J., 2012. The seismic coupling of subduction zones revisited. Journal of Geophysical Research: Solid Earth. 117(B5).

Schultz, R., 1995. Limits on strength and deformation properties of jointed basaltic rock masses. Rock Mechanics and Rock Engineering. 28(1), 1-15.

Schwarzenbach, E., Caddick, M., Petroff, M., Gill, B., Cooperdock, E., Barnes, J., 2018. Sulphur and carbon cycling in the subduction zone mélange. Scientific reports. 8(1), 1-11.

Secor, D. T., 1965. Role of fluid pressure in jointing. American Journal of Science. 263(8), 633-646.

Secor Jr, D. T., and Pollard, D. D. (1975). On the stability of open hydraulic fractures in the Earth's crust. Geophysical Research Letters, 2(11), 510-513.

Seno, T. (2009). Determination of the pore fluid pressure ratio at seismogenic megathrusts in subduction zones: Implications for strength of asperities and Andean-type mountain building. Journal of Geophysical Research: Solid Earth, 114(B5).

Shapiro, N., Campillo, M., Kaminski, E., Vilotte, J., Jaupart, C., 2018. Low-frequency earthquakes and pore pressure transients in subduction zones. Geophysical Research Letters. 45(20), 11-083.

Sharp, Z., 2017. Principles of stable isotope geochemistry.

Shelly, D. R., Beroza, G. C., Ide, S., and Nakamula, S. (2006). Low-frequency earthquakes in Shikoku, Japan, and their relationship to episodic tremor and slip. Nature, 442(7099), 188-191.

Shmulovich, K., Graham, C., and Yardley, B. (2001). Quartz, albite and diopside solubilities in H 2 O–NaCl and H 2 O–CO 2 fluids at 0.5–0.9 GPa. Contributions to Mineralogy and Petrology, 141(1), 95-108.

Sibson, R. H. (1975). Generation of pseudotachylyte by ancient seismic faulting. Geophysical Journal International, 43(3), 775-794.

Sibson, R. H. (1989). Earthquake faulting as a structural process. Journal of structural geology, 11(1-2), 1-14.

Sibson, R., 1990. Conditions for fault-valve behaviour. Geological Society, London, Special Publications. 54(1), 15-28.

Sibson, R. H. (1992). Implications of fault-valve behaviour for rupture nucleation and recurrence. Tectonophysics, 211(1-4), 283-293.

Sibson, R. H. (2003). Thickness of the seismic slip zone. Bulletin of the Seismological Society of America, 93(3), 1169-1178.

Sibson, R., Toy, V., 2006. The Habitat of Fault-Generated Pseudotachylyte: Presence vs. Absence of Friction-Melt. In Earthquakes: Radiated Energy and the Physics of Faulting (eds R. Abercrombie, A. McGarr, G. Di Toro and H. Kanamori).

Sibson, R. H. (2013). Stress switching in subduction forearcs: Implications for overpressure containment and strength cycling on megathrusts. Tectonophysics, 600, 142-152.

Simonetti, A., Heaman, L. M., Chacko, T., and Banerjee, N. R. (2006). In situ petrographic thin section U–Pb dating of zircon, monazite, and titanite using laser ablation–MC–ICP-MS. International Journal of Mass Spectrometry, 253(1-2), 87-97.

Skarbek, R. M., Rempel, A. W., and Schmidt, D. A. (2012). Geologic heterogeneity can produce aseismic slip transients. Geophysical Research Letters, 39(21).

Skarbek, R., Rempel, A., 2016. Dehydration-induced porosity waves and episodic tremor and slip. Geochemistry, Geophysics, Geosystems. 17(2), 442-469.

Skelton, A., Valley, J., Graham, C., Bickle, M., Fallick, A., 2000. The correlation of reaction and isotope fronts and the mechanism of metamorphic fluid flow. Contributions to Mineralogy and Petrology. 138(4), 364-375.

Sorensen, S. S., and Grossman, J. N. (1989). Enrichment of trace elements in garnet amphibolites from a paleo-subduction zone: Catalina Schist, southern California. Geochimica et Cosmochimica Acta, 53(12), 3155-3177.

Spandler, C., Hermann, J., Arculus, R., Mavrogenes, J., 2003. Redistribution of trace elements during prograde metamorphism from lawsonite blueschist to eclogite facies; implications for deep subduction-zone processes. Contributions to Mineralogy and Petrology, 146(2), 205-222.

Spandler, C., Hermann, J., 2006. High-pressure veins in eclogite from New Caledonia and their significance for fluid migration in subduction zones. Lithos. 89(1-2), 135-153.

Spandler, C., Hermann, J., Faure, K., Mavrogenes, J., Arculus, R., 2008. The importance of talc and chlorite "hybrid" rocks for volatile recycling through subduction zones; evidence from the high-pressure subduction mélange of New Caledonia. Contributions to Mineralogy and Petrology. 155(2), 181-198.

Spandler, C., Pettke, T., Rubatto, D., 2011. Internal and external fluid sources for eclogite-facies veins in the Monviso meta-ophiolite, Western Alps: implications for fluid flow in subduction zones. Journal of Petrology. 52(6), 1207-1236.

Spandler, C., and Pirard, C. (2013). Element recycling from subducting slabs to arc crust: A review. Lithos, 170, 208-223.

Spear, F., 1988. Thermodynamic projection and extrapolation of high-variance mineral assemblages. Contributions to Mineralogy and Petrology. 98(3), 346-351.

Spear, F.S., 1993. Metamorphic Phase Equilibria and Pressure-Temperature-Time Paths: Washington, D.C., Mineralogical Society of America, 799 p.

Spiegelman, M. (1993). Flow in deformable porous media. Part 1 Simple analysis. Journal of Fluid Mechanics, 247, 17-38.

Spinelli, G. A., and Wang, K. (2008). Effects of fluid circulation in subducting crust on Nankai margin seismogenic zone temperatures. Geology, 36(11), 887-890.

Stern, R. J., and Bloomer, S. H. (1992). Subduction zone infancy: examples from the Eocene Izu-Bonin-Mariana and Jurassic California arcs. Geological Society of America Bulletin, 104(12), 1621-1636.

Stern, R., 2002. Subduction zones. Reviews of geophysics. 40(4), 3-1.

Stern, R. J., Kohut, E., Bloomer, S. H., Leybourne, M., Fouch, M., and Vervoort, J. (2006). Subduction factory processes beneath the Guguan cross-chain, Mariana Arc: no role for sediments, are serpentinites important?. Contributions to Mineralogy and Petrology, 151(2), 202-221.

Stewart, E. M., and Ague, J. J. (2020). Pervasive subduction zone devolatilization recycles CO 2 into the forearc. Nature communications, 11(1), 1-8.

Stipp, M., StuÈnitz, H., Heilbronner, R., and Schmid, S. M. (2002). The eastern Tonale fault zone: a 'natural laboratory'for crystal plastic deformation of quartz over a temperature range from 250 to 700 C. Journal of structural geology, 24(12), 1861-1884.

Stöckhert, B., Wachmann, M., Küster, M., Bimmermann, S., 1999. Low effective viscosity during high pressure metamorphism due to dissolution precipitation creep: the record of HP–LT metamorphic carbonates and siliciclastic rocks from Crete. Tectonophysics. 303(1-4), 299-319.

Stöckhert, B., Brix, M. R., Kleinschrodt, R., Hurford, A. J., and Wirth, R. (1999). Thermochronometry and microstructures of quartz—a comparison with experimental flow laws and predictions on the temperature of the brittle–plastic transition. Journal of Structural Geology, 21(3), 351-369.

Stöcklin, J. (1968). Structural history and tectonics of Iran: a review. AAPG bulletin, 52(7), 1229-1258.

Stünitz, H., Gerald, J. F., and Tullis, J. (2003). Dislocation generation, slip systems, and dynamic recrystallization in experimentally deformed plagioclase single crystals. Tectonophysics, 372(3-4), 215-233.

Stünitz, H., Keulen, N., Hirose, T., and Heilbronner, R. (2010). Grain size distribution and microstructures of experimentally sheared granitoid gouge at coseismic slip rates–Criteria to distinguish seismic and aseismic faults?. Journal of Structural Geology, 32(1), 59-69.

Stünitz, H., Neufeld, K., Heilbronner, R., Finstad, A. K., Konopásek, J., and Mackenzie, J. R. (2020). Transformation weakening: Diffusion creep in eclogites as a result of interaction of mineral reactions and deformation. Journal of Structural Geology, 139, 104129.

Suess, E., and Whiticar, M. (1989). Methane-derived CO_2 in pore fluids expelled from the Oregon subduction zone. Palaeogeography, Palaeoclimatology, Palaeoecology, 71(1-2), 119-136.

Sun, S., McDonough, W., 1989. Chemical and isotopic systematics of oceanic basalts: implications for mantle composition and processes. Geological Society, London, Special Publications. 42(1), 313-345.

Taetz, S., John, T., Bröcker, M., Spandler, C., 2016. Fluid–rock interaction and evolution of a high-pressure/low-temperature vein system in eclogite from New Caledonia: insights into intraslab fluid flow processes. Contributions to Mineralogy and Petrology. 171(11), 90.

Taetz, S., John, T., Bröcker, M., Spandler, C., Stracke, A., 2018. Fast intraslab fluid-flow events linked to pulses of high pore fluid pressure at the subducted plate interface. Earth and Planetary Science Letters. 482, 33-43.

Tan, E., Lavier, L. L., Van Avendonk, H. J., and Heuret, A. (2012). The role of frictional strength on plate coupling at the subduction interface. Geochemistry, Geophysics, Geosystems, 13(10).

Tanaka, S., Matsuzawa, T., and Asano, Y. (2019). Shallow low-frequency tremor in the northern Japan Trench subduction zone. Geophysical Research Letters, 46(10), 5217-5224.

Tamblyn, R., Zack, T., Schmitt, A., Hand, M., Kelsey, D., Morrissey, L., Pabst, S., Savov, I., 2019. Blueschist from the Mariana forearc records long-lived residence of material in the subduction channel. Earth and Planetary Science Letters. 519, 171-181.

Tarling, M., Smith, S., Viti, C., Scott, J., 2018. Dynamic earthquake rupture preserved in a creeping serpentinite shear zone. Nature communications, 9(1), 1-8.

Tarling, M. S., Smith, S. A., and Scott, J. M. (2019). Fluid overpressure from chemical reactions in serpentinite within the source region of deep episodic tremor. Nature Geoscience, 12(12), 1034-1042.

Tarling, M. S., Smith, S. A., Scott, J. M., Rooney, J. S., Viti, C., and Gordon, K. C. (2019). The internal structure and composition of a plate-boundary-scale serpentinite shear zone: the Livingstone Fault, New Zealand. Solid Earth, 10(4), 1025-1047.

Taylor, S. R., McLennan, S. M., 1985. The continental crust: its composition and evolution.

Tewksbury-Christle, C. M., Behr, W. M., and Helper, M. A. (2021). Tracking deep sediment underplating in a fossil subduction margin: Implications for interface rheology and mass and volatile recycling. Geochemistry, geophysics, geosystems: G (3), 22(3).

Tewksbury-Christle, C. M., and Behr, W. M. (2021). Constraints from exhumed rocks on the seismic signature of the deep subduction interface. Geophysical Research Letters, e2021GL093831.

Teyssier, C., Whitney, D. L., Toraman, E., and Seaton, N. C. (2010). Lawsonite vorticity and subduction kinematics. Geology, 38(12), 1123-1126.

Thomas, A. M., Beroza, G. C., and Shelly, D. R. (2016). Constraints on the source parameters of low-frequency earthquakes on the San Andreas Fault. Geophysical Research Letters, 43(4), 1464-1471.

Thompson, J.B., 1959, Local equilibrium in metasomatic processes, in Abelson, P.H., eds., Researches in Geochemistry, Volume 1: New York, John Wiley, p. 427–457.

Thompson, G., and Humphris, S.E., 1977, Seawater-rock interactions in the oceanic basement, in Paquet, H., and Tardy, Y., eds., Proceedings of the 2nd International Symposium on Water-Rock Interaction: Strasbourg, France, p. 13–18.

Tian, M., Ague, J., 2014. The impact of porosity waves on crustal reaction progress and CO_2 mass transfer. Earth and Planetary Science Letters, 390, 80-92.

Tichelaar, B. W., and Ruff, L. J. (1993). Depth of seismic coupling along subduction zones. Journal of Geophysical Research: Solid Earth, 98(B2), 2017-2037.

Torres-Roldan, L., Garcia-Casco, A., Garcia-Sanchez, A., 2000. CSpace: an integrated workplace for the graphical and algebraic analysis of phase assemblages on 32-bit wintel platforms. Computers and Geosciences. 26(7), 779-793.

Tribuzio, R., Messiga, B., Vannucci, R., and Bottazzi, P. (1996). Rare earth element redistribution during high-pressure–low-temperature metamorphism in ophiolitic Fe-gabbros (Liguria, northwestern Italy): Implications for light REE mobility in subduction zones. Geology, 24(8), 711-714.

Trommsdorff, V., Sánchez-Vizcaíno, L., Gomez-Pugnaire, M., Müntener, O., 1998. High pressure breakdown of antigorite to spinifex-textured olivine and orthopyroxene, SE Spain. Contributions to Mineralogy and Petrology. 132(2), 139-148.

Tsujimori, T., and Ernst, W. G. (2014). Lawsonite blueschists and lawsonite eclogites as proxies for palaeo-subduction zone processes: A review. Journal of Metamorphic Geology, 32(5), 437-454.

Turner, F. J. (1981). Metamorphic petrology: Mineralogical, field, and tectonic aspects. McGraw-Hill Companies.

Ujiie, K., Yamaguchi, A., Kimura, G., Toh, S., 2007. Fluidization of granular material in a subduction thrust at seismogenic depths. Earth and Planetary Science Letters. 259(3-4), 307-318.

Ujiie, K., Tsutsumi, A., Fialko, Y., Yamaguchi, H., 2009. Experimental investigation of frictional melting of argillite at high slip rates: Implications for seismic slip in subduction-accretion complexes. Journal of Geophysical Research: Solid Earth. 114(B4).

Ujiie, K., Saishu, H., Fagereng, Å., Nishiyama, N., Otsubo, M., Masuyama, H., and Kagi, H. (2018). An explanation of episodic tremor and slow slip constrained by crack-seal veins and viscous shear in subduction mélange. Geophysical Research Letters, 45(11), 5371-5379.

Ujiie, K., Ito, K., Nagate, A., and Tabata, H. (2021a). Frictional melting and thermal fracturing recorded in pelagic sedimentary rocks of the Jurassic accretionary complex, central Japan. Earth and Planetary Science Letters, 554, 116638.

Ujiie, K., Noro, K., Shigematsu, N., Fagereng, Å., Nishiyama, N., Tulley, C., and Masuyama, H. (2021b), April). Localized megathrust slip controlled by metasomatic reactions in subduction mélanges. In EGU General Assembly Conference Abstracts (pp. EGU21-1885).

Uliana, M. A., and Biddle, K. T. (1988). Mesozoic-Cenozoic paleogeographic and geodynamic evolution of southern South America. Revista Brasileira de geociencias, 18(2), 172-190.

Ulmer, P., and Trommsdorff, V. (1995). Serpentine stability to mantle depths and subduction-related magmatism. Science, 268(5212), 858-861.

Uyeda, S., and Kanamori, H. (1979). Back-arc opening and the mode of subduction. Journal of Geophysical Research: Solid Earth, 84(B3), 1049-1061.

van der Straaten, F., Schenk, V., John, T., Gao, J., 2008. Blueschist-facies rehydration of eclogites (Tian Shan, NW-China): implications for fluid–rock interaction in the subduction channel. Chemical Geology. 255(1-2), 195-219.

van Keken, P., Hacker, B., Syracuse, E., Abers, G., 2011. Subduction factory: 4. Depth-dependent flux of H2O from subducting slabs worldwide. Journal of Geophysical Research: Solid Earth. 116(B1).

van Keken, P. E., Wada, I., Abers, G. A., Hacker, B. R., and Wang, K. (2018). Mafic high-pressure rocks are preferentially exhumed from warm subduction settings. Geochemistry, Geophysics, Geosystems, 19(9), 2934-2961.

Vannucchi, P., Remitti, F., Bettelli, G., Boschi, C., and Dallai, L. (2010). Fluid history related to the early Eocene-middle Miocene convergent system of the Northern Apennines (Italy): Constraints from structural and isotopic studies. Journal of Geophysical Research: Solid Earth, 115(B5).

Vernant, P., Nilforoushan, F., Hatzfeld, D., Abbassi, M. R., Vigny, C., Masson, F., ... and Chéry, J. (2004). Present-day crustal deformation and plate kinematics in the Middle East constrained by GPS measurements in Iran and northern Oman. Geophysical Journal International, 157(1), 381-398.

Vigny, C., Socquet, A., Peyrat, S., Ruegg, J. C., Métois, M., Madariaga, R., ... and Kendrick, E. (2011). The 2010 Mw 8.8 Maule megathrust earthquake of central Chile, monitored by GPS. Science, 332(6036), 1417-1421.

Vitale Brovarone, A., Beyssac, O., 2014. Lawsonite metasomatism: A new route for water to the deep Earth. Earth and Planetary Science Letters. 393, 275-284.

Vitale Brovarone, A., Alard, O., Beyssac, O., Martin, L., Picatto, M., 2014. Lawsonite metasomatism and trace element recycling in subduction zones. Journal of Metamorphic Geology. 32(5), 489-514.

Vitale Brovarone, A., Chu, X., Martin, L., Ague, J., Monie, P., Groppo, C., Martinez, I., Chaduteau, C., 2018. Intra-slab COH fluid fluxes evidenced by fluid-mediated decarbonation of lawsonite eclogite-facies altered oceanic metabasalts. Lithos, 304, 211-229.

Vitale Brovarone, A., Tumiati, S., Piccoli, F., Ague, J. J., Connolly, J. A., Beyssac, O., 2020. Fluid-mediated selective dissolution of subducting carbonaceous material: Implications for carbon recycling and fluid fluxes at forearc depths. Chemical geology. 119682.

von Huene, R., and Ranero, C. R. (2003). Subduction erosion and basal friction along the sediment-starved convergent margin off Antofagasta, Chile. Journal of Geophysical Research: Solid Earth, 108(B2).

Vrolijk, P., Myers, G., Moore, J., 1988. Warm fluid migration along tectonic melanges in the Kodiak accretionary complex, Alaska. Journal of Geophysical Research: Solid Earth. 93(B9), 10313-10324.

Wakabayashi, J. (2012). Subducted sedimentary serpentinite mélanges: Record of multiple burial–exhumation cycles and subduction erosion. Tectonophysics, 568, 230-247.

Wallace, L. M., and Beavan, J. (2006). A large slow slip event on the central Hikurangi subduction interface beneath the Manawatu region, North Island, New Zealand. Geophysical Research Letters, 33(11).

Wallace, L., Eberhart-Phillips, D., 2013. Newly observed, deep slow slip events at the central Hikurangi margin, New Zealand: Implications for downdip variability of slow slip and tremor, and relationship to seismic structure. Geophysical Research Letters. 40(20), 5393-5398.

Walder, J., and Nur, A. (1984). Porosity reduction and crustal pore pressure development. Journal of Geophysical Research: Solid Earth, 89(B13), 11539-11548.

Wang, K., Hyndman, R. D., and Yamano, M. (1995). Thermal regime of the Southwest Japan subduction zone: effects of age history of the subducting plate. Tectonophysics, 248(1-2), 53-69.

Wang, Z., Zhao, D., Mishra, O. P., and Yamada, A. (2006). Structural heterogeneity and its implications for the low frequency tremors in Southwest Japan. Earth and Planetary Science Letters, 251(1-2), 66-78.

Wang, X. Q., Schubnel, A., Fortin, J., David, E. C., Guéguen, Y., and Ge, H. K. (2012). High Vp/Vs ratio: Saturated cracks or anisotropy effects?. Geophysical Research Letters, 39(11).

Wang, K., Huang, T., Tilmann, F., Peacock, S., Lange, D., 2020. Role of Serpentinized Mantle Wedge in Affecting Megathrust Seismogenic Behavior in the Area of the 2010 M=8.8 Maule Earthquake. Geophysical Research Letters. 47, e2020GL090482.

Wassmann, S., Stöckhert, B., and Trepmann, C. A. (2011). Dissolution precipitation creep versus crystalline plasticity in high-pressure metamorphic serpentinites. Geological Society, London, Special Publications, 360(1), 129-149.

Wassmann, S., Stöckhert, B., 2012. Matrix deformation mechanisms in HP-LT tectonic mélanges—Microstructural record of jadeite blueschist from the Franciscan Complex, California. Tectonophysics. 568, 135-153.

Wassmann, S., and Stoeckhert, B. (2013). Rheology of the plate interface—Dissolution precipitation creep in high pressure metamorphic rocks. Tectonophysics, 608, 1-29.

Wech, A. G., and Bartlow, N. M. (2014). Slip rate and tremor genesis in Cascadia. Geophysical Research Letters, 41(2), 392-398.

Wei, M., McGuire, J. J., and Richardson, E. (2012). A slow slip event in the south central Alaska Subduction Zone and related seismicity anomaly. Geophysical Research Letters, 39(15).

Wesnousky, S. G. (2008). Displacement and geometrical characteristics of earthquake surface ruptures: Issues and implications for seismic-hazard analysis and the process of earthquake rupture. Bulletin of the Seismological Society of America, 98(4), 1609-1632.

White, R., Powell, R., Holland, T., Johnson., Green, E., 2014. New mineral activity–composition relations for thermodynamic calculations in metapelitic systems. Journal of Metamorphic Geology. 32(3), 261-286.

Whitmarsh, R. B. (1978). Seismic refraction studies of the upper igneous crust in the North Atlantic and porosity estimates for layer 2. Earth and Planetary Science Letters, 37(3), 451-464.

Whitney, D., Evans, B., 2010. Abbreviations for names of rock-forming minerals. American mineralogist. 95(1), 185-187.

Whitney, D., Fornash, K., Kang, P., Ghent, E., Martin, L., Okay, A., vitale Brovarone, A., 2020. Lawsonite composition and zoning as tracers of subduction processes: A global review. Lithos. 105636.

Widmer, T., Thompson, A. B., 2001. Local origin of high pressure vein material in eclogite facies rocks of the Zermatt-Saas Zone, Switzerland. American Journal of Science, 301(7), 627-656.

Willner, A. P., Pawlig, S., Massonne, H. J., and Hervé, F. (2001). Metamorphic evolution of spessartine quartzites (coticules) in the high-pressure, low-temperature complex at Bahia Mansa, Coastal Cordillera of south-central Chile. The Canadian Mineralogist, 39(6), 1547-1569.

Willner, A. P., Glodny, J., Gerya, T. V., Godoy, E., and Massonne, H. J. (2004). A counterclockwise PTt path of high-pressure/low-temperature rocks from the Coastal Cordillera accretionary complex of south-central Chile: constraints for the earliest stage of subduction mass flow. Lithos, 75(3-4), 283-310.

Willner, A. P. (2005). Pressure–temperature evolution of a Late Palaeozoic paired metamorphic belt in North–Central Chile (34°–35° 30′ S). Journal of Petrology, 46(9), 1805-1833.

Willner, A. P., Thomson, S. N., Kröner, A., Wartho, J. A., Wijbrans, J. R., and Hervé, F. (2005). Time markers for the evolution and exhumation history of a Late Palaeozoic paired metamorphic belt in North–Central Chile (34–35 30′ S). Journal of Petrology, 46(9), 1835-1858.

Willner, A. P., Gerdes, A., and Massonne, H. J. (2008). History of crustal growth and recycling at the Pacific convergent margin of South America at latitudes 29–36 S revealed by a U–Pb and Lu–Hf isotope study of detrital zircon from late Paleozoic accretionary systems. Chemical Geology, 253(3-4), 114-129.

Willner, A. P., Maresch, W. V., Massonne, H. J., Sandritter, K., and Willner, G. (2016). Metamorphic evolution of blueschists, greenschists, and metagreywackes in the Cretaceous Mt. Hibernia Complex (SE Jamaica). European Journal of Mineralogy, 28(6), 1059-1078.

Wiltschko, D. V., and Morse, J. W. (2001). Crystallization pressure versus “crack seal” as the mechanism for banded veins. Geology, 29(1), 79-82.

Winchester, J. A., and Floyd, P. A. (1977). Geochemical discrimination of different magma series and their differentiation products using immobile elements. Chemical geology, 20, 325-343.

Wintsch, R. P., and Yeh, M. W. (2013). Oscillating brittle and viscous behavior through the earthquake cycle in the Red River Shear Zone: Monitoring flips between reaction and textural softening and hardening. Tectonophysics, 587, 46-62.

Wood, B. J., and Walther, J. V. (1986). Fluid flow during metamorphism and its implications for fluid—rock ratios. In Fluid—rock interactions during metamorphism (pp. 89-108). Springer, New York, NY.

Worden, R. H., and Morad, S. (1999). Clay minerals in sandstones: controls on formation, distribution and evolution. Clay mineral cements in sandstones, 1-41.

Worthington, J. R., Hacker, B. R., and Zandt, G. (2013). Distinguishing eclogite from peridotite: EBSD-based calculations of seismic velocities. Geophysical Journal International, 193(1), 489-505.

Yang, H., Liu, Y., and Lin, J. (2012). Effects of subducted seamounts on megathrust earthquake nucleation and rupture propagation. Geophysical Research Letters, 39(24).

Yamato, Philippe, Thibault Duretz, and Samuel Angiboust. "Brittle/ductile deformation of eclogites: insights from numerical models." Geochemistry, Geophysics, Geosystems 20.7 (2019): 3116-3133.

Yardley, B., 1983. Quartz veins and devolatilization during metamorphism. Journal of the Geological Society. 140(4), 657-663.

Yardley, B. W. D. (1986). Fluid migration and veining in the Connemara Schists, Ireland. In Fluid—rock interactions during metamorphism (pp. 109-131). Springer, New York, NY.

Yardley, B. W. D., Rochelle, C. A., Barnicoat, A. C., and Lloyd, G. E. (1991). Oscillatory zoning in metamorphic minerals: an indicator of infiltration metasomatism. Mineralogical Magazine, 55(380), 357-365.

Yardley, B. W. (2005). 100th Anniversary Special Paper: metal concentrations in crustal fluids and their relationship to ore formation. Economic Geology, 100(4), 613-632.

Zack, T., Rivers, T., Foley, S., 2001. Cs–Rb–Ba systematics in phengite and amphibole: an assessment of fluid mobility at 2.0 GPa in eclogites from Trescolmen, Central Alps. Contributions to Mineralogy and Petrology, 140(6), 651-669.

Zack, T., Kronz, A., Foley, S. F., and Rivers, T. (2002). Trace element abundances in rutiles from eclogites and associated garnet mica schists. Chemical Geology, 184(1-2), 97-122.

Zack, T. V., Von Eynatten, H., and Kronz, A. (2004). Rutile geochemistry and its potential use in quantitative provenance studies. Sedimentary Geology, 171(1-4), 37-58.

Zack, T., John, T., 2007. An evaluation of reactive fluid flow and trace element mobility in subducting slabs. Chemical Geology. 239(3-4), 199-216.

Žák, J., Svojtka, M., Hajná, J., and Ackerman, L. (2020). Detrital zircon geochronology and processes in accretionary wedges. Earth-Science Reviews, 207, 103214.

Zhang, J., Green II, H. W., and Bozhilov, K. N. (2006). Rheology of omphacite at high temperature and pressure and significance of its lattice preferred orientations. Earth and Planetary Science Letters, 246(3-4), 432-443.

Zheng, Y., Gong, B., Li, Y., Wang, Z., Fu, B., 2000. Carbon concentrations and isotopic ratios of eclogites from the Dabie and Sulu terranes in China. Chemical Geology. 168(3-4), 291-305.

Zheng, Y., Hermann, J., 2014. Geochemistry of continental subduction-zone fluids. Earth, Planets and Space. 66(1), 93.

Zucali, M., Chateigner, D., Dugnani, M., Lutterotti, L., Ouladdiaf, B., De Meer, S., ... and Pennock, G. M. (2002). Quantitative texture analysis of naturally deformed hornblendite under eclogite facies conditions (Sesia-Lanzo Zone, Western Alps): comparison between x-ray and neutron diffraction analysis. Deformation Mechanisms, Rheology and Tectonics: Current Status and Future Perspectives, Geological Society, London, Special Publications, 200, 239-253.

10. APPENDIX A

Angiboust et al. (2021)

Jolts in the Jade factory: A route for subduction fluids and their implications for mantle wedge seismicity

Samuel Angiboust [a,*], Jesus Muñoz-Montecinos [a,b], Aitor Cambeses [a,b], Tom Raimondo [c], Damien Deldicque [d], Antonio Garcia-Casco [b,e]

[a] Universit´e de Paris, Institut de Physique du Globe de Paris, F-75005 Paris, France

[b] Department of Mineralogy and Petrology, Faculty of Sciences, University of Granada, Campus Fuentenueva s/n, 18002 Granada, Spain

[c] UniSA STEM, University of South Australia, GPO Box 2471, Adelaide, SA 5001, Australia

[d] Laboratoire de G´eologie, Ecole Normale Sup´erieure PSL, F-75005 Paris, France

[e] Instituto Andaluz de Ciencias de la Tierra, CSIC-Universidad de Granada, 18100 Armilla, Granada, Spain

*: corresponding author (samuel.angiboust@gmail.com)

Published in Earth Science-Reviews

Abstract

An increasing number of seismological studies report transient seismicity clusters in the mantle wedge several kilometers above the subduction interface. Their physical significance with respect to subduction zone seismo-tectonics remains poorly understood. Jadeitites are known to form and/or be associated with mantle wedge serpentinites in the c. 30–70 km depth range, and thus may yield information on deformation mechanisms in this region of deep subduction environments. We herein document and compare brittle-viscous features recorded in jadeitites from Polar Urals (Russia), Kashin state (Myanmar) and Motagua fault region (Guatemala) – some of the most important jadeitite occurrences worldwide. In the Polar Urals we identified ultramafic-hosted pristine jadeitite-bearing veins c. 1 km above a Devonian paleo-subduction interface, interpreted as metasomatized former felsic dyke networks crosscutting the mantle wedge peridotites. Here, both jadeitites and associated amphibole-rich dark granofels display widespread brittle-ductile deformation fabrics such as shear bands, foliated cataclasites and breccias, cemented through dissolution-precipitation processes by omphacite and sodic amphiboles, a mineral assemblage typical of high-pressure–low-temperature subduction zone conditions. Electron probe and laser ablation ICP-MS mapping indicate that these brittle-viscous networks display a substantial metasomatic imprint highlighted in the dark granofels by variations in major and trace elements. Switches between viscous and brittle deformation patterns are attested by crystallographic-preferred orientations of jadeite in some of the shear zones that crosscut the host jadeitites. Strikingly similar mineral assemblages and deformation patterns were observed in the Kashin and Motagua samples. Observed deformation features in these localities can be classified into three categories (tectonic breccias, foliated cataclasites and hydraulic breccias), which may occasionally form in sequence and exhibit mutually overprinting textures. Some of the foliated cataclasites contain fine-grained and foliated "shard-like" features forming a radial omphacite-jadeite spherulitic texture, interpreted as former pseudotachylyte that evokes a paleo-seismic origin. We interpret these healed fault networks as recording external fluid influx within fracture zones that repeatedly ruptured along former "dyke" networks. These high permeability drains likely (i) contribute to the transfer of highly pressurized plate-interface metamorphic fluids into the mantle wedge; and (ii) trigger seismic instabilities recorded in the basal part of active mantle wedge sections. These findings provide new insights into the current understanding of the rheology (e.g., serpentinization ratio) and stress state in the mantle wedge, with implications for subduction interface seismogenesis.

Keywords: Subduction, Fluids, Jadeitite, Earthquakes, Mantle wedge, Foliated cataclasites

1. Introduction

Understanding processes rooted in the mantle wedge region of subduction zones is of critical importance because its structure strongly controls the rheology of the subduction interface at the downdip end of the seismogenic zone (Hyndman and Peacock, 2003; Dessa et al., 2009; Agard et al., 2018). Fluids released by metamorphic reactions in the downgoing plate are thought to control the degree of hydration (serpentinization) of the fore-arc mantle wedge (e.g., Hacker et al., 2003; Deschamps et al., 2010; Bostock, 2013). The bulk serpentinization ratio of the mantle wedge, estimated based on the perturbation of seismic wave velocities, is generally considered low (i.e., <20 vol%; Abers et al., 2017) except for specific subduction environments where it may reach up to 60 vol% (e.g., Central Japan: Hyndman and Peacock, 2003; Mariana margin: Hussong, 1981). The serpentinized mantle wedge has long been considered as mostly aseismic due to the presence of weak minerals such as antigorite or talc that are known to substantially reduce rock strength (e.g., Hilairet et al., 2007). Yet, insights gained from detailed studies on the Sumatra 2004 (Mw = 9.1) and Maule 2010 (Mw = 8.8) mega-earthquakes have shown that some of these exceptional rupture events may nucleate or propagate at the base of the "cold nose" region (e.g., Dessa et al., 2009; Wang et al., 2020). This paradox raises important questions regarding the rheology of the partly serpentinized mantle above the subduction interface. The report of slow earthquakes near the seismogenic downdip end of several subduction megathrusts also changed our vision regarding stress distribution along the deep interface (e.g., Fu and Freymueller, 2013; Frank et al., 2015; Audet and Kim, 2016), with potential implications for mega-earthquake prediction (Obara and Kato, 2016; Bouchon et al., 2018). Whereas it is now accepted that fluids dramatically impact the mechanical stability of the deep serpentinized interface, very little in situ information is known about fluid-rock interaction processes or the feedback between upward transported fluids and seismicity (e.g., Angiboust et al., 2014; Locatelli et al., 2018).

Over the last decade, an increasing number of high-resolution seismological studies have identified the presence of seismicity nests in the partly serpentinized mantle wedge (e.g., Halpaap et al., 2019 and references therein). These events are generally interpreted as mechanically related to the influx of fluids or melts between 30 and 70 km depth (e.g., Davey and Ristau, 2011). A majority of the clusters identified in literature concentrates in the first 15 km above the plate interface (e.g., Greece: Halpaap et al., 2019; Japan: Uchida et al., 2010, Nakajima and Uchida, 2018; New Zealand: Davey and Ristau, 2011; Central Chile: Wang et al., 2020; Colombia: Chang et al., 2019) along steeply-dipping, planar features commonly seen as "vent-like" structures, apparently channelizing plate-interface fluids towards the inner wedge. Normal, strike-slip and thrust focal mechanisms are reported for a large majority of these supra-slab earthquakes, with magnitudes generally spanning a range between 2 and 5 (e.g., Halpaap et al., 2019). The physics of the rupture and the nature of the material where these earthquakes are nested remain unknown. Moreover, the source and the composition of the fluids passing through these networks is also a matter of discussion since the precise location of

hydrous mineral breakdown reactions strongly depends on the subduction thermal structure (e.g., Hermann et al., 2006; Syracuse et al., 2010).

Natural mantle wedge samples, despite their scarcity worldwide, represent a unique opportunity to shed light on these deep-seated processes (e.g., Kepezhinskas et al., 1995; Horn et al., 2020). Jadeitites are known to represent fossilized fluid pathways from the base of the hydrated mantle wedge (Harlow and Sorensen, 2005; Harlow et al., 2015). From this perspective, they may provide insights on the physical nature of supra-slab seismic events. However, primary structures from jadeitite-bearing localities have been almost systematically overprinted during long-term subduction, extensive serpentinization and exhumation (e.g., Central America: Flores et al., 2015; Kawamoto et al., 2018; Myanmar: Shi et al., 2009a; Japan: Morishita et al., 2007). In the Polar Urals (Russia), the Pus'yerka locality exhibits a relatively undisturbed contact between a jadeitite "dyke" network and its ultramafic host (e.g., Meng et al., 2011; Angiboust et al., 2021), thus providing an opportunity to identify deformation processes rooted in these jadeitite bodies. Through a combined petrological, microstructural and geochemical investigation of Polar Urals samples, we provide new evidence for brittle-ductile switches in jadeitites (and associated amphibole-phlogopite granofels) microstructures. These structures are compared with those from samples of loose jadeitite boulders from Myanmar and Guatemala, settings where pristine structures are only exceptionally exposed (e.g., Sorensen et al., 2010). We then evaluate their potential meaning in terms of fluid pathways and the genesis of seismic instabilities in the basal region of active mantle wedges.

2. Geological setting

2.1. Pus'yerka jadeitite deposit (Polar Urals, Russia)

The Polar Urals belt formed during closure of the Uralian ocean by subduction and by the eastward burial of the European continental margin under an oceanic volcanic arc (e.g., Savelieva et al., 2002). In the Polar Urals, the Main Ural Thrust (MUT; Fig. 1a) corresponds to a major crustal-scale shear zone with peridotites that were thrust over eclogitized continental crust (Marun-Keu complex; e.g., Udovkina, 1971; Dobretsov and Sobolev, 1984; Glodny et al., 2003). Rare ophiolitic, blueschist-facies m´elange exposures are restricted to the base of the MUT (e.g., Kazak et al., 1976). Locally, the MUT has been subject to moderate reactivation as a detachment fault during exhumation (e.g., Sychev and Kulikova, 2012). In the Polar Urals, three peridotite massifs (the Rai-Iz, Syum-Keu and Voikar massifs) were locally transformed into antigorite-schists along the MUT hangingwall (Fig. 1b). These large mantle exposures, mostly harzburgitic and lherzolitic in composition (Savelieva and Suslov, 2014; Shmelev, 2011), exhibit large chromite deposits and are crosscut by numerous subvertical dunitic channels interpreted as the melt extraction pathways (Batanova et al., 2011). The MUT hanging wall displays (i) a serpentinization gradient towards the underlying unit; (ii) the presence of jadeite ($NaAlSi_2O_6$) veins in the serpentinites from the hanging wall; and (iii) a high pressure–low temperature (HP-LT) metamorphic imprint in the footwall units (e.g., Dobretsov and Ponomareva, 1968; Glodny et al., 2003; Batanova et al., 2011; Shmelev, 2011; Meng et al., 2016). The Rai- Iz, Syum-Keu and Voikar peridotite massifs in the Polar Urals can thus be viewed as good

analogues of a supra-subduction setting, enabling the understanding of deep-seated processes below an inferred Paleozoic island arc (e.g., Batanova et al., 2011; Savelieva et al., 2002, 2016; Angiboust et al., 2021), in a region of the deep subduction interface that is not commonly exhumed (Guillot et al., 2009; Agard et al., 2018).

The studied Pus'yerka exposure is located along a jadeitite-bearing serpentinized shear zone that is several hundred meters thick and 5 km long, striking N-S and dipping E approximately 1 km above the Main Ural Thrust (MUT; Fig. 1b). In a recent study, Angiboust et al. (2021) have interpreted the MUT hanging wall as a rare natural case study highlighting the structure along the base of a subduction mantle wedge. This major jadeitite deposit, discovered and mined in the 1980s (Kuznetsov et al., 1986; Fishman, 2006), represents a unique locality to investigate the structural contacts between the jadeite bodies and its host (e.g., Meng et al., 2011; Angiboust et al., 2021).

The basal serpentinites as well as the jadeitite-bearing network exhibit a regional foliation parallel with the MUT (Fig. 1c). Field, geochemical and density measurements indicate serpentinization ratios in the range of 35–65 vol% (in agreement with the 45–65 vol% estimates from Makeyev, 1992), with up to 90–100% approaching the MUT and within the jadeite-bearing networks (Fig. 1b; Angiboust et al., 2021 and references therein). The serpentinite schists that host the jadeitite boudins are composed of antigorite with minor amounts of brucite, magnetite and phlogopite (Makeyev, 1992) as well as chlorite, tremolite and magnesite. Within the serpentinite shear zone, tens of whitish jadeitite lenses are observed, elongated *en echelon* and stretched parallel to the main foliation dip direction (Fig. 1b). The thickness of these lenses ranges between several tens of centimeters to several meters in the few places where the lenses were observed in situ (e.g., Kuznetsov et al., 1986; Meng et al., 2011).

Ion probe U-Pb dating of zircon crystals from the main jadeitite body yielded U-Pb ages of 404 ± 7 Ma (Meng et al., 2011) and 409 ± 3.3 Ma (Konovalov and Sergeev, 2015). These Devonian ages were interpreted by Meng et al. (2011) as dating intra-oceanic subduction initiation of the Uralian ocean realm. Angiboust et al. (2021) proposed that these jadeitite bodies derive from the metasomatic replacement of a former trondhjemitic dyke that crystallized from slab-derived melts within an ultramafic mantle wedge setting, in a subduction initiation context (i.e., at a temperature regime much higher than expected in a long-lived subduction context; e.g., Soret et al., 2016 and references therein). Ar- Ar plateau ages and multi-mineral Rb-Sr dating yield ages for phlogopite and amphibole-bearing domains ranging from 410 to 395 Ma, interpreted by Angiboust et al. (2021), in line with the pioneering study of Dobretsov and Ponomareva (1968), as marking the re-equilibration of dyke material during secular cooling from supra-solidus to HP-LT conditions (i.e., from $T > 700$ ◦C to $T < 500$ ◦C for a pressure on the order of 1.5 GPa). The studied samples were collected in the main jadeitite “dyke” (Fig. 1b, e).

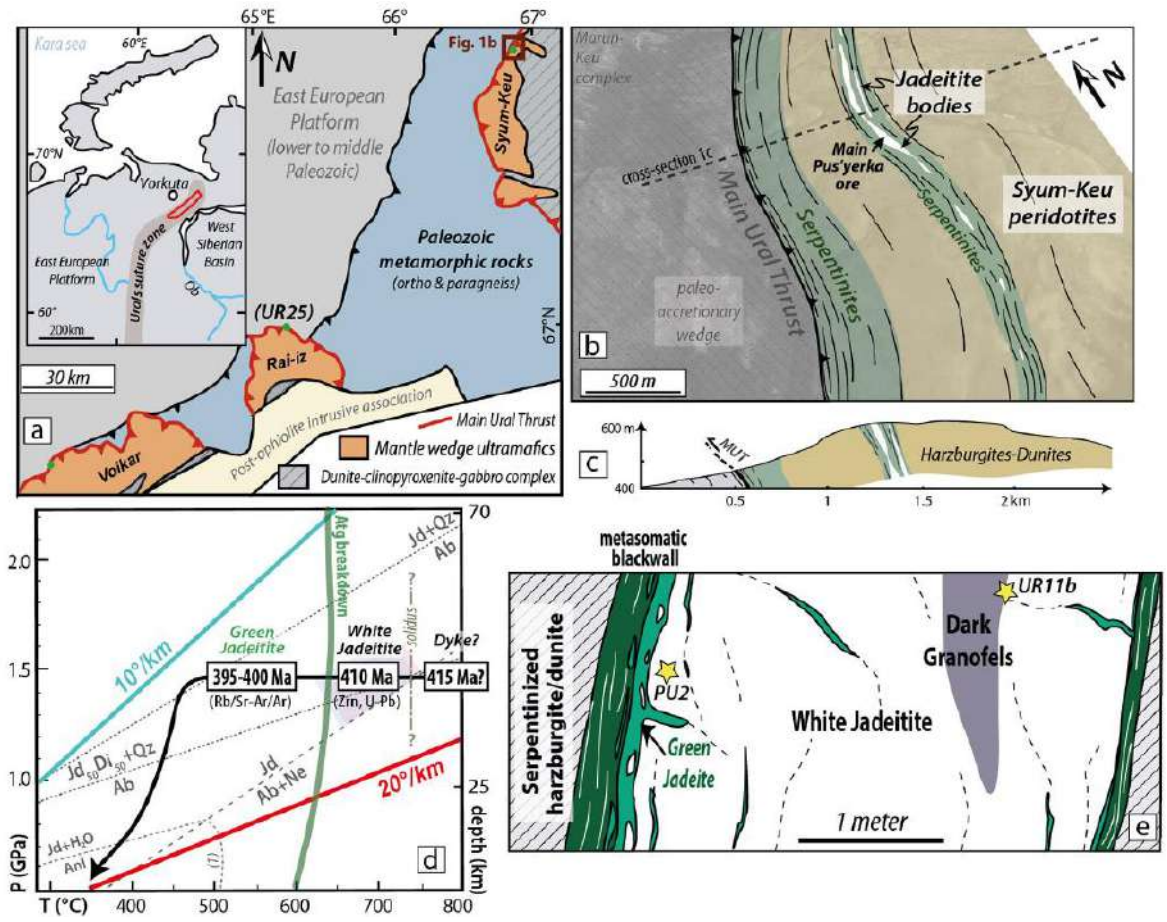

***Fig. 1**. a. Simplified geological map of the Polar Urals locating the three main mantle wedge sections exposed in this region and the study area at the base of the Syum-Keu massif. The inset localizes the Polar Urals in northern Russia. Green dots correspond to jadeitite-bearing localities (modified after Angiboust et al., 2021). b. Geological map showing the structures above the Main Ural Thrust, interpreted as an ancient subduction interface. The studied jadeitite "dyke" crops out as a boudinaged sliver wrapped by a network of sheared serpentinites, approximately 1 km above the Main Ural Thrust. c. Cross-section highlighting the geometry of the structures identified in the field (modified after Angiboust et al., 2021). d. Pressure-Temperature-time sketch summarizing the long-term evolution of the Pus'yerka jadeitite dyke structure (after Angiboust et al., 2021). $Jd_{50}Di_{50}$ reaction line is after Maruyama and Liou (1988). Reaction (1): Analcime = Albite + Nepheline. e. Schematic view of the white jadeitite "dyke" as observed in situ in the Polar Urals with dismembered patches of dark granofels and dark amphibole-phlogopite bearing blackwalls forming at the contact with the host serpentinized ultramafic rocks. Mineral abbreviations after Whitney and Evans (2010). (For interpretation of the references to colour in this figure legend, the reader is referred to the web version of this article.)*

2.2. Kashin state Jade Mines Belt (Northern Myanmar)

One of the world's largest jadeitite-bearing suture zones is exposed in the Kashin state of Myanmar in the famous Jade Mines Belt (e.g., Shi et al., 2012; Nyunt et al., 2017), where loose jadeitite fragments are found in conglomerates, river beds or exceptionally embedded within strongly-weathered antigorite schists (e.g., Harlow et al., 2015 and references therein; Ridd et al., 2019). The original jadeitite-bearing structures (likely ancient felsic dykes; e.g., Bleek, 1908) were formed within a serpentinized mantle wedge from a subduction zone of debated Late Jurassic to Late Cretaceous

age (Goff´e et al., 2002; Shi et al., 2009a, 2012; Yui et al., 2013; Harlow et al., 2016). These metasomatized dykes were extensively affected by exhumation and subsequent strike-slip deformation related to the Sagaing transform fault system (Harlow et al., 2015; Searle et al., 2007; Ridd et al., 2019). Protracted deformation led to the formation of a serpentinite m´elange in which jadeitite "dykes" and blocks were disrupted and disseminated in the antigorite schist matrix, together with other lenses of seafloor origin such as graphite schists, glaucophane schists, garnet amphibolites and garnet micaschists (Nyunt et al., 2017).

Although the original thickness of the jadeitite "dykes" is challenging to evaluate due to poor exposure conditions and late deformation, some studies mention typical thicknesses on the order of several meters (Shi et al., 2012; Harlow et al., 2015 and references therein), in line with the structures observed in situ in the Polar Urals (Fig. 1e). Texturally secondary chlorite schists ("blackwalls") as well as albitite bands are reported at the contact between the dyke structure and the host (Bleek, 1908; Chhiber, 1934). Na-amphibole-rich bands (mostly eckermannite and glaucophane; see Oberti et al., 2015 for further details on mineralogy) are also found either embedded within the jadeitite "dyke" or lining the contact with the ultramafic host (Bleek, 1908; Nyunt, 2009). Most pressure-temperature estimates for jadeitite formation in the Jade Mine Belt region span a wide range from 1.0–1.5 GPa and 300–500 ◦C (Mével and Kienast, 1986; Goff´e et al., 2002; Shi et al., 2003). The herein studied samples, provided by a local miner, were found as boulders in a conglomerate near the Lonkin township (near Hpakan).

2.3. Motagua fault zone (Guatemala)

The Guatemala suture zone is an E-W-trending major plate boundary zone that separates the Caribbean and North American plates. This strike-slip suture, which puts in contact the Maya block to the north with the Chortis block to the south (e.g., Ortega-Gutiérrez et al., 2007 and references therein), contains many mafic and ultramafic blocks as well as eclogite-, blueschist- and garnet amphibolite-facies crustal and sedimentary fragments interpreted as remnants from a Cretaceous meta-ophiolite (e.g., Brueckner et al., 2009). The Motagua fault zone separates two distinct terranes likely exhumed during two distinct collisional events: the North Motagua and the South Motagua mélanges (e.g., Beccaluva et al., 1995; Gendron et al., 2002; Harlow et al., 2004; Harlow et al., 2011). Different metamorphic ages on jadeitites and eclogites were reported for these two terranes, ranging from c. 100–60 Ma for the North Motagua and c. 160–110 Ma for the South Motagua mélanges (see Flores et al., 2013 and references therein). The highest-pressure rocks from these two mélanges are also slightly different, with 500–650 ◦C and 1.5–2.3 GPa for the North Motagua mélange (Harlow et al., 2008; Tsujimori et al., 2004) and 470–520 ◦C and 2.0–2.7 GPa (Tsujimori et al., 2006; Endo et al., 2012) for the South Motagua mélange.

Jadeitites occur as meter-sized blocks within the serpentinite mélanges but are most commonly found as pebbles within streams or as loose blocks in slope debris. As for the Jade Mines Belt in Myanmar, pristine tectonic relationships are extremely difficult to document. The mineralogy of jadeitites is

quite varied in terms of minerals and mineral abundances, and with contrasting assemblages in the north and south Motagua mélanges (Harlow et al., 2011; Flores et al., 2013). The herein studied samples were collected as loose boulders in streams from the southern Motagua mélange (Rio El Tambor area) and contain essentially jadeite plus minor omphacite and lawsonite, in agreement with the mineralogy of jadeitites from this mélange (Harlow et al., 2011).

3. Analytical methods

3.1. Electron probe microanalysis

Mineral compositions were quantified via electron probe microanalysis (EPMA) using a Cameca SXFive operated in the CAMPARIS analytical facility at Paris University. Standard analytical conditions (15 keV, 10 nA, beam diameter 5 μm) and a set of synthetic and natural crystals for calibration standards were used: Fe_2O_3 (Fe), MnTiO3 (Mn, Ti), diopside (Mg, Si), CaF_2 (F), orthoclase (Al, K), anorthite (Ca) and albite (Na). X-ray maps were acquired on the same instrument using analytical conditions of 15 keV, 250 nA, a dwell time of 60 milliseconds and a step size of 2 μm. Some of the X-ray images were processed and quantified with DWImager software (Torres-Roldan et al., 2000; see García-Casco, 2007). A scanning electron microscope (SEM) Zeiss EVO MA10 at the Institut de Physique du Globe de Paris using internal calibration standards was used for microscopic investigations, energy dispersive X-ray spectral (EDS) mapping and surface composition characterizations. Mineral abbreviations are from Whitney and Evans (2010). Clinopyroxene and clinoamphibole compositions, including estimation of Fe^{3+}, are calculated according to the schemes of Morimoto (1989) and Hawthorne and Oberti (2007), respectively. Classification of these minerals also follows the same authors.

3.2. Laser ablation inductively coupled plasma mass spectrometry

Laser Ablation Inductively Coupled Plasma Mass Spectrometry (LA-ICP-MS) trace element maps were acquired using a Resonetics M-50-LR 193 nm excimer laser coupled to an Agilent 7700× Quadrupole ICP-MS housed at Adelaide Microscopy, University of Adelaide. Instrument conditions and mapping protocols similar to that employed in this study are outlined in Raimondo et al. (2017). Pre-ablation of each raster scan was completed to minimize the effect of redeposition (19 μm, 75% overlap), followed by 15 s washout and 10 s of background measurement. A beam diameter of 19 μm, line spacing of 19 μm and repetition rate of 10 Hz were employed for sample PU2, resulting in an energy density of 3.5 J/cm^2 at the target. Standards were analyzed in duplicate every 2 h during the mapping session, including reference glasses NIST 610 (Pearce et al., 1997; Jochum et al., 2011a) and GSD-1D (Jochum et al., 2011b). A beam diameter of 51 μm was used for all standard analyses, and included 5 pre-ablation shots (51 μm, 75% overlap) followed by 20 s washout, 30 s background measurement and 40 s ablation time. Data acquisition was performed in time-resolved analysis mode as a single continuous experiment. Each analysis comprised a suite of 38 elements, and dwell times were as follows: 0.01 s (Li), 0.002 s (Na, Mg, Al, Si, K, Ca, Mn, Fe, Ni), 0.005 s (Sc, Ti, V, Cr, Nb, Ba, Hf, Th, U), and 0.008 s (Sr, Y, Zr, Ta, Pb, REEs). The total sweep time was 0.297 s. Post-

acquisition processing was performed using the software Iolite (Woodhead et al., 2007; Hellstrom et al., 2008; Paton et al., 2011), with data reduction and image processing procedures following those outlined by Raimondo et al. (2017) and Hyppolito et al. (2018).

3.3. Electron Back-Scattered Diffraction and cathodoluminescence mapping

Electron Back Scattered Diffraction mapping (EBSD) has been performed at the Laboratoire de Géologie of the Ecole Normale Supérieure of Paris using a ZEISS SIGMA Field Emission Gun Scanning Electron Microscope equipped with an EDX (Energy Dispersive X-ray Spectroscopy; X-MAX) and an EBSD detector (Nordlys Nano, Oxford Instruments). An acceleration voltage of 15 keV, a beam current of 5 nA, an aperture of 120 μm, an inclination of 70◦, an acquisition rate of 100 Hz, a working distance of 14 mm and a mapping step size of 2.8 μm were the analytical parameters chosen for the mapping. Data acquisition, post-processing treatment and statistical analysis were performed using Aztec, Channel 5 and MTEX software (Bachmann et al., 2010; Bachmann et al., 2011). For noise reduction, every single-pixel isolated data point was removed and followed by denoising MTEX procedures. Cathodoluminescence (CL) mosaic images were acquired using the Cathodyne (NEWTEC) device equipped with a motorized stage, a 12 kV and 120 μA plasma, and 2 s of image acquisition time.

3.4. Field constraints on Polar Urals jadeitite body

In the Pus'yerka locality of the Polar Urals, the ore jadeitite body is mostly formed by a white jadeitite core that represents more than 90% of the “dyke” volume (see schematic dyke structure in Fig. 1e). Locally, remnants of felsic lithologies (comprising an albitite groundmass with paragonite flakes surrounded by a jadeite-bearing corona) were observed, suggesting that the white jadeitite formed by replacement of a leucocratic dyke (see the model in Angiboust et al., 2021; see also Dobretsov and Ponomareva, 1968 and Kuznetsov et al., 1986). The whitish jadeitite-rich domains comprise weakly to strongly foliated opite crystals (sample PU2). These domains, referred hereafter to as dark granofels (sample UR11b), were interpreted by Angiboust et al. (2021) to be produced by the influx of alkali-rich fluids in a warm mantle wedge environment, before the emplacement of the leucocratic dyke. Such amphibole-rich blocks occupying a similar structural position were reported in the Jade Mine Belt area (Myanmar) by Bleek (1908); see also Harlow et al., 2015).

The white jadeitite is transected by centimeter to decimeter-long cracks filled by phlogopite as well as dark-blueish amphibole-rich domains and emerald-green Cr-rich clinopyroxene (Fig. 2a, b). While the bulk of the white jadeitite mass looks at a first sight microstructurally homogeneous, detailed observations highlight numerous locations where structures are brecciated, ranging from crackle- to mosaic-type breccias (e.g., Woodcock and Mort, 2008). Chaotic breccias, where substantial disruption of the original structure occurred, are also observed in jadeitites and associated dark granofels (Fig. 2b). Lastly, centimeter- to decimeter-thick, strongly sheared phlogopite-rich metasomatic rinds are observed along the margins of the jadeitite body at the contact with the host serpentinite (Fig. 1e; see also Kuznetsov et al., 1986 and Angiboust et al., 2021). Further south,

directly below the Rai-Iz peridotite massif, occurs a tectonic m´elange zone ("Nephrite brook", Kazak et al., 1976; Fig. 1a) that contains blocks of nephrite and rare jadeitite within a schistose serpentinite matrix. Sample UR25 represents one of these jadeitite pods, considered to be derived from a former "dyke" structure that has been fully disrupted by late subduction zone tectonic deformation.

The nomenclature used in Table 1 is defined based on the following deformation criteria: Type (I) corresponds to breccias formed by centimeter- to tens of centimeter-sized clasts exhibiting a substantial shearing component, fracturing and size reduction through indentation processes. Such breccias can typically reflect a damage zone deformation pattern. Type (II) brecciated materials are defined as a highly localized fault zone with evidence of pervasive shearing, grain comminution and flow banding, with pulverized wall clasts floating in a fine-grained matrix. Such microstructures are generally known in the vicinity of fault cores and are hereafter termed "foliated cataclasites". Type (III) corresponds to hydraulic breccias with millimeter to centimeter-sized clasts (which may have undergone rotation) cemented by clinopyroxene or amphibole. Space-filling material can be either dendritic, oscillatory, or strained.

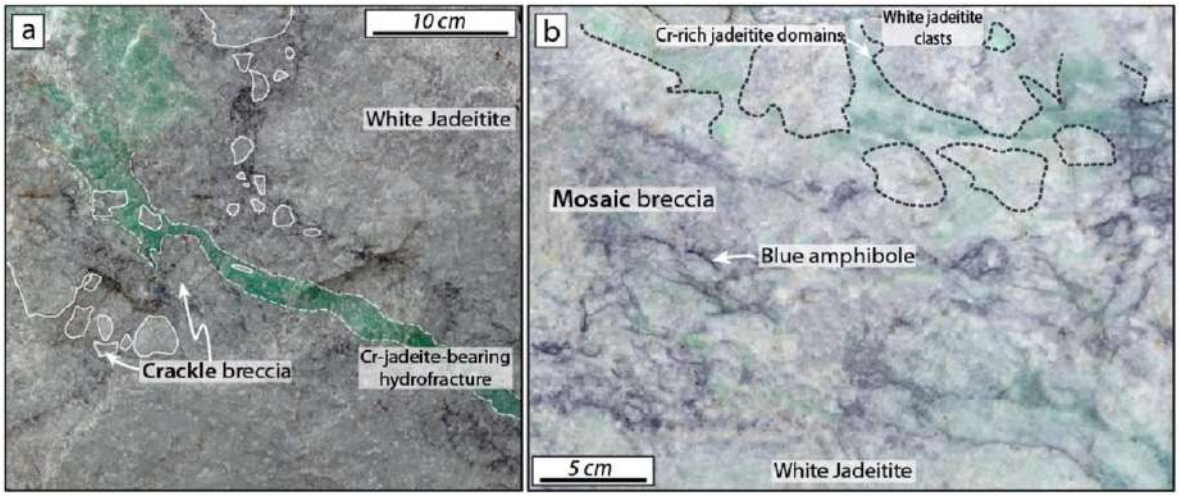

Fig. 2*. a. Field photo of a brecciated white jadeitite block, showing a discrete crackle breccia texture transected by a hydrofracture filled with green Cr- rich jadeite. b. Field photo highlighting the structure of a mosaic breccia, with disrupted white jadeitite fragments cemented by a Cr-rich jadeitic clinopyroxene. (For interpretation of the references to colour in this figure legend, the reader is referred to the web version of this article.)*

3.5. Structure of Polar Urals jadeitites

The bulk of the white jadeitite matrix is formed by idiomorphic, oscillatory and intricate 100–500 μm-long jadeite crystals (Meng et al., 2011). Their outer rims are commonly lined by Ca-rich, omphacitic compositions as well as interstitial phlogopitic micas (Angiboust et al., 2021; Fig. S1; Table 1 and Table S1). Despite an apparently homogeneous macroscopic texture, detailed petrographic investigations reveal that jadeite crystals exhibit widespread fracturing, dissolution and replacement textures (Fig. 3a, b). Vein systems that range in colour from white (jadeite composition) to green (Cr-rich jadeite or Cr-rich omphacite; Fig. 2a) are ubiquitously found crosscutting the host

jadeitite matrix (see also Franz et al., 2014). These veins are filled by idiomorphic to fibrous clinopyroxene crystals with locally oscillatory and/or dendritic textures (Kuznetsov et al., 1986; sample UR03b in Angiboust et al., 2021: Type III). Clinopyroxene crystals from brecciated samples exhibit clear evidence for pressure-solution (as shown by indentation and truncation textures), as well as solution-precipitation with fracture healing and overgrowth by a new (generally more omphacitic) clinopyroxene composition (Fig. 3a,b; Fig. S2).

The studied white jadeitite sample UR03d exhibits coarse-grained, idiomorphic and sector-zoned jadeite crystals in its matrix (Fig. 4a). These crystals, generally extremely rich in jadeitic molecule (>90 mol %), are hereafter referred to as Jd_1. The jadeite growth structures document how early structures have been transected by a localized fine-grained shear zone of oriented jadeite crystals with interstitial omphacite-rich grains. Orientation maps (Fig. 4b) show that [001] axes are dominant along the fine-grained shear zone, whereas [100] and [010] axes become important approaching the margins of the shear band. Intracrystalline misorientation EBSD maps, depicting misorientation angles between each data point and the mean orientation of the parent crystal (Fig. S3), show that grains at the shear zone margins are highly misoriented. In addition, the finer grains within the shear band are consistently devoid of intragranular misorientation except for strongly misoriented larger grains.

We interpret that the strongly misoriented clasts may represent fragmented remnants affected by brittle localized shear followed by dynamic recrystallization, resulting in the ubiquitous lack of misorientation in the surrounding finer-grained material. This pattern is highlighted by microscopic observations and strong crystallographic-preferred orientation (CPO), with [001] axes maxima but also forming a weak girdle along the stretching lineation and the foliation plane, respectively, whereas [010] and [100] display maxima subperpendicular to it (normal to and within the foliation plane, respectively; Fig. 4c). This fabric, similar SL-type tectonites, is reported in many previous omphacite (a mineral rheologically similar to jadeite and diopside) fabrics in eclogites (e.g., Philippot and van Roermund, 1992; Godard and van Roermund, 1995; Keppler et al., 2016), compatible with near-plain strain dislocation creep deformation mechanisms (e.g., Zhang et al., 2006; see also the review paper from Keppler, 2018). In addition, truncation of oscillatory zoning in jadeite crystals from the shear band denotes the contribution of solution-precipitation mechanisms. Thus, the fabrics herein observed indicate that a large part of the material involved in the shear zone (in particular the dark-shaded, fine-grained jadeite rims visible in Fig. 4a) grew syn-kinematically, most likely via crystal-plastic deformation processes coupled with dissolution-precipitation creep.

Table 1
Summary of selected samples for this comparative study, including their paragenesis and the various fracturing patterns identified therein (see text for details on the criteria used for this classification). Numbers in the last three columns refer to the chronological sequence of fracturing events identified in each sample.

	Sample	Region	Pre-fracturing assemblage	Paragenesis associated w/brittle def.	Fracturing pattern		
					Type I	Type II	Type III
Polar Urals	PU2	Pus'yerka	white Jd (Jd_1), Ed	Omp, Mg-ktp, Rct, Eck, Phl, Clc		x (1)	x (2)
	PU5	Pus'yerka	white Jd (Jd_1)	Omp, Phl, Clc (±Cal)		x	
	UR11b	Pus'yerka	Ed or Mg-ktp with Omp inc.	Jd_2, Omp, Mg-ktp, Eck/Nyb, Ttn, Chr	x		
	UR03b,03d	Pus'yerka	white Jd (Jd_1)	Jd_2, Omp			x
	UR25	Nephrite brook	white Jd (Jd_1)	Jd_2, Omp, Ttn	x		
Guatemala	MTG00	Motagua region	white Jd	Omp (not analyzed)	x		
	MTG01	South Motagua	white Jd (Jd_1)	Jd_2, Omp, Lws, Ttn	x		
	MTG02	South Motagua	white Jd (Jd_1)	Jd_2, Omp, Ttn			x
	MTG03	South Motagua	white Jd (Jd_1)	Jd_2, Omp, Ttn (±REE-rich Ep)		x	
	MTG12	South Motagua	white Jd (Jd_1)	Jd_2, Omp, Ttn		x	
Myanmar	KAS01	Hpakan (Kashin)	white Jd (Jd_1)	Jd_2, Omp, Eck	x (1)		x (2)
	KAS04	Hpakan (Kashin)	white Jd (Jd_1)	Jd_2, Omp, Eck, Clc (±Cls)	x (1)	x (2)	x (3)
	KAS06	Hpakan (Kashin)	Ed (+Omp?)	Jd_2, Omp, Rct, Eck	x		
	KAS07	Hpakan (Kashin)	white Jd (Jd1) and Mg-ktp	Jd_2, Omp, Eck, Chr		x (1)	x (2)
	KAS10	Hpakan (Kashin)	white Jd (Jd_1)	Jd_2, Eck		?	

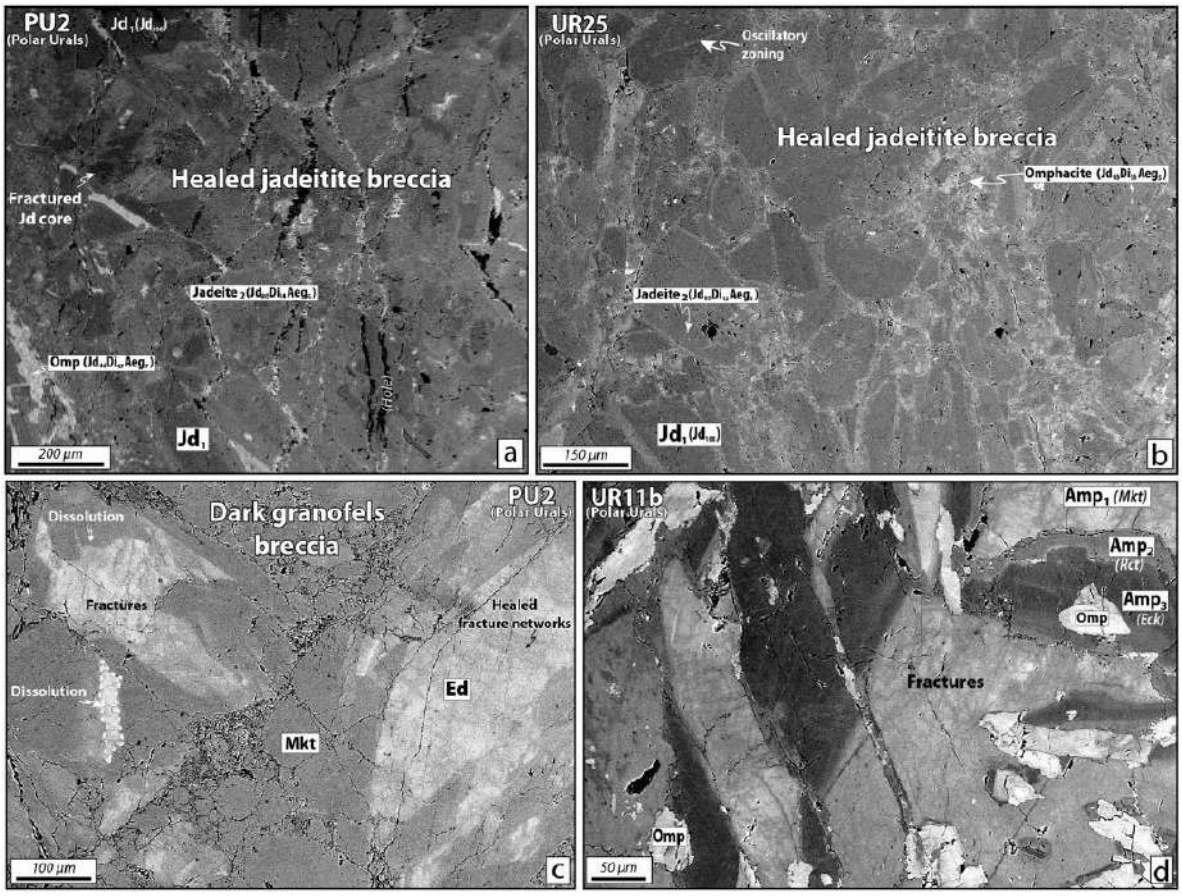

Fig. 3*. Backscattered electron (BSE) images for Polar Urals samples. a. White jadeitite specimen (PU2) showing highly disrupted clasts with evidence for fracturing, dissolution, indentation and re-precipitation. Several clinopyroxene generations can be identified with increasing diopside component towards clast rim. b. Example of a cryptic jadeitite breccia showing extensive fracturing, comminution and dissolution of dark white jadeitite clasts (locally exhibiting oscillatory zoning pattern). Location of sample UR25 given in Fig. 1a. c. Dark, amphibole-rich granofels that is heavily brecciated, with similar dissolution-reprecipitation features as well as extensive healed microfractures (sample PU2). d. Fractures associated with the growth of several amphibole compositions such as richterite (Rct) and eckermannite (Eck) overgrowing magnesio-katophorite (Mkt). Note that omphacite grows lately within a crack in textural equilibrium with Rct and Eck (sample UR11b).*

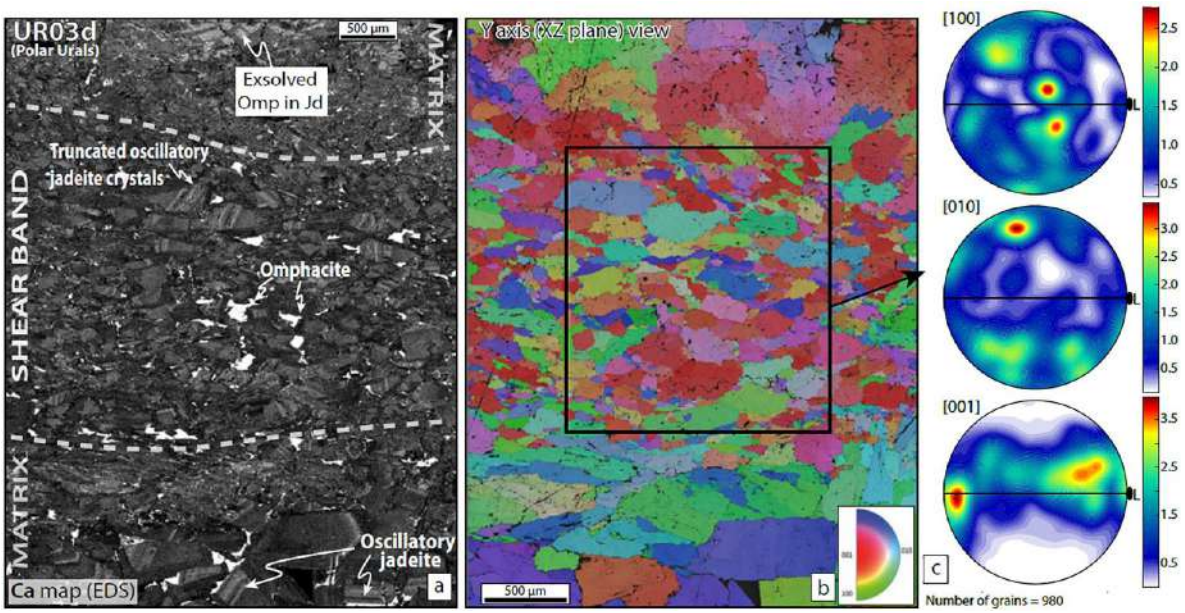

***Fig. 4**. a. EDS X-ray map (counts of Ca, brighter shades indicating greater elemental concentrations) showing the structure of a shear band that transects a white jadeitite sample (PU3) from the Pus'yerka deposit. The coarse-grained oscillatory white Jd_1 crystals are deformed within the shear band into oriented and truncated aggregates of jadeite crystals with local omphacite overgrowths. b. EBSD orientation map colored according to the inverse pole figure key (IPF) of jadeite (bottom right), showing a shape preferred orientation to the X direction of the strain ellipsoid (i.e., stretching orientation). View (XZ plane) corresponding to the Y axis of the finite strain ellipsoid. c. Pole diagrams of jadeite from the shear band (black square in panel b) represented in an upper hemisphere equal-area projection for [100], [010] and [001] crystallographic axes. Contours are multiples of uniform density distributions. The bold dot on the L axis represents the stretching lineation direction (X direction of the strain ellipsoid), and the black line represents the foliation plane.*

4. Texture and mineral chemistry of Polar Urals dark granofels

The dark granofels found within and along the white jadeitite "dykes" from the Pus'yerka locality exhibits striking evidence for ductile and brittle shearing. Coarse idiomorphic calcic to sodic-calcic amphibole cores of edenite ($NaCa_2Mg_5Si_7AlO_{22}(OH)_2$) to Mg-katophorite ($(Na(CaNa)Mg_4AlSi_7AlO_{22}(OH)_2$; *Amp1* brighter Ca-rich cores in BSE imaging mode) form a dense network of dark, sealed fractures as well as indentation and dissolution-precipitation features (Fig. 3c, d). Various mutually overgrowing generations of amphiboles ranging from Mg-katophorite (*Amp2* on Fig. 3d) to sodic amphiboles such as eckermannite ($NaNa_2(Mg_4Al)Si_8O_{22}(OH)_2$; *Amp3*) or richterite ($Na(CaNa)(Mg,Fe)_5Si_8O_{22}(OH)_2$) fill the breccia inter-clast space in apparent textural equilibrium with omphacite (see also Angiboust et al., 2021). In sample PU2, a dark granofels layer is observed (adjacent to a micro-fractured white jadeitite domain), containing oriented sodic-calcic amphibole-phlogopite (±omphacite ± clinochlore) crystals (Fig. 5a). Pervasive grain size reduction occurred through micro-brecciation (Fig. 5b, c, d) followed by further comminution that ultimately led to the formation of anastomosing foliated cataclasite networks (Fig. 5e, f, g; Type II). During (or after) grain size reduction, the large primary amphibole porphyroclasts of edenitic to magnesio-katophoritic compositions (with irregular Cr enrichments; Fig. 5c, g) were re-equilibrated along their

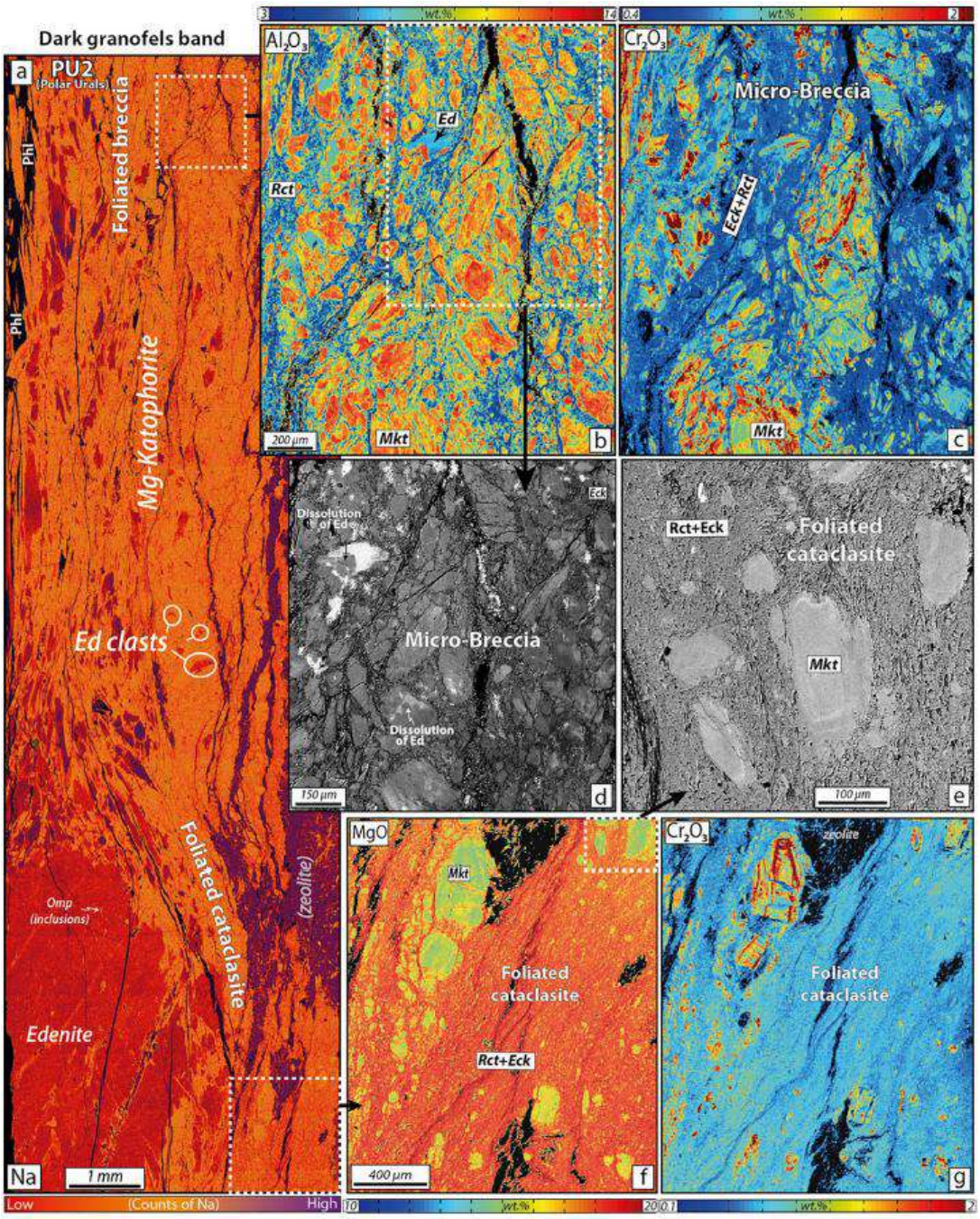

***Fig. 5**. a. EDS X-ray map (counts of Na) showing the internal structure of a shear band crosscutting a dark granofels (sample PU2, Polar Urals). Primary edenite compositions (large clast) are gradually transformed along their rims into Mg-katophorite to richteritic compositions. Remnants of the original edenite clasts are found floating in the Mg-rich domain, associated with oriented phlogopite (Phl) as well as rare omphacite and clinochlore crystals. b and c. EPMA X-ray maps showing a close-up on the foliated, matrix-rich, clast-supported chaotic breccia. d. BSE image showing dissolution features of the primary edenitic amphibole. e. BSE image showing a region of the shear band exhibiting a typical foliated cataclasite texture with Mg-katophorite clasts wrapped in a richterite+eckermannite fine-grained matrix. f and g. EPMA X-ray maps showing the internal structure of the foliated cataclasite as well as the presence of pre-fracturing Cr sector zoning in Mg-katophorite crystals. Some trace element maps for this sample are provided in Fig. S4. Texturally late Na- and Ca-rich zeolites grow as patches and along fractures parallel with the main foliation.*

rims and fractures with very fine-grained pulverized domains with richteritic to eckermannitic compositions (Fig. 5c, f). It thus appears that fracturing and milling occurred after (or during) the formation of Mg-katophorite around the edenitic rims. LA-ICP-MS trace element mapping shows that the Mg-katophorite clasts are enriched in Cr, Nd, Zr and Y, whereas the fine richterite-eckermannite intergrowths are relatively enriched in Li and Ni (see Fig. S4).

An example of Type I mosaic breccia can be seen in Fig. 6a (sample UR11b), where clasts of Mg-katophoritic composition were also heavily affected by multiple fracturing events. Remnants from the most pristine amphiboles lie along the edenite-Mg-katophorite transition (see Table S1 and Fig. S4 for chemical properties). Omphacitic clinopyroxene is very common as inclusions within clast cores as well as along sealed fractures (Fig. 6d). Several generations of Mg-katophorite (with the younger exhibiting increasing Na(B) and decreasing Ca contents; Fig. 6c) can be identified within and around the clasts. Texturally late eckermannite crystals (together with nyboïte: $NaNa_2(Mg_3Al_2)Si_7AlO_{22}(OH)_2$) are found filling the clast's cracks as well as replacing quadrangular inclusions in the cores of the fragments (Fig. 6b; see Angiboust et al., 2021 for details on mineral chemistry). The inter-clast space is filled with fine-grained Mg-katophorite fragments that coexist with zoned clinopyroxene (ranging from jadeite to omphacite in composition; Fig. 6d) as well as micrometer- to tens of micrometer-sized chromian spinel crystals (surrounded by Cr-clinopyroxene; Fig. 6b; Fig. S2). Electron probe mapping demonstrates that the inter-clast domain is relatively enriched in Al, Na, Ca and Cr with respect to the Mg-katophorite clasts (Fig. S5).

LA-ICP-MS trace element mapping of the brecciated region from the dark granofels (UR11b) shows Mg-katophorite cores exhibiting Cr oscillations equivalent to sample PU2 (Fig. 5g), revealing cryptic fractures healed with amphiboles substantially enriched in Zr, Hf, Y, Cr, Li and Ba (Fig. 6e, f, g; Fig. S5). Similar enrichments are distinguished within clinopyroxene-rich fracture-fill material (Fig. S5). Patchy enrichment in Li, Ba, Sr, Y and Ce (among other elements) is also visible in the amphibole-clinopyroxene inter-clast domain (see Fig. S5 for further maps as well as normalized trace-element spider diagrams).

4.1. Deformation and mineral chemistry of Motagua (Guatemala) jadeitite breccias

Macroscopic evidence for brecciation of the Motagua region jadeitites is widespread in the studied samples (see also Harlow et al., 2011 and references therein). Three types of deformation patterns were observed: (i) deep green fractures crosscutting white jadeitites (Type I, Fig. 7a, b); (ii) finely comminuted foliated breccia and cataclastic patterns (Type II, Fig. 7e); and (iii) hydraulic-like breccias where millimeter- to centimeter-sized angular clasts are infiltrated by a fibrous, oriented jadeitite (bluish) cement (Type III, Fig. 7c, d; see below). Whereas the clasts forming the breccias are systematically whitish to light-greenish along their rims, the fracture- and breccia-filling material is always darker, ranging from dark green (Fig. 7a, b) to deep blue (Fig. 7c, d, e). The inter-clast domain filling these breccias is always enriched in Ca, Mg and Fe and depleted in Na and Al, as a consequence of omphacite growth. The replacement of the original jadeite (Jd_1, of near pure jadeite composition)

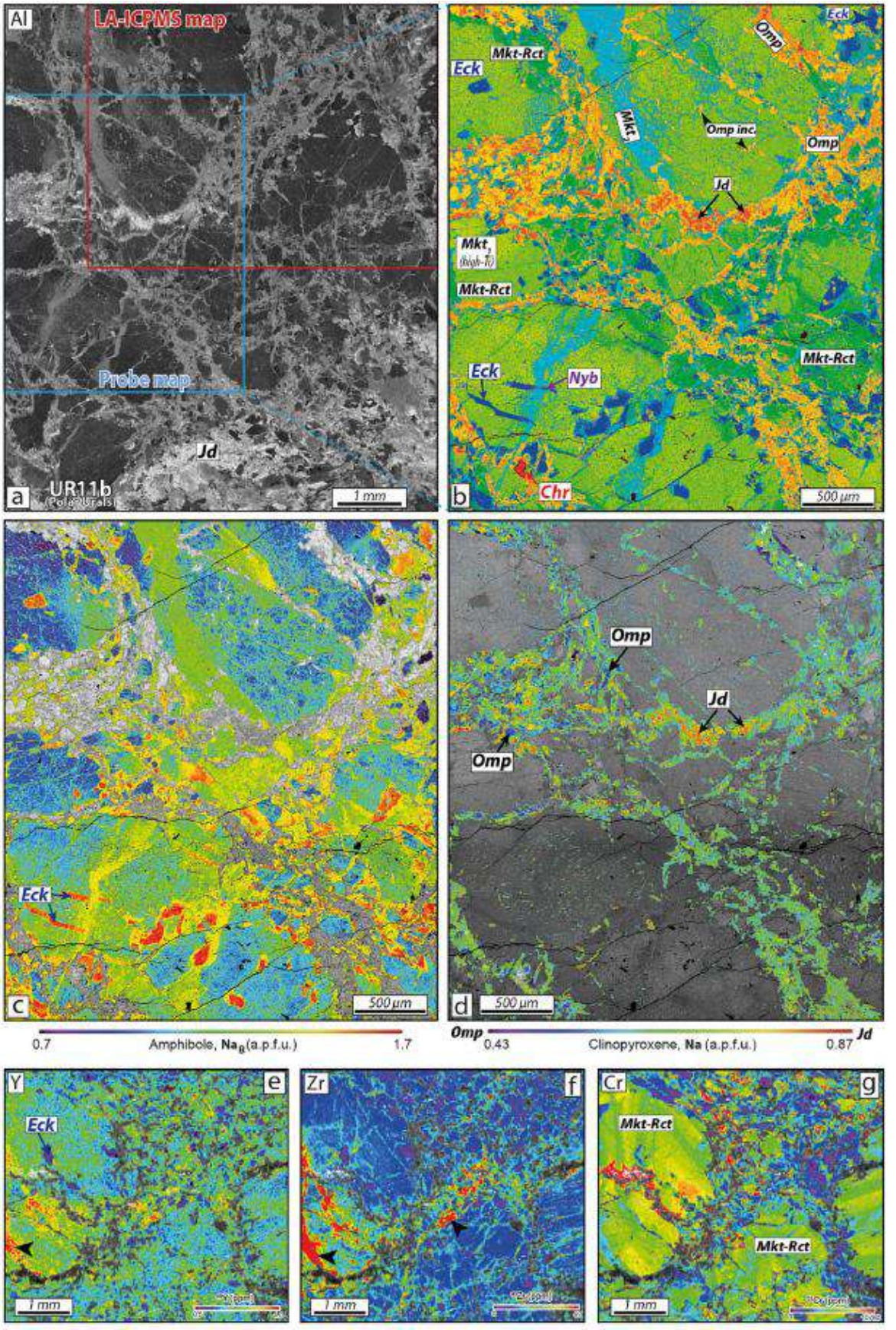
Al
LA-ICPMS map
Probe map
Jd
a
UR11b
1 mm
b
Eck
Omp
Mkt-Rct
Eck
Mkt2
Omp inc.
Omp
Jd
Mkt2 (high-Ti)
Mkt-Rct
Mkt-Rct
Eck
Nyb
Chr
500 µm
Eck
c
500 µm
Omp
Jd
Omp
d
500 µm
0.7
Amphibole, Na_B (a.p.f.u.)
1.7
Omp
0.43
Clinopyroxene, Na (a.p.f.u.)
0.87
Jd
Y
e
Eck
1 mm
Zr
f
1 mm
Cr
g
Mkt-Rct
Mkt-Rct
1 mm

Fig. 6*. a. EDS X-ray map (counts of Al, brighter shades indicating greater elemental concentrations) depicting the chaotic breccia texture with the various healed fracture networks, as well as the location of both LA-ICP-MS and electron probe maps (sample UR11b, Polar Urals). b. EPMA-based masked phase map showing the various Mg-katophorite generations (green), eckermannite (blue) and nyboïte (violet). Omphacite is in light yellow shades, jadeite in deep orange and chromite (Chr) in red. Note how the various fracture generations are mutually overprinting. c. Amphibole masked map showing the Na(B) content. Increasing Na(B) is commonly viewed as reflecting a decreasing P/T ratio (closer to HP-LT conditions). d. Masked map of Na content in clinopyroxene showing two distinct compositions in the breccia-filling material. e, f and g. LA-ICP-MS masked trace element maps (amphiboles only) showing Y, Zr and Cr concentrations (in ppm). The full analytical dataset is given in Fig. S5. Black arrows indicate Zr and Y enrichments in the healed fractures and in the inter-clast matrix. (For interpretation of the references to colour in this figure legend, the reader is referred to the web version of this article.)*

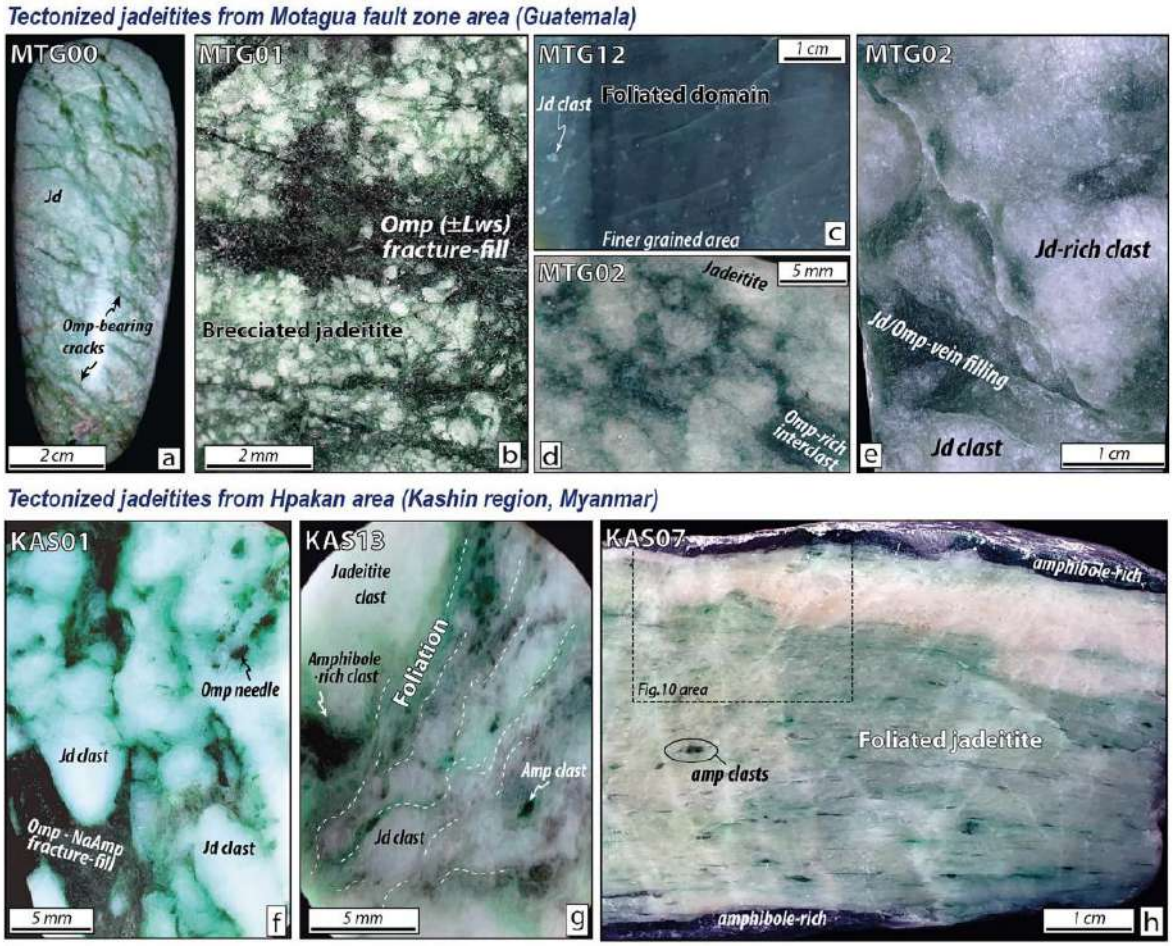

Fig. 7. a. Polished axe carved in a Motagua fault zone jadeitite. This artefact has been found in El Manati excavation (Olmec civilization, 2500–500 B·C; Veracruz state, Mexico; length: 105 mm, weight 189.5 g, density 3.24). It shows numerous omphacite-bearing fractures characteristic of a nearby fault zone system (Type I). Courtesy of F. Gendron (MNHN, Paris). b. Polished rock slab showing numerous white jadeitite domains rimmed by a dark-green omphacitic clinopyroxene. This sample is cut by a fracture that exhibits fibrous omphacite crystals as well as rare lawsonite crystals. c. Type II jadeitite sample showing the host that is transected by a foliated domain comprising white jadeitite clasts. d. Jadeitite breccia (Type III) with clasts fractured and healed by a blueish omphacite. e. Jadeitite breccia (Type III) with clasts pervasively fractured and partly recrystallized along their rims by a secondary, greyish jadeite composition, and later cemented by a deep blue ('Olmec') jadeite composition. f. White jadeitite clasts forming a breccia texture with Cr-enrichments along their rims and cemented by fibrous sodic clinopyroxenes (Type III). g. Moderately foliated breccia

showing intermixed dark amphibole-rich clasts and white jadeitite clasts. h. Strongly foliated white jadeitite matrix in between two foliated dark granofels bands (Type II). Note the large amount of blue amphibole clasts wrapped in the main clear foliation. The white boudin corresponds to a remnant of the pre-deformation pure jadeitite (Jd_1). (For interpretation of the references to colour in this figure legend, the reader is referred to the web version of this article.)

by a secondary clinopyroxene (Jd_2, commonly slightly poorer in jadeite molecule ($80 < Jd_2 < 90$ mol%) and *Omp*) is pervasive, affecting the entire breccia and not only the clast margins (Fig. 8a, b). Fracture-filling clinopyroxene exhibits feather-like omphacitic crystals (Fig. S2) as well as a texturally strained appearance (Fig. 8a). The Mg EDS map in Fig. 8a shows relict white jadeitite clast cores (also visible on the hand specimen image in Fig. 7e) affected by pervasive re-equilibration (dissolution-precipitation) by Ca-rich jadeite and omphacite compositions along crystal joints, fractures, grain boundaries and micro-faults.

In Type II fault rocks, a centimeter-thick layering with variable shades of blue-grey (Fig. 7c) is observed transecting the original white jadeitite (Fig. 9a). Pale, clast-like patches (of pure jadeite composition) are macroscopically visible both in the host jadeitite as well as within the deep blue layers (see Table S1 for representative mineral compositions). Microscopically, the bands are composed of very fine-grained (5–15 μm on average diameter) jadeitite fragments cemented by omphacite-rich compositions in interstitial positions (Fig. 9b, c, d, g). Interestingly, this apparently pulverized domain also hosts "shard-like" features ranging in size from several tens to hundreds of microns (Fig. 9e,f,g). These shards (locally showing ptygmatic folds and contortion) define a weak lamination, resembling the "fiamme" textures known in ignimbrites and other pyroclastic flow deposits. Many of these shards display a fibro-radial intergrowth of jadeite and omphacite fibers that evoke the textures reported in spherulites formed after the devitrification of a former glass (Fig. 9g). SEM-based surface estimates of these shards yield compositions ranging between those measured for jadeite and omphacite crystals (Fig. 9c, h). The shard-bearing fault zone domain shown in Fig. 9b is transected by a dark, very fine-grained omphacitite band that seems connected with the network of omphacite-bearing hydrofractures that transect the rock volume. Remnants from foliated fragments of the host (namely the white jadeitite Jd_1 but also the foliated shard-bearing domain) are observed, strongly dissolved, within this omphacitite band. A metasomatic reaction front also appears to have formed at the contact between these two domains (Fig. 9b).

5. Deformation and mineral chemistry of Hpakan (Myanmar) jadeitite breccias

Further evidence for brecciation of jadeitites can be obtained observing the hand specimens from Myanmar shown in Fig. 7f, g and h. These samples exhibit the most complex sequence of mutually crosscutting brittle events (Table 1). In Fig. 7f, white (and slightly rounded) jadeitite clasts are rimmed by omphacite (light green domains) and wrapped by dark blue amphibole (eckermannite)-clinopyroxene intergrowths (Fig. 8b). The pristine jadeitic pyroxene composition (Jd_1) is only preserved as islands in the middle of a brighter (in BSE) more omphacitic pyroxene (Jd_2 and Omp; Fig. 8c). In sample KAS10, dissolved cores exhibiting exsolution features can also be observed, with two pyroxenes forming at the expense of a former one (Fig. S2). Jd_1 seems to have been replaced

along grain boundaries by a fluid that triggered pervasive re-equilibration (mixed Type I and Type III deformation). In other samples, the same meso-scale structure exhibits a weak, omphacite-rich foliation wrapping remnants of the white jadeitite and dismembered amphibole-rich fragments (Fig. 7g). This texture suggests that viscous flow may occasionally overprint previously formed brittle (Type I) brecciated zones.

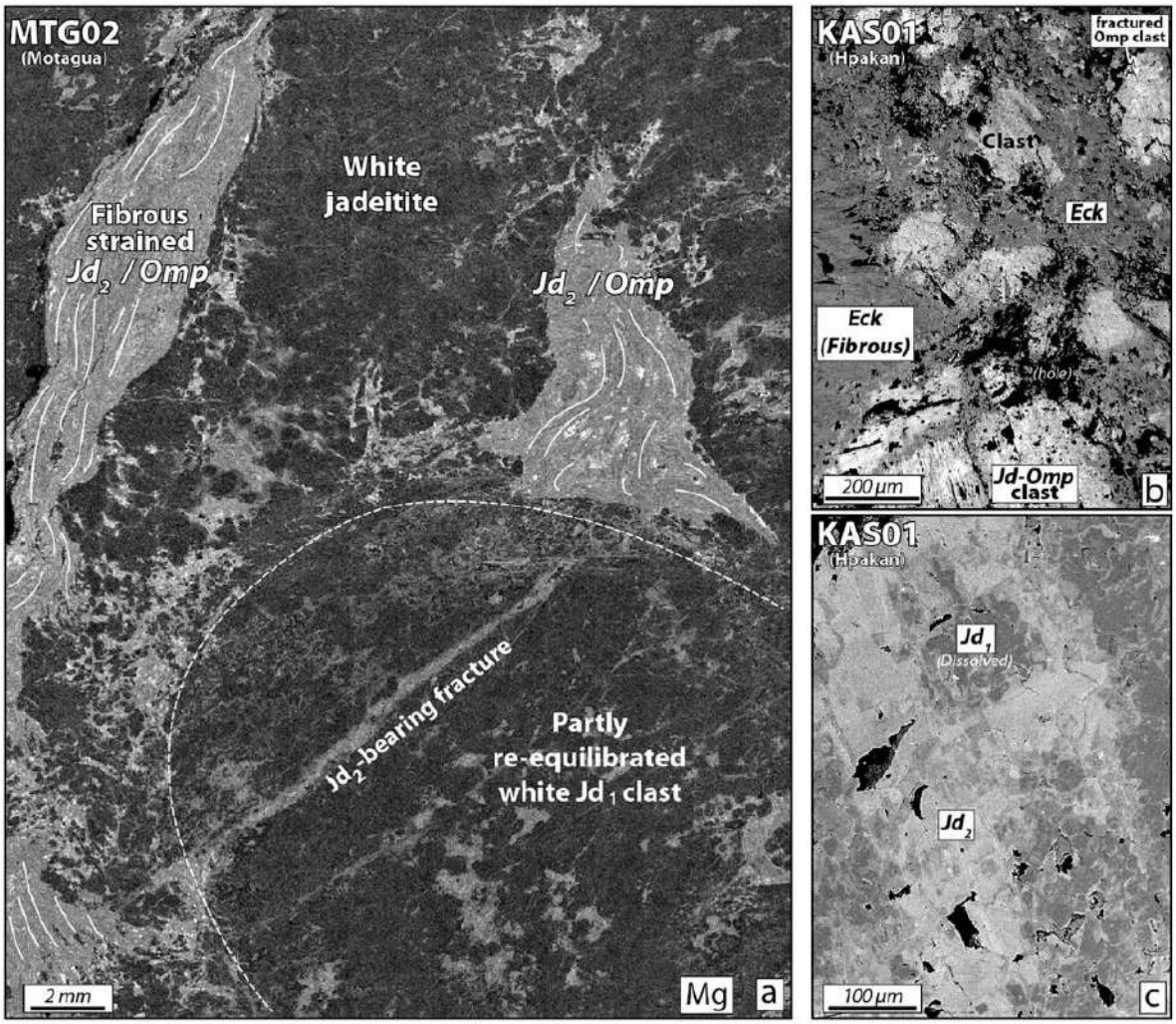

Fig. 8*. a. EDS X-ray map (counts of Mg, brighter shades indicating greater elemental concentrations) depicting a Type III hydraulic breccia texture with fibrous clinopyroxene fills (see Fig. S2 for further images; Motagua region, Guatemala). Note how the Jd_1 clasts are corroded and replaced by a secondary jadeite (richer in omphacitic component) along grain boundaries, micro-fractures as well as inside the clasts. b. BSE image of a brecciated jadeitite with fibrous eckermannite (sodic amphibole) infills (Myanmar). c. BSE image showing dissolved primary Jd_1 generation (nearly Jd_{100}) replaced by a secondary Jd_2 composition (slightly more enriched in omphacite).*

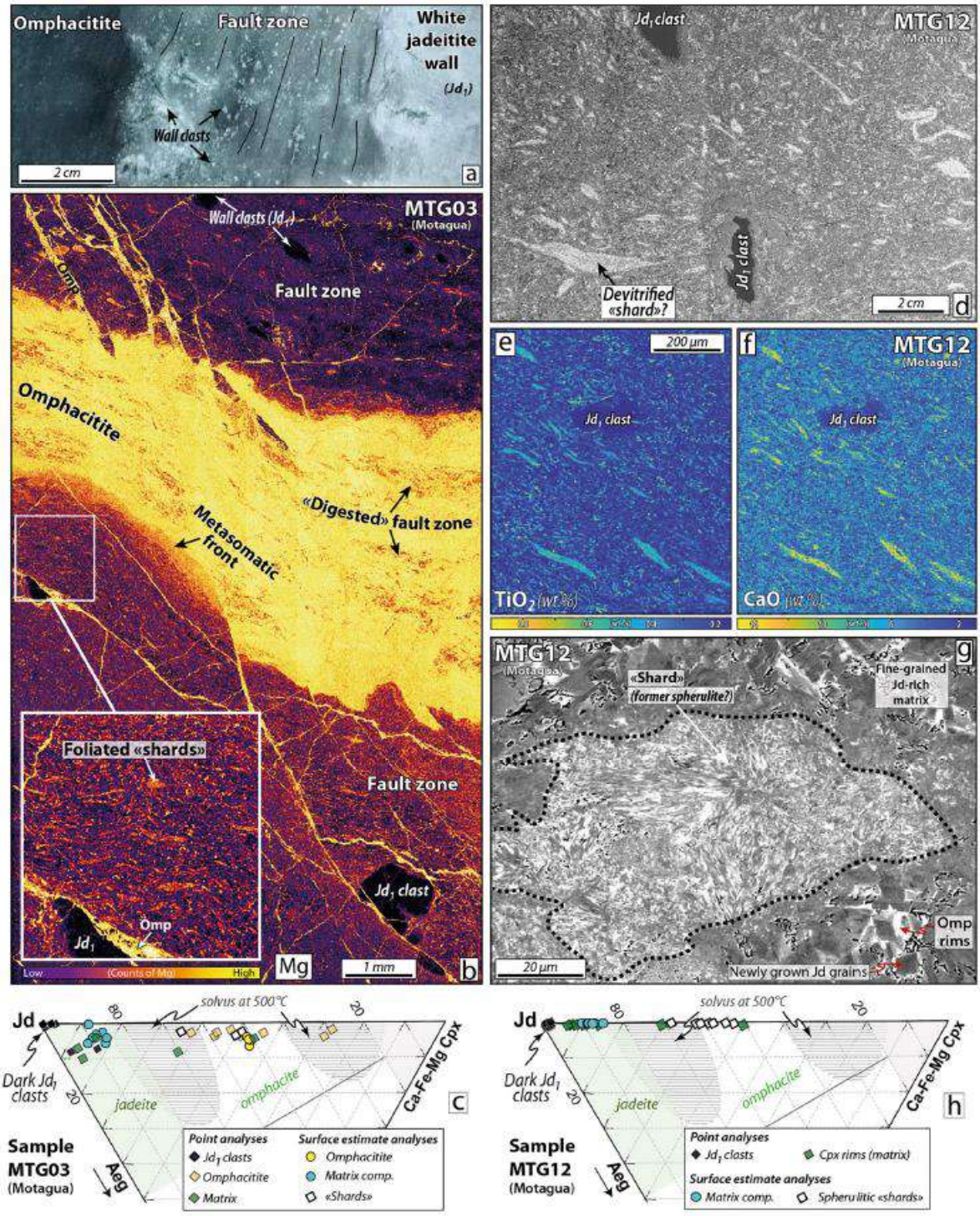

***Fig. 9**. a. Hand specimen image of a Motagua jadeitite showing deformation features of the pristine white jadeitite on the right, the foliated clast-bearing domain in the center (Type II texture) and a secondary omphacitite band on the left. b. EDS X-ray map (counts of Mg) depicting a Type II matrix hosting white jadeitite clasts (in black), foliated "shards" as well as late omphacite-bearing hydrofracture networks. c. Clinopyroxene composition in the Jd-Di-Aeg triangle (after Morimoto, 1989; MTG03). Solvus domains for clinopyroxene are derived from García-Casco et al. (2009). d. BSE image showing the typical appearance of a Type II foliated cataclasite matrix where shards and partly re-equilibrated white jadeitite clasts*

coexist. Note how the shards are randomly folded but yet define a mild foliation. e and f. Quantified EPMA X-ray maps of TiO_2 and CaO contents (in wt%) showing elemental distributions in a clast and shard-bearing, Type II foliated cataclastic matrix. g. High-magnification BSE image showing a shard that exhibits a fibro-radial internal structure that evokes devitrification spherulites. Note how the finely-comminuted clasts forming the pulverized matrix were overgrown by a new (locally facetted) omphacitic clinopyroxene composition during fault consolidation and fluid-enhanced sealing. h. Clinopyroxene composition in the Jd-Di-Aeg triangle (sample MTG12). Note how shards are systematically enriched in omphacitic content.

Sample KAS07 displays a whitish, foliated band separating two dark granofels domains (Fig. 7h). The leucocratic band comprises small, flattened dark amphibole fragments oriented parallel with the main foliation (Fig. 10a), as well as green trails characteristic of Cr-bearing omphacitic clinopyroxenes. A cathodoluminescence image (Fig. 10b) of the whitish domain reveals the presence of three distinct jadeite-forming events in a Type II pattern deformation zone. The first is a green-colored aggregate (*Jd_1;* white jadeite: $Jd_{91}Quad_5Aeg_4$ on average) wrapped within a pink-colored foliated band (mostly *Jd_2*) that hosts numerous angular, green-shaded fragments clearly derived from the green *Jd_1* aggregate on the left of the image (Fig. 10b). These green clasts range in size from several tens to hundreds of microns, and display widespread evidence of fracturing, dissolution and re-precipitation/ overgrowth by a brighter, slightly more omphacitic composition (see for example Fig. 10c; $Jd_{84}Quad_6Aeg_{10}$ on average). This fabric evokes a deformation by micro-fracturing, with substantial comminution accompanied with shearing and flow banding of the pink cataclastic domain.

In the same sample, an eckermannite-filled extensional vein (Type III) is observed crosscutting at low angles the foliated cataclastic domain (Fig. S2). A late pure jadeite formation event (*Jd_3*, in purple on Fig. 10b) also occurs as foliation parallel bands, as patchy domains in the green-colored *Jd_1 augen* on the left of the image, as well as filling late cracks that crosscut all previous features. Sheared amphibole fragments (mostly eckermannite) appear dark in the cathodoluminescence image in the main foliated area (Fig. 10b). BSE imaging and composition analysis reveal that the amphibole-rich band from the left part of this thin section (Fig. 10a) locally contains Mg-katophorite cores rimmed by eckermannite or nyboïte compositions (see Table S1 for representative mineral compositions). This brecciated amphibole-rich domain (likely a former Type I) has been cemented by a clinopyroxene-Na-amphibole mixture and foliated parallel to the adjacent foliated cataclasite domain (Figs. 7h, 10b). A striking feature of this dark domain is the systematic decrease of Ca content in amphibole from the cores (Mg-katophorite; 7 wt% CaO) to the foliated matrix, where amphiboles are extremely enriched in Na2O (>11 wt%) and depleted in CaO (<1.5 wt %). Similar observations were made in sample KAS06 where cores are edenitic (up to 10 wt% CaO), whereas crystals lining the foliation correspond to eckermannite, also closely associated with strained jadeite crystals (see Fig. S2 for EDS mapping and further details on mineral chemistry).

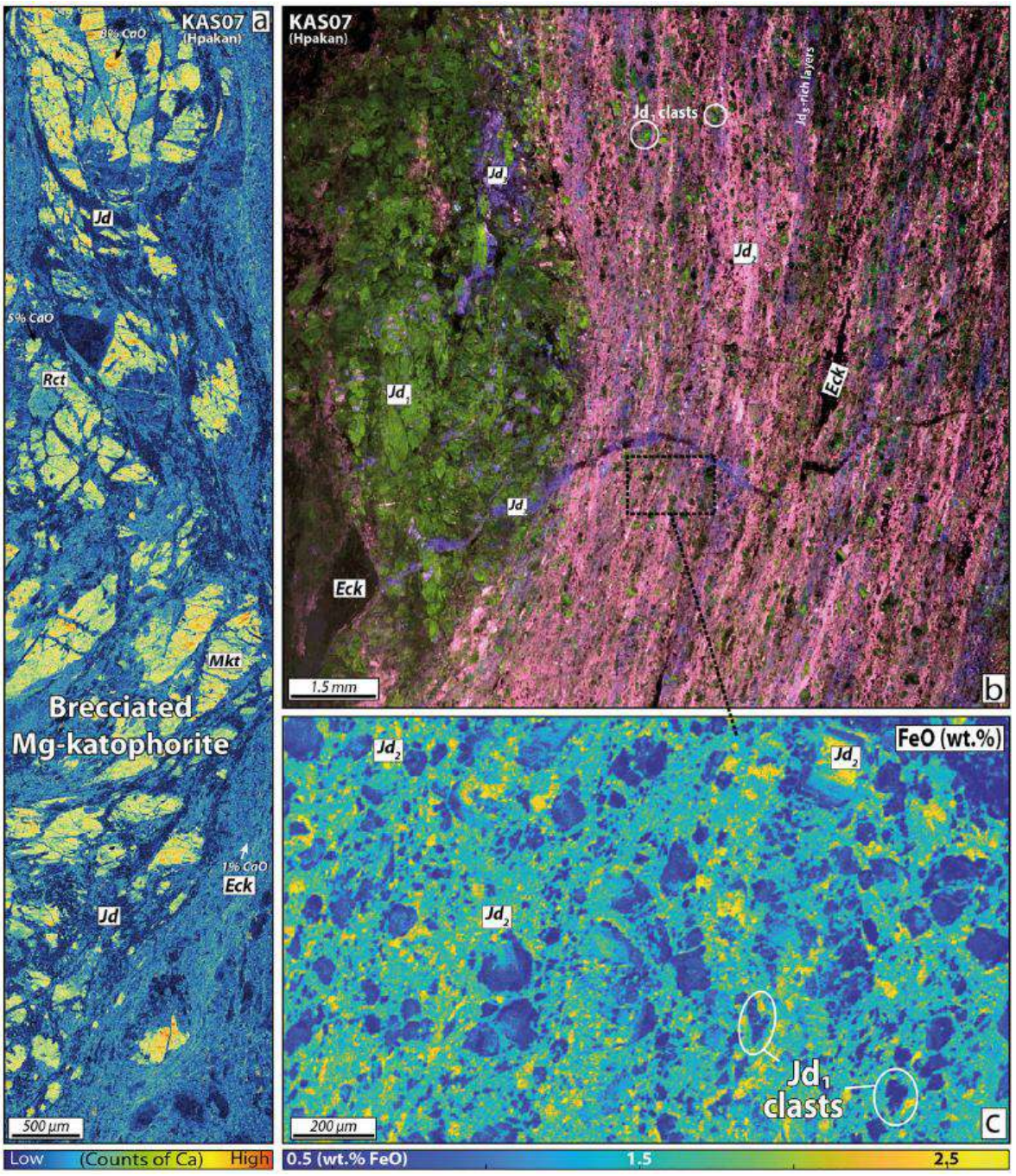

Fig. 10. *a. EDS X-ray map (counts of Ca) showing the internal structure of a foliated and brecciated dark granofels layer with Mg-katophorite cores (locally containing up to 8 wt% CaO) wrapped within a jadeite-eckermannite-bearing foliation. b. Cathodoluminescence image of the whitish, foliated part of sample KAS07. Note the white jadeitite (Jd_1; CL-colored in green) fragments now dispersed in the Type II foliated cataclasite matrix (Jd_2; CL-colored in pink) and the black trails parallel with the foliation that are mostly made of sodic amphibole (e.g., eckermannite). Late Cr-rich jadeite (Jd_3; CL-colored in purple) is also observed parallel with the main foliation as well as along cracks. c. EPMA X-ray map showing FeO distribution in the whitish foliated cataclastic domain. Note the random (Fe-poor) Jd_1 clast size distribution as well as the apparent absence of internal deformation (such as plasticity) of Jd_1 clasts. (For interpretation of the references to colour in this figure legend, the reader is referred to the web version of this article.)*

The most compelling evidence pointing to repeated brittle deformation events is exhibited in Fig. 11 (sample KAS04). Three chemically distinct domains can be distinguished: (i) the white jadeitite clasts (likely a former Type I structure); (ii) the blue amphibole fibrous veins that "inject" between breccia clasts (e.g., hydrofracture-filling material); and (iii) a very fine-grained, greenish Type II foliated omphacitite domain at the top of the sample (Fig. 11a, Fig. 12f). Locally, the contact between the blue amphibole domains and the white clasts exhibits structures that evoke Type III hydrofracturing processes (with local embayments pointing to interface-coupled dissolution-precipitation mechanisms; Fig. 11b; e.g., Putnis and Austrheim, 2013). A large surface of the same sample (KAS04) has been mapped using EDS (Fig. 11c) in order to image millimeter-scale relationships between these three domains. The largest rounded, Al-rich white jadeite clast (colored in red) is transected along its base by a sharp micro-fault plane, along which the green, very fine-grained material ("foliated cataclasite") is found. The green omphacitite domain is formed by tens of micrometer-sized crystals (Fig. 11d) that commonly contain dark clasts (in BSE mode) with a composition similar to the large white jadeitite clasts (Fig. 12f). Cathodoluminescence imaging reveals that the clasts in the foliated cataclasites have a similar purple CL colour as the large white jadeitite clasts, confirming their genetic link (Fig. 12a, b, c). These clasts are rimmed by two distinct clinopyroxene compositions (Jd_2 and *Omp*) with increasing omphacitic content (Figs. 11e, 12f), the interfaces between which appear to be dissolved (see black arrows on Fig. 11d).

Elongated patches with omphacitic composition are aligned with the main foliation, and invade the fault as well as its damage zone (Fig. 12a, b). The foliated nature of this fine-grained jadeite-omphacite rich domain is evidenced using EBSD mapping (Fig. 12d). This image shows a shape-preferred orientation, with elongated jadeitic clinopyroxene grains (aspect ratios up to 6:1) defining a lineation subparallel to the strong crystallographic-preferred orientation well visible in [001] (Fig. 12e). Similarly to Polar Urals jadeitites, the [010] crystallographic axes are highly concentrated normal to the foliation plane but [100] are aligned within the foliation plane perpendicular to [010]. This defines a fabric akin to LS-type tectonites, confirming the likely presence of crystal-plastic deformation mechanisms associated with a near-plain strain geometry, as also supported by experimental investigations and numerical simulations (Ulrich and Mainprice, 2005; Zhang et al., 2006). In addition, intragranular misorientation maps show that several highly misoriented grains are surrounded by clusters of finer-grained crystals devoid of internal deformation. The former likely represent remnant fragments, and the latter dynamically recrystallized grains along the foliation (Fig. 12d, Fig. S3).

A late faulting event that led to the precipitation of blue amphibole as well as clinochlore along micro-fault planes affects the white jadeitite domain and the foliated cataclasites (Fig. 11c, e). Celsian crystals (a Ba-rich feldspar) are commonly found texturally associated with these apparently late clinochlore-bearing fault zones (black arrows on Fig. 11c). To summarize, textural relationships visible in sample KAS04 suggest the following deformation sequence: (i) tectonic brecciation of the white jadeitite; (ii) cataclasis of some of the white jadeitite and foliation of this cataclased domain;

(iii) re-brecciation (hydraulic) of the volume and precipitation of the Na-amphibole-rich domain between brecciated and cataclased domains; and (iv) crystallization of clinochlore and celsian along late discrete fault zones oblique to the previous fault structures (Fig. 11c).

6. Discussion

6.1. Worldwide jadeitites record mixed deformation regimes

Our comparative and analytical investigation reveals that most of the studied samples from Russia, Guatemala and Myanmar display widespread and similar markers of fracturing that have received little attention in previous studies (e.g., Dobretsov and Ponomareva, 1968; Shi et al., 2009b). Brittle deformation markers span a broad range, from Type I breccias typical of damage zones (e.g., Figs. 2, 6, 10a, 13a), to Type II variably foliated cataclasites that are more diagnostic of strongly localized fault systems (e.g., Rowe et al., 2011; Angiboust et al., 2015; Oncken et al., in revision; Figs. 5, 9, 13b), to Type III hydraulic breccias thought to develop at high fluid pressure conditions as extensional veining (e.g. Woodcock et al., 2007). A common feature of all studied materials are arrays of healed mineral fractures commonly coupled with grain size reduction, crystal indentation and dissolution-precipitation processes. This pattern, sometimes hardly visible using optical microscopy, requires the use of specific analytical approaches such as cathodoluminescence imaging or electronic microscopy to be documented (e.g., Figs. 3, 12; Shi et al., 2003; Sorensen et al., 2006; Takahashi et al., 2017). Pure extensional fracturing (e.g., hydrofracturing; Type III; Fig. 13c) has been identified in several samples, with fragments of the host that appear to have been snatched into clinopyroxene or amphibole-rich veins (Fig. 10b). When several brittle events can be distinguished, Type III events always occur late in the sequence (Table 1). In all localities, it is always the original white jadeitite material (Jd_1) that undergoes shearing-related brecciation and subsequent cementation by a darker clinopyroxene (Jd_2 or *Omp;* Fig. 7e) and/or by sodic amphiboles (e.g., eckermannite; Figs. 7f, 11a).

Evidence for viscous deformation has been observed in a shear band transecting the coarse-grained Polar Urals white jadeitite body (Fig. 4a), as well as within Myanmar jadeitites (Shi et al., 2009b). This observation reveals that the white jadeitite body, once crystalized, underwent differential stresses high enough to generate crystal plasticity (most likely via dislocation creep) yielding a CPO. Following the argument developed in Angiboust et al. (2021), it is hypothesized that this shearing occurred at c. 650 ◦C, i.e., above the antigorite stability field (Fig. 14d), because no evidence for Cr enrichment was found in this shear band (even though other processes may also contribute to Cr availability in the system; e.g., Huang et al., 2019). Assuming a strain rate of 10^{-14} s^{-1} (a median value commonly inferred for ductile shear zones; e.g., Pfiffner and Ramsay, 1982) and using the experimentally-based dislocation creep flow laws from Orzol et al. (2006) and Zhang et al. (2006), it is possible to estimate the differential stresses required for creating the shear band of sample UR03 to be between 125 and 40 MPa, respectively. Note that these values likely represent an upper bound since other competing deformation mechanisms such as pressure solution creep would likely be activated at lower stress values (e.g. Godard and van Roermund, 1995). The implications of these values will be discussed hereafter.

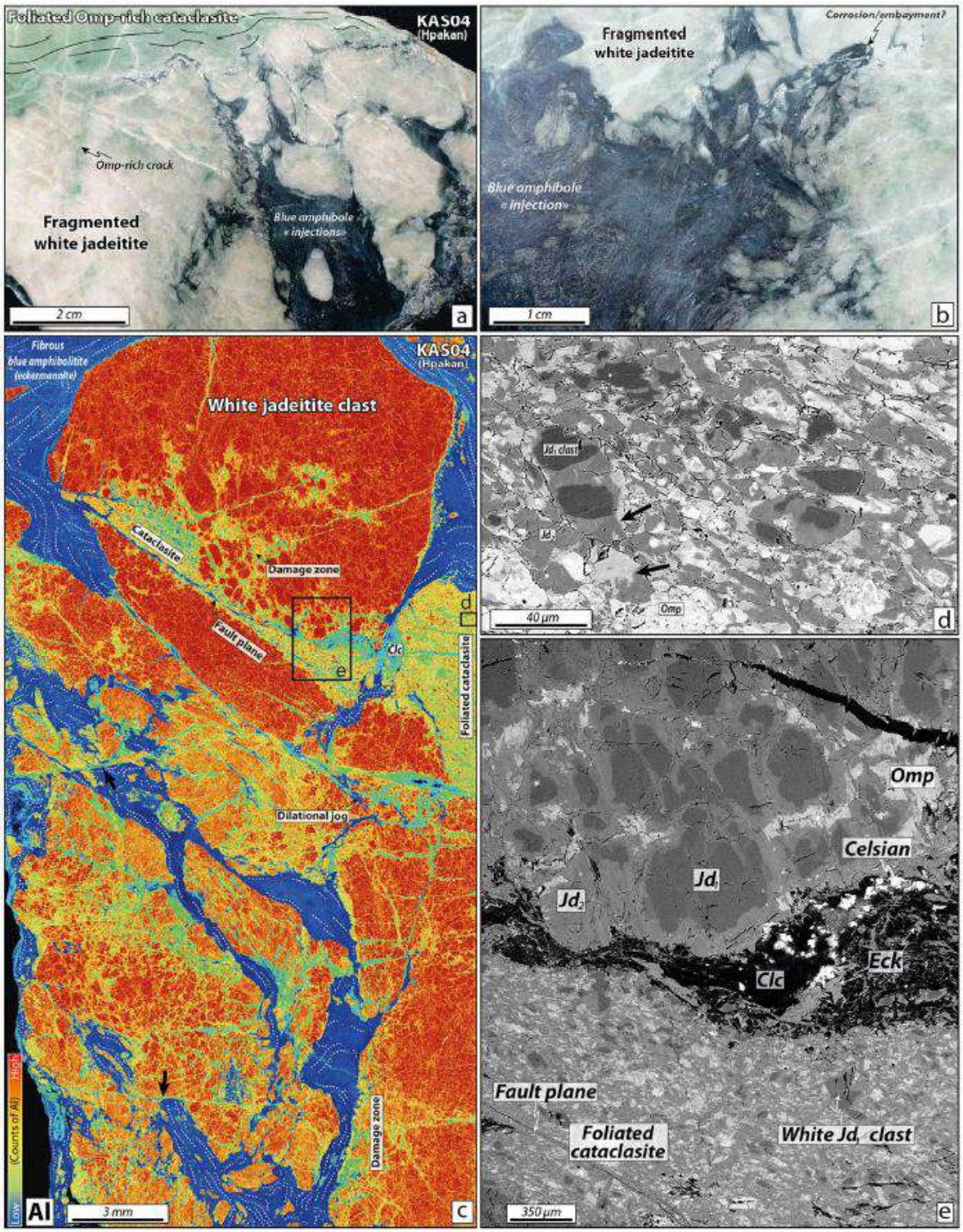

Fig. 11. *a. Polished hand specimen of a brecciated jadeitite from Myanmar (KAS04), where white jadeitite clasts are transected by a green, strongly foliated cataclastic domain (Type II). The sample is lately affected by a stage of pervasive, fibrous sodic amphibole (eckermannite) growth, infiltrating along cracks. b. Higher magnification image showing how the white jadeitite has been hydrofractured and filled by sodic amphibole, leaving embayments that may be interpreted as resulting from the dissolution by a reactive fluid. Note also the distribution of sodic amphibole fibers infiltrating the Type*

III breccia. c. EDS X-ray map (counts of Al) showing the great complexity of the internal structure in sample KAS04, where several brittle deformation and fluid-rock interaction events can be identified, including deformation features along ancient fault planes with injecting cataclastic material as well as damage zone formation. d. BSE image of the foliated cataclasite domain where white Jd_1 clasts are now dissolved and embedded within a Jd_2-omphacite matrix. e. BSE close-up image of the faulted area in panel c showing the foliated cataclasite domain, the micro-fault plane as well as the partly re-equilibrated damage zone. The contact between the large white jadeitite clast has been re-activated and filled by a clinochlore-eckermannite-celsian paragenesis. (For interpretation of the references to colour in this figure legend, the reader is referred to the web version of this article.)

The CPO observed in KAS04 sample and other Type II samples likely results from a combination of dislocation creep and solution- precipitation processes in a dominant simple shear regime but also with some degree of pure shear, as suggested by the observed LS-type fabric but also a weak girdle of [001], respectively (Figs. 4c, 12e). These deformation mechanisms have been already documented in eclogite-facies clinopyroxene by Godard and van Roermund (1995); see also Ulrich and Mainprice, 2005) (e.g., Fig. 12b). It is clear from the fragmented jadeitite clast distribution (along with the cathodoluminescence colour of the various crystals; Fig. 12b) that cataclastic flow (during brittle deformation) operated through localized faulting *before* CPO formation (see also Oncken et al., in revision; Fig. 10c). In other words, we infer that the observed foliated cataclasite structure is the protracted result of consecutive brittle flow followed by slower, viscous creep. This sequence of events may be the record of one or several seismic cycles where fast co-seismic slip is immediately followed by a slower after-slip event (e.g., Sibson, 1986; Rowe et al., 2011). Indeed, many of the reported fabrics resemble the structures documented in fault cores at shallower/colder environments where multiple episodes of particle fluidization are reported on the principal slip zone (Figs. 5f, 10c; e.g., Sibson, 1986; Snoke et al., 2014; Cox and Munroe, 2016; Muñoz-Montecinos et al., 2021a). Interestingly, the main brecciation/cataclasis event in sample KAS04 is followed by an episode of hydraulic brecciation where Na-amphibole precipitates Type III; Fig. S2). Similar deformation patterns have been observed in dark granofels that also comprise breccias (Fig. 6), foliated cataclasites (Fig. 5) and multiple fracturing events (Fig. 3c; Fig. S5; Table 1).

Exceptionally, the finding of elongated spherulitic shards in a fine-grained sheared domain (Figs. 7c, 9d) – possibly formed by the devitrification of former glass fragments – may be indicative of former pseudotachylytes (i.e., a glassy injection domain formed by melting during fault slip at seismic strain rates; e.g., Austrheim and Boundy, 1994; Austrheim and Andersen, 2004). The Jd_1 clasts found floating in the comminuted matrix display extensive fracturing, grain-size reduction and stress-driven corrosion that characterize pseudotachylyte-bearing systems (e.g., Kirkpatrick and Rowe, 2013). Glassy shards similar to those shown in Fig. 9g are mostly reported in ignimbrite deposits (e.g., Bull and McPhie, 2007) and in rocks from ancient impact craters (e.g., Dressler and Reimold, 2001). Although, to the best of our knowledge, such shard-like textures have not been described in ancient fault zones, the discovery of unreported textures must be expected because the formation environment of these slip events strongly differs from other paleo-earthquake reports made in the downgoing lithosphere (see below).

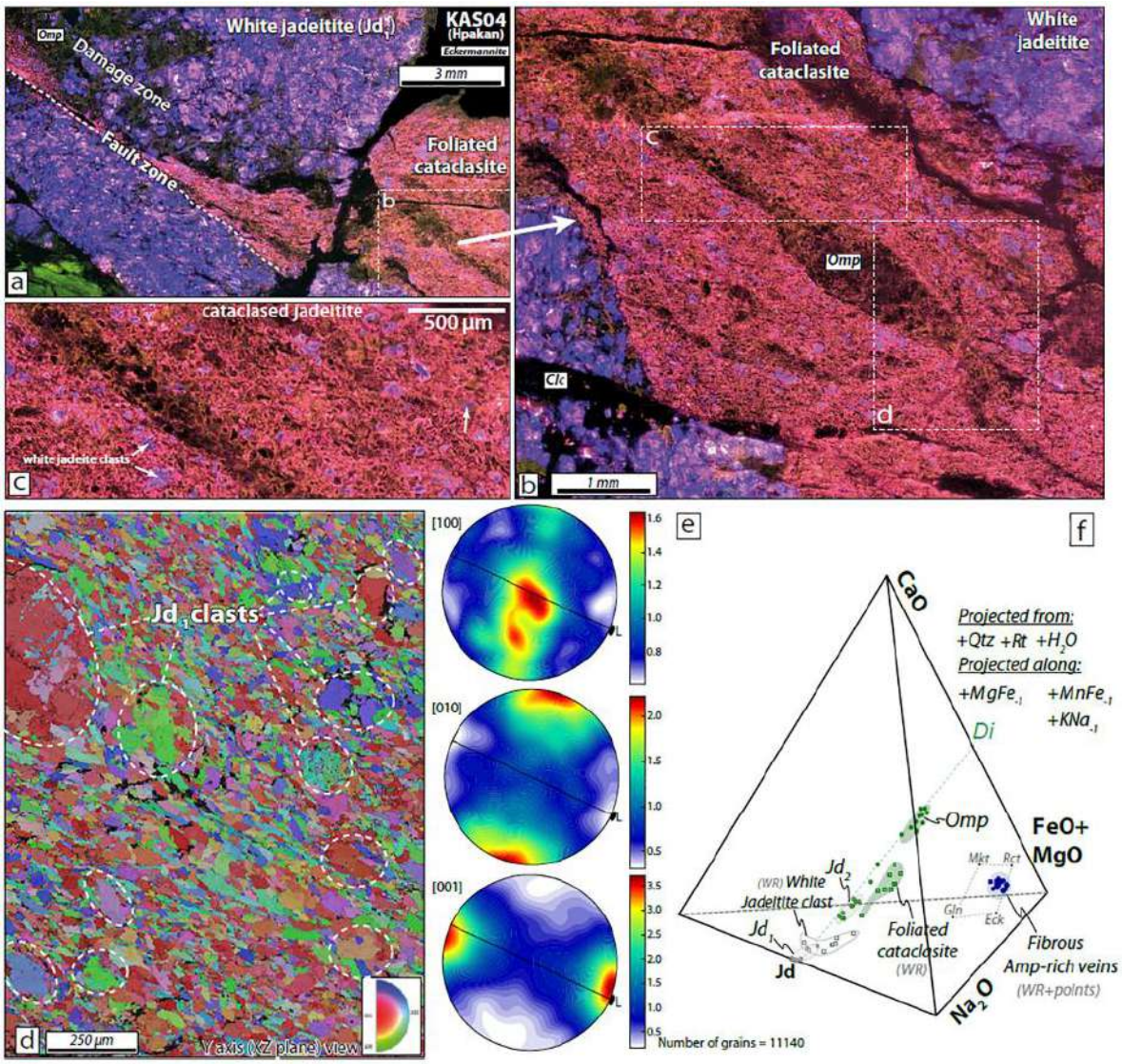

Fig. 12. a, b, c. Cathodoluminescence images showing the relationships between the different textural domains of sample KAS04. Note how the Jd_1 fragments (pink colors) are dragged within the foliated cataclasite domain. d. EBSD orientation map colored according to the inverse pole figure key (IPF) of jadeite (bottom right), showing a shape preferred orientation of jadeite to the X direction of the strain ellipsoid (i.e., stretching orientation). View (XZ plane) corresponding to the Y axis of the finite strain ellipsoid. e. Pole diagrams of jadeite crystals smaller than 100 µm in diameter (larger crystals are considered as clasts, as indicated in the figure and more detailed in Fig. S3), represented in an upper hemisphere equal-area projection for [100], [010] and [001] crystallographic axes. Contours are multiples of uniform density distributions. The bold dot on the L axis represents the stretching lineation direction (X direction of the strain ellipsoid) and the black line the foliation plane. f. Projection in a CaO-Al_2O_3-(FeO + MgO)-Na_2O system of the different groups of mineral compositions, as well as local surface estimates of bulk major element composition (WR: whole-rock). Circles are single point measurements and squares are SEM-based surface compositional estimates (WR).

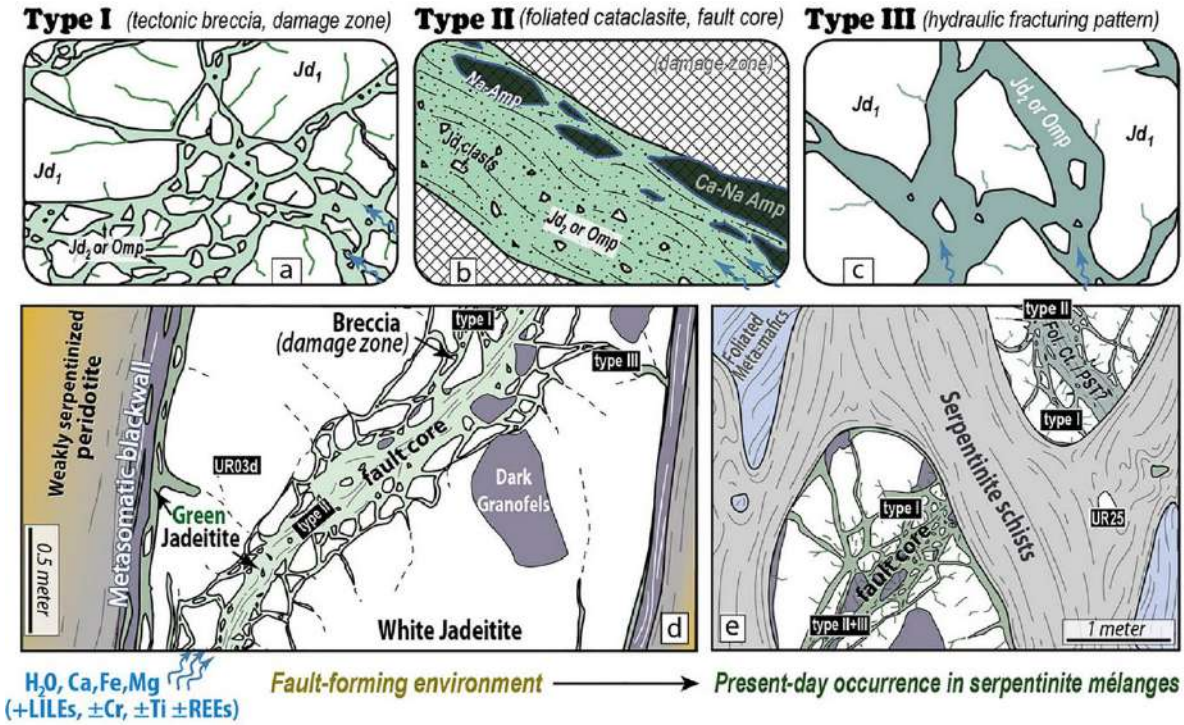

Fig. 13*. a, b and c. Sketches showing the key features of the three main categories of tectonized jadeitites identified in this comparative study. d. Sketch depicting the white jadeitite structure (derived from observations from the Pus'yerka body) at the time of brecciation, indicating the various elements identified in the field and their position with respect to the main fault and host ultramafics. e. Sketch highlighting the structure of jadeitite blocks as exposed in HP-LT serpentinite m´elanges, where they are commonly associated with blueschist and/or eclogite-facies crustal rocks. We posit that the faulting frequently observed within jadeitite blocks has been acquired earlier, when the jadeitite was a dyke-like structure hosted by weakly serpentinized mantle wedge peridotites.*

6.2. Jadeitite formation and pressure-temperature conditions of brittle deformation

In most serpentinite m´elange settings, the original structure at the time of jadeitite formation has been obliterated or disrupted by subduction zone tectonics (e.g., Harlow et al., 2015). Whereas in several cases jadeitites appear to be directly precipitated from hydrothermal fluids ("P-type" jadeitite, according the classification from Tsujimori and Harlow, 2012; e.g., García-Casco et al., 2009; Harlow et al., 2011), some localities preserve textural features typical of a replacement process ("R-type" jadeitite according to the same classification), including igneous zircon crystals with older crystallization ages (Yui et al., 2012; Yui et al., 2013; Hertwig et al., 2016) or the presence of incompletely "jadeitized" trondhjemitic remnants in the dyke volume (Angiboust et al., 2021). Indeed, early observations from Dobretsov and Ponomareva (1968) and Kuznetsov et al. (1986) in Russia, as well as Bleek (1908) and Chhiber (1934) in Myanmar, reveal that original jadeitite may form as dyke-like structures. It is plausible that these dykes were jadeitized during long-term cooling within the high-pressure field, coeval with replacement of a former felsic intrusive body formed earlier in the mantle wedge above the subduction interface, and possibly shortly after subduction initiation in a warm thermal regime (see the recent model by Angiboust et al., 2021; see also Meng

et al., 2011 and Fig. 14). Such secular cooling has also been documented above the metamorphic soles from New Caledonia (e.g. Soret et al., 2016) and Oman ophiolites (e.g. Prigent et al., 2018).

A number of recent studies (e.g., García-Casco et al., 2009; Schertl et al., 2012; Angiboust et al., 2021) have suggested that jadeitites may commonly form at temperatures far above 500 ◦C, perhaps up to 700 ◦C. García-Casco et al. (2009) and Cárdenas-Párraga et al. (2012) have also suggested that exsolution features, as observed in sample KAS10 (Fig. S2), could evidence the cooling of a clinopyroxene of intermediate jadeite-omphacite composition below the solvus at 500 ◦C. This implies that white jadeitites including the Myanmar samples formed at temperatures higher than generally expected. Consistent with this interpretation, Harlow and Sorensen (2005) suggested that the whitish colour of the relatively high temperature jadeitite may be due to Cr stability in the host ultramafic chromite and clinopyroxene crystals. In other words, it is likely that Cr-poor white jadeitite bodies formed at T conditions above the antigorite stability field, i.e., before serpentinization of the host ultramafic (Fig. 14), even though some Cr may also be hosted in high temperature chloritite blackwall (not documented in the studied localities; see Cárdenas-Párraga et al., 2012). Following this logic, it can be concluded that the systematic observation of darker-shaded clinopyroxene precipitates/overgrowths within breccias or cataclasites in many jadeitite localities indicate that fracturing and fluid-rock interaction events occurred during long-term cooling at $T < 600$ ◦C (e.g., García-Casco et al., 2009; Schertl et al., 2012; this study).

Whereas breccias and cataclasites are classically reported for rather shallow – and hence colder – environments (<15 km depth, $T < 300$ ◦C; Sibson, 1986), a number of field examples have recently shown that such features can form at depths greater than 30 km in the downgoing subducted crust (e.g., Angiboust et al., 2012, 2015; Hertgen et al., 2017; Muñoz-Montecinos et al., 2021a; Oncken et al., in revision). Minerals filling the studied breccias and growing within these fault zones encompass (i) omphacite (and locally lawsonite) in Guatemalan samples; (ii) omphacite, jadeite, phlogopite and Na-rich amphiboles in the Polar Urals samples; and (iii) Na-amphiboles, jadeitic and omphacitic clinopyroxenes in Myanmar samples. These parageneses point to HP-LT conditions ranging between 1 and 2 GPa and 300–500 ◦C as documented in the reviews of Tsujimori and Harlow (2012) and Harlow et al. (2015; Fig. 14d). Angiboust et al. (2021) have demonstrated that the phlogopite-bearing fracturing event seen crosscutting Polar Urals jadeitites occurred at least 15 Ma after the HT jadeite-forming event (see also Meng et al., 2011), thus providing an independent confirmation of the secondary nature of the brecciation process. We conclude that in the studied set of samples – and perhaps as a rule in fossil and active subduction systems – brittle deformation of jadeitites is a deep process occurring at or near peak-burial depths in a cooling environment (as suggested in Fig. 14), rather than as a consequence of late exhumation-related deformation. In order to undergo brittle deformation, the rock must be in-situ and surrounded by mechanically strong material, rather than as a tectonic block floating in a serpentinite-matrix mélange where stress is dissipated in the weak matrix.

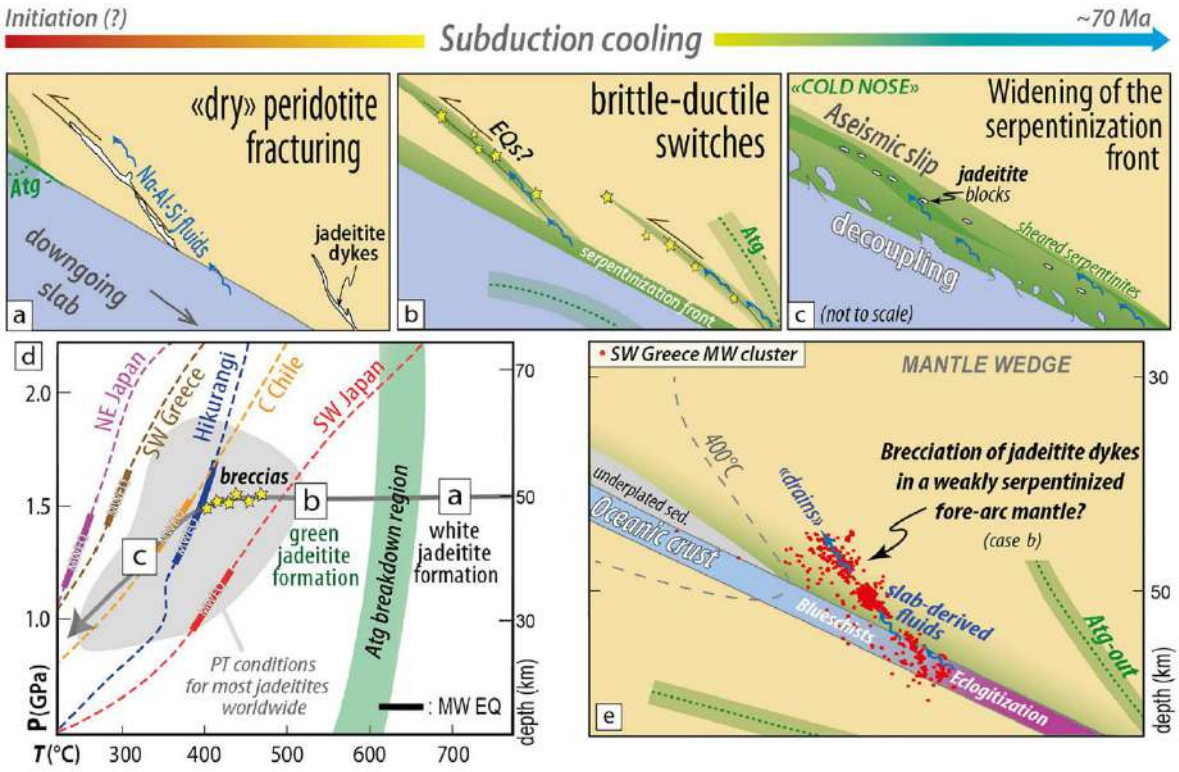

Fig. 14. a, b and c. Sketches depicting the long-term tectonic evolution of jadeitite "dykes" along the base of the mantle wedge, from their formation (by replacement of a previous dyke structure or from direct precipitation from a fluid) to their fracturing, dismembering and wrapping as blocks in a chaotic serpentinite m´elange. Previous geochronological data (Angiboust et al., 2021) confirms that several tens of millions of years of subduction activity and mantle wedge hydration are required to achieve a structure as shown in panel (c). Atg-: antigorite dehydration reaction. d. Pressure-Temperature diagram indicating the conditions of formation of the main white jadeitite bodies documented worldwide, and the conditions of the green jadeitite tectonic overprint (and associated sodic amphibole generation). After, and only after brecciation (yellow stars), the dyke fragments can be exhumed along the plate interface, provided that the hangingwall serpentinization rate is sufficiently high to enable return-flow of these dense blocks in a buoyant, serpentinized matrix (e.g., Gerya et al., 2002; Guillot et al., 2009). P-T conditions for jadeitites are sourced from the compilations by Tsujimori and Harlow (2012) and Harlow et al. (2015). Also shown are the slab-top temperature estimates as calculated by Antriasian et al. (2019, Hikurangi), Wang et al. (2020, central Chile), Halpaap et al. (2019, W Greece) and Peacock (2003, NE and SW Japan). References used for the depth of mantle wedge earthquakes (MW EQ) are provided in text. e. Location of one of the MW clusters identified by Halpaap et al. (2019) in W. Greece and interpreted as marking the trace of plate-interface fluids migrating along a vent structure. The formation of this EQ nest (corresponding to the yellow stars from panel d) likely implies that the serpentinization ratio of the subduction interface hanging wall is very low, thus pointing to a structure analogous to the sketch drawn in panel (b).

6.3. Origin of brecciated dark granofels and relationships with fluid-rock interaction events

A striking similarity characterizes the textural relationships between the dark granofels and jadeitites from the Polar Urals and Myanmar. In both localities, they occur as thin layers or pods of "amphibolites" of several tens of centimeters (Chhiber, 1934; Angiboust et al., 2021; Fig. 1e), generally striking parallel to the main "dyke" foliation and deformed coeval with the associated jadeitites. Their amphibole compositional patterns are also nearly identical, with relicts of Ca-rich amphiboles in the granofels mineral cores (mostly edenite and Mg-katophorite), and Ca-poor, Na-rich amphiboles along their rims and along highly metasomatized domains (Shi et al., 2003; Fig. S2). Field observations (Chhiber, 1934; Angiboust et al., 2021) and petrological investigations suggest that two distinct dark granofels occurrences may exist: (i) as disaggregated fragments (the "schistose amphibolite inclusions" from Chhiber, 1934; see also Harlow et al., 2015) inherited from a pre-jadeitization event; and (ii) as amphibole-rich blackwalls formed at the contact between the jadeitite body and the host ultramafic (Shi et al., 2003). The latter should in theory have formed lately at $T <$ 350 ◦C (Shi et al., 2003) and only exhibit Na-amphiboles (since no Ca chemical potential gradient exists between ultramafics and jadeitites), thus hampering the formation of calcic and sodic-calcic amphiboles such as edenite or Mg-katophorite in the reaction blackwall. The former should instead contain these sodic-calcic amphibole species (e.g., Figs. 5a, 6b, 10a) as remnants of an early HT event, associated with the infiltration of alkali-rich fluids and/or melts (likely trondhjemitic in composition) within ultramafics in a subduction initiation setting. This process is known to occur in anomalously high subduction thermal regimes (see also the discussion in Angiboust et al., 2021 and similar structures and rock assemblages in Lázaro et al., 2011 and Soret et al., 2016). Brecciation, followed by boudinage, late tectonic disaggregation and block-in-matrix deformation, most likely blurred the primary contacts, hampering an accurate reconstruction of the geometry of the original jadeitite-dark granofels boundaries (e.g., Fig. 10a).

6.4. Fluid ingress and metasomatic imprint

A common feature reported in jadeitites worldwide is the enrichment in Ca, Fe and Mg of jadeitic clinopyroxenes due to the infiltration of Ca- Fe-Mg-rich fluids associated with dissolution-precipitation processes during late fluid-rock interaction events (e.g., Sorensen et al., 2006; García-Casco et al., 2009; Harlow et al., 2011; Cárdenas-Párraga et al., 2012; Angiboust et al., 2021; this study). The formation of dissolution features (Fig. 3c), re-equilibration of clast rims (Fig. 8a) and the metasomatic overprint left in the rock record (Fig. 9b) are witnesses to the apparently corrosive nature of the infiltrating fluids, which were at thermodynamic disequilibrium with respect to the infiltrated material. The absence of carbonates in most jadeitite occurrences suggests that the fluids were CO_2-poor, most likely because the CO_2 precipitated as carbonates before reaching the jadeitite-forming location. Substantial Cr enrichments are also visible in some of the sheared domains and between breccia fragments (as shown for instance by the growth of chromian spinel around Mg-katophorite

clasts in sample UR11b; Fig. 6b; see also the green overgrowths around white jadeitite clast in Fig. 7f).

As discussed earlier, the release of Cr may be related to serpentinization of the host peridotite during fluid-rock interaction. It is important to note that (i) jadeite/omphacite is found growing within brecciated white jadeitites (Figs. 3b, 8a and 11c) and amphibole-rich dark granofels (Fig. 6d); and (ii) amphibole growth is observed in brecciated dark granofels (Fig. 5b) and between white jadeitite breccia fragments (Figs. 7f, 11a, 11b). From these observations, it appears that the incoming fluid composition was not buffered by the wall-rock composition and that brittle events contributed to a chemical and mechanical homogenization of the original dyke-forming lithologies. Furthermore, the widespread formation of texturally late micas (e.g., phlogopite in the Polar Urals: Angiboust et al., 2021, see also Fig. S1; phengite or phlogopite in Guatemala: Harlow et al., 2011; Flores et al., 2013; white mica in W. Japan: Shigeno et al., 2012) associated with enrichments in LILEs and other fluid mobile elements (Figs. S3 and S4) confirm that fluid sources were variable in time, switching from a mafic oceanic crust signature to a more hybridized composition with transient highs in sedimentary input (e.g., Sorensen et al., 2006, 2010; Morishita et al., 2007; Meng et al., 2011, 2016; Harlow et al., 2015; Chen et al., 2018; Cárdenas-Párraga et al., 2012). This temporal variability of incoming fluid chemistry from a more mafic to a more sedimentary signature could likely be explained by variations in the amount of sedimentary material undergoing devolatilization reactions in the underlying subduction channel (e.g., Bebout, 2007; Scambelluri et al., 2019). This chronological sequence confirms that the same fluid pathways (namely the jadeitite “dykes”) were used over several millions of years as major drains for highly pressurized plate-interface fluids, on their way to the partly hydrated mantle wedge (e.g. Doglioni et al., 2009; Spandler and Pirard, 2013).

The distribution of jadeitite “dykes” as seen in the Polar Urals (Fig. 1b; see also Angiboust et al., 2021) demonstrates that fluid pathways are rather discrete in the overlying plate (i.e., jadeitite does not precipitate randomly everywhere in the fore-arc mantle). It also indicates that less mechanical energy is required to re-fracture a pre- pre-existing physical discontinuity (e.g., a dyke-like structure) than creating new channels for draining plate-interface fluids. This implicitly requires that breccia sealing must have been faster than rupture recurrence to explain the mutual crosscutting relationships documented between the various events identified in our study (see also Woodcock et al., 2007). It seems clear that nearly lithostatic pore fluid pressure was sustained throughout the entire jadeitite drain activity as demonstrated by the ubiquitous evidence for fluid-rock interaction in the three types of brittle features reported here (Table 1; see also Kuznetsov et al., 1986 and Angiboust et al., 2021). Yet, transient overpressures likely triggered the formation of some of the (explosive) breccia features (Type III) within already-tectonized Type I and Type II domains (Figs. 11c, 13a, b). These findings are consistent with the episodic opening of vein systems and filling of voids by omphacitic compositions documented by García- Casco et al. (2009) and Cárdenas-Párraga et al. (2012) in the Sierra del Convento serpentinite mélange (E. Cuba), and also in other subduction HP-LT mélanges environments (e.g., Muñoz-Montecinos et al., 2021b).

6.5. Fluid ingress and metasomatic imprint

Brecciated rocks have long been recognized as potential markers of seismic deformation (e.g., Sibson, 1986; Angiboust et al., 2012; Melosh et al., 2014). Evidence of fault-zone rocks with diagnostic elements such as damage zones and fault cores (Fig. 13a, b) highlights for the first time that jadeitites (and associated dark amphibole-rich granofels) host abundant brittle deformation events, most likely along fast-slipping seismogenic fault planes. Estimating slip or strain rates along paleo-fault surfaces (or shear zones) is a challenging task, subject to great uncertainties. While Oncken et al. (in revision) have recently demonstrated that foliated cataclasites can form in slow slip environments for strain rates in the range 10^{-3} to 10^{-5} s^{-1}, the lack of well-preserved pseudotachylytes in the studied samples hampers a direct identification of seismic slip rates (i.e., on the order of m/s). However, the discovery of a foliated fault zone with abundant "shards" exhibiting structures analogous to devitrified spherulites (Fig. 9g) opens the possibility for constraining former slip events at strain rates approaching seismic slip velocities, fast enough to generate co-seismic temperatures as high as 1500 ◦C (e.g., Sibson et al., 2006; Menant et al., 2018) and trigger frictional melting. Note that chemical modification of the system is required to explain the enrichment in Ca, Fe and Mg of the shard-bearing fault zone as shown in Fig. 9b, c. As earlier stated by Magloughlin (1992) and Swanson (1992), cataclasites and pseudotachylytes may be closely intricated in fault zone rocks, both exhibiting evidence for open-system modification of the pristine host composition. Thus, the structures herein observed may have formed through (i) metasomatic fault-zone alteration associated with fluid influx within a finely-crushed cataclastic domain (likely a structure as shown in Fig. 13b), followed by (ii) fast-slip along narrow zones where local melting of the previously-formed cataclasites occurred (thus explaining the enrichment in omphacitic component of "shards" and devitrified spherulites, Fig. 9d–h). Subsequent shear deformation contributed to the apparent banding systematically observed in Type II fault rocks (e.g., Fig. 9b). It is therefore proposed that the reported features can be explained by fluctuations in slip rate velocities in a fluid-saturated fault zone.

6.6. Implications for mantle wedge seismicity and plate-interface rheology

Observations made on the Myanmar and Guatemalan loose samples are challenging to link to their respective formation context because pristine field relationships were obliterated during block-in-matrix dismembering as well as sedimentary transport into conglomerate deposits. A few exceptional observations in Myanmar document the presence of jadeitite-bearing "dykes" that are several hundred meters long and meters to tens of meters thick (e.g., Bleek, 1908), but most of these bodies have been mined. The Polar Urals Pus'yerka locality (and to a lesser extent other jadeitite localities in Siberia; Dobretsov and Ponomareva, 1968) has the potential to yield in situ information on the dimensions of ruptured bodies as well as refining the chronology of the processes at stake. Kuznetsov et al. (1986) report that jadeitite "dykes" in the Pus'yerka locality (also mined in the 1990s and mostly exhausted) were locally up to several tens of meters thick, pinching out to meter-thick bands at the northern and southern terminations of the several kilometer-long dyke structure (Fig. 1b). These observations provide critical insights into the minimum size for mantle wedge earthquakes. Assuming a planar

geometry for a single event that ruptured the Pus'yerka jadeitite body (before the dyke structure was boudinaged), a squared 3 × 3 km rupture, a 10 cm co-seismic displacement and a shear modulus of 84 GPa for jadeitite (Hao et al., 2019), a magnitude of Mw = 4.5 can be calculated (Sibson, 1989). This magnitude estimates ranges between 3 and 5 when changing fault dimensions and displacements within bounds compatible with field and structural observations.

Is this range of magnitudes comparable with the events reported in the forearc lithospheric mantle clusters in active subduction zones? Davey and Ristau (2011) report a subvertical, 10 km-large cluster of earthquakes (average maximum magnitude of 4.5 for normal, inverse and strike-slip events) above the subduction interface at 40–50 km depth in the northern Hikurangi margin. These authors note their spatial relationship with the inferred 700 ◦C isotherm, where they expect full antigorite breakdown and relate these earthquakes to dehydration embrittlement processes. Released upwelling fluids infiltrate the mantle wedge, possibly explaining volcanism in the above back-arc basin. Nakajima and Uchida (2018) have identified a nest of supra-slab micro-seismicity (Mw = 1–3) located 10–15 km above the Philippine plate in central Japan, between 25 and 35 km depth with focal mechanisms corresponding to normal and strike-slip events. Interestingly, seismic activity markedly increased after the 2011 Tohoku megathrust rupture, leading Nakajima and Uchida (2018) to consider these events as marking the trace of highly pressurized fluids, cyclically drained above the plate interface along a “highly fractured, pre-existing mature pathway”. According to this model, several months are required for these fluid pulses to travel the few kilometers that separate these nests from the megathrust area (see also White et al., 2016). Similar structural conclusions were drawn by Yu and Zhao (2020) who focused on 35–55 km depth microseismicity events in the NE Japan forearc mantle using P-wave velocity perturbations. Halpaap et al. (2019) have demonstrated that several seismicity nests ranging in magnitude from 2 to 4 occur under Western Greece in a weakly serpentinized mantle. These events (mostly extensional) occur between 45 and 55 km depth along a diffuse structure that dips at 45◦ to the subduction interface plane (see hypocenter distribution plotted in Fig. 14e). Halpaap et al. (2019) conclude that plate-interface fluids transiently migrate along fault-bounded vents, diminishing the pore pressure along the interface, thus decreasing plate-interface seismicity. This non-exhaustive list of studies confirms that fluids are unequivocally required to explain the seismotectonic features documented in the remote mantle wedge. It also appears that these nests are transient in the context of subduction zone evolution and spatially localized within well-defined structures.

The formation of mantle wedge earthquakes has critical implications for plate-interface rheology and more specifically may provide precious constraints on the volumetric abundance of serpentinite in the forearc mantle. A vibrant debate exists on the abundance and distribution of serpentinite in the mantle wedge based on the interpretation of seismic wave velocity perturbations and the effect of serpentinite anisotropy (e. g., Hyndman and Peacock, 2003; Liu et al., 2020; Luo and Wang, 2021). It is likely that serpentinite distribution is highly uneven in the mantle wedge, with the highest serpentinization rates directly above the interface and fairly low rates (likely less than 15 vol%) within

the innermost forearc mantle (e.g., Reynard, 2013; Abers et al., 2017; Halpaap et al., 2019). Stress accumulation in the mantle must be inhibited by serpentinite formation, which is known to flow at very low stresses (e. g., Escartin et al., 2001; Reynard, 2013 and references therein). The stress level required for enabling plastic deformation of jadeitites (40–125 MPa according to our calculations) is several orders of magnitude greater than the stresses required for the flow of serpentinites (approximately 1 MPa at 600 ◦C using the calibration from Hilairet et al., 2007). In order to transfer plate-interface stresses into the overlying mantle and trigger plastic deformation of jadeitites (Fig. 4), the host peridotite must have been relatively dry (i.e., with serpentinization rates far lower than 10 vol%.) as inferred for many active subduction settings (e.g., Abers et al., 2017; Halpaap et al., 2019). The triggering of multiple cataclastic events as documented by our observations (Fig. 9b) could be explained by transient increases in strain rate (during slow slip events or earthquakes), by an increase of pore fluid pressures, or by a combination of both. The latter option is supported by the discovery of fabrics typically observed in faulted jadeitites (e.g., Figs. 9, 12), as well as major and trace element chemical arguments that point to mass transfer and opening of the system to external fluids (e.g., Fig. 6), most likely sourced in the subduction interface region.

From these considerations, we can conclude that (i) the seismic events recorded above the subduction interface in several active subduction zones likely correspond to the brittle deformation of jadeitite bodies (Fig. 14d, e), which according to field observations are themselves derived from the metasomatic replacement of former felsic dyke bodies or direct precipitation from fluids (see discussion in Harlow et al., 2015 and Angiboust et al., 2021); and (ii) brittle jadeitite deformation may have occurred in the fossil subduction record and in present-day settings in a relatively dry peridotitic mantle, thus providing valuable insights into the serpentinization degree of the interface hangingwall and the stress distribution at the base of the megathrust region (Halpaap et al., 2019; Luo and Wang, 2021). This record of the deep conduits draining plate-interface fluids into the overlying mantle wedge sheds light on the structure of the “cold nose” above the subduction interface, with implications for volatile budget estimates, the rheology of the plate interface itself (including the various types of seismicity), and the interpretation of Vp/Vs and Poisson's ratios from active subduction settings worldwide.

7. Conclusions

A vein network from the Polar Urals composed of jadeitite and amphibole-phlogopite granofels is hosted in mildly serpentinized peridotites. This structure formed by metasomatic replacement of a former magmatic dyke above the subduction interface at c. 50 km depth, in a young and dry mantle wedge environment. During subsequent cooling of the subduction zone, this jadeitized “dyke” experienced mixed brittle-viscous deformation regimes associated with several serpentinite- and oceanic crust-derived fluids. Extensive fracturing, well-visible in the amphibole-rich granofels and more cryptic in the jadeitite bodies, led to the local formation of breccias and foliated cataclasites. The associated metasomatic imprint confirms the importance of these fault zones as major drains for overpressurized plate-interface metamorphic fluids. Very similar features, including omphacite- and

amphibole-rich breccias together with foliated cataclasites, are also observed in loose jadeitite boulders from Myanmar and Guatemala serpentinite mélanges. We propose that supra-slab seismicity nests recorded in present-day subduction margins (e.g., N Hikurangi, NE Japan, W Greece) may reflect the repeated fluid-assisted breakage of planar bodies formed by jadeitite "dykes". The local presence of these rupture events implies that the serpentinization rate was locally low (probably <10–15 vol%) along the base of the mantle wedge during "dyke" faulting activity. These results shed light on the importance of physical discontinuities such as jadeitite bodies for draining plate-interface fluids into the mantle wedge, and provide key constraints on the stress distribution in deep subduction margins.

Acknowledgements

Johannes Glodny (GFZ Potsdam) is acknowledged for insightful discussions that initiated this project. François Gendron (MNHN) is also warmly acknowledged for sharing his knowledge about the Motagua region and information on archeological material. Ksenia Kulikova is thanked for sharing her knowledge on the regional geology of the Urals. J.M-M express his gratitude to Ralf Hielscher, Rüdiger Kilian and Luiz Morales for assistance with the MTEX software. Michael Popov, Stephan Borensztajn, Arthur Delorme, Julia Cozzolino and the Camparis team are acknowledged for technical assistance. Michael Bostock and Gaston Godard are acknowledged for insightful discussions. The careful and efficient editorial handling by Carlo Doglioni is much appreciated. Comments from Bill Leeman and two anonymous reviewers helped to greatly increase the clarity of this manuscript. D.D. was funded by the European Research Council grant REALISM (2016-grant 681346) to Alexandre Schubnel. This study was funded with an IDEX-USPC research chair grant (#16C538) and was partly supported by the IdEx Universit´e de Paris ANR-18-IDEX-0001.

References

Abers, G. A., Van Keken, P. E., & Hacker, B. R. (2017). The cold and relatively dry nature of mantle forearcs in subduction zones. *Nature Geoscience*, *10*(5), 333-337.

Agard, P., Plunder, A., Angiboust, S., Bonnet, G., & Ruh, J. (2018). The subduction plate interface: rock record and mechanical coupling (from long to short timescales). *Lithos*, *320*, 537-566.

Angiboust, S., Agard, P., Yamato, P., & Raimbourg, H. (2012). Eclogite breccias in a subducted ophiolite: A record of intermediate-depth earthquakes?. *Geology*, *40*(8), 707-710.

Angiboust, S., Pettke, T., De Hoog, J. C., Caron, B., & Oncken, O. (2014). Channelized fluid flow and eclogite-facies metasomatism along the subduction shear zone. *Journal of petrology*, *55*(5), 883-916.

Angiboust, S., Kirsch, J., Oncken, O., Glodny, J., Monié, P., & Rybacki, E. (2015). Probing the transition between seismically coupled and decoupled segments along an ancient subduction interface. *Geochemistry, Geophysics, Geosystems*, *16*(6), 1905-1922.

Angiboust, S., Glodny, J., Cambeses, A., Raimondo, T., Monié, P., Popov, M., & Garcia-Casco, A. (2020). Drainage of subduction interface fluids into the forearc mantle evidenced by a pristine jadeitite network (Polar Urals). *Journal of Metamorphic Geology*.

Antriasian, A., Harris, R. N., Tréhu, A. M., Henrys, S. A., Phrampus, B. J., Lauer, R., ... & Barker, D. (2019). Thermal regime of the northern Hikurangi margin, New Zealand. *Geophysical Journal International*, *216*(2), 1177-1190.

Audet, P., & Kim, Y. (2016). Teleseismic constraints on the geological environment of deep episodic slow earthquakes in subduction zone forearcs: A review. *Tectonophysics*, *670*, 1-15.

Austrheim, H., & Boundy, T. M. (1994). Pseudotachylytes generated during seismic faulting and eclogitization of the deep crust. *Science*, 265(5168), 82-83.

Austrheim, H., & Andersen, T. B. (2004). Pseudotachylytes from Corsica: fossil earthquakes from a subduction complex. *Terra nova*, *16*(4), 193-197.

Bachmann, F., Hielscher, R., & Schaeben, H. (2010). Texture analysis with MTEX–free and open source software toolbox. In Solid State Phenomena (Vol. 160, pp. 63-68). *Trans Tech Publications Ltd*.

Bachmann, F., Hielscher, R., & Schaeben, H. (2011). Grain detection from 2d and 3d EBSD data—Specification of the MTEX algorithm. *Ultramicroscopy*, 111(12), 1720-1733.

Batanova, V. G., Belousov, I. A., Savelieva, G. N., & Sobolev, A. V. (2011). Consequences of channelized and diffuse melt transport in supra-subduction zone mantle: evidence from the Voykar ophiolite (Polar Urals). *J. Petrol*. 52(12), 2483-2521.

Bebout, G. E. (2007). Metamorphic chemical geodynamics of subduction zones. *Earth and Planetary Science Letters*, 260(3-4), 373-393.

Beccaluva, L., Bellia, S., Coltorti, M., Dengo, G., Giunta, G., Mendez, J., Romero, J., Rotolo, S. and Siena, F., 1995. The northwestern border of the Caribbeanplate in Guatemala: New geological and petrological data on the Motagua ophiolitic belt. Ofioliti, 20, 1-15.

Bleek, A.W.G (1908). Jadeite in the Kachin Hills, Upper Burma. *Records of the Geological Survey India*, 36(4), 254-285.

Bostock, M. G. (2013). The Moho in subduction zones. *Tectonophysics*, *609*, 547-557.

Bouchon, M., Marsan, D., Jara, J., Socquet, A., Campillo, M., & Perfettini, H. (2018). Suspected deep interaction and triggering between giant earthquakes in the Chilean subduction zone. *Geophysical Research Letters*, *45*(11), 5454-5460.

Brueckner, H. K., Lallemant, H. G. A., Sisson, V. B., Harlow, G. E., Hemming, S. R., Martens, U., ... & Sorensen, S. S. (2009). Metamorphic reworking of a high pressure–low temperature mélange along the Motagua fault, Guatemala: a record of Neocomian and Maastrichtian transpressional tectonics. *Earth and Planetary Science Letters*, *284*(1-2), 228-235.

Bull, K. F., & McPhie, J. (2007). Fiamme textures in volcanic successions: Flaming issues of definition and interpretation. *Journal of Volcanology and Geothermal Research*, *164*(4), 205-216.

Cárdenas-Párraga, J., García-Casco, A., Harlow, G. E., Blanco-Quintero, I. F., Agramonte, Y. R., & Kröner, A. (2012). Hydrothermal origin and age of jadeitites from Sierra del Convento Mélange (Eastern Cuba). *European Journal of Mineralogy*, *24*(2), 313-331.

Chen, Y., Huang, F., Shi, G. H., Wu, F. Y., Chen, X., Jin, Q. Z., ... & Nyunt, T. T. (2018). Magnesium isotope composition of subduction zone fluids as constrained by jadeitites from Myanmar. *Journal of Geophysical Research: Solid Earth*, *123*(9), 7566-7585.

Chhiber HL. 1934. *The Mineral Resources of Burma*. London: MacMillan

Cox, S. F., & Munroe, S. M. (2016). Breccia formation by particle fluidization in fault zones: implications for transitory, rupture-controlled fluid flow regimes in hydrothermal systems. *American Journal of Science*, *316*(3), 241-278.

Davey, F. J., & Ristau, J. (2011). Fore-arc mantle wedge seismicity under northeast New Zealand. *Tectonophysics*, *509*(3-4), 272-279.

Deschamps, F., Guillot, S., Godard, M., Chauvel, C., Andreani, M., & Hattori, K. (2010). In situ characterization of serpentinites from forearc mantle wedges: timing of serpentinization and behavior of fluid-mobile elements in subduction zones. *Chemical Geology*, *269*(3-4), 262-277.

Dessa, J. X., Klingelhoefer, F., Graindorge, D., André, C., Permana, H., Gutscher, M. A., ... & SUMATRA-OBS Scientific Team. (2009). Megathrust earthquakes can nucleate in the forearc mantle: Evidence from the 2004 Sumatra event. *Geology*, *37*(7), 659-662.

Dobretsov, N. L., & N. V. Sobolev (1984). Glaucophane schists and eclogites in the folded systems of northern Asia. *Ofioliti*, 9. 401-424.

Dobretsov, N. L., & Ponomareva, L. G. (1968). Comparative characteristics of jadeite and associated rocks from Polar Ural and Prebalkhash region. *International Geology Review*, 10(3), 247-279.

Dressler, B. O., & Reimold, W. U. (2001). Terrestrial impact melt rocks and glasses. *Earth-Science Reviews*, *56*(1-4), 205-284.

Endo, S., Wallis, S. R., Tsuboi, M., Torres De León, R., & Solari, L. A. (2012). Metamorphic evolution of lawsonite eclogites from the southern Motagua fault zone, Guatemala: insights from phase equilibria and Raman spectroscopy. *Journal of Metamorphic Geology*, *30*(2), 143-164.

Escartin, J., Hirth, G., & Evans, B. (2001). Strength of slightly serpentinized peridotites: Implications for the tectonics of oceanic lithosphere. *Geology*, *29*(11), 1023-1026.

Fishman, A.M. (2006): Gems in the north Ural and Timan. *Geoprint*, Syktyvkar, 88 p. (in Russian).

Flores, K. E., Skora, S., Martin, C., Harlow, G. E., Rodríguez, D., & Baumgartner, P. O. (2015). Metamorphic history of riebeckite-and aegirine-augite-bearing high-pressure–low-temperature blocks within the Siuna Serpentinite Mélange, northeastern Nicaragua. *International Geology Review*, *57*(5-8), 943-977.

Flores, K. E., Martens, U. C., Harlow, G. E., Brueckner, H. K., & Pearson, N. J. (2013). Jadeitite formed during subduction: In situ zircon geochronology constraints from two different tectonic events within the Guatemala Suture Zone. *Earth and Planetary Science Letters*, *371*, 67-81.

Frank, W. B., Shapiro, N. M., Husker, A. L., Kostoglodov, V., Bhat, H. S., & Campillo, M. (2015). Along-fault pore-pressure evolution during a slow-slip event in Guerrero, Mexico. *Earth and Planetary Science Letters*, 413, 135-143.

Franz, L., Sun, T. T., Hänni, H. A., de Capitani, C., Thanasuthipitak, T., Atichat, W., ... & Capitani, C. D. (2014). A comparative study of jadeite, omphacite and kosmochlor jades from Myanmar, and suggestions for a practical nomenclature. *J. Gemmol*, 34, 210-229.

Fu, Y., & Freymueller, J. T. (2013). Repeated large slow slip events at the southcentral Alaska subduction zone. *Earth and Planetary Science Letters*, *375*, 303-311.

García-Casco, A. (2007). Magmatic paragonite in trondhjemites from the Sierra del Convento mélange, Cuba. *American Mineralogist*, 92(7), 1232-1237.

García-Casco, A., Vega, A. R., Párraga, J. C., Iturralde-Vinent, M. A., Lázaro, C., Quintero, I. B., ... & Torres-Roldán, R. L. (2009). A new jadeitite jade locality (Sierra del Convento, Cuba): first report and some petrological and archeological implications. Contributions to Mineralogy and Petrology, 158(1), 1.

Gendron, F., Smith, D. C., & Gendron-Badou, A. (2002). Discovery of jadeite-jade in Guatemala confirmed by non-destructive Raman microscopy. *Journal of Archaeological Science*, 29(8), 837-851.

Gerya, T. V., Stöckhert, B., & Perchuk, A. L. (2002). Exhumation of high-pressure metamorphic rocks in a subduction channel: A numerical simulation. *Tectonics*, 21(6), 6-1.

Glodny, J., Austrheim, H., Molina, J. F., Rusin, A. I., & Seward, D. (2003). Rb/Sr record of fluid-rock interaction in eclogites: The Marun-Keu complex, Polar Urals, Russia. *Geochimica et Cosmochimica Acta*, *67*(22), 4353-4371.

Godard, G., & van Roermund, H. L. (1995). Deformation-induced clinopyroxene fabrics from eclogites. *Journal of Structural Geology*, 17(10), 1425-1443.

Goffe´, B., C. Rangin, and H. Maluski (2002), Jade and associated rocks from the jade Mines area, Northern Myanmar as record of a polyphased high pressure metamorphism. Himalaya–Karakoram–Tibet Workshop meeting (abstract) ,*J. Asian Earth Sc*i.,20,16–17.

Guillot, S., Hattori, K., Agard, P., Schwartz, S., & Vidal, O. (2009). Exhumation processes in oceanic and continental subduction contexts: a review. *Subduction zone geodynamics*, 175-205.

Hacker, B. R., Abers, G. A., & Peacock, S. M. (2003). Subduction factory 1. Theoretical mineralogy, densities, seismic wave speeds, and H2O contents. *Journal of Geophysical Research: Solid Earth*, 108(B1).

Halpaap, F., Rondenay, S., Perrin, A., Goes, S., Ottemöller, L., Austrheim, H., ... & Eeken, T. (2019). Earthquakes track subduction fluids from slab source to mantle wedge sink. *Science Advances*, *5*(4), eaav7369.

Hao, M., Pierotti, C. E., Tkachev, S., Prakapenka, V., & Zhang, J. S. (2019). The single-crystal elastic properties of the jadeite-diopside solid solution and their implications for the composition-dependent seismic properties of eclogite, *American Mineralogist*, *104*(7), 1016-1021.

Harlow, G. E., Hemming, S. R., Lallemant, H. G. A., Sisson, V. B., & Sorensen, S. S. (2004). Two high-pressure–low-temperature serpentinite-matrix mélange belts, Motagua fault zone, Guatemala: a record of Aptian and Maastrichtian collisions. *Geology*, *32*(1), 17-20.

Harlow, G. E., & Sorensen, S. S. (2005). Jade (nephrite and jadeitite) and serpentinite: metasomatic connections. *International Geology Review*, *47*(2), 113-146.

Harlow, G. E., Sisson, V. B., Tsujimori, T., Sorensen, S. S., & Brueckner, H. K. (2008). P–T conditions of eclogite/garnet–amphibolite from serpentinite mélanges along the Motagua fault zone, Guatemala. *Abs. Ann. Meet. Geol. Soc. Amer.: http://acs. confex. com/crops/2008am/webprogram/Paper50090. html*.

Harlow, G. E., Sisson, V. B., & Sorensen, S. S. (2011). Jadeitite from Guatemala: new observations and distinctions among multiple occurrences. *Geologica Acta*, *9*(3-4), 0363-387.

Harlow, G. E., Tsujimori, T., & Sorensen, S. S. (2015). Jadeitites and plate tectonics. *Annual Review of Earth and Planetary Sciences*, *43*, 105-138.

Harlow, G. E., Flores, K. E., & Marschall, H. R. (2016). Fluid-mediated mass transfer from a paleosubduction channel to its mantle wedge: evidence from jadeitite and related rocks from the Guatemala Suture Zone. *Lithos*, *258*, 15-36.

Hawthorne, F. C., & Oberti, R. (2007). Classification of the amphiboles. *Reviews in Mineralogy and Geochemistry*, *67*(1), 55-88.

Hellstrom, J., C. Paton, J. Woodhead, and J. Hergt (2008), Iolite: software for spatially resolved LA-(quad and MC) ICPMS analysis, *Mineralogical Association of Canada short course series*, 40, 343-348.

Hermann, J., Spandler, C., Hack, A., & Korsakov, A. V. (2006). Aqueous fluids and hydrous melts in high-pressure and ultra-high pressure rocks: implications for element transfer in subduction zones. *Lithos*, *92*(3-4), 399-417.

Hertgen, S., Yamato, P., Morales, L. F., & Angiboust, S. (2017). Evidence for brittle deformation events at eclogite-facies PT conditions (example of the Mt. Emilius klippe, Western Alps). *Tectonophysics*, *706*, 1-13.

Hertwig, A., McClelland, W. C., Kitajima, K., Schertl, H. P., Maresch, W. V., Stanek, K., ... & Sergeev, S. A. (2016). Inherited igneous zircons in jadeitite predate high-pressure metamorphism and jadeitite formation in the Jagua Clara serpentinite mélange of the Rio San Juan Complex (Dominican Republic). *Contributions to Mineralogy and Petrology*, 171(5), 48.

Hilairet, N., Reynard, B., Wang, Y., Daniel, I., Merkel, S., Nishiyama, N., & Petitgirard, S. (2007). High-pressure creep of serpentine, interseismic deformation, and initiation of subduction. *Science*, *318*(5858), 1910-1913.

Horn, C., Bouilhol, P., & Skemer, P. (2020). Serpentinization, deformation, and seismic anisotropy in the subduction mantle wedge. *Geochemistry, Geophysics, Geosystems*, *21*(4), e2020GC008950.

Huang, J., Hao, J., Huang, F., & Sverjensky, D. (2019). Mobility of chromium in high temperature crustal and upper mantle fluids. *Geochemical Perspectives Letters*, 12, 1-6.

Hussong, D. M. (1981). Tectonic processes and the history of the Mariana arc: a synthesis of the results of Deep Sea Drilling Project Leg 60. *Initial reports of the deep sea drilling project*, 60, 909-929.

Hyndman, R. D., & Peacock, S. M. (2003). Serpentinization of the forearc mantle. *Earth and Planetary Science Letters*, 212(3-4), 417-432.

Hyppolito, T., Cambeses, A., Angiboust, S., Raimondo, T., García-Casco, A., & Juliani, C. (2018). Rehydration of eclogites and garnet-replacement processes during exhumation in the amphibolite facies. *Geological Society, London, Special Publications*, 478, SP478.473. doi:10.1144/sp478.3.

Jochum, K. P., et al. (2011a), Determination of Reference Values for NIST SRM 610–617 Glasses Following ISO Guidelines, *Geostandards and Geoanalytical Research*, 35(4), 397-429.

Jochum, K.P., Wilson, S.A., Abouchami, W., Amini, M., Chmeleff, J., Eisenhauer, A., Hegner, E., Iaccheri, L.M., Kieffer, B., Krause, J., McDonough, W.F., Mertz-Kraus, R., Raczek, I., Rudnick, R.L., Scholz, D., Steinhoefel, G., Stoll, B., Stracke, A., Tonarini, S., Weis,

D., Weis, U. & Woodhead, J.D. (2011b). GSD-1G and MPI-DING Reference Glasses for In Situ and Bulk Isotopic Determination. *Geostandards and Geoanalytical Research*, 35, 193-226, doi: 10.1111/j.1751-908X.2010.00114.x.

Kawamoto, T., Hertwig, A., Schertl, H. P., & Maresch, W. V. (2018). Fluid inclusions in jadeitite and jadeite-rich rock from serpentinite mélanges in northern Hispaniola: Trapped ambient fluids in a cold subduction channel. *Lithos*, 308, 227-241.

Kazak, A.P., Dobretsov, N.L., Moldavantsev, J.E. (1976). Glaucophane schists, jadeitites, vesuvianites and nephrites of the Rai-Iz ultramafic massif. *Geology and Geophysics* (in Russian), 2, 60-66.

Kepezhinskas, P. K., Defant, M. J., & Drummond, M. S. (1995). Na-metasomatism in the island-arc mantle by slab melt—peridotite interaction: evidence from mantle xenoliths in the North Kamchatka Arc. *Journal of Petrology*, 36(6), 1505-1527.

Keppler, R., Stipp, M., Behrmann, J. H., Ullemeyer, K., & Heidelbach, F. (2016). Deformation inside a paleosubduction channel–Insights from microstructures and crystallographic preferred orientations of eclogites and metasediments from the Tauern Window, Austria. *Journal of Structural Geology*, 82, 60-79.

Keppler, R. (2018). Crystallographic preferred orientations in eclogites–A review. *Journal of Structural Geology*, 115, 284-296.

Kirkpatrick, J. D., & Rowe, C. D. (2013). Disappearing ink: How pseudotachylytes are lost from the rock record. *Journal of Structural Geology*, *52*, 183-198.

Konovalov A.L. & Sergeev S.S. (2015). About the age of zircons from jadeitite ultrabasite array of Syomke in the zone of the Main Uralian fault (the Polar Urals). *Regionalnaya geologiya i metallogeniya*. 64, 41–47. (In Russian).

Kuznetsov, Y. V., Kuznetsova, N. A., & Tsyutskiy, S. S. (1986). Features of jadeite mineralization in the Pus'yerka deposit (Polar Urals). *International Geology Review*, 28(9), 1096-1101.

Lázaro, C., Blanco-Quintero, I. F., Marchesi, C., Bosch, D., Rojas-Agramonte, Y., & García-Casco, A. (2011). The imprint of subduction fluids on subducted MORB-derived melts (Sierra del Convento Mélange, Cuba). *Lithos*, 126(3-4), 341-354.

Liu, W., Zhang, J., Cao, Y., & Jin, Z. (2020). Geneses of two contrasting antigorite crystal preferred orientations and their implications for seismic anisotropy in the forearc mantle. *Journal of Geophysical Research: Solid Earth*, *125*(9), e2020JB019354.

Locatelli, M., Verlaguet, A., Agard, P., Federico, L., & Angiboust, S. (2018). Intermediate-depth brecciation along the subduction plate interface (Monviso eclogite, W. Alps). *Lithos*, *320*, 378-402.

Luo, H., & Wang, K. (2021). Postseismic geodetic signature of cold forearc mantle in subduction zones. *Nature Geoscience*, 1-6.

Magloughlin, J. F. (1992). Microstructural and chemical changes associated with cataclasis and frictional melting at shallow crustal levels: the cataclasite-pseudotachylyte connection. *Tectonophysics*, *204*(3-4), 243-260.

Makeyev, A.B. (1992) Mineralogy of alpine-type ultramafics in the Ural. Nauka, St. Petersburg. 195 p. (in Russian).

Maruyama, S., & Liou, J. G. (1988). Petrology of Franciscan metabasites along the jadeite-glaucophane type facies series, Cazadero, California. *Journal of Petrology*, 29(1), 1-37.

Melosh, B. L., Rowe, C. D., Smit, L., Groenewald, C., Lambert, C. W., & Macey, P. (2014). Snap, Crackle, Pop: Dilational fault breccias record seismic slip below the brittle–plastic transition. *Earth and Planetary Science Letters*, *403*, 432-445.

Menant, A., Angiboust, S., Monié, P., Oncken, O., & Guigner, J. M. (2018). Brittle deformation during Alpine basal accretion and the origin of seismicity nests above the subduction interface. *Earth and Planetary Science Letters*, *487*, 84-93.

Meng, F., Yang, H. J., Makeyev, A. B., Ren, Y., Kulikova, K. V., & Bryanchaninova, N. I. (2016). Jadeitite in the Syum-Keu ultramafic complex from Polar Urals, Russia: insights into fluid activity in subduction zones. *European Journal of Mineralogy*, 28(6), 1079-1097.

Meng, F., Makeyev, A. B., & Yang, J. (2011). Zircon U–Pb dating of jadeitite from the Syum-Keu ultramafic complex, Polar Urals, Russia: constraints for subduction initiation. *Journal of Asian Earth Sciences*, *42*(4), 596-606.

Mével, C., & Kienast, J. R. (1986). Jadeite-kosmochlor solid solution and chromian sodic amphiboles in jadeitites and associated rocks from Tawmaw (Burma). *Bulletin de Minéralogie*, *109*(6), 617-633.

Morimoto, N. (1989). Nomenclature of pyroxenes. *Mineralogical Journal*, *14*(5), 198-221.

Morishita, T., Arai, S., & Ishida, Y. (2007). Trace element compositions of jadeite (+ omphacite) in jadeitites from the Itoigawa-Ohmi district, Japan: Implications for fluid processes in subduction zones. *Island Arc*, 16(1), 40-56.

Nakajima, J., & Uchida, N. (2018). Repeated drainage from megathrusts during episodic slow slip. *Nature Geoscience*, *11*(5), 351-356.

Nyunt, T. T., Massonne, H. J., & Sun, T. T. (2017). Jadeitite and other high-pressure metamorphic rocks from the Jade Mines Belt, Tawmaw area, Kachin State, northern Myanmar. *Geological Society, London, Memoirs*, *48*(1), 295-315.

Nyunt, T. T. (2009). Petrological and geochemical contribution to the origin of jadeitite and associated rocks of the Tawmaw Area, Kachin State, Myanmar. Stuttgart PhD thesis.

Obara, K., & Kato, A. (2016). Connecting slow earthquakes to huge earthquakes. *Science*, 353(6296), 253-257.

Oberti, R., Boiocchi, M., Hawthorne, F. C., Ball, N. A., & Harlow, G. E. (2015). Eckermannite revised: The new holotype from the Jade Mine Tract, Myanmar—crystal structure, mineral data, and hints on the reasons for the rarity of eckermannite. *American Mineralogist*, 100(4), 909-914.

Oncken O, **Angiboust S**, Dresen G, Slow slip in subduction zones: Reconciling deformation fabrics with instrumental observations and laboratory results, **Submitted.**

Ortega-Gutiérrez, F., Solari, L. A., Ortega-Obregon, C., Elias-Herrera, M., Martens, U., Moran-Ical, S., ... & Schaaf, P. (2007). The Maya-Chortís boundary: a tectonostratigraphic approach. *International Geology Review*, *49*(11), 996-1024.

Orzol, J., Stöckhert, B., Trepmann, C. A., & Rummel, F. (2006). Experimental deformation of synthetic wet jadeite aggregates. *Journal of Geophysical Research: Solid Earth*, *111*(B6).

Paton, C., J. Hellstrom, B. Paul, J. Woodhead, and J. Hergt (2011), Iolite: Freeware for the visualisation and processing of mass spectrometric data, *Journal of Analytical Atomic Spectrometry*, 26(12), 2508-2518.

Peacock, S. M. (2003). Thermal structure and metamorphic evolution of subducting slabs. *Geophysical Monograph-American Geophysical Union*, *138*, 7-22.

Pearce, N. J. G., W. T. Perkins, J. A. Westgate, M. P. Gorton, S. E. Jackson, C. R. Neal, and S. P. Chenery (1997), A compilation of new and published major and trace element data for NIST SRM 610 and NIST SRM 612 glass reference materials, Geostandards Newsletter - *Journal of Geostandards and Geoanalysis*, 21(1), 115-144.

Pfiffner, O. A., & Ramsay, J. G. (1982). Constraints on geological strain rates: arguments from finite strain states of naturally deformed rocks. *Journal of Geophysical Research: Solid Earth*, *87*(B1), 311-321.

Philippot, P., & van Roermund, H. L. (1992). Deformation processes in eclogitic rocks: evidence for the rheological delamination of the oceanic crust in deeper levels of subduction zones. *Journal of structural geology*, 14(8-9), 1059-1077.

Putnis, A., & Austrheim, H. (2013). Mechanisms of metasomatism and metamorphism on the local mineral scale: The role of dissolution-reprecipitation during mineral re-equilibration. In *Metasomatism and the chemical transformation of rock* (pp. 141-170). Springer, Berlin, Heidelberg.

Raimondo, T., Payne, J., Wade, B., Lanari, P., Clark, C., & Hand, M. (2017). Trace element mapping by LA-ICP-MS: assessing geochemical mobility in garnet. *Contributions to mineralogy and petrology*, *172*(4), 17.

Reynard, B. (2013). Serpentine in active subduction zones. *Lithos*, *178*, 171-185.

Ridd, M. F., Crow, M. J., & Morley, C. K. (2019). The role of strike-slip faulting in the history of the Hukawng Block and the Jade Mines Uplift, Myanmar. *Proceedings of the Geologists' Association*, *130*(2), 126-141.

Rowe, C. D., Meneghini, F., & Moore, J. C. (2011). Textural record of the seismic cycle: Strain-rate variation in an ancient subduction thrust. *Geological Society, London, Special Publications*, *359*(1), 77-95.

Savelieva, G. N., Sharaskin, A. Y., Saveliev, A. A., et al. (2002). Ophiolites and zoned mafic–ultramafic massifs of the Urals: a comparative analysis and some tectonic implications. *Mountain building in the Uralides*, 135-153.

Savelieva, G. N., & Suslov, P. V. (2014). Structure and composition of mantle peridotites at the boundary with crustal complexes of ophiolites in the Syumkeu massif, Polar Urals. *Geotectonics*, *48*(5), 347-358.

Savelieva, G. N., Batanova, V. G., & Sobolev, A. V. (2016). Pyroxene–Cr-spinel exsolution in mantle lherzolites of the Syum-Keu ophiolite massif (Arctic Urals). *Russian Geology and Geophysics*, *57*(10), 1419-1436.

Scambelluri, M., Cannaò, E., & Gilio, M. (2019). The water and fluid-mobile element cycles during serpentinite subduction. A review. *European Journal of Mineralogy*, 31(3), 405-428.

Schertl, H. P., Maresch, W. V., Stanek, K. P., Hertwig, A., Krebs, M., Baese, R., & Sergeev, S. S. (2012). New occurrences of jadeitite, jadeite quartzite and jadeite-lawsonite quartzite in the Dominican Republic, Hispaniola: petrological and geochronological overview. *European Journal of Mineralogy*, *24*(2), 199-216.

Searle, M. P., Noble, S. R., Cottle, J. M., Waters, D. J., Mitchell, A. H. G., Hlaing, T., & Horstwood, M. S. A. (2007). Tectonic evolution of the Mogok metamorphic belt, Burma (Myanmar) constrained by U-Th-Pb dating of metamorphic and magmatic rocks. *Tectonics*, *26*(3).

Shi, G. H., Cui, W. Y., Tropper, P., Wang, C. Q., Shu, G. M., & Yu, H. (2003). The petrology of a complex sodic and sodic–calcic amphibole association and its implications for the metasomatic processes in the jadeitite area in northwestern Myanmar, formerly Burma. *Contributions to Mineralogy and Petrology*, *145*(3), 355-376.

Shi, G. H., Jiang, N., Liu, Y., Wang, X., Zhang, Z. Y., & Xu, Y. J. (2009a). Zircon Hf isotope signature of the depleted mantle in the Myanmar jadeitite: implications for Mesozoic intra-oceanic subduction between the Eastern Indian Plate and the Burmese Platelet. *Lithos*, *112*(3-4), 342-350.

Shi, G., Wang, X., Chu, B., & Cui, W. (2009b). Jadeite jade from Myanmar: its texture and gemmological implications. *The journal of gemmology and proceedings of the Gemmological Association of Great Britain*, 31(5), 185.

Shi, G., Harlow, G. E., Wang, J., Wang, J., Ng, E., Wang, X., ... & Cui, W. (2012). Mineralogy of jadeitite and related rocks from Myanmar: a review with new data. *European Journal of Mineralogy*, 24(2), 345-370.

Shigeno, M., Mori, Y., Shimada, K., & Nishiyama, T. (2012). Jadeitites with metasomatic zoning from the Nishisonogi metamorphic rocks, western Japan: fluid–tectonic block interaction during exhumation. *European Journal of Mineralogy*, 24(2), 289-311.

Shmelev, V. R. (2011). Mantle ultrabasites of ophiolite complexes in the Polar Urals: petrogenesis and geodynamic environments. *Petrology*, *19*(6), 618-640.

Sibson, R. H. (1986). Brecciation processes in fault zones: inferences from earthquake rupturing. *Pure and Applied Geophysics*, *124*(1), 159-175.

Sibson, R. H., Toy, V. G., Abercrombie, R., & McGarr, A. (2006). The habitat of fault-generated pseudotachylyte: Presence vs. absence of friction-melt. *GEOPHYSICAL MONOGRAPH-AMERICAN GEOPHYSICAL UNION*, *170*, 153.

Snoke, A. W., Tullis, J., & Todd, V. R. (Eds.). (2014). *Fault-related rocks: a photographic atlas* (Vol. 410). Princeton University Press.

Sorensen, S., Harlow, G. E., & Rumble, D. (2006). The origin of jadeitite-forming subduction-zone fluids: CL-guided SIMS oxygen-isotope and trace-element evidence. *American Mineralogist*, *91*(7), 979-996.

Sorensen, S. S., Sisson, V. B., Harlow, G. E., & Avé Lallemant, H. G. (2010). Element residence and transport during subduction-zone metasomatism: evidence from a jadeitite-serpentinite contact, Guatemala. *International Geology Review*, *52*(9), 899-940.

Soret, M., Agard, P., Dubacq, B., Plunder, A., & Yamato, P. (2017). Petrological evidence for stepwise accretion of metamorphic soles during subduction infancy (Semail ophiolite, Oman and UAE). *Journal of Metamorphic Geology*, *35*(9), 1051-1080.

Swanson, M. T. (1992). Fault structure, wear mechanisms and rupture processes in pseudotachylyte generation. *Tectonophysics*, *204*(3-4), 223-242.

Sychev, S. N., & Kulikova, K. V. (2012). Structural evolution of the Main Ural Fault Zone in the western framework of the Voikar-Synya ophiolite massif. *Geotectonics*, *46*(6), 427-434.

Syracuse, E. M., van Keken, P. E., & Abers, G. A. (2010). The global range of subduction zone thermal models. *Physics of the Earth and Planetary Interiors*, *183*(1-2), 73-90.

Takahashi, N., Tsujimori, T., Kayama, M., & Nishido, H. (2017). Cathodoluminescence petrography of P–type jadeitites from the New Idria serpentinite body, California. *Journal of Mineralogical and Petrological Sciences*, *112*(5), 291-299.

Torres-Roldan, R. L., Garcia-Casco, A., & Garcia-Sanchez, P. A. (2000). CSpace: An integrated workplace for the graphical and algebraic analysis of phase assemblages on 32-bit Wintel platforms. *Computers & Geosciences*, *26*(7), 779-793.

Tsujimori, T., & Harlow, G. E. (2012). Petrogenetic relationships between jadeitite and associated high-pressure and low-temperature metamorphic rocks in worldwide jadeitite localities: a review. *European Journal of Mineralogy*, *24*(2), 371-390.

Tsujimori, T., Liou, J. G., & Coleman, R. G. (2004, November). Comparison of two contrasting eclogites from the Motagua fault zone, Guatemala: southern lawsonite eclogite versus northern zoisite eclogite. In *Geological Society of America Abstracts with Programs* (Vol. 36, No. 5, p. 136).

Uchida, N., Kirby, S. H., Okada, T., Hino, R., & Hasegawa, A. (2010). Supraslab earthquake clusters above the subduction plate boundary offshore Sanriku, northeastern Japan: Seismogenesis in a graveyard of detached seamounts?. *Journal of Geophysical Research: Solid Earth*, *115*(B9).

Udovkina, N.G. (1971). Eclogites of Polar Urals Nauka, Moscow (in Russian).

Ulrich, S., & Mainprice, D. (2005). Does cation ordering in omphacite influence development of lattice-preferred orientation?. *Journal of Structural Geology*, 27(3), 419-431.

Wang, K., Huang, T., Tilmann, F., Peacock, S. M., & Lange, D. (2020). Role of Serpentinized Mantle Wedge in Affecting Megathrust Seismogenic Behavior in the Area of the 2010 M= 8.8 Maule Earthquake. Geophysical Research Letters, 47(22), e2020GL090482.

White, L., Rawlinson N., Lister G., Tanner D., Macpherson C., and Morgan J. (2016). Pulses of earthquake activity in the mantle wedge track the route of slab fluid ascent. EGU General Assembly Conference Abstracts, 18. 2016.

Whitney, D. L., & Evans, B. W. (2010). Abbreviations for names of rock-forming minerals. *American mineralogist*, *95*(1), 185-187.

Woodcock, N. H., Dickson, J. A. D., & Tarasewicz, J. P. T. (2007). Transient permeability and reseal hardening in fault zones: evidence from dilation breccia textures. *Geological Society, London, Special Publications*, *270*(1), 43-53.

Woodcock, N. H., & Mort, K. (2008). Classification of fault breccias and related fault rocks. *Geological Magazine*, *145*(3), 435-440.

Woodhead, J. D., J. Hellstrom, J. M. Hergt, A. Greig, and R. Maas (2007). Isotopic and Elemental Imaging of Geological Materials by Laser Ablation Inductively Coupled Plasma-Mass Spectrometry, *Geostandards and Geoanalytical Research*, 31(4), 331-343.

Yu, Z., & Zhao, D. (2020). Seismic evidence for water transportation in the forearc off Northern Japan. *Journal of Geophysical Research: Solid Earth*, *125*(4), e2019JB018600.

Yui, T. F., Fukoyama, M., Iizuka, Y., Wu, C. M., Wu, T. W., Liou, J. G., & Grove, M. (2013). Is Myanmar jadeitite of Jurassic age? A result from incompletely recrystallized inherited zircon. *Lithos*, *160*, 268-282.

Yui, T. F., Maki, K., Wang, K. L., Lan, C. Y., Usuki, T., Iizuka, Y., ... & Grove, M. (2012). Hf isotope and REE compositions of zircon from jadeitite (Tone, Japan and north of the Motagua fault, Guatemala): implications on jadeitite genesis and possible protoliths. *European Journal of Mineralogy*, *24*(2), 263-275.

Zhang, J., Green II, H. W., & Bozhilov, K. N. (2006). Rheology of omphacite at high temperature and pressure and significance of its lattice preferred orientations. *Earth and Planetary Science Letters*, *246*(3-4), 432-443.

11. APPENDIX B

Holtmann et al. (submitted)

Basally-Accreted Zagros Amphibolites Record the Cretaceous Thermal Evolution of the Closing Neo-Tethyan Realm

Regina Holtmann[1], Jesús Muñoz-Montecinos[1,2], Samuel Angiboust[1,3*], Aitor Cambeses[2], Guillaume Bonnet[4,5], Allison Brown[6], Besim Dragovic[6], Zeynab Gharamohammadi[7], Mathieu Rodriguez[8], Johannes Glodny[9], Ali Kananian[6], Philippe Agard[4]

[1] *Université de Paris, Institut de Physique du Globe de Paris, CNRS, F-75005 Paris, France*

[2] *Department of Mineralogy and Petrology, Faculty of Sciences, University of Granada, Campus Fuentenueva s/n, 18002 Granada, Spain*

[3] *University of Lyon, ENS Lyon, CNRS, LGL-TPE, 46 Allée d'Italie, F-69007 Lyon, France*

[4] *Department of Earth Science, Earth Research Institute, University of California, Santa Barbara, CA, USA*

[5] *Institut des Sciences de la Terre de Paris, Sorbonne Université, Paris, France*

[6] *School of Geology, College of Science, University of Tehran, Tehran, Iran*

[7] *School of the Earth, Ocean and Environment, University of South Carolina, Columbia, SC, USA*

[8] *Laboratoire de Géologie, Ecole normale supérieure, PSL research university, CNRS UMR 8538, 24 rue Lhomond, 75005 Paris, France*

[9] *GFZ German Research Centre for Geosciences, Potsdam, Germany*

*: corresponding author *(samuel.angiboust@gmail.com), now at ENS Lyon (France)*

For submission to: Lithos

ABSTRACT

A Cretaceous paleo-accretionary wedge, the Ashin Complex, now exposed along the Zagros suture zone in southern Iran, exhibits mafic, metasedimentary and subordinate ultramafic lithologies. Field, geochemical and petrological observations point to an anomalous high-temperature event that gave rise to the formation of peritectic (trondhjemitic) melts associated with restitic garnet-bearing amphibolites in the structurally highest sliver of the Ashin Complex. Lu-Hf isotopic dating of centimetre-sized garnet porphyroblasts in amphibolite-facies metasediments yielded a crystallization age of 113.10 ± 0.36 Ma, possibly representing the age of prograde to near-peak metamorphic conditions. SHRIMP U-Th-Pb zircon dating from trondhjemitic leucosomes yields crystallization ages of 104 ± 1 Ma, interpreted as the age of the temperature peak, which occurred in the upper amphibolite-facies (c. 650-680 °C at 1.1-1.3 GPa), according to thermodynamic modelling and Ti-in-zircon thermometry. Rutile crystals from two leucosomes yield Zr-in-rutile temperatures in the range of 580-640 °C and a LA-ICP-MS U-Pb age range from 85 to 112 Ma. This spread in ages is interpreted as a consequence of partial system re-opening during incipient cooling. A late static recrystallization event is indicated by the presence of sodic clinopyroxene, sodic amphibole, Si-rich phengite, titanite overgrowths after rutile and lawsonite within leucosomes and late fractures. This mineral assemblage is interpreted as reflecting long-term isobaric cooling with a gradient value that decreased down to 7 °C/km and that occurred at least until the end of the Cretaceous, possibly as a consequence of increasing thermal age of the subducting slab. This first report of a melting event in the Zagros paleo-accretionary wedge reveals the presence of a transient, abnormally high thermal gradient of c. 18 °C/km that occurred at c. 105-113 Ma. We speculate that this elevated thermal regime could be explained by the subduction of a seafloor-related thermal anomaly such as a seamount chain, a transform fault system or, more likely, a (perhaps extinct) spreading ridge under the southern Iranian margin. The latter hypothesis is supported by paleogeographic reconstructions of the Tethyan realm suggesting the entrance of the Northern Tethyan basin ridge into the subduction zone shortly after 120 Ma.

KEYWORDS: Zagros, subduction, trondhjemites, amphibolites, geochronology, Neo-Tethys

1. INTRODUCTION

Critical information on past geodynamic processes and regional-scale paleogeographic reconstructions can be derived studying ancient convergent margins and accretionary wedges (e.g. Ernst, 1973; Stern, 2002; Willner et al., 2004; Rossetti et al., 2017; Dilek & Ogawa, 2021). A number of previous studies have demonstrated that paleo-accretionary wedges do record long-term fluctuations of the subduction thermal gradient over geological timescales (Grove & Bebout, 1995; García-Casco et al., 2008; Lázaro et al, 2009; Plunder et al., 2015; Angiboust et al., 2018). Subduction initiation, known to be marked by a hot thermal environment during the first millions of years of subduction activity (Guilmette et al., 2018; Pourteau et al., 2019; Agard et al., 2020), is invariably followed by a secular cooling of the subduction thermal gradient as convergence proceeds to reach a nearly steady-state regime (e.g. Anczkiewicz et al., 2004; Angiboust et al., 2016; Tamblyn et al., 2019). However, subduction zone thermal structure is known to be rather unstable over millions of years. Several processes such as convergence rate decrease, slab dip flattening or the subduction of a thermal anomaly (e.g. a ridge, a triple junction) can leave an imprint permanently recorded in the rock record of ancient margins or volcanic arc chemical compositions (e.g. Gutscher et al., 2000; Lagabrielle et al., 2000; Tatsumi & Hanyu, 2003; Windley & Xiao, 2018; Dragovic et al., 2020; De la Fuente et al., 2021).

Only a few areas are witnesses of the long-term thermal evolution of the Neo-Tethyan realm in Asia during Mesozoic times (e.g. Angiboust et al., 2016; Pourteau et al., 2019). Meta-ophiolitic remnants from this oceanic realm are volumetrically scarce (e.g. Agard et al., 2006; Omrani et al., 2008; Rolland et al., 2009; Burg, 2018; Saccani et al., 2018; Pirnia et al., 2020) and when present, they do not commonly record a time window long enough to shed light on the long-term thermal evolution of the subduction zone. The c. 3000 km-long Zagros belt in southern Iran, unlike most classical subduction-collisional Alpine belts, does not exhibit large exposures of paleo-accretionary rocks despite an enduring subduction history (c. 180-35 Ma; Berberian & King, 1981; Sengör et al., 1988; McCall, 1997). Remnants from the deep Neo-Tethyan paleo-accretionary wedge are particularly well-preserved in the Hajiabad-Esfandagheh region (**Fig.1A,B**) where slivers of oceanic lithosphere origin have been accreted against the Sanandaj-Sirjan zone (SaSZ). The SaSZ has been interpreted as the thinned SW margin of the Eurasian continental plate (e.g. Alavi, 1994; Agard et al., 2006; Hassanzadeh & Wernicke, 2016). Previous studies have demonstrated that metamorphic rocks in the Hajiabad-Esfandagheh region form an antiformal nappe-stack that has been metamorphosed during the Upper Cretaceous under a thermal gradient compatible with a subduction zone environment (7-10 °C/km; e.g. Agard et al., 2006; Angiboust et al., 2016; Muñoz-Montecinos et al., 2021). This led to the formation of blueschist-facies rocks, occasionally overprinting higher temperature amphibolite-facies material (the Ashin garnet micaschists described in Agard et al., 2006). The Ashin complex, which represents the structurally highest sliver of the nappe-stack (Angiboust et al., 2016), exhibits a multi-stage metamorphic history with a spread in metamorphic ages ranging between c. 120 Ma to c. 79 Ma (K-Ar: Ghasemi et al., 2002; Ar-Ar: Agard et al., 2006; Rb-Sr: Angiboust et al., 2016 and

Shafaii Moghadam et al., 2017). The Ashin rocks represent one of the very rare witnesses of the Neo-Tethyan suture across several thousands of kilometers (i.e. from Turkey to India). Thus, refining our understanding of the Pressure-Temperature-time (P-T-t) evolution of the rocks forming the Ashin complex is crucial. The variety of metamorphic ages and the ubiquitous disequilibrium textures (Angiboust et al., 2016; Shafaii Moghadam et al., 2018), which at a first sight represent an obstacle for fine-tuning the timing of the Cretaceous metamorphic imprint, may perhaps be viewed as an opportunity for understanding and quantifying the long-term evolution of the subduction thermal gradient and hence, yield crucial information for paleo-geographic reconstructions. Indeed, on a broader perspective, the precise configuration of both the northern and southern subduction zones that were active in the Neo-Tethyan basin located to the North of Arabia during Cretaceous is still unresolved (e.g. Alavi, 1994; Agard et al., 2007; Hassanzadeh & Wernicke, 2016; Burg, 2018; Bonnet et al., 2020). In this regard, the Ashin complex may constitute a cornerstone for deciphering this missing piece of the Zagros subduction history. We herein report the first evidence for partial melting of some of the rocks forming this paleo-accretionary complex, provide new P-T-t data and discuss the implications of these findings for the regional geodynamics and the long-term evolution of the Neo-Tethyan realm.

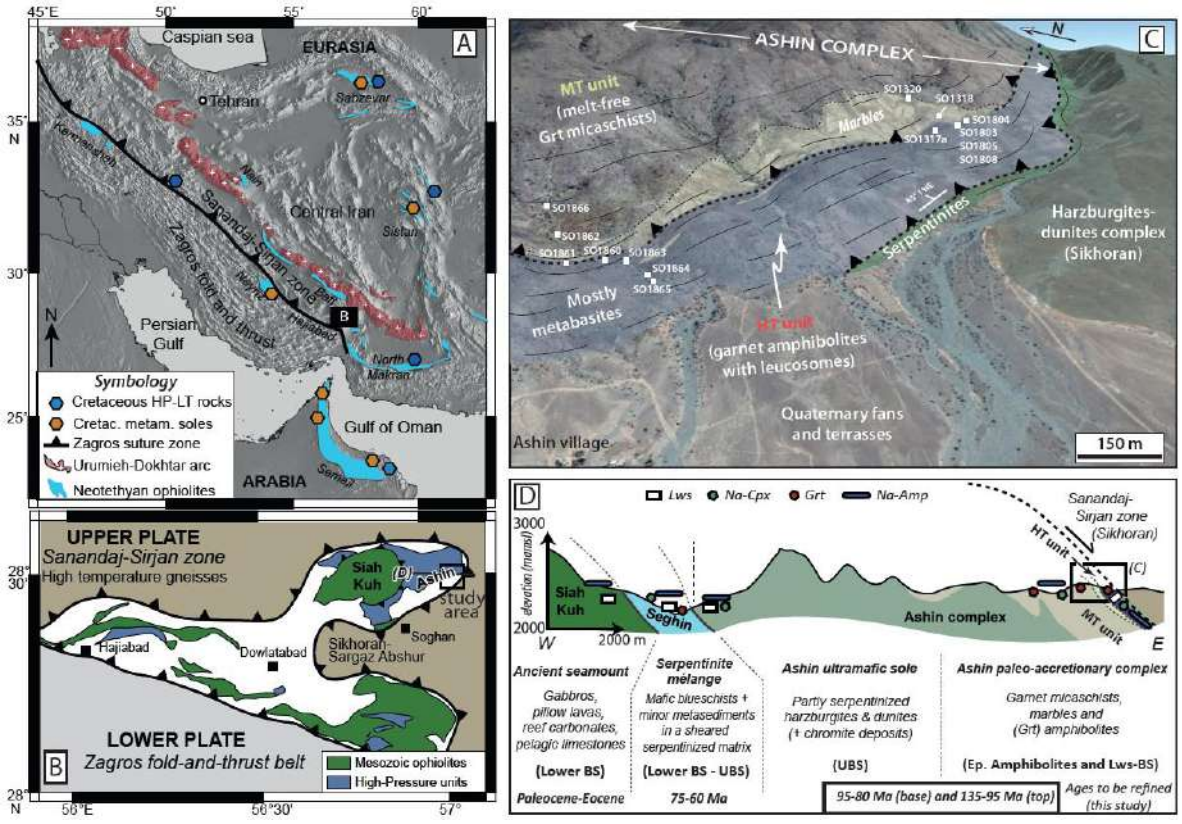

Figure 1. A*. Regional tectonic map locating the position of the Zagros suture zone, the ancient Urumieh Dokhtar arc as well as the main tectonic units reported in this study. The studied area is located in B. (modified after Bonnet et al., 2020).* ***B****. Simplified geological map of the study area locating the Mesozoic ophiolites, the units affected by a HP-LT overprint and the major thrust contacts in the area (modified after Agard et al., 2006).* ***C****. Panorama (Google Earth image) of the*

*study area (close to the Ashin village) showing the various lithologies encountered, the attitude of the foliation and the sampling locations. **D**. Simplified cross-section exhibiting the main relationships between the various units, the key index-minerals identified in the current and previous studies, and providing a summary of geological information for each of the units identified in this cross-section. References for ages are given in text.*

2. GEOLOGICAL SETTING

2.1. The Neo-Tethys Ocean

The Neo-Tethys Ocean separated Eurasia from the continents derived from Gondwana (e.g. Stampfli and Borel, 2002; Blakey, 2008). Subduction initiated in the Late Jurassic-Early Cretaceous, as recorded by several calc-alkaline volcanic arcs scattered along southern Eurasia, such as part of the Durkan volcanics in Iran (Burg, 2018; Esmaeili et al., 2020; Barbero et al., 2021) in the Sanandaj-Sirjan (SaSZ) domain. The evolution of the Northern Neo-Tethys subduction zone is mainly documented from ophiolites along the Indus-Yarlong-Tsangpo suture (e.g. Xigaze; Hébert et al., 2012). A second episode of subduction initiation occurred at 105-110 Ma (Guilmette et al. 2018), giving birth to a Southern Neo-Tethys subduction, whose ophiolitic remnants are scattered from Troodos (Cyprus) to the Spongtang ophiolite in the western Himalaya (Agard et al., 2007). The Late Cretaceous obduction of the Neiriz and Semail ophiolites North of Arabia is linked to the evolution of this Southern Neo-Tethys subduction (Agard et al., 2011).

The fabric of the Neo-Tethys Ocean commonly displays Oceanic Island Basalts (OIB), especially around 90-130 Ma (Mahoney et al., 2002; Yang and Dilek, 2015; Esmaeili et al., 2020), which testifies to an enhanced plume activity across the Neo-Tethys realm. The episode of initiation of the Southern Neo-Tethys subduction may be part of a global plate reorganization event around 105-110 Ma (Matthews et al., 2012; Rodriguez et al., 2021), well recorded in the Indian Ocean's fabric (Olierook et al., 2020). A change in the dynamics of the subduction zones surrounding the Indian Ocean is invoked as a likely driver for this event, including the deactivation of a subduction segment dipping beneath the Lhasa continental terrane (Li et al., 2018). This period of global plate reorganization may correspond to a period of global slow-down in plate velocities (Olierook et al., 2020), although the seafloor magnetic record is difficult to decipher for this time span. The evolution of the segments of the Northern Neo-Tethys subduction that used to run between Eurasia and Arabia in the Cretaceous is less documented (i.e. less well-preserved) than the segments preserved in Tibet. Two suture zones (the inner Zagros and the outer Zagros belts) are observed running parallel to the SaSZ and correspond to various remnants of the Tethyan basin that were accreted against the SaSZ during convergence and subsequent collision between the Arabian and Eurasian plates in the Cenozoic (e.g. Agard et al., 2007; Hassanzadeh & Wernicke, 2016; Ajirlu et al., 2016 and references therein).

2.2. The Zagros orogeny

The Zagros orogen is a relatively young mountain belt formed by the collision between the Arabian plate and the Iranian margin over the last 30 Ma (e.g. Berberian & King, 1981; Agard et al., 2011).

This collisional stage was preceded by a long-lasting NE verging subduction episode of the Neo-Tethyan lithosphere under the thinned Iranian margin, expected to have initiated during middle Jurassic times (c. 180 Ma; Berberian & King, 1981; McCall, 1997; Dercourt et al., 1993). Extensive calc-alkaline arc magmatism occurred in the upper plate between Jurassic and Eocene times along the SaSZ and the Urumieh Dokhtar magmatic arc (Alavi, 1994; **Fig.1A**). The SaSZ and the Urumieh Dokhtar complexes extend between the Bitlis area in Turkey down to the Makran area (Sengör et al., 1988) and were formed by a collage of various terranes against Central Iran (Ricou, 1994; Hassanzadeh & Wernicke, 2016). The SaSZ comprises a variety of pre-alpine metamorphic rocks as

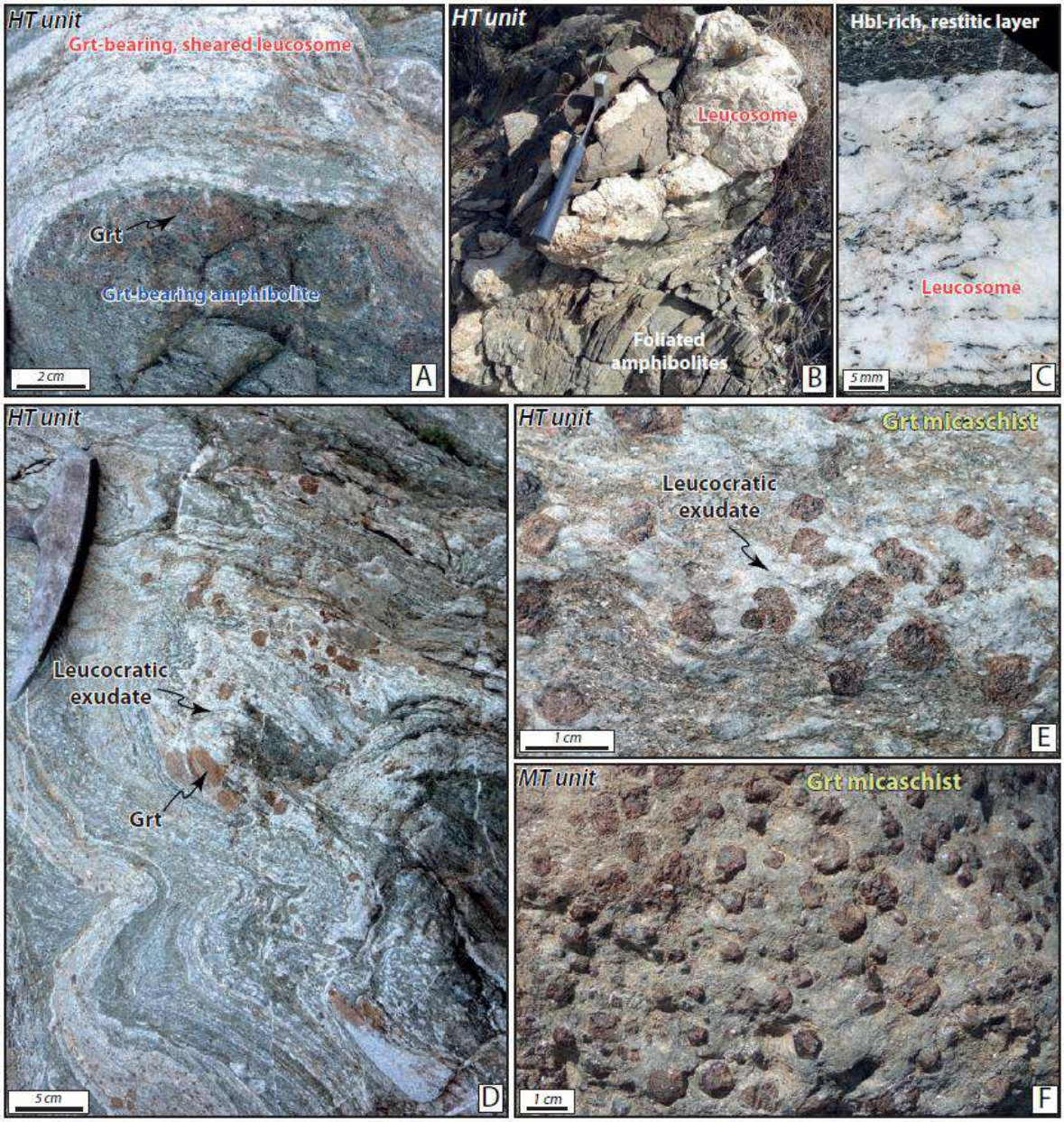

Figure 2. Field pictures of representative lithologies for HT and MT Ashin units. A. Garnet amphibolite residue with an adjacent, sheared (garnet-bearing) leucocratic domain. B. Leucocratic pocket wrapped within the amphibolite foliation. C.

Close up view of a restitic hornblende-rich and associated leucocratic domains containing blueish amphibole crystals parallel to the vein walls (sample SO1317). D. Field picture of a tightly folded leucocratic domain in a mafic and tuffaceous material exhibiting cm-sized euhedral garnet that grew within the leucocratic band. E. Close-up view of a garnet micaschist layer displaying some leucocratic, plagioclase-rich exudates wrapping garnet along the foliation (HT unit). F. View of a representative MT unit garnet micaschist, devoid of leucocratic bands.

well as accreted fragments of the Iranian margin (Arfania & Shahriari, 2009). In the studied Hajiabad-Esfandagheh area, SaSZ rocks (locally named as Sikhoran-Sargaz Abshur complex; **Fig.1B**) comprise tectonically intercalated Mesozoic and Paleozoic high temperature gneisses, exhibiting metamorphic ages between 185 and 330 Ma (Ghasemi et al., 2002; Arvin et al., 2007). These rocks, devoid of high pressure-low temperature (HP-LT) metamorphism, were inferred to occupy an upper plate position during the oceanic subduction event (Shafaii Moghadam & Stern, 2011). The origin of the metamorphic overprint affecting SaSZ rocks is debated. In the last few years, some authors have proposed that the SaSZ magmatism and metamorphism could be related to a rifting event (e.g. Azizi & Stern, 2019 and references therein).

2.3 The Hajiabad-Esfandagheh blueschists

Unlike SaSZ rocks, the Hajiabad-Esfandagheh blueschists (Sabzehei, 1974) exhibit widespread markers for HP-LT metamorphism and occur in a tectonic window under the SaSZ Sikhoran massif in the studied area (e.g. Agard et al., 2006). They are internally formed by an antiformal stack of tectonic slices of various P-T-t trajectories (Angiboust et al., 2016). The lowermost Siah Kuh unit, part of the "coloured mélange" as defined in literature (Stöcklin, 1974), is a pluri-kilometre sized ophiolitic massif that was weakly metamorphosed at the entrance of the blueschist facies (c. 250 °C at 0.7 GPa) and has recently been interpreted as an almost undisturbed seamount accreted against the SW Iranian margin during the early Cenozoic (Bonnet et al., 2019). Above this lies a serpentinite-rich block-in-matrix domain (Seghin complex), mostly comprising decametre to hectometre-sized lawsonite-blueschist facies lenses of mafic tuffs associated with minor marbles (Sabzehei, 1974; Angiboust et al., 2016; Muñoz-Montecinos et al., 2021). Peak burial conditions, typical of a cold subduction environment (500 °C, 1.6 GPa) were reached between 60 and 75 Ma according to multi-mineral Rb-Sr dating (Angiboust et al., 2016; see also Shafaii Moghadam et al., 2017). The shear zone separating the Seghin complex from the basal ultramafic part of the Ashin complex (**Figs.1C and D**) is a several hundred meter-thick serpentinized domain which comprises scarce jadeitite veins inferred to have formed at around 400-450 °C and 1.6 GPa (Oberhänsli et al., 2007; Angiboust et al., 2016).

The uppermost part of the nappe-stack is occupied by the Ashin unit (Agard et al., 2006; Angiboust et al., 2016) which is internally formed from the base to the top by (i) a variably thick (0-500 m) harzburgitic to dunitic sequence (comprising chromitite pods), (ii) slivers of blue-amphibole-bearing, phengitic quartzites, (iii) a strongly folded and foliated garnet micaschists sequence with minor meta-mafic, marble and meta-chert intercalations and (iv) an uppermost, tens-of-meters thick meta-mafic-sedimentary association (**Figs.1C and D**). Agard et al. (2006) and Angiboust et al. (2016) have

reported amphibolite-facies conditions for Ashin garnet micaschists with temperatures in the order of 550 °C and pressures close to 1 GPa. The K-Ar ages published so far for Ashin micaschists are quite scattered, at c. 79 ± 2 Ma, 82 ± 1 Ma (Ghasemi et al., 2002), 98 ± 2 Ma and 101 ± 2 Ma (Delaloye & Desmons, 1980). More recently, Agard et al. (2006) reported similar in situ white mica Ar-Ar ages of 82-102 Ma and 89-109 Ma for Ashin complex garnet micaschists. Multi-mineral-based Rb-Sr isochron ages (Angiboust et al., 2016) revealed that the base of the Ashin complex (namely the quartzites) yield end of deformation ages slightly younger (78-96 Ma) than the uppermost part (the garnet micaschists and the marbles) for which 92-101 Ma ages were reported. Interestingly, an amphibolite sample collected in the uppermost part of the Ashin complex and displaying evident textural and isotopic disequilibrium features yielded a poorly constrained, but clearly older Rb-Sr age in the range of 110-130 Ma. Equally old ages of 124-136 Ma were also reported in Shafaii Moghadam et al. (2017) using a similar methodological approach. The significance of this large age spread recorded in Ashin complex rocks will be hereafter discussed in the perspective of a new tectono-metamorphic model.

3. STRUCTURE AND LITHOLOGIES OF THE ASHIN COMPLEX

The upper part of the Ashin complex comprises subvertical to steeply SE-dipping slivers with distinct lithological compositions which were overthrust by the ultramafic lithologies from the Sikhoran-Sargaz-Abshur massif (SaSZ) in the study area (**Fig.1C**). The contact between these two units is lined by SE-dipping level of strongly sheared serpentinites, which are transected by a late, high-angle normal fault network (N060-striking) that contributed to the piedmont morphology now visible in the Ashin village region (e.g. Agard et al., 2006). In the studied locality, a pluri-kilometre-long meta-mafic sliver dominantly formed by amphibole-rich lithologies (and locally garnet amphibolites; **Fig.2A**) as well as meter-thick marble lenses and rare garnet micaschists layers were observed, interlayered within amphibolites of the mafic sliver (referred hereafter as the High Temperature unit: HT; **Fig.1C**). Leucocratic veins and segregates (**Fig.2B** and **C**) are commonly found as (i) cm-sized veinlets perpendicular with to host foliation, connecting to thicker drains and (ii) vein systems parallelized with the main foliation, commonly stretched and boudinaged along the local NE-SW striking main foliation direction (**Figs.1C and 2B**). The contacts between leucocratic and host material are sharp and irregular. Locally, dark rims can be observed in the host along the vein wall. Mafic layers are locally interleaved with more felsic, meta-tuffaceous lithologies characterized by a greater amount of white micas, also parallelized with the main foliation (**Fig.2D**). In the most pelitic facies, volumetrically rare, leucocratic exudates can be macroscopically observed along discrete layers associated with large garnet porphyroclasts (**Fig.2E**). Equally large garnet crystals are observed growing within these white exudates where they locally reach one centimetre in diameter. These leucocratic and melanocratic domains (observed only in the HT Ashin complex) display features typical of partial melting processes (according to the description of Sawyer, 2008) and are therefore referred to as leucosomes and melanosomes (or restites) in the following. Field evidence suggest that little volumes of melt formed within the amphibolite, likely less than c. 6 vol.% (see the geochemistry

section for further justification). A thick sequence of garnet micaschists (**Fig.2F**) capped by a several meters-thick, strongly foliated marble sliver (see Agard et al., 2006 for further structural and mineralogical data on these lithologies), referred hereafter to as the Medium Temperature unit (MT), immediately underlays the HT unit.

4. ANALYTICAL METHODS

4.1 Electron microprobe measurements

Petrological investigations were conducted on a set of 14 representative samples localized on **Fig.1C** and **Table S1**. Electron probe microanalyses were acquired at the GFZ Potsdam with a GEOL-JXA8230 and at the Department of Earth Sciences, University of California Santa Barbara, on a Cameca SX-100 machine under common analytical conditions (15 Kv, 20 to 10 nA, wavelength-dispersive spectroscopy mode) using a 5 µm beam. Standards used for the calibration were as follows: orthoclase (Al, Si, K), fluorite (F), rutile (Ti), Cr_2O_3 (Cr), wollastonite (Ca), tugtupite (Cl), albite (Na), MgO (Mg), Fe_2O_3 (Fe) and rhodonite (Mn). Elemental X-ray maps were performed on the same instruments with a step size of 5 and 20 µm and a dwell time of 20 ms. The resulting X-ray maps were processed using the software DWImager (Garcia-Casco, 2007). In order to highlight minerals and textures of interest, some mineral phases were masked out, and the color images of the phases of interest were overlain onto a grayscale-image base-layer calculated with the expression $\Sigma[counts/nA/s)_i * A_i$, (where A is the atomic number and i corresponds to Si, Ti, Al, Fe, Mn, Mg, Ca, Na, K, Cr) and contains the basic textural information of the scanned areas. Representative major element mineral analyses are provided in **Table S2.**

4.2 Whole rock major and trace elements geochemistry

Six representative leucocratic veins and ten amphibolites were processed for whole rock major and trace element determinations using X-ray fluorescence (XRF) and inductively coupled plasma mass spectroscopy (ICP-MS) at the Centre for Scientific Instrumentation of the University of Granada (CIC-UGR). XRF major element analyses were performed after melting using a lithium tetraborate fusion flux. Typical analytical accuracy was better than ± 1.5% for an analyte concentration of 10 wt. %. Zirconium was determined by X-ray fluorescence on the same disks, with a precision better than ± 4% for 100 µg/g of Zr. ICP-MS measurements were performed after HNO_3+HF digestion of 0.1 g of sample powder in a Teflon-lined vessel at ~180 °C and 200 psi for 30 min, evaporation to dryness, and subsequent dissolution in 100 ml of 4 vol.% HNO_3. Instrument measurements were carried out in triplicate with a PE SCIEX ELAN- 8000 spectrometer using rhodium as an internal standard. Precision determined from standards WSE, BR and AGV run as unknowns, was better than ± 2% and ± 5% for analyte concentrations of 50 and 5 µg/g, respectively. The results are offered in **Table S3**.

4.3 Rutile LA-ICP-MS measurements

In situ U–Pb and trace-element analyses of rutile were performed using the laser ablation split-stream (LASS) facility at the University of California, Santa Barbara (USA). The LASS system combines a Cetac 193-nm ArF Excimer laser and Hel-Ex2 ablation cell with a Nu Instruments Plasma HR-ES multi-collector ICP-MS for collecting U-Th-Pb data and an Agilent 7700S quadrupole ICP-MS for collecting major and trace element data. Methods used in this study follow those outlined by Kylander-Clark et al. (2013). Rutile grains were analysed in situ in thin sections and from separated crystal mounts. Rutile was ablated using a variable beam diameter, depending on the grain size of the sample, of 35 µm (for SO1866) or 50 µm spots (for all other samples), at 4 Hz repetition rate for 60 shots at a laser fluence of 1 J/cm^2, after two pre-ablation shots at 50% laser power used to remove surface contamination. U–Pb data reduction, including corrections for baseline, instrumental drift, mass bias, down-hole fractionation and uncorrected age calculations were carried out using the Iolite v. 2.5 (Paton et al., 2011), and error correlations were recalculated after Schmitz and Schoene (2007). Analyses of unknowns were bracketed (once every ~8 unknowns) by analyses of matrix-matched reference material Kragerø rutile (~1090 Ma ID-TIMS date; Luvizotto et al., 2009; Bracciali et al., 2013). Secondary rutile reference material R9826J (381.9 ± 1.1 Ma TIMS date; Kylander-Clark et al., 2008), Wodgina (2845.4 ± 0.5 Ma Tera-Wasserburg Concordia date; Ewing, 2011) were analysed concurrently (once every ~16 unknowns) and treated as unknowns to assess accuracy and precision. The uncertainty on isotopic ratios includes the internal uncertainty determined by Iolite to which a systematic percentage of uncertainty was added to ensure that the weighted mean of isotopic ratios of secondary standard R9826J analyses have a MSWD of 1. During the course of the study, we obtained ages of 386.0 ± 2.4 Ma for R9826J (n=20), and 2777.9 ± 14.6 Ma for Wodgina (n=20), within 1.1% and 2.4% of the reference values, respectively. All unknowns were additionally bracketed by analyses of international glass standard BHVO2G (Jochum et al., 2005), that was used as a primary standard for trace elements, using ^{47}Ti as the internal standard element and an assumed concentration of 59.94 wt.% Ti in rutile. For these samples, U-Pb isotopic analyses were displayed with 95%-confidence error ellipses in Tera-Wasserburg diagrams. Discordia isochron ages were calculated with IsoplotR (Vermeesch, 2018) using the least-square "York" method. In order to decipher the span of ages covered, isochrons were anchored to the common ^{207}Pb/^{206}Pb value at 100 Ma (Stacey & Kramers, 1975).

4.4 Lu-Hf garnet analysis

The methodology for initial preparation for garnet geochronology broadly follows that described by Dragovic et al. (2012). The sample was split into two sub-volumes; one for garnet separation and the other for whole rock/matrix preparation. The first sub-volume was hand-crushed using an agate mortar and pestle, sieved to between 74 and 149 µm grain size (100-200 mesh size), and run through a Frantz magnetic separator in order to remove most of the non-garnet minerals. The resultant garnet separate was divided into several fractions of ~100-150 mg each for subsequent dissolution and clean chemistry. A "matrix" sample was obtained by physical separation of garnet porphyroblasts from the

whole rock sub-volume. Both the matrix and whole rock were powdered using an agate mortar and pestle. All samples subsequently underwent a full dissolution procedure. Aliquots of the whole rock and matrix were digested using a 4:1 HF/HNO_3 solution in a Parr bomb (i.e. a high-pressure, steel-jacketed Teflon vessel) for 7 days. Additional aliquots of the whole rock and matrix, along with the garnet separates were also digested by a "tabletop" technique. This approach first involves treatment in a concentrated HF/1.5N HCl solution at 120°C. This is performed until few visible grains remain (importantly, the refractory and Hf-rich minerals zircon and rutile remain undissolved and thus do not affect isotopic analyses). Samples are then redissolved in 2:1 concentrated HNO_3/1.5N HCl to remove secondary fluorides. All samples were then equilibrated with in-house mixed ^{176}Lu-^{180}Hf spike appropriately chosen for the (elemental) Lu/Hf ratio of the samples. Following this, a two-step column chromatography procedure was performed to extract high purity Lu and Hf separates, modified after the methods of Bast et al. (2015).

Analyses were performed at the Center for Elemental Mass Spectrometry (CEMS) at the School of the Earth, Ocean and Environment, University of South Carolina, using a Thermo-Fisher Neptune Plus multi-collector inductively coupled plasma mass spectrometer (MC-ICP-MS) with an Apex Omega desolvating nebulizer. The $^{176}Lu/^{175}Lu$ was determined following Vervoort et al. (2004) based on the observation that the Yb-isotope mass fractionation on the instrument biased relative to the Lu-isotope mass fractionation. The reproducibility of the calculated natural $^{176}Lu/^{175}Lu$ (taken as $^{176}Lu/^{175}Lu = 0.02655$) is tested in different Lu/Yb elemental mixtures at the beginning of each analytical session. We used $^{173}Yb/^{171}Yb = 1.129197$ for mass fractionation and calculated the ^{176}Yb contribution to the ^{176}Lu signal using a $^{176}Yb/^{173}Yb$ (natural) value of 0.793045. Based on a plot of ^{176}Yb-interference- and fractionation-corrected $^{176}Lu/^{177}Lu$ vs. $^{173}Yb/^{175}Lu$ (proportional to elemental Yb/Lu), we determined an instrumental mass bias factor of 0.9997 on the $^{176}Yb/^{173}Yb$ ratio upon which corrected $^{176}Lu/^{177}Lu$ ratios remain constant for a range of added Yb. This mass bias factor is instrument- and introduction system-dependent and relates to the transmission of each isotope beam through the instrument, but varies between 0.9996 and 0.9998, long-term, at CEMS. The $^{176}Hf/^{177}Hf$ and Hf concentrations were determined. The $^{179}Hf/^{177}Hf$ value of 0.7325 was used for mass fractionation correction. External reproducibility on 30-ng runs of an in-house Hf standard elemental solution during the analytical session was 0.25 ε_{Hf} units (n= 10). Lastly, Lu and Hf concentrations were determined by isotope dilution, and $^{176}Lu/^{177}Hf$ ratios were calculated from that data. The resulting isotopic data and ages are presented in **Table S4**.

4.5 Zircon LA-ICP-MS and SHRIMP measurements

Zircon crystals were separated using panning, first in water and then in ethanol. This was followed by magnetic extraction of Fe-rich minerals with a NdFeB permanent magnet. Finally, zircons were handpicked using a binocular microscope. The zircons were cast on "megamounts", i.e. 35 mm epoxy discs fixed on the front of a mount holder so that no metallic parts or surface discontinuities faced the secondary ions extraction plate. The crystals were carefully studied with optical (reflected and transmitted light) and scanning electronic microscopy (backscattering and cathodoluminescence)

prior to laser ablation inductively coupled plasma mass spectroscopy (LA-ICP-MS) and SHRIMP analyses.

Trace element analyses were done at the CIC-UGR LA-ICP-MS laboratory using a Perkin Elmer NexION 350X ICP-MS coupled to a New Wave Research NR 213 laser ablation system. The analyses were performed on the same mounts used for isotope analyses using the NIST-610 glass as an external standard, which was measured after every six unknowns. Spots to be analysed were pre-ablated for 15 seconds with a laser fluency of 2.5 J cm^{-2}, and then ablated for 60 seconds with a laser fluency of 7.5 J cm^{-2}. A blank, measured in the same conditions but with zero laser energy, preceded every measurement. Data reduction was done using an in-house software written in the STATA™ programming language.

Zircon crystals were analysed at the CIC-UGR with the IBERSIMS SHRIMP IIe/mc ion microprobe for U-Th-Pb following the method described by Williams & Claesson (1987). The mount was coated with a c. 12 nm thick gold layer. Each spot was rasterized with the primary beam for 120 s prior to analysis and then analysed for 6 scans following the isotope peak sequence $^{196}Zr_2O$, ^{204}Pb, $^{204.1}$background, ^{206}Pb, ^{207}Pb, ^{208}Pb, ^{238}U, ^{248}ThO, ^{254}UO. Every peak of every scan was measured sequentially 10 times with the following total counting times per scan: 2 seconds for mass 196; 5 seconds for masses 238, 248, and 254; 15 seconds for masses 204, 206, and 208; and 20 seconds for mass 207. The primary beam, composed of $^{16}O^{-16}O^{+}$, was set to an intensity of about 5 nA, with two Köhler apertures: (1) at 120 μm and (2) at 70 μm, which generated 17 × 20 and 9 × 12 μm elliptical spots on the target to analyse cores and rims respectively (see Zircon dating results section). The secondary beam exit slit was fixed at 80 microns, achieving a resolution of about 5000 at 1% peak height. All calibration procedures were performed on the standards included on the same mount. Mass calibration was done on the REG zircon (ca. 2.5 Ga, very high U, Th and common lead content). The analytical session started by measuring the SL13 zircon (Claoue-Long et al., 1995), which was used as a concentration standard (238 ppm U). The TEMORA zircon (416.8 ± 1.1 Ma; Black et al., 2003), used as an isotope ratios standard, was then measured after every 4 unknowns. Data reduction was done with the SHRIMPTOOLS software (available from www.ugr.es/~fbea), which is a new implementation of the PRAWN software originally developed for the SHRIMP. Uncertainties are reported at the 95% confidence interval (≈2σ). Standard uncertainties (95% C.I) on the 37 replicates of the TEMORA standard measured during the analytical session were ± 0.35% for $^{206}Pb/^{238}U$ and ± 0.83 % for $^{207}Pb/^{206}Pb$. The resulting ages, isotopic ratios and element concentrations are presented in **Table S5**.

4.6 Thermodynamic modelling

The T-X(H_2O) and P-T pseudosection calculations were performed using the Perple_X software version 6.9.1 (Connolly, 2005). The selected chemical system (Na_2O-CaO-K_2O-FeO-MgO-MnO-Al_2O_3-SiO_2-TiO_2-H_2O) reflects a representative mafic amphibolite (sample SO1804, see **Table S3**) which shows a bulk major (and trace) elements composition similar to MORB (see section 6). In sake

of simplifying this chemically complex system, iron is considered as ferrous (this assumption is largely supported by the clinozoisite-rich nature of epidote observed in garnet amphibolites). This modelling approach is particularly challenging since neither mafic restite nor leucosome compositions alone properly represent the bulk composition of the system at the melt-producing conditions.

We used the following list of Perple_X solid solution models: feldspar (Fuhrman and Lindsley, 1988), clinopyroxene (Holland and Powell, 1996), chlorite (Holland et al., 1998), orthopyroxene (Powell and Holland, 1999), ilmenite (Ti-phases, White et al. 2000), amphibole (Dale et al, 2005), melt, garnet and biotite (White et al, 2007) and white mica (Smye et al., 2010). The choice of this list is motivated and justified by the consistency of results obtained in a previous study on partially molten MORB rocks (Angiboust et al., 2017) for a geological problem largely similar to the current investigation. Modelling is run using the ds5 thermodynamic database (Holland and Powell, 1998; updated in 2002).

5. PETROGRAPHY AND MINERAL CHEMISTRY

5.1 Amphibolites

The HT unit amphibolites mainly consist of medium- to coarse-grained amphibole (70-80 vol%) with subordinate amounts of plagioclase, garnet, epidote, titanite, ilmenite, rutile, quartz and chlorite. Amphiboles are euhedral to subhedral (**Figs.3A to C and E**) and correspond mostly to tschermakite and Mg-hornblende, but pargasite and edenite are locally observed (**Figs.4A, B and 5A to D**). They exhibit blueish sodic-calcic or locally sodic amphibole as well as light green actinolitic rims (**Figs.3E, 4A, B and 5A to D**). The HT amphiboles are commonly in apparent textural equilibrium with euhedral, porphyroblastic garnet or show inclusions of the latter. Within sample SO1863b, garnet (commonly chloritized along the rims and fractures) makes up to c. 5 vol% of the rock with grain diameters of commonly c. 2 mm but reaching grain sizes of up to 7 mm. Garnet is weakly zoned, with a composition in the range $Alm_{50\text{-}70}Prp_{1\text{-}10}Grs_{20\text{-}50}Sps_{1\text{-}2}$ (**Fig.4C**). Garnet from a garnet-rich layer in sample SO1860 (hereinafter referred to as “garnet-amphibolite”) exhibit atoll-like textures. Ca-Mg-Fe clinopyroxene in the range of $CEn_{33\text{-}41}CFs_{16\text{-}35}Wo_{30\text{-}49}$ (augite and diopside; **Figs.4D and E**) are observed as inclusions within garnet in the garnet-amphibolite (SO1860). Rare omphacite needles and Mg-riebeckite have been reported overgrowing prograde amphiboles in the adjacent mafic lithologies (Angiboust et al., 2016). Epidote or zoisite commonly occurs as blocky grains on the rims of or within amphibole crystals and/or in association with garnet (**Figs.3B, F** and **S1A to D**). Epidote is observed to be locally replaced by lawsonite. Myrmekitic epidote associated with albite is locally

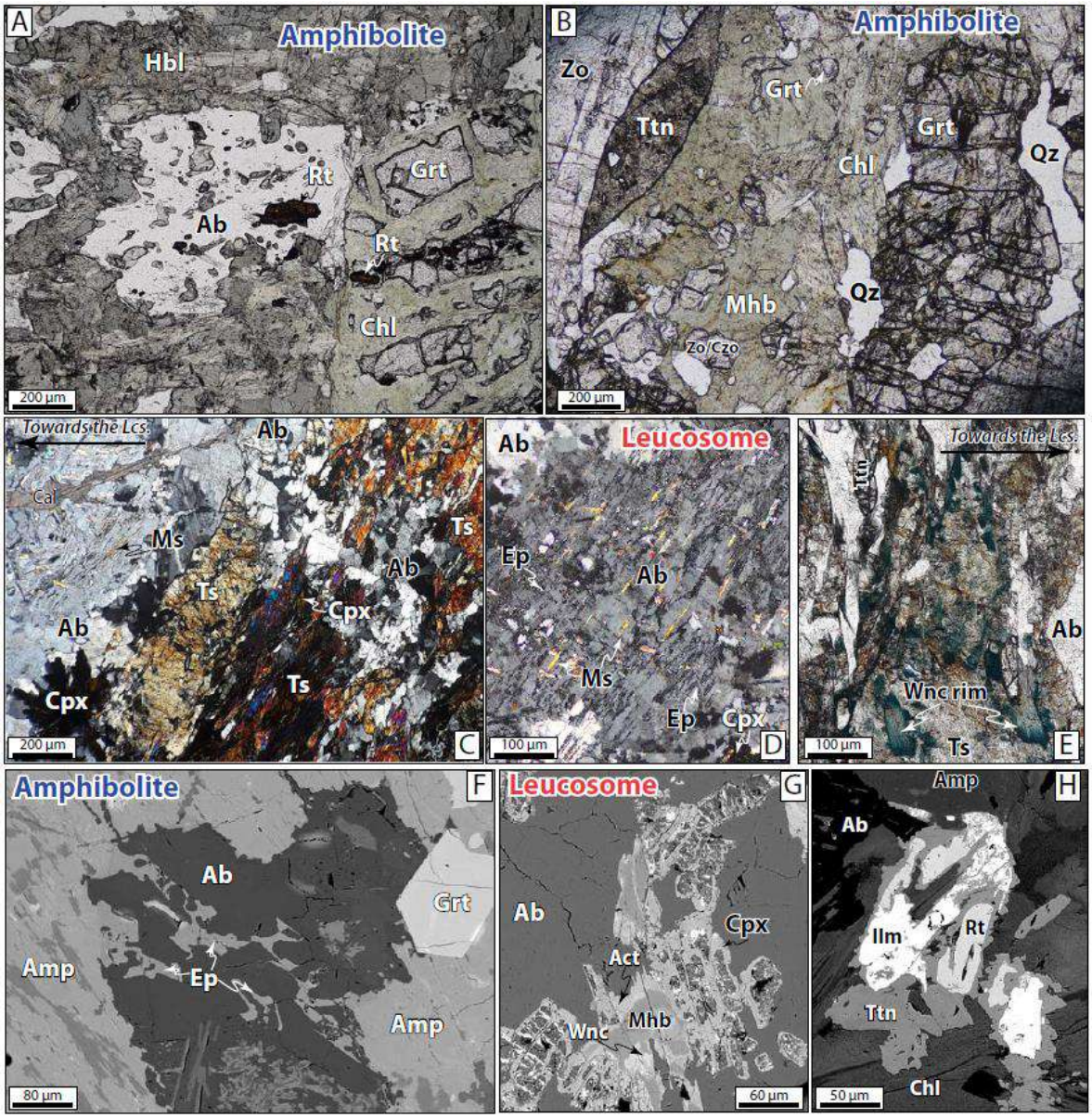

Figure 3. A to E. Optical polarized light photomicrographs (crossed polarizers used for Fig. 3C and D) of representative amphibolites and leucosome domains from the Ashin HT unit. F to H. Backscattered electron images of amphibolite and leucosome domains highlighting relevant mineral textures (see the main text) from the Ashin HT samples.

observed in interstitial leucocratic domains within the amphibolite (**Fig.3F**). Titanite displays varying grain sizes of up to millimeter size values, occurs within the rims or along the grain boundaries of amphibole (**Fig.3B**) and occasionally hosts rutile and ilmenite relicts (**Fig.3H**). Further, albite-rich plagioclase (Ab_{85-95}) and quartz are commonly found within the interstitial spaces of amphibole, epidote and garnet (**Figs.3A, H** and **5H**). In sample SO1861, clustered and oriented clinozoisite makes up a volumetrically important domain ("zoisitite"; **Fig.3B**).

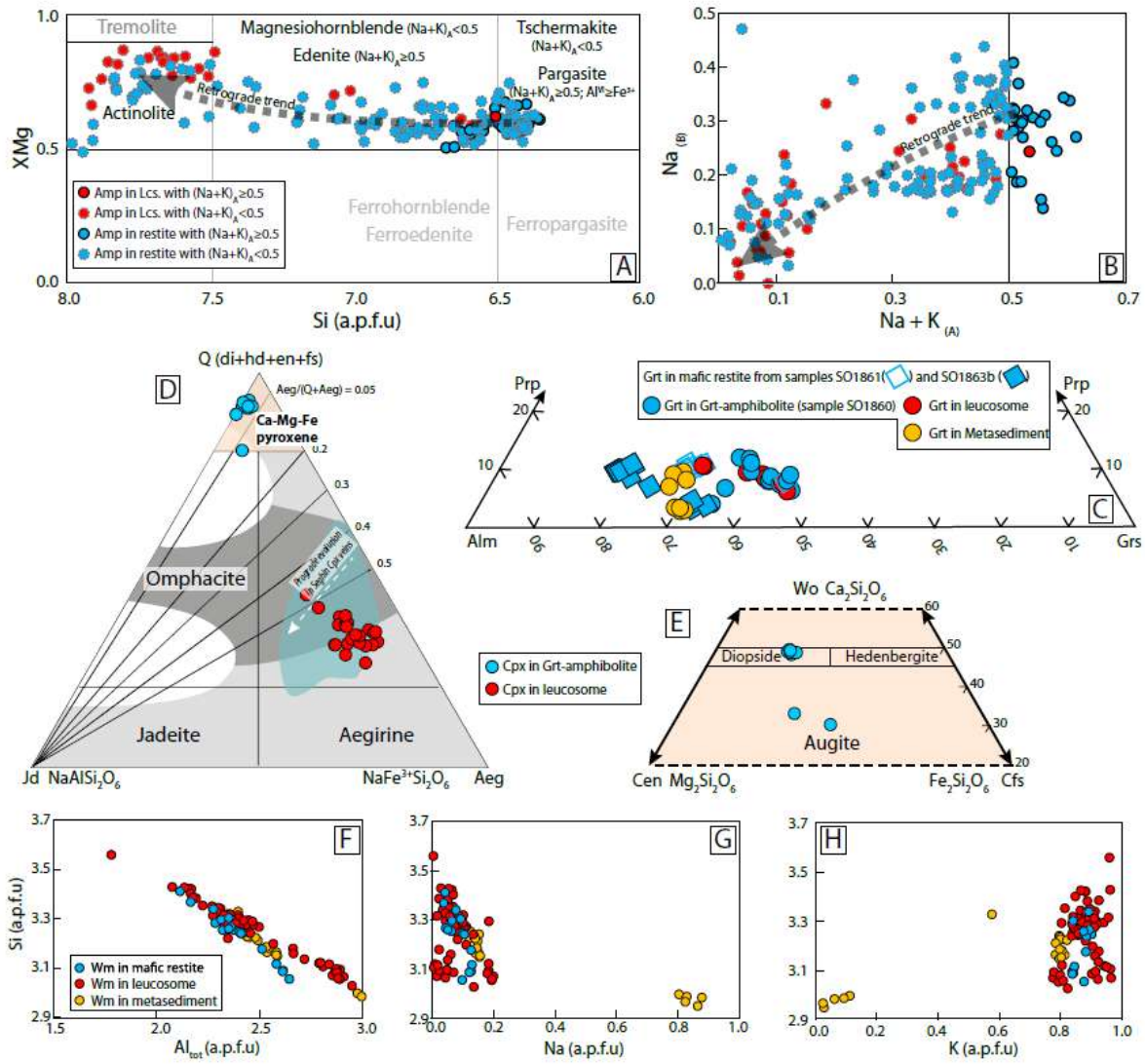

Figure 4. Summary of mineral chemistry results of amphibole (A and B), garnet (C), clinopyroxene (D and E) and white mica (F to H) in samples from Ashin HT unit material. Additional epidote and white mica mineral chemistry diagrams are offered in Figures S1A to D.

5.2 Leucocratic exhudates

Leucocratic veins (hereafter referred to as leucosomes) from the HT unit comprise coarse-grained plagioclase + quartz and subordinate phengitic white mica + amphibole + titanite + rutile + chlorite + epidote ± clinopyroxene ± lawsonite (**Figs.3C** and **D**). The interfaces between amphibolite and the leucosome domains generally follow the overall layering/orientation of the amphibole crystals. Both domains are spatially connected through plagioclase-rich microchannels in the amphibolite (**Fig.3C**). The leucosomes are chiefly made of albitic plagioclase (up to 80 vol%; Ab_{80-99}), although X-ray mapping and cathodoluminescence imaging revealed the presence of a clear patchy zoning pattern with oligoclase domains (**Figs.5H and S2**). White mica occurs as 100µm-1mm laths, randomly oriented inclusions within or along the cleavage of coarse plagioclase crystals, or as dense clusters

associated with epidote (**Figs.3C, D and G**) in "saussuritized" domains. Muscovite cores commonly exhibit thin phengitic rims showing a clear Tschermak substitution trend with increasing Mg and Si at the expenses of Al, while Na-richer cores are locally observed (**Figs.4F, 5E, F and G**). Large rutile grains (which were separated for Zr-in-rutile thermometry, see below) are commonly rimmed by titanite (e.g. **Fig.5E**). Some acicular actinolite grains grow along the cleavage planes of medium-grained plagioclase crystals in sample SO1317. Single small crystals of Mg-hornblende have been identified within the leucosomes. In the leucosome-restite interface (**Figs.5A to D**), amphibole is strongly zoned with compositions ranging from Mg-hornblende to tschermakite (locally edenite and pargasite) in the cores and winchite to actinolite towards the rims. Some elements such as Al and Ti are particularly enriched in the cores, the latter showing an exceptionally well-defined pattern (**Fig.5C**). The calculated XMg ($Mg/(Mg+Fe^{2+})$) values are generally high (above 0.5) with higher values towards the actinolitic rims but never reaching tremolitic values (**Figs.4A and 5D**). Epidote is commonly Fe^{3+}-poor (**Fig.S1**) and occurs associated with or overgrowing amphibole (e.g. **Fig.5A**). Furthermore, minor amounts of dark brown, prismatic clinopyroxene (of aegirine composition; **Fig.4D**) occur as fine-grained aggregates or fibro-radial clusters (**Figs.3C and G**). They seem to have nucleated on other minerals such as hornblende or a previous (now pseudomorphed) clinopyroxene (**Fig.3G**). Interestingly, lawsonite is observed overgrowing plagioclase within the leucosome or filling micro-fractures (**Fig.5H**). Pumpellyite and calcite occur in the leucosomes as patches and late veins (**Fig.S2B**), respectively. The paragenetic sequence observed in amphibolites and associated leucosome domains is summarized in **Fig.6**.

5.3 Garnet micaschists

Garnet micaschists from the HT unit are observed interleaved with amphibolite and tuffaceous levels (characterized by their relatively high white mica contents). Their mineral assemblages comprise garnet + white mica + quartz + albite + rutile as well as scarce amphibole crystals. Garnet micaschists from the MT unit comprise garnet + white mica + quartz + albite + rutile + ilmenite + rutile + epidote + chlorite + calcite (see **Fig.S3**). Their mineralogy as well as thermo-barometric constraints has been given in Agard et al. (2006, see also Angiboust et al., 2016 for further petrological information). Rutile occurs as oriented grains within garnet rims as well as along the main metamorphic foliation, whereas titanite forms large automorphous crystals within garnet mantles (apparently connected to the matrix via fracture networks) and rimming rutile crystals in the matrix. Ilmenite inclusions found in garnet cores are oriented along a previous foliation. Garnet is essentially almandine with XMg contents exhibiting a slight increase towards the rims (XMg: core = 0.01, rim = 0.11, see **Fig.S3**). White mica displays three generations with phengitic cores (Si=c.3.3 apfu), muscovitic mantles (Si=c.3.1 apfu) and thin outer rims of phengitic composition (Si=c.3.4 apfu; **Fig.S3**). In addition, rare paragonite (K=c.0.03 to 0.1 apfu) has been observed within the matrix around garnet (**Figs.4G and H**).

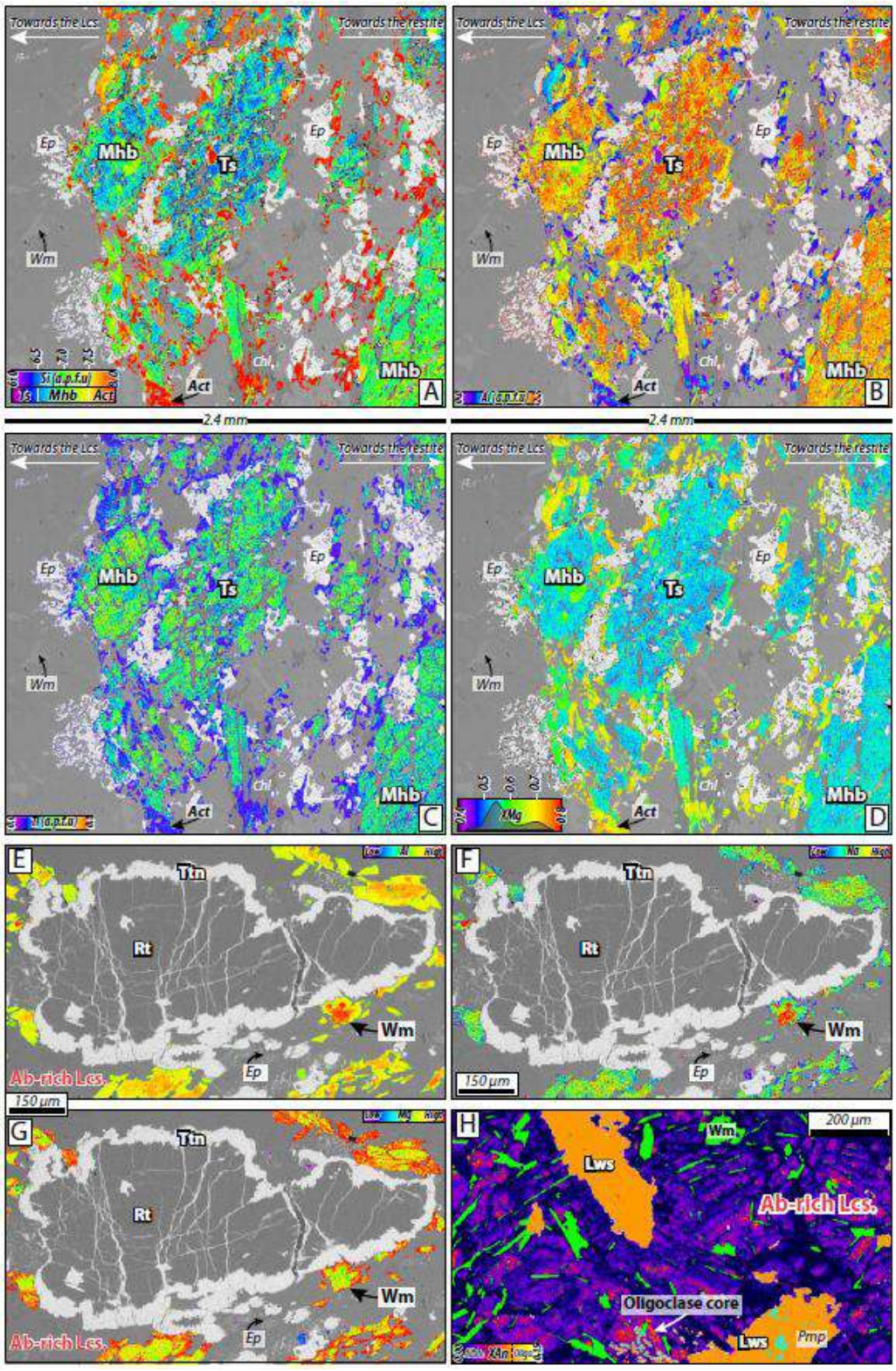

Figure 5. X-rays maps from Ashin HT unit samples highlighting multiple recrystallization and metamorphic events recorded in these rocks. A to D. Leucosome-restite interface emphasizing amphibole textures. E to G. Leucosome view highlighting rutile and white mica mineral textures. H. Albite-rich leucosome depicting mineral zoning characterized by higher anorthite component towards plagioclase cores. Note the occurrence of lawsonite overgrowing the leucosome fabric.

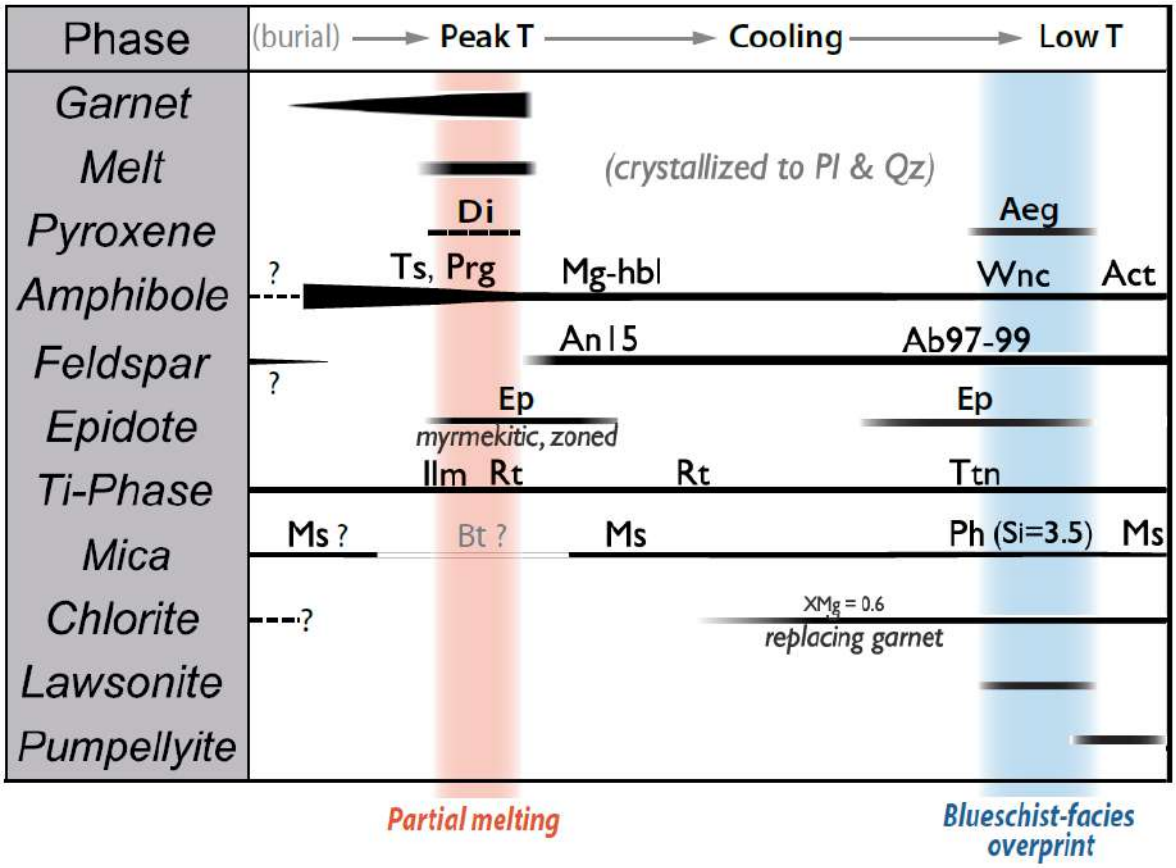

Figure 6. Occurrence table summarizing the paragenetic evolution throughout the metamorphic history recorded by Ashin HT unit samples.

6. WHOLE-ROCK GEOCHEMISTRY

6.1 Amphibolites

Garnet amphibolite and amphibolites show major element compositions with SiO_2 varying between 41 and 55 wt.% and Na_2O+K_2O varying between 1.7 and 7.4 wt.% (excluding the zoisite-rich sample SO1861b), belonging thus to the picro-basalts and basalts fields in a TAS diagram (up to basaltic trachy-andesite for one sample; **Table S3**). The chondrite-normalised Rare Earth Elements (REEs) pattern shown in **Fig.7A** for Ashin HT unit amphibolites span a range between N-MORB and OIB end-members. Their Heavy Rare Earth Elements (HREEs) generally define a nearly flat pattern, whereas some amphibolites show relatively enriched Light Rare Earth Element (LREE) concentrations. The Th/Yb versus Nb/Yb diagram from Pearce (2008) (**Fig.7B**) is generally used for tracking mantle sources (Nb/Yb) and the effect of crustal components (Th/Yb), making use of two highly and nearly equally incompatible elements in mafic magmas (Th and Nb). The two elements are considered as sensitive indicators of crustal involvement due to magma-crust interaction or to inheritance of subduction components (Pearce, 2008). In this diagram, the Ashin HT unit rocks are distributed between normal N-MORB patterns (four samples) and substantially enriched signatures (five samples) showing considerable higher Th/Yb ratios than the MORB-OIB array.

6.2 Leucosomes

Major element data from Ashin HT leucosomes yields SiO_2 contents ranging between 62 and 66 wt.%, very high Na_2O contents between 9 and 11 wt.% and low K_2O and CaO contents (0.2-0.8 wt.% and 1.1-4.4 wt.%, respectively; **Table S3**). Iron and magnesium contents are also very low (<0.4 wt.%). These leucosomes thus belong to the trachytic field in a TAS diagram. Several of these samples correspond to the field of trondhjemites according to the classification of O'Connor (1965) and with the fields of Barker (1979) as shown in **Fig.7C**. The chondrite-normalized pattern from **Fig.7A** shows considerably low REE concentrations overlapping with trondhjemitic signatures from other localities such as Isla Diego de Almagro and Sierra del Convento and La Corea case studies (Garcia-Casco et al., 2008). Some of them show an increase in LREEs, possibly indicating some degree of fractionation. In the Th/Yb vs Nb/Yb diagram (**Fig.7B**), the Ashin leucosomes also overlap with those from the Sierra del Convento locality, spanning a range between average OIB and E-MORB compositions.

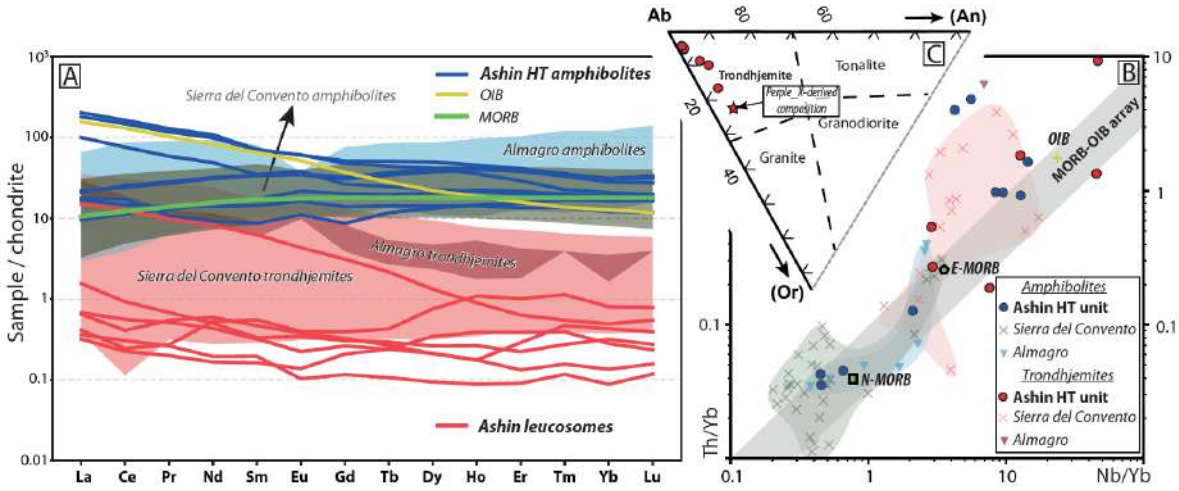

Figure 7. A. Chondrite-normalized trace element patterns for the suite of studied samples including Ashin leucosomes and amphibolites. Data from other geological settings (Diego de Almagro Island, Patagonia; Angiboust et al., 2017 and Sierra del Convento-La Corea areas, Cuba; Lazaro et al., 2011; Blanco-Quintero et al., 2011) as well as OIB and MORB patterns are shown for comparison. B. Trace element Th/Yb versus Nb/Yb diagram (from Pearce, 2008). For reference, the composition of several trondhjemite samples were also plotted in this diagram originally designed for primitive basaltic rocks. C. classification of granitoids in the An-Ab-Or normative projection (after the classification of Barker, 1979). The red star is the theoretic composition predicted at 680 °C and 1.2 GPa using thermodynamic modelling.

7. Garnet Lu-Hf dating

The Lu and Hf concentrations, $^{176}Lu/^{177}Hf$ and $^{176}Hf/^{177}Hf$ ratios for all samples are reported in **Table S4**. Hf isotope data are reported against the JMC-475 Hf standard value of $^{176}Hf/^{177}Hf = 0.282160$ (Vervoort and Blichert-Toft et al. (1999). For age calculations, an uncertainty of 0.5% is used for $^{176}Lu/^{177}Hf$ ratios. Uncertainties in the $^{176}Hf/^{177}Hf$ ratios are reported as the internal precision (shown as 2 σ S.E. in Table X) of the analyses, are determined by within-run statistics.

Lu and Hf concentrations in analysed garnets display consistent concentrations of ~1.8 µg/g and ~0.04 µg/g, respectively (**Table S4**). Resultant $^{176}Lu/^{177}Hf$ ratios in garnet range from ~5.6 to ~6.1, suggestive of clean separates lacking the incorporation of deleterious Hf-rich inclusions during the full dissolution process (i.e. zircon). The tabletop-digested whole rock and matrix have significantly lower Hf concentrations than the bomb-digested whole rock and matrix (~0.1 and ~0.05 µg/g vs. ~5.1 and 3.5 µg/g, respectively), with resultant higher $^{176}Lu/^{177}Hf$ ratios (~0.66 and ~0.77 vs. ~0.02 and ~0.01, respectively), suggesting incorporation of Hf-rich zircon during bomb digestion.

The Lu-Hf garnet isochron for the Ashin micaschist is shown in **Fig.8**. The isochron age was calculated with the online version of the program IsoplotR (Vermeesch, 2018) using a ^{176}Lu decay constant of 1.867×10^{-11} yr^{-1} (Söderlund et al., 2004). A regression through five garnet fractions, the tabletop-digested whole rock and matrix, and the bomb-digested whole rock and matrix yields a relatively poor (9-point) isochron date of 111.80 ± 0.26 Ma (2σ S.E.; MSWD = 21) with an initial $^{176}Hf/^{177}Hf = 0.2829036 \pm 12$. The high MSWD likely results from inclusion of the bomb-digested whole rock and matrix samples into the isochron age calculation. Scherer et al. (2000) noted that the influence of zircon results in erroneous Lu-Hf garnet age calculations. This is corroborated by the high measured Hf concentrations of the bomb-digested whole rock and matrix (5.1 and 3.5 µg/g, respectively). In the case provided by Scherer et al. (2001), dissolution and incorporation of inherited zircon has the effect of pulling the whole rock below the "true" isochron. Here, removing the bomb-digested whole rock and matrix, yields a more reliable (7-point) isochron date of 113.10 ± 0.36 Ma (2σ S.E.; MSWD = 1.8) with an initial $^{176}Hf/^{177}Hf = 0.282790 \pm 10$. **Fig.8** shows that the bomb-digested whole rock and matrix lie above the 7-point, ~113 Ma isochron. This is suggestive of incorporation of relatively young zircon into solution during bomb digestion (see section 9). As such, we use the 7-point isochron age of 113.10 ± 0.36 Ma in further interpretations and discussion.

8. RUTILE U-Pb DATING AND ZR-IN-RUTILE TEMPERATURES

Rutile crystals were separated from two leucosomes (SO1803 and SO1808, HT unit), a garnet micaschist (SO1866) and a mafic amphibolite (SO1862) from the underlying MT unit. Rutile from samples SO1803 and SO1808 were sufficiently radiogenic to be dated (see results in **Fig.9**). In both samples, most analyzed grains are ~100 µm large, which corresponds to closure temperatures of the U-Pb system of ~650 °C (with a 10 °C/Ma cooling rate, Dodson, 1973; Cherniak, 2000), of the same order as the temperature recorded by the Zr-in-rutile thermometer (see below). Analyses from sample SO1808 are too scattered to yield a meaningful Tera-Wasserburg discordia age. Instead, assuming model common Pb compositions at 100 Ma for the upper intercept (Stacey and Kramers, 1975), the analyses likely reflect a scatter of dates between c. 112 and 85 Ma (without a significant correlation of dates with Zr concentrations; **Fig.9A**). Sample SO1803 yields a Tera-Wasserburg isochron age of 88.5 ± 2.8 Ma (2σ, n=138, MSWD = 1.9). The initial $^{207}Pb/^{206}Pb$ value of 0.841 ± 0.01 (2σ) defined by the isochron agrees with the model common Pb composition at 92 Ma ($^{207}Pb/^{206}Pb_i$ of 0.841; Stacey and Kramers, 1975). However, high uncertainty might be linked to different rutile generations

(although not distinguishable on the basis of trace element patterns), U or Pb loss, and all rutile analyses could correspond to ages scattered between c. 112 and 85 Ma **(Fig.9B)**, similar to what is deduced from sample SO1808.

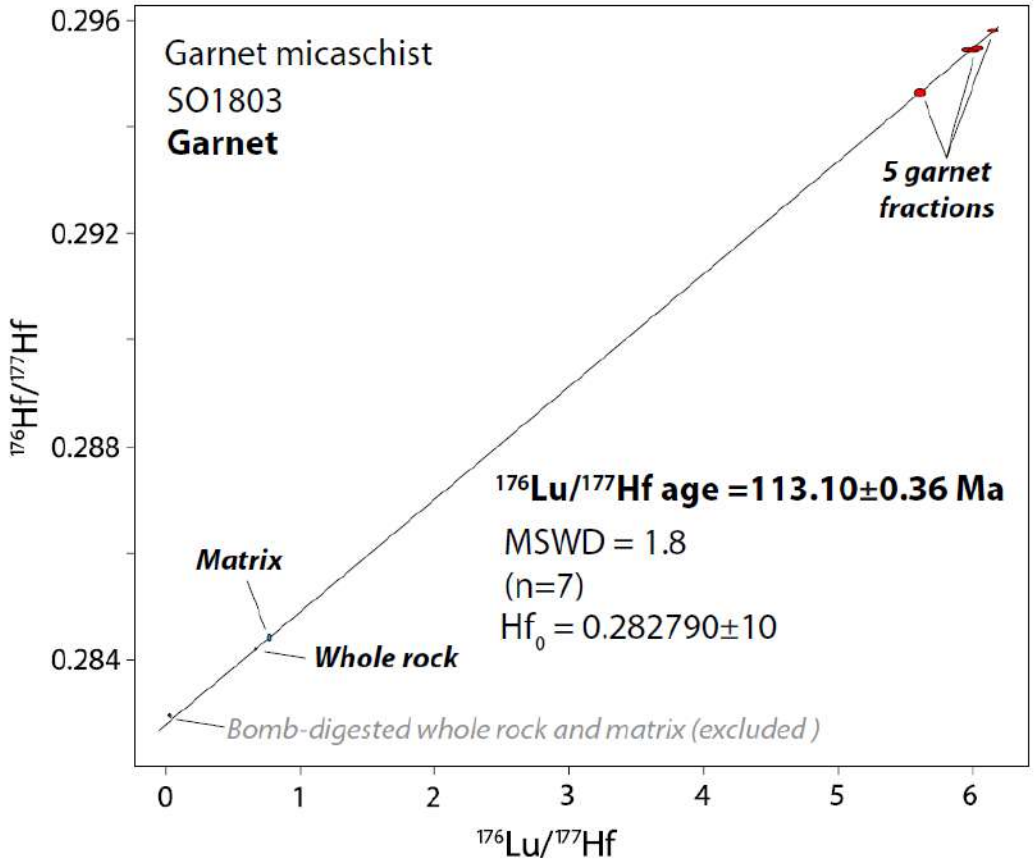

Figure 8. Lu-Hf garnet geochronology. Seven-point (five garnet fractions, tabletop-dissolved whole rock and matrix) isochron age, uncertainty, MSWD and initial Hf composition for the Ashin HT garnet micaschist. Note that the bomb-digested whole rock and matrix analyses fall off the isochron (see main text for discussion).

The amount of Zr-in-rutile (ZiR) is considered to reflect peak metamorphic contents and conditions (Zack et al., 2004; Kohn, 2020) as rutile equilibrates its Zr content during prograde metamorphism (e.g. Penniston-Dorland et al., 2018), but seems to act as a relatively closed system during retrograde cooling (Ewing et al., 2013). After sorting the data by their 2σ confidence intervals, temperatures have been calculated for each rutile grain using the Tomkins et al. (2007) calibration, considered to be most precise for temperatures below 700 °C. The statistical uncertainties (2σ) are in the range of ±15-20 °C. An a priori 1.2 GPa pressure value has been chosen for the ZiR thermometer calculations, as revealed by pressure estimates calculated in the following section, and in line with previous estimates calculated for the Ashin complex (Agard et al., 2006 and Angiboust et al., 2016). The calculated temperatures, presented in Fig.10, indicate that HT unit samples experienced temperatures

at least in the range of 620-660 °C (c. 180-350 ppm of Zr) while sensibly cooler temperatures are derived for the MT unit (560-620 °C, c.80-180 ppm of Zr).

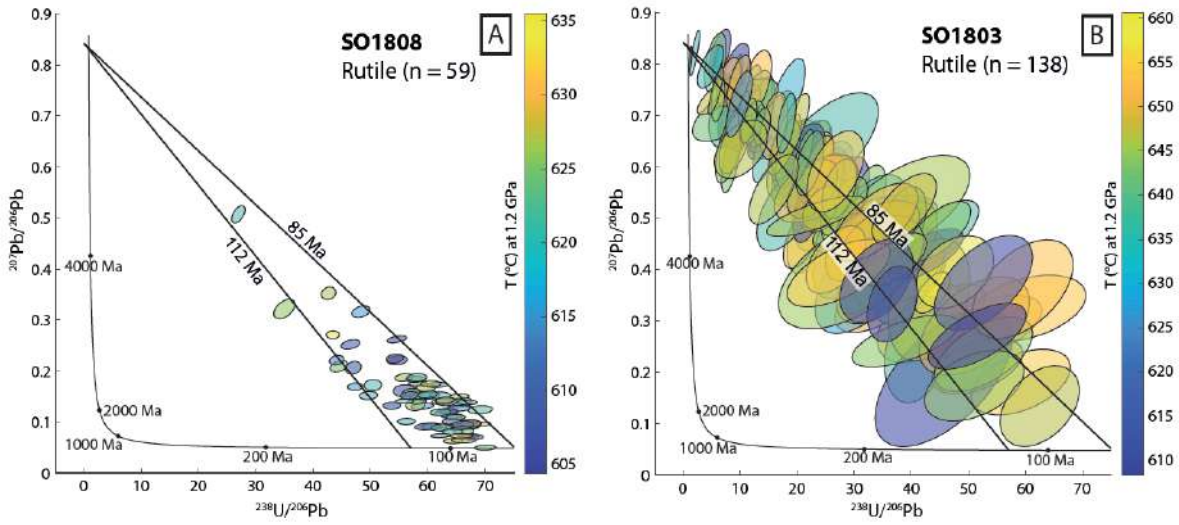

Figure 9. A. Tera-Wasserburg diagram for rutile crystals in sample SO1803, with the fitted discordia line. 95% confidence ellipses are color-coded for Zr-in-rutile temperatures. B. Tera-Wasserburg plot for rutile in sample SO1808, excluding analyses below 0.5, with the fitted discordia line. 95% confidence ellipses are color-coded for Zr-in-rutile temperatures.

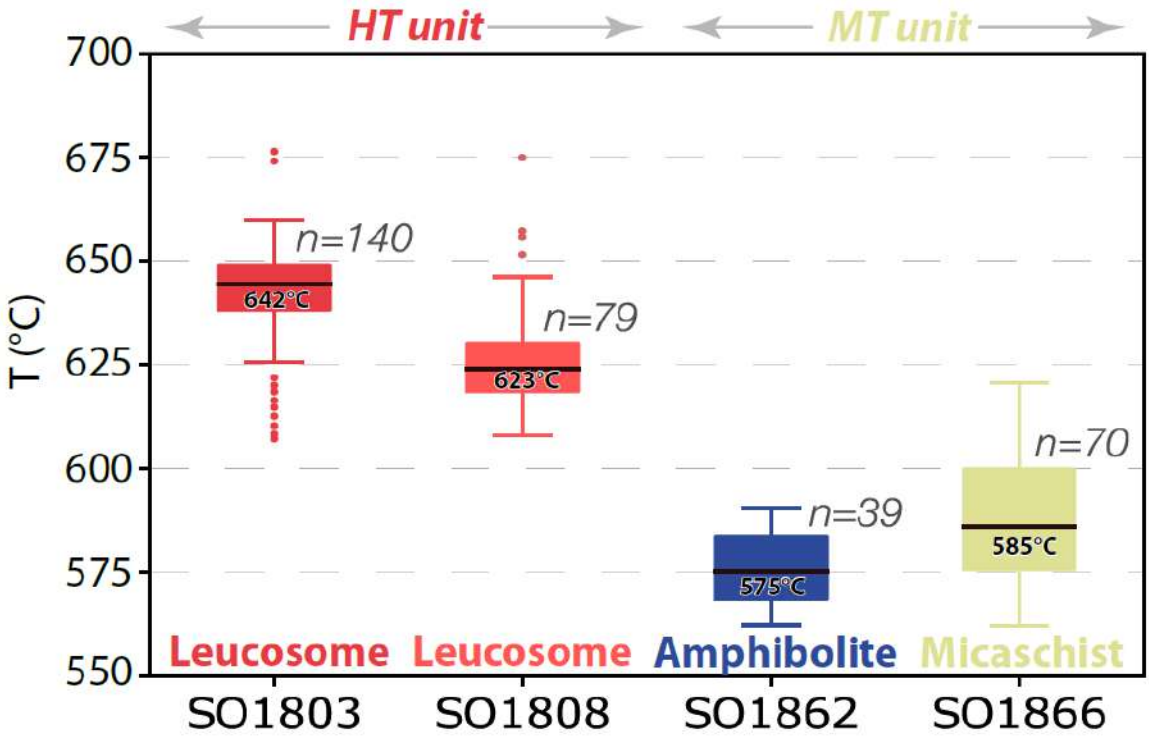

Figure 10. Zr-in-rutile results according to the Tomkins et al. (2007) calibration at 1.2 GPa for two HT unit and two MT samples.

9. ZIRCON U-PB DATING, TRACE ELEMENTS AND TI-IN-ZIRCON TEMPERATURES

Sample SO1805C (a leucocratic vein) contains abundant zircon grains with several morphologies from euhedral to subhedral elongated prims with bipyramidal terminations (200 μm × 50 μm) to stubby euhedral and equant to elongated bipyramidal prisms (250 μm × 100 μm) (**Fig.11A**). Most grains are colourless and transparent, although some are pinkish translucent crystals. Cathodoluminescence imaging reveals two textural types: one population is oscillatory, patchy zoned and unzoned core grains in some cases showing metamict textures (**Fig.11A**). The second population comprises small rims, 40 μm × 20 μm, with low cathodoluminescence overgrowths partially dissolving previous group zircon grains (**Fig.11A**).

U-Th-Pb measurements on 26 different zircon cores yielded low to high concentrations of U (316–2168 ppm) and low Th (3–70 ppm) with Th/U <0.1 and little common lead ($f^{206} \leq 0.22\%$) (**Table S5**). All analyses are concordant (discordance −2.6 to 5.0 %) (**Fig.11B**). The weighted means (errors reported at 2σ) of the uncorrected and 207- corrected $^{206}Pb/^{238}U$ are identical, at 104 ± 1 Ma (MSWD = 2.14) and 104 ± 1 Ma (MSWD = 1.96), respectively (**Fig.11B**). Fourteen measurements on 14 zircon rims (second population) yielded low contents of U (2-185 ppm) and very low Th (0-3 ppm) with Th/U <0.02 (**Table S5**). The rims have a high common lead component (f^{206} 9-378 %), thus all analysed points are discordant (discordance 9 to 76 %) (**Fig.11C**). However, the data points define a discordia line with a lower Concordia intercept at 104 ± 3 Ma (MSWD 2.61), an age identical within uncertainty to the age of zircon cores (**Fig.11C**). A summary of available ages for the Ashin complex, including these new U-Pb zircon ages is given in **Fig.12**.

Trace element composition for zircon cores was obtained in the same spots of SHRIMP analysis. Due to the larger spot size of LA-ICPMS only eight measurements were conducted on rims. The zircon trace element composition for core and rim are similar, with high REE abundances (569-6369 ppm; see **Table S5**). In the chondrite-normalized REE pattern diagram both populations have steep MREE-HREE patterns (Lu_N/Gd_N = 88–3839) (**Figs.S1E and F**) with mainly negative Eu (Eu/Eu* = 0.06–1.02) and positive Ce (Ce/Ce* =0.75–30.03) anomalies.

For temperature estimations, we used the Ti-in-zircon thermometer of Ferry and Watson (2007). Because both quartz and rutile are found in the leucocratic veins possibly representing a part of the incipient cooling assemblage together with zircon, their αSiO_2 and αTiO_2 activities were assumed to be 1 (e.g. Ferry and Watson, 2007; Li et al., 2016). Zircon cores contain 1.45 to 36.3 ppm of Ti (**Table S5**), the corresponding temperatures determined are in a range of 592-883 °C with a weighted mean of 720± 70 ºC (**Figs.13A and B**). Zircon rims have Ti amounts of 2–8.44 ppm (**Table S5**) and show Ti-in-zircon temperatures of 614-730 °C yielding a weighted mean of 663±40 ºC virtually identical than cores within error (**Figs.13A and C**).

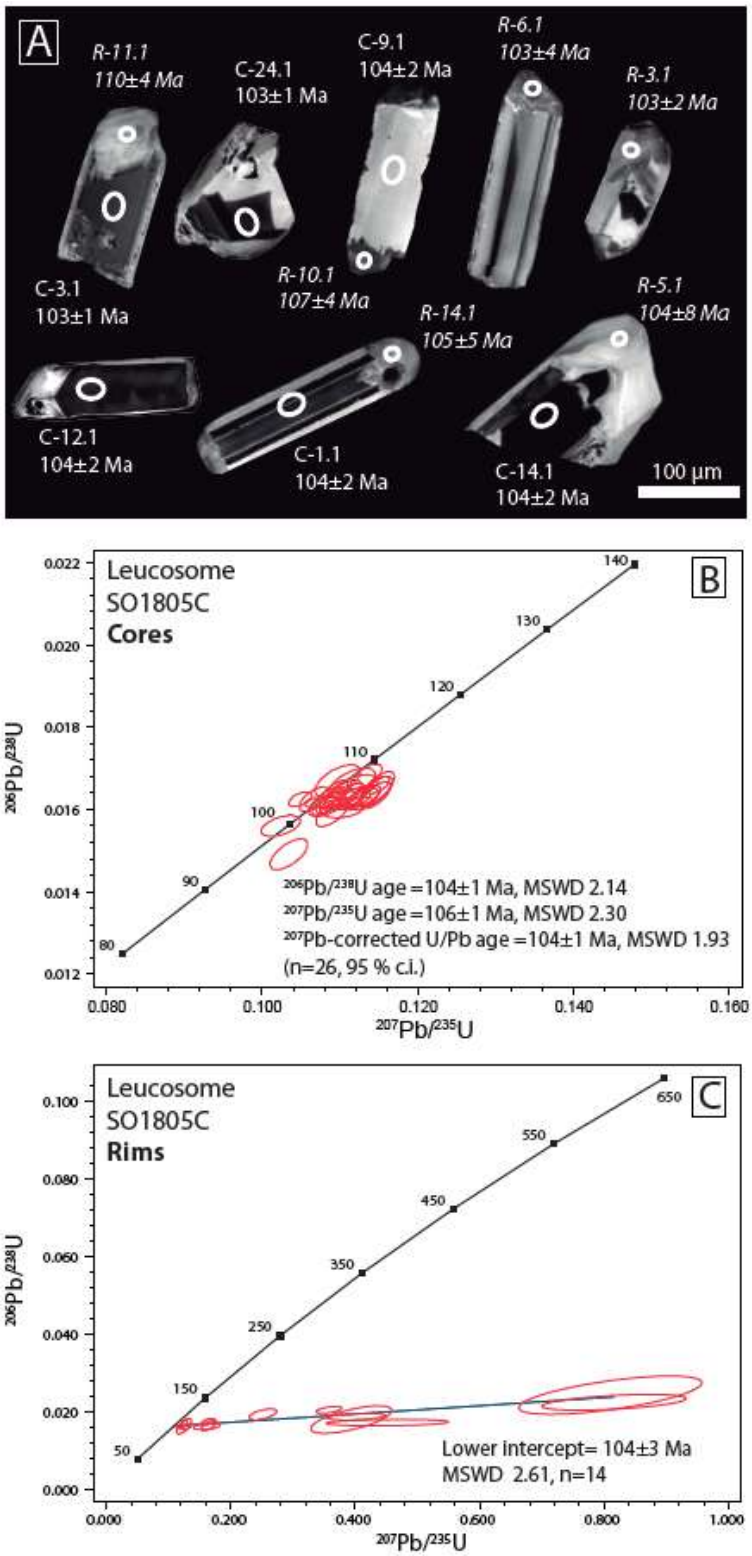

Figure 11. A. Cathodoluminescence images and 206Pb/238U ages of representative analysed zircon grains from the leucosome SO1805. Note the core-rim texture, C and R, respectively. Wetherill concordia plots for core (B) and rim (C) populations. Cores of the analysed grains are all concordant, while rims contain large contributions of common Pb that explain discordant points.

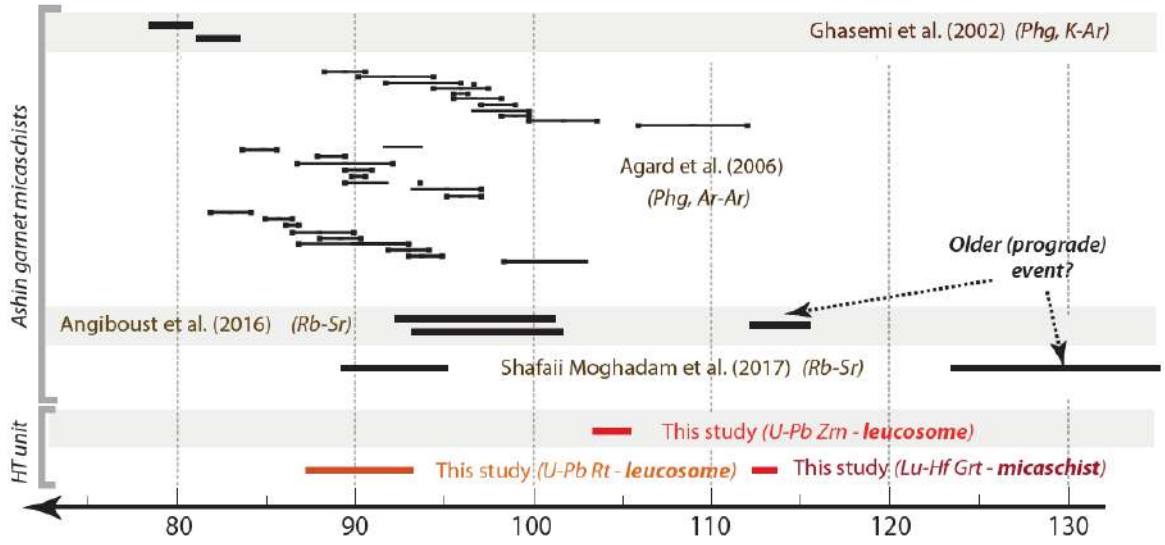

Figure 12. Summary of available geochronological constraints for upper Ashin MT and HT metamorphic rocks.

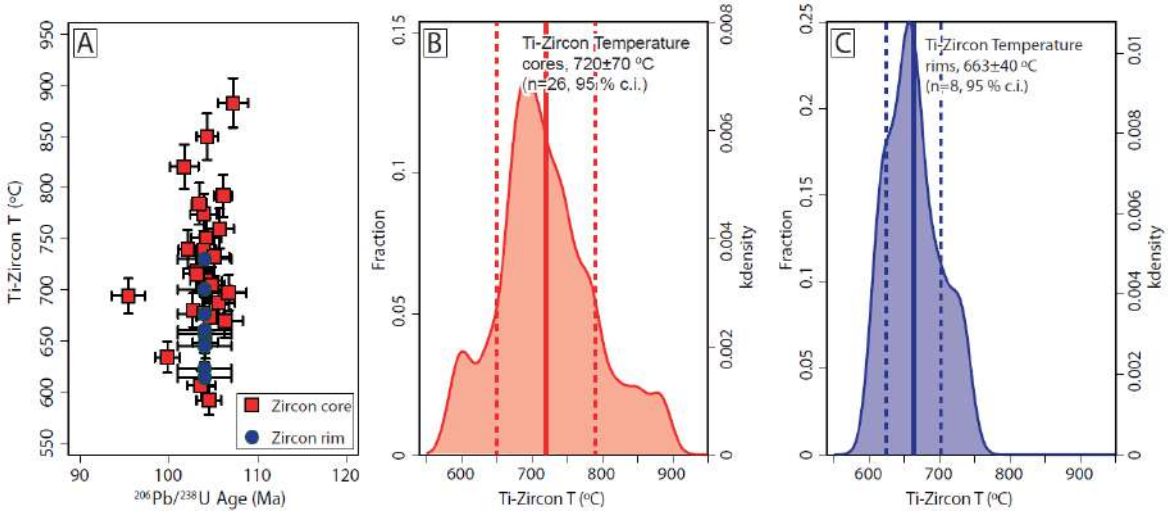

Figure 13. A. Ti-in-zircon temperatures versus crystallization ages of cores and rims. B and C. Distribution of Ti-in-zircon temperatures of cores and rims, respectively.

10. PSEUDOSECTION MODELLING

First, temperature-XH_2O pseudosections for mafic amphibolites (500-750 °C vs 0-5 wt.% H_2O; **Fig.14A**) were plotted at different pressures (1.1, 1.2 and 1.3 GPa) and compositional transects were examined at 620, 650 and 680 °C in order to determine a pressure range with melt appearance consistent with further temperature estimates and mineral assemblages (e.g. best fit field in **Fig.14A** limited by the zo-out and melt-in curves). This approach is motivated by the calculated range of Zr-in-rutile and Ti-in-zircon temperatures (on samples belonging to the HT unit) which span an approximate range near 620 to 720 °C (see sections 8 and 9). Pseudosection modelling and phase abundance transects as a function of H_2O contents (**Figs.14A and B)**, indicates that the best fit field

between observed parageneses, mineral modes and modelled phase relationships is obtained for the 1.5-2.9 wt.% H_2O range at 680 °C and 1.2 GPa. A complementary transect at 650 °C and 1.2GPa also gives a very similar H_2O range (**Fig.S4**), which is also in good agreement with the observed paragenesis. For this range, between 0 and 10 vol.% melt is predicted, in line with field-based leucosome volumetric amount estimates (<10 vol%). Further, 70 vol.% of a hornblendic amphibole is expected, in agreement with textures and mineral chemistry (**Fig.5**). A median value of 2.2 wt.% H_2O has thus been selected to calculate a P-T pseudosection in the 1.0-1.3 GPa and 500-750 °C window (**Fig.14C**).

From this model, we conclude that the best-fit region (in red) is expected for the field Amp-Grt-Cpx-Pl-Bt-Zo-Qz-Rt-melt, above the melt-in curve and below the zo-out reaction curve, in agreement with the presence of zoisite in the studied samples; **Figs.3, 6 and S1**). The red field in Fig 14C largely overlaps with the Zr-in-rutile and Ti-in-zircon temperatures calculated above. The changes in the paragenetic sequence along a hypothetic prograde burial path of 18 °C/km (see dotted lines on **Fig.14C**) is depicted in **Fig. 14D**. There, it appears that the peritectic reactions in this field involve the consumption of amphibole, plagioclase and zoisite and the associated formation of garnet, clinopyroxene and melt (in agreement with processes already documented by Vielzeuf & Schmidt, 2001 for a MORB system in laboratory experiments). Note that the main discrepancy of the model with natural observations is the prediction of biotite (approximately 6 vol.% at best-fit conditions) while it has not been observed in the set of samples selected for this study. The model also does not predict ilmenite while it is commonly observed associated with rutile in the studied samples. All garnet isopleths are nearly vertical and therefore not helpful for constraining the pressure within the red field accurately. From these pseudosection investigations together with independent zircon and rutile thermometry, we conclude that the likely peak burial PT conditions reached by the HT unit mafic lithologies reached between c. 650 and 680 °C and 1.1 to 1.3 GPa (considering the uncertainties inherent with this modelling approach; e.g. Palin et al., 2016).

11. DISCUSSION

11. Partial melting in the Zagros paleo-accretionary wedge

Our field and petrographic investigations have revealed that the internal structure of the Ashin complex is less homogeneous than initially described by Agard et al. (2006) and Angiboust et al. (2016). Indeed, a several tens of meters' thick sliver occupying the uppermost structural position (the HT unit), just under the non-subducted SaSZ-derived Sikhoran complex (**Figs.1B and C**), exhibits clear evidence for partial melting of mafic, intermediate and metapelitic lithologies (**Fig.2**). While

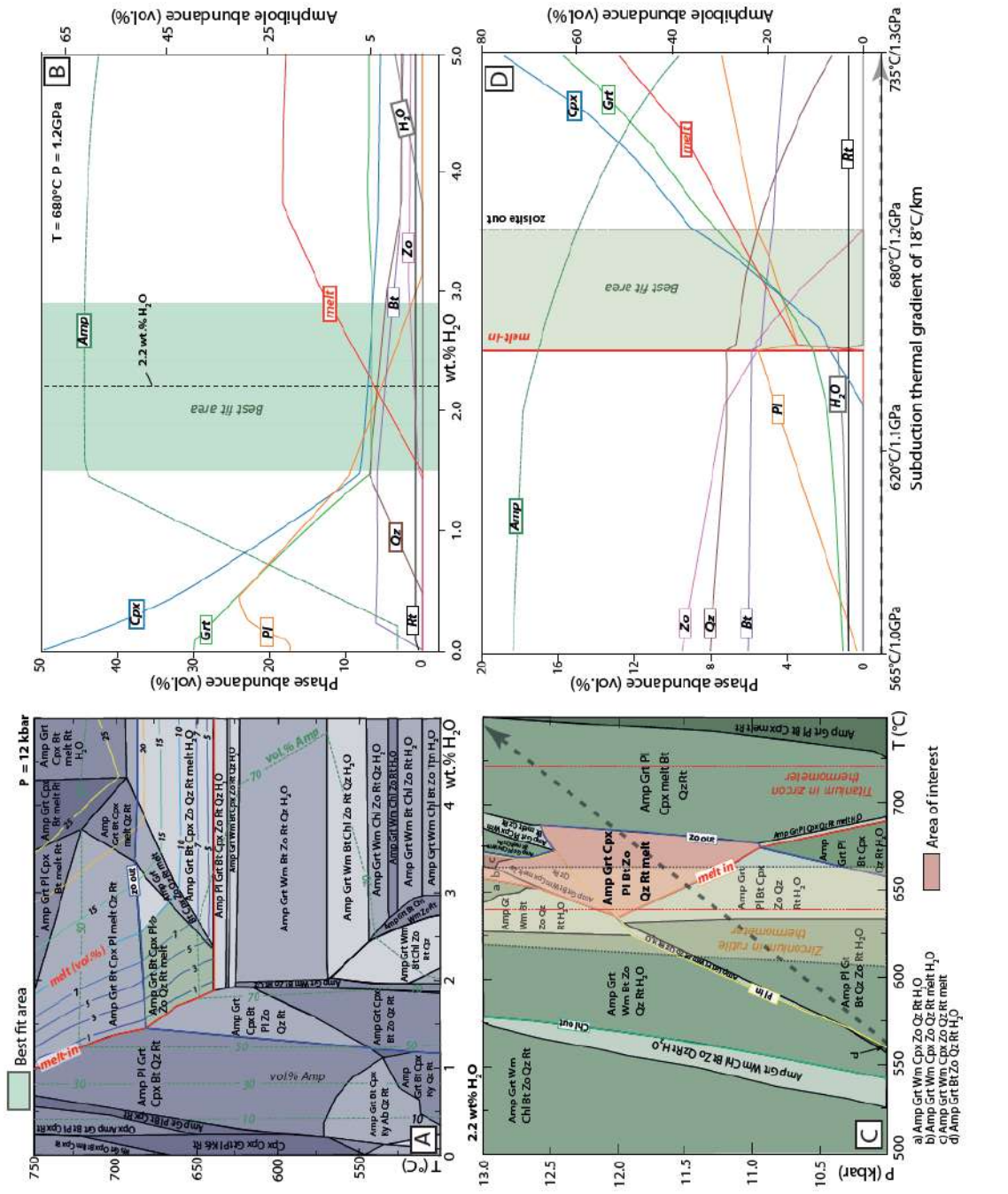

Figure 14. Thermodynamic modelling results on sample SO1804. A. T-X(H_2O) pseudosection showing fields, melt and amphibole volumetric abundances as well as the region that fits better petrological observations and measurements. B. Phase abundances relative to H_2O variations at fixed P-T conditions (1.2 GPa and 680 °C). Highlighted in green is the best-fit range (see text for further details). C. P-T pseudosection calculated with a fixed 2.2 wt.% H_2O amount. Highlighted in red the best-fit conditions as deduced from field and sample observations. The range of temperatures calculated for sample SO1803 using the Zr-in-rutile thermometry (calibration from Tomkins et al. (2007) and for sample SO1805C using Ti-in-zircon thermometry (calibration from Ferry and Watson 2007) are shown for comparison. The dotted line marks the P-T trajectory followed by a sample buried along a 20 °C/km thermal gradient. D. Phase abundances calculated along the prograde thermal gradient displayed in panel C. Best-fit conditions (see details of the approach in text) are highlighted with a green transparent band.

sub-solidus peak temperatures in the range of 500-600 °C were proposed in the immediately underlying MT unit garnet micaschists (Agard et al., 2006; Angiboust et al., 2016), the identification of leucosomes in mafic and pelitic lithologies reveals warmer conditions prevailing in the HT unit during peak burial conditions.

Although these rocks were extensively overprinted during subsequent metamorphic re-equilibration (**Fig.5**), it is possible to determine, using pseudosection modelling and Ti-in zircon temperatures, that supra-solidus temperature conditions nearing 680 °C were reached in this HT sliver (**Fig.14C**), in line with the experimental data from Vielzeuf & Schmidt (2001; **Fig.15A**). Zr-in-rutile thermometry also yielded temperature estimates beyond the MORB wet solidus, i.e above 650 °C (**Fig.10**). Pressures deduced from pseudosection modelling suggest that peak burial conditions of 1.1-1.3 GPa were attained during peak T conditions, in line with the absence of an omphacitic clinopyroxene in the peritectic assemblage which would signify pressures greater than 1.5 GPa according to Vielzeuf & Schmidt (2001; **Fig.14C**). Furthermore, at estimated peak conditions (e.g. 680 °C and 1.2 GPa), the theoretical melt composition is trondhjemitic, in agreement with analysed leucosome samples (**Fig.7C**). A discrepancy between our observations and the modelling results is the absence of biotite in our samples, while 6 wt.% is predicted using a MORB composition with 2.2 wt.% H_2O. While (rare) biotite inclusions in garnet from the Ashin complex have been reported by Agard et al. (2006), this discrepancy within our samples can be explained (i) by the use of a starting model composition with K_2O contents greater than in the average MORB composition, and (ii) the full destabilization of all the biotite crystals present in the system during retrograde overprinting.

Vestiges of subduction-related melting of oceanic crust are rare on Earth (e.g. Catalina Schists: Sorensen and Barton, 1987; Cuba: Lazaro et al., 2009 and Blanco-Quintero et al., 2011; Iran: Rossetti et al., 2010; Chilean Patagonia: Angiboust et al., 2017). The relatively enriched pattern in LREE as well as departure from the MORB fields towards OIB and higher Th/Yb ratios for some of the amphibolites (**Fig.7B**), may indicate (i) a contribution from a sedimentary source in the mafic protolith (as expected for instance in tuffaceous lithologies), (ii) a metasomatic overprint of the N-MORB protolith by sediment-derived fluids during metamorphism and/or (iii) slight modification of the pristine MORB signature due to melt extraction. Evidence for local melting of mafic MORB-related protolith, as expected for a paleo-accretionary environment, is supported by low Zr, HFSE and REE concentrations and the presence of trondhjemite-like signatures in the leucosomes (**Figs.7A to C and Table S3**; see also Rapp et al., 1991; Lazaro et al., 2011; Blanco-Quintero et al., 2011; Angiboust et al., 2017). The relatively flat HREE pattern (**Fig.7A)** suggests that the REE pattern of the mafic lithologies has been only weakly modified by melt extraction processes. Such elements are potentially partitioned in garnet, rutile and epidote; the stable phases during melting. The high concentration of hornblende crystals in some parts of the HT unit amphibolites and garnet amphibolites (**Figs. 2A and C**) confirms the restitic nature of partially molten material and indicates melt loss during the peak T event (process also visible in the residual geochemical signature of some mafic samples; **Table S3**; **Fig.7A**; see for example Sawyer, 2008). On the one hand, the formation of

a garnet-amphibole-bearing residue in some samples (**Fig.2A**) as well as the observation of leucosome patches, melt channels and veinlets of melt segregations may suggest that local partial melting occurred before dehydration of prograde amphibolite (e.g. Drummond & Defant, 1990; Foley et al., 2002). On the other hand, an external aqueous fluid source during melting must have been required to explain the relatively high amount of H_2O inferred in our pseudosection modelling approach to fit the observed parageneses (1.5-2.9 wt.%; **Fig.14**). Such H_2O-rich external fluids, also expected to explain the formation of Na-rich melts such as trondhjemite (Prouteau et al., 2001) as well as albitites (Johnson & Harlow, 1999) were likely derived from prograde dehydration reactions in the underlying oceanic lithosphere. These H_2O-rich conditions required for melting are also supported by the occurrence of only few crystals of clinopyroxene in the amphibolites, a phase that is systematically inhibited during melting at H_2O-rich conditions and high pressure conditions (e.g. Winther and Newton, 1999; Garcia-Casco et al., 2008).

The timing of prograde metamorphism – at least during amphibolite-facies at pre-melting conditions (see below) – has been illuminated through Lu-Hf dating of garnet within a metasediment from the HT unit. While the age of the peak T melting event has been possible to elucidate through dating of zircon crystals (inferred to have formed during melt crystallization) from a leucosome vein (**Fig.2B**). Garnet dating yields an age of 113.10 ± 0.36 Ma, sensibly older than the leucosome crystallization age in the range c. 104-105 Ma calculated for zircon cores and rims (**Fig.12**). We note that zircon trace element patterns, particularly HREEs, depict strong positive anomalies (**Figs.S1E and F**), compatible with zircon crystallization in the absence of garnet from the leucosome, a mineral with strong affinities for HREEs (e.g. Rubatto, 2002). Thus, the older garnet ages relative to zircon as well as HREEs patterns, allow us to conclude that leucosome zircon crystallized from a melt in the absence of garnet, the latter dating prograde metamorphism prior to peak T conditions. Within zircon, similar ages and trace element patterns as well as Ti-in-zircon temperatures (**Figs.S1E, F and 13A to C**) among cores and rims, suggest different stages of dissolution/precipitation, probably related to variable influx of melt during the partial melting process. Note that zircon ages are older than most of the ages obtained on the underlying marbles and garnet micaschists (78-101 Ma; Ghasemi et al., 2002; Agard et al., 2006; Angiboust et al., 2016). Rutile U-Pb dates span a range (85-112 Ma) which partly overlaps the age obtained using zircon U-Pb dating (**Figs.9A and B**). This spread in the dates may reflect partial isotopic re-equilibration of peak T rutile crystals during incipient cooling in the T range 550-650 °C as determined for the same rutile crystals using Zr-in-rutile thermometry (**Fig.10**). These observations support the inferred peak T conditions in the range of 650 to 680 °C, which are slightly hotter than the maximum temperatures estimated from Zr-in-rutile thermometry but well within the values obtained using the Ti-in-zircon thermometer.

Field relationships also suggest that this melting stage occurred in a host already exhibiting a structural fabric, thus implying a tectono-metamorphic history prior to partial melting, which is extremely challenging to decipher due to extensive recrystallization as a consequence of the protracted metamorphism. The existence of pre-113 Ma subduction activity and the formation of an

associated paleo-accretionary wedge is inferred from (i) the presence of probable arc magmatism culminating at c.170 Ma all along the SaSZ (e.g. Hassanzadeh & Wernicke, 2016 and references therein) and (ii) the finding of relatively old Rb-Sr multi-mineral ages in the range 110-130 Ma (with large uncertainty due to mineral isotopic disequilibrium) in the uppermost part of the Ashin complex further to the SW (Sokhan region; Angiboust et al., 2016; Shafaii Moghadam et al., 2017), which are here interpreted as non-equilibrated domains of this paleo-accretionary system. The report of eclogites in the SaSZ in the North Shahrekord region (Davoudian et al., 2008, 2016) dated at 170-185 Ma using Ar-Ar on phengite also supports the idea of a subduction margin already active earlier during the Mesozoic. The value of the metamorphic gradient before 105 Ma remains unknown.

11.2 A record of the secular cooling of the Zagros paleo-accretionary wedge

The HT Ashin locality is one of the very few places worldwide where lawsonite is observed replacing mineral phases originally crystallized in an anatectic leucosome. For instance, in Sierra del Convento and La Corea regions (Cuba), blocks of mafic rocks now exposed in a serpentinite mélange have experienced partial melting followed by isobaric cooling (at 1.5 GPa) down to lawsonite blueschist-facies over a c.15-Ma time period (e.g. Garcia-Casco, 2007; Lázaro et al., 2009; Blanco-Quintero et al., 2011). The assemblage herein reported also points to a similar cooling history, as blue amphibole, lawsonite, titanite and high-Si phengite are coevally observed, statically overgrowing the previous HT assemblage (**Figs.3, 4 and 15A**). Even though the pressure cannot be precisely constrained for the LT overprint, the reported paragenesis points to lower lawsonite-blueschist facies conditions, i.e. P-T conditions approaching 300 °C and pressures less than 1.2 GPa, based on phase relationships and mineral stability (e.g. Evans, 1990). The presence of at least four metamorphic events in Ashin HT unit metabasites and metasediments (including a very minor, exhumation-related overprint; **Fig.6**) therefore caused extensive mineral textural disequilibrium with fluid-assisted dissolution-reprecipitation processes accompanied by isotopic disequilibria. This may explain (i) the spread in rutile U-Pb ages and (ii) the difficulty of obtaining well-constrained isochrons with the multi-mineral Rb-Sr method for phengite-bearing lithologies.

Even though similar cooling-related parageneses and fabrics have been observed and reported in the immediately underlying Ashin MT unit (e.g. the garnet micaschists on **Fig.1C**), we emphasize that no evidence for partial melting is observed in these rocks, which according to previous Raman thermometry estimates, did not reach temperatures greater than 550 °C (Agard et al., 2006; Angiboust et al., 2016). We note that pressure estimates (0.9-1.2 GPa) for the melt-free garnet micaschist from the underlying MT unit (Agard et al., 2006) are not drastically different from those estimated for the overlying HT unit (**Fig.15A**). Geochronological studies on these rocks have not yielded ages older than those obtained for the melt-bearing sliver (see references above). From these observations, it may be speculated that (i) two slivers with distinct peak burial P-T-t conditions coexist in the upper part of the Ashin complex, (ii) they were juxtaposed after the melting within the trondhjemite-bearing HT sliver, likely around 95 Ma (according to Rb-Sr ages for the marble-bearing mylonites lining the

shear zone at the base of the HT sliver; **Fig.1C**; Angiboust et al., 2016) and (iii) they underwent cooling together down to lawsonite blueschist facies until the end of the Cretaceous (**Fig.15A**).

The record of long-term cooling in paleo-accretionary material is a rather rare event, known for instance in the circum-Pacific sutures (Franciscan: Grove & Bebout, 1995; Anczkiewicz et al., 2004; South-Central Chile: Hyppolito et al., 2014; Chilean Patagonia: Angiboust et al., 2018) as well as in the Caribbean (Dominican Republic: Krebs et al., 2008; Cuba: Lázaro et al., 2009; Blanco-Quintero et al., 2011). This model implies a long-term cooling of the northern Zagros subduction thermal gradient (at least in the Ashin area) from 18 °C/km down to 7 °C/km within a c. 40-Ma time window (**Fig.15A**), confirming preliminary observations reported by Angiboust et al. (2016) on the Soghan region. Corresponding cooling rates range between 8 and 10 °C/Ma (considering uncertainties on the age at which the 7 °C/km gradient has been achieved), in line with cooling rate estimates obtained by previous studies on other localities (e.g. Anczkiewicz et al., 2004; Krebs et al., 2008). Higher cooling rates of c. 25 °C/Ma were proposed for the isobaric cooling event in Cuba (Lazaro et al., 2009; Blanco-Quintero et al., 2011).

11.3 Implications for Northern Tethyan margin geodynamic evolution

Our understanding of the geodynamic history along the northern active margin of the Tethyan realm during the Cretaceous is hampered by the extreme scarcity of geological witness for this time period. In that perspective, Ashin complex rocks provide a unique window, as no other Cretaceous paleo-accretionary HP rocks are reported along the entire Zagros suture zone across 2500 km from NW Iran to the Makran region. Oceanic subduction along the northern Tethyan active margin proceeded continuously from the Lower Jurassic until the Oligocene when the Arabian continent collided with Eurasia (Agard et al., 2011; Ajirlu et al., 2016). In the meantime, the rock imprint recorded in the Ashin complex documents a steady and long-term cooling of the subduction environment from 18 °C/km down to 7 °C/km, which can be easily explained with the subduction of a seafloor with progressively older thermal age, at least between c.95 and 65 Ma (Angiboust et al., 2016 and Bonnet et al., 2020; see also Peacock, 2003). The paleo-geographic reconstructions shown in **Figs.15B to D** (from Seton et al., 2012) confirm that a progressively older and cooler oceanic lithosphere is expected between the 105 Ma thermal event and the early Cenozoic basin closure history.

The thermal pulse recorded in the Ashin complex HT unit was not identified yet in the geological record and is more challenging to link with a specific geodynamic event. The paleo-geographic reconstructions of Seton et al. (2012) and Müller & Seton (2015) predict the entrance into the subduction zone of the Neo-Tethyan mid-ocean ridge under the northern basin margin at around 120 Ma. According to Müller & Seton (2015), this ridge subduction event is inferred to have occurred at 110-120 Ma, which may, within uncertainties, be linkable to the ~105 Ma event recorded in Ashin region rocks. This event, inferred to have considerably increased the thermal gradient, may constitute one explanation, though it is (to our knowledge) not yet supported by geological observations in the region. Note that in the case of active ridge subduction, the inferred thermal gradient is expected to

be much warmer than herein estimated (in the order of 40 °C/km as for instance for the southern Chile triple junction area; e.g. Lagabrielle et al., 2000). Instead, the burial of an ancient spreading ridge, which possibly had gone extinct prior to its subduction, may have provided sufficient persistent heat to trigger partial melting in the deep parts of the Zagros paleo-accretionary wedge along the northern Tethyan subduction active margin (**Fig.15E**; see also Frassi et al., 2020 for another example in Turkey). The warm gradient calculated for these HT rocks is also compatible with the one expected for the subduction of a very young and hence, hot oceanic lithosphere, as known for instance in the Cascades or SW Japan subduction environments (e.g. Abers et al., 2013). Alternatively, the subduction of a seamount derived from a plume-lithosphere interaction, as known for the nearby Siah Kuh massif (Bonnet et al., 2020) or further east in the Durkan region (Makran; Barbero et al., 2021) could also have contributed to transient heating of the subduction thermal structure at 30-40 km depth.

Another possibility is to invoke a change in the configuration of the Africa-Eurasia convergent plate boundary around 105-115 Ma as part of the "global plate reorganization event" recorded at this period (Matthews et al., 2012). Indeed, the decrease of convergence velocity documented at most convergent plate boundaries for this period would contribute to the re-equilibration of the thermal structure and a warming of subduction interface material, prior to the shift towards faster convergence rates from the Late Cretaceous to the Eocene deduced from magnetic anomalies and geological field evidence (Larson, 1991; Agard et al., 2006, 2011; Matthews et al., 2012; Olierook et al., 2020). However, such a decrease in the convergence rate between Arabia-Africa and Eurasia is not clearly documented for the time span around 105-110 Ma, because of the coeval magnetic quiet period (Granot et al., 2012). Moreover, the convergence rate does not necessarily reflect the subduction rate (Brun & Faccenna, 2008), which thus cannot be directly reconstructed using the Ashin complex rock record.

Last, we stress that the assembly of Cimmerian blocks is a very complex and poorly resolved geodynamic issue, and the location and activity of subduction margins in the Tethyan realm during the Cretaceous remains a matter of discussion, in particular in the light of the 105-115 Ma plate reorganization event identified recently (e.g. Matthews et al., 2012). The new constrains provided by Ashin HT rocks provide an anchor point for future paleomagnetic works and geodynamic reconstructions, helping to refine the timing of basin opening, subduction initiation and thus contributing to enhance our understanding of the geodynamic processes that shaped the northern Tethyan active margin in the Cretaceous.

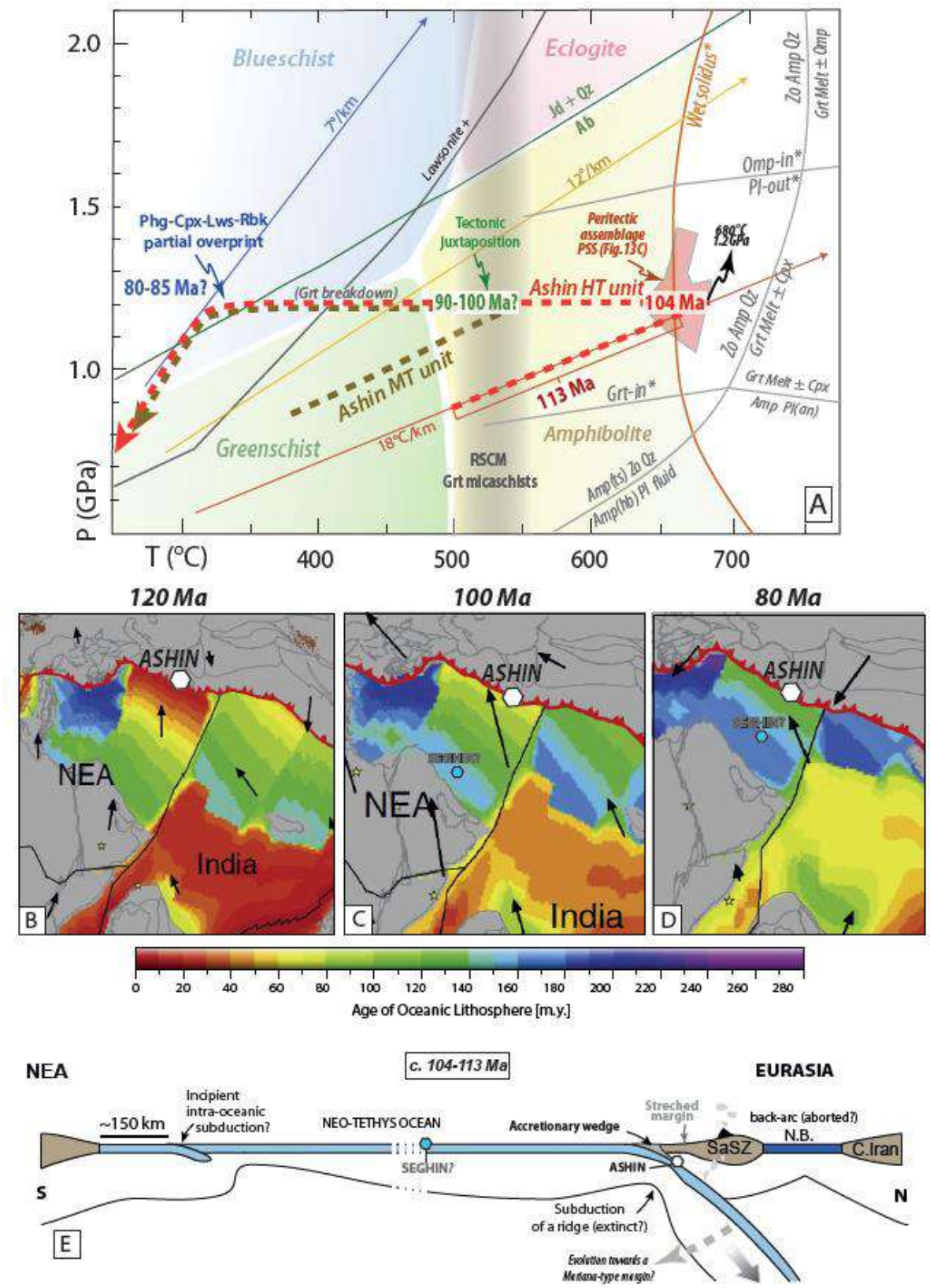
Blueschist
Eclogite
Greenschist
Amphibolite
7°/km
12°/km
Lawsonite +
Jd + Qz
Ab
Wet solidus*
Zo Amp Qz
Grt Melt ± Omp
Omp-in*
Pl-out*
Phg-Cpx-Lws-Rbk
partial overprint
80-85 Ma?
(Grt breakdown)
Tectonic
Juxtaposition
90-100 Ma?
Peritectic
assemblage
PSS (Fig. 13C)
680°C
1.2GPa
Ashin HT unit
104 Ma
Zo Amp Qz
Grt Melt ± Cpx
Ashin MT unit
113 Ma
Grt-in*
Grt Melt ± Cpx
Amp Pl(an)
18°C/km
RSCM
Grt micaschists
Amp(ts) Zo Qz
Amp(hb) Pl fluid
A
P (GPa)
T (°C)
2.0
1.5
1.0
400
500
600
700
120 Ma
100 Ma
80 Ma
ASHIN
NEA
India
B
C
D
0
20
40
60
80
100
120
140
160
180
200
220
240
260
280
Age of Oceanic Lithosphere [m.y.]
NEA
c. 104-113 Ma
EURASIA
~150 km
Incipient
intra-oceanic
subduction?
NEO-TETHYS OCEAN
Accretionary wedge
Streched
margin
back-arc (aborted?)
N.B.
SaSZ
C.Iran
SEGHIN?
ASHIN
S
N
Subduction
of a ridge (extinct?)
E
Evolution towards a
Mariana-type margin?

Figure 15. A. P-T diagram summarizing available thermobarometric and geochronological data for Ashin HT and MT units (RSCM: Raman Spectroscopy of Carbonaceous Matter; see data in Agard et al., 2006 and Angiboust et al., 2016). Grey-colored reaction lines and reactions marked with an asterisk symbol are derived from the experiments from Vielzeuf & Schmidt (2001) on MORB material. We explain the difference in peak burial temperatures and the spread of ages in the upper Ashin complex by the tectonic juxtaposition of two distinct units that occurred likely around 90-100 Ma through underplating processes occurring at c.40km depth, i.e. towards the base of the basal accretion region of a paleo-accretionary wedge. B to D: Paleogeographic reconstruction of the geodynamic evolution of the Tethyan ocean between 120 and 80 Ma, revealing a ridge subduction event as well as the subduction of gradually cooler oceanic lithosphere under the Iranian margin. Absolute plate velocity vectors are denoted as black arrows (modified after Seton et al., 2012). NEA – Northeast African plate. E: Schematic geodynamic cross-section across the Tethyan realm showing the location of Ashin complex rocks, the Northern Tethyan subduction accretionary wedge and the inferred "extinct" ridge subducted under the SaSZ at c. 105 Ma (modified after Bonnet et al., 2020 and Burg, 2018). The arrow illustrating a potential evolution towards a Mariana-type margin is based on the investigations from Muñoz-Montecinos et al. (Submitted) on Seghin blueschists.

14. CONCLUSIONS

The upper part of the Ashin complex in the Zagros Cretaceous paleo-accretionary wedge records an upper amphibolite-facies melting event (c. 650-680 °C at 1.1-1.3 GPa) that occurred at c. 104-113 Ma, leading to the formation of leucocratic veins of trondhjemitic affinity, a typical feature of partially molten mafic crust. Such a high temperature overprint requires a former warm subduction gradient (c.18 °C/km) that overprinted the rocks forming the base of an existing wedge at near 40 km depth. The origin of this thermal anomaly that has not been documented thus far, remains a matter of discussion. We favor the hypothesis of the subduction of a warm segment of the Neo-Tethyan lithosphere - such as an extinct spreading center or a seamount chain - under the Sanandaj-Sirjan buttress. This thermal imprint left on the basally-accreted Ashin complex rocks has been followed by the underplating of another, slightly cooler unit under the thermally-overprinted Ashin HT unit, likely in the 90-100 Ma time window. Cooling down of the subduction environment to a gradient of 7 °C/km proceeded towards the very end of the Cretaceous, as recorded by the HP-LT overprint of previously-underplated Ashin complex material. Ashin complex basally-accreted rocks thus provide a unique window into a poorly known time period of the northern Neo-Tethyan basin evolution, with key implications for paleo-geographic reconstructions and regional geodynamic evolution.

ACKNOWLEDGEMENTS

The four field campaigns in the Ashin region (2013-2018) would have not been possible without the logistical support from Jafar Omrani (GSI Tehran), who is warmly acknowledged. Mohammadreza Tofighi is also acknowledged for kind assistance during the last field expedition. Oona Appelt (GFZ Potsdam) is acknowledged for technical assistance with EPMA work. Gareth Seward is acknowledged for his help with BSE and EPMA analyses and Andrew Kylander-Clark for his help with LASS analyses. M. Bizimis at the Center for Elemental Mass Spectrometry at UofSC is acknowledged for considerable assistance with Lu-Hf mixed spike generation and aspects of the mass spectrometry. G.B. was funded by the "E-FIRE" project (NSF award OIA 1545903), with additional financial support from Bradley Hacker. JMM is deeply thankful to the German Academic Exchange

Service (DAAD) for a mobility grant at GFZ Potsdam. This paper benefited from thoughtful comments from A. Garcia-Casco. This study was supported by the IdEx ANR-18-IDEX-0001 as well as through an excellence research chair attributed to S.A. This is the IBERSIMS publication n. XX.

REFERENCES

Abers, G. A., Nakajima, J., van Keken, P. E., Kita, S., & Hacker, B. R. (2013). Thermal–petrological controls on the location of earthquakes within subducting plates. Earth and Planetary Science Letters, 369, 178-187.

Agard, P., Monié, P., Gerber, W., Omrani, J., Molinaro, M., Meyer, B., ... & Yamato, P. (2006). Transient, synobduction exhumation of Zagros blueschists inferred from P-T, deformation, time, and kinematic constraints: Implications for Neotethyan wedge dynamics. Journal of Geophysical Research: Solid Earth, 111(B11).

Agard, P., Jolivet, L., Vrielynck, B., Burov, E., & Monie, P. (2007). Plate acceleration: the obduction trigger?. Earth and Planetary Science Letters, 258(3-4), 428-441.

Agard, P., Omrani, J., Jolivet, L., Whitechurch, H., Vrielynck, B., Spakman, W., ... & Wortel, R. (2011). Zagros orogeny: a subduction-dominated process. Geological Magazine, 148(5-6), 692-725.

Agard, P., Prigent, C., Soret, M., Dubacq, B., Guillot, S., & Deldicque, D. (2020). Slabitization: Mechanisms controlling subduction development and viscous coupling. Earth-Science Reviews, 103259.

Ajirlu, M. S., Moazzen, M., & Hajialioghli, R. (2016). Tectonic evolution of the Zagros Orogen in the realm of the Neotethys between the Central Iran and Arabian Plates: An ophiolite perspective. Central European Geology, 59(1-4), 1-27.

Alavi, M. (1994). Tectonics of the Zagros orogenic belt of Iran: new data and interpretations. Tectonophysics, 229(3-4), 211-238.

Anczkiewicz, R., Platt, J. P., Thirlwall, M. F., & Wakabayashi, J. (2004). Franciscan subduction off to a slow start: evidence from high-precision Lu–Hf garnet ages on high grade-blocks. Earth and Planetary Science Letters, 225(1-2), 147-161.

Angiboust, S., Agard, P., Glodny, J., Omrani, J., & Oncken, O. (2016). Zagros blueschists: Episodic underplating and long-lived cooling of a subduction zone. Earth and Planetary Science Letters, 443, 48-58.

Angiboust, S., Hyppolito, T., Glodny, J., Cambeses, A., Garcia-Casco, A., Calderón, M., & Juliani, C. (2017). Hot subduction in the middle Jurassic and partial melting of oceanic crust in Chilean Patagonia. Gondwana Research, 42, 104-125.

Angiboust, S., Cambeses, A., Hyppolito, T., Glodny, J., Monié, P., Calderón, M., & Juliani, C. (2018). A 100-my-long window onto mass-flow processes in the Patagonian Mesozoic subduction zone (Diego de Almagro Island, Chile). Bulletin, 130(9-10), 1439-1456.

Arfania, R., & Shahriari, S. (2009). Role of southeastern Sanandaj–Sirjan Zone in the tectonic evolution of Zagros Orogenic Belt, Iran. Island arc, 18(4), 555-576.

Arvin, M., Pan, Y., Dargahi, S., Malekizadeh, A., & Babaei, A. (2007). Petrochemistry of the Siah-Kuh granitoid stock southwest of Kerman, Iran: Implications for initiation of Neotethys subduction. Journal of Asian Earth Sciences, 30(3-4), 474-489.

Azizi, H., & Stern, R. J. (2019). Jurassic igneous rocks of the central Sanandaj–Sirjan zone (Iran) mark a propagating continental rift, not a magmatic arc. Terra Nova, 31(5), 415-423.

Barbero, E., Pandolfi, L., Delavari, M., Dolati, A., Saccani, E., Catanzariti, R., ... & Marroni, M. (2021). The western Durkan Complex (Makran Accretionary Prism, SE Iran): A Late Cretaceous tectonically disrupted seamounts chain and its role in controlling deformation style. Geoscience Frontiers, 12(3), 101106.

Barker, F. (1979). Trondhjemite: definition, environment and hypotheses of origin. In Developments in petrology (Vol. 6, pp. 1-12). Elsevier.

Bast, R., Scherer, E.E., Sprung, P., Fischer-Gödde, M., Stracke, A., Mezger, K. (2015). A rapid and efficient ion-exchange chromatography for Lu-Hf, Sm-Nd, and Rb-Sr geochronology and the routine isotope of sub-ng amounts of Hf by MC-ICP-MS. Journal of Analytical and Atomic Spectrometry, 30, 2323.

Berberian, M., & King, G. C. P. (1981). Towards a paleogeography and tectonic evolution of Iran. Canadian journal of earth sciences, 18(2), 210-265.

Black, L. P., Kamo, S. L., Allen, C. M., Aleinikoff, J. N., Davis, D. W., Korsch, R. J. & Foudoulis, C. (2003). TEMORA 1: a new zircon standard for Phanerozoic U–Pb geochronology. Chemical Geology 200(1-2), 155-170.

Blakey, R.C. "Gondwana paleogeography from assembly to breakup—A 500 my odyssey." Geological Society of America Special Papers 441 (2008): 1-28.

Blanco-Quintero, I. F., Rojas-Agramonte, Y., García-Casco, A., Kröner, A., Mertz, D. F., Lázaro, C., ... & Renne, P. R. (2011). Timing of subduction and exhumation in a subduction channel: Evidence from slab melts from La Corea Mélange (eastern Cuba). Lithos, 127(1-2), 86-100.

Bonnet, G., Agard, P., Angiboust, S., Fournier, M., & Omrani, J. (2019). No large earthquakes in fully exposed subducted seamount. Geology, 47(5), 407-410.

Bonnet, G., Agard, P., Whitechurch, H., Fournier, M., Angiboust, S., Caron, B., & Omrani, J. (2020). Fossil seamount in southeast Zagros records intraoceanic arc to back-arc transition: New constraints for the evolution of the Neotethys. Gondwana Research, 81, 423-444.

Bracciali, L., Parrish, R. R., Horstwood, M. S., Condon, D. J., & Najman, Y. (2013). UPb LA-(MC)-ICP-MS dating of rutile: New reference materials and applications to sedimentary provenance. Chemical Geology, 347, 82-101.

Brun, J. P., & Faccenna, C. (2008). Exhumation of high-pressure rocks driven by slab rollback. Earth and Planetary Science Letters, 272(1-2), 1-7.

Burg, J. P. (2018). Geology of the onshore Makran accretionary wedge: Synthesis and tectonic interpretation. Earth-Science Reviews, 185, 1210-1231.

Cherniak, D. J. (2000). Pb diffusion in rutile. Contributions to Mineralogy and Petrology, 139(2), 198-207.

Claoue-Long, J., Compston, W., Roberts, J. & Fanning, C.M. (1995). Two carboniferous ages: a comparison of SHRIMP zircon dating with conventional zircon ages & 40Ar/39Ar analysis. In: Berggren, W.A., Kent, D.V., Aubry, M.P., Hardenbol, J. (eds) Geochronology, Time Scales & Stratigraphic Correlation. SEPM Special Publication 54, 1-22.

Connolly, J. A. (2005). Computation of phase equilibria by linear programming: a tool for geodynamic modeling and its application to subduction zone decarbonation. Earth and Planetary Science Letters, 236(1-2), 524-541.

Dale, J., Powell, R., White, R. W., Elmer, F. L., & Holland, T. J. B. (2005). A thermodynamic model for Ca–Na clinoamphiboles in Na2O–CaO–FeO–MgO–Al2O3–SiO2–H2O–O for petrological calculations. Journal of Metamorphic Geology, 23(8), 771-791.

Davoudian, A. R., Genser, J., Dachs, E., & Shabanian, N. (2008). Petrology of eclogites from north of Shahrekord, Sanandaj-Sirjan Zone, Iran. Mineralogy and Petrology, 92(3), 393-413.

Davoudian, A. R., Genser, J., Neubauer, F., & Shabanian, N. (2016). 40Ar/39Ar mineral ages of eclogites from North Shahrekord in the Sanandaj–Sirjan Zone, Iran: implications for the tectonic evolution of Zagros orogen. Gondwana Research, 37, 216-240.

de la Fuente, D., Figueroa, Ó., Demaiffe, D., Mella, M., Duhart, P., Quiroz, D., ... & Oliveros, V. (2021). Upper Cretaceous intrusives in the Coastal Cordillera near Valdivia: forearc magmatism related to the passage of a triple junction?. Andean geology: Formerly Revista geológica de Chile, 48(1), 24-53.

Delaloye, M., & Desmons, J. (1980). Ophiolites and mélange terranes in Iran: a geochronological study and its paleotectonic implications. Tectonophysics, 68(1-2), 83-111.

Dercourt, J., L. E. Ricou, and B. Vrielynck. "Atlas Tethys Palaeoenvironmental Maps Gauthier-Villars." Paris 307pp 14 (1993).

Dilek, Y., & Ogawa, Y. (2021). Subduction zone processes and crustal growth mechanisms at Pacific Rim convergent margins: modern and ancient analogues. Geological Magazine, 158(1), 1-12.

Dodson, M. H. (1973). Closure temperature in cooling geochronological and petrological systems. Contributions to Mineralogy and Petrology, 40(3), 259-274.

Dragovic, B., Samanta, L., Baxter, E.F., Selverstone, J. (2012). Using garnet to constrain the duration and rate of water-releasing metamorphic reactions during subduction: An example from Sifnos, Greece. Chemical Geology, 314-317, 9-22.

Dragovic, B., Angiboust, S., & Tappa, M. J. (2020). Petrochronological close-up on the thermal structure of a paleo-subduction zone (W. Alps). Earth and Planetary Science Letters, 547, 116446.

Drummond, M. S., & Defant, M. J. (1990). A model for trondhjemite-tonalite-dacite genesis and crustal growth via slab melting: Archean to modern comparisons. Journal of Geophysical Research: Solid Earth, 95(B13), 21503-21521.

Ernst, W. G. (1973). Blueschist metamorphism and PT regimes in active subduction zones. Tectonophysics, 17(3), 255-272.

Esmaeili, R., Xiao, W., Ebrahimi, M., Zhang, J. E., Zhang, Z., Abd El-Rahman, Y., ... & Aouizerat, A. (2020). Makran ophiolitic basalts (SE Iran) record Late Cretaceous Neotethys plume-ridge interaction. International Geology Review, 62(13-14), 1677-1697.

Evans, B. W. (1990). Phase relations of epidote-blueschists. Lithos, 25(1-3), 3-23.

Ewing, T. A. (2011). Hf isotope analysis and U-Pb geochronology of rutile: Technique development and application to a lower crustal section (Ivrea-Verbano Zone, Italy).

Ewing, T. A., Hermann, J., & Rubatto, D. (2013). The robustness of the Zr-in-rutile and Ti-in-zircon thermometers during high-temperature metamorphism (Ivrea-Verbano Zone, northern Italy). Contributions to Mineralogy and

Petrology, 165(4), 757-779.

Ferry, J. M., & Watson, E. B. (2007). New thermodynamic models and revised calibrations for the Ti-in-zircon and Zr-in-rutile thermometers. Contributions to Mineralogy and Petrology, 154(4), 429-437.

Foley, S., Tiepolo, M., & Vannucci, R. (2002). Growth of early continental crust controlled by melting of amphibolite in subduction zones. Nature, 417(6891), 837-840.

Frassi, C., Rebay, G., Marroni, M., Sayit, K., Göncüoğlu, M. C., Ellero, A., ... & Pandolfi, L. (2020). Metamorphic imprint of ridge subduction on the Neo-Tethyan ophiolites from the Saka Unit (Central Pontides, northern Turkey). Journal of Asian Earth Sciences, 200, 104468.

Fuhrman, M. L., & Lindsley, D. H. (1988). Ternary-feldspar modeling and thermometry. American mineralogist, 73(3-4), 201-215.

García-Casco, A. (2007). Magmatic paragonite in trondhjemites from the Sierra del Convento mélange, Cuba. American Mineralogist, 92(7), 1232-1237.

García-Casco, A., Lázaro, C., Rojas-Agramonte, Y., Kröner, A., Torres-Roldán, R. L., Núñez, K., ... & Blanco-Quintero, I. (2008). Partial melting and counterclockwise P–T path of subducted oceanic crust (Sierra del Convento mélange, Cuba). Journal of Petrology, 49(1), 129-161.

Ghasemi, H., Juteau, T., Bellon, H., Sabzehei, M., Whitechurch, H., & Ricou, L. E. (2002). The mafic–ultramafic complex of Sikhoran (central Iran): a polygenetic ophiolite complex. Comptes Rendus Geoscience, 334(6), 431-438.

Granot, R., Dyment, J., & Gallet, Y. (2012). Geomagnetic field variability during the Cretaceous Normal Superchron. Nature Geoscience, 5(3), 220-223.

Grove, M., & Bebout, G. E. (1995). Cretaceous tectonic evolution of coastal southern California: insights from the Catalina Schist. Tectonics, 14(6), 1290-1308.

Guilmette, C., Smit, M.A., van Hinsbergen, D.J.J., Gürer, D., Corfu, F., Charette, B., Maffione, M., Rabeau, O., Savard, D., 2018. Forced subduction initiation recorded in the sole and crust of the Semail Ophiolite of Oman. Nature geosciences 11,

Gutscher, M. A., Maury, R., Eissen, J. P., & Bourdon, E. (2000). Can slab melting be caused by flat subduction?. Geology, 28(6), 535-538.

Hassanzadeh, J., & Wernicke, B. P. (2016). The Neotethyan Sanandaj-Sirjan zone of Iran as an archetype for passive margin-arc transitions. Tectonics, 35(3), 586-621.

Hébert, R., Bezard, R., Guilmette, C., Dostal, J., Wang, C. S., & Liu, Z. F. (2012). The Indus–Yarlung Zangbo ophiolites from Nanga Parbat to Namche Barwa syntaxes, southern Tibet: First synthesis of petrology, geochemistry, and geochronology with incidences on geodynamic reconstructions of Neo-Tethys. Gondwana Research, 22(2), 377-397.

Holland, T., & Powell, R. (1996). Thermodynamics of order-disorder in minerals: II. Symmetric formalism applied to solid solutions. American Mineralogist, 81(11-12), 1425-1437.

Holland, T., Baker, J., & Powell, R. (1998). Mixing properties and activity-composition relationships of chlorites in the system MgO-FeO-Al2O3-SiO2-H2O. European Journal of Mineralogy, 395-406.

Holland, T. J. B., & Powell, R. T. J. B. (1998). An internally consistent thermodynamic data set for phases of petrological interest. Journal of metamorphic Geology, 16(3), 309-343.

Hyppolito, T., García-Casco, A., Juliani, C., Meira, V. T., & Hall, C. (2014). Late Paleozoic onset of subduction and exhumation at the western margin of Gondwana (Chilenia Terrane): Counterclockwise P–T paths and timing of metamorphism of deep-seated garnet–mica schist and amphibolite of Punta Sirena, Coastal Accretionary Complex, central Chile (34 S). Lithos, 206, 409-434.

Jochum, K. P., Willbold, M., Raczek, I., Stoll, B., & Herwig, K. (2005). Chemical Characterisation of the USGS Reference Glasses GSA-1G, GSC-1G, GSD-1G, GSE-1G, BCR-2G, BHVO-2G and BIR-1G Using EPMA, ID-TIMS, ID-ICP-MS and LA-ICP-MS. Geostandards and Geoanalytical Research, 29(3), 285-302.

Johnson, C. A., & Harlow, G. E. (1999). Guatemala jadeitites and albitites were formed by deuterium-rich serpentinizing fluids deep within a subduction zone. Geology, 27(7), 629-632.

Kohn, M. J. (2020). A refined zirconium-in-rutile thermometer. American Mineralogist: Journal of Earth and Planetary Materials, 105(6), 963-971.

Krebs, M., Maresch, W. V., Schertl, H. P., Münker, C., Baumann, A., Draper, G., ... & Trapp, E. (2008). The dynamics of intra-oceanic subduction zones: a direct comparison between fossil petrological evidence (Rio San Juan Complex, Dominican Republic) and numerical simulation. Lithos, 103(1-2), 106-137.

Kylander-Clark, A. R. C., Hacker, B. R., & Mattinson, J. M. (2008). Slow exhumation of UHP terranes: titanite and rutile ages of the Western Gneiss Region, Norway. Earth and Planetary Science Letters, 272(3-4), 531-540.

Kylander-Clark, A. R., Hacker, B. R., & Cottle, J. M. (2013). Laser-ablation split-stream ICP petrochronology. Chemical Geology, 345, 99-112.

Lagabrielle, Y., Guivel, C., Maury, R. C., Bourgois, J., Fourcade, S., & Martin, H. (2000). Magmatic–tectonic effects of high thermal regime at the site of active ridge subduction: the Chile Triple Junction model. *Tectonophysics*, *326*(3-4), 255-268.

Larson, R. L. (1991). Latest pulse of Earth: Evidence for a mid-Cretaceous superplume. Geology, 19(6), 547-550.

Lázaro, C., García-Casco, A., Rojas Agramonte, Y., Kröner, A., Neubauer, F., & Iturralde-Vinent, M. (2009). Fifty-five-million-year history of oceanic subduction and exhumation at the northern edge of the Caribbean plate (Sierra del Convento mélange, Cuba). Journal of metamorphic Geology, 27(1), 19-40.

Lázaro, C., Blanco-Quintero, I. F., Marchesi, C., Bosch, D., Rojas-Agramonte, Y., & García-Casco, A. (2011). The imprint of subduction fluids on subducted MORB-derived melts (Sierra del Convento Mélange, Cuba). *Lithos*, *126*(3-4), 341-354.

Li, W. C., Chen, R. X., Zheng, Y. F., Tang, H., & Hu, Z. (2016). Two episodes of partial melting in ultrahigh-pressure migmatites from deeply subducted continental crust in the Sulu orogen, China. Bulletin, 128(9-10), 1521-1542.

Li, S. M., Wang, Q., Zhu, D. C., Stern, R. J., Cawood, P. A., Sui, Q. L., & Zhao, Z. (2018). One or two Early Cretaceous arc systems in the Lhasa Terrane, southern Tibet. Journal of Geophysical Research: Solid Earth, 123(5), 3391-3413.

Luvizotto, G. L., Zack, T., Meyer, H. P., Ludwig, T., Triebold, S., Kronz, A., ... & von Eynatten, H. (2009). Rutile crystals as potential trace element and isotope mineral standards for microanalysis. Chemical Geology, 261(3-4),

346-369.

Mahoney, J. J., Graham, D. W., Christie, D. M., Johnson, K. T. M., Hall, L. S., & Vonderhaar, D. L. (2002). Between a hotspot and a cold spot: isotopic variation in the Southeast Indian Ridge asthenosphere, 86 E–118 E. Journal of Petrology, 43(7), 1155-1176.

Matthews, K. J., Seton, M., & Müller, R. D. (2012). A global-scale plate reorganization event at 105− 100 Ma. Earth and Planetary Science Letters, 355, 283-298.

McCall, G. J. H. (1997). The geotectonic history of the Makran and adjacent areas of southern Iran. Journal of Asian Earth Sciences, 15(6), 517-531.

Müller, R. D., Seton, M., Zahirovic, S., Williams, S. E., Matthews, K. J., Wright, N. M., ... & Cannon, J. (2016). Ocean basin evolution and global-scale plate reorganization events since Pangea breakup. Annual Review of Earth and Planetary Sciences, 44, 107-138.

Müller, R. D., & Seton, M. (2015). Paleophysiography of ocean basins. Encyclopedia of Marine Geosciences.

Muñoz-Montecinos, J., Angiboust, S., Garcia-Casco, A., Glodny, J., & Bebout, G. (2021). Episodic hydrofracturing and large-scale flushing along deep subduction interfaces: Implications for fluid transfer and carbon recycling (Zagros Orogen, southeastern Iran). Chemical Geology, 571, 120173.

Muñoz-Montecinos, J., Angiboust, S., & Garcia-Casco, A. (2021). Blueschist-facies paleo-earthquakes in a serpentinite channel (Zagros suture, Iran) enlighten seismogenesis in Mariana-type subduction margins. Earth and Planetary Science Letters, 573, 117135.

Oberhänsli, R., Bousquet, R., Moinzadeh, H., Moazzen, M., & Arvin, M. (2007). The field of stability of blue jadeite: a new occurrence of jadeitite at Sorkhan, Iran, as a case study. The Canadian Mineralogist, 45(6), 1501-1509.

O'Connor, J. T. (1965). A classification for quartz-rich igneous rocks. Geol. Surv. Prof. Pap, 525, 79.

Olierook, H. K., Jourdan, F., Whittaker, J. M., Merle, R. E., Jiang, Q., Pourteau, A., & Doucet, L. S. (2020). Timing and causes of the mid-Cretaceous global plate reorganization event. Earth and Planetary Science Letters, 534, 116071.

Omrani, J. (2008). The geodynamic evolution of Zagros: Tectonic and petrological constraints from the internal zones (Doctoral dissertation, Paris 6).

Palin, R. M., Weller, O. M., Waters, D. J., & Dyck, B. (2016). Quantifying geological uncertainty in metamorphic phase equilibria modelling; a Monte Carlo assessment and implications for tectonic interpretations. Geoscience Frontiers, 7(4), 591-607.

Paton, C., Hellstrom, J., Paul, B., Woodhead, J., & Hergt, J. (2011). Iolite: Freeware for the visualisation and processing of mass spectrometric data. Journal of Analytical Atomic Spectrometry, 26(12), 2508-2518.

Peacock, S. M. (2003). Thermal structure and metamorphic evolution of subducting slabs. Geophysical Monograph-American Geophysical Union, 138, 7-22.

Pearce, J. A. (2008). Geochemical fingerprinting of oceanic basalts with applications to ophiolite classification and the search for Archean oceanic crust. Lithos, 100(1-4), 14-48.

Penniston-Dorland, S. C., Kohn, M. J., & Piccoli, P. M. (2018). A mélange of subduction temperatures: Evidence from Zr-in-rutile thermometry for strengthening of the subduction interface. Earth and Planetary Science Letters, 482, 525-535.

Pirnia, T., Saccani, E., Torabi, G., Chiari, M., Goričan, Š., & Barbero, E. (2020). Cretaceous tectonic evolution of the Neo-Tethys in Central Iran: Evidence from petrology and age of the Nain-Ashin ophiolitic basalts. Geoscience Frontiers, 11(1), 57-81.

Plunder, A., Agard, P., Chopin, C., Pourteau, A., & Okay, A. I. (2015). Accretion, underplating and exhumation along a subduction interface: From subduction initiation to continental subduction (Tavşanlı zone, W. Turkey). Lithos, 226, 233-254.

Prouteau, G., Scaillet, B., Pichavant, M., & Maury, R. (2001). Evidence for mantle metasomatism by hydrous silicic melts derived from subducted oceanic crust. Nature, 410(6825), 197-200.

Pourteau, A., Scherer, E. E., Schorn, S., Bast, R., Schmidt, A., & Ebert, L. (2019). Thermal evolution of an ancient subduction interface revealed by Lu–Hf garnet geochronology, Halilbağı Complex (Anatolia). Geoscience Frontiers, 10(1), 127-148.

Powell, R., & Holland, T. (1999). Relating formulations of the thermodynamics of mineral solid solutions; activity modeling of pyroxenes, amphiboles, and micas. American mineralogist, 84(1-2), 1-14.

Rapp, R. P., Watson, E. B., & Miller, C. F. (1991). Partial melting of amphibolite/eclogite and the origin of Archean trondhjemites and tonalites. Precambrian Research, 51(1-4), 1-25.

Ricou, L. E. (1994). Tethys reconstructed: plates, continental fragments and their Boundaries since 260 Ma from Central America to South-eastern Asia. Geodinamica acta, 7(4), 169-218.

Rodriguez, M., Arnould, M., Coltice, N., & Soret, M. (2021). Long-term evolution of a plume-induced subduction in the Neotethys realm. Earth and Planetary Science Letters, 561, 116798.

Rolland, Y., Billo, S., Corsini, M., Sosson, M., & Galoyan, G. (2009). Blueschists of the Amassia-Stepanavan suture zone (Armenia): Linking Tethys subduction history from E-Turkey to W-Iran. International Journal of Earth Sciences, 98(3), 533-550.

Rossetti, F., Nasrabady, M., Vignaroli, G., Theye, T., Gerdes, A., Razavi, M. H., & Vaziri, H. M. (2010). Early Cretaceous migmatitic mafic granulites from the Sabzevar range (NE Iran): implications for the closure of the Mesozoic peri-Tethyan oceans in central Iran. Terra Nova, 22(1), 26-34.

Rossetti, F., Monié, P., Nasrabady, M., Theye, T., Lucci, F., & Saadat, M. (2017). Early Carboniferous subduction-zone metamorphism preserved within the Palaeo-Tethyan Rasht ophiolites (western Alborz, Iran). Journal of the Geological Society, 174(4), 741-758.

Rubatto, D. (2002). Zircon trace element geochemistry: partitioning with garnet and the link between U–Pb ages and metamorphism. Chemical geology, 184(1-2), 123-138.

Sabzehei, M. (1974). Les Mélanges ophiolitiques de la région d'Esfandagheh (Iran méridional): étude pétrologique et structurale, interprétation dans le cadre iranien (Doctoral dissertation, Université Scientifique et Médicale de Grenoble).

Saccani, E., Delavari, M., Dolati, A., Marroni, M., Pandolfi, L., Chiari, M., & Barbero, E. (2018). New insights into the geodynamics of Neo-Tethys in the Makran area: Evidence from age and petrology of ophiolites from the Coloured Mélange Complex (SE Iran). Gondwana Research, 62, 306-327.

Sawyer, E. W. (2008). Atlas of migmatites (Vol. 9). NRC Research press.

Şengör, A. M. C., Altıner, D., Cin, A., Ustaömer, T., & Hsü, K. J. (1988). Origin and assembly of the Tethyside orogenic collage at the expense of Gondwana Land. Geological Society, London, Special Publications, 37(1), 119-181.

Schmitz, M. D., & Schoene, B. (2007). Derivation of isotope ratios, errors, and error correlations for U-Pb geochronology using 205Pb-235U-(233U)-spiked isotope dilution thermal ionization mass spectrometric data. Geochemistry, Geophysics, Geosystems, 8(8).

Seton, M., Müller, R. D., Zahirovic, S., Gaina, C., Torsvik, T., Shephard, G., ... & Chandler, M. (2012). Global continental and ocean basin reconstructions since 200 Ma. Earth-Science Reviews, 113(3-4), 212-270.

Shafaii Moghadam, H.S., & Stern, R. J. (2011). Geodynamic evolution of Upper Cretaceous Zagros ophiolites: formation of oceanic lithosphere above a nascent subduction zone. Geological Magazine, 148(5-6), 762-801.

Shafaii Moghadam, H.S., Bröcker, M., Griffin, W. L., Li, X. H., Chen, R. X., & O'Reilly, S. Y. (2017). Subduction, high-P metamorphism, and collision fingerprints in South Iran: Constraints from zircon U-Pb and mica Rb-Sr geochronology. Geochemistry, Geophysics, Geosystems, 18(1), 306-332.

Smye, A. J., Greenwood, L. V., & Holland, T. J. B. (2010). Garnet–chloritoid–kyanite assemblages: eclogite facies indicators of subduction constraints in orogenic belts. Journal of Metamorphic Geology, 28(7), 753-768.

Söderlund, U., Patchett, P.J., Vervoort, J.D., Isachsen, C.E. (2004). The ^{176}Lu decay constant determined by Lu-Hf and U-Pb isotope systematics of Precambrian mafic intrusions, Earth and Planetary Science Letters, 219, 311-324.

Sorensen, S. S., & Barton, M. D. (1987). Metasomatism and partial melting in a subduction complex Catalina Schist, southern California. Geology, 15(2), 115-118.

Stacey, J. T., & Kramers, 1. (1975). Approximation of terrestrial lead isotope evolution by a two-stage model. Earth and planetary science letters, 26(2), 207-221.

Stampfli, Gérard M., and G. D. Borel. "A plate tectonic model for the Paleozoic and Mesozoic constrained by dynamic plate boundaries and restored synthetic oceanic isochrons." Earth and Planetary Science Letters 196.1-2 (2002): 17-33.

Stern, R. J. (2002). Subduction zones. Reviews of geophysics, 40(4), 3-1.

Stöcklin, J. (1974). Possible ancient continental margins in Iran. In The geology of continental margins (pp. 873-887). Springer, Berlin, Heidelberg.

Tamblyn, R., Zack, T., Schmitt, A. K., Hand, M., Kelsey, D., Morrissey, L., ... & Savov, I. P. (2019). Blueschist from the Mariana forearc records long-lived residence of material in the subduction channel. Earth and Planetary Science Letters, 519, 171-181.

Tatsumi, Y., & Hanyu, T. (2003). Geochemical modeling of dehydration and partial melting of subducting lithosphere: Toward a comprehensive understanding of high-Mg andesite formation in the Setouchi volcanic belt, SW Japan. Geochemistry, Geophysics, Geosystems, 4(9).

Tomkins, H. S., Powell, R., & Ellis, D. J. (2007). The pressure dependence of the zirconium-in-rutile thermometer. Journal of metamorphic Geology, 25(6), 703-713.

Vermeesch, P. (2018). IsoplotR: A free and open toolbox for geochronology. Geoscience Frontiers, 9(5), 1479-1493.

Vervoort, J.D. & Blichert-Toft, J. (1999). Evolution of the depleted mantle: Hf isotope evidence from juvenile rocks

through time. Geochimica et Cosmochimica Acta, 63, 533-556.

Vervoort, J.D., Patchett, P.J., Sönderlund, U., Baker, M. (2004). Isotopic composition of Yb and the determination of Lu concentrations and Lu/Hf ratios by isotope dilution using MC-ICPMS. Geochemistry, Geophysics, Geosystems, 5 (11).

Vielzeuf, D., & Schmidt, M. W. (2001). Melting relations in hydrous systems revisited: application to metapelites, metagreywackes and metabasalts. Contributions to Mineralogy and Petrology, 141(3), 251.

White, R. W., Powell, R., Holland, T. J. B., & Worley, B. A. (2000). The effect of TiO2 and Fe2O3 on metapelitic assemblages at greenschist and amphibolite facies conditions: mineral equilibria calculations in the system K2O-FeO-MgO-Al2O3-SiO2-H2O-TiO2-Fe2O3. Journal of Metamorphic Geology, 18(5), 497-511.

White, R. W., Powell, R., & Holland, T. J. B. (2007). Progress relating to calculation of partial melting equilibria for metapelites. Journal of metamorphic Geology, 25(5), 511-527.

Williams, I. S. & Claesson, S. (1987). Isotopic evidence for the Precambrian provenance and Caledonian metamorphism of high grade paragneisses from the Seve Nappes, Scandinavian Caledonides. Contributions to mineralogy and petrology 97(2), 205-217.

Willner, A. P., Glodny, J., Gerya, T. V., Godoy, E., & Massonne, H. J. (2004). A counterclockwise PTt path of high-pressure/low-temperature rocks from the Coastal Cordillera accretionary complex of south-central Chile: constraints for the earliest stage of subduction mass flow. Lithos, 75(3-4), 283-310.

Windley, B. F., & Xiao, W. (2018). Ridge subduction and slab windows in the Central Asian Orogenic Belt: Tectonic implications for the evolution of an accretionary orogen. Gondwana Research, 61, 73-87.

Winther, K. Tobias. "Experimental melting of hydrous low-K tholeiite: evidence on the origin of Archean cratons." Bull Geol Soc Den 39 (1991): 213-228.

Yang, G., & Dilek, Y. (2015). OIB-and P-type ophiolites along the Yarlung-Zangbo Suture Zone (YZSZ), Southern Tibet: Poly-Phase melt history and mantle sources of the Neotethyan oceanic lithosphere. Episodes, 38(4), 250-265.

Zack, T., Moraes, R., & Kronz, A. (2004). Temperature dependence of Zr in rutile: empirical calibration of a rutile thermometer. Contributions to Mineralogy and Petrology, 148(4), 471-488.

15. Supplementary figures and tables

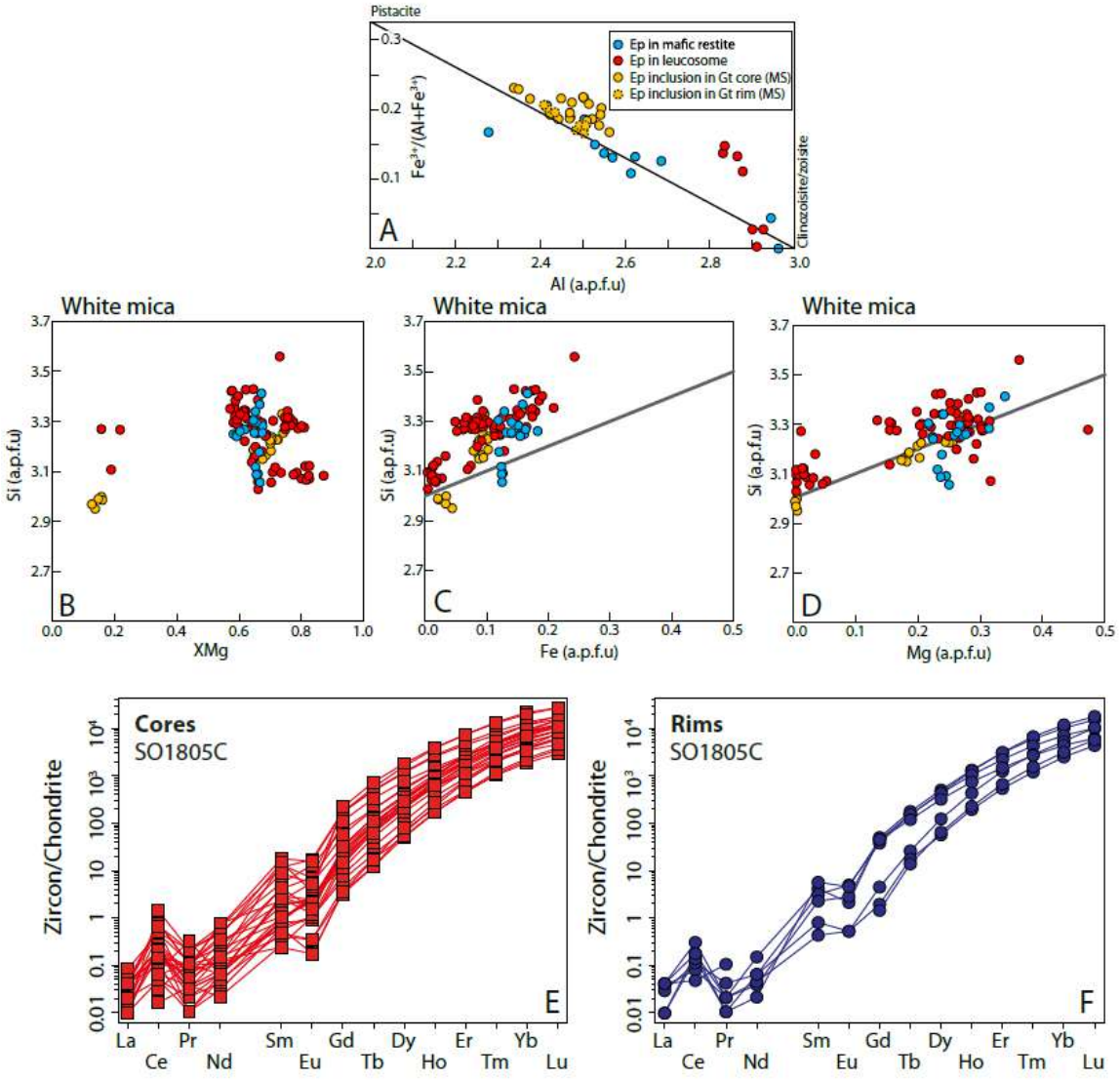

Figure 11.S1. Mineral chemistry diagrams for (A) epidote, white mica (B to D) and zircon (E and F).

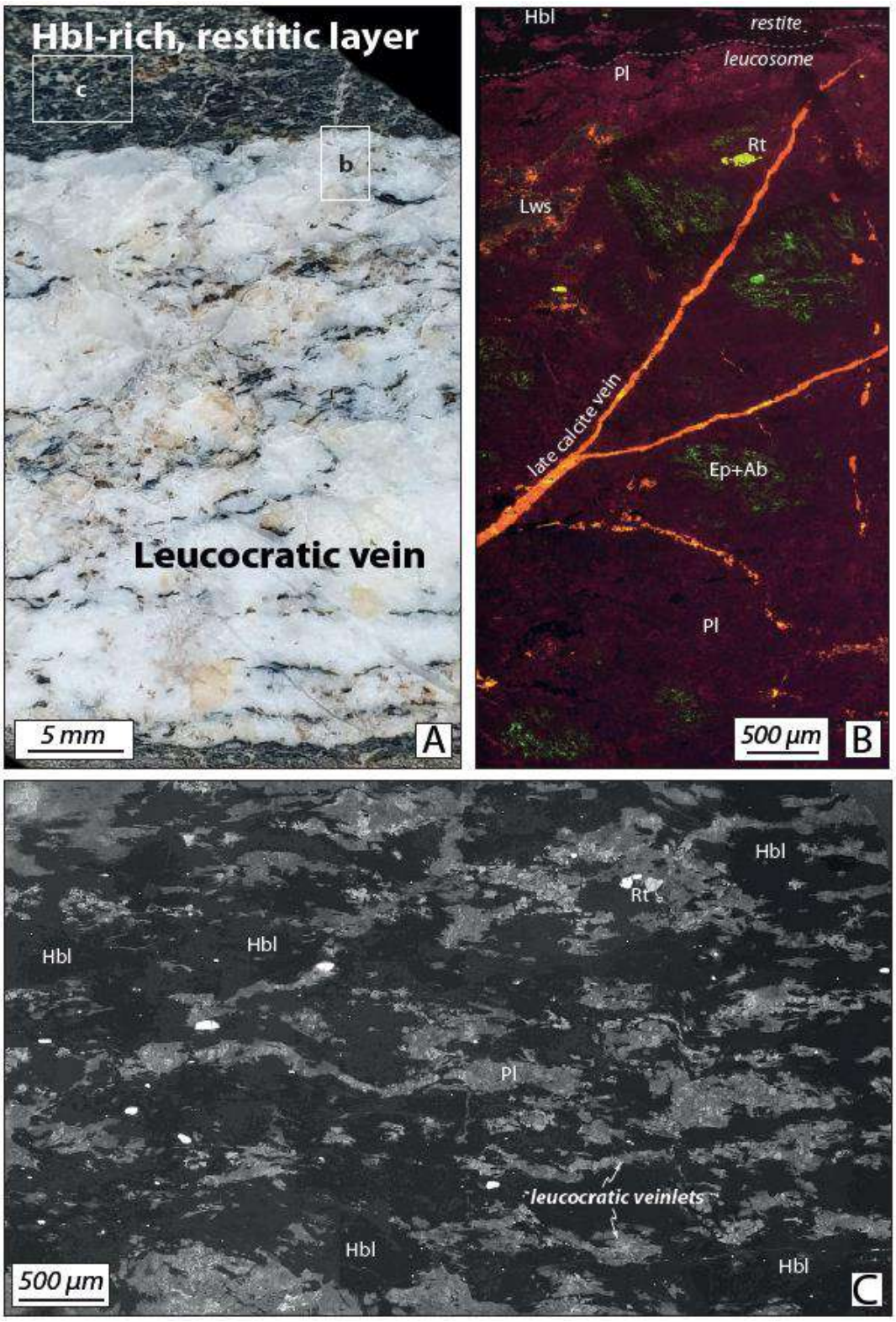

Figure 11.S2: Additional data for sample SO1317. A. The hand specimen section for overview. B. Cathodoluminescence images showing the structure of a leucocratic domain. C. A grey-scale colored cathodoluminescence image of a restitic domain, showing the foliation-parallel leucocratic veinlets separating Hbl-rich areas.

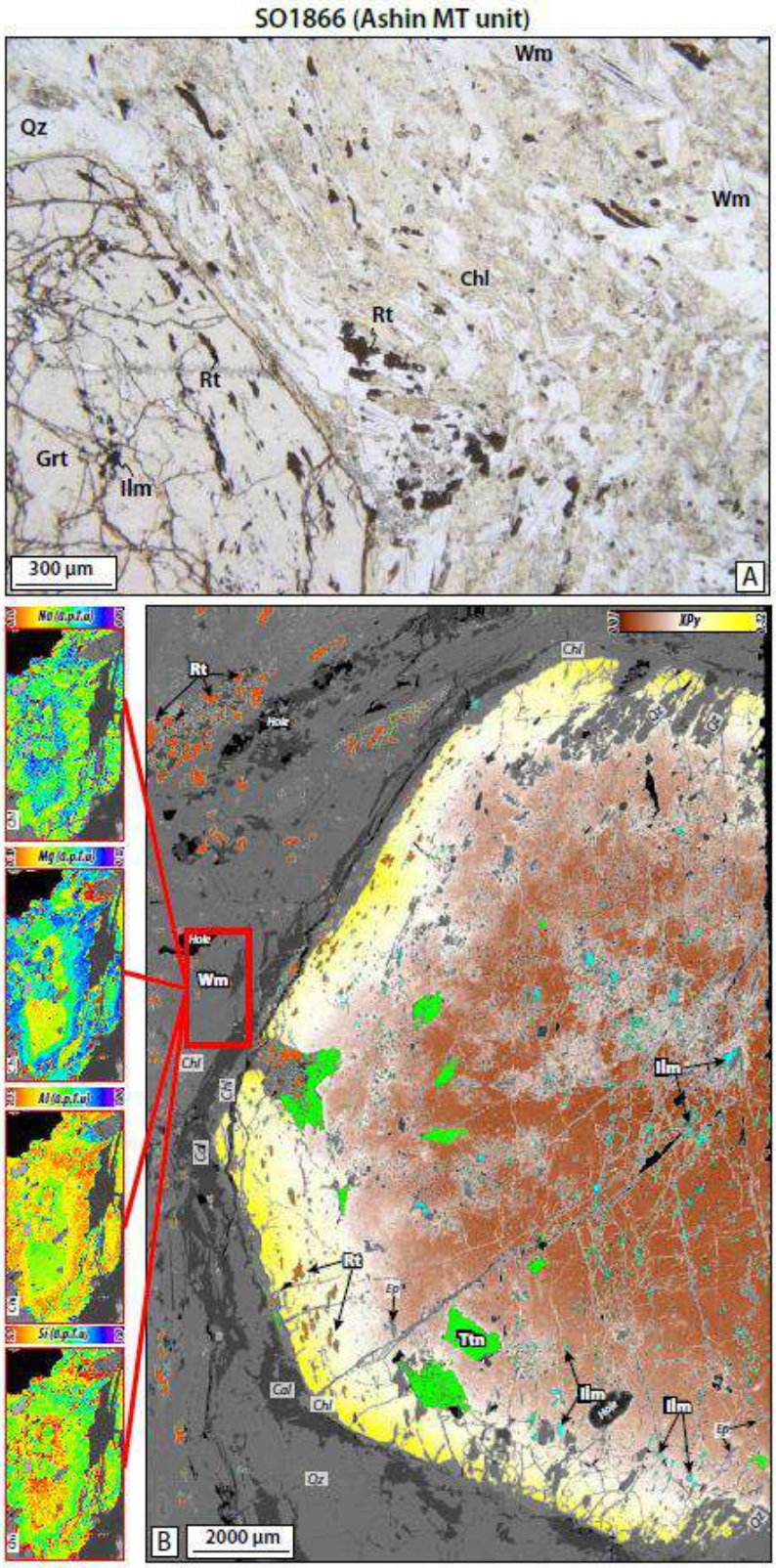

Figure 11.S3. Photomicrograph (A) and X-ray maps (B) of a garnet micaschist from the Ashin MT unit.

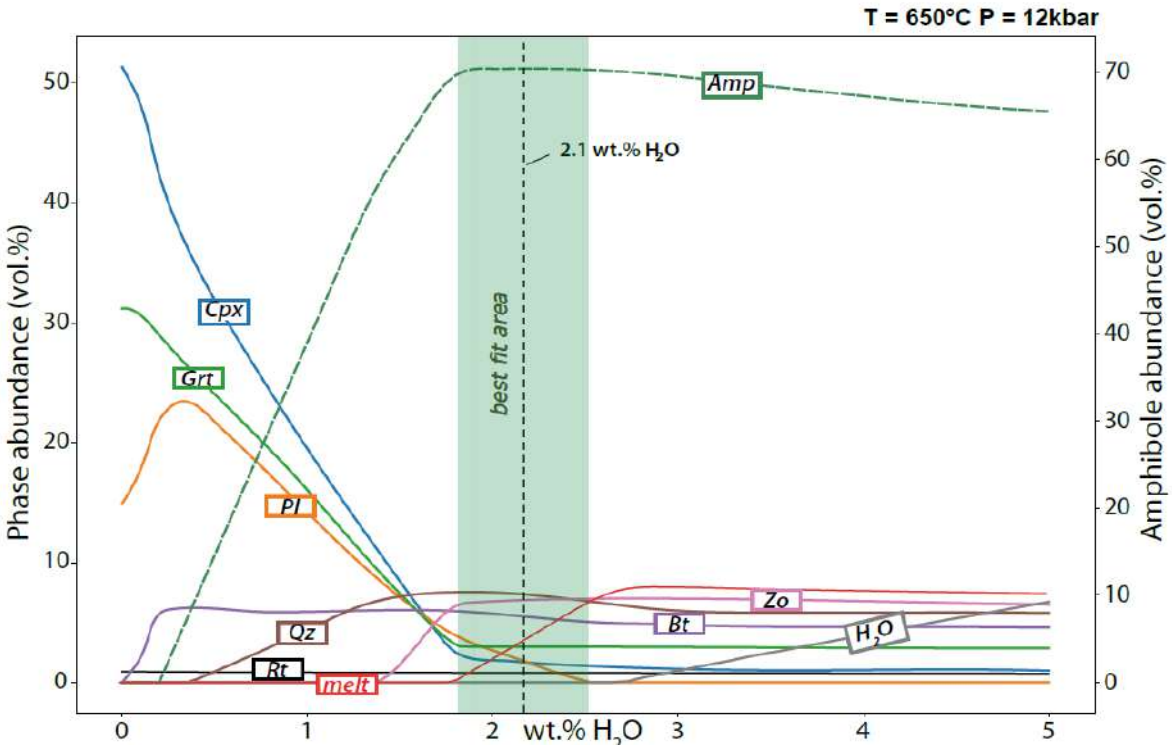

Figure 11.S4. Phase abundances relative to H_2O variations at fixed PT conditions (1.2 GPa and 650 °C).

Table S1. Location and lithologies studied in the Ashin complex

Unit	Sample	Rock type	Minerals observed (+ Pl+Qz+Ep+Ms/Phg+Chl)	Latitude (N 28°)
MT	SO1866	Grt Micaschist	Grt-Ilm-Rt-Ttn	29' 53"
MT	SO1862	Grt Micaschist	Grt-Ilm-Rt-Ttn	29' 49"
HT	SO1317	Restite+Leucosome	Amp-Cpx-Rt-Ttn-Lws-Stlp	29' 56"
HT	SO1803	Grt Micaschist+Leucosome	Amp-Grt-Rt-Ttn-Lws	29' 55"
HT	SO1804	Amphibolite	Amp-Ttn-Pmp	29' 55"
HT	SO1805c	Leucosome	Amp-Ttn-Pmp	29' 55"
HT	SO1808	Restite+Leucosome	Amp-Rt-Ttn-Pmp	29' 54"
HT	SO1860	Amphibolite	Amp-Grt-Cpx-Rt-Ttn	29' 43"
HT	SO1861	Amphibolite + zoisite-rich bands	Amp-Grt-Ilm-Rt-Ttn	29' 41"
HT	SO1863b	Amphibolite	Amp-Grt-Ilm-Rt-Ttn	29' 42"
HT	SO1863b	Leucosome	Amp-Grt-Ilm-Rt-Ttn-Lws-Pmp	29' 42"
HT	SO1864	Restite+Leucosome	Amp-Ilm-Rt-Ttn-Pmp	29' 41"
HT	SO1865	Leucosome	Amp-Grt-Ilm-Rt-Ttn-Pmp	29' 40"
HT	SO1865c	Restite+Leucosome	Amp-Grt-Ilm-Rt-Ttn-Pmp	29' 40"

Table S2. Selected electro microprobe analyses of mineral compositions and cations per formula unit in the Ashin complex

Mineral or group	Sample	Id	Unit-lithology	Zone	SiO_2	TiO_2	Al_2O_3	Cr_2O_3	FeO	MnO	MgO	CaO	Na_2O	K_2O	Total	Si	Ti	Al	Fe3+	Fe2+	Mn	Mg	Ca	Na	K	XMg	$(Na+K)_A$
					(wt%)	(wt%)	(wt%)	(wt%)	(wt%)	(wt%)	(wt%)	(wt%)	(wt%)	(wt%)		(a.p.f.u)	(a.p.f.u)	(a.p.f.u)	(a.p.f.u)	(a.p.f.u)	(a.p.f.u)	(a.p.f.u)	(a.p.f.u)	(a.p.f.u)	(a.p.f.u)		
Pargasite	SO1863b	A-SO1863b-C11	HT-Amphibolite	Host	43.67	0.52	14.06	0.18	16.21	0.06	9.87	10.25	2.73	0.30	97.84	6.42	0.06	2.44	0.34	1.66	0.01	2.16	1.61	0.78	0.03	0.57	0.52
Tchermakite	SO1861	A-SO1861-A10	HT-Amphibolite	Host	44.09	0.61	13.58	0.07	14.17	0.17	11.00	11.20	1.88	0.72	97.49	6.47	0.07	2.35	0.23	1.51	0.02	2.41	1.76	0.54	0.07	0.62	0.43
	SO1861	A-SO1861-E5	HT-Amphibolite	Leucosome	43.83	0.64	14.53	0.08	14.71	0.14	9.95	11.18	1.85	0.89	97.79	6.44	0.07	2.52	0.15	1.66	0.02	2.18	1.76	0.53	0.08	0.57	0.41
Mg-Hbl	SO1317	A-SO1317-A16	HT-Amphibolite	Host	44.63	0.69	12.85	0.05	15.22	0.20	10.99	10.64	2.32	0.36	97.96	6.52	0.08	2.21	0.34	1.52	0.03	2.39	1.67	0.66	0.03	0.61	0.45
	SO1317	M-SO1317-D8	HT-Amphibolite	Leucosome	49.11	0.36	9.95	0.03	10.85	0.23	14.01	11.22	1.94	0.20	97.90	7.01	0.04	1.67	0.13	1.16	0.03	2.98	1.72	0.54	0.02	0.72	0.31
Edenite	SO1864	A-SO1864-D5	HT-Amphibolite	Host	44.79	0.63	12.32	0.00	15.68	0.26	10.43	10.38	2.81	0.54	97.84	6.60	0.07	2.14	0.22	1.71	0.03	2.29	1.64	0.80	0.05	0.57	0.55
	SO1317	A-SO1317-B18	HT-Amphibolite	Leucosome	45.02	0.70	13.34	0.07	14.20	0.24	11.40	10.91	2.67	0.33	98.88	6.51	0.08	2.27	0.23	1.48	0.03	2.46	1.69	0.75	0.03	0.62	0.54
Actinolite	SO1317	A-SO1317-A10	HT-Amphibolite	Host	55.03	0.04	1.90	0.02	12.07	0.22	16.28	11.84	0.59	0.05	98.02	7.83	0.00	0.32	0.10	1.33	0.03	3.45	1.80	0.16	0.00	0.72	0.04
	SO1317	M-SO1317-B4	HT-Amphibolite	Leucosome	54.41	0.05	2.70	0.00	12.16	0.20	16.54	11.07	0.72	0.10	97.95	7.73	0.01	0.45	0.15	1.30	0.02	3.50	1.69	0.20	0.01	0.73	0.06
Garnet	SO1860	G-SO1860-C9	HT-Amphibolite	Host	39.39	0.06	21.86	0.02	20.60	6.85	1.33	9.85	0.04	0.00	100.01	3.12	0.00	2.04	0.00	1.37	0.46	0.16	0.84	0.01	0.00	0.10	N.A.†
	SO1860	G-SO1860-A14	HT-Amphibolite	Leucosome	39.36	0.07	21.99	0.07	20.50	2.35	1.74	14.15	0.05	0.00	100.28	3.08	0.00	2.03	0.00	1.34	0.16	0.20	1.18	0.01	0.00	0.13	N.A.†
	SO1866	G-So1866-A-41	MT-Micaschist	Host	37.77	0.07	21.21	0.08	28.34	0.00	2.40	9.79	0.00	0.00	99.67	3.00	0.00	1.99	0.00	1.88	0.00	0.28	0.83	0.00	0.00	0.13	N.A.†
Epidote	SO1861	E-SO1861-E1	HT-Amphibolite	Host	39.69	0.08	31.47	0.00	2.26	0.01	0.01	24.16	0.01	0.02	97.71	3.03	0.00	2.83	0.14	0.00	0.00	0.00	1.98	0.00	0.00	N.A.†	N.A.†
	SO1317	M-Ap-SO1317-C5	HT-Amphibolite	Host	39.18	0.03	34.35	0.02	0.13	0.03	0.02	24.17	0.02	0.00	97.95	2.96	0.00	3.06	0.01	0.00	0.00	0.00	1.96	0.00	0.00	N.A.†	N.A.†
	SO1865c	M-E-So1865c-D-7	HT-Amphibolite	Host	38.92	0.00	32.89	0.00	2.13	0.24	0.07	23.75	0.02	0.07	98.09	2.96	0.00	2.94	0.14	0.00	0.02	0.01	1.93	0.00	0.01	N.A.†	N.A.†
Pyroxene	SO1860	9 / 1 .	HT-Amphibolite	Host	53.07	0.07	1.88	0.04	9.51	0.28	11.59	22.93	0.92	0.00	100.29	1.98	0.00	0.08	0.02	0.28	0.01	0.64	0.92	0.07	0.00	0.70	N.A.†
	SO1317	36 / 1 .	HT-Amphibolite	Host	54.42	0.55	2.94	0.01	19.46	0.17	4.32	8.35	9.51	0.00	99.73	2.01	0.02	0.13	0.51	0.09	0.01	0.24	0.33	0.68	0.00	0.72	N.A.†
Plagioclase	SO1317	F-SO1317-C4	HT-Amphibolite	Host	67.24	0.00	20.55	0.00	0.04	0.00	0.01	1.30	10.95	0.01	100.11	2.95	0.00	1.06	0.00	0.00	0.00	0.00	0.06	0.93	0.00	N.A.†	N.A.†
	SO1317	F-SO1317-D3	HT-Amphibolite	Host	68.98	0.00	19.15	0.00	0.01	0.00	0.01	0.02	11.46	0.00	99.63	3.03	0.00	0.99	0.00	0.00	0.00	0.00	0.00	0.98	0.00	N.A.†	N.A.†
White Mica	SO1866	M-Hgl-So1866-A-43	MT-Micaschist	Host	47.32	0.65	32.86	0.03	1.70	0.02	1.75	0.05	1.21	9.44	95.02	3.15	0.03	2.58	FALSE	0.09	0.00	0.17	0.00	0.16	0.80	0.65	N.A.†
	SO1866	M-Q-So1866-B-12	MT-Micaschist	Host	46.95	0.07	40.82	0.13	0.64	0.00	0.05	0.33	6.71	0.30	96.01	2.97	0.00	3.04	FALSE	0.03	0.00	0.00	0.02	0.82	0.02	0.13	N.A.†
	SO1317	M-SO1317-C9	HT-Amphibolite	Host	47.11	0.00	35.73	0.01	1.34	0.07	0.18	0.02	0.08	11.15	95.69	3.12	0.00	2.79	FALSE	0.07	0.00	0.02	0.00	0.01	0.94	0.19	N.A.†
	SO1864	M-SO1864-B2	HT-Amphibolite	Host	51.44	0.03	27.67	0.00	2.93	0.02	2.64	0.02	0.50	10.40	95.66	3.42	0.00	2.17	FALSE	0.16	0.00	0.26	0.00	0.07	0.88	0.62	N.A.†
Chlorite	SO1863b	C-SO1863b-F14	HT-Amphibolite	Host	27.07	0.09	20.91	0.32	21.73	0.03	18.09	0.01	0.03	0.01	88.29	2.77	0.01	2.52	FALSE	1.86	0.00	2.76	0.00	0.01	0.00	0.60	N.A.†
	SO1866	M-Ch-So1866-E-21	MT-Micaschist	Host	26.14	0.06	21.47	0.01	23.91	0.00	16.42	0.01	0.01	0.01	88.04	2.71	0.00	2.63	FALSE	2.08	0.00	2.54	0.00	0.00	0.00	0.55	N.A.†
Lawsonite	SO1863b	M-P-So1863b-A-20	HT-Amphibolite	Host	39.92	0.00	31.26	0.00	0.02	0.00	0.00	16.93	0.00	0.01	88.15	2.10	0.00	1.94	0.00	0.00	0.00	0.00	0.96	0.00	0.00	N.A.†	N.A.†

N.A.† = Not applicable

Table S3. Whole rock major and trace elements

Rocktype	Leucosome						Amphibolite									
Sample	SO1803B	SO1803b	SO1805c	SO1808	SO1808a	SO1859	SO1801a	SO1801D	SO1804B	SO1807A	SO1817B	SO1823	SO1831	SO1857	SO1861b	SO1867
SiO_2 (wt%)	62.4	62.4	62.4	66.4	66.2	64.7	44.1	43.3	46.9	40.8	42.6	45.1	50.4	47.6	38.3	55.1
Al_2O_3	21.7	21.6	18.5	20.1	20.0	20.6	14.0	13.9	15.5	13.0	12.7	14.8	13.8	14.7	21.5	16.0
Fe_2O_3	0.29	0.17	0.36	0.37	0.36	0.48	11.6	13.2	10.6	15.0	11.7	13.7	9.63	18.41	8.72	5.08
MnO	0.01	0.01	0.01	0.00	0.01	0.01	0.17	0.20	0.15	0.23	0.21	0.16	0.16	0.30	0.33	0.10
MgO	0.22	0.15	0.11	0.15	0.14	0.38	11.70	10.26	9.31	9.80	3.37	5.34	7.43	5.24	2.64	3.48
CaO	1.89	3.36	4.38	1.06	1.35	1.70	12.98	11.21	10.30	11.63	13.93	9.20	9.24	7.36	20.49	5.01
Na_2O	9.46	9.14	10.26	10.72	10.89	10.25	1.95	2.53	2.57	2.08	4.43	3.12	2.89	1.26	0.78	4.29
K_2O	0.84	0.73	0.16	0.21	0.16	0.58	0.52	0.54	0.59	0.80	1.05	0.06	1.41	0.50	0.39	3.07
TiO_2	0.14	0.21	0.05	0.1	0.03	0.09	0.83	1.93	1.05	3.27	1.57	1.99	0.83	3.45	1.36	0.71
P_2O_5	0.01	0.01	0.02	0.01	0.01	0.01	0.07	0.36	0.07	0.29	0.18	0.21	0.07	0.46	0.04	0.13
LOI	1.29	1.81	3.35	0.90	0.79	1.06	2.02	1.94	2.65	1.87	7.85	5.69	3.50	0.39	4.65	6.41
Total	98.3	99.66	99.55	99.92	99.94	99.88	98.76	99.34	99.66	98.73	99.61	99.40	99.27	99.65	99.19	99.37
Li (ppm)	2.42	1.55	1.39	1.24	0.9	5.08	31.4	23.1	28.4	8.9	11.4	18	51.7	14.3	19.1	18.2
Rb	4.62	6.1	1.38	1.24	1.15	5.03	10.7	12.9	11.8	36.8	2.16	39.3	34.4	5.5	10.5	112
Cs	0.22	0.23	0.11	0.12	0.13	0.23	0.31	0.43	0.36	1.1	0.07	1.48	1.92	2.08	1.56	5.63
Be	1.01	0.99	0.33	0.27	0.18	0.99	0.92	0.33	1.52	0.82	0.48	0.44	2.54	1.52	2.9	1.46
Sr	177	250	25.0	17.4	5.5	91.6	548	91.5	104	287	62.4	38.4	60.2	689	176	151
Ba	208	140	34.7	85.3	18.2	449	64.2	44.9	80.6	158	10.7	144	33.6	68	37.6	443
Sc	3.57	2.99	2.49	2.79	3.82	4.71	39.6	52.8	49.9	53.9	59.9	55.4	43.4	24.7	27.8	18.8
V	5.13	4.21	13.5	5.31	7.9	12.5	294	324	386	334	430	298	490	169	178	125
Cr	85.2	28.9	23.9	156.4	25.6	48.3	657	403	391	176	236	641	75	162	232	151
Co	115	20.8	20.3	210	20.4	93.8	174	106	122	80.6	116	363	145	17.4	34.5	72.7
Ni	22.6	4.1	3.7	9	2.8	7.6	356	129	269	57.7	78.4	145	41	55.5	141	67.2
Cu	30.4	9.3	9.3	40.6	41.1	28.2	88.3	51.3	111	76.2	65.2	23.6	89.8	102	19.2	59.4
Zn	3.72	1.28	2.77	1.06	2.9	0.35	109	114	199	118	150	94.8	202	63.5	157	90.7
Ga	6.5	5.67	7.71	7.61	6.53	9.68	21.1	16.8	22.6	20.3	21.7	13.4	26.8	27.8	9	23
Y	0.3	1.50	2.07	0.18	0.52	0.73	30.3	31	42	52.9	49.6	21.2	52.2	44.1	24	36.7
Nb	0.29	3.9	0.4	0.68	0.21	0.37	23.2	1.4	50.4	2.4	3.1	4.3	49.6	25	35.6	15.3
Ta	0.59	0.43	0.06	0.85	0.06	0.4	1.97	0.29	3.87	0.31	0.46	2.31	3.68	2.39	3.36	1.36
Zr	0.5	5.51	3.66	2.21	10.5	1.17	17.2	7.09	28.3	45.8	42.1	6.68	19.3	9.65	7.8	61.4
Hf	0.04	0.14	0.14	0.11	0.27	0.06	1.18	0.68	1.76	1.82	1.83	0.59	0.98	0.27	0.29	2.41
Mo	19.0	4.92	3.16	31.2	4.49	9.81	14.9	6.40	11.3	4.78	5.96	8.29	12.6	0.46	0.24	5.86
Sn	0.24	0.35	0.26	0.3	0.31	0.29	1.18	0.6	2.39	1.42	1.39	0.61	4.52	4.32	3.21	4.28
Tl	0.08	0.07	0.04	0.03	0.03	0.04	0.08	0.08	0.07	0.27	0.02	0.29	0.21	0.06	0.09	0.6
Pb	5.66	6.42	0.8	2.85	1.14	4.03	9.59	2.38	5.35	2.54	2.68	1.78	10.9	55	7.25	7.94
U	0.02	0.25	0.03	0.02	0.04	0.02	0.79	0.11	1.68	0.32	0.41	0.08	1.72	4.06	0.5	2.58
Th	0.04	0.91	0.04	0.02	0.04	0.01	2.7	0.14	5.74	0.19	0.22	0.26	5.07	21.7	2.57	14.5
La	0.16	3.60	0.1	0.09	0.15	0.08	23.7	2.27	42.9	5.19	4.93	4.01	48.2	80.12	4.25	43.6
Ce	0.34	7.69	0.15	0.19	0.25	0.14	46.6	6.96	90.6	14.7	15.6	9.02	100	159	10.5	88.4
Pr	0.05	0.93	0.03	0.03	0.05	0.02	5.57	1.23	11.1	2.58	2.69	1.31	12.2	18.1	1.03	10.1
Nd	0.2	3.85	0.25	0.09	0.28	0.08	22.9	6.98	46.5	14.5	15	6.57	50.5	67.1	4.34	38.4
Sm	0.05	0.96	0.09	0.03	0.07	0.03	5.31	2.66	10.7	5.18	5.22	2.20	10.9	12.2	1.33	7.84
Eu	0.01	0.25	0.02	0.01	0.02	0.01	2.21	1.26	3.53	2.06	2.02	0.95	3.51	2.89	0.64	1.56
Gd	0.05	0.64	0.08	0.02	0.07	0.04	5.48	4.14	9.9	6.61	6.30	2.87	10.5	9.73	1.78	7.02
Tb	0.01	0.08	0.02	b.d.l	0.01	0.01	0.95	0.74	1.66	1.36	1.29	0.53	1.90	1.45	0.44	1.14
Dy	0.05	0.34	0.19	0.02	0.05	0.09	5.72	5.21	10.5	10.3	9.52	3.6	12.7	7.99	3.37	7.12
Ho	0.01	0.05	0.06	0.01	0.01	0.02	1.22	1.26	2.02	2.59	2.26	0.81	2.59	1.54	0.83	1.49
Er	0.02	0.11	0.17	0.02	0.05	0.06	3.27	3.58	4.83	6.77	6.32	2.23	6.81	4.34	2.55	4.06
Tm	0.00	0.01	0.03	b.d.l	0.01	0.01	0.47	0.51	0.58	0.88	0.85	0.35	0.91	0.68	0.43	0.56
Yb	0.02	0.08	0.14	0.02	0.07	0.05	2.80	3.19	3.54	5.30	4.81	2.06	5.29	4.55	2.82	3.66
Lu	0.00	0.01	0.02	b.d.l	0.01	0.01	0.43	0.5	0.5	0.8	0.7	0.3	0.85	0.7	0.42	0.55

b.d.l = Below detection limits

Table S4. Lu-Hf isotopic data and garnet age

Sample	sample wt. (mg)	Lu (µg/g)	Hf (µg/g)	176Lu/177Hf	$^{176}Hf/^{177}Hf$	± 2 SE (abs)	Age (Ma)†	2σ age uncert. (Ma)	MSWD
grt B	120	1.80	0.046	5.61	0.294644	0.000052			
grt C	106	1.77	0.042	6.03	0.295489	0.000019			
grt E	124	1.83	0.043	6.01	0.295449	0.000016			
grt F	156	1.80	0.043	5.96	0.295458	0.000023	**113.10**	**0.36**	**1.8**
grt H	155	1.82	0.042	6.15	0.295809	0.000016			
whole rock (tt*)	56.8	0.474	0.101	0.665	0.284193	0.000019			
matrix (tt)	41.8	0.277	0.051	0.770	0.284425	0.000038			
whole rock (bb)	20.0	0.550	5.09	0.015	0.282934	0.000003			
matrix (bb)	20.0	0.335	3.54	0.013	0.282942	0.000005			

* tt - tabletop digestion; bb - Parr bomb digestion

† 7-point isochron age consisting of 5 garnet fractions, tabletop whole rock and matrix

12. Location of the Zagros samples collected in 2018

Table of samples

Samples ID	Type	Host type	Lat	Long
SO 18.11	Vein	Blueschist	28°31'32.84"N	56°54'38.95"E
SO 18.12	Vein	Serpentinite	28°31'28.43"N	56°54'32.06"E
SO 18.13	Vein	Serpentinite	28°31'27.20"N	56°54'30.50"E
SO 18.14	Vein	Blueschist	28°31'17.75"N	56°54'19.58"E
SO 18.15	Vein	Blueschist	28°31'6.36"N	56°54'13.44"E
SO 18.16	Vein	Blueschist	28°31'16.25"N	56°54'11.62"E
SO 18.17 A	Host	Marble	28°31'13.90"N	56°54'13.00"E
SO 18.17 B	Vein	Blueschist	28°31'13.90"N	56°54'13.00"E
SO 18.17 C	Vein	Blueschist	28°31'13.90"N	56°54'13.00"E
SO 18.18	Vein	Blueschist	28°31'20.43"N	56°54'18.33"E
SO 18.20	Vein	Serpentinite	28°30'35.90"N	56°53'52.90"E
SO 18.21 A	Vein	Blueschist	28°30'35.90"N	56°53'52.90"E
SO 18.21 B	Vein	Blueschist	28°30'35.90"N	56°53'52.90"E
SO 18.22	Vein	Blueschist	28°30'35.90"N	56°53'52.90"E
SO 18.23	Vein	Blueschist	28°30'35.90"N	56°53'52.90"E
SO 18.24 A	Vein	Blueschist	28°30'35.90"N	56°53'52.90"E
SO 18.24 B	Vein	Blueschist	28°30'35.90"N	56°53'52.90"E
SO 18.25	Vein	Blueschist	28°30'40.46"N	56°53'55.40"E
SO 18.26	Vein	Blueschist	28°30'43.13"N	56°53'57.69"E
SO 18.27	Host	Serpentinite?	28°30'47.90"N	56°53'59.80"E
SO 18.28	Vein	Blueschist	28°30'49.24"N	56°53'59.68"E
SO 18.29C	Vein	Blueschist	28°30'49.24"N	56°53'59.68"E
SO 18.30	Vein	Blueschist	28°30'55.40"N	56°54'6.50"E
SO 18.31	Vein	Blueschist	28°30'55.95"N	56°54'8.42"E
SO 18.32	Vein	Blueschist	28°30'56.50"N	56°54'9.60"E
SO 18.33	Vein	Blueschist	28°30'56.37"N	56°54'11.51"E
SO 18.34	Vein	Blueschist	28°30'52.82"N	56°54'2.83"E
SO 18.35	Vein	Blueschist	28°30'52.82"N	56°54'2.83"E
SO 18.36	Host	Marble	28°30'51.00"N	56°53'59.20"E
SO 18.37	Vein	Serpentinite	28°30'33.35"N	56°53'50.50"E
SO 18.38	Vein	Blueschist	28°30'33.35"N	56°53'50.50"E
SO 18.39	Vein	Serpentinite	28°30'31.00"N	56°53'48.60"E
SO 18.40	Vein	Blueschist	28°30'25.66"N	56°53'43.27"E
SO 18.41	Vein	Serpentinite	28°30'21.50"N	56°53'39.90"E
SO 18.42	Vein	Blueschist	28°30'12.47"N	56°53'37.74"E
SO 18.43	Vein	Blueschist	28°29'57.00"N	56°53'32.20"E
SO 18.44	Vein	Serpentinite	28°29'57.00"N	56°53'32.20"E
SO 18.45	Vein	Serpentinite	28°29'57.00"N	56°53'32.20"E
SO 18.46	Host	Blueschist	28°29'57.00"N	56°53'32.20"E
SO 18.47	Host	Impure marble	28°29'50.40"N	56°53'1.40"E
SO 18.48	Vein	Impure marble	28°29'50.40"N	56°53'1.40"E
SO 18.49	Host	Impure marble	28°29'50.40"N	56°53'1.40"E
SO 18.50	Vein	Blueschist	28°29'50.40"N	56°53'1.40"E
SO 18.51	Host	Impure marble	28°29'50.40"N	56°53'1.40"E
SO 18.52	Vein	Metasediments	28°29'50.40"N	56°53'1.40"E
SO 18.53	Host	Impure marble	28°29'50.40"N	56°53'1.40"E
SO18.67	Host	Metasediments	28°30'11.80"N	56°53'37.90"E
SO18.68	Vein	Blueschist	28°30'11.80"N	56°53'37.90"E
SO18.69	Vein	Serpentinite	28°30'11.80"N	56°53'37.90"E
SO18.70	Host	Blueschist	28°30'11.80"N	56°53'37.90"E
SO18.71 A	Host	Blueschist	28°30'11.80"N	56°53'37.90"E
SO18.71 B	Host	Blueschist	28°30'11.80"N	56°53'37.90"E
SO18.72	Vein	Blueschist	28°30'11.80"N	56°53'37.90"E
SO18.73	Vein	Blueschist	28°30'11.80"N	56°53'37.90"E
SO18.74	Vein	Blueschist	28°30'11.80"N	56°53'37.90"E
SO18.75	Vein	Blueschist	28°30'11.80"N	56°53'37.90"E
SO18.76	Vein	Blueschist	28°30'11.80"N	56°53'37.90"E
SO18.77	Host	BS-breccia	28°30'11.80"N	56°53'37.90"E
SO18.78	Host	BS-breccia	28°30'11.80"N	56°53'37.90"E
SO18.79	Vein	Blueschist	28°30'11.80"N	56°53'37.90"E
SO18.80	Vein	Serpentinite	28°30'11.80"N	56°53'37.90"E
SO18.81	Vein	Blueschist	28°30'11.80"N	56°53'37.90"E
SO18.82	Vein	Serpentinite	28°30'11.80"N	56°53'37.90"E